Scholarly Products Resulting In Part From NIJ Funds

Published or Presented as of July 2019

Published Conference Proceedings Containing Dissertation Content

Cole ME, Stout SD, Agnew AM. March 2019. Image processing techniques for extracting complex three-dimensional cortical pore networks from high-resolution micro-computed tomography (micro-CT) images of the human femoral neck and rib. Program of the 88th Annual Meeting of the American Association of Physical Anthropologists. American Journal of Physical Anthropology 168(S68): 46.

Cole ME, Stout SD. February 2018. The use of high-resolution micro-computed tomography (micro-CT) for quantifying vascular pore networks across whole cross sections of human cortical bone. Proceedings of the American Academy of Forensic Sciences 24:61

Cole ME, Stout SD. April 2018. Automated extraction of two-dimensional cortical porosity descriptors from histological and micro-computed tomography serial sections. Program of the 87th Annual Meeting of the American Association of Physical Anthropologists. American Journal of Physical Anthropology 165(S66):51-52.

Unpublished Conference Papers Containing Dissertation Content

Cole ME, Stout SD. March 2018. Expedited extraction of 2D bone porosity descriptors from 3D micro-CT and serial section images. Paper presented at the 32nd Edward F. Hayes Graduate Research Forum, Columbus, OH.

Archived Dissertation

Cole ME. 2019. Optimizing Bone Loss Across the Lifespan: The Three-Dimensional Structure of Porosity in the Human Femoral Neck and Rib As a Metric of Bone Fragility [Doctoral Dissertation]. Submitted to OhioLINK Electronic Thesis and Dissertation Center.

Public or Guest Lectures Including Dissertation Content

Cole ME. May 15th, 2019. Optimizing Bone Loss Across the Lifespan: The Three-Dimensional Structure of Porosity in the Human Femoral Neck and Rib As a Metric of Bone Fragility [Public Doctoral Defense].

Cole ME. January 25th, 2019. Optimizing Bone Loss Across the Lifespan: The Three-Dimensional Structure of Porosity in the Human Femoral Neck and Rib As a Metric of Bone Fragility [Invited Research Presentation to the University of Akron Department of Biology]

Cole ME. November 26th, 2018. Bone Histology. [Guest Lecture for ANTHROP 5686: Forensic Field School at The Ohio State University]

Cole ME. February 7th, 2018. Skeletal Biology: The Basic Biology of Bone. [Guest Lecture for Columbus Torah Academy: High-School Anatomy and Physiology]

Book Chapters Containing Dissertation Content

Brickley M, Ives R, Mays S. In Press. The Bioarchaeology of Metabolic Bone Disease, 2nd ed. Elsevier: New York. [Contributed Micro-CT Images]

Websites

Ongoing project images and results are located at http://u.osu.edu/microCT
This website will be transferred to a personal domain following graduation.

THE OHIO STATE UNIVERSITY

Graduate School

250 University Hall
230 N. Oval Mall
Columbus, OH 43210

614-292-9490 Phone
614-292-3556 Fax

www.gradsch.osu.edu

June 6, 2019

RE: Mary Elizabeth Cole

To Whom It May Concern:

This is to certify that Mary Elizabeth Cole has completed all academic requirements for the Doctor of Philosophy degree from the Graduate Program in Anthropology at The Ohio State University.   The diploma for the degree Doctor of Philosophy will be awarded at the commencement ceremony held on August 4, 2019. Please contact Tim Watson at 614-247-7292 or watson.11@osu.edu with any questions.

Sincerely,

Tim Watson
Director-Graduation Services
Graduate School
247 University Hall | 230 N. Oval Mall | Columbus, OH 43210
614-292-6031 | 614-292-3656 (fax)
watson.11@osu.edu | www.gradsch.osu.edu

Mary Cole 200261473, cole.674@osu.edu

Report On Final Examination Status: COMPLETED
Created: May 13, 2019 08:54 AM
[Help](#)

Graduation Level
    Doctoral
Graduation Plan
    ANTHROP-PH - Anthropology
Graduation Degree
    PHD
Graduation Term
    Summer 2019 Term

Oral Exam
    05-15-2019 11:00 AM - 1:00 PM
Location
    4094   Smith Labortatory
Category M Approved
    No
Video Conference
    No

Committee Members

Advisor
    Samuel D. Stout (stout.126@osu.edu) - ANTHROP-PH, Category P, Faculty Type: EMER
Co-advisor
    (none)
Committee Members

- Douglas E Crews (crews.8@osu.edu) - ANTHROP-PH, Category P, Faculty Type: CURR
- Clark Spencer Larsen (larsen.53@osu.edu) - ANTHROP-PH, Category P, Faculty Type: CURR
- Amanda Marie Agnew (agnew.17@osu.edu) - ANTHROP-PH, Category P, Faculty Type: CURR

External Members

    (none)

Grad Faculty Representative

- Sarah-Grace Heller (heller.64@osu.edu) - FRNITA-PH, Category P, Faculty Type: CURR

Advisor Approval Info

Permitted to take second examination

Comments

No comments

Mary Cole 200261473, cole.674@osu.edu

Report On Final Document Status: COMPLETED
Created: May 13, 2019 08:54 AM
[Help](#)

Graduation Level
    Doctoral
Graduation Plan
    ANTHROP-PH - Anthropology
Graduation Degree
    PHD
Graduation Term
    Summer 2019 Term

Committee Members

Advisor
    Samuel D. Stout (stout.126@osu.edu) - ANTHROP-PH, Category P, Faculty Type: EMER
Co-advisor
    (none)
Committee Members

- Clark Spencer Larsen (larsen.53@osu.edu) - ANTHROP-PH, Category P, Faculty Type: CURR
- Amanda Marie Agnew (agnew.17@osu.edu) - ANTHROP-PH, Category P, Faculty Type: CURR
- Douglas E Crews (crews.8@osu.edu) - ANTHROP-PH, Category P, Faculty Type: CURR

External Members

    (none)

Grad Faculty Representative

- Sarah-Grace Heller (heller.64@osu.edu) - FRNITA-PH, Category P, Faculty Type: CURR

Comments

No comments

Optimizing Bone Loss Across the Lifespan: The Three-Dimensional Structure of Porosity in the Human Femoral Neck and Rib As a Metric of Bone Fragility

Dissertation

Presented in Partial Fulfillment of the Requirements for the Degree Doctor of Philosophy

in the Graduate School of The Ohio State University

By

Mary Elizabeth Cole

Graduate Program in Anthropology

The Ohio State University

2019

Dissertation Committee

Dr. Samuel D. Stout, Advisor

Dr. Clark S. Larsen

Dr. Douglas E. Crews

Dr. Amanda M. Agnew

Copyrighted by

Mary Elizabeth Cole

2019

Abstract

Rather than resisting microscopic damage, human bone tissue is adapted to disperse energy through temporary plastic deformation, which it later repairs. Under low strains, bone cells continually turn over aging bone as a stochastic maintenance operation. Under high strains, stochastic remodeling is repressed, but microscopically damaged regions are resorbed and replaced through targeted remodeling. The triggering of bone remodeling by two opposing strain environments has long confounded attempts to link bone microstructure consistently to mechanical stimuli. Additionally, bone cells become uncoupled from mechanical control as they age, and begin eroding the cortex through more extensive and unrepaired bone resorption. Intracortical porosity is often treated as a consequence of aging, when it is accumulated enough to impact bone strength and fracture risk. Yet because cortical pores are produced by both stochastic and targeted remodeling activity, they are constantly forming in all strain environments and over the lifespan. This raises the question of whether pores in high-strain environments are morphologically "optimized" or resistant to the high risk of microcrack initiation and propagation in those regions. Moreover, does porosity increase fracture risk with age not only because it is increasing porosity, but because it is reshaping it morphologically?

This study fundamentally asked whether the three-dimensional geometry of pore networks is **morphologically optimized** to resist local mechanical strain. The hypothesis

of structure-strain pore morphotypes in the human right-side femoral neck, a common site of osteoporotic fracture, and the human right-side midshaft fourth rib, a relatively unloaded control, for one male and one female per age decade from 20s to 80s. Extracted regions of each bone are visualized with high-resolution micro-CT imaging to reconstruct complete three-dimensional pore networks from 10 mm thick cross-sections of bone. These images are processed with custom routines that automatically extract and characterize porosity by bone type, pore type, and cross-sectional region.

Intraskeletally, the femoral neck and rib do vary significantly in pore morphometry, but not as expected. The more highly strained femoral neck is significantly more porous than the rib throughout the lifespan, apparently due to more permissive and uniform resorption at its endosteum, which the rib suppresses in its pleural cortex. However, regional comparions along the increasing strain gradient in the femoral neck can significantly confirm that high strain regions are distinct in pore morphometry. High-strain pores are significantly less densely populated, produce lower percentages of open and total porosity, are less convergent with other systems, and are more longitudinally oriented. Such isolated systems would be less vulnerable to the initiation and propagation of microdamage than the dense, broad, and widely convergent pore network permitted in lower strain regions. The pleural cortex of the rib, which has been hypothesized to experience relatively higher strain in some anatomical models, embodies a majority of these high-strain porosity markers. However, reduced mechanical control of the rib increases its sensitivity to physiological co-variates such as age and sex. While the pace of age-related effects is highly individualized, aging consistently and significantly

iv

reduces pore separation through convergence. This would increase vulnerability to

microcrack initiation and propagation in high-strain regions.

Dedication

For my parents, Michael and Dorothy Cole, who always encouraged me to go forward in

knowledge. When I was a child, you bought me a small microscope instead of a

telescope. Thank you - I don't think I would have liked astronomy quite so much as

histology.

Acknowledgments

This research would not have been possible without the enthusiasm, encouragement, and intellectual curiosity of Dr. Samuel Stout and Dr. Amanda Agnew. Dr. Stout first suggested that I extend Dr. Agnew's early work on cortical porosity in the rib for my master's thesis. My desire to capture porosity in its full three-dimensional configuration grew out of viewing those rib histological sections as an intriguing but inscruitable cross-section of an incredibly complex structure. Dr. Agnew has provided extensive and invaluable research support through provision of PMHS samples, DXA data, tissue storage and processing facilities, and enthusiasm for the project. Both Dr. Stout and Dr. Agnew have dedicated countless hours to assisting in applications for funding, the academic job search, and general early career mentoring. Their considerable bodies of work are driven by their passion for simply knowing more, and they inspire me to embody this attitude in my own career. I would also like to acknowledge and appreciate my two other dissertation committee members, Dr. Clark S. Larsen and Dr. Doug E. Crews, who also dedicated their time to serve on my master's thesis and candidacy exam committees. Dr. Larsen has always provided access to the Bioarchaeology Research Lab for sample processing and histological visualization. His work on cross-sectional geometry has inspired me to consider these metrics in my research, rather than viewing bone microstructure as isolated from bone shape. Dr. Crews

vii

provided considerable support in my many years as a Graduate Teaching Associate and Graduate Teaching Fellow in his role as faculty course coordinator. His work with aging in living humans reminds me to consider that human tissue is the sum of lived experiences, and is more complex than a set of metric measurements.

values for continuing analysis of this data. Dr. James Gosman provided powerful computing resources essential for this project.

Thank you to my parents and siblings for their support and encouragement of my long academic endevour. Thank you especially to Dr. Matthew Chamberlain for invaluable computing access, and for five years of listening, encouraging, and caring.

Vita

2008……………………………………………………......…..Sunrise Academy

2012………………………………………………..B.A. Cultural Anthropology

University of Maryland, Baltimore County

2012…………………………………..…………………..B.S. Biological Sciences

University of Maryland, Baltimore County

2014……………………………..……………………..M.A. Anthropology

University of Maryland, Baltimore County

2012 to 2013………………………………………………….University Fellow

Department of Anthropology, The Ohio State University

2013 to 2017…………………………………….......Graduate Teaching Associate

Department of Anthropology, The Ohio State University

2015 to 2016………………………………………...........Graduate Teaching Fellow

Department of Anthropology, The Ohio State University

2016 to 2017…………………………………………..Graduate Administrative Associate

Department of Anthropology, The Ohio State University

2016 to 2017……………..………………………………….......Graduate Consultant

Center for the Study and Teaching of Writing, The Ohio State University

x

2017 to Present…………………...National Institute of Justice Graduate Research Fellow

in Science, Technology, Engineering, and Mathematics

2018 to Present………………………………………….…………...Presidential Fellow

The Ohio State University Graduate School

Publications

2019. Stout SD, **Cole ME**, Agnew AM. Histomorphology: Deciphering The Metabolic

Record. In: *Identification of Pathological Conditions in Human Skeletal*

Remains, 3rd Edition. Eds. Buikstra, JE, Bolhofner KL. Amsterdam: Elsevier, Inc.

pp. 91 - 167

2018. Stout SD, **Cole ME**. Skeletal Histomorphometry. In: *The International*

Encyclopedia of Biological Anthropology. Ed. Trevathan W. Hoboken, NJ: John

Wiley and Sons, Inc. doi: 10.1002/9781118584538.ieba0238.

2016. Stout SD, Gocha TP, **Cole ME,** Agnew AM. Bone Histology. In: *Oxford*

Bibliographies in Anthropology. Eds. Jackson Jr. JL, Cavanaugh J, Coskunsu G,

Egorova Y, Hoffman KE. New York: Oxford University Press.

doi:10.1093/obo/9780199766567-0148.

Fields of Study

Major Field: Anthropology

Table of Contents

List of Tables

xxi

List of Figures

1. Introduction: Bone Loss, The Universal Human Pathology

1.1. Introduction: Statement of the Problem

1.1.1. Anthropological Context of the Problem

Anthropologists have extensively studied how physical activity changes the shape of the bones used for physical behaviors (Ruff et al., 2006). When mechanical demand changes from an optimal level, bone is formed or resorbed (removed) until it restores the balance of bone meeting mechanical needs. Bone forms on surfaces where demand is increased, and bone is resorbed on surfaces where demand is decreased (Lanyon, 1982). The cross-sectional distribution of bone mass in limb bones in particular has been broadly tracked across fossil and archaeological populations to detect trends in bone strength associated with the evolution of bipedalism, transition to agriculture, division of labor, roughness of terrain, and tool use (30+ studies reviewed in Ruff and Larsen, 2014).

The relationship between mechanical demand and bone shape becomes more complicated when anthropologists examine the internal structures of bone tissue. The cortical "wall" of bone accounts for more than 90% of bone strength in the femoral neck, compared to the trabecular bone that more loosely fills a bone's marrow cavity (Holzer et al., 2009). Although cortical bone appears solid to the naked eye, it is microscopically perforated with hundreds (in the rib) to thousands (in the femur) of canal systems, which carry the blood vessels that supply bone cells (Agnew and Stout, 2012; Cole and Stout,

1

2015). These vascular pores penetrate the cortex as part of bone remodeling, a cellular process that tunnels through old or damaged bone to replace it with new, freshly vascularized bone. Surrounding each new vascular pore is a circular region of new bone, termed a secondary osteon. Bone-forming osteoblast cells trapped during this process convert to mechanosensory osteocyte cells, which can trigger future bone formation or resorption in that region. Vascular pores, (primary) osteons, and osteocyte lacunae are also present in remnants of primary bone, which is increasingly remodeled with age. (Burr and Akkus, 2014).

However, cortical pores have a functional role beyond serving as passageways for the vascular structures that transport and nourish bone cells. Remodeling is triggered under three circumstances: 1) mechanical demand decreases, so pores form to remove "excess" bone, 2) mechanical demand increases, damaging the bone, so the microscopically cracked tissue is removed through remodeling, or 3) the cellular processes underlying remodeling become de-sensitized and dis-regulated with age, leading to increased porosity beyond what is mechanically stimulated (Agnew and Bolte, 2012, Burr and Akkus, 2014). Since these contradictory mechanical stimuli can all lead to porosity, anthropologists have sought to untangle the relationship between mechanical demand and pore number, shape, and location. Age-associated increases in porosity are also a key marker of bone fragility – decreased bone strength and increased fracture risk – both in archaeological (e.g. Cho and Stout, 2002) and modern populations (e.g. Yeni et al., 1997). About 70% of age-related bone loss in appendicular bones is cortical bone loss, which primarily occurs through the formation of pores (Power et al., 2004; Cooper

2

et al., 2004; Zebaze and Seeman, 2014). At least 76% of the reduction in femoral cortical strength with age results from porosity (McCalden et al., 2003). This is because vascular pores are stress concentrators where microscopic cracks can initiate and then propagate into a spontaneous fracture (Reilly and Currey, 1999, Ebacher et al., 2007). One in three women and one in five men over the age of 50 will experience at least one fracture due to severe bone loss (osteoporosis) (Melton et al., 1992, 1998, Kanis et al., 2000).

1.1.2. *Inconsistency in Mechanical Predictions of Microstructural Morphometry*

Bone functional adaptation is the theoretical link between mechanical demands and bone structure (Ruff et al., 2006). In this model, bone is resorbed on bone surfaces where the local mechanical load falls below an optimal level, and formed on bone surfaces when the local mechanical load exceeds this optimum (Lanyon, 1982). Mechanical load can be standardized as strain (ε), the fractional change in bone length during formation (Robling et al., 2014). Mechanosensory osteocyte cells sense these strain changes and appropriately recruit or inhibit bone-forming osteoblast cells and bone-resorbing osteoclast cells (Weinbaum et al., 1994; Komori, 2013; Plotkin and Bivi, 2014).

Osteoclasts resorb bone at very low strains ($<50 – 100$ $\mu\varepsilon$), leaving large pores called resorption bays. Bone routinely remodels to replace old bone at moderate strains (100 μ - $1,500$ $\mu\varepsilon$) (Frost, 2003). Osteoclasts tunnel through old bone, and osteoblasts mostly fill the tunnel with concentric rings of new bone, creating a secondary osteon with a central

3

pore (Burr and Akkus, 2014). Osteoblasts create new bone through modeling at high strains, primarily during growth (~2,000-3000 µε) (Frost 2003). Blood vessels surrounded by modeled bone also become pores. At very high strains (8000-10,000 µε) (Reilly and Currey, 2000), linear microcracks ("microdamage") form and also stimulate remodeling for targeted repair. An estimated 10 – 30% of remodeling activity is targeted at repairing microdamage, with remainder being untargeted for routine bone turnover (Burr and Martin, 1993, Li et al., 2001).

Knowledge of cellular activity at varying mechanical strains should theoretically predict how microstructure will appear in a given mechanical loading environment. However, a review of the literature (Table 1.1) indicates that intra-skeletal and intra-regional comparisons of microstructure nested within many studies contradict mechanical predictions nearly as often as they agree with them.

4

Table 1.1 Microstructural Confirmation and Contradiction of Mechanical Predictions

Micro-Structure	Predicted Association With Increasing Mechanical Strain	Intraskeletal or Regional Comparison(s) Confirm Prediction	Intraskeletal or Regional Comparison(s) Contradict Prediction
Vascular Porosity	Percent porosity decreases under high strain to avoid fragility fractures	Agnew and Stout, 2012 Cole and Stout, 2015 Skedros et al., 1994a	Cole and Stout, 2015 Hunter and Agnew, 2017
Remodeling Activity **(Osteon Population Density)**	Decreased remodeling due to inhibition by high strain	Hattner and Frost, 1963 Frost, 1969 Cho and Stout, 2011 Gocha and Agnew, 2016 Mason et al., 1995 Mulhern, 2000 Mulhern and Van Gerven, 1997 Portigliatti Barbos et al., 1983 Skedros et al., 1996	Robling and Stout, 2003 Mason et al., 1995 Zedda et al., 2015 Mayya et al., 2013
Osteon Size and Shape	Smaller and more circular, to improve chances of trapping or deflecting more frequent microcracks	Britz et al., 2009 Yeni et al., 1997 Skedros et al., 1994a,b Skedros et al., 1997 Skedros et al., 2001, Skedros et al., 2004	Britz et al., 2009 Crescimanno and Stout, 2012 Goliath et al., 2016 Pfeiffer, 1998 Pfeiffer et al., 2006 Mason et. al, 1995 Yeni et al., 1997 Skedros et al., 1994b
Osteocyte Lacunae	Denser populations needed to detect more frequently damaged tissue and trigger repair	Hunt and Skedros, 2001 Skedros et al., 2004 Skedros et al., 2005	Skedros et al., 2005 Hunter and Agnew, 2017

Microstructural features of bone tissue are thought to collaborate across multiple hierarchal levels to compensate for their individual deficiencies. A tissue structure that appears mechanically compromising in isolation may be adaptive in concert with other features. Human bone has a high toughness, meaning that it dissipates energy plastically through microscopic damage which it later repairs through targeted remodeling. "Toughening mechanisms" within bone microstructure encourage energy dispersal through this plastic deformation while limiting propagation of the permitted minor damage into catastrophic failure (Wang and Gupta, 2011). At the microscale, histological features such as secondary osteon cement lines and crack bridging mechanisms stop or redirect propagating microcracks (Nalla et al., 2005). Other microstructural features are created by the osteocyte cell network that detects strain changes and tissue damage (lacunae and canaliculi) or are artifacts of the remodeling processes that turn over old bone and repairs damaged bone (osteons, vascular porosity). Correlations between microstructural variables can become apparent when making regional comparisons of mechanical strain at varying hierarchal levels. These levels may include intraskeletal variation, anatomical region within a cross-section, and intracortical proximity to the low-strain marrow cavity, quantified as containment within the pericortical, mid-cortical, or endocortical bone "envelope". (e.g., Agnew and Stout, 2012, Dominguez and Agnew, 2016; Gocha and Agnew; 2016).

Vascular pores provide a prime example of this compensation, as they are mechanically compromising structures formed as a consequence of cellular processes that

mechanically strengthen bone tissue. Porosity is generally perceived as negatively affecting bone strength, because these voids concentrate stress and serve as initiation sites and propagation networks for microcracks (Ebacher et al., 2007). However, a vascular pore resulting from completed remodeling replaces old bone or repairs prior microdamage, making it a trade-off for old or damaged bone. Extending the vascular network into an aging or damaged region readies a transport pathway for bone cells to reach adjacent tissue that may soon be in need of remodeling (Martin, 2003). The mechanical compromise of the pore is further compensated by the new bone of surrounding osteon, with a cement line that can contain, halt, or divert propagating microcracks (Nalla et al., 2005). Viewing the full histological picture contextualizes the actual mechanical impact of individual histological features. This context may also help explain why individual histological features do not always follow theoretical models of the size, shape, and distribution that would be most mechanically advantageous in a given region.

1.1.3. *Structure-Strain Relationships Become Disregulated During Aging*

Aging breaks down the hierarchal and lateral connections between these tissue properties. Collagen and mineral degrade in quality, microdamage accumulates in brittle tissue beyond bone's capacity for repair, and lagging bone formation leaves the cortex perforated and thinned. (reviewed in Pearson and Lieberman, 2004). Age-associated bone loss can be simply understood as the rate of bone resorption outpacing the rate of bone formation. The cortical walls of bones become porous and thin, while the spongy,

7

trabecular bone buttressing the marrow cavity is increasingly thinned and separated. Bone fragility may be compromised not by the existence of individual histological features, but by their decreasing capacity to coordinate with their mechanical stimuli and with other hierarchal levels that compensate for their weaknesses. As histological structures become disregulated, it is important to incorporate multiple lines of histological evidence to understand what cellular processes are responsible.

Bone loss broadly follows trends associated with age and sex. However, the pace and extent of bone loss is highly individualized, varying with physical activity, nutrition, reproductive stress, and other mechanical and physiological co-variates that influence the activity of bone cells (Agarwal, 2008). Socio-cultural and economic access to dietary supplements for bone health may play a particularly important role in the varying health outcomes of different populations (Cho and Stout, 2003). The role of calcium and vitamin D in achieving and maintaining bone mineralization is well-studied. However, meta-analyses of clinical trials indicate that bone mineral density is also significantly affected by dietary access to vitamin C (proline and lysine hydroxylation in collagen synthesis), vitamins K1 and K2 (calcium ion binding by proteins osteocalcin, matrix Gla-protein, and protein S), vitamins B_6 and B_{12} (aldehyde cross-linking during collagen assembly; oxidative stress reduction), and silicon (modifies ratios of RANKL and osteoprotegerin). Positive associations have also been found between bone retention and magnesium (tissue sensitivity to PTH and vitamin D metabolites), potassium (pH buffering), zinc (IGF-1 production), boron (regulates vitamin D_3 use), long-chain polyunsaturated fatty acids (promote osteoblast activity), selenium (reduces oxidative

8

stress), strontium (reduces calcium loss), and copper (collagen cross-linking by lysyl oxidase; bone mescenchymal stem cell differentiation) (reviewed in Rondanelli et al., 2013; Weaver, 2013; Qu et al., 2018).

1.1.4. Limitations of Inferences from Two-Dimensional Imaging

Traditionally, anthropologists have examined porosity by cutting a ~100 micrometer thick cross-section of a bone. The cross-sections of pore systems on this slice of bone are then counted and measured (Agnew and Stout, 2012) However, pore networks are highly complex in three-dimensions, frequently splitting, merging, and branching at varied angles. In two-dimensional cross-section, pore shapes and numbers are distorted (Stout et al., 1999; Bell et al. 2001). Traditional histological slide preparation also involves grinding away several hundred micrometers of structural information between adjacent cross-sections, making it impossible to accurately reconstruct and follow pore structures as they change along a bone (Cho, 2012). Consequently, previous studies have not agreed on how pores respond in number, size, and orientation to different mechanical demands in different bone types or regions (reviewed in Stout *et al.* 1999 and Gocha and Agnew 2016). Additionally, manual selection and measurement of hundreds to thousands of individual pores is time-intensive, discouraging consistent and complete quantification of this microstructural morphometry (Agnew and Stout 2012, Cole and Stout, 2015).

1.1.5. Limitations of Inferences from Bone Mineral Density

Copyright Notice

9

Some text in this section is drawn from the author's contributor to the submitted version of the following book chapter: Stout SD, **Cole ME**, Agnew AM. Histomorphology: Deciphering The Metabolic Record. In: *Identification of Pathological Conditions in Human Skeletal Remains, 3rd Edition.* Eds. Buikstra, JE, Bolhofner KL. Amsterdam: Elsevier, Inc. pp. 9– 167, **which has been published in final form in:** https://www.elsevier.com/books/ortners-identification-of-pathological-conditions-in-human-skeletal-remains/buikstra/978-0-12-809738-0

Senescent changes are most noticeable when they are exacerbated in osteopenia and osteoporosis, which will be defined here. Age-associated changes in bone mass are typically clinically quantified in terms of bone mineral density (BMD) through dual-energy X-ray absorptiometry (DXA or DEXA) at sites such as the proximal femur, lumbar spine, and forearm (Kanis et al., 2008). The World Health Organization (WHO) published diagnostic criteria for low or decreased BMD in postmenopausal women through comparison to the BMD of young, healthy women. Osteopenia describes BMD between 1.0 and 2.5 standard deviations (T-score of -1.0 to -2.5) below this standard. Osteoporosis describes BMD more than 2.5 standard deviations (T-score less than or equal to -2.5) below this standard (WHO 2007). The International Osteoporosis Foundation (Kanis and Glüer, 2000) and the International Society of Clinical Denistometry (Binkley et al., 2006) recommend that the young adult standard for BMD be the femoral neck measurements of white women aged 20 to 29, as collected in the

NHANES III (Third National Health and Nutrition Examination Survey) reference database (Looker et al., 1997; Looker et al., 1998).

Osteoporosis increases the risk of "low force" or "fragility" fractures in response to mild or moderate trauma. In severe cases, normal physical activities can result in spontaneous fractures (Dolinak, 2008). Falls are responsible for approximately 80-90% of all fractures in older adults (Sjogren and Bjornstig 1989; Kannus et al., 1999). Despite its clinical prevalence, BMD is under-predictive of actual fracture risk. For example, a study of hip fracture patients in the United States found that 54% were not defined as osteoporotic at the hip (T-score > -2.5) and 6% were not even diagnostically osteopenic (T-score > -1.0) (Wainwright et al., 2005). BMD only explains a doubling of the fracture risk between ages 60 and 80, when fracture risk actually increases 13-fold (De Laet et al., 1997). This metric cannot quantify age-associated changes in the three-dimensional structure of cortical or trabecular bone tissue, which independently reduce bone strength and increase fracture risk (Chen et al., 2010). The National Bone Health Alliance (NBHA), composed of clinicians and clinical scientists from the National Osteoporosis Foundation and the American Society for Bone and Mineral Research, recommends an expanded toolkit for diagnosing osteoporosis in postmenopausal women and men over age 50. Even when BMD does not indicate osteoporosis (T-score > 2.5), a diagnosis may be made if an individual is at increased risk for future fractures. Risk factors include a prior low-trauma fracture at the hip for all patients, and a prior low-trauma fracture located in the vertebrae, proximal humerus, pelvis, or (in some cases) the distal forearm for patients diagnosed with osteopenia (Siris et al., 2014). The NBHA also recommend

11

the use of the FRAX® (Kanis, 2008), a tool sponsored by the World Health Organization that aggregates epidemiological data from large patient cohorts in North America, Europe, Australia, and Asia. FRAX® algorithms provide the 10-year probability of experiencing hip fracture or any major osteopororic fracture (hip, spine, forearm, or shoulder). This risk is calculated based on a combination of demographic data (age, sex, nationality, ethnicity), clinical risk factors (e.g. prior fracture, medical conditions, smoking and drinking), and femoral neck or total hip BMD.

The diagnostic challenges seen in modern populations are exacerbated in bioarchaeological contexts, which lack this patient data. Beauchesne and Agarwal (2017) note that, in contrast to surveys of modern Western populations, bioarchaeological studies often find bone loss at younger ages for both sexes, similarities between sexes in age-associated bone loss, and a low frequency of fragility fractures. One explanation for this unexpected scarcity of fragility fractures may be the survival of healthier individuals to older ages in archaeological populations (Bricker and Agarwal 2003), also described as the osteological paradox or the hidden heterogeneity of frailty (Wood et al., 1992). Beauchesne and Agarwal (2017) suggest that literature inconsistency may also be due to sampling at dissimilar skeletal sites, which differ in the rate or extent of bone loss because they vary in mechanical loading or tissue type (e.g. cortical or trabecular bone).

While fractures are visible in macroscopic examination, it is difficult to distinguish fragility-related fractures from traumatic fractures, or even post-mortem fractures (Agarwal, 2008). Like clinicians, bioarchaeologists have turned to methods than can detect a decline in the structural or material properties of bone tissue prior to fracture.

12

However, methodological differences in describing bone loss can contribute to literature inconsistency regarding patterns of bone loss in the past. A method's quantification of bone loss is specific to the skeletal site being analyzed and the bone type (cortical or trabecular) targeted. The measurement used as a proxy of bone quality also differs between methods, with the most common metrics including cortical geometry (radiogrammetry), bone mineral density (bone densiometry, typically DXA), trabecular structure (micro-CT or pQCT), and histological markers of remodeling (cortical bone histomorphometry) (Agarwal, 2008; Beauchesne and Agarwal, 2017). In radiogrammetry, radiographs are taken of a bone to measure its cortical thickness, which can be converted to its cortical index (percentage of total bone width) (Beauchesne and Agarwal, 2017). The second metacarpal is commonly chosen for radiogrammetry in archaeological studies (e.g. Pfieffer and King, 1983; Ekenman et al., 1995; Mays, 1996; Mays, 2001; Lazenby, 2002; Ives and Brickley, 2004; Glencross and Agarwal, 2011; Beauchesne and Agarwal, 2014; Beauchesne and Agarwal, 2017) due to its circular shape and nearly central medullary cavity, although it is not a common site of osteoporotic fracture (Ives and Brickley, 2004). Other bioarchaeological studies have applied radiogrammetry to the femur (Ericksen, 1976; Ekenman et al., 1995; Mays et al., 1998), radius (Ekenman et al., 1995; McEwan et al., 2005), humerus (Ericksen, 1976), and lumbar vertebrae (Pfieffer and King, 1983). In modern clinical contexts, densiometric analyses of bone mineral density (BMD) have replaced radiogrammetry (Beauchesne and Agarwal, 2017). Bone densiometry has also seen application in archaeological contexts at common clinical sites such as the proximal femur (Mays et al., 1996; Ekenman et al.,

13

1995; Lees et al., 2003; Mays et al., 2006), femoral neck (Hammerl et al., 1990; Poulsen et al., 2001; Turner Walker et al., 2001; Lees et al., 2003; McEwan et al., 2004; Holck, 2007), midshaft and distal radius (Perzigian, 1973; McEwan et al., 2004; McEwan et al., 2005), lumbar vertebrae (Agarwal and Grynpas, 2009) as well as the midshaft humerus and tibia (Ekenman et al. 1995). The emergence of three-dimensional imaging technology, such as micro-CT and peripheral quantitative computed tomography (pQCT), has popularized the analysis of changes in trabecular bone architecture in archaeological populations. Highly trabecular regions chosen for analysis include the fourth lumbar vertebra (Kneissel et al. 1997; Agarwal et al. 2004; Agarwal 2012; Beauchesne and Agarwal 2017), the proximal femur (Ryan and Shaw, 2014), and the epiphyses of appendicular bones (Chirchir et al., 2015). Cortical bone histomorphometry, which is the focus of this project, has largely been applied to quantify bone loss in archaeological studies of the femur (Martin and Armelagos, 1979; Richman et al., 1979; Ericksen, 1980; Thompson et al., 1981; Thompson and Gunness-Hey, 1981; Martin and Armelagos, 1985; Burr et al., 1990), rib, (Stout and Teitelbaum, 1976; Stout, 1983; Stout and Lueck, 1995; Mulhern, 2000; Beauchesne and Agarwal, 2017), or femur and rib comparatively (Pfeiffer, 1998; Cho and Stout, 2003; Robling and Stout, 2003; Cho and Stout, 2011; Pfeiffer et al., 2006).

1.2. Proposed Structure-Strain Model for Porosity

This study fundamentally tests the hypothesis that porosity is morphologically optimized for its localized mechanical loading environment. In other words, is pore

14

geometry less prone to microdamage in high-strain regions, where microscopic damage is more likely to occur?

While porosity has not been three-dimensionally visualized on a broad regional scale in human bone, some hypotheses can be drawn from the morphometry of secondary osteons surrounding each pore. Strain changes and microscopic damage are both sensed by osteocyte cells embedded in the bone matrix, which then trigger bone formation or resorption. Bone regions under relatively higher strain (e.g. compression) have been hypothesized to accrue more microscopic damage, triggering more frequent remodeling for repairs (Lanyon and Baggot, 1976). These targeted repairs should theoretically produce more numerous but also smaller and less connected pore systems. Two-dimensional studies have found that secondary osteons tend to be smaller (Skedros et al., 1994, 1997, 2004) and more numerous under compression (Lanyon et al., 1979; Mason et al., 1995; Riggs et al., 1993a,b; Skedros et al., 1997, 2004). However, other studies have found denser secondary osteon populations in low-strain (e.g. tensed bone), which they attribute to more frequent remodeling for bone renewal (e.g. Portigliatti et al., 1983; Mason et al., 1995; Skedros et al., 1996a; Gocha and Agnew, 2016). Pores have complex three-dimensional patterns of branching that distort two-dimensional inferences of pore number and size (Stout et al., 1999; Maggiano et al., 2016).

Small, isolated pores would be more advantageous under high-strain compression, as they would be a smaller target for the microdamage that initiates and propagates within pore systems in this loading condition. Bone regions under relatively lower strain (e.g. tension) do not show a significant association between porosity and fracture risk (Ebacher

15

et al., 2007). Total porosity is greater in tensed regions of mule deer calcanei and human ribs (Skedros et al., 2004; Agnew and Stout, 2012). In human ribs, this porosity accumulates through expansion and coalescence of existing pore systems in particularly low-strain regions adjacent to the marrow cavity (Cole, 2014). Coalescence, branching, and interconnection increases the obliqueness of the pore canal to the long axis of the bone (Hennig et al., 2015).

I hypothesize an overarching structure-strain model in which:

1) High-strain regions accumulate smaller, more isolated, longitudinally oriented pores due to more frequent remodeling

2) Low-strain regions accumulate larger, more highly connected, obliquely oriented pores due to more frequent disuse-related resorption.

Two-dimensional studies of femoral neck porosity suggest that fracture risk is related to deviation from a theoretical ideal. Osteoblasts' capacity for bone formation slows with age, decreasing their ability to keep pace filling resorption bays (Agnew and Bolte, 2012). Bone resorption also increases in response to the lowered strains of weakening muscles and declining physical activity (Thomas et al., 2005). After age 60, femoral neck porosity increases ~30% per decade. Pore diameter increases while pore number and spacing decrease, suggesting that pores are coalescing (Chen and Kubo, 2014; Milovanovic et al., 2014). These changes are exacerbated in aging women (Chen and Kubo, 2014) due to declining estrogen levels at menopause that increase bone resorption (Robling et al., 2014). In individuals without fractures, two-dimensional porosity increases along the superoinferior axis, which is loaded during gait. In

16

individuals who eventually fracture the femoral neck, porosity becomes concentrated anteriorly through pore coalescence into "giant canals" potentially due to the weakening psoas major and iliacus muscles. This weakens the cortex along the inferoanterior to superoposterior axis, the same direction that deformation occurs during a sideways fall. (Bell 1999a,b). Analysis of other structural contributors is limited by the absence of three-dimensional data (Bousson et al., 2001)

1.3. Research Questions and Hypotheses

The femoral neck and rib both display regional variation in strain within a given tranverse cross-section of their long axis. The femoral neck is bent superiorly in tension and inferiorly in compression. However, compression by the hip abductor muscles eliminates tension superiorly, creating a superior-to-inferior gradient of increasing compression. (Lovejoy, 1988; Ohman, 1997; Ruff, 2013). If the proposed model is correct, then pores should gradually shift from the hypothesized low-strain to high-strain pore morphologies along this superior-to-inferior gradient. The human rib is comparatively isolated from body weight and dynamic loading (Bellemare et al., 2003). As the ribcage expands during inspiration, the cutaneous region (skin side) and pleural region (lung side) experience opposing loading modes. In one model, the cutaneous region is tensed under low strain, and the pleural region (lung side) is compressed under high strain (Agnew and Stout, 2012). Two-dimensional studies of the midshaft rib have found that the cutaneous region is significantly more porous and trabecularized than the pleural region. This could suggest that the cutaneous region is loaded under lower strain, which is more permissive to bone resorption (Agnew and Stout, 2012; Agnew et al.,

17

2013; Cole and Stout, 2015; Dominguez and Agnew 2016). However, it is unknown if this difference is related to regional strain patterning, thus it may not reflect the true loading environment of the rib or its effects on three-dimensional pore structure (Dominguez and Agnew, 2016).

This model will be tested with these research questions [RQ] and hypotheses [H]:

[**RQ1**]: Does three-dimensional pore volume, connectivity, and orientation significantly vary between high strain and low strain regions?

[**H1A**] The femoral neck will display a high-strain morphotype (significantly smaller, less connected, more longitudinal pores) compared to the matched rib of an individual.

[**H2A**] Within a given cross-section, three-dimensional morphometry will significantly vary between anatomical divisions that describe strain distribution: superior-to-inferior femoral neck octants, and pleural/cutaneous rib halves.

[**RQ2**:] Does dynamic loading result in significantly more variation between individuals in patterns of strain, and associated pore structure?

[**H2**:] In the femoral neck, compared to the rib, body weight and physical activity will produce [**H2A**] significantly larger inter-individual variability in three-dimensional pore morphometry in a given anatomical region and [**H2B**] larger effect sizes for co-variates related to physical size.

[**RQ3**:] Does bone maintain a structure-strain relationship with age?

18

[H3A]: With age, pores in high-strain regions will increasingly resemble low-strain morphology. **[H3B]:** This change will be more significant in women, compared to men. **[H3C]:** The rib will show these changes earlier because it remodels more frequently than the femoral neck.

1.4. Significance of the Structure-Strain Context of Bone Microstructure

1.4.1. Anthropology: Bone Morphometry As a Predictor of Physical Behavior

Biological anthropologists are broadly interested in how variation in the human body reflects variation in environmental and cultural factors, both now and in the past. Age-associated bone loss occurs worldwide and can distinguish health outcomes for subsets of modern and archaeological populations based on factors such as sex, nutrition, and socioeconomic status (Agarwal, 2008; Beauchesne and Agarwal, 2014). Bone quality and strength are not derived from individual structural or material properties, but are the consequence of the interaction, negotiation, and compensation between these properties. Humans have an unusually high prevalence of remodeled bone, even compared to most primates, due to our skeletal adaptation for toughness. Humans are heavy and dynamically active enough to accumulate microdamage, but also live long enough that the microdamage needs to be repaired (Burr, 2011; Currey, 2003). Changes in these tissue components have been associated with aging in many studies, but rarely as part of a comprehensive reconstruction of bone loss from the microscale to the macroscale. Complicating these associations is our incomplete knowledge of the "normal" appearance of tissue structures in young, healthy individuals, given the significant range of variation

19

of many histological features both within the skeleton and between individuals. Historical reliance on two-dimensional imaging has limited our understanding of the complex, three-dimensional shape of bone tissue and its internal structures as they change over the lifespan.

1.4.2. Forensic: Difficulty of Distinguishing Traumatic and Spontaneous Fractures in Elderly Populations

In older adults (65 years and older), accidental and non-accidental causes of bone fracture are particularly difficult to distinguish (Dolinak, 2008). Severe bone loss (osteoporosis) in older adults increases their risk of accidental "low force" or "fragility" fractures due to mild or moderate trauma, such as a fall (Dolinak, 2008). Approximately 80-90% of all fractures in older adults occur during falls (Sjogren and Bjornstig 1989; Kannus et al., 1999). In severely osteoporotic individuals, bone can also spontaneously fracture during normal physical activities (Dolinak, 2008). At the same time, elderly adults are at increased risk for non-accidental fractures incurred through physical abuse by caretakers. An estimated 0.2 to 1.8% of older adults experience physical abuse from caretakers (Laumann et al., 2008; Acierno et al., 2010; Amstadter et al., 2011; Burnes et al., 2015) with higher percentages in adults with a disability (12%) (Powers et al., 2008) or dementia (19.7%) (Cooney et al., 2006). The National Research Council (2003) notes that markers of physical abuse have been studied in children, but similar guidelines for older adults are largely absent. They call for research into the characteristics of common injuries, such as hip fractures, so that accidental and inflicted causes may be distinguished. One research objective of the proposed research is to investigate normal

changes over the lifespan in a marker of bone fragility and fracture risk, cortical porosity.

This baseline would aid in distinguishing accidental fractures, which are predisposed by

abnormal pore structure, from non-accidental fractures of normal bone.

1.4.3. Clinical: Increasing Incidence of Osteoporotic Fracture with Aging Populations

With aging populations worldwide, the already high incidence of osteoporosis and

fragility fractures will require advances in detection and treatment. One in three women

and one in five men over the age of 50 will experience at least one fracture due to

osteoporosis (Melton et al., 1992; Melton et al., 1998; Kanis et al., 2000). An estimated

1.25 million osteoporotic femoral neck fractures occur worldwide every year, and

incidence is projected to increase by 240% in women and 310% in men by 2025

(Gullberg et al., 1997). Hip fractures have been reported to increase mortality 2.4-fold

(Browner et al., 1991), 3-fold, (Panula et al., 2011), or even 6-fold (Cauley et al., 2000).

Mortality risk from rib fracture is 2-fold to 5-fold greater in older adults (>64 or 65)

(Melton et al., 1998; Bergeron et al., 2003).

This project's comprehensive mapping of microstructural contributors of bone

strength has wide-reaching biomedical implications for understanding why certain

regions of bone (e.g., the superior-anterior femoral neck) are prone to fracture. It will also

broaden our fundamental understanding of the cellular activity (remodeling, osteocyte

presence) underlying microstructural deterioration, an essential foundational step for

targeting more effective osteoporosis treatments to the responsible cellular processes.

21

2. Cellular Basis of Bone Formation and Resorption

2.1. Introduction: Cellular Roles in Bone Modeling and Remodeling

Bones change in mass and shape drastically during subadult growth, but the amount and distribution of bone mass continues to change throughout the lifetime in response to mechanical and physiological demands. Modeling refers to the uncoupled resorption or formation of new bone on a bone surface. Remodeling is a coupled process, in which pre-existing bone is resorbed and then replaced by new bone formation (Frost, 2003). There are two forms of remodeling: targeted and stochastic. In targeted remodeling, bone responds to a specific, localized mechanical need for bone resorption or repair. In stochastic remodeling, physiological needs of the body regulate bone formation and resorption (Martin, 2002, Eriksen, 2010).

Modeling and remodeling are carried out by **osteoblasts**, the bone-forming cells, and **osteoclasts**, the bone-resorbing cells. Bone cell recruitment and activity is regulated by the local presence of paracrine factors (produced by nearby cells) and autocrine factors (produced by the cell itself) (Plotkin and Bivi, 2014). Production of local factors is influenced by mechanical demand and physiological demand on the body. Local mechanical demand changes when the mechanical loading environment of the bone is altered or when the bone accumulates microscopic damage (microdamage) that compromises its previous strength. **Osteocytes**, which are terminally differentiated

22

osteoblasts embedded in pre-existing bone during formation, sense these alterations (reviewed in Seeman, 2006). They produce local factors that activate osteoblast bone formation and/or osteoclast bone resorption, reshaping and repairing bone to withstand the new mechanical loading environment. Levels of local factors are also regulated by endocrine factors (produced by distant cells), particularly systemic hormone levels. These hormonal signals are not the direct consequence of mechanical demand, but a physiological response to other processes in the body (Martin, 2002, Eriksen, 2010).

Modeling occurs on the surface of bone and does not require synchrony between osteoclast and osteoblast activity. However, remodeling requires osteocytes to coordinate action between osteoclasts and osteoblasts through the formation of a BMU (basic multicellular unit). The transition from osteoclast bone resorption to osteoblast bone formation is known as "coupling." It is propagated by the release of local factors from resorbed bone, as well as a complex array of signals within and between osteoclasts and osteoblasts (Martin and Sims, 2014). In cortical bone, the BMU tunnels into the cortex, with osteoclasts resorbing bone in a "cutting cone," and osteoblasts following behind in a "closing cone" to form new bone. Osteoblasts leave a central Haversian canal for the central blood vessel (Eriksen, 2010). This structure is called a secondary osteon, in contrast to the primary osteons that form when modeled bone surrounds a blood vessel on the surface of the bone (Burr and Akkus, 2014).

Figure 2.1 Pore Shape Varies with Cross-Sectional Plane
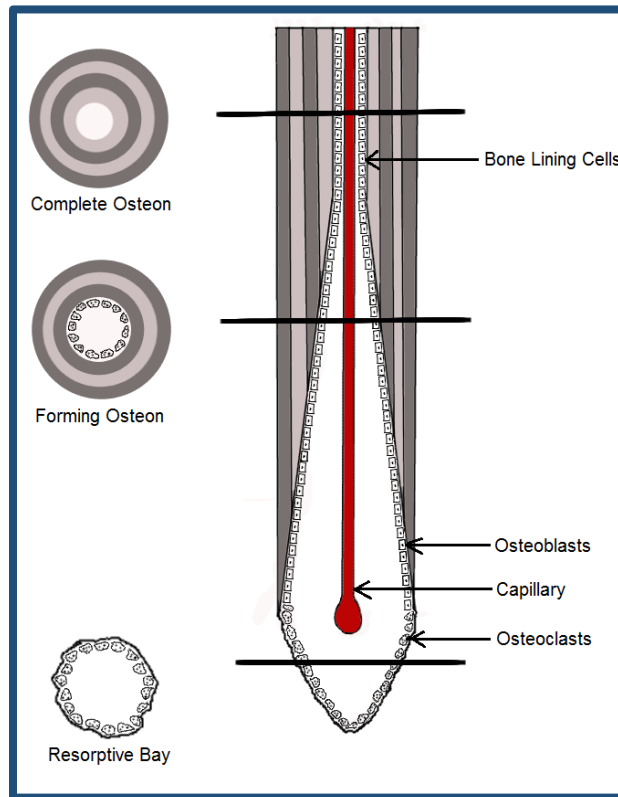
From Stout and Cole (2018)

Secondary osteons are distinguished by a cement line, the highly mineralized

border that marks remodeling reversal, where osteoclast resorption ends and osteoblast

resorption begins (Skedros et al., 2005). In trabecular bone, the BMU sits on the exposed

surface of the trabecula. Osteoblasts resorb bone, forming a trench, which is then filled

with bone by osteoblasts (Sims and Martin, 2014). This structure is called a hemiosteon.

In very thick trabeculae, complete osteons can form by tunneling through the trabecula

(Burr and Akkus, 2014). The BMU is covered by a canopy cells of mesenchymal origin,

forming the bone remodeling compartment (BRC) (Sims and Martin, 2014). In trabecular

bone, the canopy forms through retraction of bone lining cells, and it is penetrated by

24

marrow capillaries (Hauge et al., 2001). In cortical bone, the canopy forms at the end of

the closing cone, and is penetrated by the central blood vessel (Eriksen, 2010).

2.2. Development of a Paradigm for Mechanical and Physiological Interaction

Between about 1900 and 1960, it was not understood that osteoclasts and

osteoblasts were coupled in their recruitment and activity by osteocytes in response to

mechanical signals. Bone cells were thought to respond to genetic and hormonal signals

alone (Frost, 2003). However, a purely physiological perspective faces what Rauch and

Schoenau (2001) call the "blind steering" problem. Hormones and other physiological

influences increase and decrease bone mass in the same way that the wheels move a car

backwards and forwards, but cannot steer its direction. Instead, bone is adapted to be as

strong as possible, which requires regulation of both the amount of bone mass and its

distribution in space (Rauch and Shoenau, 2001). Bone's strength at a given point, in

resistance to a given plane of mechanical loading, is influenced by its length, as well as

its radial distribution. As discussed at length in Chapter 3, bone's tissue mechanics give it

a long period of plastic deformation, during which it incurs microdamage to dissipate

energy rather than fracturing. For healthy individuals, this microscopic damage can be

detected and repaired by osteocytes to restore bone strength. Martin (2003a) estimates

that bones would have to be heavier by 20% or more to sustain mechanical loading if

they could not dissipate energy through microdamage. Physiological influences cannot

tell how much bone mass already exists. They cannot detect how much more or less bone

is needed, or where it should be positioned, to make bone strong enough to withstand

typical mechanical demands on the skeleton. They do not detect when bone has

25

mechanically failed at a microscopic level and is in need of repair (Rauch and Schoenau 2001). "Steering" the amount and distribution of bone mass requires a destination (Rauch and Schoenau 2001).

2.3. Mechanical Strain as a Map for Bone Modeling and Remodeling

Emerging out of the "new bone biology" or the "Utah Paradigm," the mechanostat is a model for how bone adapts to withstand its typical mechanical loading environment. This model came together initially through at the University of Utah's Hard Tissue Workshops (Jee, 2001). The underlying concept is that bone models and remodels to keep its typical strains within a preset range, or "setpoint" (Frost, 1987). Strain is defined as the deformation of the bone during mechanical loading, and is measured as its fractional change in length. This deformation is described in terms of microstrain (µE), with one microstrain equivalent to a fractional deformation of 10^{-6} in length. The setpoint refers to the range of deformation a bone can withstand without triggering modeling or remodeling. Changes in typical mechanical loading on a bone can move it above or below its setpoint range. Typical mechanical loading on a bone changes in magnitude and direction as the body grows in size and develops its adult structure. Throughout the lifespan, changes in behavior that alter physical activity patterns can also change mechanical loading. Increased mechanical loading deforms bone above the setpoint, while decreased mechanical loading deforms bone less than its setpoint. Bone can return to its original amount of deformation by altering the amount and/or distribution of bone mass. Bone therefore models or remodels until the new configuration of bone mass deforms at its setpoint when experiencing the new mechanical loading environment.

26

Bone can also move away from the setpoint if damage to its tissue makes it weaker and more deformable in response to the same load. Triggers for modeling and remodeling may follow microscopic damage from repetitive stress or the bone loss that occurs with physiological changes during senescence.

The strain triggers for bone modeling and remodeling are what Frost (2003a) terms "minimum effective strain" thresholds (MES). Microstrains below the disuse-mode remodeling threshold (MESr) of 50 – 100 $\mu\epsilon$ (or ~400 $\mu\epsilon$, see Frost, 2000) result in bone resorption by resorptive drift or by a basic multicellular unit (BMU) (Frost, 2003a). Frost (2003b) calls this range "diuse-mode" remodeling, where bone cells resorb more bone than they form. (Frost, 2003b). Strains above MESr but below the modeling threshold (MESm) of 1,000 – 1,500 μE trigger maintenance remodeling by a BMU, replacing bone that is old or contains microdamage (Frost, 2003a). Frost (2003b) calls this range "conservation mode" remodeling, where bone cells form as much bone as they resorb, provided they complete the formation process. Strains towards ~2,000 $\mu\epsilon$ decrease remodeling (Frost, 1990). Strains between MESm and the microdamage threshold (MESp) of ~3000 μE stimulate bone modeling to increase bone mass and withstand the increased load. Above MESp, strains cause more extensive microdamage than can be repaired by the pace of bone remodeling. Microdamage accumulates in bones experiencing these strains (Frost, 2003). Strains that exceed the ultimate strength (Fx) of the bone, which is about ~25,000 $\mu\epsilon$ in early adulthood, result in bone failure (Frost, 1990, Frost, 2003).

27

2.4. Physiological Processes Move the Mechanical Threshold Setpoints

In recent decades, physiological and mechanical perspectives have merged as researchers have increasingly mapped the biochemical signaling relationships between osteoblasts, osteoclasts, osteocytes. Elucidation of interaction or "cross-talk" between these pathways has produced theoretical mechanisms for mechanotransduction, meaning how osteocytes sense mechanical strain and trigger bone formation and resorption. A biochemical perspective reveals that many endocrine factors act on bone by enhancing or repressing components of the signaling pathways for bone formation, resorption, and mechanotransduction. Current thinking in skeletal biology is that bone is shaped by mechanical demand, but that its response to this demand can be augmented by physiological needs of the body (Rauch and Shoenau, 2001). Essentially, endocrine factors move or expand the range of the strain setpoint that is "acceptable" to the mechanostat (Rauch and Shoenau, 2001, Robling et al., 2014). Physiological activation of bone formation, as with sex steroids and intermittent parathyroid hormone expression, create bone even when it is not mechanically necessary. This raises the preset strain thresholds for resorption, making the mechanostat "accept" an unusually low amount of strain. Physiological activation of bone resorption, as with estrogen loss, prolonged parathyroid hormone expression, or inflammation, resorb bone below its mechanically optimal amount. This lowers the preset strain thresholds for formation, making the mechanostat "accept" an unusually high amount of strain. Outlining biochemical mechanisms for osteoblast and osteoclast recruitment, osteoblast mechanotransduction,

28

and coupling of these systems allows subsequent illumination of the points at which physiological factors can exert influence.

2.5. Local Factors Influencing Osteoblast Differentiation and Maturation

Osteoblasts deposit the organic matrix of bone, both during initial modeling and during remodeling as replacement for resorbed bone. Osteoblasts are polarized in their distribution of organelles, meaning that their protein-producing rough endoplasmic reticulum is close to the bone surface (Bellido et al., 2014). Their numerous cytoplasmic extensions penetrate the osteoid, or unmineralized bone, as it is newly deposited (Long, 2012, Franz-Odendaal et al., 2006). To create this osteoid, osteoblasts secrete large amounts of type I collagen. Other chief products include osteocalcin, which is a non-collagenous protein that controls deposition and binding of calcium to the osteoid, and alkaline phosphatase, which blocks pyrophosphates from inhibiting this mineralization (Long, 2012, Burr and Akkus, 2014). Accumulation of hydroxyapatite, or calcium phosphate, to mineralize the matrix is mediated by these osteoblast-produced factors (Long, 2012).

Osteoblasts arise from mesenchymal stem cells (MSCs), which originate in the bone marrow. In addition to osteoblasts, mesenchymal stem cells also normally give rise to marrow stromal cells (form a scaffold for hematopoietic cells), chondrocytes (cartilage forming cells), myocytes (muscle cells), tendinocytes (tendon cells), and adipocytes (fat cells) (Gurkan and Akkus, 2008, Bae et al 2011). Mesenchymal stem cells are additionally capable of giving rise to normally endodermal hepatocyte-like cells (liver cells) and normally ectodermal neuron-like cells (Bae et al 2011, Wu and Tao 2012).

29

Since mesenchymal stem cells are multipotent, extracellular and intracellular processes are required to start and then sustain the process of osteoblast differentiation, maturation, and activity. During osteoblastogenesis, cells progress from mesenchymal progenitors to osteoblasts. Mesenchymal stem cells commit to become osteo-chondroprogenitors, marked by expression of RUNX2 (runt-related transcription factor 2) and type I collagen. Expression of OSX (Sp7/osterix) marks the transition to osteoprogenitors. Mature osteoblasts express osteocalcin and type I collagen. (Rodda and McMahon 2006, Long 2012). The two primary promoters of osteoblast differentiation are Wnt signaling and BMP/TGF-β signaling (Bellido et al., 2014). Both of these pathways are intertwined with expression of RUNX2/OSX and then osteocalcin, along with other osteoblast differentiation markers. Many factors within and beyond these pathways are acted upon by mechanical loading, hormonal influences, or both.

A survey of these pathways is necessary to understand how these mechanical and hormonal influences regulate bone formation. The following pathways describe locally produced cytokines/growth factors, and their intercellular protein and transcription factor products. Locally produced means that the factors are produced near the site where osteoblast differentiation occurs. In contrast, hormones are produced by glands and circulate widely in the body. (Plotkin and Belvi 2014). Both mechanical demands and hormones act on these pathways through modifying concentrations of ligands triggering their activation and/or interacting with signaling components within the pathways. Therefore a brief description of signaling components accompanies each local factor description. Signaling pathways also do not act in isolation, but can positively or

30

negatively regulate other pathways through "cross-talk". This interaction influences the progression from mesenchymal stem cell to mature osteoblast.

RUNX2 (runt-related transcription factor 2) and **OSX** (Sp7/osterix) are transcription factors expressed by osteoblasts during osteoblast differentiation and mature activity (Long and Ornitz 2013). RUNX2 is also called Cbfa1/AML3 (core binding factor alpha/acute myelogenous leukemia) (Lian et al., 2006). RUNX2 and OSX are necessary for both endochondral ossification and intramembranous ossification (Long 2013) No osteoblasts are found in mice with homozygous deletion of *Runx2* or deletion of OSX (Komori et al. 1997, Otto et al. 1997). Mice without Runx2 do not form mineralized skeletons and die shortly in the perinatal period (Lian et al., 2006). Haploinsufficiency of Runx2 in mice and RUNX2 humans results in underdeveloped collarbones and delayed closure of skull fontanelles, as seen in cleido-cranial dysplasia (Choi et al., 2001). Osteo-chondroprogenitors first express RUNX2, and then express both RUNX2 and OSX as they mature into osteoprogenitors. This is known because RUNX2 levels remain normal when OSX is deleted in mouse embryos, but homozygous deletion of the *Runx2* gene in mice prevents *Osx* gene expression (Nakashima *et al.,* 2002). Key pathways in osteoblastogenesis regulate this transition, including canonical and non-canonical Wnt signaling and BMP (bone morphogenic protein) action.

RUNX2 acts upstream of canonical (β-catenin dependent) **Wnt signaling** to promote OSX expression for osteoblast differentiation and early maturation (Hill et al. 2005). Wnts are a family of secreted proteins having 19 members in mammals, and specifically in humans (Wodarz and Nusse 1998, Bellido et al., 2014). In canonical Wnt

31

signaling, the extracellular Wnt ligand binds to the seven-pass transmembrane protein FZD (Frizzled) and its co-receptors, single-pass transmembrane proteins LRP5 (low-density lipoprotein receptor-related protein 5) and LRP6. This binding stabilizes the protein β-catenin inside the cell (Long and Ornitz 2013). Normally, β-catenin is bound by a complex of axin, APC (Adenomatous polyposis coli), CK1 (casein kinase 1), and GSK-3β (glycogen synthase kinase-3β). CK1 and GSK-3β both phosphorylate β-catenin, marking it for ubiquitination and then degradation by the 26S proteasome. Wnt binding causes phosphorylation to activate Dsh (Dishevelled) which phosphorylates and inactivates GSK-3β. Wnt binding also causes axin to bind to the LRP5/6 cytoplasmic domain. β-catenin is thereby released from its binding complex and translocates to the nucleus (Lian et al., 2006, Plotkin and Bivi, 2014). Inside the nucleus, β-catenin forms a complex with LEF (lymphoid enhancer-binding factor) and TCF1 (T cell factor 1), TCF3, and TCF4 (Long, 2012). The β-catenin-Tcf/LEF complex then activates target gene promoters (Lian et al., 2006).

β-catenin-Tcf/LEF gene targets focus on osteoblast differentiation and early maturation. β-catenin is required for OSX expression (Hu et al 2005). Mice with deletion of β-catenin in osteo-chondroprogenitors do not develop into mature osteoblasts, and instead switch their to chondrocytes, forming ectopic cartilage (Day et al. 2005, Hill et al. 2005, Hu et al. 2005, Hilton et al. 2005, Rodda and McMahon 2006). In early osteoblastogenesis, β-catenin-Tcf/LEF also activate RUNX2 transcription, creating positive feedback for this signaling pathway (Gaur et al., 2005). Other target genes include cell cycle promoters (cyclin-D, Myc), AP-1 transcription factors promoting

32

differentiation (c-Jun, Fra-1), promoters of other differentiating pathways (BMP-4, FGF-18, Cx43), negative regulators of differentiating pathways (axin, Smad6) and mature osteoblast markers (osteocalcin) (Chau et al., 2009, Li and Stocum 2014, Bellido et al., 2014, Plotkin and Bivi, 2014). Wnt10b, acting through β-catenin and TCF, also suppresses transcription factors PPARγ (peroxisome proliferatoractivated receptor-γ) and C/EBPα (CCAAT/enhancer-binding protein-α), which would otherwise promote mesenchymal stem cell differentiation into an adipocyte rather than an osteoblast (Ross et al., 2000). β-catenin is required for OSX positive osteoprogenitors to express osteocalcin at initial low levels, but prevents expression at high levels. This suggests that Wnt/β-catenin signaling is necessary for early osteoblast maturity, but must be downregulated before later maturity (Rodda and McMahon 2006).

Non-canonical (β-catenin) Wnt pathways also function in bone to promote osteoblast differentiation. There appears to be a Wnt pathway independent of LRP5/6 and β-catenin for progression to OSX expression. Tu et al. (2007) found that Wnt3a and Wnt7b signal through G-protein subunit $G\alpha_{q/11}$ to activate PKCδ (an isoform of protein kinase C), which progresses cells from RUNX2 positive to OSX positive through an unknown mechanism. Also independent of β-catenin, Wnt5a methylates histones of the promoters of adipogenic genes, blocking the transcriptional activity of PPARγ (Takada et al., 2007).

Suppression of osteoblast differentiation can occur through Wnt antagonists. Dickkopfs 1 and 2 (Dkk-1, Dkk-2) bind to LRP5/6 using Kremen 1 (Krm) or Kremen 2 as a co-receptor (Lian 2006). A complex formed by Krm, Dkk-1, and LRP6 promotes

33

endocytosis of the Wnt receptor from the plasma membrane (Mao et al., 2002). Sclerostin and Wise also bind to LRP5/6 to inhibit Wnt signaling (Plotkin and Bivi, 2014). Secreted frizzled-related proteins (sFRPs), Wnt inducible factor (WIF-1), and Cereberus bind to the Wnt ligand directly (Kawano and Kypta 2003).

In addition to being required for osteoblast differentiation, RUNX2 and OSX are necessary for mature osteoblast activity (Ducy et al., 1999). They regulate gene expression for proteins related to deposition and organization of organic matrix such as BGLAP (osteocalcin), SPP1 (osteopontin), MMP13 (matrix metalloprotease 13 / collagenase 3), ALP (alkaline phosphatase), and VEGF (vascular endothelial growth factor). They also regulate the osteoblast expression of genes coding for proteins that regulate osteoclast activity (OPG = osteoprotegerin, RANKL = Receptor activator of nuclear factor κ-B ligand) (Lian *et al*., 2006, Jonason et al., 2009, Bellido *et al*., 2014) RUNX2 increases expression of the Wnt inhibitor Sclerostin in osteoblasts during matrix mineralization (Seveston et al., 2004).

As RUNX2 and OSX are transcription factors, many other nuclear factors modify their activity. Nuclear factors can stimulate osteoblast differentiation by increasing RUNX2 expression (MSX2, BAPX1, GLI2, DLX5, DLX3), serving as a RUNX2 co-activator (TAZ), or increasing RUNX2 activity (MAF, RB). Alternatively, nuclear factors can block osteoblast differentiation through inhibiting RUNX2 DNA binding (Twist, HAND2, GLI3), nuclear translocation (STAT1), expression (ZPF521, HOXA1), or activity (HES, HEY). Since RUNX2 functions in mature osteoblasts, degradation of RUNX2 reduces bone mass (Schnurri 3). Similarly, nuclear factors may increase OSX

34

transcriptional activity (NFATC1, DLX5) or decrease OSX levels (p53) to stimulate and suppress osteoblast differentiation, respectively (Long and Ornitz 2012, Long 2013, Lan et al., 2006).

Members of the transforming growth factor β protein superfamily, including **BMPs** (bone morphogenic proteins) and **TGF- β isoforms,** also promote osteoblastogenesis through RUNX2, crosstalk with Wnt signaling, and their own gene targets. In general, BMPs promote osteoblast differentiation and mature functions while TGF- βs confine osteoblasts to early differentiation (Plotkin and Bivi, 2014). TGF- β will induce bone formation only near bone. BMPs can induce bone when injected into ectopic sites, such as muscle, where they were first identified (Lee et al., 2000) Short-term expression of BMP-2 induces irreversible bone formation (Noel et al., 2004), but its absence causes spontaneous, non-healing fractures in mice (Tsuji et al., 2006). BMP-4 is osteogenic, but normal development of the limb bones will occur in its absence (51) BMP-7 expression results in osteoblastic differentiation, but postnatal growth and maintenance of limb bones will occur in its absence as other BMPs compensate (Tsuji et al., 2010). BMP-2 is therefore necessary and sufficient for osteoblast differentiation, and cannot be compensated, unlike other BMPs. Conversely, BMP-3 binds to the BMP type II to inhibit BMP2 and BMP4 signaling, thereby maintaining appropriate bone mass. BMP3 is produced by osteoblasts and osteocytes postnatally, creating a negative feedback mechanism for bone formation (Long, 2012). TGF-β isoforms include TGF-β1, TGF-β2, and TGF-β3. TGF-β1 is the most prevalent isoform in bone (Plotkin and Bivi, 2014).

35

Osteoblast cell membranes contain TGF-β receptors that are dimers of type I and type II serine/threonine kinase receptors (Plotkin and Bivi, 2014). In **canonical TGF-β signaling**, binding of the TGF-β superfamily member causes the type II receptor to phosphorylate the type I receptor. In the case of BMP, receptor association is also regulated by Neogenin, another transmembrane protein. (Chen et al., 2012). The type I receptor then phosophorylates Smad transcription factors inside the cell. BMPs work through Smads 1, 5, and 8, and while TGF-β isoforms work through Smads 2 and 3. The phosphorylated Smads associate with Smad 4 and the complex translocates to the nucleus for regulation of transcription (Chen et al., 2012, Plotkin and Bivi, 2014). Other Smads (Smad6 for BMPs and Smad7 for TGF-β isoforms) can compete with the phosphorylated Smads for association with Smad4. This competition blocks translocation of the Smad complex to the nucleus, blocking osteoblastogenesis (Chen et al., 2012). A number of other negative regulators exist for the BMP-Smad pathway, including extracellular matrix antagonists that bind BMPs (e.g. noggin, chordin, gremlin), a decoy BMPR receptor, Smurf1/Smurf2/E3 ubiquitin ligase mediated ubiquitination of Smads for proteosomal degradation, and Ski and Sno inhibitors of Smad once it translocates to the nucleus (Chau et al., 2009) In **non-canonical TGF-β signaling**, the type I receptor phosphorylates TAK1 (TGF-β activated kinase 1) instead of Smads. TAK1 can activate kinase-dependent (phosphorylation-based) signaling cascades, such as MAPK/ERK (mitogen-activated protein kinases/extracellular signal-regulated kinase) also known as Ras-Raf-MEK-ERK after its cascade components. This cascade ends in the nucleus (Lian et al., 2006, Jonason et al., 2009)

36

Both BMP-2 and TGF-β1 interact with RUNX2 in the nucleus. In the presence of RUNX2, both pathways prevent myogenesis by suppressing MyoD. Both pathways also increase expression of genes for type I collagen, the major component of bone matrix, and fibronectin, a noncollagenous extracellular matrix glycoprotein (Lee et al., 2000). BMPs create a complex between Smad and RUNX2. This requires RUNX2 to be phosphorylated by non-canonical MAPK/ERK signaling, which promotes RUNX2 association with CBP (CREB-bunding protein (Afzal et al., 2005, Chen et al., 2012) Smad and RUNX2 then interact as a co-regulatory complex on promoters for genes specific to osteoblasts, producing osteoblast markers such as ALP (alkaline phosphatase) and osteocalcin (Lee et al., 2000). In contrast, TGF-β1 does not interact with Smad to produce these mature osteoblast markers. TGF-β1 Smad3-RUNX2 interactions actually inhibit expression of osteocalcin (Alliston et al., 2001, Kang et al., 2005) Research has yet to discover the exact action of TGF-β1 on osteoblasts, but it seems to promote early osteoblast differentiation while inhibiting maturation (Kang et al., 2005, Plotkin and Bivi, 2014)

Other pathways do not require prior RUNX2 presence in the nucleus. Both TGF-β1 and BMP-2 upregulate transcription of RUNX2 itself, in a pathway involving canonical Smads activating the protein junB, and non-canonical MAPK activating p38 (Lee et al., 2002). BMP-2 induced Smads may act independent of RUNX2, but mediated by DLX5, to induce OSX expression (Lee et al., 2003) Non-canonical BMP signaling through AKT also phosphorylates OSX and DLX5 to increase their stability and transcriptional activity (Jeong et al., 2011, Choi et al. 2011). TGF-β2 induces a non-

37

canonical MAPK/ERK cascade that stimulates osteoblast differentiation, especially

during rapid marrow expansion (Lee et al., 2006) TGF-β1 induces a non-canonical

MAPK to p38 cascade resulting in type I collagen expression. A non-canonical JNK

pathway may mediate TGF-β1 induction of fibronectin expression (Lee et al., 2000).

These pathways reinforce the concept that BMP activity markers span osteoblast

differentiation, while TGF-β is focused on earlier differentiation.

The BMP/ TGF-β1 distinction is also evident in crosstalk with Wnt signaling.

One component of the canonical BMP signaling pathway, Smad1, forms a complex with

Dsh, a component of canonical Wnt signaling. As previously discussed, Wnt binding

phosphorylates Dsh to inhibit GSK-3β, allowing β-catenin to translocate to the nucleus.

Liu et al., (2006) found that BMP-2 signaling promotes Smad1-Dsh interaction,

preventing Dsh use in Wnt signaling, inhibiting β-catenin accumulation in the nucleus.

BMP-2 may thereby temporarily suspends Wnt signaling for differentiation, while

promoting later osteoblast maturation n through the BMP-2 mechanisms previously

discussed (Liu et al., 2006). Prior Wnt signaling seems to reinforce this process by

protecting Smad-1 dependent BMP signaling. The same complex that binds and degrades

β-catenin may also degrade Smad1 (Logan and Nusse, 2004). Wnt3a signaling inhibits

this degradation by phosphorylation of the binding complex (Fuentealba et al., 2007) By

guarding mechanisms that negatively regulate its own signal, Wnt signaling allows the

progression from differentiation to maturation. Conversely TGF-β1 canonical (Smad3)

and non-canonical (ALK5, PKA, PI3K) pathways converge to stabilize β catenin by

inactivating GSK-3 and increasing nuclear translocation. They also increase β-catenin

38

transcriptional activity (Zhou, 2011). This promotes osteo-chondroprogenitor progression to osteoprogenitors, as previously discussed (Lian et al., 2006). However, the same TGF-β1non-canonical pathways ALK5 and PKA, along with JNK, inhibit later osteoblast differentiation (Matsuguchi et al, 2009, Zhou, 2011).

FGF (fibroblast growth factors) ligands and receptors play diverse roles in osteoblast differentiation and osteoblast maturity. The FGF family of proteins has 22 members, and FGF1, 2, 6, 7, 8, 9, 17, and 18 are known to act in bone, although not across all skeletal elements (Long and Ornitz, 2013). FGFs bind to a tyrosine kinase receptor (FGFR1 through 4). The osteoblast cell membrane expresses FGFR1, FGFR2, and FGFR3 (Plotkin and Bivi, 2014). These receptors phosphorylate and activate diverse intercellular pathways, including MAPK/ERK, PI3K/AKT, STAT 1, and PLC-γ → PKC (Eswarakumar et al., 2005, Turner and Grose, 2010, Plotkin and Vivi, 2014) Growth factors FGF-2, FGF-4, and FGF-6 all induce differentiation, although this effect is greatest for FGF-2 (Chen et al., 2012). Without FGF-2, more mesenchymal stem cells differentiate into adipocytes (Plotkin and Bivi, 2014).

FGF-2 is expressed by osteoprogenitors and mature osteoblasts (Plotkin and Bivi, 2014). FGF-2 promotes RUNX2-induced osteoblast maturation, such as transcription of the osteocalcin BGLAP gene, through a complex pathway (Plotkin and Bivi, 2014). Niger et al., (2012) hypothesize that FGF-2 binding to its receptor triggers an intercellular pathway through MAPK/ERK. Additionally, FGF-2 binding activates intercellular PLCγ, which works through IMPK and IP6K to converts the *inositol* pyrophosphate InsP3 into higher order InsP6 and InsP7. These InsPs activate PKCδ is translocation to the nucleus,

39

where it interacts with RUNX2 to promote expression of RUNX2's osteogenic target genes. MAP/ERK also modulates RUNX2 transcriptional activity (Niger et al., 2013). FGF-2 binding also causes PKCδ to dock at the intercellular domain of Cx43 (Connexin 43), the most common gap junction protein in osteoblasts. (Niger et al., 2010). This docking may be promoted by InsP7 from the other pathway. InsP7 may even exit the cell through the gap junction to promote osteoblastogenesis in other cells (Niger et al., 2013). Once recruited by Cx43, PKCδ also translocates to the nucleus to promote RUNX2 expression, as in the other pathway.

The type of receptor is important for FGF function. FGFR1 promotes early preposteoblast differentiation, without RUNX2 expression (Long and Ornitz, 2013). However, it inhibits mineralizing activity of mature osteoblasts, although its mechanism is unknown (Jacob et al., 2008). FGFR2 promotes differentiation partially through increasing RUNX2 expression (Eswarakumar et al., 2002, 2004). It also promotes mature osteoblast bone formation (Yu et al., 2003). FGFR3 seems to suppress early differentiation and promote mineralization. Mice without FGFR3 have more osteoblasts, but less mineralization of osteoid (Valverde-Franco et al., 2004)

In terms of cross-talk, FGF-2 apparently acts downstream of the early differentiating function of TGF-β signaling (Chen et al., 2012). In mice without the receptor TGF-βR2, exogenously applied FGF-2 restores early differentiation (Sasaki et al., 2006). However, it still supports TGF-β signaling by increasing TGF-β expression, as does FGF-9 (Fakhry et al., 2009) FGF-2 and FGF-9 also both increase BMP-2 expression (Fakhry et al., 2009). FGF-2 appears to be an upstream regulator of BMP-2 actions on

40

mature osteoblast activity (Chen et al., 2012) In mice lacking FGF-2, BMP-2 driven nuclear accumulation of RUNX2 is decreased, and BMP-2 induced bone formation is also diminished. (Naganawa et al., 2008) FGF-2 supports BMP signaling by upregulating expression of BMPR-IB receptor (Singhatanadgut et al., 2006) Conversely, FGF-1 signaling appears to antagonize Wnt signaling (Lin and Hankenson 2011). FGF-1 inhibits Wnt3a-induced transcription of genes for osteoblastogenesis (Ambrosetti et al., 2008). A potential pathway is FGF activation of SOX2, which then binds to β-catenin to block it from jointing with TCF/LEF for gene transcription (Mansukhani et al., 2005)

IGFs (insulin-like growth factors) promote osteoblast differentiation, mature function, and survival (Plotkin and Bivi, 2014). IGFs are induced by the presence of somatotropin/growth hormone (GH), which is produced in the pituitary gland (Long and Ornitz, 2013). GH binds to its transmembrane receptor GHR, and Janus kinase 2(JAK2) associated with the GHR intracellular domain causes this domain to dimerize. STATs (signal transducers and activators of transcription) dock at the GHR receptor and are then translocated to the nucleus (DiGirolamo et al., 2007, Perrini et al., 2010, Bellido and Gallant, 2014). About 75% of IGF-1 is produced in the liver in response to GH and enters circulation. Most of the remainder is produced and stored in skeletal tissue and in adipose tissue. Mature osteoblasts produce and store IGF-1 in skeletal tissue, and it is release during bone resorption (Long, 2012, Plotkin and Bivi, 2014). Ligand IGF-1 is active during both embryonic and postnatal growth, while IGF-2 is downregulated after its embryonic role (Plotkin and Bivi, 2014). All effects of ligand IGF-1, and most effects

41

of ligand IGF-2, are mediated by the type I receptor (IGF-IR) (Long and Ornitz 2013), although there is also a type I receptor (IGF-IIR) (Plotkin and Bivi, 2014).

IGF-R1, a tetramer receptor, has two extracellular α subunits for IGF binding and two intercellular β subunits with tyrosine kinase activity to phosphorylate several pathways (Plotkin and Bivi, 2014). IGF-1 binding triggers phosphorylation of intercellular Shc and IRS-1. These trigger to a MAPK/ERK pathway leading to transcription of genes promoting differentiation (Plotkin and Bivi, 2014). Shc and IRS-1 also trigger a PI3K/AKT pathway that enhances protein synthesis by activating mTOR (mechanistic target of rapamycin) and p70S6 kinase. PI3K/AKT additionally prevents osteoblast apoptosis by deactivating pro-apoptotic protein BAD (Blc-2-associated death promoter (Petley et al., 1999, Perinni et al., 2010). IGF-1 may cooperate with BMP-2 to induce OSX expression through the MAPK pathway (Celil and Campbell, 2005). Interestingly, GH acting through JAK2 can also activate both Shc and IRS1-3, activing these MAPK/ERK and PI3K/AKT pathways for cell survival (Perinni et al., 2010) PI3K/AKT pathways from GH are linked in particular to inhibition of capase 3, a proapoptotic protein (Sanders et al., 2006). However, GH cannot induce bone formation directly, but must act through IGF-1 at the osteoblast's receptor. Deletion of IGF1R in osteoblasts prevents their differentiation in response to growth hormone (DiGirolamo et al., 2007). IGFR1 overexpression in osteoblasts increases bone formation, while deletion of the receptor decreases bone formation (Zhang et al., 2002, Zhou et al., 2000).

PTHrP (parathyroid hormone-related peptide) and **PTH** (parathyroid hormone) signal through the same receptor PTH1-R (parathyroid hormone/parathyroid hormone-

42

related peptide receptor). PTHrP is produced by cells in many tissues, why PTH

produced and secreted by the parathyroid gland (Chau et al., 2009). PTHrP and PTH

share eight of the first thirteen amino acids, and only the first 34 amino acids control

biological activity (Plotkin and Bivi, 2014). PTHrP is necessary and more important than

PTH for endochondral development because it also regulates chondrocytes during

formation of cartilage templates (Amizuka et al., 2004).

Upon PTHrP or PTH ligand binding, conformational changes in the receptor

activate G-protein signaling. This pathway continues through the cyclic AMP (cAMP),

which activates PKA (protein kinase A). PKA phosphorylates and activates transcription

factors including CREB (cAMP response element binding protein), AP-1 members (c-

jun, fosB, JunB, fra1, and fra2), and RUNX2 enhance differentiation (Datta and Abou-

Samra, 2009, Plotvin and Bivi, 2014). PKA signaling also promotes cell survival by

deactivating pro-apoptotic protein BAD and increasing transcription of anti-apoptotic

protein Bcl2 (Yamamoto et al., 2007, Yamashita et al., 2008). PTH1-R can also signal

through PLCβ (phospholipase C β) to PKC (protein kinase C) (Datta and Abou-Samra,

2009) PTH1-R can also signal through a MAP/ERK pathway to induce cyclin D1 in

proliferating progenitors, enhancing cell growth (Datta et al., 2007). In already

differentiated but maturing osteoblasts, continued PTH expression blocks the MAP/ERK

pathway, reducing cyclin D1 and arresting cell growth (Datta et al., 2005) Cyclin D1

inhibition may be through PTH upregulation of p21 and p27 (Qin et al., 2005)

PTH1-R also enhances differentiation through cross-talk with other pathways,

primarily through increasing expression of their signaling components (Datta and Abou-

43

Samra, 2009). PTH and PTHrP up-regulate mRNA expression of Wnt receptor components Frizzled and LRP6, along with β-catenin, while decreasing expression of Wnt antagonist Dikkopf-1 (Kulkami et al., 2012). PTH increases expression of TGF-β pathway components, including TGF-β1, TGF-β2, and Smad3 (Sowa et al., 2003) Long exposure to PTH stimulates IGF-I release in fetal rats and mice, and IGF-I and IGF-II release in adult mice, which will be discussed further as a coupling mechanism (Canalis et al., 1989, Linkhart and Mohan, 1989). However, IGF-1 may also promote PTH activity, as mice lacking iGF-1 have less bone formation (Miyakoshi et al., 2001). PTHrP increases expression of the BMP-IA receptor in mesenchymal stem cells that are still plutipotent (Chan et al., 2003) FGF-2 and FGF-2R are also increased by PTH (Hurley et al., 1999)

PTH1-R also provides temporary desensitization to differentiating signals from its own and other pathways, which is important for coupling bone formation with resorption. Ligand binding triggers association of β-arrestin-1 and β-arrestin-2 to PTH1-R, causing the complex to internalize and also reduce its affinity for cAMP (Plotkin and Bivi, 2014). Receptors are either destroyed or recycled to the surface (Datta and Abou-Samra, 2009). The PTH1-R receptor similarly complexes with the TGF-β receptor TGF-βII. TGF-βII phosphorylates the cytoplasmic domain of PTH1-R, causing desensitization, while PTH1-R draws both receptors into the cell. (Chen et al., 2012). High levels of RUNX2 seem to blunt differentiating effects of PTH, perhaps to support RUNX2's maturation activities (Merciris et al., 2001)

ATF4 (Activating transcription factor 4) is expressed during late osteoblast differentiation and therefore contributes to mature osteoblast activity (Long and Ornitz 2013). It directly regulates osteocalcin expression and RANKL expression in osteoblasts (Yang et al 2004, Elefteriou et al 2006). Nuclear factor FIAT, as suggested by its name (factor inhibiting ATF4-mediated transcription), suppresses this expression (Yu et al., 2005). ATF4 also interacts with FOXO family transcription factors for efficient import of amino acids for protein synthesis. (Yang, et al. 2004).

AP-1 family transcription factors (Fos, FosB, Fra-1, Fra2, Jun, JunB, JunD) have a complex role in osteoblast differentiation (Chau et al., 2009). Different members are expressed early and late in differentiation, and stimulate or suppress transcription (Bellido et al., 2014). For example, Fra-1 (FOS-related antigen 1) and ΔFosB (splicing variant of FBJ murine osteosarcoma viral oncogene homolog B) increase bone mass by stimulating osteoblast differentiation, although Fra-1 does not affect the number of osteonblasts (Jochum et al., 2000, Sabatakos et al. 2000, Eferl et al., 2004, Kveiborg et al. 2004). JunB (Jun b proto-oncogene) reduces osteoblast differentiation (Kenner et al., 2004) Atf4 controls mature osteoblast expression of collagen type 1 and osteocalcin (Yang et al., 2004)

The intertwined pathways of local factors regulating osteoblast differentiation allow the body to precisely regulate the number and maturity of recruited osteoblasts. They also provide numerous targets, both in terms of ligands and signaling pathway components, to be targeted by mechanical and hormonal influences. To generalize and summarize the above discussion, RUNX2 and OSX are transcription factors required for

45

osteoblast differentiation, maturation, and function. Canonical Wnt signaling operates

through differentiation and early maturation but must be reduced for full maturity. TGF-

βs appear to confine osteoblasts to early differentiation, while BMPs function through

osteoblastogenesis. IGFs promote differentiation, maturation, and survival. FGFs have

diverse roles in advancing oteoblastogenesis. PTH and PTHrP have a complex role, in

that they appear to promote osteoblast differentiation and maturation markers, positively

and negatively regulate differentiating effects of other pathways, arrest cell cycle growth

in late maturing osteoblasts, and prevent apoptosis. Many other local factors affect

osteoblast recruitment and function, but they will be discussed as components of

resorption-formation coupling and/or hormone interaction.

2.6. Local Factors Influencing Osteoclast Differentiation and Maturation

Osteoclasts are responsible for resorption of bone. They are polykaryons, meaning

that they have multiple nuclei resulting from the fusion of multiple progenitors (Ross,

2013, Bellido et al., 2014). Osteoclasts are attached to the bone surface through the

integrin heterodimer αvβ3 embedded in their plasma membrane (Ross, 2013). Within

minutes of attachment, rings of filamentous actin surface on the osteoclast plasma

membrane. After several hours these unite into a podosome belt, creating a sealed

compartment between the osteoclast and bone surface (Bellido et al., 2014). Within this

sealing zone, the osteoclast plasma membrane takes on a "ruffled" appearance due to the

fusion of vesicles, for secretion of its bone-resorbing products (Ross, 2013). A

H^+/ATPase (ATP61) and chloride channel CIC-7 (H^+/Cl- exchange transporter 7) in the

osteoclast plasma membrane pump H^+ and Cl^- into the sealing zone. A bicarbonate

46

HCO3/CL- exchanger outside the sealing zone sustains the osteoclast's H^+ and Cl^- supply. The HCl acidifies the sealing zone, causing the hydroxyapatite mineral in the bone to dissolve and exposing the type I collagen. Osteoclasts digest this matrix by secreting enzymes such as cathepsin K and matrix metalloproteinases (MMP-9, MMP-13, MMP-14), along with TRAP (tartrate-resistant acid phosphatase), which may promote reactive oxygen species formation (Ross, 2013, Bellido et al., 2014). After resorption, osteoclasts undergo cell death through apoptosis, which is mediated by osteoclast detachment and potentially integrin detachment (Bellido et al., 2014).

Like osteoblasts, osteoclast progenitors are produced in bone marrow. Osteoclasts arise from hematopoietic stem cells (HSCs), which also produce immune elements in the blood, including white blood cells (monocytes, macrophages, neutrophils, eosinophils), red blood cells and their progenitors (erthyroblasts / erythrocytes), and platelets and their progenitors (megakaryocytes) (Cabrita et al., 2003). Unlike osteoblasts, osteoclasts have a fairly simple signaling mechanism that triggers their differentiation and mature activity.

M-CSF (macrophage colony stimulating factor) is normally secreted by osteoblasts, osteoblast precursors, and osteocytes (Bellido et al., 2014). M-CSF binds to the CSF-1R/c-Fms on the hematopoietic stem cell, triggering pathways through PI3K/AKT, GRB2 (growth-factor-receptor bound protein 2) → ERK, and MITF → BCL-2 (B-cell lymphoma 2) (McGill et al., 2002, Ross and Teitelbaum, 2005). These pathways promote cell survival by blocking apoptosis and reorganize the cytoskeleton to promote cell migration and spreading. They also simulate osteoclasts to express RANK (receptor activator of nuclear factor-κB), which is trimeric receptor expressed on the osteoclast

47

surface (Bellido et al., 2014). Although osteoblasts also express RANKL, as previously

discussed, osteoclasts have higher expression (Moriishi et al., 2012).

RANKL (receptor activator of nuclear factor-κB ligand), also known as

TNFSF11 (tumor necrosis factor ligand super family member 11), is a cytokine from the

tumor necrosis factor (TNF) (Takayanagi, 2007). The ligand for RANKL is RANK

(receptor activator of nuclear factor-κB), which is expressed on the surface of osteoblasts

and osteocytes, and can also be secreted in soluble form (Bellido et al., 2014). RANK

binding to RANKL causes the adapter molecule TRAF6 to bind to RANKL's

cytoplasmic domain. This trimerization triggers signaling through IKK (inhibitor of NF-

κB kinase) → NF-κB (receptor activator of nuclear factor-κB) and separately through

MAPK → c-FOS → AP1 (activator protein 1). Both of these pathways result in

activation of NFATc1 (nuclear factor of activated T cells, cytoplasmic 1). After

translocation to the nucleus, NFATc1 forms a complex on DNA with transcription factors

PU.1, CREB, MITF (microphthalmia-associated transcription factor), and AP1. One set

of target genes, DC-STAMP (Dendritic-cell-specific transmembrane protein) and

ATP6V0D2 (ATPase, H+ Transporting, Lysosomal 38kDa, V0 Subunit D2), promote

fusion of osteoclast progenitors, creating the mutli-nucleated cell. Other target genes are

the previously discussed components of matrix degradations (cathepsin K, MMP9, CIC-

7, ATP61) (Takayanagi, 2007). Upon migrating to the bone surface, the osteoclast binds

through its integrin αvβ3 heterodimers. This creates a signal cascade through c-src that

promotes formation of the podosome belt and ruffled border (Ross, 2013). The exact

signaling mechanism has been debated, but results in the movement of vesicles, F-actin,

48

and cytoskeletal microtubules to the basal side of the osteoblast, facing the bone (Horne et al., 2005, Zou et al., 2007).

OPG (Osteoprotegerin/tumor necrosis factor receptor superfamily member 11B) is a soluble factor secreted by osteoblasts and osteocytes (Bellido et al., 2014). It can also bind to RANKL on the osteoclast, but this binding does not result in osteoclast differentiation. Since OPG competes with RANK for access to RANKL, the ratio of OPG to RANK to the osteoclast's environment determines which factor is likely to bind. When RANKL is more abundant than OPG, osteoclastogenesis is more probable, but when RANKL is low in respect to OPG, blocking osteoclastogenesis is more likely (Takayanagi, 2007, Kajiya et al., 2010, Ross, 2013, Bellido et al., 2014)

2.7. Mechanisms of Osteocyte Mechanotransduction

2.7.1. *Osteocyte Differentiation*

Approximately 65% of osteoblasts die through apoptosis following bone formation (Parfitt, 1990). Estimates for the number that terminally differentiate into osteocytes range from 10% to 30% (Parfitt, 1990, Aubin and Liu, 1996, Banks, 1974). Osteoblasts surviving on the surface of the newly formed bone differentiate into bone lining cells (Bellido et al., 2014). Since osteocytes accumulate in bone tissue through many modeling and remodeling events, they compose 90 – 95% of all bone cells at a given time (Himeno-Ando, et al., 2012). Osteocytes become embedded in the osteoid secreted by themselves and neighboring osteoblasts (Franz-Odendall 2006). Palumbo et al. (1990) theorizes that losing connection with the active osteoblasts on the forming bone surface causes osteocytes to commit to their terminal differentiation. The molecular

49

mechanism may involve downregulation of TGF-β signaling through Smad3 (Borton et al., 2001). Osteocyte cell bodies are housed in lacunae, which are connected to other lacunae through canaliculi. Osteocytes extend their ~50 dendrites into the canaliculi to communicate with other osteocytes (Himeno-Ando et al., 2012, Robling et al., 2014). Cx43 is an important gap junction for this intracellular communication (Bivi et al. 2012).

2.7.2. Strain-Induced Mechanotransduction

To trigger modeling and remodeling in line with the mechanostat, osteocytes must both sense mechanical strain and transduce the message to osteoblasts and osteoclasts. Researchers are just beginning to probe the details of this mechanism, but it seems to be related to detecting fluid flow (Komori et al., 2013). The lacunae and canaliculi form a dense interconnected network of space within bone. Bone by weight is about 10% water. Of this, about 40% is bound within collagen fibers, with the remainder unbound within lacunar-canalicular and vascular pore networks in the cortex (Burr and Akkus, 2014). Strain on bone tissue causes fluid flow from high pressure to low pressure regions (Robling et al., 2014). Osteocytes and their dendrites are suspended within the lacunar-canalicular space by integrins, which are associated with actin filaments inside the osteocyte cytoplasm (Turner, 2006, Robling et al., 2014). In the Weinbaum (1994) model, fluid flow deflects and shortens the osteocyte's tethering apparatus. This stretches the osteocyte cell membrane, amplifying the strain signal 10 - 100x. Actin filaments inside the cell also reorganize into bundles called stress fibers (Meazzini et al., 1998). This shear stress acts on L-type voltage-sensitive calcium channels and mechano-sensitive channels, causing extracellular calcium to flow into the cell (Turner, 2006).

50

Intercellular calcium is also released from storage inside the osteocyte by signaling through a MAP/ERK pathway ATP (adenosine triphosphate) to the receptors P2X and P2Y, which release PGE2 (prostaglandin E2) (Burger and Klein-Nulend, 1999, You et al., 2001, Turner, 2006). PGE2 acts on its receptors EP2 and EP4 through a cAMP → PKA pathway to activate transcription factor CREB. This leads to the expression of genes for osteoblast proliferation, differentiation, and survival, thereby signaling for bone formation (Plotkin and Bivi, 2014). Fluid flow also stimulates activity of NOS (nitric oxide synthase) and the release of NO (nitric oxide). NO inhibits bone resorption by decreasing RANKL expression and increasing OPG expression, thereby preventing osteoclast recruitment and protecting forming bone (Burger and Klein-Nulend, 1999, Turner, 2006, Komori, 2013). Osteocytes can also inhibit bone formation in response to fluid flow (Komori, 2013, Pajevic, 2013). In mice, SOST (sclerostin) is produced during hindlimb unloading, but suppressed during hindlimb loading (Robling et al., 2008, Lin et al., 2009). Sclerostin decreases osteoblastogenesis by inhibiting canonical Wnt signaling by binding to LRP5/6, and by antagonizing BMP signaling (Bellido et al., 2014). Finally, mechanical loading helps regulate matrix mineralization by increasing transcription of proteins DMP-1 and PEX, which promote mineralization, and MEPE, which inhibits mineralization (Gluhak-Heinrich et al., 2003, Harris et al., 2007, Burr and Akkus, 2014).

2.7.3. *Damage-Induced Mechanotransduction*

Osteocytes can also sense microdamage in their environment and signal for local repair. Mechanism for this targeted remodeling is likely osteocyte apoptosis. Linear microcracks disrupt lacunar-canalicular fluid transport between osteocytes. (Tami et al.,

2002) This break in fluid flow impairs nutrient transport and cell-cell signaling, causing hypoxic stress followed by osteocyte apoptosis (Martin, 2003, Herman et al., 2007). Verborgt et al (2000) found that within one day of cyclic loading on the rat ulna, osteocyte apoptosis occurred in regions within 100 μm of the resulting microdamage. Within one week, resorption spaces appeared in these same locations. Osteocyte apoptosis ends in rupture of the cell membrane, releasing TNF-α (tumor necrosis factor α), IL-6 (interleukin 6), and IL-7 (interleukin 7). These pro-inflammatory cytokines flow through lacunar-canalicular and vascular pores to the bone surface (Lotze and Tracey 2005). IL-6 and IL-7 induce expression of RANKL, promoting osteoclastogenesis (Shandala et al., 2012). This process appears to recruit osteoclasts to the damage periphery, as RANKL is low near damage and apoptotic osteocytes but high 100 – 500 μm away (Kennedy et al., 2011). Larger cracks result in a greater RANKL increase (Mulcahy et al., 2011). IL-6 and IL-7 also induce ICAM-1 in osteoclast progenitors, making them adhere to endothelial cells lining the vasculature to aid transport to the site (Cheung et al., 2012).

2.8. Coupling of Resorption and Formation During Remodeling

The first stage of remodeling is activation. This stage is characterized by formation of the canopy and growth of the blood vessel to penetrate the BMU. Osteoblast and osteoclast progenitors arrive in the BMU through this circulation. The capillary grows towards the BMU and penetrates the canopy, allowing hematopoietic stem cell progenitors of osteoclasts to enter from circulation in the blood (Kristensen et al., 2013). As previously indicated, mechanical loading stimulates osteocytes to produce RANKL,

inducing osteoclast differentiation in hematopoietic stem cells (Shandala et al., 2012).

Once differentiated, osteoclasts initiate the second stage, resorption. Specialized bone

lining cells may remove exposed collagen and deposit the cement line (Allen and Burr,

2014).

The third stage is reversal, in which osteoclastic resorption ends and osteoblastic

formation begins. The exact signaling mechanisms for reversal is unclear (Burr and

Akkus, 2014). This stage requires coupling, meaning that the amount of bone formation

should be matched to bone resorption, unless disuse remodeling is occurring (Frost

2003b, Sims and Martin, 2014). Harris and Heaney (1969) note that healthy individuals

have similar overall rates of resorption and formation. Martin and Sims (2014) provide a

comprehensive overview of the latest theories for coupling mechanisms. Resorption of

bone by osteoclasts releases active TGF-β and IGF-1 from the matrix, which helps recruit

mesenchymal stem cells for osteoblastogenesis, as previously discussed (Tang et al 2009,

Xian et al 2012). As osteoblasts are recruited, they also produce and release TGFβ and

IGF-1 in biologically inert form. PTH and vitamin D (1,25-dihydroxyvitamin-D$_3$)

enhance the ability of osteoblasts to serve as plasminogen activators (Fukomoto et al

1992, Fukomoto et al 1994). The plasminogen activator / plasminogen system generates

plasmin, which activates the latent forms of TGFβ and IGF-1 (Yee et al., 1993, Campbell

et al., 1992). The hormonal influences of PTH and vitamin D essentially allow

osteoblasts to renew and amplify their own recruitment signal.

By themselves, factors released from the resorbed matrix are not sufficient for

coupled formation (Martin and Sims 2005, Sims et al., 2004). Active signaling by

53

osteoclasts also appears necessary (Sims and Martin, 2014). Resorbing osteoclasts express CT-1 (Gp130 signaling cytokine cardiotrophin-1) *(Walker et al 2008).* Coupling activity is dependent on secretion of gp130, which is assisted by IL-6 produced by osteocytes (Martin and Sims 2005, Sims et al., 2004). Global deletion of CT-1 in mice results in low osteoclast and osteoblast activity (Walker et al 2008). Osteoclasts also secrete BMP-6 and Wnt10b, two signaling pathways of osteoblastogenesis, although levels may not be high enough to be effective (Henrikson et al., 2012). However, these pathways do enhance RANKL action on osteoclastogenesis (Quinn et al., 2001, Maeda et al., 2012). During active resorption, osteoclasts additionally secrete the proteins CTHRC1 (Collagen triple helix repeat containing 1) and Afamin, which both stimulate bone formation (Kim et al., 2012, Takeshita et al., 2013). Non-resorbing osteoclasts secrete PDGF-BB, which may inhibit and induce migration of mesenchymal stem cells and preosteoblasts at different stages of remodeling *(*Kreja et al 2010, Sanchez-Fernandez et al 2008, Kubota et al 2002, Sims and Martin, 2014). Additionally, osteoclasts express EphrinB2 on the plasma membrane, which facilitates bidirectional cell-cell signaling when in contact with EphB4 on the osteoblast plasma membrane *(Allan et al 2008,* Irie et al 2009*).* This signal inhibits osteoclast differentiation and promotes osteoblast differentiation (*Zhao* et al., 2006). This coupling pathway is also promoted by PTH, which causes a rapid 10x increase in EphrinB2 expression *(*Allan et al 2008). Semaphorin proteins help prevent coupling from progressing too quickly (Martin and Sims, 2014). Osteoclasts secrete Sema4D, which inhibits osteoblast differentiation, helping forestall progression (Negishi-Koga et al., 2011). Osteoblasts secrete Sema3B, which enhances

54

RANKL action to promote continued resorption (Sutton et al., 2008). Vitamin D (1,25-dihydroxyvitamin-D$_3$) also increases Sema3B action. Following promoting of osteoblastogenesis during reversal, remodeling enters the fourth stage of bone formation. Osteoblasts lay down osteoid and begin primary mineralization. Mature osteoblasts secrete Wnt5a and PTHrP to promote differentiation of additional mesenchymal stem cells into osteoblasts through the previously discussed pathways (Miao et al 2005, Tu et al 2007). Secondary mineralization continues as remodeling enters the final resting, or quiescence, stage (Allen and Burr, 2014).

2.9. Physiological Control of Growth During Skeletal Development

2.9.1. *Interaction of Sex Steroids with Longitudinal Growth*

Growth hormone (GH), also called somatotropin, is a key hormonal determinant of the longitudinal growth of bone. Its target IGF-1 promotes proliferation of chondrocytes in the growth plate (Mackie et al., 2011).As previously discussed, growth hormone is produced in the pituitary gland and stimulates production of IGF in the liver, skeletal tissue, and adipose tissue (Long and Ornitz, 2013). GH directly stimulates IGF-1 production by growth plate chondrocytes. GH-stimulated IGF-1 produced in the liver also enters the growth plate through the circulatory system. (Nilsson et al 2005, Pass et al 2009) IGF-2 is expressed by growth plate chondrocytes independent of GH stimulation (DeChiara et al 1991) IGF-2 is necessary for embryonic growth, but is downregulated after birth (Plotkin and Bivi, 2014). Low GH levels are associated with infants small for gestational age (Weaver and Fuchs, 2014). Deficiency in GH during childhood is

55

associated with reduced height during the growth spurt in puberty, and with adult short stature (Weaver and Fuchs, 2014, Bellido and Gallent, 2014). The GH/IGF-1 axis can also be suppressed during childhood by inflammatory cytokines produced by chronic inflammatory conditions, leading to growth defects (Pass et al., 2009).

Thyroid hormone T3 (triiodothyronine) interacts with thyroid hormone receptor α to upregulate canonical Wnt4 signaling and increase the presence of FGFR3 for FGF signaling. Both of these pathways accelerate chondrocyte hypertrophy (Barnard et al., 2005, Wang et al., 2007, Mackie et al., 2011). IGF-1 may promote this pathway, as IGF-1 inhibitors also partially inhibit T3 activity (Wang et al., 2010). Hypothyroidism in humans impairs chondrocyte hypertrophy, thins the growth plate, and slows longitudinal growth (Mackie et al., 2011).

Sex steroids mediate the effects of the GH/IFG-1 axis on longitudinal bone growth (Callewaert et al., 2010a). Androgens are secreted by testes, ovaries, and adrenal glands. In males, the testes secrete 95% of the main male androgen, testosterone. In females, 25% of testosterone is produced by the ovaries, 25% by the adrenal glands, and 50% by conversion from other sex steroids in peripheral tissues such as adipose tissue. Estrogens are secreted primarily by the ovaries in women, although they can also be produced in adipose tissue. In men, over 80% of estrogen is produced in the adipose tissue by P450 aromatase conversion from androgens. A small amount is also produced by the testes (Weaver and Fuchs, 2014). In male neonates, testosterone secretion establishes the pattern of GH secretion (Jansson et al., 1985). In male mice, longitudinal

56

bone growth during the perinatal secretion of androgens is a key determinant of adult length of the femur and tibia (Sims et al., 2006).

Fetal and infant growth is rapid, but slows during childhood. During puberty, GnRH (gonadotropin-releasing hormone / gondaoliberen) triggers the production of low levels of androgens and estrogen (Weaver and Fuchs, 2014). Estrogen in females, and testosterone aromatized to estrogen in males, stimulates GH secretion in the hypothalamus and pituitary glands. GH circulates to the liver and stimulates IGF-1 production, which enhances longitudinal bone growth as previously described (Leung et al., 2004). IGF-1 action on the growth plate produces the pubertal growth spurt in both males and females (Vanderschueren et al., 1997, Vidal et al., 2000, Callewaert et al., 2010a). Males and females do not have major differences in absolute growth rate, but females enter puberty earlier, while males stay in puberty longer (Seeman, 2002, Iuliano-Burns et al., 2009, Callewaert et al., 2010a). Males thereby achieve a higher peak height velocity and adult height (Weaver and Fuchs, 2014). Female mean height velocity is 5.5 cm/year at age 10, peaks at 8.5 cm/year by age 12, and is close to zero by age 16. Male mean height velocity rises to 5 cm/year starting at age 12, peaks at 9.5 cm/year by age 14, and is close to zero by age 17 (Heaney et al., 2000). In late puberty, rising estrogen levels close the growth plate and stimulate epiphyseal fusion. This closure is delayed by disorders involving resistance to estrogen (e.g. Turner's syndrome) or deficiency in aromatase conversion (Leung et al., 2004, Weaver and Fuchs, 2014).

2.9.2. *Interaction of Sex Steroids with Radial Expansion and Endosteal Preservation*

Testosterone increases periosteal bone formation and estrogen increases endosteal bone formation (Turner et al 1989, 1990a,b). Frost (1992) hypothesized that estrogen lowers the mechanostat setpoint for modeling, so that more endocortical bone is formed than is mechanically necessary. During fetal growth, placental estrogen levels are high, inhibiting endosteal resorption. When this estrogen supply is cut off at birth, the setpoint is raised, and mechanically unnecessary endocortical bone is resorbed. As the marrow cavity expands, directly determined bone density decreases by about 30% within the first six postnatal months (Trotter and Hixon 1974). In females, the mechanically-driven endosteal expansion associated with radial growth is reversed by high levels of estrogen expression at the end of puberty. Bone is added at the endosteum (Martin, 2003, Robling et al., 2014). During the reproductive period, females store more mineral than men of the same age and lean body mass (Ferretti et al., 1998). However, when estrogen levels decline through menopause, the mechanostat setpoint is raised again, and bone resorption increases at the endosteum (Robling et al., 2014). Activation frequency of resorption increases by 33%, substantially increasing erosion of the marrow cavity (Han et al., 1997).

In recent years, mechanisms have emerged for estrogen's capacity to lower the mechanostat setpoint and induce excess bone formation. When PGE2 and nitric oxide are produced by osteocytes in respond to fluid flow, estrogen signals through its receptor ERα to upregulate their expression (Joldersma et al., 2001, Bakker et al., 2005, Price)

58

Estrogen also increases expression of β-catenin in respond to fluid flow (Yeh et al., 2010). Estrogen may also act through the GH/IGF-1, but studies have not been consistent (Callewaert et al., 2010b). As previously discussed, these pathways promote bone formation by triggering osteoblastogenesis. Estrogens amplify the mechanical signal for bone formation, thereby producing more bone than is mechanically necessary. In females only, estrogen also signals through its ERβ receptor to limit periosteal expansion in response to mechanical loading (Callewaert et al., 2010a). Female mice with disruption of ERβ form more periosteal bone after loading (Saxon et al., 2007).

Testosterone increases bone strength by promoting periosteal expansion, distributing mass further from the neutral axis. In males, the periosteal and endosteal radii increases steadily during growth and then stay fairly constant until middle age. During senescence, the periosteal and endosteal radii slowly expand again (Martin, 2003a). Due to their enhanced periosteal formation, males have larger bone diameters at peak bone mass compared to females (Burr and Akkus, 2014). Testosterone signals through the androgen receptor AR to promote normal periosteal and endosteal bone growth. AR signaling lowers expression of sclerostin and nitric oxide, which osteocytes produce to inhibit osteoblastogenesis during mechanical unloading (Callewaert et al., 2010a, Callewaert et al., 2010d). Testosterone thereby raises the mechanostat's tolerance for periosteal formation beyond mechanical demand (Callewaert et al., 2010a). AR action on the mechanostat is likely mediated through GH-IGF-1. Androgens secreted during the male neonatal period imprint male patterns GH secretion. This imprinting allows males to secrete higher levels of IGF-1 than females (Callewaert et al., 2010c). Males also signal

through ERα with testosterone aromatized to estrogen, and this signal is necessary for AR promotion of periosteal bone growth (Callewaert et al., 2010b). Male humans and mice with resistance to estrogen or lack of aromatase have low bone mass (Callewaert et al., 2010b). However, ERα does not significantly modify bone's response to mechanical loading in males as it does in females (Callewaert et al., 2010a, Price et al., 2011).

2.9.3. *Estrogen Deficiency Also Contributes to Bone Loss in Elderly Men*

In men, approximately 50% of cases of osteoporosis have a direct cause, and are termed secondary osteoporosis (Pietschmann et al., 2001). Approximately 85% of cases of secondary osteoporosis in men are endocrine related (corticosteroid excess in Cushing's syndrome, testosterone deficiency in primary or secondary hypogonadism) or behaviorally induced (exogenous corticosteroid use, alcoholism, tobacco use, inadequate calcium or vitamin D intake) (reviewed in Ebeling 2008; Sim and Ebeling 2013). When no secondary cause is discerned, the osteoporosis is termed primary or idiopathic (Pietschmann et al., 2001).

Estrogen, particularly estradiol (E$_2$), plays a key role in primary osteoporosis in elderly men. After age 70, declining bioavailability of estradiol is associated with accelerated cortical bone loss (Khosla et al. 2005; Riggs et al. 2008), increased markers of bone turnover (Szulc et al., 2001; Khosla et al., 2001; Gennari et al., 2003; Van Pottelbergh et al., 2003), and decreased bone mineral density (Bourdel et al., 1989; Slemenda et al., 1997; Greendale et al., 1997; Khosla et al., 1998; Ongphiphadhanakul et al., 1998; Center et al., 1999; Amin et al., 2000; Szulc et al., 2001; Khosla et al., 2001; Khosla et al., 2005; Van Pottelbergh et al. 2003). Khosla et al. (2001, 2005) in particular

60

demonstrated that older men can fall below the threshold of bioavailable estrogen needed to protect against bone loss. Total levels of testosterone and the estrogen hormone estradiol (E_2) remain largely constant over male lifespan (Khosla et al., 2001). However, bioavailable testosterone declines 26% in middle-aged men (40 – 59 years) and 60% in older men (>60 years) compared to young men. Similarly, bioavailable estradiol declines 9% in middle-aged men and 38% in older men compared to young men. This shrinking bioavailability appears to be due largely to an age-associated increase of the sex-hormone binding globulin (SHBG), which binds estradiol. SHBG is 16% higher in middle-aged men and 76% higher in older men (Khosla et al., 2005). Pietschmann (et al., 2001) similarly found that men diagnosed with primary osteoporosis have significantly lower serum estradiol and free androgen, and significantly higher SHBG concentrations, compared to controls.

Bioavailable testosterone affects bone mass indirectly through its aromatization to estrogen. In men, over 80% of estrogen is produced in the adipose tissue by aromatase conversion from androgens. A small amount is also produced by the testes (Weaver and Fuchs, 2014). Men's ability to aromatize testosterone to estradiol may actually increase with age. However, the decline in bioavailable testosterone as a substrate for this process further reduces bioavailable estradiol (Khosla et al., 2001). In a nursing home study of elderly men, up to 66% of hip fractures and 20% of spinal fractures occurred in hypogonadal men with abnormally low serum testosterone (Abbasi et al., 1995). Gennari et al. (2003) also found that aromatase activity increased with age, but was lower in osteoporotic men compared to controls.

61

Compared to other estrogens and testosterone, bioavailable estradiol is the most significant predictor of bone resorption markers and BMD in elderly men (Khosla et al., 2001). The level of bioavailable estradiol also shows a significant positive association with cortical and trabecular vBMD in the male lumbar spine, femoral neck, distal radius, and distal tibia, even after adjusting for age (Khosla et al., 2005). Khosla et al. (2001) found that elderly men with Bio-E$_2$ level above the sample median lost minimal or no bone at the radius and ulna, while men falling below this median threshold lost progressively bone at a progressively higher rate as Bio-E$_2$ levels decreased. Khosla et al. (2005) similarly found that men with Bio-E2 levels below the sample median significantly declined in trabecular vBMD and cortical vBMD at several skeletal sites. In their sample of subjects from Rochester, MN, ~90% of postmenopausal women, ~50% of elderly men, and ~25% of middle-aged men fellow below this median threshold, suggesting that they were at risk of developing osteoporosis (Khosla et al., 2001) Gennari et al. (2003) also observed that men above a sample median threshold of bioavailable estradiol were relatively protected from bone loss, while men below this threshold were at risk for bone loss.

3. Mechanical Basis of Bone Formation and Resorption

Copyright Notice

3.1. Introduction: Mechanical Behavior of Materials

How can we infer mechanical strain without destructive mechanical testing of bone tissue? The type or "mode" of mechanical loading experienced by bone can be used as a proxy of relatively higher or lower strain, allowing comparisons to other tissue regions or skeletal elements. Mechanical loading mode can be inferred from how the bone is loaded by body weight and/or physical activity, as described in this subchapter. Additionally, spontaneous fractures tend to concentrate at specific anatomical sites (e.g. vertebrae, femoral neck) that experience heavy mechanical demand from dynamic loading or body weight. These sites are more vulnerable to changes in bone quality that increase bone fragility with age. Pathological fractures may be distinguished by their occurance at less

common anatomical sites, dissociated from the usual life conditions and age-associated changes that typically predict traumatic fractures. Understanding how the biomechanical configuration of a bone affects mechanical demand and eventual fracture risk can help identify pathological sources of fracture.

3.1.1. Elastic and Plastic Deformation

A force-displacement curve can describe the behavior of a sample as a whole structure, not normalized for sample mass and geometry. A stress-strain curve represent the sample's material properties, as it normalized for mass and geometry (Robling et al., 2014). **Stress** (σ) is force of the applied load divided by area, and corresponds to the force on the y-axis of a force-displacement curve (Einhorn, 1992, Robling et al., 2014). The stress on this y-axis can be compression, tension, shear, or torque (torsion) (Einhorn, 1992). **Strain** (ε) is the net change in length ($\Delta L/L$), and corresponds to the displacement (δ) on the x-axis of a force-displacement curve. Since strain describes a net change in length, it does not have dimensions (Einhorn, 1992, Robling et al., 2014). Generally strains are measured in microstrains ($\mu\varepsilon$) where 1 $\mu\varepsilon$ is equal to a 10^{-6} net change in length. This change in length can be shortening (compression) or lengthening (tension) (Robling et al., 2014).

The initial part of a stress-strain curve is linear, with stress and strain increasing proportionally. This is called the **elastic (or pre-yield) region**, which refers to bone's capacity to return to zero displacement with no energy lost, such that bone is not permanently deformed (Einhorn, 1992, Robling et al., 2014). The slope of the stress-

64

strain curve gives Young's modulus of elasticity, which corresponds to **stiffness** or

rigidity (Einhorn, 1992, Burr, 2011, Robling et al., 2014). Young's modulus (E) is the

proportionality constant between stress and strain given by Hooke's law as $\sigma = E\varepsilon$. Since

strain has no dimensions, Young's modulus has the same units as stress, pascals (Pa),

which are pounds per square inch (Robling et al., 2014). Increased stiffness (larger slope)

is favorable mechanically in the sense that a larger stress is required for a given

deformation. Decreased stiffness (smaller slope) indicates that a smaller stress is required

for a given deformation (Einhorn, 1992).

For loading in one direction (x) perpendicular to the plane of interest, strain is

given by a rearrangement of Hooke's law: $\varepsilon_x = \sigma_x / E$. Stresses in other planes (σ_y, σ_z) are

zero. However, since the material is lengthened or shortened in the x direction, it also

changes its deformation in other planes. For example, if the material is stretched in the x

direction, the y and z directions must shorten to provide the stretched material. This

relationship is described by Poisson's ratio (v), where $v = -\varepsilon_y / \varepsilon_x = -\varepsilon_z / \varepsilon_x$. Poisson's

ratio ranges from perfectly incompressible (0) to perfectly compressible (0.5) and is ~0.3

to 0.35 in bone. Combinations of Hooke's law and Poisson's ratio can be used to derive

equations for stress and strain in x, y, and z planes from uniaxial loading or loading along

multiple axes (Ebacher et al., 2014, Robling et al., 2014).

Generally, the elastic region of the stress-strain curve is offset by 0.2% strain

compared to the force-displacement curve (Robling et al., 2014). **Resilience** describes the

energy under the stress-strain curve stored by bone up to the yield point, and recoverable

after unloading (Einhorn, 1992). Following the elastic region, stress and strain are not

proportional. The end of the elastic region on the stress-strain curve is the yield point, and

the stress at this point is the yield stress (σ_y) (Robling et al., 2014). The yield point is also

called the elastic limit (Einhorn, 1992) After this point, the material enters the **plastic**

(post-yield) deformation region, where energy is lost, the material is permanently

deformed even after unloading. Strain (deformation) continues to increase without a

proportionally large increase in stress (force/area) (Einhorn, 1992, Robling et al., 2014).

At the maximum stress (σ_{ult}), corresponding to ultimate or structural strength, failure of

the material begins (Robling et al., 2014). Therefore the **strength** of bone is calculated as

the maximum stress (height of the stress-strain curve) at which the bone fails (Einhorn,

1992, Burr, 2011). It should be noted that some writings refer to strength as bone's

hardness, which is its resistance to plastic deformation (e.g. Ritchie, 2011). **Ductility**

describes the strain at the point of failure. Brittle materials, such as chalk or osteopetrotic

bone, have minimal or no post-yield deformation, but break soon after reaching the yield

point. (Einhorn, 1992). The total area under the stress-strain curve is **toughness**, which

represents the total energy that the material absorbs before failing (Einhorn, 1992,

Robling et al., 2014). Toughness corresponds to work on the force-displacement curve

(Robling et al., 2014).

3.2. Mechanical Loading Environment of Bone

3.2.1. Mechanical Loading Modes Experienced by Bone

Bone is loaded uniformly along its long axis during **axial loading**. In axial

compression, the ends of bones are pushed together and length decreases. For example,

vertebrae in humans are compressed axially by body weight during upright posture, and

66

during daily activities such as bending or lifting with the back (Cooper et al. 2002). The vertebrae, especially in the thoracolumbar spine, are a common site of traumatic axial compression injuries (Gertzbein et al. 1992). These fractures are common in patients with bones weakened by osteoporosis or certain cancers, such that the compression fracture can occur with minimal loading (Wood et al. 2014). Between 12% and 23.5% of individuals over age 50, both male and female, have at least one vertebral fracture related to osteoporosis (Cooper et al. 1992; Melton et al. 1993; O'Neill et al. 1996; Jackson et al. 2000).

In **axial tension,** the ends of bones are pulled apart and length increases. Bone is weaker in tension than compression (Reilly and Burstein 1974, 1975). Since compression exerts comparatively higher magnitude loads than tension, there is rarely a net tensile strain in bone. Tensile strains can occur regionally, as in bending, or due to pull from muscle attachments, as violently demonstrated in evulsion fractures (Currey, 1968; Einhorn, 1992).

Over 70% of longitudinal forces in bone are due to **bending** (Biewener and Bertram 1993). In bending, cortical regions are tensed and compressed by the same applied load. When a limb pushes against the ground, an equal and opposite Ground Reaction Force (GRF) originates at the center of gravity and pushes back (Lieberman et al., 2004). For example, at midstance, the ground reaction force vector in response to a limb pushing against the ground is nearly vertical. In pure bending (e.g. neglecting axial compression), regions of cortex anterior to the GRF are compressed, while regions of cortex posterior to the GRF are tensed (Lieberman et al.2004). Compressive and tensile

67

stresses in the plane of bending decrease towards the neutral axis, and the net stress is zero where they meet (Robling et al., 2014). Since bone will be formed or resorbed regionally at the periosteal or endosteal surface in relation to these regional strains, quantifying cross-sectional geometry (the distribution of bone in a cross-section) can help infer the causative direction of non-axial loading (Ruff, 2006), and will be discussed in a later section.

Bone is weaker in tension than compression (Reilly and Burstein 1974, 1975). When cyclical loaded to the same magnitude, bone fails more quickly in tension than compression (Caler and Carter 1989, Pattin et al.,1996). Lanyon and Baggott (1976) observed that, in bending, compressed regions of bone have higher strain (x1.9) than tensed regions. In the sheep radius, compressed and tensed regions did not vary substantially in thickness, but the compressed region "seemed further advanced" in remodeling. Tension tests are not necessarily predictive of bone's tensile behavior in bending. Currey (1999) notes that a bending specimen has his tensile stresses in a small surface volume opposite to the central loading point. Tension specimens, being uniformly stressed throughout their volume, have a greater volume in which they can fail at weak points and flaws. Therefore, yield stress in tension under-predicts the bending strength of bone by ~40% (Currey, 1999). Bone yields in tension before compression. In compression, the stress-strain curve has a long elastic region and a comparatively short plastic region. In tension, the elastic region before the yield point is shorter but the plastic region is longer. Due to its large plastic region, tensed bone can withstand a significant

68

amount of inelastic strain (~2%) while increasing comparatively little in stress (<2 GPa) (Wang and Gupta, 2011).

Another force that bone can experience is **shear**, in which the ends of bones move in parallel but opposite directions due to a transverse load (Einhorn, 1992). In this case, the plane experiences shear stress (τ) oriented transverse to the plane. Shear strain (γ) is also measured as $\Delta L/L$, but this gives the radian change in angle between the original vertical orientation of the plane and the sheared, slanted angle of the plane. Shear can be modeled on a stress/strain curve as previously described, with the same stress/strain proportionality $\tau = G\gamma$. In this case, the G constant is the modulus of rigidity in shear (Robling et al, 2014). In **torsion**, the ends of bones are twisted relative to one another. Torsion induces a combination of normal stresses and shear stresses along the entire length of the bone depending on the angle of rotation of the plane (Einhorn, 1992). Shear stress is maximum and normal stress is zero at 0° and 90°, while shear stress is zero and normal stress is maximum at the principle directions, 45° and 135°. In between these angles, bone experiences a combination of shear and normal stress (Robling et al., 2014).

In practice, bones can experience a combination of axial, bending, torsion, and shear loads (Einhorn, 1992, Ruff et a. 1993, Skedros et al. 2005, Lieberman at al. 2004). Bone has **anisotropy**, meaning that its resistance to a force depends on the direction of force (Melton et al., 1988) For example, vertebrae are most resistant to compression (Galante et al., 1970). The proximal femur is resistant to loads parallel to its trabecular architecture (Brown and Ferguson 1978). The femur is more resistant to longitudinal loading than transverse loading (Burnstein, 1976, Einhorn, 1992).

69

Falls provide an example of how mechanical loading modes combine exert force on and fracture bone regions. Approximately 80-90% of all fractures in older adults (age 65+) occur during falls (Sjogren and Bjornstig 1989; Kannus et al., 1999). Forearm fractures, commonly of the distal radius or ulna from a "fall onto an outstretched hand" (FOOSH), comprise an estimated 18.5% of osteoporotic fractures worldwide, with a high prevalence in women (80%) (Johnell and Kanis 2006). Most distal radius fractures occur when the hand strikes the ground with wrist in dorsiflexion (palm-first). The palmar aspect first fails in tension, further bending the wrist in dorsiflexion and compressing the dorsal aspect.

3.2.2. Trade-Offs Between Strength and Toughness in Fracture Resistance

As demonstrated in the comparison of compression and tension, bone cannot maximize both its resistance to plastic deformation (hardness) and its resistance to fracture and crack propagation within the plastic region (toughness) (Ritchie, 2011). Toughness can be measured as the total energy needed for failure as previously describe (Einhorn, 1992, Robling et al., 2014). Bone's resistance to fracture is defined not by its strength, meaning its maximum stress, but by the energy it can absorb before breaking (Burr, 2011). Tough materials dissipate more energy before failure by releasing energy in the form of limited plastic deformations that do not fully fracture the bone. For this reason, toughness can also be calculated from the fracture mechanics needed to initiate or propagate a crack. Therefore, a very hard material that resists plastic deformation cannot also be tough (Ritchie, 2011). A brittle material has high stiffness and high hardness but low toughness because it fails early in plastic deformation (Einhorn, 1992). For example,

70

overly mineralized osteopetrotic bones are very dense and strong. However, these bones are fragile because they can absorb little energy before failure. Conversely, osteoporotic bones are less strong and stiff, but can absorb more energy before failure. Therefore they resist fracture less than a normal bone, but more than an osteopetrotic bone (Burr, 2011).

As a fracture grows, tough materials such as bone actually develop greater resistance to fracture (fracture toughness). This is called resistance curve (R-curve) behavior (Wang and Gupta, 2011). Intrinsic toughening mechanisms elongate plastic deformation, allowing bone to deform more before it initiates or propagates a crack. These mechanisms tend to occur in nanometer hierarchy. Extrinsic toughening mechanisms cannot stop crack initiation, but they can slow or stop an initiated crack (Ritchie, 2011). Intrinsic mechanisms in bone include the flexibility and sliding mechanism of its collagen fibrils (Ritchie, 2011). Mineralized tissue toughness is mostly derived from extrinsic toughening mechanisms, including dissipation of energy through microdamage, crack deflection at secondary osteon cement lines, and crack bridging (Nalla et al., 2005) Microscopic damage is actually an advantage to bone in small amounts because it dissipates energy in the plastic deformation region that would fracture a more brittle material (Martin, 2003). Even though microdamage does weaken bone, mechanosensory mechanisms allow bone to target and remodel the damaged area. Microdamage threatens bone when it accumulates quicker than it can be repaired, due to very high strain (Frost, 2003) or senescence of bone's cellular targeting and remodeling mechanisms.

3.3. Bone Functional Adaptation

Bone is a mechanical organ, and the cellular processes that create its histological components are primarily driven by mechanical stimuli. In order to distinguish pathological bone, one must first understand the impact of mechanical loading on the variability of these histological features. Pathological conditions drive cellular activity and its histomorphometric products outside of this normal variation. In this subsection we discuss the theoretical basis for interpreting histomorphometry that links biomechanical inputs to cellular activity outputs.

Bone functional adaptation is a theoretical concept that explains how bone adjusts the amount and distribution of its mass to withstand that bone's typical mechanical loads. While this concept is regularly applied to the external size and shape of the bone, tissue within the bone cortex also adapts. Bone functional adaptation is a feedback-based model in which increasing mechanical strain leads to bone deposition, while decreasing mechanical strain leads to bone resorption. Equilibrium strains that fall within a range of "optimum customary strain level" do not produce a net change in bone deposition (Lanyon et al., 1982). The strain level perceived to be "optimal" by bone during its typical mechanical loading likely is determined by a combination of factors, including skeletal location, genetics, hormonal and other physiological influences, and the breakdown of these influences with senescence and disease (Heaney et al., 2000; Ruff et al., 2006; Robling et al., 2014). More specifically, bone is known to adapt to regional strains, not total strains (Lanyon et al., 1982; Ruff et al., 2006). Lanyon et al. (1982) found that when strain is distributed regionally bone forms preferentially on the periosteal

72

surface of the region under higher strain, rather than uniformly around the circumference of the bone.

Frost's (1987a) mechanostat provides a strain-based mathematical model for how this feedback might occur. Strains falling below a disuse threshold result in bone resorption, strains within the equilibrium range produce remodeling to repair and maintain bone, and strains above the equilibrium range stimulate modeling, meaning the formation of new bone where it was previous absent. Higher strains produce the accumulation of fatigue damage, and ultimately result in failure (Frost, 1987a). Mechanical studies on bone allowed Frost to update his model with quantifiable strain magnitudes for these thresholds (Frost, 2003). See Pearson and Lieberman (2004) for a comprehensive overview of alternative models for bone functional adaptation.

3.4. Predicting Stochastic vs. Targeted Remodeling

In targeted remodeling, bone responds to a specific mechanical need for bone resorption or repair. In stochastic remodeling, physiological needs of the body regulate bone formation and resorption (Martin, 2002, Eriksen, 2010). The relative contributions of targeted and stochastic processes to overall remodeling have been particularly debated. Many studies have shown that resorption spaces are not randomly associated with microdamage, but specifically target its location (e.g. Burr et al., 1985, Burr and Martin, 1993, Mori and Burr, 1993, Li et al., 2001). For example, Burr et al., (1985) found that resorption spaces in cortical bone of dog ulnas were associated with repair of fatigue microdamage 44 times more often than by chance alone. Just because remodeling is

73

capable of targeting microdamage does not mean that this is the primary impetuous for remodeling. Mori and Burr (1993) estimated that about 30% of total remodeling in dog radii is targeted remodeling. Conversely, Li et al., (2001) found that 90% of resorption spaces were not associated with microcracks in beagle ribs. O'Conner et al., (1982) found that maximum strain rate accounted for $68-81\%$ of total variance in bone formation at the surface (e.g., modeling). However, maximum strain rate accounted for but 43.7% of total variance in remodeling within cortical bone. Other histological structures produced by remodeling also have a complex association with mechanical loading, such as the distribution of secondary osteons and osteocyte lacunae (Skedros et al., 2004). Martin (2002) proposed that these associations between remodeling activity and microdamage may be irrelevant, since remodeling complexes (BMUs or Basic Multicellular Units) can progress several millimeters through bone. He created a mathematical model showing that all remodeling in cortical bone could result from targeting, provided that BMUs can "steer" towards microdamage. Concentrating on histomorphology alone would seem to place mechanical and physiological influences at an unresolvable impass. However, careful examination of the biochemical pathways underlying mechanical and physiological modeling and remodeling shows that these two influences are intimately linked. Physiological factors influence bone shape by regulating the sensitivity of bone to mechanical demands (Rauch and Shoenau, 2001, Robling et al., 2014). This allows bone to pursue a mechanically optimal amount and distribution of mass in healthy individuals, while reserving the capacity to suspend this optimization in times of physiological need.

74

3.5. Structural Properties of Whole Bone in Cross-Section

Remodeling alters the material properties of bone by reorganizing its internal structures, such as its lacunar-canalicular architecture, vascular porosity, and lamellar organization. The structural properties of bone are altered by changes to its external size and shape produced by modeling or resorption on periosteal or endosteal surfaces (Martin, 1993). The size and shape of cortical bone in cross-section is largely established by modeling during growth. However, periosteal apposition and endosteal resorption accelerate during senescence and can either preserve or compromise bone strength, dependeing on their balance.

3.5.1. Radial Expansion of the Cross-Section Results From Growth in Length

During growth, increases in bone length impose more strain on the bone during bending. Modeled as a beam, the deflection of a bone is given by the equation $ML^2/8EI$, where M is the bending moment (combination of forces and moments on a region), L is length, E is Young's modulus, and I is the area moment of inertia. In other words, bone deflection increases with the square of its length (Turner, 2006). Bones grow in length before they grow in mass during the pubertal growth spurt in both sexes, during which they have a higher rate of fracture (Rauch and Shoenau, 2001). This strain drives radial expansion of the whole bone in cross-section.

Hollow tubes are more resistant to bending and torsion when their mass is distributed further from the neutral axis (Ruff and Hayes, 1983, Einhorn, 1992). For a given bending moment, bone can decrease its deflection by increasing the area moment of inertia (I). For a tubular bone, $I = \frac{\pi}{4}(r_p^4 - r_e^4)$, where r_p is the periosteal (outer) radius

75

and r_e is the endosteal (marrow cavity) radius. In mammals, the periosteal radius is about 1.8 times the endosteal radius, so $I \approx 0.71 r_p^4$. In other words, bone can compensate for the deformation induced by its increasing length by increasing its periosteal radius (Turner, 2006). For example, an 8% increase in periosteal radius is associated with a 36% increase in bone rigidity (stiffness) (Turner, 2006). During periosteal expansion, the endosteum is resorbed, maintaining the ratio between their radii (Martin, 2003). Cortical area, the amount of cortical bone in a transverse cross-section, is also proportional to resistance to axial compression loads caused by body weight (Skedros, 2011). Increasing body mass during growth also contributes to the mechanical demand for radial expansion through modeling (Rauch and Shoenau, 2001).

As discussed in Chapter 2.9, estrogen increases endosteal bone formation, and its declining levels during menopause lead to cortical bone resorption at the endosteum. For example, in a modern Australian population, midshaft femoral cross-sectional dimensions are comparable between young males and females when adjusted for height. Femora became larger and more circular with age in both sexes, expanding significantly in height normalized mediolateral diameter (~18% male, ~10% female) and anteroposterior diameter (~%6 male and female). However, male bone dimensions exceed those of females during and after menopause (Feik et al., 2000). Schlecht et al. (2015) found that young women (20 – 35 years old) have significantly less (6-25%) cortical area than expected from their body size and external bone size (robustness). In males, this periosteal apposition compensates for age-associated endosteal resorption. Periosteal apposition needs to restore only ~30% of the bone resorbed at the endosteum

to preserve resistance to bending or torsion, since distribution of mass further from the neutral axis is more mechanically effective (Martin, 1993). For example, in the femur, males and females decline equally in material strength related to bone composition, but female structural strength declines with age while male structural strength is preserved by periosteal apposition (Martin and Atkinson, 1977). Males, but not females, similarly preserve or expand cortical area and its associated cross-sectional measurements of resistance to bending or torsion in the tibia (Ruff and Hayes, 1988), radius (Burr and Martin, 1983), and vertebral body (Mosekilde and Mosekilde, 1990).

Loss of cross-sectional robustness is associated with decreased stiffness and reduced resistance to fracture, as demonstrated in the tibia (Armstrong et al., 2004; Jepsen et al., 2013), femur, humerus, radius, second metacarpal (Schlecht et al., 2014), and rib (Murach et al. 2017). Aging males still experience reduced bone strength and increased fracture risk due to previously discussed declines in bone quality (Martin, 1993). One in three women and one in five men over age 50 will experience an osteoporotic fracture (Melton et al., 1992; Melton et al., 1998; Kanis et al., 2000). However, male preservation of structural properties of bone strength helps explain their lower overall incidence of osteoporotic fracture. Females experience 1.6 times as many osteoporotic fractures as males, or 61% of the worldwide incidence of all fractures. Prevalence is particularly high in females for osteoporotic fractures of the forearm (80%), humerus (75%), hip (70%), and vertebrae (58%) (Johnell and Kanis, 2006).

77

3.5.2.   *Cortical Drift During Growth Alters Cross-Sectional Shape*

Strain-responsive modeling is not uniform within a cross-section, but instead varies between planes such as the anterior-posterior or medial-lateral axis. Within a given plane, resistance to bending is also approximated by area moment of inertia (I). The equation $I = \int y^2 \delta A$ ^{2} integrates small units of area (δA) along the plane of interest with their perpendicular distance (y) from the neutral axis (Skedros, 2011). The need for resistance to bending in a given plane determines the distribution, and therefore shape, of bone in a given cross-section (Ruff and Hayes 1983). During growth, bones use cortical (modeling) drift to adapt their shape to the mechanical demands of a changing body structure and capacity for physical activity. In this modeling process, bone is formed on the periosteum and resorbed from the endosteum to shift a region of cortex in a given plane (Frost, 2003) This high activation frequency creates large concentrations of intracortical porosity as the periosteal cortex is resorbed and the endosteal cortex is trabecularized in the direction of drift (Frost, 1969; Agnew et al., 2013). The actively drifting cortex results in extreme tissue heterogeneity that may indicate whether a bone is more or less likely to resist loading. Agnew et al. (2013) found that in growing human ribs the percentage of Haversian bone in a cross-section, as opposed to primary bone, has a positive relationship with elastic modulus. During aging, changes in gait can again activate cortical drift. In Feiket al.'s (2000) modern Australian population, the anterior cortex expands with age in both females (9.3% increase) and males (3.1% increase). They attribute this anterior drift to a stooping posture, which thrusts the hips, head, and thorax forward.

78

The endosteal lamellar pocket (ELP), so named by Maggiano et al. (2011), is a histological remnant of this cortical drift that remains in the adult cross-section. ELPs are large regions of primary bone that form at the endosteum as hemicircumferential lamellae. In the adult femur, they border approximately one-sixth to one-half of the medullary cavity and commonly cover half of the cortical thickness in this region. ELPs have few longitudinally oriented secondary osteons marking remodeling activity, and are instead vascularized instead by radially oriented transverse canals (Maggiano et al. 2011). For example, the midshaft femur drifts rapidly posteriorly and medially in toddlers and slowly anteriorly and laterally starting in childhood (Goldman et al., 2009). To move the femur laterally, the lateral cortex forms bone on its periosteal surface and resorbs bone on its endosteal surface. The medial cortex also moves laterally through the reverse pattern of periosteal resorption and endosteal formation. The primary bone formed on the medial endocortex forms an ELP that persists in the adult femur, although its anterior or posterior positioning varies between individuals (Maggiano et al., 2011). These ELPs are more prominent in the distal femur (Maggiano et al., 2015). ELPs in the adult humerus instead reflect torsional loading during growth. The midshaft and distal diaphysis display clockwise drift, wherein the periosteal bone rotates from posterior-medial to posterior, and the endosteal bone rotates from anterio-medial to anterio-lateral (Maggiano et al., 2015).

3.5.3. *Assessment of Axial Loading Differences With Relative Cortical Area*

Cross-sectional size and shape are modeled by mechanical loading, primarily during growth. Physical activity patterns, diet, health, and aging can alter typical

79

mechanical loading, so groups that vary in these biocultural circumstances will also vary in cross-sectional size and shape. Over the last few decades, bioarchaeologists and paeleoanthropologists have used population and group differences in cross-sectional geometry to make inferences about the evolution of bipedalism, along with shifting patterns of subsistence, division of labor, and mobility (reviewed in Ruff and Larsen, 2014).

Relative cortical area (RCA), also called percent cortical area (%Ct.Ar), can be used to infer changes in bone mass between groups or over time (Sladek et al., 2006). %Ct.Ar is measured as Cortical Area (Ct.Ar) / Total Area (Tt.Ar), and therefore describes the proportion of total area of a cross-section that contains cortical bone. For example, a %Ct.Ar of 0.5 indicates that 50% of the total area (i.e., transverse size) of cross-section contains cortical bone (Peck and Stout, 2007). %Ct.Ar is not standard for an individual, but varies intraskeletally. For example, Auerbach and Ruff (2006) determined that the humerus shows a right-side bias in midshaft diaphyseal breadth. They attribute this difference to human prevalence of right-handedness. Similarly, skeletal samples of the upper limb from Neandertals to the present show significant variability in upper limb asymmetry along the shaft (Trinkaus et al., 1994). Peck and Stout (2007) and Stewart et al. (2015) both found that the midshaft rib has significantly lower %Ct.Ar than the dynamically loaded long bones of the upper and lower limbs. In the upper limb, humeri have a relatively low %Ct.Ar while radii and ulnae have a relatively high %Ct.Ar, reflecting more diverse limb use. Potentially due to their shared and constant role in bipedalism, the femur and tibia have very similar %Ct.Ar, grouping with (Stewart et al.

80

2015) or without (Peck and Stout, 2007) the non-weight bearing fibula. Two immobilized quadriplegic individuals had extremely low femoral %Ct.Ar compared to the mobile group (Peck and Stout, 2007) providing evidence for reduction in bone with pathological disuse.

%Ct.Ar does not quantify the absolute magnitude of axial load, but is simply used to compare the relative values between individuals. For example, Sladek et al. (2006) inferred that Late Eneolithic and Early Bronze Age central Europeans had similar patterns of mobility due to their similar tibial %Ct.Ar values. Diet also contributes to the capacity of bone to form and retain mass. Cho and Stout (2011) detected higher cortical bone turnover and loss in females compared to males in an Imperial Roman population. While female bone loss is probably partially due to menopause and lactation, Cho and Stout (2011) also implicate lesser access to calcium-rich marine foods in this population.

3.5.4. Cross-Sectional Shape as a Metric of Loading Direction

Since most loading during locomotion is not axial, differences in physical activity and limb use between groups are better inferred by relative cross-sectional shape than by relative cross-sectional size (Ruff and Larsen, 2014). Cross-sectional shape analysis quantifies the distribution of bone along planes of bending within the cross-section. Area moment of inertia (I), also called second moment of area, essentially measures the distribution of bone around the neutral axis, as previously described (Ruff and Hayes, 1983). It is often used to measure resistance to bending perpendicular to anatomical planes, or around the principal axes in a cross-section. Bending about the planes of shortest distribution of tissue (the minor axis) gives the greatest resistance to bending

81

(I_{max}), whereas bending about the longest distribution of tissue (the major axis) gives the least resistance to bending (I_{min}) (Ruff and Hayes, 1983). Circularity of the bone is given by the ratio of any two perpendicular area moments of inertia, most typically $I_{max}/I_{min.}$ When the bone is more circular, I_{max} and I_{min} are closer in value, so the circularity ratio is closer to 1 (Ruff and Hayes, 1983).

Several additional calculations may be derived from area moment of inertia (I) to summarize the section's overall resistance to bending. The polar moment of inertia (J), often used as an estimate of resistance to torsion, is given by the sum of two perpendicular area moments of inertia, such as $I_{max} + I_{min}$ (Ruff and Hayes, 1983). The section modulus (Z), is calculated as I_{max}/c, where I is the area moment of inertia and c is the maximum radius of the cross-section (Juvinall and Marshek, 1991). Z approximates the cross-section's resistance to loading best by considering distribution of tissue. It has been shown to be strongly correlated with the strength of bone in mechanical tests of bending or torsion (Klenerman et al., 1967; Martin and Burr, 1984b; Murach et al. 2017).

Over the last few decades, anthropologists have used these estimates of mechanical loading history to make inferences about past behavior and physical activities (Ruff and Larsen, 2014). In paleoanthropology, cross-sectional geometry has been broadly applied to fossil remains to track changes in the bending environment associated with shifting locomotion patterns, limb length, and body size (e.g. Endo and Kimura, 1970; Lovejoy and Trinkaus, 1980; Kennedy, 1983; Trinkhaus and Ruff, 1989; Abbott et al., 1996; Ruff, 1993; Trinkaus et al., 1998; Ruff, 1999; Ruff et al., 1999; Trinkaus and Ruff, 1999a; Trinkhaus and Ruff, 1999b; Trinkaus et al., 1999; Ruff, 2009; Kupervage

and Eckhardt, 2009; Bleuz, 2012). In bioarchaeology, cross-sectional geometry has been shown to shift at the population level with changes in subsistence, division of labor, mobility, and tool use (reviewed in Ruff and Larsen 2014).

3.5.5. *The Parabolic Index: An Overlooked Cross-Sectional Indicator of Osteoporosis*

Cross-sectional geometry calculations are not intended to accurately represent absolute values of bending or torsional resistance for individuals (Ruff et al. 2006). Absolute values are generally only reported in depth for individual fossil hominins, due to the small sample size. Even then, these hominins are almost always contextualized by cross-sectional measurements from larger populations of other hominin fossils, primates, and/or anatomically modern humans (e.g. Gruss, 2007; Ruff, 2009; Bleuze et al., 2012). Most bioarchaeological analyses look for broader population or sub-population patterns and distributions in cross-sectional shape and size, since individuals are not guaranteed to be representative of the entire population.

Conversely, the parabolic index is an old but largely overlooked cross-sectional measurement that does have potential for assessing bone strength in individuals. First proposed by Epker and Frost (1964), this metric incorporates both the percentage of bone mass in the cross section and its distribution around the centroid. The parabolic index (Y) is a ratio of the relative cortical area to the relative marrow area, also written as follows:

$$Y = (\text{Cortical Area} * \text{Marrow Area}) / (\text{Total Area}^2)$$

Regardless of their individual percentages, relative cortical area and relative marrow area sum to 1.00, meaning 100% of the total area of the cross-section. The parabolic index (Y)

reaches a maximum value of 0.25 when relative cortical area and relative marrow area are both equal to 0.5, each composing 50% of the total area. Epker and Frost (1964) derived the parabolic index from the mechanics of hollow cylinders loaded slightly off center, wherein the "parabolic formula for nominally concentrically loaded columns" has an optimal wall-to-lumen ratio of 0.5 to 0.5 (Olsen, 1956, Popov, 1952, cited in Epker and Frost 1964:472). Hollow cylinders closer to this ratio better withstand longitudinal compression loads (Takahashi and Frost, 1966). The parabolic index also incorporates a non-axial loading component because "it is assumed that the column is loaded slightly off center so that there is a definite bending or buckling tendency" (Epker and Frost, 1964:472). Both Epker and Frost (1964) and Takahashi and Frost (1966) found that metabolically normal ribs approached the maximum parabolic index of 0.25, while osteoporotic ribs did not exceed a parabolic index threshold of 0.19.

Takahashi and Frost (1966) noted that, in their modern population, males steadily decline in the parabolic index after age 35. Females remain near the maximum parabolic index until a rapid post-menopausal drop after age 50. Males and females both approach an osteoporotic parabolic index after age 70. In contrast, Cho and Stout (2003) and Beauchesne and Agarwal (2017) do not detect sex differences in Imperial Roman populations at Isola Sacra and Velia, respectively. However, the Velia population also lacks the significant sex differences seen in modern populations for other cortical geometric measurements (metacarpal cortical index, rib relative cortical area), as well as rib cortical histomorphometry and vertebral trabecular bone volume. While no ribs in the Velia population fall below the parabolic index threshold for osteoporosis (0.19), the

84

parabolic index does decline significantly with age in both males and females (Beauchesne and Agarwal, 2017).

Frost (1963) argues that, due to their high remodeling rate, ribs reflect physiological changes in bone biology due to age and disease earlier then appendicular bones. This suggests that different skeletal elements within an individual might differ in the parabolic index. The threshold indicative of osteopenia or osteoporosis might also vary between types of bones. A comprehensive study of intraskeletal variability in the parabolic index in metabolically normal and pathological individuals would improve the applicability of this metric in archaeological and forensic contexts. Preliminary examination of a small sample from Cole and Stout (2016) suggest that the midshaft femur, tibia, and rib of the same individuals do significantly differ in the parabolic index. However, correcting for cortical porosity brings these skeletal elements into greater agreement as to whether an individual falls above or below the 0.19 threshold for osteoporosis.

4. Mechanical Predictions of Microstructural Patterning Over the Lifespan

4.1. Introduction: Normal Trajectory of Remodeling Rate Over the Lifespan

Variation in remodeling rate depends not only on mechanical stimuli, but on changes in celluar activity over the lifespan, particularly during growth and senescence. A driving force behind toughening mechanisms in bone is their hierarchal structure, with organization from the molecular level to the macroscale (Allen and Burr, 2008; Ritchie, 2011; Wang and Gupta, 2011). Since material properties of bone are most strongly associated with remodeling (Martin, 1993), the rate of remodeling is a major determinant of bone strength as it relates to these properties. Children have high remodeling rates during growth, which slow with adulthood. Remodeling rates reach a minimum at about

age 35 and then begin to increase again (Martin, 1993). One reason for this increase in the remodeling rate in individuals over 35 years of age is a decline in muscle strength and physical activity (Thomas et al., 2005). This decline can trigger increasing amounts of disuse remodeling, in which more bone is resorbed than is formed in its place (Frost, 2003). A second driving force behind the increase in remodeling rate is that stimuli for remodeling (such as fatigue damage) continue, but bone's cellular capacity to form new bone declines. High remodeling rates in youth lead to a positive bone balance, but high remodeling rates in age lead to a net bone loss (Seeman and Delmas, 2006).

In growth and adulthood, estrogen promotes endosteal bone formation, while testosterone promotes periosteal bone formation. As hormone levels decline with age, osteoblasts are no longer driven by these additional signals for bone formation (Pearson and Lieberman, 2004). Osteoblasts and their progenitors also undergo senescence with age, evidenced by a decline in production of alkaline phosphatase (an enzyme that is a byproduct of bone formation) and osteoprotegerin (a protein produced by osteoblasts that inhibits osteoclastogenesis), which indicate a decline in capacity for differentiation and a reduced sensitivity both to chemical and mechanical signaling pathways (Tanaka and Liang, 1996; Nishida et al., 1999; Makhluf et al., 2000; Batge et al., 2000). Researchers are still debating why this senescence occurs and have considered hypotheses such as the accumulation of reactive oxygen species, irreversible epigenetic modifications, and telomere shortening (Pearson and Lieberman, 2004). Biocultural factors can also modify age-associated bone loss. In both modern and archaeological population, bone loss is associated with inadequate nutrition (e.g. calcium and vitamin D deficiency, increased

87

animal protein and phosphorus, malnutrition). Reproductive stress (pregnancy, lactation) and lifestyle choices (lack of physical activity, smoking, drinking) also appear to be risk factors for osteoporosis (reviewed in Agarwal, 2008). Remodeling in old age does not reap the mechanical benefits of remodeling in youth due to the net loss of bone (Martin, 1993).

4.2. Sexual Dimorphism in Trabecular Bone Loss with Age

Unlike the cortical bone loss associated with aging, trabecular loss begins during sex hormone sufficiency in early adulthood. Riggs (et al., 2008) compared cortical and trabecular bone loss across the lifespan in the distal radius, distal tibia, and lumbar spine. They found that, before age 50, women have already lost 37% and men have lost 42% of the total amount of trabecular bone they will lose over their lifetimes. One potential cause of this early trabecular bone loss is a decline in serum IGF-I (56% in women, 24% in men) and serum IGFBP3, a sign of growth hormone (GH) secretion (10% in women, 15% in men) between ages 20 and 50. Trabecular bone loss also accelerates at periomenopause in women, as estrogen levels decline, and after age 65 in men, as sex steroid levels decline. In comparison, only 6% of lifetime cortical bone loss occurs before age 50 in women, and only 15% in men (Riggs et al., 2008). Trabecular bone loss in early adulthood has also been detected in the proximal femur (Riggs et al., 2004) and lumbar spine (Meier et al., 1984; Kalender et al., 1989. Yu et al., 1999. Riggs et al., 2004).

Men tend to lose cancellous bone through trabecular thinning, while women decline in trabecular number. This variation may contribute to the lower fracture risk in males. In their study of the distal radius, Khosla et al. (2005) found that cortical thickness

88

and cortical vBMD declines largely after age 50 in both and women. However, age-associated changes in trabecular bone structure begin earlier. Trabecular bone volume/tissue volume (BV/TV) decreases similarly in women (-27%) and men (-26%) between ages 20 and 90. Young men have thicker trabecular than young women. Between ages 20 and 49, trabeculae become thinner in men, increasing trabecular number as struts are perforated and separated. In contrast, aging women experience trabecular loss, signified by decreased trabecular number and increased trabecular spacing (Khosla et al. 2005). The iliac crest displays similar patterns of female trabecular loss as opposed to trabecular thinning (Parfitt et al. 1983; Han et al. 1996). For the same loss of trabecular volume, a reduction in trabecular number reduces bone strength and Young's modulus two to five times more than trabecular thinning (Silva and Gibson, 1997). This structural compensation for trabecular volume loss in aging men may contribute to their lower fracture risk (Khosla et al., 2005).

4.3. Nanoscale: Collagen and Mineral Mechanics

4.3.1.   Organization of the Mineralized Matrix

By weight, bone is 65% hydroxyapatite mineral, 25% organic component, and 10% water. The water is either bound to the collagen and mineral or flows through lacunar-canalicular and vascular channels, as described in Question 1: Mechanotransduction. The organic matrix is 90% collagen, mostly type I collagen with small amounts of type III and V. The other 10% of the organic matrix consists of non-collagenous proteins (NCPs). Of these NCPs, 15% are found within bone cells and 85% outside bone cells (Burr and Akkus, 2014). Collagen is defined as a structural protein

containing a collagen triple helix motif, meaning three polypeptide chains with Gly-X-Y amino acid repeats. Type I collagen contains two α1 chains and one α2 chain (Van der Rest and Garrone, 1991).

After type I collagen is secreted by osteoblasts, its non-helical N- and C-telopeptides are cleaved by a protease. This allows the molecules of collagen to assemble into fibrils (Rossert and de Crombrugghe, 2002). Individual collagen molecules are 1.5 x 300 nm in size, and they organize into collagen fibrils 80 – 100 nm in diameter (Wang and Gupta, 2011). Within the fibril, collagen molecules are quarter-staggered, meaning that they one end of each molecule overlaps with the 40-nm space between two adjacent molecules (Rossert and de Crombrugghe, 2002) The combination of the gap and overlap creates the characteristic 67 nm D banding pattern seen in electron microscopy (Rossert and de Crombrugghe, 2002, Burr and Akkus, 2014). These gaps are filled by carbonated apatite platelets measuring about 50 x 25 x (1.5 – 4 nm), oriented parallel to the long axis of the fibril (Wang and Gupta, 2011). Even though non-collagenous proteins are associated with mineralized collagen, there is actually a large space between these structures. Atomic force microscopy shows that the surfaces of collagen fibrils are covered with significant amounts of apatite mineral (Sasaki et al., 2002, Hassenkam et al., 2004, Hansma et al., 2005). Bundles of parallel collagen fibrils are called collagen fibers, which is the structural unit typically discussed at the tissue level (Rossert and de Crombrugghe, 2002). Typically, these fibers are 150 nm in diameter and 10 µm long (Burr and Akkus, 2014). Osteoporotic bone has reduced mean collagen fibril diameter,

which may explain some of its increased fragility (Kafantari et al., 2000, Tzaphlidou and

Kafantari 2000)

4.3.2. *Loading at the Nanoscale*

The first nanoscale model of collagen and matrix visualized mineral platelets in

rows parallel to collagen (Akiva et al., 1998). The strength of bone predicted from this

model was limited by the weak ductile collagen rows in between brittle mineral rows in

the fibril. Collagen is ductile and has a low Young's modulus (stiffness) (Wang and

Gupta, 2011). Jager and Fratzl (2000) proposed the quarter-staggered array of collagen

and mineral platelets previously described. In this model, the collagen fibrils stretch in

shear to transfer the tensile load to the mineral platelets. In turn, the platelets carry the

tensile load (Gupta et al., 2005, Wang and Gupta, 2014). The strain ratio of fibril to

mineral is 5:2 in tension, but collagen transfers this strain to the mineral platelets. This

coupled process shields the minerals by distributing the force of the load (Fratzl et al.,

1994, Gao et al., 2003). Consequently, mineral in bone can support twice the fracture

load as bulk hydroxyapatite (Gupta et al., 2006). In turn, the mineral platelets compensate

for collagen's low stiffness. Composite stiffness (E) is proportional to $G_p\rho^2$, where G_p is

the protein stiffness and ρ is the aspect ratio of the mineral platelets (Gao, 2006). Since

mineral platelets have a high aspect ratio ρ (length/height) of ~30 to 40, they raise the

composite stiffness of the mineralized matrix and compensate for the low protein

stiffness G_p (Wang and Gupta, 2014). Mineral and collagen interfaces occur both within

collagen fibrils and at the surfaces between mineral-coated fibrils, as previously

discussed (Wang and Gupta, 2011). Gupta et al. (2005, 2006) found through synchrotron

91

X-ray scattering that collagen fibril strain is almost constant in the inelastic region. They proposed that Jager and Fratzl (2000)'s model is replicated at the collagen fibril scale. When loaded, the fibrils deform in tension and shear in the extrafibrillar matrix, spreading the tensile stress between adjacent fibrils (Gupta et al., 2006). Mineral is therefore a key determinant of nanoscale elastic and plastic properties, while collagen is responsible for viscoelastic properties, which resist shear flow (Kim and Elias, 2014). The ultimate strength of bone against failure is a consequence of the individual strengths of collagen and mineral platelets, along with their interfacial interaction (Gao, 2006).

4.3.3. *Intraskeletal Variation in Nanoscale Mechanical Properties*

Variation in mineralization helps explain how the mechanical properties of bone tissue change with tissue and location. Higher mineralization promotes stiffness, while lower mineralization promotes energy dissipation (Burr, 2011). In the rat cortex, the mineral to matrix ratio explains 54% of variation in Young's modulus and 62% of variation in hardness as measured by nanoindentation (Pathak et al., 2011). However, newly formed (and therefore less mineralized) cortex has a larger capacity for dissipating energy (Donnelly et al., 2010)

Additionally, the mode of loading on a skeletal region can change its strain distribution between mineral and collagen. Gupta et al. (2005, 2006) found that bovine bone tensed in the elastic range distributes its strain in a ratio of 12 (overall tissue) : 5 (collagen) : 2 (mineral). However, bovine bone compressed in the elastic range distributes its strain in a ratio of 1.6 (overall tissue) : 2 (collagen) : 1 (mineral). Even though the elastic modulus is the same, the strain distribution is different. Raghavan et al.

92

(2008) found that minerals became more ordered in bovine bone loaded under tension. Wang and Gupta (2011) hypothesize that bone geometry may complicate this strain distribution.

4.3.4. Deformation at the Nanoscale

In recent years, models have emerged to explain how damage begins at the nanoscale. Gupta et al. (2005, 2006) used synchrotron structural data and thermal activation analysis to propose that ionic bonds break between collagen and mineral within fibrils (intrafibrillar decohesion) or between fibrils (interfibrillar decohesion). Mercer et al. (2006) noted that bovine bone did not show a significant change in initial loading modulus. They inferred that collagen and mineral platelets within fibrils slip apart at a thin adhesive layer between them. Early in this slip, before shear stress reaches a critical value, friction keeps the collagen and mineral intact. Slip then moves from the edges of the mineral platelet to the center. This explains the increase in stress following yield, which results from collagen stretching in this model (Mercer et al., 2006, Wang and Gupta, 2011). Wang and Gupta (2011) also argue that local breaks could coalesce into cracks visible in confocal or light microscopy. For example, diffuse microdamage occurs below the size of lamellae (1 – 3 µm) and may even occur at the collagen fibril level (> 1 µm) (Diab et al., 2006, Braidotti et al., 1997)

Bone can display R-curve behavior with increasing resistance to a growing fracture even at the nanoscale. Noncollagenous proteins (NCPs) coat the surface of the collagen fibril, serving as an adhesive with adjacent fibrils (Hansma et al., 2005). When bone is deformed, these NCPs dissipate energy by stretching in length and breaking

"sacrificial bonds" (Hansma et al., 2005, Fatner et al., 2007). After unloading, these bonds quickly reform (Seref-Ferlengez et al., 2015) For example, osteopontin and osteocalcin have roles in regulating mineralization (George, 2008) but they also appear to be involved in this toughening mechanism (Fratzl and Weinkamer, 2007, Fatner et al., 2007)

4.3.5. *Changes with Age: Collagen Cross-Linking*

The post-yield behavior of bone is related both to collagen content, as discussed, and to collagen cross-linking (Ruppel et al., 2008). Enzymatically mediated cross-links cross-links connect adjacent collagen molecules at their N- and C- terminuses (Burr and Akkus, 2014). These cross-links begin as divalent cross-links, formed by the condensation of hydroxyallysine (HYL). The enzyme lysyl oxidaze links two Hyl residues with a Hyl from the α-helix, forming pyridinoline (PYD), or with a lysine from the α-helix, forming deoxypyridinoline (DPD) (Ruppel et al., 2008). These stable and mature trivalent cross-links increase up to a tissue age of 10 – 15 years (Garnero et al., 2006) Enzymatically mediated crosslinks are important for the tensile and viscoelastic properties of the collagen matrix (Yamauchi et al., 1998a, 1998b). For example, high PYD content has been linked to higher strength to failure (Banse et al., 2002). Remodeling reduces the mean tissue age of the bone, increasing the number of immature divalent cross-links (Robins and Brady, 2002). Mineralization of new bone can also slow the maturation of divalent cross-links (Eyre, 1981). Paradoxically, osteoporotic individuals decrease in the number of divalent cross-links, which increases their PYD

94

ratio. However, this may be due to variations in maturation rate or to post-translational modifications to the collagen (Paschalis et al., 2004).

Non-enzymatic cross-links can be formed randomly between collagen molecules and collagen fibrils by advanced glycation end products (AGEs). These condensations of arginine, lysine, and ribose accumulate in the extracellular matrix (Burr and Akkus, 2014). AGEs form over years and therefore accumulate with tissue age (Monier, 1989) AGE accumulation reduces collagen elasticity and is associated with markers of bone brittleness, including declining toughness and strain to failure (Ruppel et al., 2008). Experimental studies have shown that cracks grow more easily in bones with non-enzymatically cross-linked collagen (Vashishth et al., 2001, Vashishth 2009). While these cross-links do stiffen bone, they significantly reduce toughness in terms of the post-yield energy required to fracture the bone (Tang et al., 2009)

Extracellular sugars are associated with non-enzymatic cross-link formation, which is one source of fragility in diabetic bone (Ruppel et al., 2008). In addition to forming non-enzymatic cross-links, AGEs bind to the RAGE receptor on the osteocyte plasma membrane, activating NF-κB and stimulating the release of pro-inflammatory cytokines (IL-1α, IL-6, TNF-α). Tpphis inflammation enhances osteoclast activation and bone destruction (Ding et al., 2006, Nyman et al., 2007).

4.3.6. Changes with Age: Secondary Mineralization

About five to ten days after osteoid deposition, the matrix begins to mineralize through nucleation of the crystals (Parfitt, 1987). The mineral crystal established by primary mineralization is 50 – 70% of its maximal value (Amprino and Engstrom, 1952,

95

Marotti et al., 1972, Bala et al., 2010) Based on animal studies, the mineral crystal

establishes up to 80% of its indentation stiffness during this period (Busa et al., 2005,

Bala et al., 2010). Mineralization speed slows significantly after a few days or weeks

(Bala et al., 2013). Secondary mineralization, during which the crystal matures, occurs

over an ensuing time period that researchers have estimated as less than a year to thirty

years (Fuchs et al., 2008, Handschin and Stern, 1994, Akkus et al., 2003). The apatitic

core of a mineral crystal is enveloped by a hydrated layer and then surrounding fluid. The

hydrated layer contains exchangeable mineral ions that facilitate mineral maturation. As

the mineral crystal matures, its apatitic core grows in size, and its hydrated layer shrinks

(Bala et al., 2013). After elongating into a plate, the mineral crystal thickens (Fratzl et al.,

1991) The mineral crystal also increases in crystallinity, which refers to the size and

perfection (order) of the crystal lattice (Bala et al., 2013). Finally, the crystal may alter its

substitution of carbonate ions for PO_4^{3-} or OH^- which decreases its atomic order (Fuchs et

al., 2008). With crystal maturity, carbonate has been found to both increase (Pellegrino

and Blitz, 1972, Yerramshetty et al., 2006, Fuchs et al., 2006, Akkus et al., 2003) and

decrease (Paschalis et al., 1996, Ouyang et al., 2004). Since the mineral crystal must still

fit into the organic matrix, crystal growth stops at about 95% of the theoretical maximum

(Bala et al., 2013). At this point, the organic matrix is said to be "fully mineralized"

(Akkus et al., 2003).

Crystals with more perfect lattice structures, such as diamond, have a very high

Young's modulus (stiffness). However, these crystals are sensitive to atomic-level flaws.

Inorganic minerals in bone, teeth, and shell have a comparatively lower Young's modulus

96

and lower strength, which makes them tolerant of cracks of tens to hundreds of nanometers in size. While these crystals would be brittle if they were larger than their crack tolerance, keeping them at the nanoscale makes them insensitive to such flaws (Gao, 2006). Therefore, even though mineral crystals becoming larger as they mature sounds like a mechanical advantage, it actually makes them more brittle (Boskey, 2003). In turn, the mismatched crystals tend to reduce the stiffness of the bone (Jager and Fratzl 2000). Mineral crystals can become abnormally large in osteogenesis imperfecta (Landis, 1995) and sodium fluoride treatment (Fratzl et al., 1994). Studies have varied in whether osteoporosis is associated with normal (Rubin et al., 2003, Lundon et al., 1994, Simmons et al., 1991) or large crystals (Thompson et al., 1983, Burnell et al., 1982, 183). At the same time, pathologically small crystals will not be able to carry out their previously discussed role in resisting load. There is thought to be an optimal mineral crystal size for maximum strength (Boskey, 2003).

The length of secondary mineralization has been controversial. Some researchers have found that mineral content and mineral crystallinity (size, and/or perfection) increases for a period of up to thirty years. Akkus et al (2003) used Ramen microspectroscopy to measure mineral content, mineral crystallinity, and carbonate substitution in primary lamellar bone of human femoral diaphyses. From formation to third decade, mineral content increased 24%, and mineral size also significantly increased. Carbonate substitution for phosphate also decreased, making the crystal more perfect. Handschin and Stern (1994) similarly report that mineral crystallinity increased by up to 20% between age zero and age twenty five. In contrast, Fuchs et al. (2008) found

97

that secondary mineralization was completed within 350 days of bone formation in the tibial diaphyses of New Zealand white rabbits. Marotti et al., (1972) found that secondary osteons completely mineralized within eight months. Huang et al. (2003) found that cortical tissue was fully mineralized after one year in adult female cynomolgus monkeys. Fuchs et al. (2008) attributes the age related mineralization increases seen in Akkus et al. (2003) to hyper-mineralization, in which osteocyte lacunae and canaliculi become filled with mineral. Indeed, Jowsey (1966) reports that Haversian canals can be completely plugged for 500 µm along their length, and partially plugged for an additional 500 µm. Less than 0.5% of Haversian canals are occluded between age 20 and 50, but individuals over age 50 have 1 – 2% of their canals plugged, regardless of osteoporotic state (Jowsey, 1966).

Remodeling rate influences both the mean degree of mineralization (DMB) and the overall heterogeneity of mineral distribution in bone tissue (Martin, 1993, Bala et al., 2013). When remodeling rate is low, there is more time for complete secondary mineralization. Mean DMB increases and bone becomes more homogenously mineralized (Bala et al., 2013). This association is upheld clinically for anti-catabolic (resorption reducing) bisphosphonate osteoporosis treatment (Chavassieux et al., 1997, Boivin et al., 2000, 2003, Zoehrer et al., 2006, Borah et al., 2006, Misof et al., 2008, Boskey et al., 2009, Bala et al., 2011) osteopetrosis (Boskey and Marks, 1985, Chavassieux et al., 2007) and necrosis (Hemar et al., 2012) among other pathologies (Bala et al., 2013) When remodeling rate is high, bone turnover occurs before full secondary mineralization. Mean DMB decreases and bone becomes more

98

heterogeneously mineralized due to matrix in various stages of mineralization (Bala et al.,2013). This connection is upheld clinically for the increased remodeling experienced during menopause (Recker et al., 2004), postmenopausal osteoporosis (Roschger et al., 2001, 2008, Misof et al., 2003, Ciarelli et al., 2003, Zoehrer et al., 2006, Bovin et al., 2008), anabolic (bone-forming) PTH osteoporosis treatment (Misof et al., 2003, Paschalis et al., 2005), and mild primary hyperparathyroidism (Bovin and Meunier, 2002, Roschger et al., 2007). Either extreme of remodeling and mineralization is disadvantageous. Bone with high mineralization, such as osteopetrotic bone, is stronger (maximum stress) and stiffer. However, it has a short plastic deformation region and is more likely to fracture. Additionally, its mineral homogeneity reduces its ability to stop or deflect cracks, as will be discussed under microstructure. Bone with low mineralization, such as osteoporotic bone, can deform more in strain, but have lower strength and stiffness (Ruppel et al., 2008). When bone is too flexible, it can crack even under normal loading (Seeman and Delmas, 2006).

4.4. Microdamage as an Energy-Dissipating Mechanism

4.4.1. Microdamage As an Exception to Mechanostat Predictions

Using histomorphometry to infer remodeling activity and its mechanical stimulus appears straightforward with the setpoints outlined in the mechanostat model. However, as Martin (2000b) identifies, the remodeling range of the mechanostat model does not have a high enough setpoint to target microdamage. Remodeling is initiated both at low strains, in response to disuse, and high strains, in response to microdamage. Attempts to

99

infer mechanical demand from histomorphometry must consider whether the remodeling is likely to represent stochastic bone turnover or targeted bone repair.

Martin (2000b) notes that placing remodeling and its adaptive window out of the range of microdamage repair implies that targeted remodeling is not adaptive. However, microdamage serves as a toughening mechanism to resist bone failure. Bone trades some of its elastic stiffness for toughness. While it yields earlier, it can deform plastically and resist fracture for increasing amounts of strain (Ritchie, 2011). Bone dissipates energy without failure through forming small diffuse cracks under tension and larger microcracks under compression. This energy release increases the total energy required to break the bone (Martin, 2003). Microdamage also is an important consideration for predicting histomorphometry because it both initiates and is initiated by histological features. Microcracks are removed through targeted remodeling bone (Burr and Martin 1993; Li et al., 2001), creating the secondary osteons, vascular pores, and lacunar canalicular architecture associated with remodeled bone. However, microdamage can also be initiated by these same vascular pores and osteocyte lacunae (Ebacher et al. 2007).

Microdamage is an important consideration for interpreting the mechanical loading environment of bone tissue. The concept of microdamage appends Frost's mechanostat model of bone turnover, such that remodeling activity can be triggered both at moderate strains and at strains high enough to induce microdamage (Burr, 1993; Li et al., 2001). Microdamage accumulation also helps explain increased fragility of bone in association with age and pathologies that increase mineralization, accumulate vascular

100

porosity, and promote osteocyte apoptosis or death. In particular, vascular porosity is created by microdamage-targeted remodeling, and subsequently this stress-concentrating porosity becomes a risk factor for initiation propagation of microcracks into fracture (Ebacher et al., 2007)

4.4.2. *Aging of the Nanostructure Contributes to Microdamage*

Microdamage is known to accumulate with age in the cortex of the weight-bearing femoral mid-diaphysis, proximal femoral head, femoral neck, and tibial diaphyses (Mori et al., 1997, Norman and Wang, 1997, Schaffler et al., 1995). Trabecular microfractures have also been found to increase with age in human femoral heads (Koszyca et al., 1989,) and human vertebral bodies (Vogel et al. 1993). Wasserman et al. (2005) make the argument that microdamage occurs preferentially in aging tissue because of its previously discussed decline in quality. With age, tissue increases in its non-enzymatic collagen cross-linking, mineral size and shape, and potentially carbonate substitutions, which destabilize crystal structure. As mineralization increases, hydration of the matrix also decreases (Wasserman et al., 2005). Nanoindentation of the human tibia shows that interstitial bone is stiffer and harder than secondary osteonal bone, likely due to higher mineralization (Schuit et al., 2004, Ruppel et al., 2008) Most microdamage accordingly accumulates in older, interstitial regions of bone (Norman and Wang, 1997, Schaffler et al., 1995) Wasserman et al. (2005) used Ramen microspectroscopy to determine that microcracks did significantly co-localize with regions of comparatively high mineralization in human midshaft femora. Increasing mineralization decreases the

101

yield strain of bone, which helps explain why microdamage is highly localized to these brittle regions (Norman and Wang, 1997, Schaffler *et al*., 1995, Wasserman et al. 2005, Ebacher *et al.,* 2005). Burr et al. (1998) found that microdamage to less than 0.1% of the cortex, on average, was sufficient to cause stiffness losses in excess of 15%.

Interstitial regions are remnants of primary circumferential lamellar bone or old osteons that have not been recently remodeled, and are therefore more mineralized (Wasserman et al., 2005). Primarily lamellar bone adjacent to the endosteum is resorbed with age, and much of the intracortical bone is replaced with secondary osetonal bone through remodeling. However, primary lamellar bone can remain as interstitial bone near the periosteal surface across the lifespan. Therefore, aged individuals do have regions of old tissue even if their remodeling rate has increased, as in post-menopausal osteoporosis (Akkus et al., 2003). Simmons et al., (1990) noted that elderly individuals had increased numbers of new, mineralization secondary osteons relative to 40 – 45 year olds, due to increases in remodeling rate with senescence. However, they notes that secondary osteons seemed to "avoid" remodeling interstitial regions. As discussed in Question 1: Mechanotransduction, osteocytes must be active within ~100 µm of microdamage to activate targeted remodeling (Verborgt et al. 2000). Osteocytes are estimated to have a lifespan of approximately twenty years (Frost, 1960, Parfitt, 1993). Age-related diseases are also associated with osteocyte apoptosis. For example, Zarrinkalam et al. (2012) found that empty osteocyte lacunae increased 1.7-fold in the lumbar spine and 2.1-fold in the iliac crest of osteoporotic sheep compared to controls. In aged individuals, microdamage may accumulate both because the interstitial tissue has declined in

102

mechanical quality, and because osteocytes in that region are dead and cannot target

remodeling (Schaeffler et al., 1995, Burr, 2011).

4.4.3. *Morphology of Microdamage Depends on Loading Mode*

While diffuse microdamage and linear cracks are visible at the microscale, they

begin with nanoscale-level structural changes in the bonds between collagen, mineral,

and non-collagenous proteins (NCPs). Osteoporotic bone has reduced mean collagen

fibril diameter, which may explain some of its increased fragility (Kafantari et al., 2000;

Tzaphlidou and Kafantari 2000). Fibers with a similar banding pattern have been

reported for relatively ancient bone (Ascenzi, 1955; Wyckoff, 1965), suggesting that

collagen fibers are preserved for analysis in such bone. When subjected to cyclic

bending, bone tends to fail through interlamellar debonding in tensed regions and through

oblique or longitudinal cracking in compressed regions (Carter and Hayes, 1977). Many

of bone's material properties are anisotropic, meaning they accumulate differently based

on direction, and microdamage is no exception (Burr et al., 1998).

Tension and compression loading differ in the strain threshold and resulting

morphology of microdamage in bone. Pattin et al. (1996) observed modulus degradation

and an increase in the cyclic dissipation of energy starting at 2,500 $\mu\varepsilon$ in cadaveric

femoral cortical bone loaded under tension, compared to a damage threshold of 4,000 $\mu\varepsilon$

under compression. Diab and Vashishth (2005) found that tensed regions accumulate

four-fold more diffuse microdamage than compressed regions, while compressed regions

accumulate twice as much linear microcracking as tensed regions. Regions under tension

preferentially develop diffuse damage, a mesh of many small cracks ~2 to 10 µm wide

oriented transversely to the tensile stress (Schaffler et al., 1994; Zioupos and Currey, 1994; Boyce et al., 1998; Reilly and Currey, 1999; Reilly and Currey, 2000; Vashishth et al., 2000; Ebacher et al., 2007). However, this microdamage does not coalesce into large (> 100 µm) microcracks that are capable of penetrating Haversian systems until high strains are reached, just prior to failure. Bone tissue regions under compression first begin to develop microcracks at high strains but these cracks are likely to continue growing and lead to bone fracture (Reilly and Currey, 1999). Linear microcracks are 40 to 100 µm long and 1 to 2 µm wide in cross-section, but can run 300 to 500 µm in the longitudinal plane of the bone (Burr and Martin, 1993; Taylor and Lee, 1998). Burr et al. (1998) found that tensile cortices had significantly more (25%) damage than compressed cortices, since diffuse microdamage begins in tensed regions at lower strains than microcracks begin in compressed regions.

4.4.4. *Diffuse Microdamage as an Energy-Dissipating Mechanism*

Since bone is weaker and deforms under lower strain in tension, it is able to dissipate energy by forming diffuse cracks that are less likely to propagate into fracture than those formed under compression. This mechanism increases the fatigue life of the bone (Reilly and Currey, 1999; Diab et al. 2005; Green et al., 2011). Reilly and Curry (1999; 2000) found that diffuse microdamage appears even before the yield point in the load/deformation curve signifying any loss of stiffness. Until a 15% loss of stiffness, only these small, isolated cracks appear in bone (Burr et al., 1998). Up to a stiffness loss of 20%, bone does not suffer significant changes in the energy it can absorb before failing (Boyce et al., 1996; Martin et al., 1997; Reilly and Curry, 2000). Energy dissipation

104

through microdamage was also found in Ebacher et al.'s (2007) study of four-point bending of machined cortical sections and whole cadaveric tibiae. After the bone yields to plastic deformation in tension, the neutral axis shifts towards the compressive surface, redistributing longitudinal (axial) strains towards the tensile surface. Due to this redistribution, the compressive surface experiences higher stress, while the tensile surface is pulled further apart and experiences higher strain. Therefore, compression is a key determinant of the maximum stress that bone can withstand prior to failure (Wang and Gupta, 2011). However, transverse strains are redistributed towards the compressive surface. This is because the tensile surface expands in volume in the transverse plane (as measured by Poisson's ratio) through the formation of cracks and voids, while volume is largely conserved on the compressive surface (Ebacher et al., 2007).

This concept of diffuse microdamage as an adaptive energy-dissipating mechanism was challenged by the finding that diffuse microdamage does not stimulate remodeling. Herman et al. (2010) found that loading the rat ulna produced osteocyte apoptosis and activated remodeling at sites of linear microcracks but not diffuse microdamage. Seref-Ferlenguez et al. (2014) used creep loading to generate in vivo diffuse damage in the rat ulna. They found that diffuse damage was reduced and the 15% loss in stiffness recovered within 14 days after loading. Seref-Ferlenguez et al. (2014) hypothesize that diffuse damage is repaired through mineral deposition regulated by osteocyte-produced proteins, and through the repair of ionic bonds in the matrix. In trabecular bone, complete fractures of trabeculae (microfractures) remodel through endochondral ossification (Burr, 2011).

105

4.4.5. *Microdamage Tends to Initiate at Stress-Concentrating Voids*

Early researchers recognized that microdamage could initiate at stress concentrators such as vascular canals and osteocyte lacunae (e.g. Currey, 1962). Ebacher et al. (2007) observed that tensile diffuse microdamage can initiate both within Haversian systems and throughout interstitial bone. However, they found that compressive microcracks preferentially initiated within Haversian systems during bending. Crack initiation has been linked both to the concentration of stress within these canals and to their low shear strength as a consequence of low mineralization, resulting in a low elastic modulus within the Haversian system (Ascenzi and Bonucci, 1972; Reilly and Currey, 1999). A microcrack would have to pass into an older, stiffer bone region in order to escape the Haversian system (He and Hutchinson, 1989). This interface increases resistance to cracking outside of the Haversian system, such that microdamage often remains restricted to the system in which it initiated (Ebacher et al., 2007).

Ebacher et al. (2007) argue that microdamage and fracture are highly influenced by pore number, size, and canal geometry in regions under compression, but not tension. Since compressive microdamage largely is restricted to Haversian systems surrounding vascular canals, the amount of porosity in an individual should influence bone failure in compressed regions. Tensed regions can initiate microdamage in interstitial bone, so they should not be as sensitive to individual differences in porosity. In Ebacher et al.'s (2007) study of four-point bending of machine cortical sections and whole cadaveric tibiae, compression regions from different individuals did indeed show variance in the shape and magnitude of their stress-strain curves. Tension regions showed very uniform stress-

106

strain curves between individuals, supporting the argument that failure under tension is not very sensitive to inter-individual variation porosity. Even though tensed regions accumulate significantly more porosity than compressed regions (e.g., Frost, 1990; Skedros et al., 1994b; Skedros et al., 2005a), they are not very sensitive to microdamage and failure as a direct consequence of this porosity.

4.4.6. Changes With Age: Increased Mineralization Accelerates Microdamage Accumulation

In mechanical testing, microdamage reduces both stiffness (Burr et al., 1998) and overall strength of bone (Carter and Hayes, 1977). The cracked region of bone cannot be re-cracked to release energy unless it is remodeled. This effect decreases bone's capacity to resorb energy (toughness) (Burr, 2011). While large amounts of microdamage can be induced in mechanical testing, these levels are rarely, if ever, found *in vivo* (Burr, 2011). In experimental animal models, increased microdamage does reduce toughness, but not at the levels of physiologically normal microdamage accumulation (Allen et al., 2006; Mashiba et al., 2000; Mashiba et al., 2001; Komatsubara et al., 2003). Burr (2011) argues that microdamage typically accrued *in vivo* is not a significant mechanical detriment to bone unless it is not remodeled, due to turnover suppression or failure to detect the damage.

Microdamage does eventually become mechanically compromising if allowed to accumulate (Ebacher et al., 2007). Microdamage is known to accumulate with age in the cortex of the weight-bearing femoral mid-diaphysis, proximal femoral head, femoral

107

neck, and tibial diaphyses (Mori et al., 1997; Norman and Wang, 1997; Schaffler et al., 1995). Trabecular microfractures have also been found to increase with age in human femoral heads (Koszyca et al., 1989,) and human vertebral bodies (Vogel et al., 1993). Preferential formation of less damaging diffuse microdamage *in vivo* also shifts with age (Diab and Vashishth, 2007). Younger individuals form many localized diffuse cracks, while older individuals form fewer, longer linear microcracks (Allen and Burr, 2008).

Age and pathology alter mineral content and quality, inviting microdamage accumulation in brittle tissue regions. Higher mineralization promotes stiffness, while lower mineralization promotes energy dissipation (Burr, 2011; Donnelly et al., 2010). Increasing mineralization decreases the yield strain of bone before plastic deformation, which helps explain why microdamage is highly localized to these brittle regions (Norman and Wang, 1997; Schaffler et al., 1995; Wasserman et al., 2005; Ebacher et al., 2005). Wasserman et al. (2005) used Ramen microspectroscopy to determine that microcracks significantly co-localized with regions of comparatively high mineralization in human midshaft femora. Most microdamage accordingly accumulates in older, interstitial regions of bone tissue (Norman and Wang, 1997; Schaffler et al., 1995).

Microcrack length and orientation are the strongest predictors of the decline in stiffness. Burr et al. (1998) found that microdamage to less than 0.1% of the cortex, on average, was sufficient to cause stiffness losses in excess of 15%. Akkus et al. (2003) found that a metric incorporating crack length and orientation had a stronger association with elastic modulus degradation than the number of microcracks (66% greater) or the sum of crack lengths (33% greater). Bone can slow this decline in stiffness by deflecting

108

the crack away from its propagating force, or by shortening the length of the crack. Norman and Wang (1997) found that in the human midshaft tibia and proximal femur, 62.4% of all microcracks are deflected around osteons in the border between the cement line (which marks remodeling reversal) and the interstitial bone. Similarly, Schaffler et al. (1995) found that in human femora 87% of microcracks either initiated in interstitial bone, presumably due to high mineralization, or intersected with cement lines.

4.5. Changes With Age: Older Tissue Loses Osteocyte Sensitivity to Microdamage

Due to continual remodeling throughout life, regions of bone tissue vary in tissue age and do not match the chronological age of an individual. However, interstitial regions that do persist for decades will eventually lose osteocyte sensitivity, allowing microdamage to accumulate without detection and repair. Interstitial regions are remnants of primary circumferential lamellar bone or old osteons that have not been recently remodeled, and are therefore more mineralized (Wasserman et al., 2005). Primarily lamellar bone adjacent to the endosteum is resorbed with age, and much of the intracortical bone is replaced with secondary osteonal bone through remodeling. However, primary lamellar bone can remain as interstitial bone near the periosteal surface across the lifespan. Therefore, aged individuals do retain regions of old tissue even if their remodeling rate has increased, as in post-menopausal osteoporosis (Akkus et al., 2003). Simmons et al., (1991) note that individuals over age 60 have increased numbers of new, mineralized secondary osteons relative to 40 to 45 year olds, due to increases in remodeling rate with senescence. However, individuals over age 60 also

109

retain more of their older, more highly mineralized bone, which was previously targeted for remodeling.

Osteocyte activity is essential for microdamage detection and repair. After depositing osteoid, approximately 10% to 30% of the bone-forming osteoblast cells become trapped in the new matrix and differentiate into osteocytes (Banks, 1974; Parfitt, 1993; Aubin and Liu, 1996). Osteocyte cell bodies are housed in lacunae, and they extend their approximately 50 dendrites through fluid-filled channels called canaliculi to communicate with other osteocytes (Himeno-Ando et al., 2012). Osteocytes sense local changes in mechanical strain and trigger cellular pathways for bone modeling and remodeling to compensate for these changes (Komori et al., 2013). However, they can also sense microdamage their environment and signal for local repair. The mechanism for this "targeted" remodeling is likely osteocyte apoptosis. Linear microcracks disrupt lacunar-canalicular fluid transport between osteocytes. (Tami et al., 2002) This break in fluid flow impairs nutrient transport and cell-cell signaling, causing hypoxic stress followed by osteocyte apoptosis (Martin, 2003; Herman et al., 2010).

Osteocyte activity is highly localized, as the cells must be active within ~100 µm of microdamage to activate targeted remodeling (Verborgt et al., 2000). Osteocytes were originally estimated by Frost (1960a) to have a lifespan of approximately twenty years. Bonewald (2017) notes that osteocytes in regions with slow bone turnover may survive for decades, compared to the days-long lifespan of osteoclasts and weeks-long lifespan of osteoblasts. However, empty osteocyte lacunae do accumulate with age. In aged individuals, microdamage may accumulate both because the interstitial tissue has

110

declined in mechanical quality, and because osteocytes in that region are dead and cannot target remodeling (Schaeffler et al., 1995; Burr, 2011).

4.6. Intraskeletal Variability in Microdamage Accumulation

Under models of bone functional adaptation, such as Frost's (1987a) mechanostat, high strain suppresses remodeling activity related to routine bone turnover. Yet strains high enough to induce microdamage also trigger targeted remodeling activity, composing an estimated 10% to 30% of all remodeling activity (Burr and Martin, 1993; Li et al., 2001). Considering both models, in circumstances of higher mechanical strain, the routine remodeling rate might be suppressed, but the targeted remodeling rate might be accelerated in response to more frequent microdamage. Perhaps in part due to methodological variation, this uncertainty regarding remodeling rate is also reflected to some degree in the literature.

Some have hypothesized that skeletal elements experiencing higher mechanical loads accrue more microscopic damage, triggering more frequent remodeling for repairs (Lanyon and Baggot, 1976). For example, Robling and Stout (2003) found that the femur exceeds the rib in remodeling rates. They link this conclusion to dynamic loading, which is produced by movement in the femur but is relatively uncommon in the rib. However, other studies conversely claim higher remodeling rates in the rib compared to the femur (Hattner and Frost, 1963; Frost, 1964; Cho and Stout, 2011; Mulhern, 2000; Mulhern and Van Gerven, 1997). Similarly, other authors have found denser secondary osteon populations in skeletal elements or tissue regions under low strain, which the authors

111

attribute to more frequent remodeling for bone renewal (e.g. Portigliatti et al., 1983; Mason et al., 1995; Skedros et al., 1996; Gocha and Agnew, 2016).

If remodeling rate varies between skeletal elements, microdamage accumulation may similarly vary. For example, Frost (1960c) did not find a significant relationship between microdamage and age in his sample of human ribs. Schaffler et al. (1995) attribute this difference from results of their femoral study to the relatively higher remodeling rate in the rib. They argue that the rib can minimize microdamage accumulation over the lifespan through its high turnover rate. Cho and Stout (2011) hypothesize that the rib accumulates more microdamage than the femur due to loading cycles induced by respiration. This microdamage produces greater rates of targeted remodeling in the rib. Frost (1963) stated that the high remodeling rate in ribs also causes them to reflect changes in bone mass from disease and aging earlier than appendicular bones. Relative to long bones, the human rib is isolated from irregular dynamic loading, being similarly loaded between individuals by the musculature associated with breathing (Bellemare et al., 2003). Agnew et al. (2017) found that in the human sixth rib midshaft linear microcrack length, density, and surface density significantly varied between elderly individuals. This suggests that inter-individual metabolic variations in remodeling rate can cause significant differences in microdamage accumulation, even between similarly aged individuals. However, as Agnew et al. (2015) note, the relationship between age, microdamage, and mechanical properties is still not firmly established in the rib, and is the subject of ongoing study.

4.7. Lacunar- Canalicular Architecture Reflects Osteocyte Activity

The preceding section discussed the bone remodeling process, how histomorphological features relate to it, and how histomorphometric analysis can be used to assess aspects of this important metabolic process, e.g., bone formation rate, in skeletal remains. The following section addresses how an often overlooked aspect of the microarchitecture of bone, lacunar-canalicular achitecture, can provide useful information about bone strength.

4.7.1. *Osteocyte Lacunar Density and Volume Increases With Higher Strain*

Osteocyte lacunae concentrate stress and have been observed to serve as initiation points for microscopic cracks (Reilly and Currey, 2000). Osteocyte lacunar density has been shown to weaken deer calcanei and equine third metatarsals because it is negatively correlated with stiffness, ultimate stress, and yield, and elastic energy (Skedros et al., 2003). While these elastic properties are important, osteocytes are necessary for continually sensing and repairing bone's plastic deformation, microdamage. Qiu et al. (2005) found that the likelihood of microdamage was 3.8x higher in bone with osteocyte lacunar density less than 728/mm^2. They examined ribs from women aged 50 to 60 and found that about 73% of the microcracks were associated with interstitial bone fragments without osteocyte lacunae.

Two-dimensional counts of osteocyte lacunae do not consistently reflect mechanical predictions for osteocyte activity. New osteocyte lacunae are created through modeling or remodeling in a region. Osteocyte lacunae are removed if the surrounding

113

tissue is resorbed, or if the osteocyte dies and the lacuna is filled in (Carter et al., 2014).

Some pericellular modification of the lacuna may also be possible (Qing and Bonewald, 2009; Tang et al. 2012). Theoretically, compressed regions should contain a higher density of osteocyte lacunae than tensed regions. Compressed regions are under higher strain, so more osteocytes should be present to detect and repair fatigue damage (Skedros et al., 2005a). This pattern has been confirmed in compressed and tensed regions of adult equine radii, equine calcani, and artiodactyl calcani (Hunt and Skedros, 2001, Skedros et al., 2004, Skedros et al., 2005a). However, the inverse pattern is found in equine third metacarpals, where osteocyte lacunae have a denser population in the tensed region compared to the compressed region (Skedros et al., 2005a).

Notably, osteocyte lacunar density is a quantification of the number of lacunae in the two-dimensional area of a cross-section, and does not consider the volume of lacunae or their canalicular connections. Two-dimensional methods for quantifying osteocyte lacunar density rely largely on point-counts of the osteocyte lacunae seen in cross-section, sometimes with geometric extrapolations to three dimensions. These methods cannot detect variations along the thickness of the cross-section (Hannah et al., 2010). Three-dimensional analysis of osteocyte lacunar volume with confocal microscopy and synchrotron μCT suggests osteocytes in regions of higher strain trend towards denser concentrations, higher lacunar volume, and larger surface area. (Carter et al., 2013a; Carter et al., 2013b; Carter et al., 2014; Hannag et al., 2012; Himeno-Ando et al., 2012) The increase in lacunar volume appears to be related to metabolic activity, as cytoplasm volume is increased but nuclear volume is not (Himeno-Ando et al., 2012)

114

4.7.2. Changes With Age: Osteocyte Lacunar Density Decreases

Osteocyte lacunar density generally decreases with age, as reviewed in Hunter and Agnew (2016). In cortical bone, age-associated declines in osteocyte lacunar density have been observed significantly (Busse et al., 2010; Vashishth et al., 2000; Hunter and Agnew, 2016) or insignificantly (Carter et al. 2013a) in the midshaft femur, and insignificantly in the distal radius and midshaft rib (Hunter and Agnew, 2016). In trabecular bone, osteocyte lacunar density declines significantly with age in the femoral head (Mori et al., 1997) and the iliac crest (Mullender et al., 1996; Qui et al., 2002; Bach-Gansmo et al., 2016). Osteocyte lacunar density also declines with age in the parietal bone (Torres-Lagares et al. 2016). Cortical porosity increases with age due to the same factors that drive osteocyte apoptosis: increased targeted remodeling and resorption and cellular senescence in osteoblast functionality (Thomas et al., 2005, Pearson and Lieberman, 2004). As osteocyte lacunar density decreases with age, it shows a significant association with increasing cortical porosity, a relationship seen in the cortices of the midshaft femur (Vashishth et al., 2000; Vashishth et al., 2002; Dong et al., 2014; Hunter and Agnew, 2016), femoral neck (Power et al., 2001), distal radius, and midshaft rib (Hunter and Agnew, 2016), and in the trabecular bone of the vertebral body (Vashishth et al., 2005).

This decline in osteocyte lacunar density may be attributed to several age-associated challenges to osteocyte survival and function. First, as previously discussed, osteocytes in unremodeled tissue may exceed their lifespan, precluding future local

115

remodeling triggered by mechanical strain changes or microdamage (Schaeffler et al., 1995; Burr, 2011). Osteocyte lacunae can remain empty after death, or else become filled with hypermineralized matrix through a process known as micropetrosis (Frost, 1960b). Second, as previously discussed, osteocytes may also die through apoptosis in response to microdamage, which is increasingly common with age. Older bone tissue is more vulnerable to microdamage because it is brittle due to age-associated changes in mineral size, shape, and composition (Wasserman et al., 2005). A microcrack's disruption of lacunar-canalicular fluid flow causes apoptosis of local osteocytes (Martin, 2003, Herman et al., 2010), releasing pro-inflammatory cytokines that recruit osteoclasts for bone resorption (Lotze and Tracey, 2005; Kennedy et al., 2011). Third, osteocyte apoptosis also increases systemically with age, without triggering remodeling activity, in response to increased levels of reactive oxygen species and decreased lysosomal function (Noble et al., 1997; Jilka et al., 2013), as reviewed by Jilka and O'Brien (2016).

Mechanical loading promotes osteocyte survival (Hamrick et al., 2006), so declining physical activity and increasing muscle weakness with age may be another factor driving osteocyte apoptosis. Accordingly, Hunter and Agnew (2016) found that osteocyte lacunar density declined with age at the highest rate and with the greatest inter-individual variability in the midshaft femur, followed by the distal radius and then the midshaft rib. The femur and distal radius are dynamically loaded, making their microstructure more sensitive to inter-individual and age-associated variation in physical activity, while the rib is cyclically loaded by breathing throughout life (Hunter and Agnew, 2016).

116

Age-associated declines in osteocyte survival appear in many bones of the human body, but the extent can vary widely between individuals and sampling sites, as explored by Frost (1960a). Dunstan et al. (1993) found that osteocyte viability (showing lactate dehydrogenase activity) decreases with age in the trabecular bone of the femoral head, but not that of the second lumbar vertebra. The femoral head has a low remodeling rate compared to the lumbar vertebrae, so osteocytes are more likely to exceed their lifespan before replacement. Dunstan et al. (1993) and Wong et al. (1987) noted that in osteonecrosis and osteoarthritis cases complete loss of osteocyte viability is localized to deep trabecular bone in the femoral head, which is particularly susceptible to this pathology. Wong et al. (1985) found that in the trabecular bone of the femoral head nearly all osteocytes are viable before age 25. Viability significantly decreases with age, especially in the older tissue deep in trabeculae, similarly in healthy individuals, cases of degenerative joint disease, and chronic alcoholism. Osteocyte survival is also reduced with age in the ilium (Delling, 1973). Even in the parietal bone, which has low bone turnover, osteocyte lacunar density and percentage of occupied lacunae both decline with age in cortical and trabecular bone (Torres-Lageres et al. 2010).

4.7.3. Changes With Age: Percent Occupied Lacunae Decreases

Osteocyte lacunar density approximates osteocyte survival (Hunter and Agnew, 2016). However, the distinction between a lacuna and its osteocyte occupant is important in some pathological cases. Osteocyte lacunar density can decline because the osteocytes are formed in fewer numbers, or because the osteocytes die more frequently and their

117

empty lacunae are filled by micropetrosis (Qiu et al., 2003). For example, in Qiu et al.'s (2003) study of the trabecular bone of the iliac crest, healthy patients experienced increasing osteocyte apoptosis with age, declining both in osteocyte lacunar density and percent occupied lacunae. Yet patients with vertebral fractures experienced decreased osteocyte formation with age, perhaps due to premature osteoblast apoptosis, causing a decline in osteocyte lacunar density while percent occupied lacunae remained stable. These changes were localized to deep (older) trabecular bone in healthy individuals, but targeted both superficial and deep bone in fracture patients (Qiu et al., 2003).

Osteoporosis can alter the rate at which osteocyte lacunar density declines with age, although reports are not consistent. Mori et al. (1997) found that femoral neck fracture predicted a ~30% (insignificant) lower osteocyte lacunar density in the trabecular bone of the femoral head, compared to healthy controls. Qiu et al. (2003) similarly found that vertebral fracture predicted a 34% (significant) lower osteocyte lacunar density in the trabecular bone of the iliac crest, compared to healthy controls. Conversely, Mullender et al. (1996) found that osteoporotic individuals experienced significantly less of a decline in osteocyte lacunar density with age in the trabecular bone of the iliac crest, compared to healthy controls. They did not see a significant correlation of percent empty lacunae with age in either healthy or osteoporotic individuals, leading them to suggest that osteoporosis does not accelerate osteocyte apoptosis. McCreadie et al. (2004) similarly found no significant difference in osteocyte lacunar density between fracture cases and controls in the trabecular bone of the femoral head.

4.8. Changes With Age: Altered Lacunar-Canicular Architecture

The absolute number of osteocyte lacunae may be less important than the volume and connectivity of the whole network in fluid flow and inter-cellular communication (Robling and Turner, 2002; Skedros et al., 2005a). Canaliculi appear to be thinner, but more branched and numerous, in more highly loaded bone (Himeno-Ando et al. 2012). Milovanovic et al. (2013) found that aged individuals have ~30% fewer canaliculi per lacuna, and that aging decreases canalicular number, connectivity, extent, a phenomenon also seen in mice (Kobayashi et al., 2015).

Age and pathology can also alter osteocyte lacunar size and shape, although reports are not always consistent. Lacunar size has been found to both decrease with age (Mullender et al., 1996; Carter et al., 2013a) and increase with age (Bach-Gansmo, et al. 2016). Osteoporosis has been described variably as increasing (Wright et al., 1978; Van Hove et al., 2009), decreasing (Mullender et al., 1996), or causing no change (McCreadie et al., 2004) in osteocyte lacunar size. **Osteopenic** osteocytes are reported to be relatively large and elongated, **osteopetrotic** osteocytes are small and discoid, and **osteoarthritic** osteocytes are smallest and round (Van Hove et al., 2009). Smaller and more spherical osteocytes are more sensitive to small strains, producing more nitrous oxide (NO) in response to mechanical loading and thereby inhibiting osteoclast activity (Bacabac et al., 2008). Smaller osteocytes, with their high mechanosensitivity, might contribute to the osteoclast inhibition and high BMD that characterizes osteopetrosis. Enlarged osteocytes, being less sensitive to mechanical loading, could permit the excessive osteoclastic resorption seen in osteopenia and osteoporosis (Van Hove et al., 2009).

119

4.9. Secondary Osteon Size and Shape as Toughening Mechanisms

4.7.4. Small, Circular Osteons Are Associated With Higher Mechanical Strain

Secondary osteon size also varies according to mechanical strain differences within single skeletal elements. High strain represses remodeling activity, which should theoretically result in a smaller osteon area (Abbott et al., 1996). A finite element model from van Oers (et al. 2008) suggests that relatively small changes in strain are sufficient to cause large variations in osteon diameter. Smaller osteons also allow bone to pack more osteons into the same space, taking advantage of their toughening mechanisms to resist high strain. Regions with smaller osteons have higher fracture toughness in tension and shear, as seen in the human femur (Yeni et al., 1997). Within a cross-section, compressed regions experience higher strain and tend to produce smaller osteons than tensed regions. This pattern is see in the human femur (Yeni et al., 1997), and in the calcaneus of adult elk, sheep (Skedros et al. 1997), horse (Skedros et al. 1994b; Skedros et al. 1997), and mule deer (Skedros et al. 1994a, Skedros et al. 2001, Skedros et al. 2004). However, size differences were not detected between compressed and tensed regions of the horse radius (Mason et al., 1995) or human tibia (Yeni et al., 1997). In the mule deer calcaneus, osteons are also smaller in the endocortical region, where strain is lowest, compared to the middle and pericortical regions (Skedros et al., 1994b), although this pattern was not detected in the elk, sheep, or horse calcaneus (Skedros et al., 1997).

120

Higher strain from increased mobility and body weight can also reduce osteon size in the same skeletal element. Schlecht et al. (2012) found that individuals with normal mobility have smaller osteons than quadriplegic individuals in the femur, tibia, humerus, and radius. In the ulna and fibula, which are not so highly loaded by body weight or limb use, osteon area falls within the same range for mobile and quadriplegic individuals, although mobile individuals still have slightly smaller osteons. Robust Pleistocene humans have significantly smaller (~25%) osteons in the femur and tibia compared to modern humans (Abbott et al., 1996). Osteons near the periosteum of the anterior midshaft femur significantly decrease in size as body weight increases (Britz et al., 2006).

Sexual dimorphism in osteon size is likely a proxy for higher physical activity and body weight in males, which tends to produce smaller osteons in weight-bearing bones, such as the femur (Dominguez and Agnew, 2016). For example, males were observed to have significantly smaller osteons than females in the anterior midshaft femur of the 14th - 19th century Pecos Pueblo population (Burr et al., 1990) and throughout the midshaft femoral cortex in a late medieval Nubian population (Mulhern and Van Gerven, 1997). However, this Nubian population did not display the same sexual dimorphism in osteon size in the rib, which lacks the weight bearing and dynamic loading environment of the femur (Mulhern, 2000). Similarly, sex differences in osteon size were not detected in the rib at the Early Archaic Windover, Middle Woodland Gibson, and Late Woodland Ledders sites (Stout and Lueck, 1995), or in modern individuals (Dominguez and Agnew, 2016). Even in the femur, osteon size is not consistently correlated with sex. Pfeiffer (1998; et al., 2006) observed no significant sex differences in osteon size in the femur or

121

rib of 18th century English Huguenots (Spitalfields), 19th century British Canadians (St. Thomas), or Later Stone Age or 20th century South Africans (University of Capetown). Britz et al. (2009) found that females in a modern Australian population unexpectedly have significantly smaller osteons than males in the anterior midshaft femur, but these differences are due to outlier individuals. Dominguez and Crowder (2015) suggest an endocrine role due to their observation that, in the anterior femur, younger females have larger osteons and older females have smaller osteons compared to age-matched males.

Intraskeletal comparisons do not maintain the pattern of high mechanical strain and smaller osteon size seen regionally within skeletal elements. The weight bearing and dynamic loading in the femur might be predicted to produce smaller osteons than those seen in the rib. However, the femur has significantly larger osteons than the rib in both modern (Goliath et al., 2016) and archaeological (Pfeiffer, 1998; Pfeiffer et al., 2006) populations. The smaller cross-sectional area of ribs compared to femora may favor a smaller osteon size (Goliath et al., 2016), especially given that even within the ribs Dominguez and Agnew (2016) noted a relationship between osteon size and the amount of available cortex (Ct.Ar) for remodeling to occur . The more variable loading experienced by the femur could also contribute to its greater variability in osteon size (Pfeiffer et al., 2006).

The smaller osteons that form under higher mechanical strain also tend to be more circular in shape. The circularity index of an osteon is measured as $4\pi(\text{area/perimeter}^2)$, where values approaching zero represent more elongated osteons and where approaching one represent more circular osteons (Goliath et al., 2016). In the mule deer calcaneus,

122

osteons are smallest and most circular in the high strain regions under compression and near the periosteum (Skedros et al., 1994b). Near the periosteum of the anterior midshaft femur, increased body weight is associated with increased circularity, as well as smaller size (Britz et al., 2009). Sex differences and intraskeletal differences in circularity are not significant in the rib, humerus, and femur (Britz et al., 2009; Crescimanno and Stout, 2012; Goliath et al., 2016). Hennig et al. (2015) caution that the circularity index is highly sensitive to minor variations in perimeter, such as errors in closure of a digital outline of an osteon. They recommend substituting the inverse of the osteon aspect ratio, quantified as (major axis/minor axis)$^{-1}$, where zero is infinitely elongated and one is perfectly circular.

4.10. Changes With Age: Secondary Osteons Become Smaller and More Circular

Age-associated declines in physical activity and muscle strength might be expected to relieve high strains and thereby produce larger, more elliptical osteons. However, the literature supports an opposite trend towards smaller, more circular osteons with age. Smaller osteons have long been noted in human bones such as the femur (Currey, 1964; Singh and Gunberg, 1970; Evans, 1976; Thompson, 1980; Martin et al., 1980; Watanabe et al., 1998; Burr et al., 1990; Eriksen, 1991; Pfeiffer, 1998; Britz et al., 2009; Hennig et al., 2015; Goliath et al., 2016), tibia (Singh and Gunberg, 1970; Ortner, 1975; Evans, 1976; Thompson and Galvin, 1983), fibula (Evans, 1976), humerus (Iwamoto et al., 1978; Martin et al., 1980; Yoshino et al., 1994), metacarpal (Martin et al., 1980), rib (Pfeiffer, 1998; Dominguez and Agnew, 2016; Goliath et al., 2016), and

123

mandible (Singh and Gunberg, 1970). Osteon area also decreases with age in animal models, including the femora of rhesus macaques (Burr, 1992; Havill, 2004) and the rat femur, tibia, and mandible (Singh and Gunberg, 1971). As a caveat, a statistically significant decrease of osteon area with age has not been upheld in some case studies of these same human bones (Jowsey 1964; Black et al., 1974; Mulhern and Van Gerven, 1997; Pfeiffer, 1998; Pfeiffer et al., 2006). Osteons have also been observed to increase in circularity with age in the femur (Currey, 1964; Britz et al., 2009; Goliath et al., 2016), and rib (Goliath et al., 2016).

Histological studies of osteon geometry have historically relied on two-dimensional cross-sections. Yet osteons form complex, interconnected three-dimensional networks, much like the vascular pores they contain (Maggiano et al., 2016). Hennig et al. (2015) wondered whether Haversian systems were altering their three-dimensional shape with age, or whether they were merely changing in orientation, thereby skewing their two-dimensional cross-section. If a Haversian system does not change its three-dimensional geometry, but alters its orientation relative to the plane of section, it can alter its cross-sectional area and circularity. Hennig et al. (2015) matched three-dimensional µCT reconstructions of vascular canal orientation to two-dimensional inverse osteon aspect ratio of the surrounding osteons. More obliquely oriented osteon would be expected to appear more elongated in cross-section. However, as vascular canals became more obliquely oriented with age due to interconnection and convergence, their surrounding osteons actually become more circular in cross-section. Increasing obliqueness perpendicular to the major axis of the osteon could theoretically increase

124

circularity, but this would also increase cross-sectional area, contrary to the observed age-associated reduction of osteon size (Hennig et al. 2015). Britz et al. (2009) similarly reject an orientation-based explanation for increased circularity because osteon diameter decreases with age. Osteons with similar canal orientations also display a large variation in cross-sectional shape. These results suggest that osteons are actually altering their three-dimensional size and shape with age, becoming smaller and more circular, rather than merely altering their orientation (Hennig et al., 2015).

Do age-associated changes in osteon size and shape stem from senescence, adaptation, or continuation of normal remodeling activity? Supporting a senescent explanation, Martin et al. (1980) propose that osteoclasts decline in their capacity to extend the borders of the cutting cone, producing smaller osteons. Takahashi et al. (1965) and Seeman (2013) suggest that larger osteons have a higher probability of being removed by remodeling as osteon population density increases with age. An adaptive argument advanced by Burr et al. (1990) is that changes in osteon shape and size help compensate for age-associated reductions in bone quality. Specifically, smaller osteons can accommodate a higher osteon population density, increasing the cement line interfaces for toughening mechanisms such as microcrack deflection and osteon pullout (Dominguez and Agnew, 2016). Smaller osteons would also require smaller resorption bays, reducing the size of temporary but stress-concentrating defects (Goliath et al., 2016). Conversely, Hennig et al. (2015) argue that the thinning, porous cortex can interact with weight gain during aging to inflict higher strain on skeletal elements. In this

125

scenario, the trend towards smaller, more circular osteons is a continuation of the

relationship with high strain seen in youth.

4.11. Vascular Porosity Reflects Resorption Activity
4.11.1. Vascular Porosity Reflects Regional Mechanical Strain

Pores related to the vascularization of bone, including resorption bays and

Haversian canals, are the product of mechanically-induced modeling and remodeling.

Bone modeling involves concentric lamellae of bone surrounding a blood vessel,

producing a primary osteon with a central pore containing vasculature (Stout et al. 1999;

Burr and Akkus, 2014). Bone remodeling begins with osteoclasts tunneling through the

bone, forming a "cutting cone" that, in cross-section, appears as a large, irregularly

shaped pore called a "resorption bay" (Stout and Crowder, 2011; van Oers et al., 2008).

If mechanical strain and physiological capacity is sufficient to induce the formation of

new bone, the resorption bay is filled in with concentric lamellae of bone, producing a

secondary osteon with a central pore called a "Haversian canal" (Burr and Akkus, 2014).

If bone formation is not complete, the resorption bay will remain as a large pore.

Adjacent resorption bays near the marrow cavity can coalesce into huge "trabecularized"

pores if their interstitial regions are resorbed (Zebaze et al., 2009).

Individual vascular pores form a complex three-dimensional network

interconnected by branching events and transverse canals, sometimes called "Volkmann's

canals" (Tappen, 1977; Stout et al., 1999). While transverse canals and Volkmann's

canals are sometimes used as interchangeable terms, Maggiano et al. (2016) notes the

126

historical distinction. Volkmann's (1863) original description referred to vascular canals that formed during osteomyelitis, breaking out of their Haversian system to canalize adjacent bone. Therefore, these Volkmann's canals lack surrounding lamellae (Jaffe, 1929, Cooper et al., 1966). Tappen (1977) describes transverse canals that are surrounding by lamellae because they are contiguous with a remodeling event, either the cutting cone "breaking out" laterally from an existing BMU or "swinging around" during remodeling. Maggiano et al. (2016) used synchrotron μCT to determine that transverse canals generally emerge through one of the following processes: 1) lateral branching of a smaller diameter canal from a larger diameter canal, 2) dichotomous branching, wherein a canal splits into two canals similar in size to produce a "dumbbell" shaped osteon, or 3) intraosteonal remodeling, involving a younger Haversian system remodeling an existing, older Haversian system and potentially reusing its blood vessel. Branching events have been reported to occur on average every 2.5 mm (Beddoe, 1977) to 3 mm (Koltze, 1951) along a canal.

According to Frost's (1990) mechanostat model, high strain represses bone resorption and should reduce bone porosity, while low strain is permissive to bone resorption and should increase bone porosity. Since porosity is the product of remodeling, intraskeletal variance in porosity should reflect intraskeletal variance in remodeling rate (Cho and Stout, 2011). For example, due to their high turnover rates, ribs are thought to lose bone earlier than more dynamic and weight-bearing skeletal elements (Epker et al., 1965; Agnew and Stout, 2012). However, Hunter and Agnew (2016) did not find significant differences in percent porosity between the distal radius, midshaft rib, and

127

midshaft femur of the same individuals. Similarly, Cole and Stout (2015) did not observe significant differences in percent porosity at the midshafts of the femur, tibia, and rib of the same individuals in a small sample. However, they found that the rib displayed significantly greater trabecularized porosity than the femur or tibia, which preferentially formed cortical pores (Cole and Stout, 2015). The rib experiences extensive trabecularization of the cortex with age, as pores adjacent to the endosteum coalesce with each other and the marrow cavity. Since these pores are united with the marrow cavity, they are likely to be excluded from pore quantification during analysis, obscuring the true relationship of porosity to aging and bone strength (Hunter and Agnew 2016; Dominguez and Agnew, 2014). Zebaze et al. (2009) found that exclusion of the trabecularized cortex underestimates porosity by ~2.5 fold.

In the mid-thoracic (4-7) ribs, subtraction of porous voids makes cortical area a better predictor of the peak force, structural stiffness, and total energy required to fracture the rib. These improvements are significant but small, suggesting that bone loss at the endosteum reflected in measures of cross-sectional bone quantity is more important for predicting bone strength in ribs (Dominguez et al., 2016). Similarly, in the distal radius, the total reduction in bone mass between ages 50 and 80 is due largely to porous trabecularization at the endosteum (47%), followed by trabecular bone thinning (32%) and then formation of pores within the cortex (21%) (Zebaze et al., 2010). The primacy of this "invisible" trabecularized porosity in some skeletal elements helps explain why certain pathological conditions appear to accelerate intracortical pore formation in some bones but not others. For example, Villanueva et al. (1966) found that osteoporotic ribs

128

had normal intracortical porosity, but experienced an expansion of the marrow cavity with associated cortical thinning. Conversely, Jowsey (1964) described extensive intracortical remodeling with increasing numbers of incomplete osteons in osteoporotic femora.

Porosity has been shown to vary within a cross-sectional plane according to regional strain differences. Endosteal skeletal regions experience lower magnitude strains compared to regions located closer to the periosteum and consequently are more porous. Skeletal biologists have long recognized that porosity increases from the periosteum to the endosteum in various long bones (e.g. Jowsey, 1960; Atkinson, 1965; Martin et al., 1980; Martin and Burr, 1984a; Thomas et al., 2005; Zebaze et al., 2010). Strains are lowest at the endosteum because these regions are closest to the neutral axis, where strain is minimized (Martin, 1993; Thomas et al., 2005). While females do lose bone preferentially at the endosteum with age, porosity is highest at the femoral endosteum across the lifespan in both sexes (Bousson et al., 2001). Similarly, compressed regions of a cross-section experience high strain and are less porous, while tensed regions experience low strain and are more porous, as demonstrated in the calcanei of Rocky Mountain Mule Deer (Skedros et al., 1994b). Two-dimensional studies of the midshaft rib have found that the cutaneous region is significantly more porous and trabecularized than the pleural region (Agnew and Stout, 2012; Agnew et al., 2013; Cole and Stout, 2015; Dominguez and Agnew 2016). However, it is unknown if this difference is related to regional strain patterning, thus it may not reflect the true loading environment of the rib or its effects on three-dimensional pore structure (Dominguez and Agnew, 2016).

129

4.11.2. Mechanical Strain Directs Three-Dimensional Secondary Osteon Orientation

The tunneling orientation of the cutting cone during bone remodeling appears to be mechanically directed. Like the vascular pores they contain, secondary osteons tend be longitudinally oriented (90˚) in long bones to align with the principal direction of loading. For example, the femur has a mean osteon orientation of 79˚ (Hennig et al., 2015). Tappen (1977) traced BMUs through serial sections and found that osteons commonly tunnel both proximally and distally, forming a structure described by Johnson (1964) as a "double-ended osteon". In dogs, the proximal-distal tunnel comprises 34.7% of Haversian systems in the tibia and 42.1% of Haversian systems in the humerus, not considering osteons that extended beyond the serial sectioned volume (Tappen, 1977). Van Oers et al. (2008) used a finite element model of bone remodeling to demonstrate that proximal-distal tunneling emerges from the strain environment around the initial resorption cavity. During longitudinal loading, strains around the resorption bay are high in the transverse direction, inhibiting osteoclast resorption, while strains in the longitudinal direction are low, permitting osteoclast resorption proximally and distally.

As the osteon tunnels longitudinally, it can also "drift" laterally (Fig. 6.7). The drifting osteon morphotype results from continuous resorption on one side and continuous formation on the opposing side of a lateral plane through the osteon. In the cross-sectional plane, this osteon morphotype appears as a Haversian canal surrounded by four to eight concentric lamellae, which continue on one side of the osteon as a "tail" of

130

semi-circular lamellae (Robling and Stout, 1999). Robling and Stout (1999) comprehensively examined drifting osteons in serial sections of two baboon midshaft fibulae, a human third metatarsal, and a human proximal phalanx. They found that most drifting osteons do not consistently trend in a single direction, but change direction slightly (e.g., 3°) or even significantly (e.g., 188°). The finite element model of van Oers (et al. 2008) predicts that the drifting osteon morphotype emerges when a steep lateral gradient of strain permits resorption on the lesser strained side and inhibits resorption on the higher strained side. Robling and Stout (1999) observed substantial changes in drift direction occurred between adjacent osteons and within single osteons at the same cross-sectional level, so strain gradients would need to be highly localized and change direction frequently to "steer" this drift. Cooper et al. (2011) suggest that microcracks may provide such a temporary localized stimuli for targeted remodeling, causing the cutting cone to drift toward and remodel the damaged region. Osteons do generally exhibit an overall drift toward the lower strains at the endosteum (Koltze, 1951; Cohen and Harris, 1958; Epker and Frost, 1965; Burton et al., 1989; Maggiano et al., 2012). Drifting osteons have been reported to form across the lifespan (Robling and Stout, 1999), but with a significant reduction in frequency of formation with age (Sedlin et al., 1963; Coutelier, 1976; Streeter, 2011).

Most of the BMUs observed by Tappen (1977) originated as lateral "breakout zones" from existing BMUs before tunneling proximally and distally. Maximum Haversian system length has been reported as ranging from 5.4 mm to 10 mm (Filogamo, 1964; Johnson, 1964; Cooper et al., 2006). Osteons have been described as terminating in

131

resorption bays on the endosteal surface (Koltze, 1951; Cohen and Harris, 1958; Maggiano et al., 2012). More rarely, osteons narrow to end in a "blind" or "sealed" osteon. Prevalence of this secondary osteon morphotype has been reported as <0.1% in non-primate bone (Henrie et al., 2014), 1% to 2.2% in healthy human femora and tibiae (Pazzaglia et al., 2013; Henrie et al., 2014), and 4-5% in tibia following traumatic amputation (Congiu and Pazzaglia, 2011). Due to its higher prevalence in trauma cases, sealed osteons may be related to a reduction or severance of blood supply (Henrie et al., 2014).

4.12. Changes With Age: Increased Vascular Porosity Weakens Bone

` It is well established that intracortical porosity increases with age as resorption rate outpaces formation rate and capacity (Jowsey, 1960; Jowsey, 1964; Bell et al., 2001). Osteoblasts' capacity for bone formation slows with age, decreasing their ability to keep pace filling resorption bays (Pearson and Lieberman, 2004). Bone resorption also increases in response to the lowered strains of weakening muscles and declining physical activity (Thomas et al., 2005). After age 60, porosity increases 31-33% per decade in the femoral neck (Chen et al., 2010). Pore diameter increases while pore number and spacing decrease, suggesting that pores are coalescing (Chen and Kubo, 2014; Milovanovic et al., 2014). These changes are exacerbated in women due to declining estrogen levels at menopause that increase bone resorption (Chen and Kubo, 2014).

Expansion and coalescence of existing pores is a key driver of age-associated increases in porosity. Pore size plays a central role in variation in porosity in general.

132

Thomas et al. (2005) found that mean pore area explained ~81% of regional variation in porosity in the midshaft femur, with only 12-16% additionally explained by pore density. With age, pore expansion and coalescence further eclipses pore density as a driver of porosity. Bousson et al. (2001) and Cooper et al. (2007a) both noted that, in the midshaft femur, pore number increases up to age 60. After this threshold, pore number declines as canals increase in size and decrease in spacing, indicating that these canals are coalescing and interconnecting. Chen et al. (2010) similarly found that, in the femoral neck, cortical porosity increases two-fold, canal diameter increases 65-77%, and canal number decreases 16-17% between middle-aged and elderly groups of men and women. Percent porosity increases with age even as the absolute number of pores decreases, because formerly distinct pores are combining through resorption of their prior tissue boundaries. For example, Bell et al. (2001) found that, in individuals older than 75 years, giant coalesced canals (>385 µm in diameter) accounted for 27% of femoral neck porosity despite being 1% of the number of canals. Sex differences in age-associated porosity also appear to be driven by pore size. In the anterior femoral neck midshaft, the significantly higher porosity seen in women is derived from their significantly larger canal diameter (Cooper et al. 2007a). The higher porosity seen in the femoral neck in women can also be attributed to their significantly larger canals, but not to significant differences in canal number or spacing. Large canals are concentrated at the endosteum of the femoral neck in elderly men, but also occur at the periosteum in elderly women (Chen et al. 2010).

Variation in where this coalescence occurs may help explain inter-individual variation in fracture risk, as described by Bell et al. (1999a, b) for the human femoral

133

neck. In this region, the superior cortex is least compressed and experiences the lowest strain during gait, while the inferior cortex is the most compressed and experiences the highest strain. Accordingly, in individuals without femoral neck fractures, porosity decreases as strain increases along this superoinferior axis. However, in women with femoral neck fractures, this gradient is disrupted as porosity increases by 41% in the anterior cortex. This concentration is related to a doubling of pore coalescence into "giant canals" (>385 µm) in this region. Age-associated restriction of physical activities that load the anterior cortex, such as hip extension and adduction, may contribute to the increased porosity of this region in fracture cases. This coalescence weakens the femoral neck along the inferoanterior to superoposterior axis, the same direction that deformation occurs during a sideways fall (Bell et al., 1999a, b).

Despite this age-associated increase in porosity, the extent of vascular pore accumulation is highly individualized. Age explains only 12.1% of the variation in porosity between individuals, even when controlled for height, weight, and sex (Stein et al., 1999). Agnew and Stout (2012) found that elderly individuals displayed vascular porosity covering between 6.24% and 41.95% of the cortex at the midpoint of sixth ribs. Individual factors such as severe osteoporosis, poor diet, and low physical activity can contribute to higher percentages of porosity in a given age category (Cho and Stout, 2011; Thomas et al., 2005; Agnew and Stout, 2012). Porosity reflects the biological age of tissue, rather than the chronological age of the individual (Thomas et al., 2005). Pathological conditions that alter remodeling rates can also affect the prevalence and shape of vascular porosity.

134

Increases in vascular porosity compromise bone's resistance to elastic and plastic deformation. Vascular porosity is associated either with the complete resorption of a mineralized bone region, or its partial replacement with less mineralized new bone. Therefore, vascular porosity causes declines in stiffness and hardness, which are associated with mineralization as previously discussed. Currey (1999) compared 67 compact tissues from 32 species and found that most samples with low mineral (<220 m/g) had high porosity (>8%) and lower values of Young's modulus. Changes in porosity in the human femur account for 76% in the reduction of strength (ultimate stress) in tension with age (McCalden et al., 2003). An increase in porosity from 4% to 10% reduces peak stress before fracture by more than half. An increase in porosity from 4% to 20% reduces bone's ability to deform without cracking by threefold (Martin and Burr, 1989). Since vascular pores concentrate stress, they also serve as initiation and propagation sites for microcracks (Ebacher et al., 2007). Ex-vivo experiments show that a 4% increase in vascular porosity decreases initiation toughness by 4% and increases crack propagation by 84% in bone tissue (Ural and Vashishth, 2007; Diab and Vashishth, 2005). The secondary osteons that form around vascular pores have a cement line that deflects microcracks and serves as a toughening mechanism. However, these interfaces will still be weaker against catastrophic failure (Martin, 1993). Secondary bone is 80-90% as strong and 87-91% as stiff as primary bone (Reilly and Burnstein, 1974; Vincentelli and Grigorov, 1985).

135

5. Materials and Methods for Data Collection

5.1. Introduction: Research Design

This project examines the structure-strain relationship of cortical pore morphometry in an age series of the human rib and femoral neck, using high-resolution micro-computed tomography imaging. The focus on post-mortem human subjects (PMHS) is intended capture the life-long trajectory and hierarchal variation of microstructural responses to human-specific dynamic activities. An age series of the right-side fourth rib and matched right-side femoral neck was extracted from PMHS, including one male and one female per decade from the 20's to the 80's. Subjects were represented by demographic data, DXA scans of areal bone mineral density (aBMD), and gross geometry of the proximal femur and femoral neck quantified during dissection. Whole cross-sections of the midshaft rib and the distal femoral neck were extracted and three-dimensionally visualized over a 1 cm length using high-resolution micro-CT, at a resolution (6.4097 µm) suitable for visualizing cortical porosity.

Micro-CT images were then processed through a cascade of routines all custom-coded for this project. Images were adjusted for brightness and contrast in ImageJ (NIH), and then oriented to a transverse cross-section in DataViewer (Bruker). Femoral necks, which had to be cut into three columns to fit in the micro-CT field of view, were oriented more precisely to align along their cuts in Dragonfly (3D). A custom macro for CT-

136

Analyser then binarized the image through adaptive neighborhood thresholding, resulting in a white cortical shell perforated with black pore spaces. In order to isolate these pore spaces, the periosteal boundary needed to be sealed and removed, and the endosteal boundary needed to be trimmed of trabecular projections. A custom macro was developed for CT-analyser to extract and smooth the marrow boundary, removing trabecular struts and trabecularized pore adhesions. The output of this routine was a series of image stacks representing 1) the isolated marrow cavity, 2) a filled cortical shell, 3) cortical bone stripped of trabeculae, 4) isolated pore spaces, 5) isolated trabecular architecture, 6) isolated trabecular spaces, and 7) all isolated pore and trabecular spaces.

In order to asses mechanical effects on pore type, a custom macro was developed for ImageJ to divide the stack of isolated pore spaces into "cortical" and "trabecularized", based on pore diameter in comparison to distance from the marrow cavity. To assess regional variation in pore morphometry, a custom macro was developed in ImageJ to draw the major axis on a the cortical shell of a rib, and output separate shells of cutaneous and pleural cortex on either side of the major axis. For the femoral neck, the major axis was rotated at 45° intervals around the cross-section to create octants representing a superior to inferior gradient. In both cases, the isolated region served as a region of interest "mask" to analyze only the pores contained within that region. An additional utility quantified relative cortical area and the parabolic index automatically by batch-processing, wherein each isolated marrow image was measured for marrow area, merged with the cortical shell, measured for total area, and saved as a total area mask. This ROI was used to mask the binarized cortical shell, so that CT-Analyzer 2D morphometry

137

could quantify the cross-sectional geometry, relative cortical volume, and cross-sectional thickness of the cortical shell.

Finally, pore morphometry was quantified using CT-Analyzer 3D morphometry. This routine requires an input to be measured (total, cortical, or trabecularized pores) and a region of intest to set the boundaries of the measurement (total or regional mask). Morphometric measurements included pore prevalence, percent porosity, connectivity, directional alignment, and network complexity, as will be detailed in the section on analytical methods.

5.1.1. *Mechanical Patterning of the Human Femoral Neck*

In order to clearly link pore morphometry to intracortical strain variation, a cross-section with a consistent, predictable strain gradient was required. The unique bipedal configuration of the human femoral neck produces such a gradient. During bipedal walking, the femoral head of the planted leg serves as the axis of medial rotation to swing the pelvis and the opposing leg forward. Medial rotaion at the hip is accomplished by the hip abductors tensor fasciae latae, gluteus minimus, and anterior fibers of gluteus maximus. Lateral rotation at the hip is accomplished by quandratus femoris, gluteus maximus, piriformis, and triceps coxae (obturator internus, superior gemelli, inferior gemelli). These muscles compress the head and neck of the femur into the acetabulum to stabilize the joint (Moore et al., 2014). This compression eliminates tension superiorly, creating a superior-to-inferior gradient of increasing compression. (Lovejoy, 1988, Ohman, 1997, Ruff, 2013). In bone, peak longitudinal strains occur in compressed

138

regions, while tension exerts comparatively low magnitude strains (Tanako et al. 1999, Skedros et al., 2005). Therefore, the femoral neck should exhibit **low strain superiorly, and a gradient of increasing strain inferiorly.** This strain gradient is the source of the relatively thin superior cortex and thickened inferior cortex of the human femoral neck. The ape femoral neck is bent superiorly in tension and inferiorly in compression, creating a circular femoral neck without superior-inferior thickness variation (Lovejoy, 1988, Ohman, 1997). Femoral neck cross-sectional geometry suggest an intermediate bipedal gait in Australopithecines, falling between non-human apes and humans (Ruff and Higgens, 2013).

Additionally, the femoral neck has significant clinical relevance. Approximately 50% of femoral fractures occur at the femoral neck (Koval et al., 1996). Cortical bone accounts for >90% of bone strength in the femoral neck (Holzer et al., 2009). Two-dimensional studies implicate porosity in the cortical thinning associated with fracture cases (e.g. Bell 1996a,b). Three-dimensional analysis is vital for understanding how porosity contributes to hip fragility (Bousson et al., 2001).

5.1.2. *Mechanical Patterning of the Human Rib*

The rib serves as a relatively "unloaded" control, as it is similarly loaded between individuals by intercostal muscles in breathing (Bellemare et al., 2003). The rib experiences more systemic bone loss with age, with minimal sensitivity to an individual's dynamic activity patterns (Robling and Stout, 2003). The "unloaded" rib should

theoretically display low-strain patterning in comparison to the high-strain patterning of the dynamically loaded, weight-bearing femoral neck.

In a simplified model, as the ribcage expands during inspiration, the cutaneous region (skin adjacent) is tensed under low strain, and the pleural region (lung adjacent) is compressed under high strain (Agnew and Stout, 2012). The cutaneous cortex has been demonstrated to significantly exceed the pleural cortex in percent porosity (Agnew and Stout, 2012; Cole and Stout, 2015; Hunter and Agnew 2016; Dominguez and Agnew, 2014). However, it is uncertain whether the cutaneous cortex of the rib is actually experiencing lower mechanical strain at the midshaft (Hunter and Agnew 2016; Dominguez and Agnew, 2014).

During breathing, the thoracic cage is elevated and expands both transversely and anterio-posteriorly. The lower ribs (primarily 7 – 10) expand the thoracic cage transversely through a "bucket handle" movement, wherein their midshaft regions move laterally and upwards. As the sternal and vertebral ends are fixed, this movement bends the rib inwards. The cutaneous (skin-side) cortex is tensed, a low strain mode, while the pleural (lung-side cortex) is compressed, a high strain mode (Agnew and Stout, 2012). However, the upper ribs (primarily 2 – 6) expand the upper thorax anterio-posteriorly through a "pump handle motion." The sternum moves anteriorly, and the sternal end of the associated ribs moves anteriorly and superiorly (Moore et al. 2014). This has the effect of bending the rib outwards, against its curvature, which could potentially reverse the loading modes of the cutaneous and pleural cortices (Agnew, 2011). Additionally, the thoracic cage expands in both transverse and anterio-posterior dimensions during forced

140

inspiration (Moore et al. 2014), potentially complicating the theoretically simple loading environment of the human rib.

5.2. Sample Description

5.2.1. Sample Origin

Samples were collected from the right side due to a slight right leg dominance in most modern humans (Gilligan et al., 2013). Ribs do not show significant right-left laterality in porosity (Agnew and Stout, 2012). Right-side femoral necks and midshaft fourth ribs were sourced from full-bodied post-mortem human subjects (PMHS). Dissection from full-bodied individuals was essential to ensure that the femoral neck and rib pair came from the same individual, and were not removed or damaged antemortem or perimortem in a surgical or traumatic context. PMHS were sourced from The Ohio State University College of Medicine Division of Anatomy Body Donor Program, through the generous provision of Dr. Amanda Agnew (Skeletal Biology Research Lab, Injury Biomechanics Research Center, The Ohio State University). An additional individual, a 39 year old female (I.D. 39F), was provided by Dr. Alex Robling (Department of Anatomy and Cell Biology, Indiana University of Medicine).

5.2.2. Sample Demographics

The sample used in this study is an age series of fourteen individuals (age range 26 – 88, mean age 54.79 years), with each individual represented by a matched right femoral neck and right fourth rib midshaft (Table 5.1). Each decade of life from the 20's to the 80's is represented by one male and one female. Individuals were selected from

141

post-mortem human subjects (PMHS) available through the Body Donor Program if they fit the age and sex requirements of the age series, if they were full-bodied cadavers, and if they had no recent trauma involving the right proximal femur and thoracic cage.

Table 5.1 Sample Demographic Information and Cause of Death

ID	Age	Sex	Descent	Cause of Death
26M	26	M	European	Suicide
28F	28	F	European	Breast cancer
34M	34	M	European	Acute anoxia (suicide by hanging)
39F	39	F	European	Hepatic cirrhosis, hepatic encephalopathy
41M	41	M	European	Unknown
49F	49	F	European	Non-ST-elevation myocardial infarction Pre-mortem: Right transtibial amputee
50F	50	F	European	Cardiac arrest
56M	56	M	European	Pneumonia
60F	60	F	European	Small cell carcinoma with brain metastesis
67M	67	M	European	Pneumonia
70F	70	F	European	Unknown
77M	77	M	European	Cardiac arrest, lung cancer, myocardial infarction
82F	82	F	European	Cerebrovascular accident (stroke) Pre-mortem: Type 2 diabetes mellitus (DM2)
88M	88	M	European	Pneumonia Pre-mortem: Left leg and knee amputated at approximately midshaft

The potential effect of body size on cortical pore structure is suggested by the previously discussed alignment of bone microstructure with mechanical demand derived from weight bearing and dynamic activity. Height, weight, and body mass index (weight / height^2) at the time of death were recorded for each full-bodied individual (Table 5.2). Per Agnew et al. (2019), body mass index is treated both as a continuous variable (kg/m^2) and as a categorical variable using its World Health Organization (1995) defined divisions into underweight (15.0 – 19.9), normal weight (20.0 – 24.9), overweight (25.0 –

142

29.9), and obese (30.0+). Individual 39F was originally procured for medical instruction and was embalmed, so certain demographic information (height, weight, BMI) is not available for this individual.

Table 5.2 Body Size and Body Mass Index (BMI)

ID	Age	Sex	Weight (kg)	Height (m)	Continuous BMI (kg/m^2)	Categorical BMI
26M	26	M	77.56	1.8288	23.2	Normal
28F	28	F	34.5	1.626	13	Underweight
34M	34	M	81.19	1.905	22.4	Normal
39F	39	F	NA	NA	NA	NA
41M	41	M	67.13	1.7018	23.2	Normal
49F	49	F	59.87	1.651	22	Normal
50F	50	F	77.56	1.7018	26.8	Overweight
56M	56	M	92.98	1.7526	30.3	Obese
60F	60	F	54.55	1.7018	18.8	Normal
67M	67	M	60.8	1.7272	20.4	Normal
70F	70	F	69.4	1.7018	24	Normal
77M	77	M	74.8	1.7018	25.8	Overweight
82F	82	F	65.3	1.651	24.0	Normal
88M	88	M	98.4	1.905	27.1	Overweight

5.3. Bone Mineral Density (aBMD)

In order to measure areal bone mineral density (aBMD), dual X-ray absorptiometry (DXA/DEXA) scans were performed on the total body of each individual in the Injury Biomechanics Research Center using a GE Lunar Prodigy. Regional foci included the anterior-posterior (AP) view of lumbar spine (L1 – L4), left forearm (distal radius and ulna), right and left side femoral neck, and right and left side of the proximal femur. For this study, aBMD (g/cm^2) was considered as a continuous variable for the total body (Table 5.3) and for the right femoral neck (Table 5.4).

143

T-score represents the standard deviation of the individual's aBMD from a "young adult," calculated as *(individual's BMD − young-adult mean BMD)/SD*. For the GE Lunar Prodigy, the young adult (ages 20-40) reference database for the total body is derived from the Bone Mineral Density in Childhood Study (BMDCS) and the Third National Health and Nutrition Examination Survey (NHANES III) as recommended by the International Committee for Standards in Bone Measurement (ICSBM). The International Osteoporosis Foundation (Kanis and Glüer, 2000) and the International Society of Clinical Denistometry (Binkley et al., 2006) recommend that the young adult standard for BMD be the femoral neck measurements of women of European descent aged 20-29, as collected in the NHANES III reference database (Looker et al., 1997, 1998). Kanis et al. (2008) argue that these standards can accommodate postmenopausal women and men of any ethnic descent over age 50. At the femoral neck specifically, the NHANES III database is also used for female individuals. For male individuals, a proprietary GE Lunar Prodigy male reference database is used for femur scan foci due to the lack of conversion equations for femoral neck NHANES III data in men. This DXA also computes a Z-score which is an aBMD standard deviation from a population matched for age, sex, weight, and ethnicity (Binkley *et al.* 2005).

After Agnew *et al.* (2019), T-score was also considered both as a continuous variable and a categorical variable for the total body and for the right femoral neck. In 1994, the World Health Organization (WHO) published diagnostic criteria for low or decreased BMD in postmenopausal women through comparison with the BMD of young, healthy women. Osteopenia describes BMD between 1.0 and 2.5 standard deviations (T-

144

score of -1.0 to -2.5) below this standard. Osteoporosis describes BMD more than 2.5

standard deviations (T-score less than or equal to -2.5) below this standard (WHO, 2007).

Table 5.3 Total Body DXA Areal Bone Mineral Density (aBMD)

ID	Age	Sex	aBMD (gm/cm²)	T-Score	Z-Score	T-Score Category
26M	26	M	1.354	1.5	1.5	Normal
28F	28	F	1.089	-0.4	0.9	Normal
34M	34	M	1.29	0.9	0.8	Normal
39F	39	F	NA	NA	NA	NA
41M	41	M	1.123	-0.8	-0.3	Normal
49F	49	F	0.985	-0.9	-0.5	Normal
50F	50	F	1.444	3.6	3.4	Normal
56M	56	M	1.266	0.6	-0.1	Normal
60F	60	F	0.984	-1	0.4	Normal
67M	67	M	1.3	1	2.1	Normal
70F	70	F	1.024	-0.6	0.6	Normal
77M	77	M	1.232	0.3	1.1	Normal
82F	82	F	1.403	3.2	4.9	Normal
88M	88	M	1.347	1.5	1.6	Normal

Table 5.4 Femoral Neck DXA Areal Bone Mineral Density (aBMD) and Right-Left Asymmetry

ID	Right Femoral Neck				Left Femoral Neck				Femoral Neck Difference			Dual Total Femur Difference	
	aBMD (gm/cm²)	T-Score	Z-Score	T-score Category	aBMD (gm/cm²)	T-Score	Z-Score	T-score Category	aBMD (gm/cm²)	T-Score	Z-Score	T-Score	Asym-metry
26M	1.816	5.7	5.6	Normal	1.577	3.9	3.8	Normal	0.239	1.8	1.8	1.4	Sig.
28F	0.93	-0.4	0.3	Normal	0.932	-0.4	0.3	Normal	0.002	0	0	0	None
34M	1.394	2.5	2.5	Normal	1.306	1.8	1.9	Normal	0.052	0.4	0.4	0.4	None
39F	NA	NA	NA	NA	NA	NA	NA	NA	NA	NA	NA	NA	NA
41M	1.044	-0.2	0.4	Normal	1.044	-0.2	0.4	Normal	0	0	0	0.4	None
49F	0.746	-2.1	-1.2	Osteopenia	0.864	-1.2	-0.4	Osteopenia	0.118	0.8	0.8	0.6	Mild
50F	1.386	2.5	3	Normal	1.277	1.7	2.2	Normal	0.109	0.8	0.8	0	None
56M	1.028	-0.3	0.4	Normal	1.089	0.1	0.6	Normal	0.061	0.5	0.5	0.2	None
60F	0.38	-1.5	0	Osteopenia	1.204	1.2	2.7	Normal	0.374	2.7	2.7	1.3	Sig.
67M	1.002	-0.5	1	Normal	0.999	-0.5	1	Normal	0.003	0	0	0.3	None
70F	0.692	-2.5	-0.9	Osteoporosis	0.617	-3	-1.4	Osteoporosis	0.075	0.5	0.5	0.1	None
77M	1.088	0.1	1.7	Normal	1.144	0.6	2.1	Normal	0.055	0.4	1.9	0.1	None
82F	0.978	-0.4	1.8	Normal	1.042	0	2.3	Normal	0.064	0.5	0.5	0.2	None
88M	2.046	7.5	8.8	Normal	0.988	-0.6	0.7	Normal	1.058	8.1	8.1	4.5	Sig.

146

5.4. Sample Collection

5.4.1. Gross Dissection Techniques

Femoral neck samples were dissected from PMHS by removal of the articular cartilage of the knee joint, shaving adherent muscle tissue from the femoral diaphysis, removing the iliofemoral ligament, and carefully perforating the synovial membrane of the hipjoint. After breaking the seal on the membrane, the femur could be rotated out of the acetabulum without damaging the femoral neck. Similarly, ribs were treated by removing intercostal muscles, cutting the cartilage at the sternal end, and then carefully popping the rib head out of its vertebral articulation. All bone samples were fresh frozen and wrapped in saline-soaked gauze and stored in freezer bags in a -20ºC freezer when not in use, to prevent deterioration.

5.5. Metric Variables Collected During Gross Dissection

Femoral neck geometry (femoral neck axial length, neck-shaft angle, maximum neck diameter) was quantified with standard sliding calipers (Meeusen et al., 2015) and a handheld goniometer (Gilligan et al., 2013). These metrics were based on a literature review of femoral neck morphometry, as detailed in the following table.

147

Table 5.5 References for Collection of Femoral Neck Gross Geometric Variables

Variable Name	Variable Units	Variable Description	Reference
FemMxLng	mm	Femoral shaft length measured with osteometric board from most superior femoral head to most inferior distal condyles	DiMichele and Hunt (2015); Bass (1995); Standards (1994);
FemSub TrAPDia	mm	A-P (sagittal) subtrochanteric diameter	DiMichele and Hunt (2015); Bass (1995); Standards (1994); Zoebeck (1983)
FemSub TrMLDia	mm	M-L (transverse) subtrochanteric diameter	DiMichele and Hunt (2015); Bass (1995); Standards (1994); Zoebeck (1983)
FemHead SIDi	mm	Maximum vertical head diameter	DiMichele and Hunt (2015); Zoebeck (1983); Martin and Saller (1957); Pearson (1917); NMNH (1995)
FemHead HzDia	mm	Maximum horizontal head diameter	DiMichele and Hunt (2015); Zoebeck (1983); Martin and Saller (1957);
FemNeck SL	mm	Superior neck length	Murlimanju *et al.* 2012
FemNeck IL	mm	Inferior neck length	Murlimanju *et al..* 2012
FemNeck VDia	mm	Vertical neck diameter (minimum)	DiMichele and Hunt (2015); Zoebeck (1983); NMNH (1995)
FemNeck TDia	mm	Transverse neck diameter (minimum)	Custom
FNAL Cent	mm	Femoral neck axial length to head apex	Michelloti and Clark, 1999
FNAL Apex	mm	Femoral neck axial length to head center	Meeseun *et al.,* 2013
OFF	mm	Offset of shaft axis to head center	Michelloti and Clark, 1999
Neck-Shaft Angle	degrees	Neck-shaft axis to neck axis angle	Gregory et al. 2008

Table 5.6   Femoral Neck Gross Geometry

ID	Femoral Shaft Dimensions			Femoral Head Dimensions		Femoral Neck Dimensions				Femoral Neck Orientation			
	Fem Mx Lng (mm)	Fem Sub Tr APDia (mm)	Fem Sub Tr MLDia (mm)	Fem Head SIDia (mm)	Fem Head HzDia (mm)	Fem Neck SL (mm)	Fem Neck IL (mm)	Fem Neck VDia (mm)	Fem Neck TDia (mm)	FNAL Cent (mm)	FNAL Apex (mm)	OFF (mm)	Neck-Shaft Angle (degree)
26M	496	27.95	30.79	48.58	48.08	18.19	36.98	27.23	33.15	104.5	84.7	47.01	125º
28F	411	25.03	26.02	43.15	43.06	18.33	34.2	25.56	26.89	91.2	71.6	37.12	135º
34M	484	30.84	40.11	53.55	53.1	29.01	32.67	38.52	27.35	118.6	101.7	58.46	130º
39F	NA	30.5	29.27	46.09	45.98	21.42	31.61	31.27	24.1	98.6	78.3	45.64	135º
41M	464	30.05	41.95	48.83	48.78	17.88	33.15	29.26	37.35	103.7	86.6	52.24	135º
49F	439	26.81	27.59	43.56	43.46	20.72	34.4	28.77	23.51	89.6	76.61	39.45	130º
50F	NA	26.33	31.14	49.34	49.65	23.06	34.26	30.55	27.9	99	89.9	41.01	140º
56M	480	28.74	33.19	50.19	50.15	20.54	34.87	35.21	27.32	102.2	83	43	135º
60F	452	26.07	27.3	42.57	42.57	22.11	37.54	29.77	23.38	88.2	73.2	35.39	145º
67M	455	32.29	35.02	50.48	49.65	23.93	27.57	38.32	30.4	99	82.7	47.86	135º
70F	NA	26.52	31.86	44.43	44.27	14.33	35.74	24.52	32.13	89.1	74.3	38.18	140º
77M	440	26.8	34.1	49.1	49.2	22.9	29	34	33.8	100.9	84.1	39.2	140º
82F	435	33	28.2	44	47	21.5	37.3	40	25.5	94.2	77.5	45.2	135º
88M	NA	41.9	48.5	54.4	54.1	25.3	39.4	42.1	29	112.4	94.3	57.3	130º

149

5.5.1. Fine Dissection Techniques

A 2-inch segment was cut from each whole rib at the midshaft, 50% of the

distance from the tubercle to the sternal end, using a Dremel XPR (Agnew and Stout,

2012). The rib was notched on the sternal end in order to retain orientation.The entire

femoral neck was extracted from the proximal femur with Stryker saw by removing the

femoral head and then cutting the neck from the trochanters. The femoral neck was

notched on the superior and anterior orientations of the proximal (head) end. Soft tissue

was removed to expose the bone of the femoral neck or rib. These extracted samples were

subsequently refined to a 1 cm thickness by clamping into a metal chuck and cutting the

unfixed, unembedded bone on an Isomet. The femoral neck was cut just medial to the

intertrochanteric line, where it is most distinct from non-human primates (Ohman et al.,

1997, Ruff, 2013). However, the entire span of the femoral neck was often approximately

1 cm as centered on its superior aspect, especially in females. The angle of the cut was

oriented to align with the long axis of the femoral neck. Marrow was washed out of the

resulting segment with a WaterPik. Femoral necks were too wide to fit within the field of

view (17.178 mm x 17.178 mm) at imaging resolution (6.4097 µm). Extracted femoral

necks were further divided into an anterior, middle, and posterior column with two cuts

on the Isomet parallel to its major axis on the distal face. The kerf of this diamond

wafering blade was 0.010" (254 µm). However, the extracted whole femoral necks were

first micro-CT scanned at low resolution (35.028 µm) to visualize the intact trabecular

150

bone architecture for future study. Ribs were scanned whole along their extracted 1 cm

length.

Figure 5.1 Cut Angle for Femoral Neck
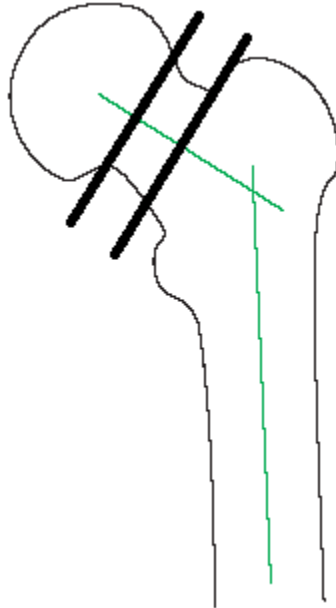
Modified from Rüedi and Murphy (2000)

Figure 5.2 Sample Refinement with Isomet

151

5.6. Preparation for Micro-CT Imaging

It is essential that the bone not dry out during the long micro-CT scan. Drying will cause slight sample movement that prevents accurate reconstruction of the final image. Additionally, all samples were scanned with a bone mineral density phantom and a vial of phosphate-buffered saline to allow calibrartion for volumetric bone mineral density. For accurate vBMD calculation, the sample must remain moist. Each rib or femoral neck column was wrapped in a saline-soaked kimwipe, and then in a thin layer of parafilm, Sample orietations were marked on the parafilm. The sample was then wrapped in a layer of transparent cellophane tape. Finally, the sample was mounted vertically on a plastic disc using commercial sticky-tack reinforced with a coating of gel superglue. The sample was allowed to dry in this orientation overnight in a refrigerator to avoid the bone freezing and then moving as it heated up during the scan. To mount the sample in the micro-CT, its plastic disc was adhered to the micro-CT vBMD phantom mounted on a metal sample holder, both adhered with double-sided tape.

Figure 5.3 Sample Wrapping and Mounting

Figure 5.4 Sample Mounted on vBMD Phantom and Inside the HeliScan Micro-CT
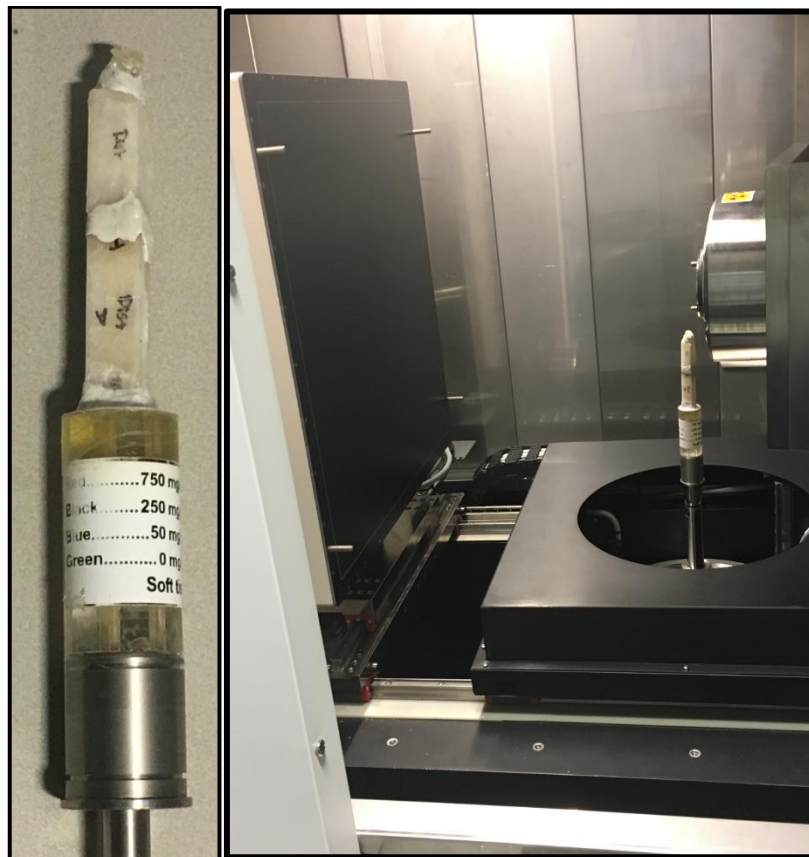
Micro-computed tomography (micro-CT) reconstructs three-dimensional structures by interpolating X-ray images of a rotating sample from hundreds of angles (Cooper et al., 2004). Samples were micro-CT scanned at the Center for Electron Microscopy and Analysis (CEMAS) at The Ohio State University using the FEI HeliScan. Cross-sections were cut at 10 mm thickness in order to scan the maximum depth (6 – 10 mm) reported for complete pore systems (Filogamo, 1964; Johnson, 1964; Cooper et al., 2006). This depth was also analyzed in order to capture branching events, which occur at minimum every 2.5 to 3 mm (Koltze, 1951; Beddoe, 1977). It should be noted that the final image stack after completed analysis was sometimes slighty smaller than 10 mm in length, either because the femoral neck was biologically smaller (e.g., 49F), or due to diminishing sample brightness at the periphery of images. For this reason, morphometric measurements are normalized for sample volume. The smallest resolution that could accommodate a 10 mm thick sample in its field of view was 6.4097 µm. Imaging resolution for cortical pores in human bone must be approximately 5 – 10 µm (Cooper et al., 2007). Because the sample rotates, the field of view must fit the diagonal of this sample (14.142 mm). The field of view at this resolution is 17.178 mm wide, which can fit the sample with some room for error. The HeliScan has a micro-positoning stage for precise sample placement.

154

Table 5.5 HeliScan Acquisition Settings for All High-Resolution Scans

60 kV	Key Field Spacing = 45
80 uA	Test Spacing = 80
Focus Mode M	Do Offset Calibration
Camera (Detector Y) = 379.5 mm	Clearfields = 10
Sample Y = 17.5 mm	Darkfields = 2
1 x 1 binning (6.5 um)	Z position = 1.00 mm
Exposure time: 0.400 ms (6.5 um)	Type = Both
Detector X Start Position: 0	Detector x shift columns = 9
Averaging to Skip: 0	Specify Exposure Time = no
Averaging: 5	Trajectory = Space Filling
Use Averaging for Snap: No	Z stage initial steps = 10
Warmup Time = 2 min	Projections Per Revolution = 2880

Two ribs (56M and 77M) were initially experimentally scanned at slightly higher (>0.23 µm more) resolution, but were resampled in X, Y, and Z dimensions before continued analysis. With 14 ribs and 14 femoral necks with three segments each, this project required scanning 56 individual bone segments. A rib of this size (~15 µm long) requires approximately a 2.5 hour scan, while a femoral neck (~40 µm long) requires approximately a 6.5 hour scan. Unfortunately, one segment of each of four femoral necks moved slightly during scanning. It may be possible to rescue these images with additional image processing, or simply rescan them. For this analysis, femoral neck sample size was reduced.

Figure 5.6 Movement Artifacts in 28F Femoral Neck
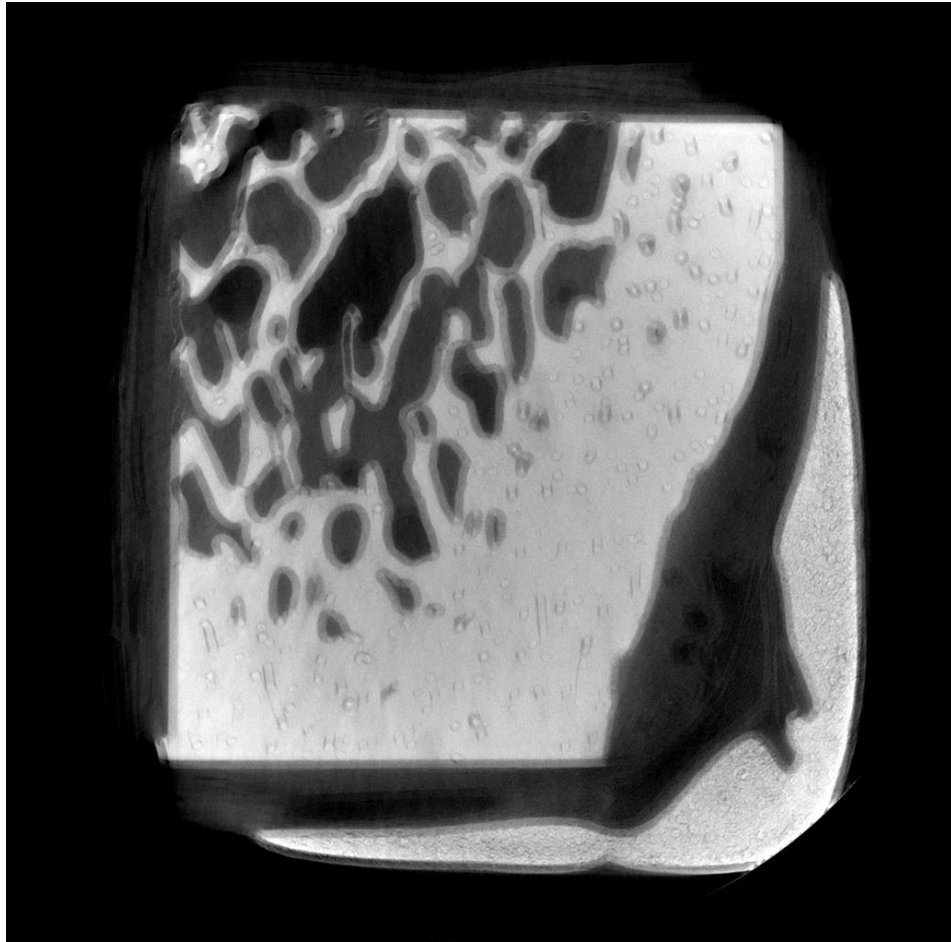
6. Image Analysis Methods

6.1. Introduction: Challenges in Segmenting Human Cortical Bone

At the high resolution used in this study, a 10 mm length of bone contains 1,561 individual slices, each of 6.4097 µm thickness. With trabecular bone, typically visualized at 30 – 100 µm resolution, it is more common for analysis to include manual tracing of the endosteal border, slice by slice. Some approaches include computerized assistance to grow regions or snap to binarized pixel boundaries, but there is a manual component in region selection and confirmation (Buie et al., 2007). Manual definition is unrealistic for the number of slices used in this study. Additionally, reliance on manual segmentation is vulnerable to inter-observer error, as the difficult placement of the endosteal border is a matter of experience and, to some degree, opinion (Buie et al., 2007). With fully automated segmentation, all samples are processed identically, and samples retain exact pixel borders of untouched boundary regions.

Several previous studies have explored methodology for fully automated segmentation of cortical and trabecular bone from micro-CT scans. Buie et al. (2007) developed a widely-cited (399+ studies) "dual threshold" methodology for automatic segmentation of cortical and trabecular bone in lower resolution micro-CT scans (10-82 µm) based on pixel brightness thresholds. Their methodology relies on the differing pixel brightness of the endosteal and periosteal borders at this resolution, owing to adjacency to

157

cortical and trabecular bone, respectively. These thresholds are manually set for each sample by the operator. However, experimentation with this method was not successful for the current data set. At the lower micro-CT or CT resolution typically used for trabecular architecture analysis, cortical pores are not visible unless they are very large. Cortical pores are essentially lost in the noise of the cortical bone at trabecular imaging resolution. When marrow-adjacent cortical pores become resolvable at the resolution used in this study, they are too similar in pixel brightness to adjacent trabecular cavities to be differentiated by thresholding. A single threshold for a boundary will either include adjacent trabecular cavities or cut in to large cortical pore spaces.

Martin-Badosa et al., (2003) separated cortical and trabecular bone using a similar resolution (6.65 mm) to the present study. They developed this method on synchrotron images of the distal metaphysis of the murine femur. Similar to Buie et al., (2007), they differentiated cortical and trabecular bone by neighborhood (adaptive) thresholding of endosteal and periosteal borders. They then examined the histogram of hole sizes of the entire stack, including both cortical pores and trabecular spaces. This produced a size histogram with a peak for cortical pores and a larger peak for trabecular spaces. To close cortical pores, they automatically filled all holes below a size threshold manually decided from each stack histogram. However, the images show that trabecularized pores that open to the marrow cavity – and are therefore not closed holes – were joined with the marrow ROI. Buie et al., (2007) also developed their method on mice, which rarely form remodeling units in comparison to humans and consequently have more limited porosity, limiting application of such methods to human bone (Schnieder et al, 2013). Carriero et

158

al. (2014) automatically segmented open porosity in synchrotron images of murine tibial and humeral diaphyses by performing a morphological closing operation on trabecularized spaces. However, this approach did not include removal of trabecular connections.

Given the lack of a fully automated cortical segmentation routine suitable for the densely trabecular bone of the human femoral neck, a custom image processing approach was developed for this study. Two coding environments were employed. The ".ijm" coding language in the free, open source software FIJI/ImageJ (NIH) was used for image pre-processing (brightness / contrast adjustment, femoral neck segment merging) as well as modification of pore images (pore type differentiation, regional mask creation, relative cortical area calculation). CT-Analyser (Bruker) is a SkyScan micro-CT branded software that allows custom macro-building of morphological operations on grayscale images. Pore extraction, marrow bounding, and 2D/3D morphometric analysis were conducted in CT-Analyser. Dragonfly (ORS) was used for three-dimensional visualization and femoral neck segment alignment. The full text of all ImageJ macros is available in Appendix A. A laboratory computer with 196 GB of RAM was used for the initial reorientation step, in which images are re-sliced from the axial dimension produced by the micro-CT (~5,000-7,000 slices) to a tranverse cross-section of the femoral neck (~2,200 slices). After this reorientation, all processing could be performed on a personal computer with 32 GB of RAM.

159

6.2. Brightness/Contrast Adjustment

If the entire 16-bit pixel range is applied to a pixel range (65,535 gray levels), the resulting imaging will be very dull and indistinct. The pixel brightness range must be restricted to at least a minimum value to exclude dull pixels, and present them as "black." First, images are normalized at 0.3% saturation to stretch their gray levels to fit the entire 0 – 65535 pixel brightness range, using the ImageJ function "Enhance Contrast."

All micro-CT images in this study produced a similar pixel brightness histogram after normalization, including a peak representing dark regions (space, pores), a peak representing gray regions (mounting wrap, soft tissue), and a peak representing white regions (bone). The ideal pixel minimum is the minimum value between the gray peak and the white peak. Setting the threshold here excludes the kimwipe, parafilm, and cellophane tape, as well as any soft tissue, while including maximum white pixels representing bone.

160

Figure 6.1 34M Slice Before and After Normalization With Histograms

Count: 6832996	Min: 0
Mean: 9236.092	Max: 18667
StdDev: 5218.924	Mode: 0 (1470407)
Bins: 256	Bin Width: 72.918

Count: 6832996	Min: 0
Mean: 34174.139	Max: 65535
StdDev: 19309.025	Mode: 0 (1470407)
Bins: 256	Bin Width: 255.996
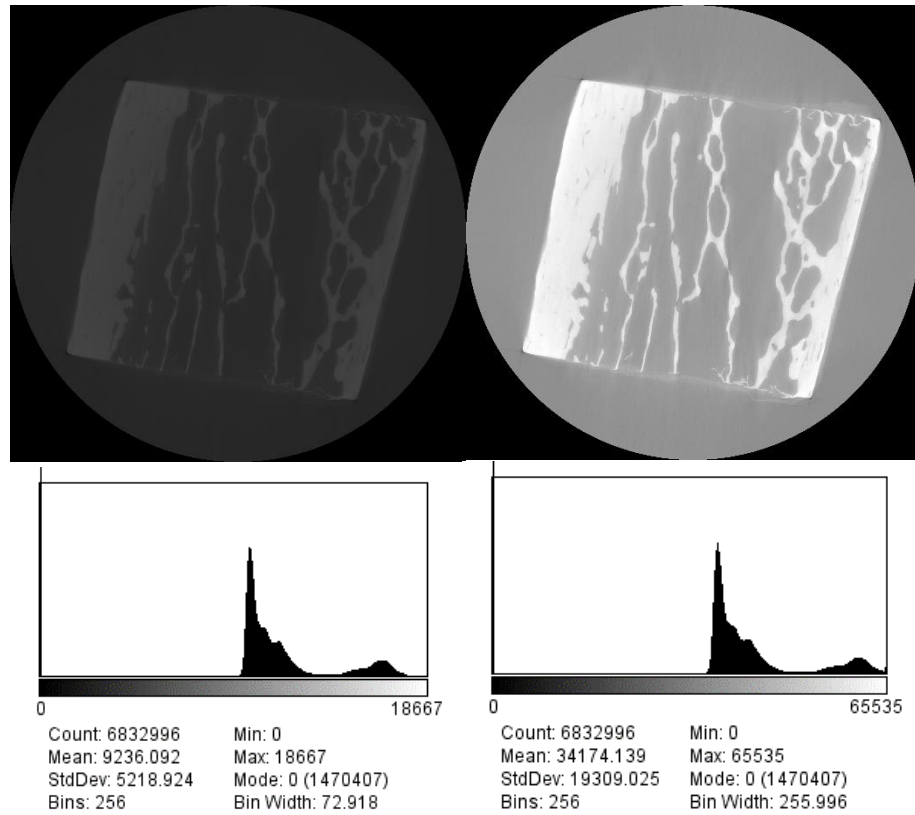
Ribs could be represented by a single pixel minimum, because the image brightness does not vary substantially during their short scans. A custom ImageJ macro, "Batch Histogram," was designed to iterate through all images in a stack and find the pixel minimum of their combined histogram. By batch processing, the user does not need to open the entire 5,000-7,000 image stack, allowing this operation to be performed even on a computer with 16 GB of RAM.

161

Figure 6.2 34M Slice and Histogram After "Batch Histogram" Processing

Count: 6832996 Min: 0
Mean: 5153.735 Max: 65535
StdDev: 13876.394 Mode: 0 (5871202)
Bins: 256 Bin Width: 255.996
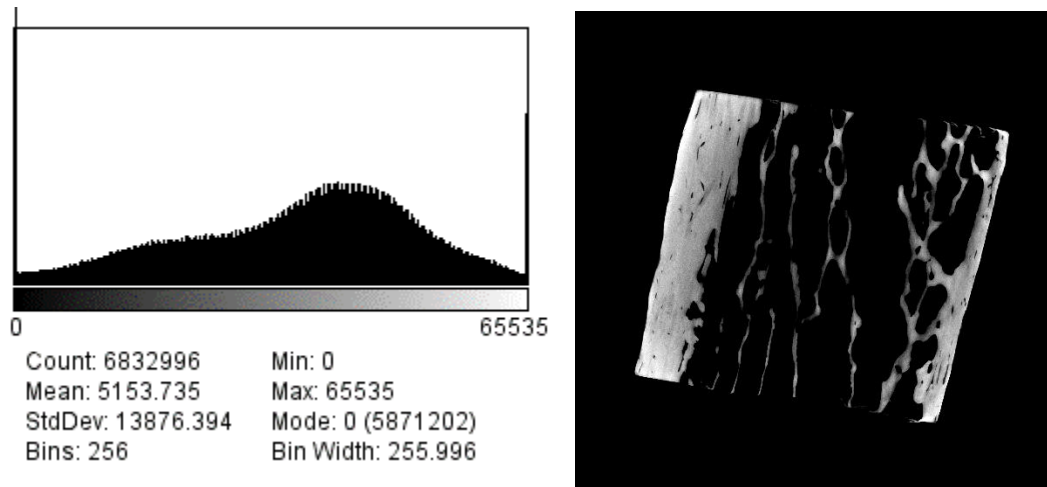
For the long scans of the femoral neck (6.5+ hours), the target current sometimes dropped after a long imaging period. This resulted in reduced brightness at one end of the image stack, so that a uniform value could not be applied to the entire stack. Therefore, an additional ImageJ macro "Slice Histogram" was coded to iterate through the entire stack and pick the ideal minimum value between the gray (mounting) and white (bone) peaks for each slice.

162

Figure 6.3 Tip Fading in 60F (Top, Bottom Left) Corrected With Slice Histogram Code (Bottom Right)
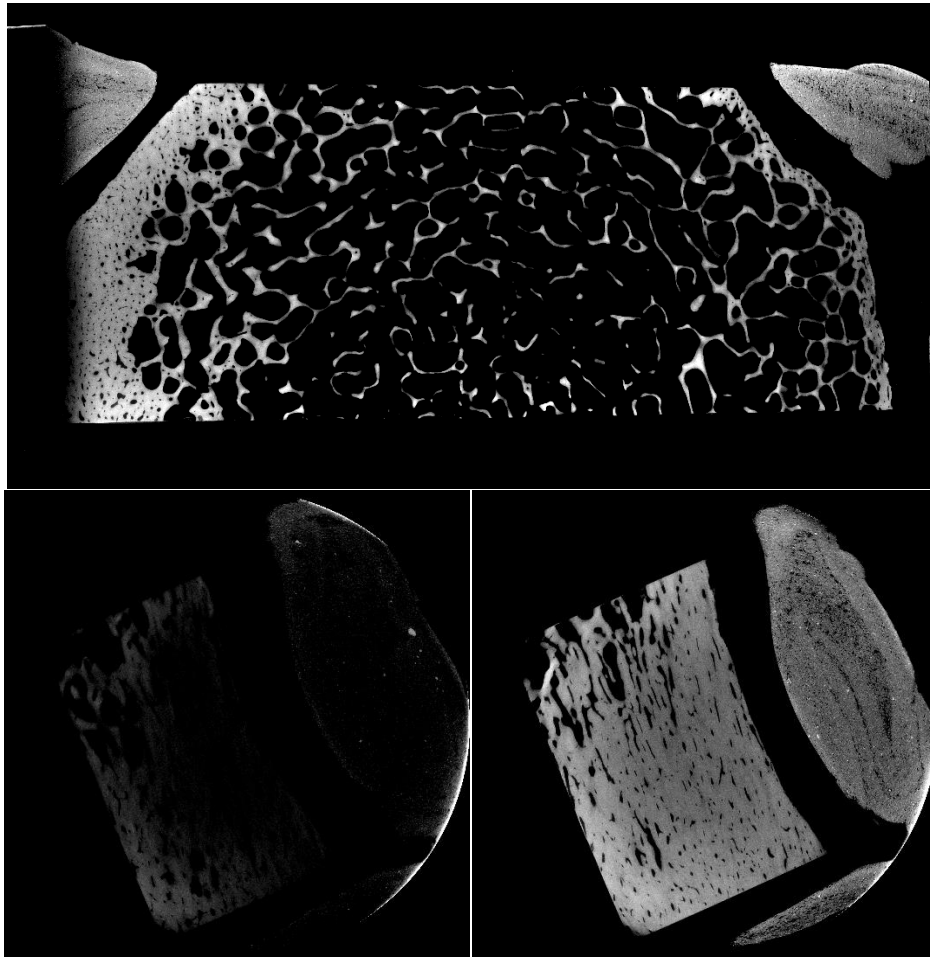
6.3. Axial to Transverse Reorientation

The HeliScan exports cross-sectional slices in an axial format from the top to bottom of the scan. To save image processing time, 5,000-7,000 produced slices can be loaded into DataViewer and resliced as a transverse cross-section. Rib images are also reoriented to transverse slices in DataViewer, and are then ready for pore extraction. However, the three femoral neck columns must be oriented to their final alignment before pore extraction. Any stack rotation following binarization will cause the creation of grayscale

163

shadowing where the change has been interpolated. Therefore, the three femoral neck columns are aligned in the free 3D visualization software DragonFly, which permits visualization both slicewise and three-dimensionally.

Figure 6.4 Axial to Transverse Cross-Section Reorientation in DataViewer
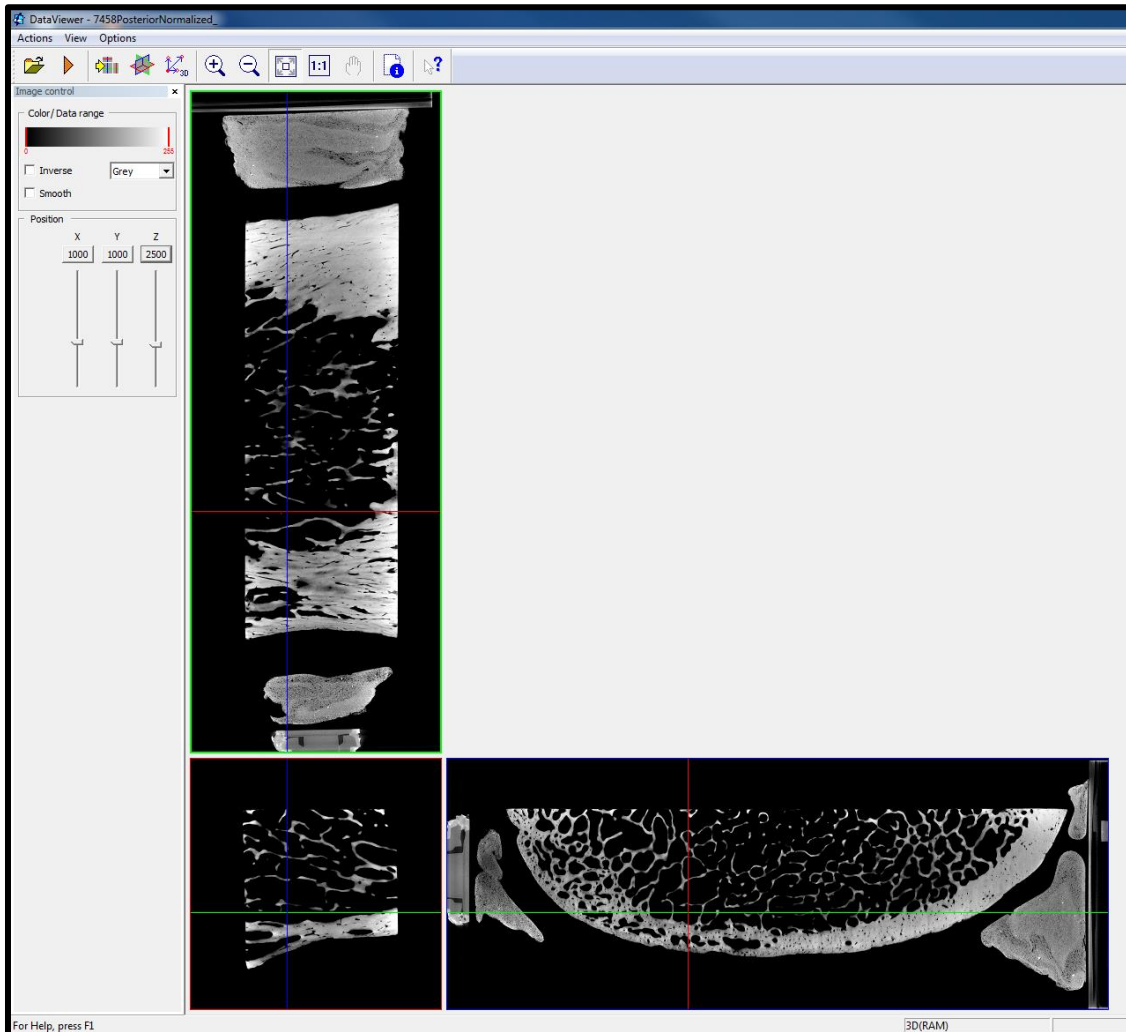
Figure 6.5 Alignment of Adjacent Femoral Neck Columns in Dragonfly
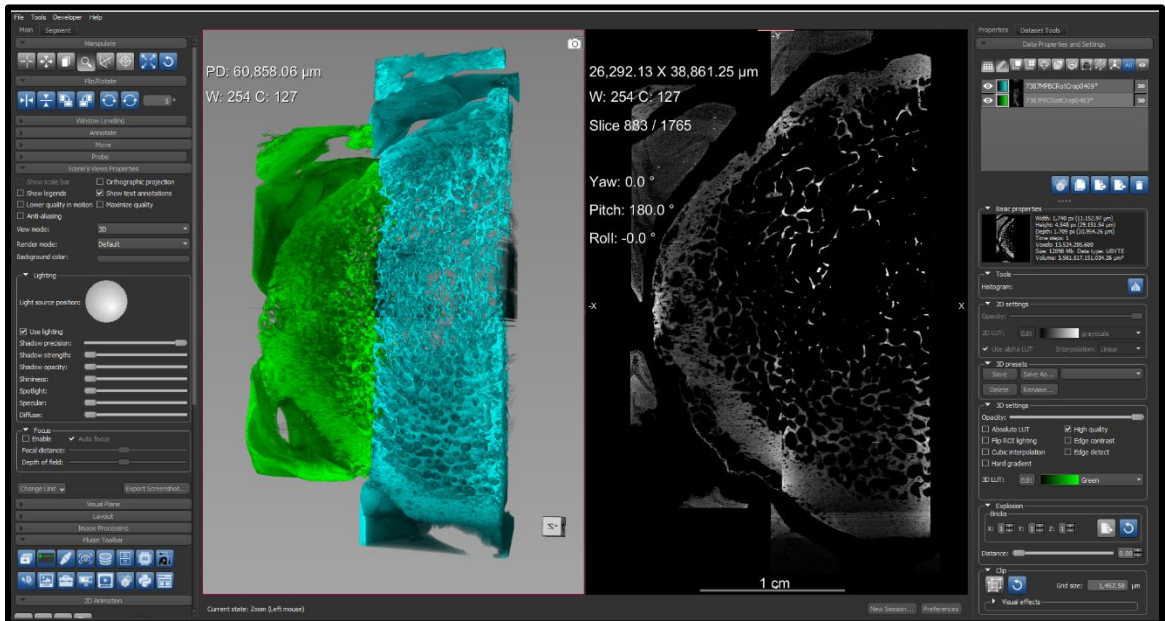
6.4. Pore Extraction and Mounting Fixture Removal

An essential step in morphological analysis is segmentation, where grayscale pixels are binarized either white or black. This is typically accomplished through global thresholding, where a single pixel brightness threshold determines whether pixels will be black (below) or white (above) that threshold. However, global thresholding excludes faint pores and tends to erode and fragment the faint margins of trabeculae.

To avoid losing data, a custom macro was built in CT-Analyser using their adaptive thresholding capabilities. In adaptive thresholding, the threshold of a given pixel is determined by a statistic (mean, median, max+min) about the thresholds of the neighboring pixels in a given radius. This pixel-by-pixel thresholding compensates for variations within a frame in brightness and sharpness of desired extractable features. All visible pores can be extracted through this adaptive thresholding routine:

165

1) **Gaussian Blur filter** (2 pixel radius, round): *Removes random noise*

2) **Mean-C Adaptive Thresholding** (1 pixel radius, round, 35 – 255 pre-thresholding): *Sets a pixel threshold based on mean in a 1 pixel radius*

3) **Despeckle white** < 5 pixels: *Removes white noise*

4) **Despeckle black** < 5 pixels: *Removes black noise*

5) **3D Morphological Opening Operation** (2 pixel radius, round): *Smooths noise at pore boundaries*

In this study, the sticky tack used to mount samples on the micro-CT imaging chuck was visible in the resulting scans. To remove this fixture, the pore extraction routine performs some additional steps using the "Region of Interest" (ROI) clipboard:

1) **ROI Shrink Wrap 3D** – *Creates a filled ROI mask of the entire cortex*

2) **Despeckle ROI 3D** – *Sweeps all but the largest object (the filled mask) in 3D*

3) **Remove Pores ROI 2D** – *Removes any large pores included in the filled mask*

4) **Bitwise Image = ROI AND Image** – *Uses the filled mask of the cortex to mask the mounting fixture on the image*

167
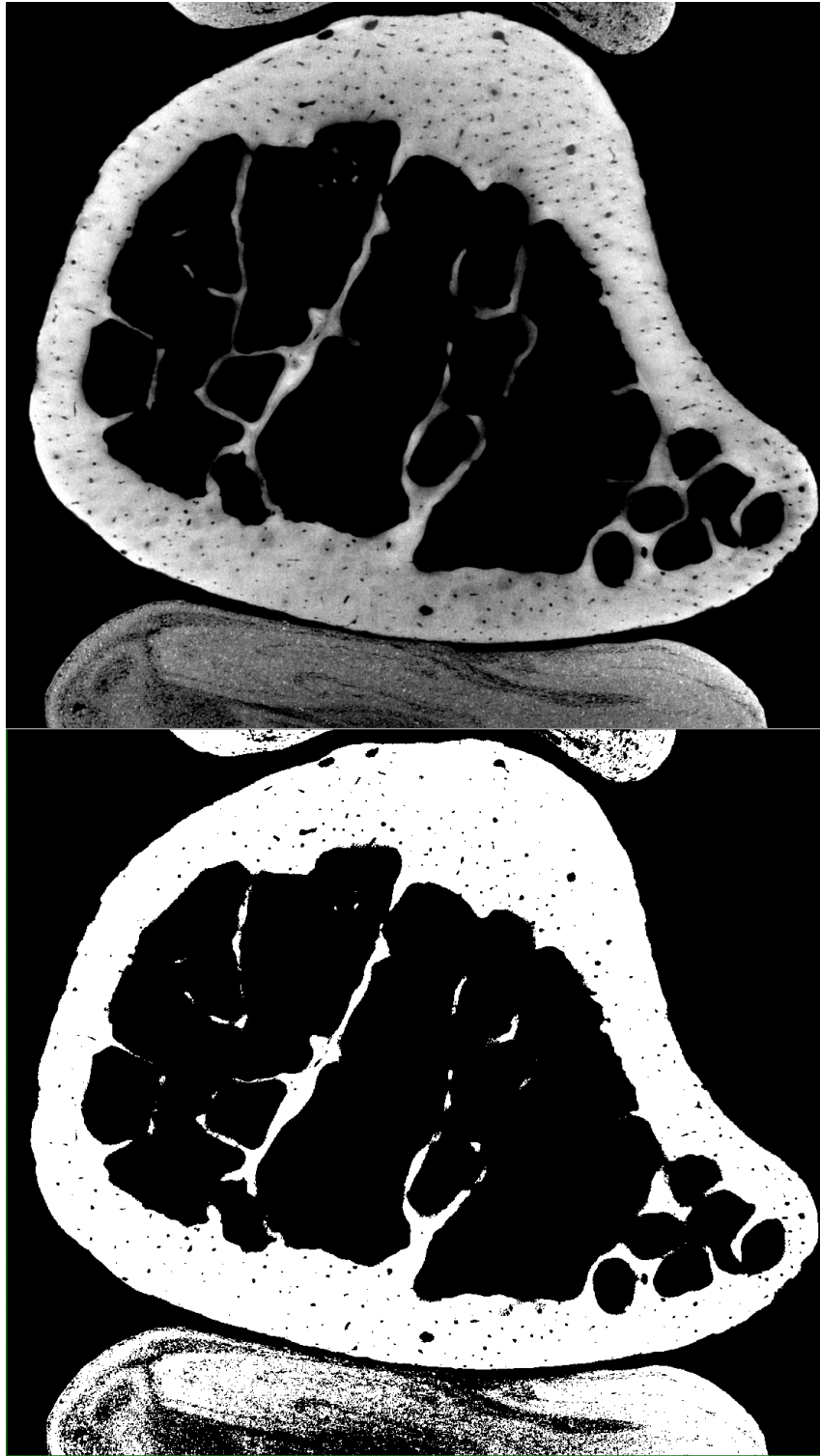
Figure 6.7 All Visible Pores Extracted With Adaptive Thresholding in 34M

168
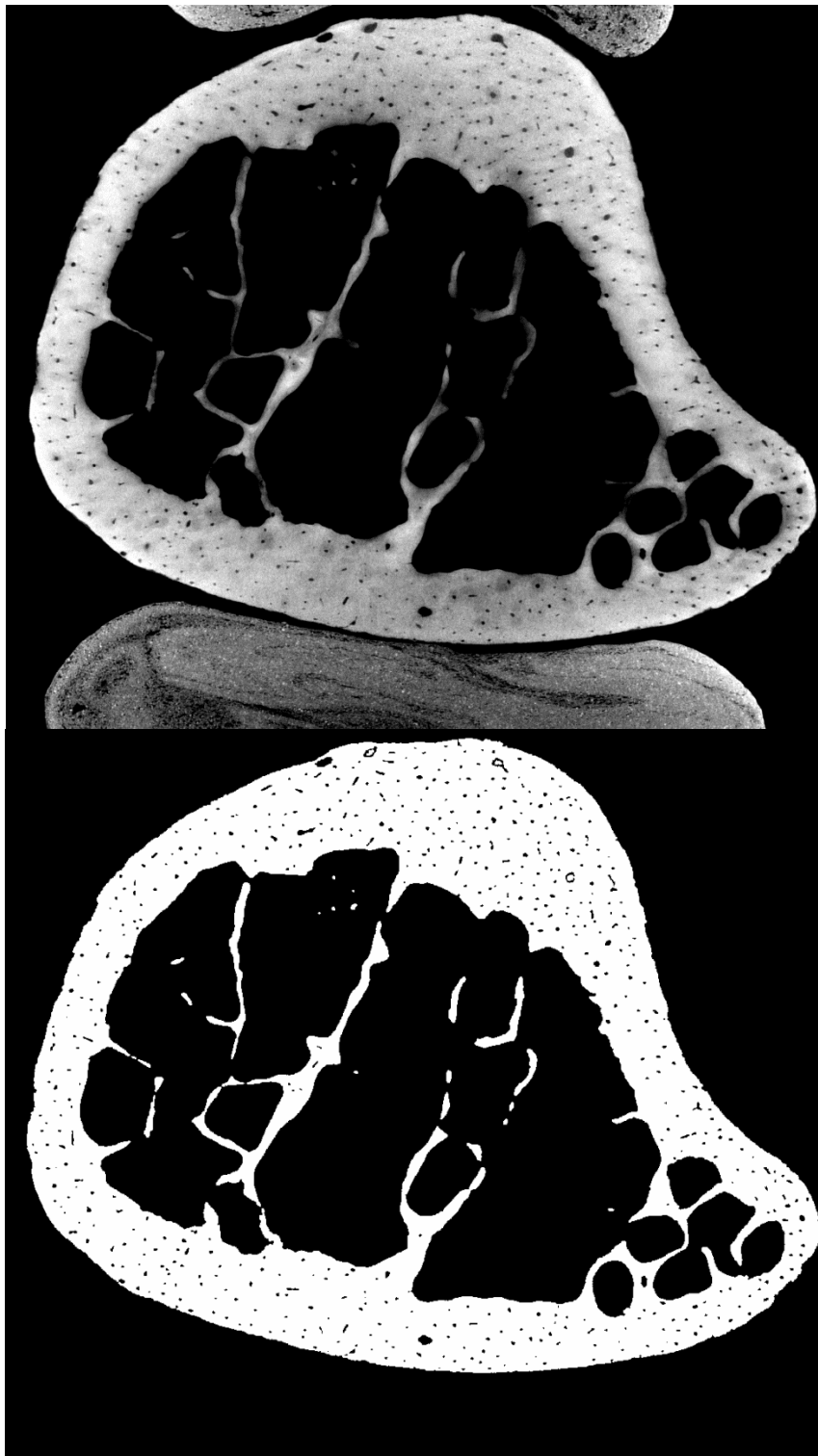
6.5. Femoral Neck Column Merging

After pore extraction and mounting fixture cleaning, the rib is prepared for marrow bounding to differentiate cortical from trabecular bone. However, the three columns of the femoral neck must still be merged. These columns have been aligned in Dragonfly, so they do not need to be reoriented, but merely pasted together. ImageJ has an inbuilt utility "Paste Control Transparent Zero" that copies and pastes the white area of binarized images without overlapping their black boundaries. However, this utility only works on a manual, slice-by-slice basis. A custom ImageJ macro was created to copy and paste anterior and posterior femoral segments onto the middle segment at the same slice in each stack. Additionally, the code automatically crops the image stack to the boundaries of the merged image. The user manually sets the coordinates in the macro editor as follows:

1) Open MergeFemora in the ImageJ macro editor

2) Open the macro recorder to view a readout of actions

3) Set Edit → Paste Control to Transfer mode: transparent-zero

4) Open the middle image

5) Image → Adjust → Canvas Size → Center, Width = 6000 pixels

6) Open the anterior image

7) Draw a rectangle to the boundaries of the anterior image, copy and paste onto the middle image

8) Use the rectangle tool to move the copied anterior cortex into position, then click the rectangle again

169

9) Note the first two readout values in macro recorder makeRectangle, and paste these into ax and ay values in the MergeFemora

10) Repeat for the posterior segment and px and py values in the MergeFemora code

It is advisable to run this macro on a small subset of slices from a spread within the cortex before processing the entire stack, in order to make fine adjustments to positioning.

Figure 6.8 Femoral Merging Input and Output in 67M
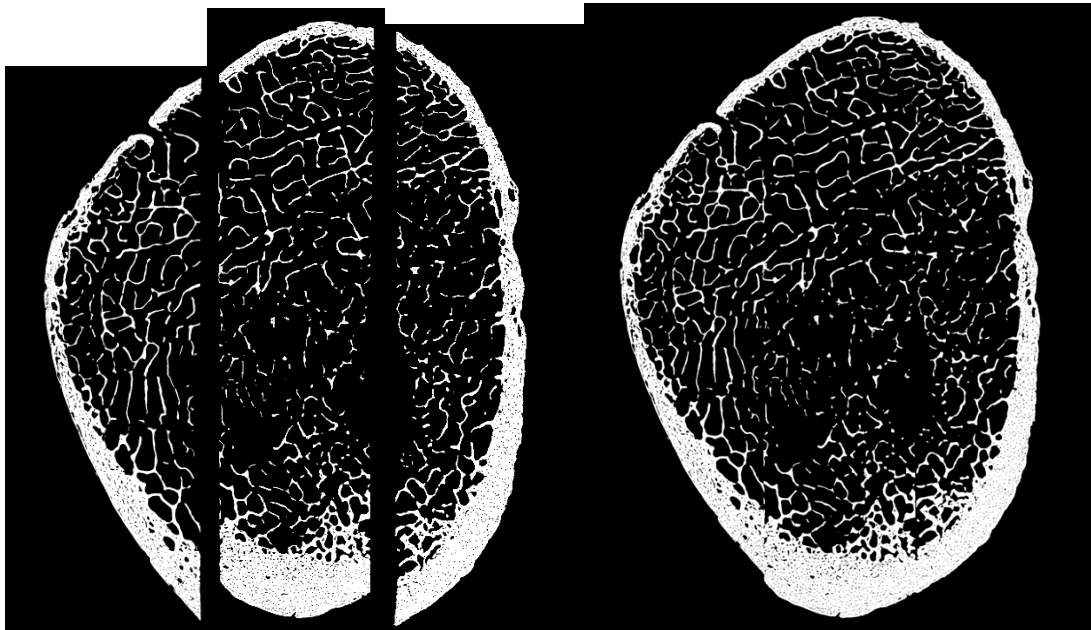
6.6. Marrow Bounding

In the marrow bounding routine developed for CT-Analyser, the endocortical boundary is not drawn so much as its irregularities are smoothed. To ensure consistency between individuals, the same smoothing thresholds were preserved for marrow bounding. A maximum of 30 pixels for filling cortical pores, clipping trabeculae, and

170

sealing trabecularized pores was effective at extracting the cortical shell in all ribs and femoral necks in this sample.

The workflow is complex, and fully detailed in Appendix 11.4. First, the periosteal border is shrink-wrapped and morphologically closed to seal large perosteal openings. This filled total area mask is then superimposed on the original image to isolate the marrow cavity. Trabeculaer struts and trabecularized pores are irregularities in this border that can be removed through morphological erosion and dilate, also of 30 pixels. An additional 30 pixel closing operation is applied to trabecular struts. Once the endosteam is isolated, it can be inverted and combined with the original filled cortex to create a solid cortical mask of the bone. This cortical mask is used to extract isolated pore networks in the remainder of the macro. The cortical mask is also the region of interest (ROI) used to normalize pore morphometry for tissue volume in later 3D morphometric analysis. The output from this macro is several folders of image stacks depicting varying divisions of cortex, porosity, and trabeculature. In addition to the cortical mask, cortical pores, cortical bone, and trabecularized bone shown below, this macro outputs image stacks of the isolated marrow cavity, isolated trabecular spaces, and all spaces (cortical + trabecular).

171

Figure 6.9 Marrow Bounding Workflow Summary
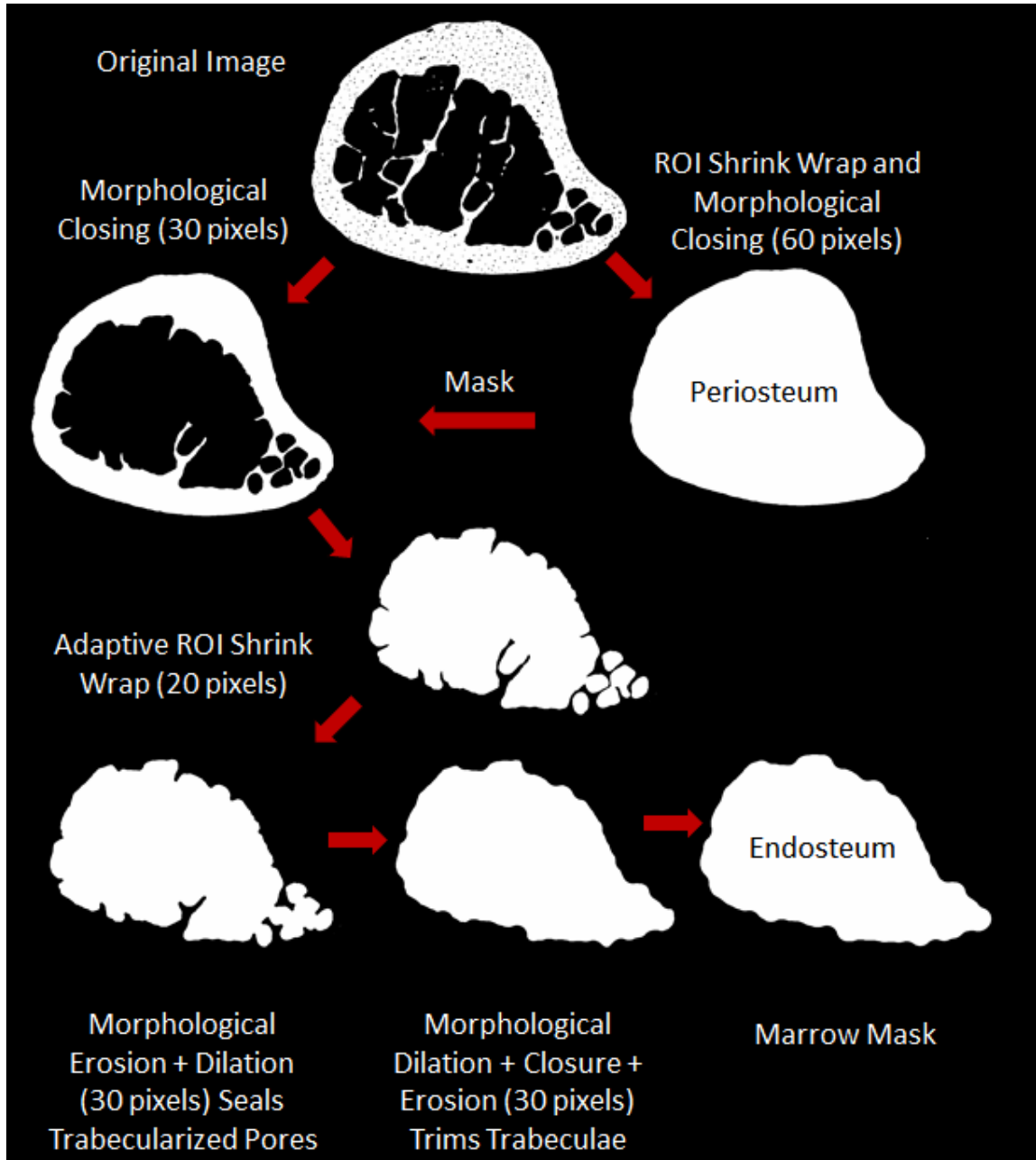
Figure 6.10 Marrow Bounding Output Image Stacks
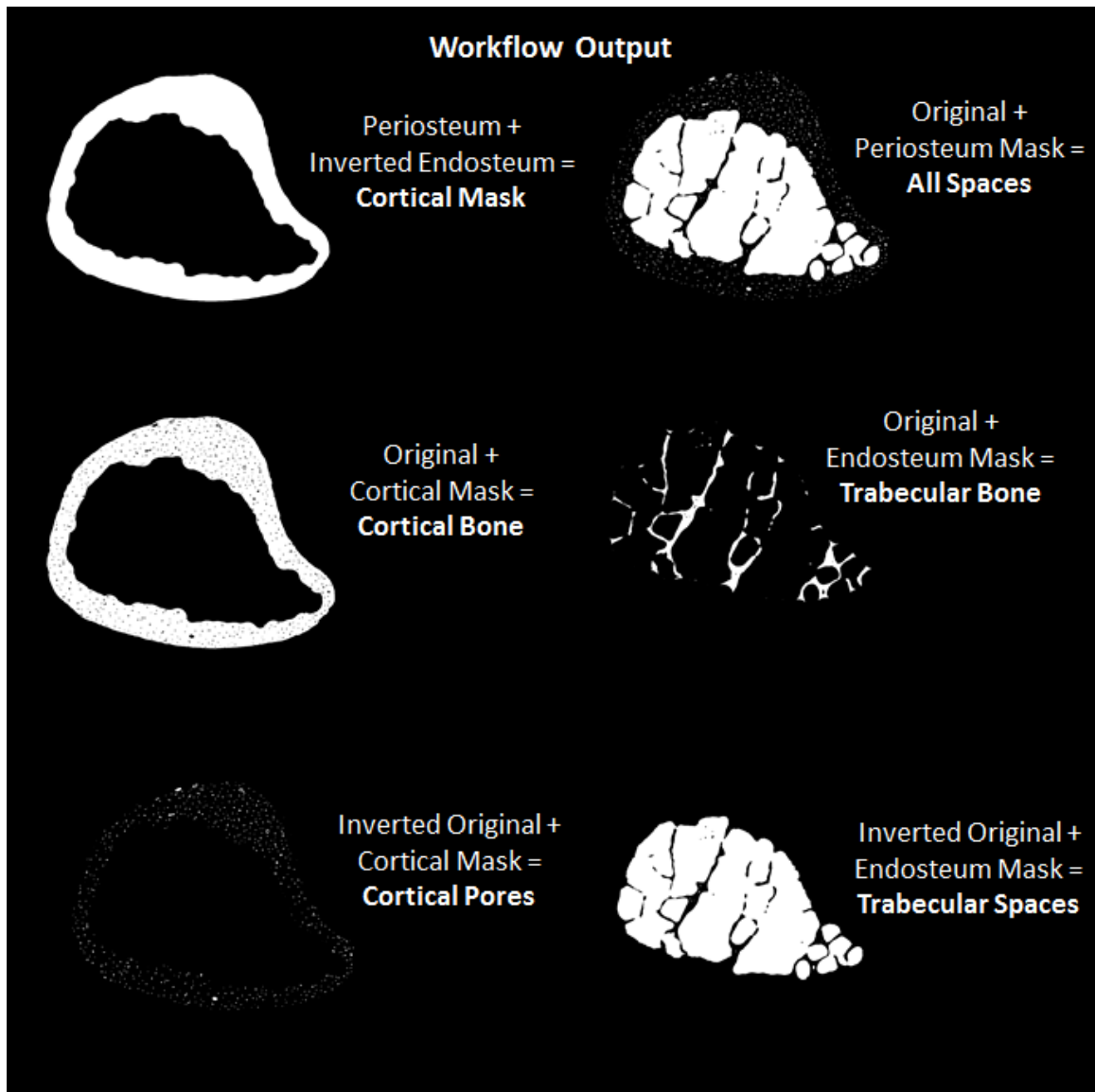
6.7. Pore Type Differentiation

The custom ImageJ macro used in this research generates separate image stacks of cortical and "trabecularized" pores. Keshawarz and Recker (1984) defined a pore as "trabecularized" if its minimum diameter exceeded its distance from the marrow cavity. At the start of this macro, pores undergo a binary dilate, close, fill holes, erode operation

that fills the lumen of hollow pores. This macro subsequently isolates pores using the

Analyze Particles plugin, and then superimposes these pores on a Euclidean Distance

Map of the marrow cavity. An EDM is a visual representation of distance from an object

as a pixel brightness value. For example, a pore located 10 pixels from the marrow cavity

will have a very low pixel brightness of 10. This macro measures the minimum gray

value (distance from the marrow in pixels) inside each pore, and compares this distance

to the pore's minimum feret (caliper) diameter. Pores are sorted into separate cortical and

trabecularized image stacks. This macro also collates two-dimensional morphometric

measurements of pore geometry from each slice.

Figure 6.11 Pore Type Differentiation Stages
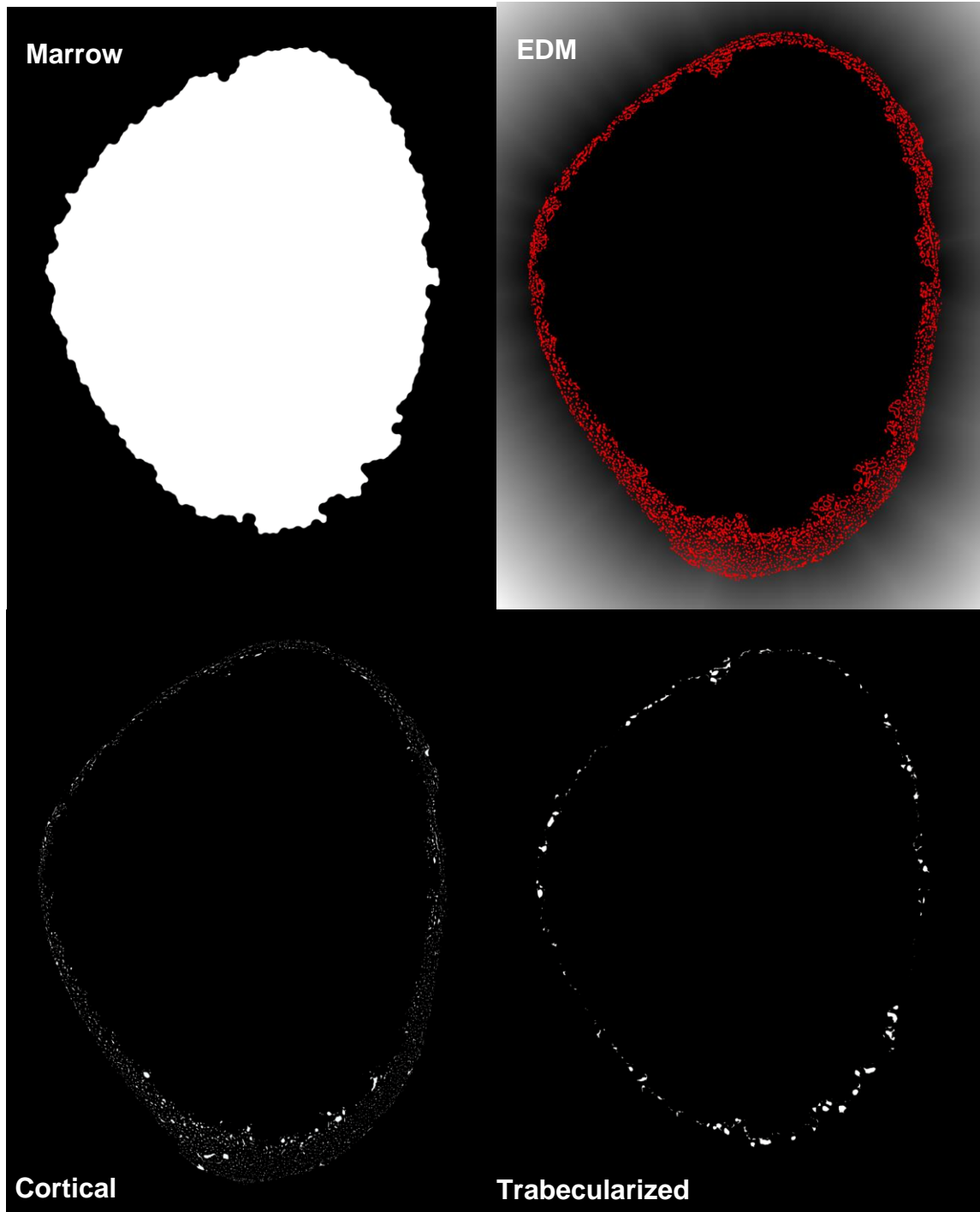
6.8. Regional Differentiation

For the rib, a custom ImageJ macro takes the input of the cortical shell and extracts coordinates of the major axis from the plugin BoneJ (Doube et al., 2010). This macro generates separate image stacks of the cutaneous cortex and the pleural cortex, as individually defined for each slice to account for changing bone morphometry along the image length. These separate regions may be used as ROI masks in CTan to compare the morphometry of pores (total, cortical, or trabecularized) between the two cortices of the rib.

For the femoral neck, a custom ImageJ macro similarly takes the input of the cortical shell and extracts coordinates of the major axis from BoneJ output. Using the major axis, octants are generated every 45 degrees to create regions along the superior-to-inferior strain gradient of the femoral neck. Calculating octant division for each slice allows the octants to remain aligned with the major axis of that slice, even as cortical shape is changing over the bone segment length. While these octants are not selected to be equal in size, they are consistently aligned with the superior to inferior axis of interest in this study. Additionally, other regions studies of cortical morphometry in the femur rely on octants that are not equal in area (e.g. Thomas et al., 2005; Gocha et al., 2018).

This macro initially loops through all cortical shell images without actually modifying them, and determines the coordinates for the bounding rectangle that best fit each octant on each slice. The macro also draws the octants on a stack output for reference. After this loop, the macro determines the maximum rectangle required to bound all octants of a certain anatomical type. It then loops back through and crops octant

176

images, as well as the total, cortical, and trabecularized pores they mask. By reducing the size of images through cropping unused space outside an octant, this macro improves analytical efficience. CT-Analyser's 3D morphometry requires approximately 10-20 minutes with cropping, and 45-60 minutes without cropping.

Figure 6.12 Femoral Neck Drawn Octants with Extracted Inferior Octant in 67M
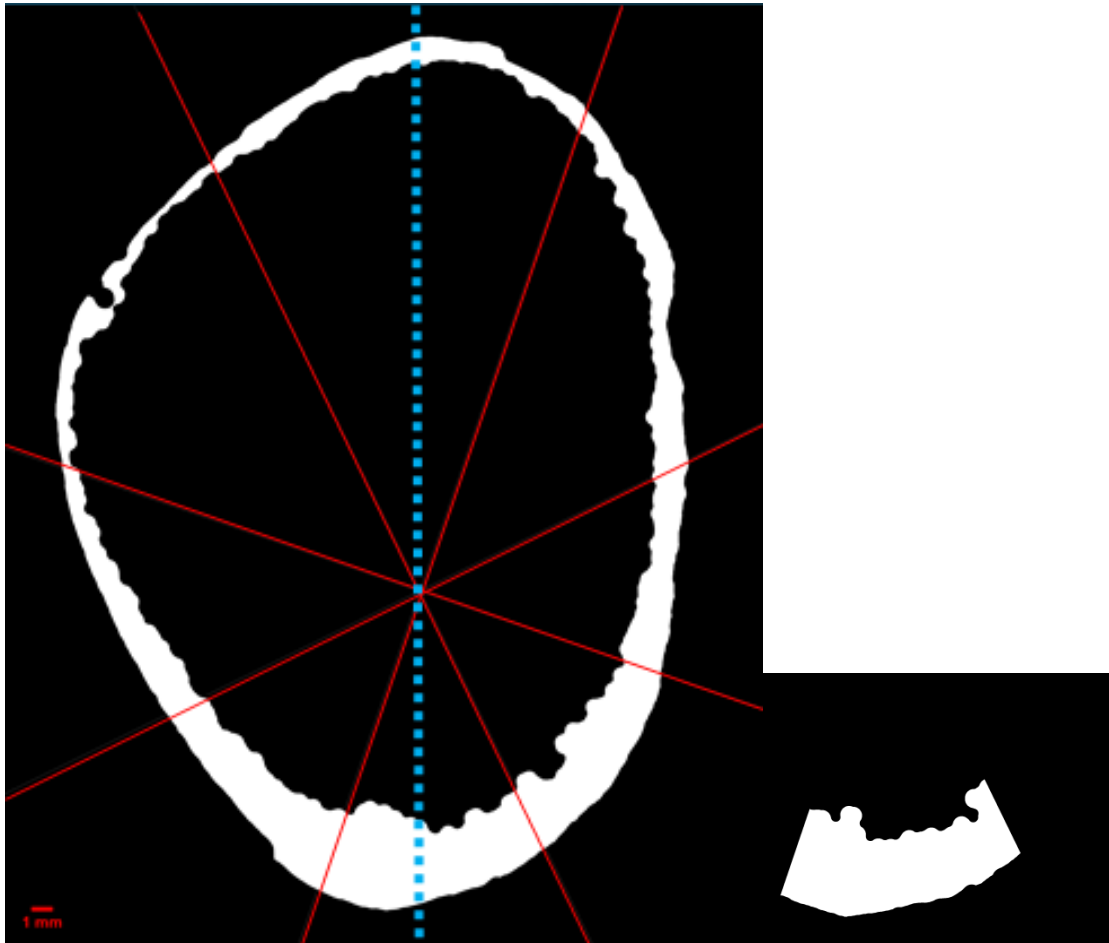
6.9. Relative Cortical Area and Parabolic Index

The final custom macro created for this project forms a mask of the total cortical area by merging the isolated marrow and the cortical shell created by marrow bounding.

177

During this process, total area and marrow area are quantified in order to calculate

Relative Cortical Area [(Total Area –Marrow Area / Total Area)*100] and the Parabolic

Index [Y = (Cortical Area * Marrow Area) / Total Area^2]. In addition to producing a table

of RCA and PI values by slice, this macro determines whether bones are osteoporotic

according to the parabolic index. The total area is then output as an image stack, so that it

can serve as an ROI mask for the filled cortical shell for calculations of the cross-

sectional geometry of the cortex.

6.10. Three-Dimensional Pore Morphometry

All of these image processing routines cumultate in three pore stacks (total,

cortical, trabecularized) and two ROI masks delineating the cortical boundaries of pore

analysis (whole and region). In CT-Analyser, both the file for analysis and the ROI mask

are loaded for three-dimensional morphometric analysis. The table below describes the

pore morphology parameters measured by CT-Analyser.

178

Table 6.1 Pore Morphometric Variables Measured By CT-Analyser

Variable	R Variable Name	Derived From	Units	Description
Percent Porosity	*percent_ porosity*	Cleaned Cortex	%	Pore Volume / Cortical Mask Volume
Percent Closed Porosity	*percent_ closed_ porosity*	Cleaned Cortex	%	Pores surrounded by white voxels on all sides in 3D
Percent Open Porosity	*percent_ open_ porosity*	Cleaned Cortex	%	Pores with any connection to the boundaries of the cortical mask
Proportion of Open Pores	*percent_ open_ pores*	Cleaned Cortex + Isolated Network	%	Number Open Pores / Number Total Pores
Proportion of Closed Pores	*percent_ closed_ pores*	Cleaned Cortex + Isolated Network	%	Number Closed Pores / Number Total Pores
Pore Density	*pore_ density*	Cleaned Cortex + Isolated Network	$1 / \mu m^3$	Number Total Pores / Cortical Mask Volume
Pore Thickness	*structure_ thickness*	Isolated Network	μm	Diameter of largest sphere enclosing a point (Trabecular Thickness equivalent)
Pore Separation	*structure_ separation*	Isolated Network	$1/\mu m$	Diameter of largest sphere enclosing a space (Trabecular Separation equivalent)
Standard Deviation of Pore Thickness	*stdv_ structure_ thickness*	Isolated Network	μm	Size is a proxy of the range of pore separation
Standard Deviation of Pore Separation	*stdv_ structure_ separation*	Isolated Network	$1/\mu m$	Size is a proxy of the range of pore thickness

179

Table 6.2 Pore Morphometric Variables Measured By CT-Analyser (Continued)

Variable	R Variable Name	Derived From	Units	Description
Pore Fragmentation Index	*fragmenta tion_ index*	Isolated Network	$1 / \mu m$	Compares volume and surface of solid before and after dilation by a single voxel as (S1-S2)/(V1 – V2) Inverse connectivity index, where higher values correspond to disconnected structures, and lower values correspond to "nodes" and higher connectivity.
Pore Connectivity Density	*connectivity _density*	Isolated Network	$1 / \mu m^3$	Number of redundant connections between pore structures per unit volume – derived from euler characteristic analysis
Degree of Anisotropy	*DA*	Isolated Network		Describes the degree to which structures are aligned (anisotropic) with a directional axis, as measured through mean intercept length analysis. Ranges from 0 (total isotropy) to infinity (total anisotropy)
Pore Linear Density	*structure_ linear_ density*	Isolated Network	μm	1 / (structure thickness + structure spacing) Implies number of intersections with pore network on a random linear path (Trabecular Number equivalent)
Cortex Fractal Dimension	*fractal_ dimension_ cortex*	Cleaned Cortex	Ratio	Index of complexity of the binarized cortical bone as a ratio of change in detail to change in scale – higher values are more complex structures
Pore Fractal Dimension	*fractal_ dimension_ pores*	Isolated Network	Ratio	Index of complexity of the isolated pore network as a ratio of change in detail to change in scale – higher values are more complex structures

7.   Results

7.1. Introduction: Methodological Considerations

Statistical testing must consider repeated measures, as pore morphometry is being compared within an individual (rib vs. femoral neck) or within regions of the same cross-section. While a repeated measures ANCOVA is the more traditional approach to this type of analysis, linear mixed models (LMM) are increasingly used to compare group means (Kruger and Tian, 2004). LMM models individual subjects as random effects to account for their repeated measurements, so it can directly characterize nonlinear individual attributes. LMM also better handles missing data and unbalanced model design (Kruger and Tian, 2004), such as the unequal number of males and females in the femoral neck dataset, or the unequal number of samples when comparing the rib (n = 14) and femoral neck (n=10). All statistical analysis was performed in the free, open source coding language R, version 3.6.0. The LMM designed for this analysis employs the "nlme" package in R. A sample code is provided in the R Statistical Code appendix.

For intraskeletal analysis, each pore morphometric variable is compared between the different levels of a given regional comparison, including bone type (rib vs. femoral neck), pore type (cortical vs. trabecularized), and region (rib cutaneous/pleural cortices or femoral neck octants. Co-variates are age, cortical thickness, and sex, as well as their interactions. This relationship is modeled as:

181

lme(poremorphometry ~ regionalcomparison + age * cs.th * sex, random = ~

1 | ID, datasetname, method = "REML", na.action = na.exclude)

The variance in pore morphometry explained by each model may be quantified with a

pseudo R^2 in a LMM. Marginal R^2 is the variance explained by the fixed factor(s), which

is the regional comparison in this model. Conditional R^2 is the variance explained by

both fixed factors and random factors – in this case, the individual with the repeated

measurements (Nakagawa and Schielzeth 2013). Cohen's d can quantify the effect size of

significant associations with fixed factors or co-variates by dividing the difference of

group means by the average of their standard deviaton. A d of 1 corresponds to a single

standard deviation between group means. Cohen suggested that effect size be quantified

as small or trivial (d = 0.2), medium (d = 0.5), and large (d=0.8). The positive or negative

term of Cohen's d describes the positive or negative relationship of the predictor with the

dependent variable (Cohen 1977). Unlike traditional analysis of variance metrics, LMM

do not require normal distribution of the dependant variables. However, the residuals

should be normally distribued. Normality of the residuals is checked with a quantile-

quantile (QQ) plot to examine deviations from normality and look for outliers. If a

Shapiro-Wilk test of the residuals is non-normal, the model is instead run through a

penalized quasilikelihood (PQL) general linear mixed model that can accommodate non-

normal data. Cohen's d and marginal and condition R^2 are also provided for glmmPQL

tests, as described in a sample code in the R Statistical Code appendix.

Pore separation and its standard deviation were not calculated for cortical and

trabecularized subsets of the femoral neck and rib data. Removing trabecularized pores

182

artificially increases pore separation for individuals who actually had more convergent pore networks. Therefore, a univariate model was run only on the effects of bone type and co-variates. A glmmPQL can again rescue non-normal residuals.

For regional comparisons between femoral neck octants, only total porosity was analyzed for this project, without division into pore types. This required only changing the equation of the LMM:

lme(poremorphometry ~ octant + age * cs.th * sex, random = ~ 1 | ID, data = datasetname, method = "REML", na.action = na.exclude)

This analysis was also complemented with tests for Cohen's d effect size, marginal R^2, and a Shapiro-Wilk test of normality for residuals. Again, a glmmPQL model could correct non-normal LMM residuals.

To visualize differences in two-factor groups, such as rib vs. femoral neck, cortical vs. trabecularized pore type, or cutaneous vs. pleurl rib region, a post-hoc is not required because the two levels must vary from one another. Scatterplots with marked medians are instead compared between the levels to discern the direction of difference. For comparisons of femoral neck octant distribution of pore morphometry, a post-hoc test must be applied to dertemine which specific octants vary from one another. Pairwise comparisons with a Tukey correction for multicollinearity were performed in the package "emmeans" for LMM and "glht" for glmmPQL. To quantify the nature of any significant octant differences, pore morphometry values were mapped onto octant positions using radar graphs, and medians were assessed for each octant by sex and by total sample.

183

7.2. Definition of Variables for Analysis

Table 7.1 Variable List of Demographic and Body Size Co-variates

Variable Name	R Name	Type	Units	Description
Age	*age*	Continuous	Years	Age at time of death
Sex	*sex*	Categorical	Male, Female	Biological sex
Height	*height*	Continuous	m	Known height at time of death
Weight	*weight*	Continuous	kg	Known weight at time of death
Continuous Body Mass Index	*BMI_con*	Continuous	kg/m^2	Weight / Height^2
Categorical Body Mass Index	*BMI_cat*	Categorical	Underweight Normal Overweight Obese	World Health Organization (1995) defined categories for continuous BMI: Underweight (15.0 – 19.9), Normal (20.0 – 24.9), Overweight (25.0 – 29.9), Obese (30.0+)

184

Table 7.2 Variable List of Bone Mineral Density Co-variates

Variable Name	R Name	Type	Units	Description
Continuous Total Body aBMD	*BMD_ total_ con*	Continuous	gm/cm^2	Total body aBMD measured by DXA after death
Continuous Total Body T-score	*T_total_ con*	Continuous	None	Standard deviation of total body aBMD from young adult NHANES III total body standard
Categorical Total Body T-Score	*T_total_ cat*	Categorical	Normal Osteopenia Osteoporosis	World Health Organization (1994) defined categories: Normal (> -1.0) Osteopenia (-1.0—2.5) Osteoporosis (=< -2.5)
Continuous Total Body Z-score	*Z_total_ con*	Continuous	None	Standard deviation of total body aBMD from age/sex/weight/ethnicity matched standard
Continuous Right Femoral Neck aBMD	*BMD_ neck_ con*	Continuous	gm/cm^2	Right femoral neck aBMD measured by DXA after death
Continuous Right Femoral Neck T-score	*T_neck_ con*	Continuous	None	Standard deviation of right femoral neck aBMD from young adult NHANES III femur standard (females) or GE Lunar standard (males)
Categorical Right Femoral Neck T-Score	*T_neck_ cat*	Categorical	Normal Osteopenia Osteoporosis	World Health Organization (1994) defined categories: Normal (> -1.0) Osteopenia (-1.0—2.5) Osteoporosis (=< -2.5)
Continuous Right Femoral Neck Z-score	*Z_neck_ con*	Continuous	None	Standard deviation of right femoral neck aBMD from age/sex/weight/ethnicity matched standard

Table 7.3 Variable List of Femoral Neck Gross Geometry Co-variates

Variable Name	R Name	Type	Units	Description
FemMx Lng	*fem_mx_lng*	Continuous	mm	Femoral shaft length measured with osteometric board from most superior femoral head to most inferior distal condyles
FemSub TrAPDia	*fem_sub_tr_ap_dia*	Continuous	mm	A-P (sagittal) subtrochanteric diameter
FemSub TrMLDia	*fem_sub_tr_ml_dia*	Continuous	mm	M-L (transverse) subtrochanteric diameter
FemHead SIDi	*fem_head_si_dia*	Continuous	mm	Maximum vertical head diameter
FemHead HzDia	*fem_head_hz_dia*	Continuous	mm	Maximum horizontal head diameter
FemNeck SL	*fem_neck_sl*	Continuous	mm	Superior neck length
FemNeck IL	*fem_neck_il*	Continuous	mm	Inferior neck length
FemNeck VDia	*fem_neck_v_dia*	Continuous	mm	Vertical neck diameter (minimum)
FemNeck TDia	*fem_neck_t_dia*	Continuous	mm	Transverse neck diameter (minimum)
FNAL Cent	*fnal_cent*	Continuous	mm	Femoral neck axial length to head apex
FNAL Apex	*fnal_apex*	Continuous	mm	Femoral neck axial length to head center
OFF	*off*	Continuous	mm	Offset of shaft axis to head center
Neck-Shaft Angle	*neck_shaft_angle*	Continuous	degrees	Neck-shaft axis to neck axis angle

186

Table 7.4 Variable List of Cross-Sectional Geometry Co-variates

Variable Name	R Name	Type	Units	Description	Source
Mean Slice Relative Cortical Area	*rca_ mean_ slice*	Continuous	%	Mean of all slice [(Cortical Area / Total Area) * 100]	Custom ImageJ Macro *RCA* calculates RCA per slice
Mean Stack Relative Cortical Area	*rca_ mean_ stack*	Continuous	%	(Stack Mean Cortical Area / Stack Mean Total Area) * 100	CTan 2D Morphology: Cortical Shell with Total Area ROI
Relative Cortical Volume	*rcv*	Continuous	%	(Cortical Volume / Total Volume) * 100	CTan 3D Morphology: Cortical Shell with Total Area ROI
Mean Slice Parabolic Index	*pi_ mean_ slice*	Continuous	None	Mean of all slice [Y = (Cortical Area * Marrow Area) / Total Area^2]	Custom ImageJ Macro *RCA* calculates PI per slice
BoneJ Mean Minimum Principle Moment of Inertia (Imin)	*imin_ mean_ bonej*	Continuous	μm^4	Mean of all slice Imin values	BoneJ via custom ImageJ macro *RibRegion* or *FemoralNeckRegion*
CTan Mean Minimum Principle Moment of Inertia (Imin)	*imin_ mean_ ctan*	Continuous	μm^4	Mean of all slice Imin values	CTan 2D Morphology: Cortical Shell with Total Area ROI
BoneJ Mean Maximum Principle Moment of Inertia (Imax)	*imax_ mean_ bonej*	Continuous	μm^4	Mean of all slice Imax values	BoneJ via custom ImageJ macro *RibRegion* or *FemoralNeckRegion*

187

Table 7.5 Variable List of Cross-Sectional Geometry Co-variates (Continued)

Variable Name	R Name	Type	Units	Description	Source
CTan Maximum Principle Moment of Inertia (Imax)	*imax_min_ctan*	Continuous	μm^4	Mean of all slice Imax values	CTan 2D Morphology: Cortical Shell with Total Area ROI
BoneJ Mean Polar Moment of Inertia (J)	*j_mean_bonej*	Continuous	μm^4	Mean of all slice (Imax + Imin)	BoneJ via custom ImageJ macro *RibRegion* or *FemoralNeckRegion*
CTan Mean Polar Moment of Inertia (J)	*j_mean_ctan*	Continuous	μm^4	Mean of all slice (Imax + Imin)	CTan 2D Morphology: Cortical Shell with Total Area ROI
Mean Eccentricity	*ecc*	Continuous	None	Mean of all slice eccentricity, where e = $\sqrt{1 - \frac{b^2}{a^2}}$ for a fitted ellipse with major axis *2a* and minor axis *2b*	CTan 2D Morphology: Cortical Shell with Total Area ROI
Cross-sectional Thickness	*cs.th*	Continuous	μm	2 / (surface/volume) from 2D integration	CTan 2D Morphology: Cortical Shell with Total Area ROI

188

7.3. Co-variate Refinement and Selection

7.3.1. *Appropriateness of Parametric Tests for Co-variate and Pore Morphometry Analysis*

To determine whether to take a parametric or non-parametric approach to analysis, Shapiro-Wilk Normality tests were applied to continuous co-variates and pore morphometric variables separately in the rib and femoral neck due to the slightly different structure of these sample sets.

Table 7.6 Shapiro-Wilk Normality Test for Rib Co-Variates and Total Pores

Variable	W	p-value
Age	0.960301	0.728055
Weight	0.97335	0.93077
Height	0.843963	***0.023822***
Continous BMI	0.948251	0.57204
Continous Total BMD	0.920341	0.253527
Continous Total T-score	0.904911	0.15618
Continous Total Z-score	0.895549	0.11619
rca_mean_slice	0.95213	0.594233
Mean Parabolic Index	0.883923	0.066116
Mean Imin BoneJ	0.888201	0.076153
Mean Imax BoneJ	0.953401	0.614642
Mean J BoneJ	0.939091	0.406798
rca_mean_stack	0.955112	0.642482
Mean Imin	0.887791	0.075128
Mean Imax	0.953688	0.619293
Mean J	0.939575	0.412908
Mean Eccentricity	0.77844	***0.002735***
Cross-sectional Thickness	0.89041	0.08194
Relative Cortical Volume	0.955087	0.642073
Cortical Fractal Dimension	0.94807	0.531165
% Closed Porosity	0.953008	0.608313
% Open Porosity	0.914301	0.181933
% Porosity	0.913138	0.175006

189

	W	p-value
Pore Thickness	0.985672	0.995516
Pore Separation	0.966448	0.825918
Structure Linear Density	0.892276	0.087178
Fragmentation Index	0.963235	0.775807
DA	0.881683	0.061417
Pore Network Fractal Dimension	0.947339	0.520214
Connectivity Density	0.938969	0.405274
StDv Pore Thickness	0.885126	0.068792
StDv Pore Separation	0.779286	***0.002799***
Proportion Open Pores	0.873823	***0.047498***
Proportion Closed Pores	0.873823	***0.047498***
Pore Density	0.937425	0.386327

Significant values (p < 0.05) are ***bolded***

Table 7.7 Shapiro-Wilk Normality Test for

Femoral Neck Continuous Co-Variates

Variable	W	p-value
Age	0.97278	0.915356
Weight	0.968161	0.878561
Height	0.76155	0.007377
Continous BMI	0.979268	0.960404
Continous Total BMD	0.883874	0.172403
Continous Total T-score	0.883466	0.170722
Continous Total Z-score	0.894054	0.219515
Continous R Femoral Neck BMD	0.945053	0.635975
Continous R Femoral Neck T-score	0.89683	0.234194
Continous R Femoral Neck Z-score	0.959725	0.795435
FemMxLng	0.862298	0.15872
FemSubTrAPDia	0.859836	0.075969
FemSubTrMLDia	0.926683	0.416067
FemHeadSIDi	0.926534	0.414681
FemHeadHzDia	0.947649	0.640778
FemNeckSL	0.889713	0.16832
FemNeckIL	0.935773	0.507008
FemNeckVDia	0.957103	0.752402
FemNeckTDia	0.92574	0.407325
FNALCent	0.861099	0.078619
FNALApex	0.873731	0.110467

OFF	0.896249	0.199174
Neck-Shaft Angle	0.910848	0.28687
Mean RCA by Slice	0.899846	0.218246
Mean Parabolic Index	0.921327	0.368156
Mean Imin BoneJ	0.942772	0.584253
Mean Imax BoneJ	0.792893	***0.011883***
Mean J BoneJ	0.949015	0.656864
Mean RCA by Stack	0.909137	0.275113
Mean Imin CTan	0.969664	0.887712
Mean Imax CTan	0.814679	***0.02185***
Mean J CTan	0.875554	0.115971

Significant values (p < 0.05) are ***bolded***

Shapiro-Wilk Normality Test for

Femoral Neck Continuous Co-Variates (Continued)

Variable	W	p-value
Relative Cortical Volume	0.909017	0.274308
Cortical Fractal Dimension	0.864125	0.085332
% Closed Porosity	0.934119	0.489602
% Open Porosity	0.931545	0.463258
% Porosity	0.928939	0.437536
Pore Thickness	0.837274	***0.040926***
Pore Separation	0.886402	0.154415
Structure Linear Density	0.926978	0.41883
Fragmentation Index	0.561825	***1.95E-05***
DA	0.917054	0.333039
Pore Network Fractal Dimension	0.903998	0.242254
Connectivity Density	0.974226	0.927028
StDv Pore Thickness	0.754107	***0.004004***
StDv Pore Separation	0.847592	0.054377
Proportion Open Pores	0.844734	0.05027
Proportion Closed Pores	0.844734	0.05027
Pore Density	0.934136	0.489779

Significant values (p < 0.05) are ***bolded***

191

7.3.2. Refinement of Cross-Sectional Geometry Calculations

Cross-sectional geometry is calculated from each rib or femoral neck represented as a binarized, filled cortical shell. Custom ImageJ macros *RCA, RibRegion,* and *FemoralNeckRegion* report cross-sectional metrics (Table 7.10, Table 7.11) for each slice within a stack using the ImageJ plugin BoneJ (Doube *et al.,* 2010). Ct-analyser 2D and 3D morphometry reports similar or the same values for the input of the cortical shell with an ROI mask of the total area. Both BoneJ and Ct-analyser calculate Imin, Imax, and J slicewise, and take the mean for the stack value. Relative cortical area is more methodologically variable in its calculation within this study. The custom ImageJ macro *RCA* calculates relative cortical area for each slice from total area and marrow area slice input images, reflecting the traditional histological approach. CTan 2D morphometry reports the mean object (cortical) area for the entire image stack, which can be divided by the mean ROI (total) area for the stack to produce a single stack relative cortical area value. CTan 3D morphometry reports the object (cortical) volume / ROI (total) volume ratio, which is equivalent to relative cortical volume.

192

Table 7.8 Cross-Sectional Geometry: Rib

ID	RCA Mean Slice (%)	RCA Mean Stack (%)	RCV (%)	BoneJ Mean Imin (μm^4)	CTan Mean Imin (μm^4)	BoneJ Mean Imax (μm^4)	CTan Mean Imax (μm^4)	BoneJ Mean J (μm^4)	CTan Mean J (μm^4)	PI Mean Slice (Y)	Ecc	Cs.Th. (μm)
26M	53.68	53.70	53.68	1.95E+14	1.95E+14	5.40E+14	5.40E+14	7.35E+14	7.35E+14	0.25	0.80	1215.80
28F	53.93	52.53	52.50	4.04E+13	4.04E+13	1.32E+14	1.32E+14	1.72E+14	1.72E+14	0.25	0.83	813.16
34M	42.54	42.55	42.53	3.33E+14	3.33E+14	3.51E+14	3.51E+14	6.85E+14	6.85E+14	0.24	0.22	1047.40
39F	41.50	41.53	41.51	5.58E+13	5.58E+13	1.55E+14	1.55E+14	2.11E+14	2.11E+14	0.24	0.80	718.46
41M	24.59	24.85	24.83	8.56E+13	8.78E+13	2.15E+14	2.16E+14	3.01E+14	3.03E+14	0.19	0.77	499.79
49F	42.52	42.56	42.53	1.99E+13	1.99E+13	3.53E+13	3.53E+13	5.52E+13	5.52E+13	0.24	0.66	545.69
50F	48.02	48.06	48.04	1.15E+14	1.15E+14	3.07E+14	3.07E+14	4.22E+14	4.22E+14	0.25	0.79	972.98
56M	26.59	26.61	26.59	1.93E+14	1.93E+14	2.96E+14	2.96E+14	4.89E+14	4.89E+14	0.20	0.59	620.77
60F	34.46	34.46	34.43	1.91E+13	1.91E+13	9.98E+13	9.98E+13	1.19E+14	1.19E+14	0.23	0.90	438.38
67M	21.80	21.83	21.80	1.22E+14	1.22E+14	2.47E+14	2.47E+14	3.69E+14	3.69E+14	0.17	0.71	488.26
70F	32.38	32.41	32.38	8.95E+13	8.95E+13	1.97E+14	1.97E+14	2.87E+14	2.87E+14	0.22	0.74	618.60
77M	31.46	31.42	31.40	9.56E+13	9.56E+13	1.67E+14	1.67E+14	2.62E+14	2.62E+14	0.22	0.65	611.20
82F	62.58	62.60	62.58	8.95E+13	8.95E+13	1.76E+14	1.76E+14	2.65E+14	2.65E+14	0.23	0.70	1156.40
88M	28.20	28.21	28.20	1.89E+14	1.89E+14	4.41E+14	4.41E+14	6.30E+14	6.30E+14	0.20	0.75	644.55
Shapiro-Wilk Sig.	0.5942	0.6425	0.6421	0.07615	0.07513	0.6146	0.6193	0.4068	0.4129	0.06612	***0.002735***	0.08194

*Significant values ($p < 0.05$) are **bolded.***

193

Table 7.9 Cross-Sectional Geometry: Femoral Neck

ID	RCA Mean Slice (%)	RCA Mean Stack (%)	RCV (%)	BoneJ Mean Imin (μm^4)	CTan Mean Imin (μm^4)	BoneJ Mean Imax (μm^4)	CTan Mean Imax (μm^4)	BoneJ Mean J (μm^4)	CTan Mean J (μm^4)	PI Mean Slice (Y)	Ecc	Cs.Th. (μm)
34M	27.12	31.17	31.15	1.55E+16	1.80E+16	4.78E+16	4.62E+16	5.11E+16	6.42E+16	0.20	0.78	2060.00
39F	19.76	19.93	19.91	8.33E+15	8.46E+15	1.33E+16	1.35E+16	2.16E+16	2.19E+16	0.16	0.60	1100.00
49F	18.39	19.19	19.17	4.67E+15	4.74E+15	8.48E+15	8.61E+15	1.32E+16	1.33E+16	0.15	0.67	998.00
50F	23.93	23.77	23.76	1.29E+16	1.30E+16	1.70E+16	1.71E+16	2.99E+16	3.02E+16	0.18	0.47	1400.00
56M	15.81	15.94	15.93	1.22E+16	1.24E+16	1.74E+16	1.76E+16	2.96E+16	3.00E+16	0.13	0.53	1080.00
60F	19.73	19.68	19.66	5.52E+15	5.62E+15	8.80E+15	8.96E+15	1.43E+16	1.46E+16	0.16	0.60	1070.00
67M	16.57	16.73	16.72	1.24E+16	1.25E+16	2.20E+16	2.22E+16	3.44E+16	3.47E+16	0.14	0.65	1240.00
70F	17.26	17.35	17.33	7.87E+15	7.99E+15	1.91E+16	1.93E+16	2.70E+16	2.73E+16	0.14	0.75	1120.00
77M	19.65	21.64	21.63	1.08E+16	1.08E+16	1.92E+16	1.98E+16	3.00E+16	3.06E+16	0.16	0.67	1370.00
88M	25.69	25.80	25.79	1.45E+16	1.48E+16	2.37E+16	2.39E+16	3.82E+16	3.87E+16	0.19	0.61	1570.00
Shapiro-Wilk Sig.	0.2182	0.2751	0.2743	0.5843	0.8877	***0.011883***	***0.02185***	0.6569	0.116	0.3682	0.9093	***0.0333***

*Significant values ($p < 0.05$) are **bolded.***

194

The three calculations of relative cortical area were normally distributed for both the rib and femoral neck. These values could subsequently be compared through a parametric approach. A linear mixed model for repeated measures, with the individual as the error term (Table 7.9), was used to compare the RCA calculation from the mean slice, mean stack, and volume methods. Considering an ANOVA of this linear model, there was no significant difference in RCA output for either the rib ($p = 0.52$) or the femoral neck ($p = 0.06$), and the calculation method alone explained less than 1% of the variance. Given this equivalence, Relative Cortical Volume was chosen as the representative co-variate for Relative Cortical Area, as it additionally considers thickness between the slices in its calculation.

Table 7.10 ANOVA of Linear Mixed Model for RCA Calculation Method

	Sum Sq	Mean Sq	Num DF	Den DF	F value	p-value	R^2 marginal	R^2 conditional
Rib	0.06	0.03	2.00	28.00	0.66	0.52	1.09E-05	1.00
Femoral Neck	3.46	1.73	2.00	20.00	3.30	0.06	0.01	0.97

*Significant values ($p < 0.05$) are **bolded**.*

BoneJ and CTan derived values for Imax, Imin, and J were all normally distributed, with the exception of the femoral neck BoneJ Mean Imax ($p = 0.011883$) and CTan Mean Imax ($p = 0.02185$) A series of paired t-tests compaired BoneJ and CTan derivations for the parametric values (Table 7.12 and found no significant differences. The non-parametric paired t-test equivalent, a Wilcoxon Signed Rank Test with the Pratt (1959) method for handling ties, compared CTan Mean Imax and BoneJ Mean Imax, and found no significant

195

difference (Z = -1.8074, p-value = 0.08008). To remain consistent with the use of CTan 2D/3D morphometry for RCA calculation, CTan 2D/3D morphometry values were also selected as the moment of inertia co-variates.

Table 7.11   Paired T-Tests for Moments of Inertia Calculation Method

Paired T-Test	Mean Difference	t	p-value (two-tailed)	df	95% Confidence Interval of Difference	
					Lower	Upper
Rib Imin	-1.6E+11	-1	0.335561	13	-5E+11	1.82E+11
Rib Imax	-7.1E+10	-1	0.335561	13	-2.3E+11	8.29E+10
Rib J	-1.4E+11	-1	0.335561	13	-4.5E+11	1.66E+11
Femoral Neck Imin	-3.62E+14	-1.5154	0.163974	9	-9.02E+14	1.78E+14
Femoral Neck J	-1.62E+15	-1.26933	0.236163	9	-4.51E+15	1.27E+15

*Significant values (p < 0.05) are **bolded**.*

7.3.3.   Correlation Matrix Between Co-variates

Correlations between co-variates were analyzed separately for the rib and femoral neck due to their varying sample sizes and gross and cross-sectional co-variates. The strength of the linear relationship between pairs of co-variates was measured with the Pearson r. The strength of relationship was categorized as None or Very Weak (r < 0.3), Weak (r = 0.3 – 0.5), Moderate (r = 0.5 – 0.7), or Strong (r>0.7). Correlation tables were visualized in R using package ggcorplot (Figures 7.1., 7.2, 7.3)

196

Figure 7.1 Rib Co-variate Correlation Matrix with Pearson R, Ordered by Variable List
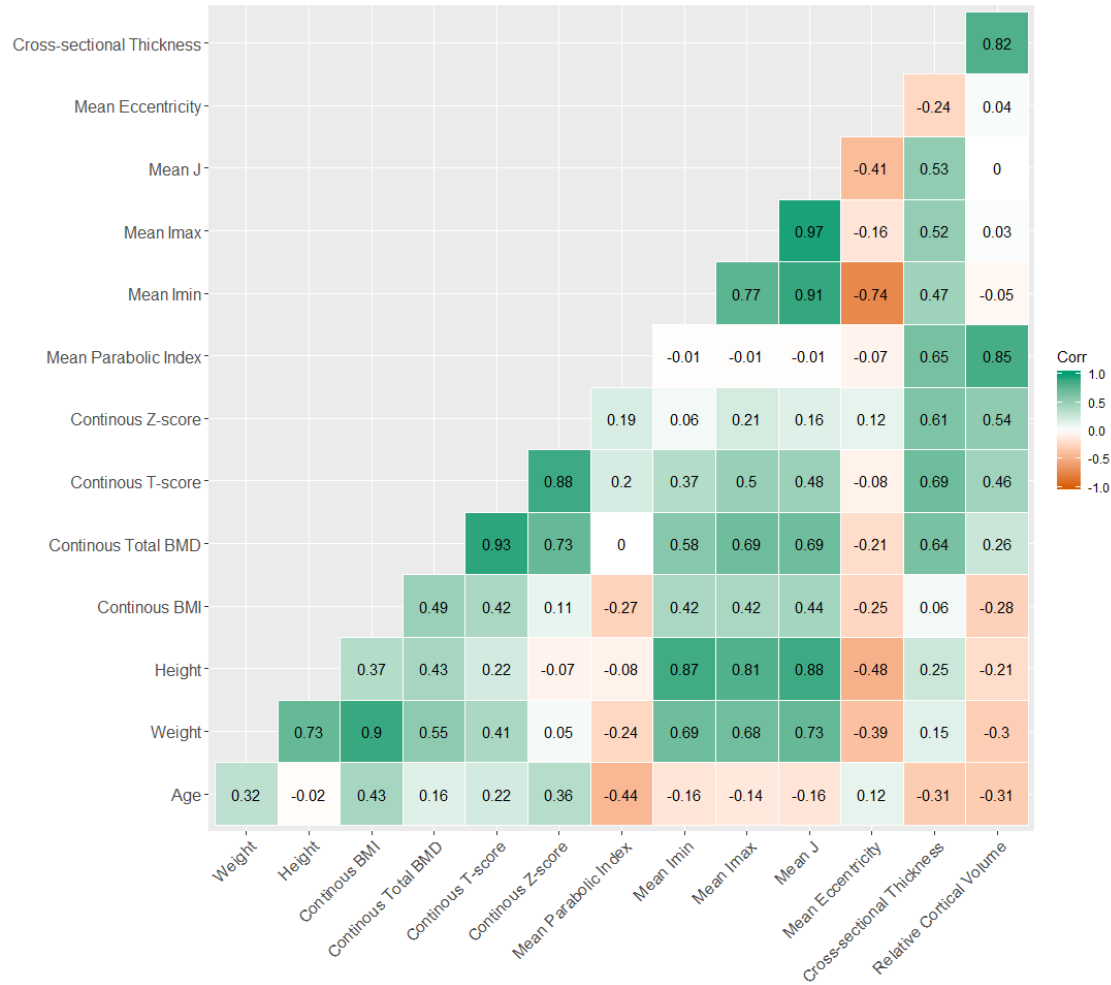
Figure 7.2 Rib Co-variate Correlation Matrix with Pearson R, Reordered by Hierarchal Clustering
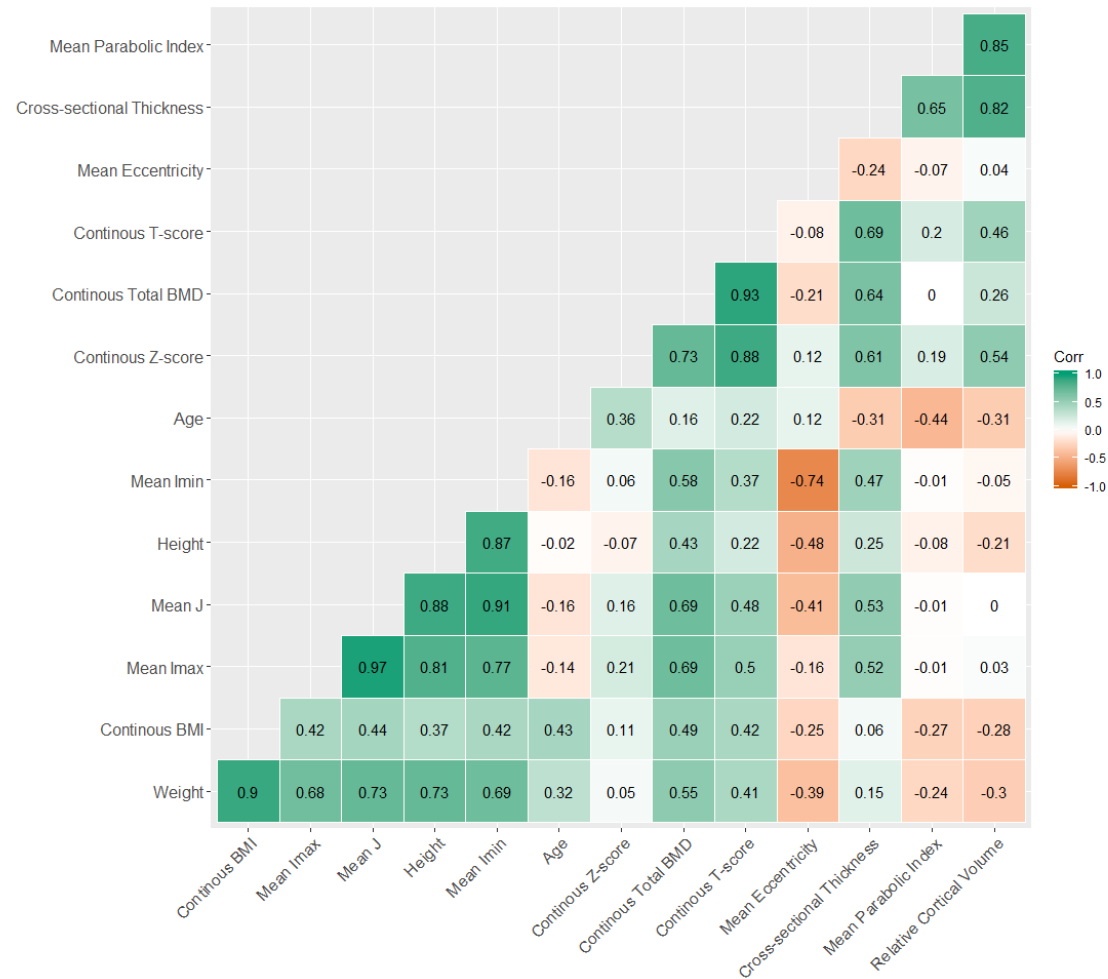
Figure 7.3 Rib Co-variate Correlation Matrix Showing Significant P-Values, Ordered by Variable List

199
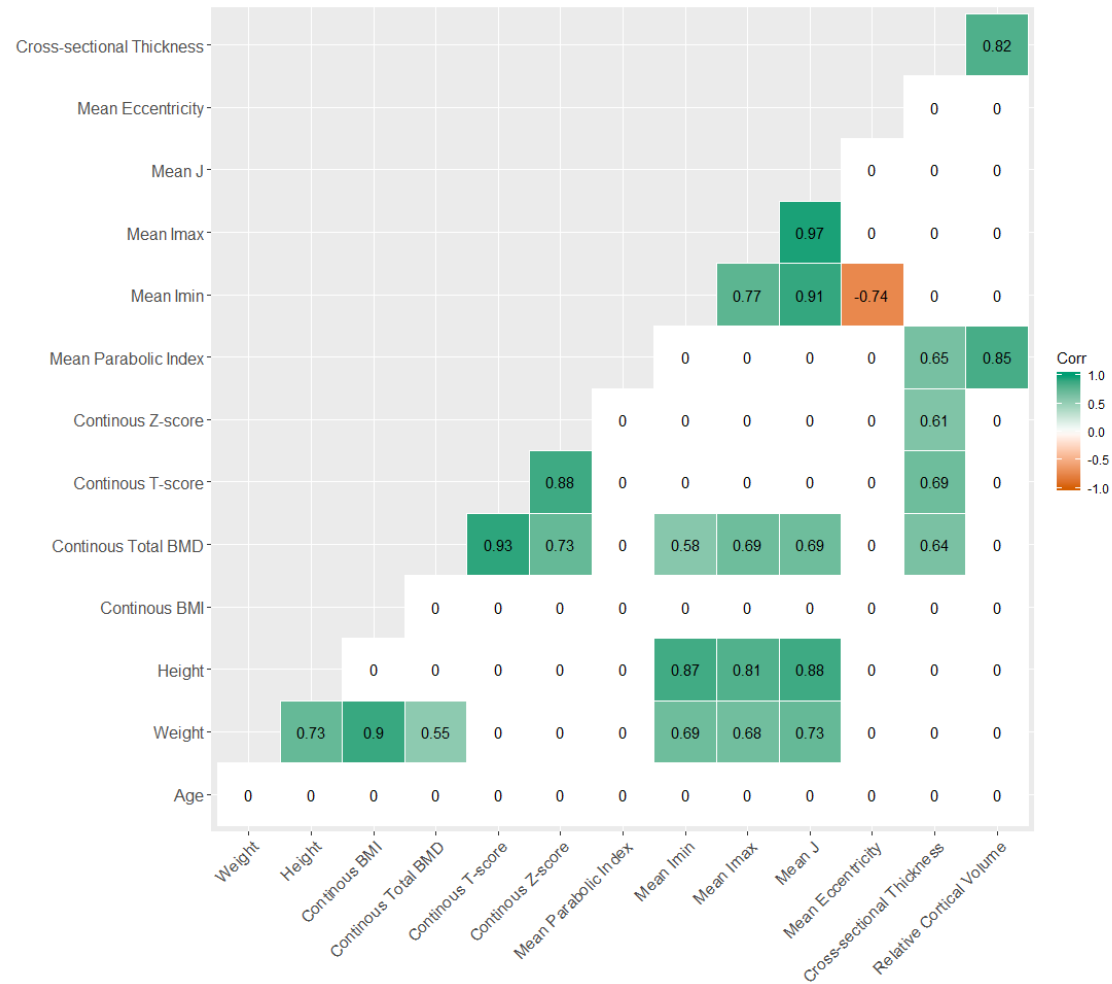
Rib Related Metrics: Most of the strong and significant correlations in the rib are due to inter-related co-variate groups of body size (height, weight, continuous BMI), BMD (total BMD, T-score, Z-score), moments of inertia (mean I_{max}, mean I_{min}, J) and bone mass (relative cortical volume, cross-sectional thickness, mean parabolic index). However, a few trends or significant correlations do exist between demographic or BMD variables and cross-sectional metrics.

Age: Chronological age is not strongly or significantly correlated with any of the continuous demographic, body size, BMD, or cross-sectional metrics in the rib. The small sample size may play a role in reducing the significance of these interactions. Age is weakly negative correlated with relative cortical volume, cross-sectional thickness, and mean parabolic index, reflecting cortical thinning with age. Age is weakly positively correlated with continuous Z-score, but it is also an inherent adjustment to this calculation. Age also weakly positively correlates with weight and continuous BMI, as all four overweight or obese individuals in the sample are older than 50 years.

Body Size: Height and weight are both moderately to strongly and significantly positively correlated with rib cross-sectional moments of inertia (mean I_{max}, mean I_{min}, mean J), reflecting the increased stiffness required by increasing body size. However, relative cortical volume and mean parabolic index are weakly negatively correlated with body size, potentially due to the tendency of older individuals to skew larger. Interestingly, mean eccentricity is moderately

200

but insignificantly negatively correlated with height and weight, suggesting slightly more circular (less eccentric) ribs with increased body size. Weight is moderately and significantly correlated with continuous total BMD, and a moderate but insignificant correlation exists with continuous total t-score. This correlation is absent for total continuous z-score, which is adjusted for body size

Bone Mineral Density: Continuous total BMD is moderately and significantly correlated with rib cross-sectional moments of inertia (mean Imax, mean Imin, mean J). All BMD metrics are moderately and significantly correlated with cross-sectional thickness.

Cross-Sectional Size and Shape: Moments of inertia signifying rib shape are not significantly correlated with metrics of bone mass (relative cortical volume, mean parabolic index, cross-sectional thickness in the rib. The single significant and moderately strong negative correlation in the rib, between mean Imin and mean eccentricity, is geometric. As mean eccentricity increases and the cross-section elongates, Imin (calculated **around** the minor axis by both CTan and BoneJ) decreases.

201

Figure 7.4 Femoral Neck Co-variate Correlation Matrix with Pearson R, Ordered by Variable List
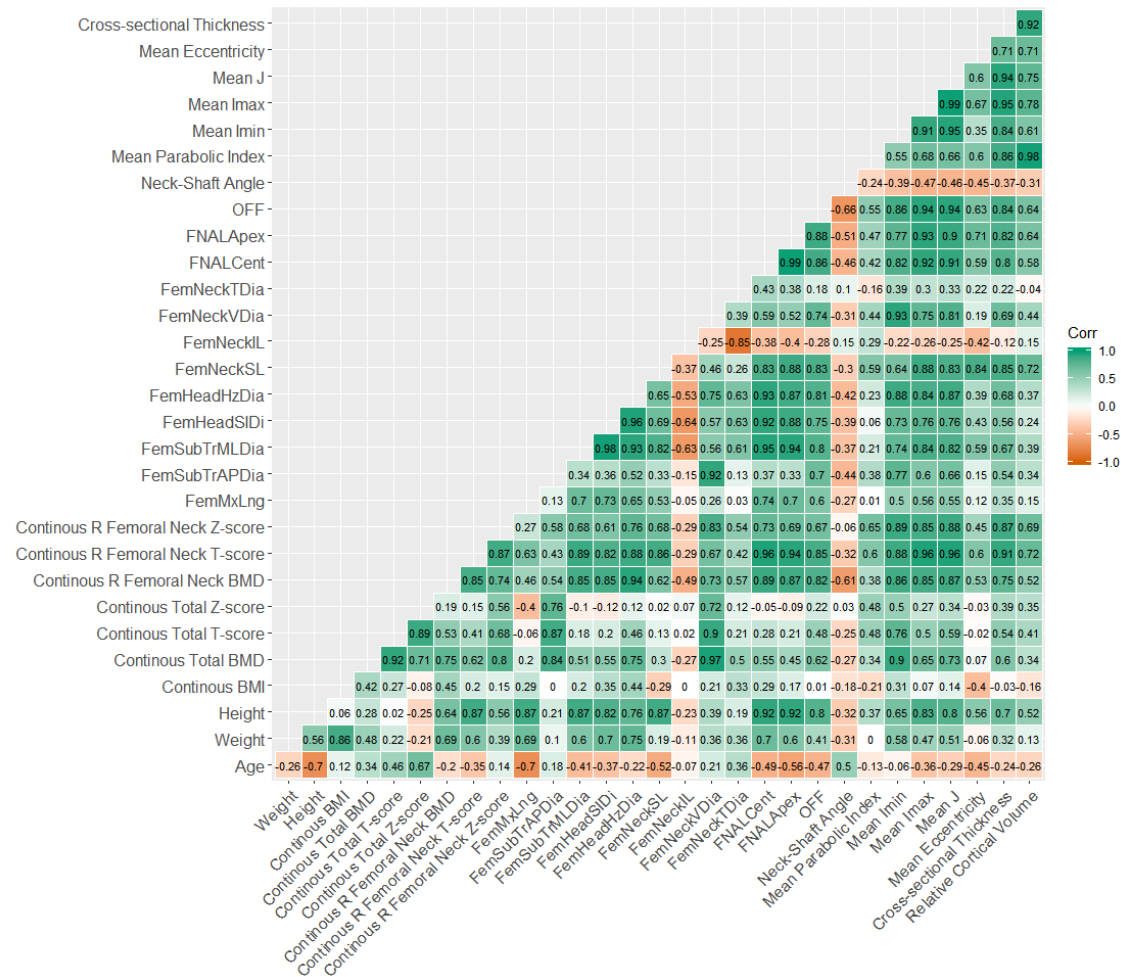
Figure 7.5 Femoral Neck Co-variate Correlation Matrix with Pearson R, Reordered by Hierarchal Clustering
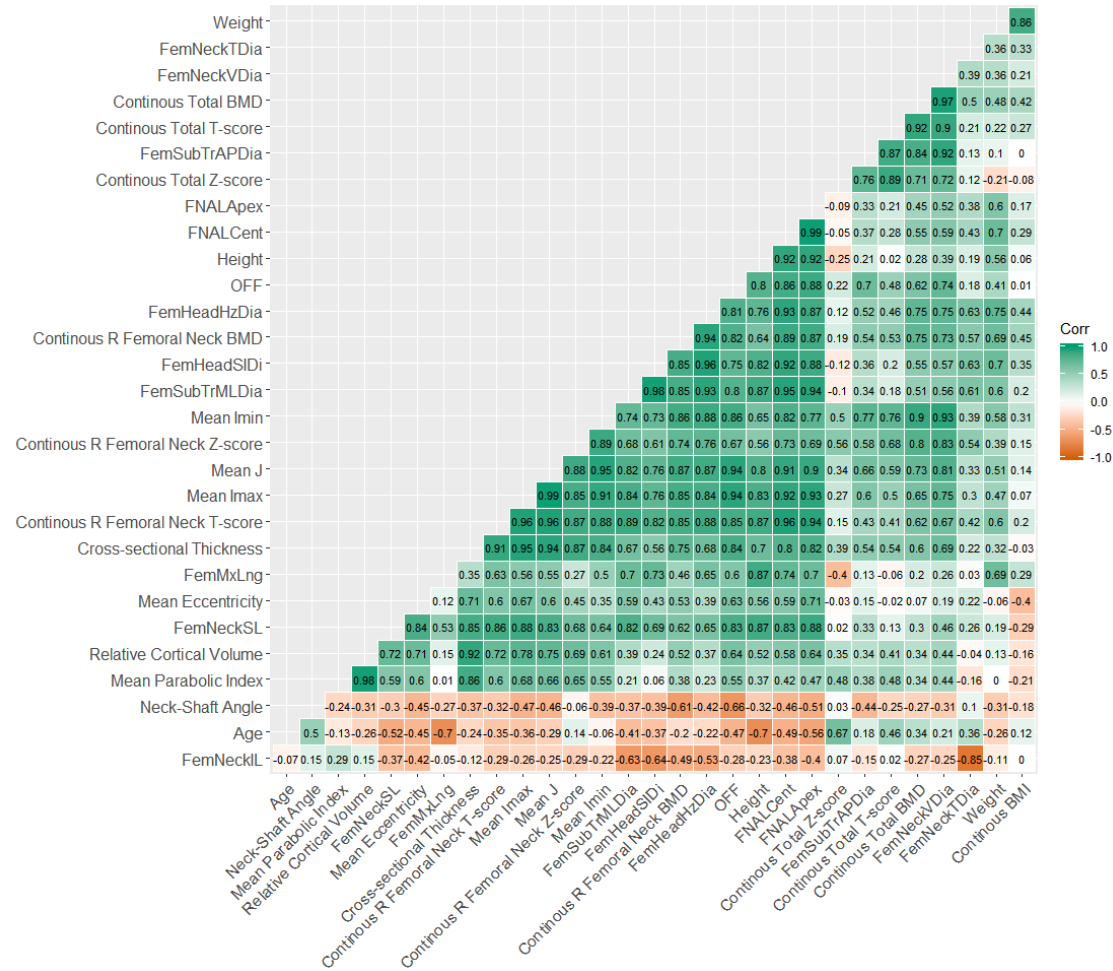
Figure 7.6 Femoral Neck Co-variate Correlation Matrix Showing Significant P-Values, Ordered by Variable List
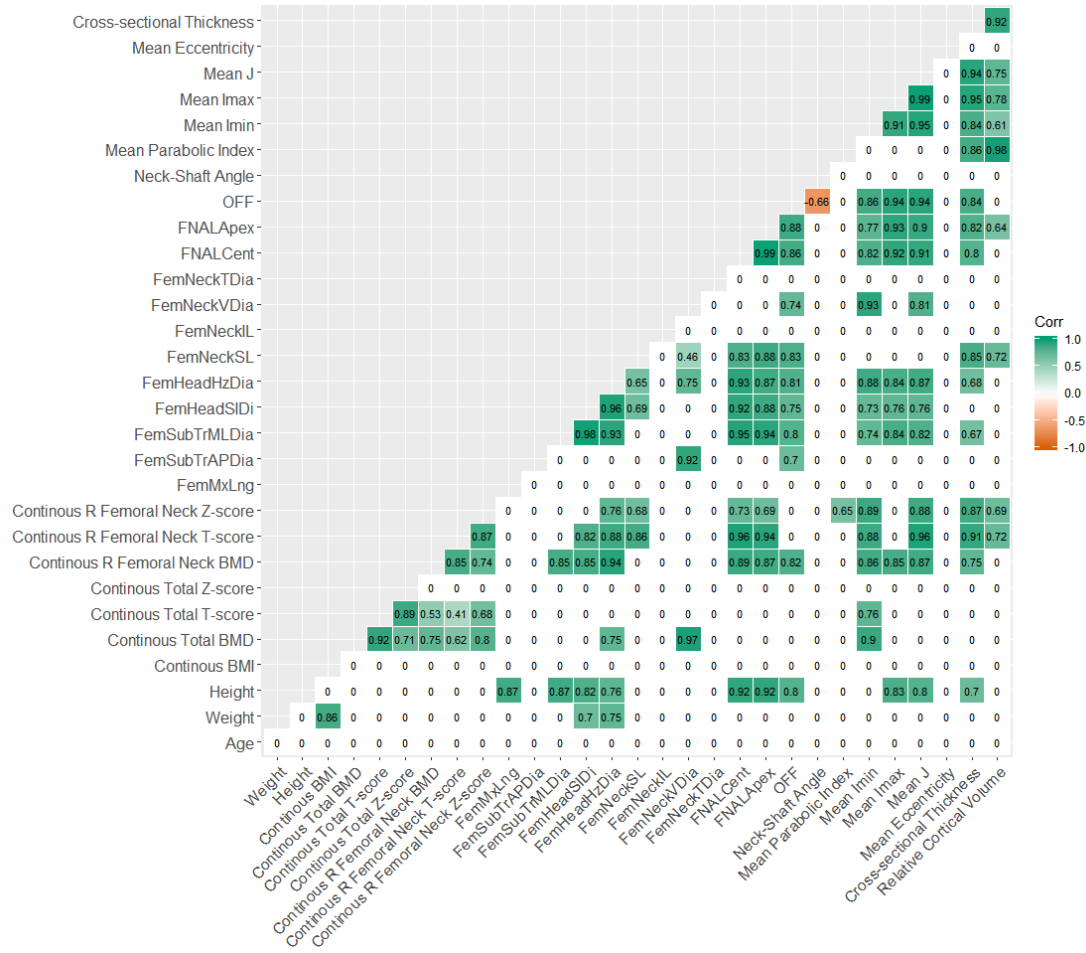
Femoral Neck Related Metrics: Many of the strong and significant positive correlations within femoral neck co-variates are positive correlations between multiple aspects of femoral neck gross geometry. The sole strong and significant negative correlation is again geometric in nature. As neck shaft angle increases, the femoral head is pulled superiorly and its offset decreases.

Age: Again, no significant correlations exist between chronological age and body size, BMD, gross-geometry, or cross-sectional geometry of the femoral neck. Like the rib, age is weakly negative correlated with relative cortical volume, cross-sectional thickness, and mean parabolic index of the femoral neck, reflecting cortical thinning with age. Weak negative correlations with cross-sectional shape (mean Imax, mean eccentricity) also suggest that the femoral neck becomes more circular with age. While age is very weakly or weakly positively correlated with total BMD and T-score in both the rib and femoral neck, age is actually weakly *negatively* correlated with right-femoral neck specific BMD and T-score, but not the matched Z-score. Ubiquitous weak negative correlations between femoral neck gross geometry and age are likely due to the slightly older ages of females in the sample, as these individuals tend to have smaller femoral neck dimensions.

Body Size: As a weight-bearing region, several gross geometric aspects of the femoral neck are strongly and significantly positively correlated with body size. Weight and height are both strongly and significantly positively correlated with femoral head vertical and horizontal diameter. Height is strongly and significantly

205

positively correlated with the femoral shaft dimensions of femoral subtrochanteric ML: diameter and logically with femoral shaft maximum length. Height also strongly and significantly positively correlates with femoral neck axial length (to head center and apex), and femoral head offset, suggesting a longer femoral neck in taller individuals. Finally, height is strongly and significantly positively correlated with cross-sectional shape (mean imax, mean imin) and cross-sectional thickness in the femoral neck. Converse to the rib, mean eccentricity is moderately positively correlated with height and not correlated with weight, suggesting that taller individuals have less circular femoral neck cross-sections.

Bone Mineral Density: Total values for bone mineral density (BMD, T-score, Z-score) are all strongly and significantly positively correlated with right femoral neck specific BMD values. Considering metrics of right femoral neck BMD specifically, strong and significant positive correlations with gross geometry include shaft dimensions (femoral subtrochanteric AP diameter and ML diameter), femoral head dimensions (vertical and horizontal), and femoral neck axial length (to head and center, and femoral head offset). Femoral neck cross-sectional shape (Imin, Imax, J), and mass (cross-sectional thickness, relative cortical volume) are also strongly and significantly positively correlated with femoral neck BMD.

Cross-Sectional Size and Shape: Strong and significant positive correlations with femoral neck gross geometry suggest that cross-sectional shape and cross-sectional thickness increases in correlation with dimensions of the femoral head

206

(vertical and horizontal diameter), shaft width (subtrochanteric ML diameter), femoral neck vertical diameter, and femoral neck length (to femoral head apex and center, and femoral head offset). Relative cortical volume strongly and significantly positively correlates with femoral neck length (superior length and femoral neck axial length to apex) in particular.

7.3.4. Correlation Between Co-Variates and Dependent Pore Morphometry

Co-variates were analyzed for correlations with dependent variables to determine which co-variates should be retained for subsequent linear mixed models. Correlations between co-variates were analyzed separately for the rib and femoral neck due to their varying sample sizes and gross and cross-sectional co-variates. The strength of the linear relationship between pairs of co-variates was measured with the Pearson r. The strength of relationship was categorized as None or Very Weak ($r < 0.3$), Weak ($r = 0.3 – 0.5$), Moderate ($r = 0.5 – 0.7$), or Strong ($r > 0.7$). Correlation tables were visualized in R using package ggcorplot for the rib (Figures 7.3 and 7.4) and the femoral neck (Figures 7.5 and 7.6).

207

Table 7.12 Pore Morphometry: Total Pores for Whole Bone

ID	Bone	Cortex Fractal Dimension	%Closed Porosity	%Open Porosity	%Porosity	Pore Thickness	Pore Separation	Pore Linear Density	Fragmentation Index	Degree of Anisotrooy	Pore Fractal Dimension	Connectivity Density	StDv PoreThickness	StDv Pore Separation	Proportion Open Pores	ProportionClosed Pores	Pore Density
Units		NA	%	%	%	µm	µm	1/µm	1/µm	NA	NA	1/µm³	µm	µm	%	%	1/µm³
26M	rib	2.39	0.06	5.54	5.60	153.29	326.02	3.65E-04	3.94E-02	3.35	2.21	5.53E-08	133.14	79.60	83.86	16.14	1.05E-07
28F	rib	2.32	0.05	5.72	5.76	170.75	388.60	3.37E-04	3.62E-02	2.79	2.06	5.49E-08	112.21	129.99	85.55	14.45	9.58E-08
34M	rib	2.41	0.06	3.22	3.27	58.83	306.38	5.55E-04	4.49E-02	4.47	2.19	7.18E-08	51.95	74.71	82.40	17.60	1.20E-07
34M	neck	2.58	0.09	11.10	11.20	325.00	362.00	3.45E-04	2.93E-02	2.55	2.45	6.15E-08	229.00	108.00	72.53	27.47	8.56E-08
39F	rib	2.36	0.04	7.58	7.61	139.17	347.85	5.46E-04	3.10E-02	3.47	2.14	7.92E-08	99.49	110.86	92.38	7.62	1.36E-07
39F	neck	2.53	0.07	11.40	11.40	206.00	312.00	5.51E-04	2.96E-02	1.49	2.40	9.38E-08	153.00	101.00	74.98	25.02	1.29E-07
41M	rib	2.35	0.02	6.06	6.08	108.08	291.43	5.61E-04	3.82E-02	3.22	2.10	1.33E-07	89.46	83.80	93.59	6.41	2.18E-07
49F	rib	2.49	0.06	14.63	14.68	121.73	198.71	1.20E-03	3.34E-02	2.73	2.38	1.96E-07	85.70	61.49	69.59	30.41	3.22E-07
49F	neck	2.55	0.03	15.20	15.30	137.00	137.00	1.10E-03	1.10E-03	1.67	2.46	1.13E-07	96.10	83.40	83.22	16.78	1.20E-07
50F	rib	2.45	0.06	8.65	8.70	128.90	292.60	6.74E-04	3.27E-02	3.04	2.31	1.08E-07	104.89	78.80	90.33	9.67	1.73E-07
50F	neck	2.55	0.11	11.10	11.20	229.00	331.00	4.85E-04	2.99E-02	1.66	2.42	8.90E-08	158.00	112.00	72.75	27.25	1.24E-07
56M	rib	2.43	0.10	6.30	6.40	76.96	261.95	8.29E-04	3.67E-02	3.41	2.23	1.19E-07	59.72	78.06	80.55	19.45	1.74E-07
56M	neck	2.55	0.04	10.70	10.80	141.00	255.00	7.58E-04	2.96E-02	2.05	2.45	1.21E-07	113.00	74.40	72.42	27.58	1.55E-07

208

Table 7.13 Pore Morphometry: Total Pores for Whole Bone (Continued)

ID	Bone	Cortex Fractal Dimension	%Closed Porosity	%Open Porosity	%Porosity	Pore Thickness	Pore Separation	Pore Linear Density	Fragmentation Index	Degree of Anisotrooy	Pore Fractal Dimension	Connectivity Density	StDv PoreThickness	StDv Pore Separation	Proportion Open Pores	ProportionClosed Pores	Pore Density
Units		NA	%	%	%	µm	µm	1/µm	1/µm	NA	NA	1/µm³	µm	µm	%	%	1/µm³
60F	rib	2.40	0.01	7.43	7.44	96.73	246.91	7.66E-04	3.77E-02	3.46	2.18	1.70E-07	80.23	68.98	97.38	2.62	2.81E-07
60F	neck	2.56	0.03	14.20	14.20	194.00	257.00	7.27E-04	2.61E-02	2.03	2.46	1.02E-07	156.00	72.00	82.90	17.10	1.13E-07
67M	rib	2.40	0.04	7.24	7.28	105.92	242.39	6.85E-04	3.91E-02	3.22	2.18	1.56E-07	92.91	65.91	92.60	7.40	2.35E-07
67M	neck	2.50	0.11	5.64	5.74	115.00	264.00	4.97E-04	4.02E-02	2.54	2.37	1.49E-07	112.00	72.10	72.09	27.91	2.15E-07
70F	rib	2.42	0.07	6.82	6.88	100.59	271.51	6.82E-04	3.92E-02	3.13	2.24	1.56E-07	89.77	79.39	91.15	8.85	2.46E-07
70F	neck	2.49	0.06	14.40	14.40	469.00	261.00	3.07E-04	3.00E-02	1.71	2.41	1.50E-07	516.00	72.30	81.30	18.70	1.68E-07
77M	rib	2.40	0.04	8.88	8.92	127.22	274.42	6.99E-04	3.38E-02	3.05	2.22	1.61E-07	97.30	79.67	95.45	4.55	2.26E-07
77M	neck	2.56	0.06	11.00	11.10	177.00	286.00	6.23E-04	2.77E-02	2.07	2.45	9.25E-08	151.00	83.70	78.54	21.46	1.15E-07
82F	rib	2.52	0.03	10.97	10.99	180.23	253.99	6.09E-04	3.01E-02	4.00	2.39	7.94E-08	187.62	64.27	91.64	8.36	1.02E-07
82F	neck	2.58	0.10	18.10	18.20	415.00	266.00	4.37E-04	2.88E-02	1.63	2.50	1.20E-07	372.00	83.70	75.84	24.16	1.54E-07
88M	rib	2.41	0.03	8.50	8.54	138.48	275.34	6.15E-04	3.59E-02	3.08	2.23	1.38E-07	111.47	73.72	93.03	6.97	2.30E-07

Table 7.14 Pore Morphometry: Cortical and Trabecularized Pores for All Bone

ID	Bone	Pore Type	Cortex Fractal Dimension	%Closed Porosity	%Open Porosity	%Porosity	Pore Thickness	Pore Linear Density	Fragmentation Index	Degree of Anisotroy	Pore Fractal Dimension	Connectivity Density	StDv PoreThickness	Proportion Open Pores	Proportion Closed Pores	Pore Density
Units			NA	%	%	%	µm	µm	1/ µm	1/ µm	NA	NA	1/ µm^3	µm	µm	%
26M	rib	Ct	2.37	0.11	2.60	2.71	0.04	5.97E-04	4.45E-02	4.18	2.15	5.39E-08	113.00	83.51	16.49	1.08E-07
26M	rib	Tb	2.08	0.20	2.70	2.89	254.00	1.14E-04	1.21E-02	1.39	1.93	4.94E-10	113.00	88.24	11.76	1.14E-09
28F	rib	Ct	2.28	0.11	1.65	1.75	0.05	4.39E-04	1.83E-04	3.60	1.93	5.30E-08	21.10	84.89	15.11	9.90E-08
28F	rib	Tb	2.12	0.08	3.94	4.01	228.00	1.76E-04	1.18E-02	1.48	1.97	1.04E-09	85.20	91.58	8.42	2.05E-09
34M	rib	Ct	2.41	0.07	2.85	2.92	45.60	6.39E-04	4.54E-02	4.43	2.18	5.82E-08	28.10	76.16	23.84	1.01E-07
34M	rib	Tb	2.04	0.06	0.26	0.32	169.00	1.89E-05	2.02E-02	2.10	1.65	1.64E-10	72.00	82.31	17.69	4.38E-10
34M	neck	Ct	2.54	0.56	4.12	4.66	182.00	2.56E-04	3.69E-02	2.13	2.37	5.30E-08	144.00	68.81	31.19	8.06E-08
34M	neck	Tb	2.26	0.54	5.93	6.44	383.00	1.68E-04	1.50E-02	1.14	2.10	6.80E-09	233.00	82.62	17.38	1.00E-08
39F	rib	Ct	2.31	0.48	2.56	3.03	0.04	5.36E-04	4.16E-02	3.25	2.01	7.47E-08	26.80	90.50	9.50	1.44E-07
39F	rib	Tb	2.16	0.64	3.97	4.58	192.00	2.38E-04	1.42E-02	1.58	1.87	2.18E-09	94.60	74.39	25.61	4.72E-09
39F	neck	Ct	2.51	0.69	3.07	3.74	102.00	3.65E-04	3.95E-02	1.83	2.28	7.11E-08	86.40	66.20	33.80	1.15E-07
39F	neck	Tb	2.31	0.26	7.27	7.51	229.00	3.25E-04	1.98E-02	1.99	2.12	1.84E-08	151.00	94.10	5.90	2.62E-08
41M	rib	Ct	2.34	0.13	3.42	3.54	0.04	9.75E-04	4.39E-02	3.57	2.32	7.21E-08	32.40	91.34	8.66	1.74E-07
41M	rib	Tb	2.15	0.12	2.42	2.54	0.02	1.37E-04	1.71E-02	1.47	1.79	2.03E-09	88.00	94.72	5.28	4.12E-09
49F	rib	Ct	2.45	0.50	4.74	5.22	0.05	1.16E-03	4.74E-02	2.74	2.25	1.71E-07	20.80	69.40	30.60	3.51E-07
49F	rib	Tb	2.28	0.30	9.19	9.46	162.00	5.82E-04	1.80E-02	1.18	2.03	1.00E-08	80.70	93.19	6.81	1.75E-08
49F	neck	Ct	2.53	0.98	5.69	6.61	89.10	7.39E-04	3.14E-02	1.67	2.34	7.86E-08	60.00	70.30	29.70	1.09E-07
49F	neck	Tb	2.35	0.33	7.93	8.23	151	5.41E-04	2.44E-02	2.07	2.21	2.31E-08	98	90.68	9.32	3.69E-08

210

Table 7.15 Pore Morphometry: Cortical and Trabecularized Pores for All Bone (Continued)

ID	Bone	Pore Type	Cortex Fractal Dimension	%Closed Porosity	%Open Porosity	%Porosity	Pore Thickness	Pore Linear Density	Fragmentation Index	Degree of Anisotrooy	Pore Fractal Dimension	Connectivity Density	StDv PoreThickness	Proportion Open Pores	ProportionClosed Pores	Pore Density
Units			NA	%	%	%	μm	μm	1/μm	1/μm	NA	NA	1/μm³	μm	μm	%
50F	rib	Ct	2.42	0.35	3.95	4.28	0.02	2.18E-04	4.02E-02	1.17	1.91	2.24E-09	100.00	88.98	12.39	4.92E-09
50F	rib	Tb	2.14	0.34	4.09	4.42	203.00	2.18E-04	1.67E-02	1.17	1.91	2.24E-09	100.00	74.78	25.22	4.92E-09
50F	neck	Ct	2.52	0.87	2.93	3.77	115.00	3.26E-04	4.00E-02	1.81	2.31	7.20E-08	92.60	64.93	35.07	1.14E-07
50F	neck	Tb	2.29	0.34	6.92	7.23	262.00	2.74E-04	1.77E-02	1.72	2.13	1.37E-08	160.00	92.45	7.55	1.99E-08
56M	rib	Ct	2.42	0.21	4.74	4.95	53.30	9.25E-04	3.97E-02	3.37	2.20	1.15E-07	29.50	79.93	20.07	1.77E-07
56M	rib	Tb	2.13	0.22	1.23	1.45	147.00	9.83E-05	2.35E-02	1.60	1.71	2.04E-09	75.00	88.66	11.34	4.11E-09
56M	neck	Ct	2.54	0.67	4.40	5.04	78.30	6.42E-04	3.65E-02	2.21	2.37	9.49E-08	62.90	63.49	36.51	1.46E-07
56M	neck	Tb	2.30	0.34	5.20	5.53	184.00	2.98E-04	2.34E-02	1.74	2.08	1.80E-08	119.00	87.89	12.11	2.91E-08
60F	rib	Ct	2.39	0.19	4.15	4.33	0.04	9.31E-04	4.44E-02	3.34	2.12	1.60E-07	21.00	96.65	3.35	2.86E-07
60F	rib	Tb	2.19	0.36	2.76	3.11	164.00	1.90E-04	1.95E-02	1.26	2.19	4.23E-09	83.60	86.64	13.36	8.02E-09
60F	neck	Ct	2.54	0.84	5.92	6.70	127.00	5.28E-04	3.34E-02	2.03	2.36	7.19E-08	110.00	71.11	28.89	1.02E-07
60F	neck	Tb	2.33	0.58	6.65	7.19	213.00	3.35E-04	2.26E-02	2.04	2.14	2.01E-08	155.00	89.52	10.48	3.06E-08
67M	rib	Ct	2.40	0.10	4.28	4.38	0.04	9.37E-04	2.46E-02	3.68	2.14	1.51E-07	24.70	92.27	7.73	2.40E-07
67M	rib	Tb	2.16	0.06	2.83	2.90	192.00	1.51E-04	1.79E-02	1.67	1.79	2.64E-09	90.80	96.10	3.90	4.71E-09
67M	neck	Ct	2.55	0.48	3.57	4.03	72.80	5.52E-04	3.94E-02	2.44	2.40	1.07E-07	68.10	67.17	32.83	1.55E-07
67M	neck	Tb	2.24	0.29	3.40	3.67	195.00	1.87E-04	2.26E-02	1.47	2.00	1.31E-08	116.00	87.99	12.01	2.12E-08

211

Table 7.16 Pore Morphometry: Cortical and Trabecularized Pores for All Bone (Continued)

ID	Bone	Pore Type	Cortex Fractal Dimension	%Closed Porosity	%Open Porosity	%Porosity	Pore Thickness	Pore Linear Density	Fragmentation Index	Degree of Anisotrooy	Pore Fractal Dimension	Connectivity Density	StDv PoreThickness	Proportion Open Pores	ProportionClosed Pores	Pore Density
Units			NA	%	%	%	µm	µm	1/µm	1/µm	NA	NA	1/µm³	µm	µm	%
70F	rib	Ct	2.41	0.24	3.92	4.15	0.04	8.98E-04	4.48E-02	3.14	2.19	1.49E-07	23.40	90.46	9.54	2.51E-07
70F	rib	Tb	2.15	0.21	2.52	2.73	180.00	1.51E-04	1.87E-02	1.29	1.72	3.46E-09	93.90	86.58	13.42	6.05E-09
70F	neck	Ct	2.48	0.51	4.51	4.99	93.40	5.33E-04	3.68E-02	1.83	2.34	1.27E-07	76.60	75.27	24.73	1.57E-07
70F	neck	Tb	2.22	0.22	9.00	9.21	627.00	1.46E-04	2.23E-02	2.43	2.01	1.75E-08	514.00	90.99	9.01	2.60E-08
77M	rib	Ct	2.38	0.28	4.22	4.49	0.04	7.94E-04	4.11E-02	3.21	2.13	1.53E-07	30.10	94.41	5.59	2.33E-07
77M	rib	Tb	2.17	0.35	4.09	4.43	196.00	2.26E-04	1.60E-02	1.49	1.91	3.62E-09	92.90	86.74	13.26	6.18E-09
77M	neck	Ct	2.54	0.31	5.43	5.72	0.03	7.06E-04	7.06E-04	2.04	2.39	8.58E-08	48.40	77.03	22.97	1.18E-07
77M	neck	Tb	2.26	0.52	4.70	5.20	0.01	1.91E-04	1.91E-04	1.88	1.93	2.22E-09	167.00	78.35	21.65	3.76E-09
82F	rib	Ct	2.49	0.32	5.45	5.75	58.90	9.75E-04	3.58E-02	3.57	2.32	7.21E-08	32.40	89.05	10.95	1.07E-07
82F	rib	Tb	2.14	0.89	4.38	5.23	0.01	1.69E-04	1.34E-02	1.33	1.94	1.24E-09	202.00	71.22	28.78	2.88E-09
82F	neck	Ct	2.57	0.72	6.97	7.64	202.00	3.77E-04	3.62E-02	1.56	2.42	9.71E-08	203.00	67.86	32.14	1.44E-07
82F	neck	Tb	2.30	0.33	9.92	10.20	492.00	2.07E-04	2.24E-02	2.48	2.16	1.66E-08	410.00	90.74	9.26	2.77E-08
88M	rib	Ct	2.38	0.23	3.71	3.93	0.02	2.18E-04	4.40E-02	1.19	1.88	2.51E-09	105.00	89.05	10.95	4.89E-09
88M	rib	Tb	2.17	0.43	4.18	4.60	0.02	2.18E-04	1.51E-02	1.19	1.88	2.51E-09	105.00	88.04	11.96	4.89E-09

212

Table 7.17 Pore Morphometry: Cutaneous and Pleural Regions of the Rib

ID	Region	Pore Type	Cortex Fractal Dimension	%Closed Porosity	%Open Porosity	%Porosity	Pore Thickness	Pore Linear Density	Fragmentation Index	Degree of Anisotrooy	Pore Fractal Dimension	Connectivity Density	StDv PoreThickness	Proportion Open Pores	ProportionClosed Pores	Pore Density
Units			NA	%	%	%	µm	µm	1/µm	1/µm	NA	NA	1/µm^3	µm	µm	%
26M	Cut	Ct	2.36	0.12	2.83	2.95	47.20	6.23E-04	4.13E-02	4.14	2.11	5.40E-08	25.90	82.90	17.10	9.58E-08
26M	Ple	Ct	2.36	0.09	2.40	2.49	42.80	5.80E-04	4.75E-02	4.12	2.16	5.41E-08	24.20	84.26	15.74	1.20E-07
26M	Cut	Tb	2.11	0.18	4.70	4.87	254.00	1.92E-04	1.23E-02	1.60	1.98	8.07E-10	98.90	90.14	9.86	1.90E-09
26M	Ple	Tb	2.05	0.20	0.96	1.16	252.00	4.62E-05	1.21E-02	1.90	1.79	2.48E-10	156.00	85.00	15.00	5.61E-10
28F	Cut	Ct	2.30	0.15	2.26	2.40	43.00	5.55E-04	4.23E-02	4.00	1.97	8.00E-08	22.70	91.11	8.89	1.32E-07
28F	Ple	Ct	2.23	0.07	1.22	1.28	34.50	3.69E-04	5.21E-02	3.26	1.88	5.28E-08	17.50	89.84	10.16	1.09E-07
28F	Cut	Tb	2.15	0.17	7.21	7.36	227.00	3.24E-04	1.18E-02	1.63	1.98	1.81E-09	85.80	90.20	9.80	3.63E-09
28F	Ple	Tb	2.06	0.00	1.23	1.23	208.00	5.90E-05	1.37E-02	1.27	1.81	6.64E-10	75.70	99.17	0.83	1.19E-09
34M	Cut	Ct	2.37	0.08	2.68	2.75	44.10	6.20E-04	4.88E-02	3.81	2.09	7.90E-08	28.40	84.57	15.43	1.49E-07
34M	Ple	Ct	2.40	0.05	3.14	3.19	46.30	6.87E-04	4.59E-02	4.08	2.14	6.70E-08	27.60	86.25	13.75	1.28E-07
34M	Cut	Tb	2.10	0.06	0.28	0.34	153.00	2.21E-05	2.42E-02	3.17	1.63	2.06E-10	69.20	89.29	10.71	5.77E-10
34M	Ple	Tb	2.10	0.03	0.30	0.32	164.00	1.97E-05	2.19E-02	2.29	1.65	2.30E-10	75.10	85.84	14.16	5.41E-10
39F	Cut	Ct	2.33	0.53	3.46	3.97	56.10	7.05E-04	4.01E-02	3.41	2.03	1.17E-07	25.50	94.41	5.59	2.05E-07
39F	Ple	Ct	2.26	0.45	1.92	2.35	56.60	4.14E-04	4.37E-02	2.96	1.95	4.49E-08	28.30	85.25	14.75	1.03E-07
39F	Cut	Tb	2.22	0.80	6.57	7.32	201.00	3.64E-04	1.35E-02	1.49	1.92	3.48E-09	97.30	83.36	16.64	6.91E-09
39F	Ple	Tb	2.09	0.51	2.09	2.59	165.00	1.57E-04	1.60E-02	1.73	1.77	1.44E-09	79.50	67.00	33.00	3.75E-09

213

Table 7.18 Pore Morphometry: Cutaneous and Pleural Regions of the Rib (Continued)

ID	Region	Pore Type	Cortex Fractal Dimension	%Closed Porosity	%Open Porosity	%Porosity	Pore Thickness	Pore Linear Density	Fragmentation Index	Degree of Anisotrooy	Pore Fractal Dimension	Connectivity Density	StDv PoreThickness	Proportion Open Pores	ProportionClosed Pores	Pore Density
Units			NA	%	%	%	µm	µm	1/ µm	1/ µm	NA	NA	1/ µm^3	µm	µm	%
41M	Ple	Ct	2.33	0.04	3.02	3.06	44.50	6.84E-04	4.64E-02	3.53	2.05	1.20E-07	22.70	95.19	4.81	2.18E-07
41M	Cut	Ct	2.32	0.23	3.92	4.14	55.10	7.47E-04	4.14E-02	3.27	2.00	1.42E-07	28.30	91.16	8.84	2.31E-07
41M	Ple	Tb	2.10	0.00	1.46	1.46	164.00	8.89E-05	1.81E-02	1.38	1.70	2.12E-09	71.80	98.80	1.20	3.74E-09
41M	Cut	Tb	2.17	0.27	3.61	3.88	194.00	2.00E-04	1.69E-02	1.61	1.83	1.97E-09	93.00	91.22	8.78	4.89E-09
49F	Cut	Ct	2.44	0.55	4.98	5.50	44.20	1.24E-03	4.74E-02	2.59	2.24	1.81E-07	20.60	72.14	27.86	3.64E-07
49F	Ple	Ct	2.41	0.41	4.51	4.90	45.10	1.08E-03	4.83E-02	3.01	2.19	1.62E-07	21.00	68.26	31.74	3.51E-07
49F	Cut	Tb	2.29	0.44	10.80	11.20	159.00	7.06E-04	1.83E-02	1.23	2.06	1.12E-08	79.30	92.63	7.37	2.08E-08
49F	Ple	Tb	2.22	0.13	7.35	7.48	160.00	4.68E-04	1.93E-02	1.22	1.94	9.77E-09	80.80	96.28	3.72	1.78E-08
50F	Ple	Ct	2.42	0.40	4.29	4.67	50.60	9.19E-04	3.88E-02	3.21	2.22	1.06E-07	24.00	89.55	10.45	1.78E-07
50F	Cut	Ct	2.40	0.25	3.67	3.91	50.10	7.77E-04	4.22E-02	3.43	2.18	9.85E-08	24.40	89.04	10.96	1.89E-07
50F	Ple	Tb	2.15	0.40	4.52	4.91	190.00	2.58E-04	1.70E-02	1.14	1.92	2.69E-09	101.00	75.97	24.03	6.06E-09
50F	Cut	Tb	2.13	0.16	3.80	3.95	215.00	1.83E-04	1.69E-02	1.27	1.87	2.25E-09	98.90	79.94	20.06	4.56E-09
56M	Cut	Ct	2.41	0.17	5.00	5.15	52.10	9.86E-04	4.03E-02	2.92	2.18	1.16E-07	29.00	78.05	21.95	1.83E-07
56M	Ple	Ct	2.40	0.25	4.54	4.77	54.20	8.78E-04	3.99E-02	3.71	2.18	1.16E-07	29.80	83.03	16.97	1.82E-07
56M	Cut	Tb	2.15	0.19	1.52	1.71	148.00	1.15E-04	2.50E-02	1.98	1.72	3.17E-09	76.60	96.16	3.84	5.61E-09
56M	Ple	Tb	2.12	0.22	1.01	1.23	146.00	8.41E-05	2.27E-02	1.39	1.66	1.15E-09	73.20	80.35	19.65	3.25E-09

214

Table 7.19 Pore Morphometry: Cutaneous and Pleural Regions of the Rib (Continued)

ID	Region	Pore Type	Cortex Fractal Dimension	%Closed Porosity	%Open Porosity	%Porosity	Pore Thickness	Pore Linear Density	Fragmentation Index	Degree of Anisotrooy	Pore Fractal Dimension	Connectivity Density	StDv PoreThickness	Proportion Open Pores	ProportionClosed Pores	Pore Density
Units			NA	%	%	%	µm	µm	1/µm	1/µm	NA	NA	1/µm³	µm	µm	%
60F	Cut	Ct	2.37	0.18	4.50	4.68	47.60	9.76E-04	4.19E-02	3.09	2.08	1.71E-07	21.80	96.20	3.80	2.76E-07
60F	Ple	Ct	2.37	0.20	3.83	4.02	44.70	8.94E-04	4.70E-02	3.52	2.12	1.51E-07	19.90	97.06	2.94	3.01E-07
60F	Cut	Tb	2.21	0.33	3.16	3.48	148.00	2.35E-04	2.10E-02	1.54	1.70	5.93E-09	78.70	87.17	12.83	1.14E-08
60F	Ple	Tb	2.16	0.33	2.45	2.77	175.00	1.58E-04	1.80E-02	1.19	1.71	2.82E-09	83.30	87.77	12.23	5.56E-09
67M	Ple	Ct	2.38	0.13	4.17	4.29	46.50	9.17E-04	4.44E-02	3.84	2.13	1.31E-07	24.50	91.42	8.58	2.24E-07
67M	Cut	Ct	2.37	0.07	4.42	4.48	46.40	9.61E-04	4.36E-02	3.35	2.10	1.76E-07	25.00	93.61	6.39	2.70E-07
67M	Ple	Tb	2.16	0.10	3.15	3.24	202.00	1.61E-04	1.70E-02	1.50	1.81	2.82E-09	93.20	95.49	4.51	4.89E-09
67M	Cut	Tb	2.16	0.02	2.49	2.52	178.00	1.41E-04	1.96E-02	1.88	1.76	2.48E-09	85.50	97.28	2.72	4.72E-09
70F	Cut	Ct	2.39	0.27	4.39	4.65	45.10	1.02E-03	4.40E-02	3.14	2.18	1.76E-07	22.50	89.64	10.36	2.79E-07
70F	Ple	Ct	2.39	0.21	3.52	3.72	46.80	7.92E-04	4.60E-02	3.46	2.16	1.26E-07	24.20	91.51	8.49	2.32E-07
70F	Cut	Tb	2.16	0.24	2.50	2.74	167.00	1.64E-04	2.14E-02	1.66	1.68	3.15E-09	97.50	84.35	15.65	6.71E-09
70F	Ple	Tb	2.13	0.18	2.55	2.73	188.00	1.45E-04	1.65E-02	1.32	1.75	3.91E-09	88.70	90.12	9.88	5.97E-09
77M	Ple	Ct	2.38	0.30	4.31	4.59	59.40	7.70E-04	3.98E-02	3.26	2.16	1.36E-07	30.30	94.20	5.80	2.12E-07
77M	Cut	Ct	2.34	0.24	4.11	4.34	51.20	8.42E-04	4.38E-02	3.12	2.06	1.81E-07	29.10	95.17	4.83	2.77E-07
77M	Ple	Tb	2.15	0.49	3.14	3.61	176.00	2.05E-04	1.73E-02	1.40	1.89	3.94E-09	84.80	84.79	15.21	6.63E-09
77M	Cut	Tb	2.20	0.13	5.50	5.62	207.00	2.71E-04	1.56E-02	1.69	1.90	3.84E-09	96.40	93.29	6.71	6.80E-09

215

Table 7.20 Pore Morphometry: Cutaneous and Pleural Regions of the Rib (Continued)

ID	Region	Pore Type	Cortex Fractal Dimension	%Closed Porosity	%Open Porosity	%Porosity	Pore Thickness	Pore Linear Density	Fragmentation Index	Degree of Anisotrooy	Pore Fractal Dimension	Connectivity Density	StDv PoreThickness	Proportion Open Pores	ProportionClosed Pores	Pore Density
Units			NA	%	%	%	µm	µm	1/µm	1/µm	NA	NA	1/µm^3	µm	µm	%
82F	Cut	Ct	2.45	0.38	5.56	5.91	56.50	1.04E-03	3.67E-02	3.26	2.28	9.53E-08	31.20	90.28	9.72	1.45E-07
82F	Ple	Ct	2.47	0.19	5.47	5.66	60.70	9.30E-04	3.57E-02	3.89	2.29	7.78E-08	33.30	92.15	7.85	1.10E-07
82F	Cut	Tb	2.17	0.72	6.82	7.49	346.00	2.16E-04	1.33E-02	1.33	1.95	2.53E-09	216.00	85.25	14.75	4.82E-09
82F	Ple	Tb	2.11	0.72	2.39	3.09	217.00	1.43E-04	1.49E-02	1.54	1.84	1.64E-09	131.00	76.82	23.18	3.26E-09
88M	Ple	Ct	2.37	0.15	3.25	3.40	49.60	6.82E-04	4.57E-02	3.81	2.12	1.12E-07	26.90	95.18	4.82	2.14E-07
88M	Cut	Ct	2.37	0.31	4.23	4.52	51.90	8.65E-04	4.27E-02	2.92	2.14	1.53E-07	27.30	89.75	10.25	2.60E-07
88M	Ple	Tb	2.14	0.17	3.91	4.07	239.00	1.71E-04	1.29E-02	1.36	1.89	1.69E-09	111.00	91.81	8.19	3.12E-09
88M	Cut	Tb	2.18	0.72	4.49	5.18	185.00	2.79E-04	1.69E-02	1.26	1.87	3.45E-09	93.00	86.49	13.51	6.98E-09

216

Table 7.21 Pore Morphometry: Femoral Neck Octants

ID	Octant	Cortex Fractal Dimension	%Closed Porosity	%Open Porosity	%Porosity	Pore Thickness	Pore Separation	Pore Linear Density	Fragmentation Index	Degree of Anisotroöy	Pore Fractal Dimension	Connectivity Density	StDv PoreThickness	StDv Pore Separation	Proportion Open Pores	ProportionClosed Pores	Pore Density
		NA	%	%	%	µm	µm	1/ µm	1/ µm	NA	NA	1/ µm³	µm	µm	%	%	1/ µm³
34M	A	2.52	0.04	13.70	13.70	377.00	332.00	3.63E-04	2.72E-02	2.90	2.39	5.32E-08	258.00	79.70	76.89	23.11	7.26E-08
34M	I	2.56	0.14	8.20	8.33	322.00	410.00	2.58E-04	3.39E-02	2.75	2.43	5.43E-08	191.00	111.00	65.91	34.09	8.51E-08
34M	IA	2.54	0.09	5.40	5.49	286.00	387.00	1.91E-04	3.72E-02	2.94	2.38	5.35E-08	242.00	86.70	74.85	25.15	8.23E-08
34M	IP	2.49	0.11	5.11	5.22	220.00	422.00	2.37E-04	3.83E-02	2.38	2.31	6.52E-08	142.00	124.00	68.94	31.06	1.04E-07
34M	P	2.51	0.06	4.87	4.93	174.00	376.00	2.83E-04	3.71E-02	2.74	2.34	6.60E-08	137.00	104.00	76.12	23.88	9.70E-08
34M	S	2.55	0.05	17.00	17.00	275.00	275.00	6.18E-04	2.40E-02	2.96	2.44	8.09E-08	177.00	70.00	80.60	19.40	9.65E-08
34M	SA	2.49	0.05	16.30	16.30	336.99	337.00	4.84E-04	2.43E-02	3.26	2.36	7.39E-08	249.00	75.90	77.50	22.50	9.33E-08
34M	SP	2.56	0.05	19.10	19.20	375.80	376.00	5.09E-04	2.43E-02	3.25	2.45	5.38E-08	233.00	84.20	75.32	24.68	7.43E-08
39F	A	2.42	0.04	7.80	7.83	143.00	315.00	5.41E-04	3.36E-02	1.69	2.23	7.69E-08	96.00	115.00	81.87	18.13	1.23E-07
39F	I	2.52	0.09	8.56	8.64	191.00	321.00	4.51E-04	3.41E-02	2.01	2.38	5.90E-08	131.00	98.90	68.19	31.81	1.06E-07
39F	IA	2.44	0.05	6.61	6.66	174.00	364.00	3.78E-04	3.45E-02	1.76	2.25	6.22E-08	131.00	124.00	80.39	19.61	1.01E-07
39F	IP	2.52	0.10	10.20	10.30	210.00	303.00	4.89E-04	3.20E-02	1.86	2.38	1.03E-07	159.00	97.30	74.96	25.04	1.52E-07
39F	P	2.49	0.08	19.00	19.10	255.00	257.00	7.46E-04	2.74E-02	1.41	2.38	1.09E-07	178.00	90.40	78.59	21.41	1.63E-07
39F	S	2.45	0.08	10.00	10.10	145.00	265.00	6.89E-04	3.12E-02	1.78	2.31	1.33E-07	99.20	85.00	80.20	19.80	1.84E-07
39F	SA	2.39	0.04	9.01	9.05	136.00	273.00	6.61E-04	3.09E-02	2.00	2.20	8.73E-08	92.20	97.50	83.75	16.25	1.35E-07
39F	SP	2.47	0.19	21.20	21.40	232.00	223.00	9.19E-04	2.82E-02	1.77	2.35	1.28E-07	166.00	87.60	80.63	19.37	1.85E-07

217

Table 7.22 Pore Morphometry: Femoral Neck Octants (Continued)

ID	Octant	Cortex Fractal Dimension	%Closed Porosity	%Open Porosity	%Porosity	Pore Thickness	Pore Separation	Pore Linear Density	Fragmentation Index	Degree of Anisotrooy	Pore Fractal Dimension	Connectivity Density	StDv PoreThickness	StDv Pore Separation	Proportion Open Pores	ProportionClosed Pores	Pore Density
		NA	%	%	%	µm	µm	1/ µm	1/ µm	NA	NA	1/ µm^3	µm	µm	%	%	1/ µm^3
49F	I	2.58	0.03	7.91	7.94	128.00	279.00	6.16E-04	3.15E-02	2.72	2.47	9.63E-08	121.00	80.90	81.53	18.47	1.24E-07
49F	A	2.43	0.03	19.92	19.94	140.00	210.00	1.41E-03	2.00E-02	1.64	2.34	1.83E-04	90.20	81.30	87.00	13.00	0.00E+00
49F	IA	2.54	0.04	14.50	14.50	161.00	257.00	8.95E-04	2.49E-02	2.09	2.45	1.18E-07	115.00	82.60	82.90	17.10	1.39E-07
49F	IP	2.54	0.02	11.10	11.10	135.00	273.00	8.20E-04	2.57E-02	2.76	2.43	7.11E-08	95.10	90.30	89.23	10.77	9.21E-08
49F	P	2.52	0.03	19.30	19.30	145.00	236.00	1.32E-03	2.09E-02	1.63	2.43	7.48E-08	87.10	89.00	91.30	8.70	9.09E-08
49F	S	2.41	0.04	16.60	16.60	108.00	202.00	1.52E-03	2.54E-02	1.80	2.31	1.67E-07	75.40	78.00	84.79	15.21	1.98E-07
49F	SA	2.42	0.08	21.70	21.80	118.00	183.00	1.82E-03	2.56E-02	1.43	2.32	1.33E-07	71.50	75.10	88.15	11.85	1.80E-07
49F	SP	2.40	0.08	18.30	18.30	112.00	196.00	1.61E-03	2.61E-02	1.59	2.29	1.12E-07	70.70	81.00	85.27	14.73	1.57E-07
50F	A	2.47	0.10	10.50	10.60	206.00	268.00	5.12E-04	3.62E-02	1.83	2.33	1.26E-07	141.00	88.80	75.73	24.27	1.99E-07
50F	I	2.47	0.10	12.80	12.80	272.00	370.00	4.70E-04	2.87E-02	1.25	2.31	5.65E-08	174.00	146.00	74.30	25.70	9.42E-08
50F	IA	2.45	0.12	8.73	8.84	238.00	329.00	3.69E-04	3.65E-02	1.53	2.29	7.92E-08	172.00	121.00	76.39	23.61	1.28E-07
50F	IP	2.45	0.08	7.09	7.16	207.00	356.00	3.45E-04	3.55E-02	1.57	2.26	7.27E-08	171.00	123.00	76.75	23.25	1.16E-07
50F	P	2.45	0.05	7.27	7.32	153.00	312.00	4.75E-04	3.48E-02	2.01	2.29	1.05E-07	114.00	107.00	80.44	19.56	1.52E-07
50F	S	2.48	0.08	15.00	15.10	212.00	259.00	7.07E-04	2.86E-02	1.46	2.35	9.75E-08	142.00	81.50	79.38	20.62	1.41E-07
50F	SA	2.52	0.11	14.20	14.30	216.00	276.00	6.57E-04	2.76E-02	1.67	2.41	9.44E-08	155.00	91.10	75.12	24.88	1.43E-07
50F	SP	2.42	0.13	10.80	10.90	185.00	289.00	5.89E-04	3.21E-02	1.52	2.25	9.65E-08	119.00	95.80	74.73	25.27	1.60E-07

218

Table 7.23 Pore Morphometry: Femoral Neck Octants (Continued)

ID	Octant	Cortex Fractal Dimension	%Closed Porosity	%Open Porosity	%Porosity	Pore Thickness	Pore Separation	Pore Linear Density	Fragmentation Index	Degree of Anisotropy	Pore Fractal Dimension	Connectivity Density	StDv Pore Thickness	StDv Pore Separation	Proportion Open Pores	ProportionClosed Pores	Pore Density
		NA	%	%	%	μm	μm	1/ μm	1/ μm	NA	NA	1/ μm³	μm	μm	%	%	1/ μm³
56M	A	2.52	0.06	12.60	12.60	159.00	221.00	7.88E-04	3.32E-02	2.02	2.43	1.49E-07	123.00	68.20	72.85	27.15	2.11E-07
56M	I	2.54	0.04	8.50	8.54	156.00	273.00	5.44E-04	3.16E-02	3.11	2.43	6.98E-08	145.00	76.00	71.39	28.61	1.07E-07
56M	IA	2.50	0.03	9.96	9.99	130.00	238.00	7.64E-04	3.22E-02	2.53	2.40	1.08E-07	111.00	68.90	66.64	33.36	1.72E-07
56M	IP	2.49	0.02	7.24	7.26	115.00	303.00	6.25E-04	3.06E-02	2.79	2.34	6.56E-08	86.70	86.30	83.46	16.54	9.34E-08
56M	P	2.46	0.02	11.60	11.60	138.00	251.00	8.35E-04	3.02E-02	2.08	2.34	1.25E-07	101.00	84.00	82.94	17.06	1.60E-07
56M	S	2.44	0.04	12.20	12.20	119.00	222.00	1.02E-03	2.75E-02	2.26	2.31	1.63E-07	81.80	70.30	82.74	17.26	1.98E-07
56M	SA	2.48	0.04	12.50	12.60	125.00	226.00	9.97E-04	2.94E-02	2.01	2.38	1.26E-07	85.00	68.40	74.76	25.24	1.80E-07
56M	SP	2.48	0.06	11.70	11.80	140.00	216.00	8.39E-04	3.40E-02	1.98	2.37	1.78E-07	108.00	66.90	71.34	28.66	2.59E-07
60F	A	2.47	0.05	19.10	19.10	200.00	222.00	9.52E-04	2.54E-02	1.57	2.36	9.82E-08	140.00	75.00	80.07	19.93	1.27E-07
60F	I	2.61	0.04	11.70	11.70	186.00	267.00	6.25E-04	2.83E-02	2.51	2.51	8.56E-08	153.00	75.10	80.43	19.57	1.07E-07
60F	IA	2.57	0.04	18.00	18.00	241.00	243.00	7.46E-04	2.45E-02	2.07	2.48	8.88E-08	196.00	72.20	84.19	15.81	1.10E-07
60F	IP	2.57	0.02	9.39	9.41	176.00	264.00	5.31E-04	3.22E-02	2.47	2.45	7.76E-08	162.00	75.10	81.41	18.59	1.07E-07
60F	P	2.49	0.03	9.07	9.09	158.00	271.00	5.72E-04	3.19E-02	2.09	2.37	1.03E-07	144.00	80.00	88.12	11.88	1.29E-07
60F	S	2.37	0.02	16.00	16.00	139.00	212.00	1.15E-03	2.64E-02	1.84	2.23	1.30E-07	89.70	74.50	89.75	10.25	1.60E-07
60F	SA	2.45	0.04	18.00	18.10	176.00	226.00	1.02E-03	2.70E-02	1.14	2.34	1.07E-07	113.00	76.50	81.78	18.22	1.49E-07
60F	SP	2.33	0.03	15.20	15.20	143.00	204.00	1.05E-03	2.86E-02	1.82	2.17	1.54E-07	103.00	74.20	94.00	6.00	1.92E-07

219

Table 7.24 Pore Morphometry: Femoral Neck Octants (Continued)

ID	Octant	Cortex Fractal Dimension	%Closed Porosity	%Open Porosity	%Porosity	Pore Thickness	Pore Separation	Pore Linear Density	Fragmentation Index	Degree of Anisotropy	Pore Fractal Dimension	Connectivity Density	StDv PoreThickness	StDv Pore Separation	Proportion Open Pores	ProportionClosed Pores	Pore Density
		NA	%	%	%	μm	μm	1/ μm	1/ μm	NA	NA	1/ μm³	μm	μm	%	%	1/ μm³
67M	A	2.59	0.08	7.30	7.37	154.00	281.00	4.76E-04	3.69E-02	2.80	2.48	1.04E-07	120.00	73.80	71.78	28.22	1.45E-07
67M	I	2.53	0.10	6.37	6.47	161.00	281.00	4.00E-04	3.96E-02	2.61	2.41	1.34E-07	127.00	72.80	75.34	24.66	1.83E-07
67M	IA	2.59	0.05	8.50	8.55	163.00	274.00	5.23E-04	3.18E-02	3.05	2.49	8.38E-08	143.00	68.90	75.39	24.61	1.07E-07
67M	IP	2.49	0.03	6.03	6.06	84.00	278.00	7.18E-04	3.22E-02	3.18	2.35	8.80E-08	68.20	75.90	79.09	20.91	1.12E-07
67M	P	2.41	0.06	8.77	8.82	109.00	235.00	8.01E-04	3.04E-02	3.17	2.26	1.48E-07	82.40	68.60	79.59	20.41	1.84E-07
67M	S	2.49	0.10	9.34	9.44	125.00	239.00	7.50E-04	3.18E-02	2.76	2.37	1.73E-07	98.70	68.70	75.63	24.37	2.35E-07
67M	SA	2.43	0.09	9.70	9.79	125.00	231.00	7.77E-04	3.33E-02	2.54	2.30	1.40E-07	102.00	71.00	66.21	33.79	2.28E-07
67M	SP	2.56	0.05	19.10	19.20	125.13	376.00	5.09E-04	3.33E-02	3.25	2.45	5.38E-08	233.00	84.20	75.32	24.68	7.43E-08
70F	A	2.36	0.06	31.20	31.20	484.00	239.00	6.43E-04	2.73E-02	1.84	2.33	8.90E-08	318.00	76.10	75.52	24.48	1.16E-07
70F	I	2.56	0.08	6.53	6.61	131.00	266.00	5.02E-04	3.67E-02	2.50	2.47	2.45E-07	114.00	66.70	84.40	15.60	2.76E-07
70F	IA	2.51	0.06	5.30	5.36	84.40	263.00	6.31E-04	3.62E-02	3.02	2.39	1.56E-07	72.20	66.10	81.71	18.29	1.73E-07
70F	IP	2.39	0.06	6.12	6.18	131.00	266.00	4.68E-04	3.69E-02	2.48	2.32	1.71E-07	140.00	72.60	83.93	16.07	2.07E-07
70F	P	2.34	0.03	11.60	11.60	125.00	271.00	9.27E-04	2.46E-02	3.23	2.31	7.87E-08	74.80	86.20	82.72	17.28	8.81E-08
70F	S	2.28	0.06	12.10	12.20	122.00	249.00	9.92E-04	2.61E-02	2.52	2.18	1.54E-07	74.80	90.80	85.95	14.05	1.81E-07
70F	SA	2.41	0.07	33.70	33.80	872.00	246.00	3.87E-04	2.78E-02	1.61	2.36	8.82E-08	535.00	75.20	74.53	25.47	1.14E-07
70F	SP	2.30	0.04	14.30	14.40	155.00	237.00	9.23E-04	2.46E-02	2.77	2.27	1.20E-07	104.00	73.20	83.02	16.98	1.36E-07

220

Table 7.25 Pore Morphometry: Femoral Neck Octants (Continued)

ID	Octant	Cortex Fractal Dimension	%Closed Porosity	%Open Porosity	%Porosity	Pore Thickness	Pore Separation	Pore Linear Density	Fragmentation Index	Degree of Anisotrooy	Pore Fractal Dimension	Connectivity Density	StDv PoreThickness	StDv Pore Separation	Proportion Open Pores	ProportionClosed Pores	Pore Density
		NA	%	%	%	µm	µm	1/ µm	1/ µm	NA	NA	1/ µm³	µm	µm	%	%	1/ µm³
77M	I	2.55	0.13	6.62	6.74	206.00	325.00	3.27E-04	3.69E-02	2.82	2.41	6.92E-08	169.00	87.40	74.81	25.19	1.04E-07
77M	IA	2.56	0.07	7.60	7.67	157.00	301.00	4.86E-04	3.32E-02	2.70	2.43	8.19E-08	133.00	83.80	74.22	25.78	1.11E-07
77M	IP	2.50	0.08	8.22	8.30	184.00	305.00	4.48E-04	3.17E-02	2.26	2.35	6.85E-08	179.00	87.10	78.96	21.04	9.50E-08
77M	P	2.40	0.02	13.30	13.30	130.00	244.00	1.01E-03	2.57E-02	2.36	2.27	1.22E-07	86.90	80.30	89.99	10.01	1.49E-07
77M	S	2.47	0.03	14.10	14.10	143.00	245.00	9.80E-04	2.38E-02	2.28	2.36	9.37E-08	99.70	80.60	80.67	19.33	1.08E-07
77M	SA	2.54	0.04	15.90	16.00	203.00	253.00	7.85E-04	2.47E-02	2.37	2.44	1.06E-07	149.00	71.60	74.23	25.77	1.50E-07
77M	SP	2.38	0.02	14.60	14.70	137.00	236.00	1.06E-03	2.37E-02	2.25	2.24	1.17E-07	86.20	77.50	87.90	12.10	1.42E-07
82F	A	2.26	0.16	26.00	26.10	444.00	190.00	5.85E-04	3.54E-02	1.70	2.13	1.66E-07	361.00	84.90	79.31	20.69	2.83E-07
82F	I	2.56	0.12	11.80	11.90	289.00	290.00	4.11E-04	3.44E-02	1.70	2.45	9.35E-08	225.00	97.60	75.26	24.74	1.50E-07
82F	IA	2.48	0.08	14.40	14.50	230.00	250.00	6.27E-04	3.14E-02	1.32	2.37	1.26E-07	201.00	84.60	80.52	19.48	1.81E-07
82F	IP	2.54	0.07	14.30	14.30	325.00	272.00	4.38E-04	3.39E-02	1.58	2.43	8.06E-08	279.00	92.90	79.03	20.97	1.36E-07
82F	P	2.54	0.05	22.20	22.30	367.00	239.00	6.04E-04	2.96E-02	1.44	2.48	9.47E-08	290.00	84.30	81.87	18.13	1.46E-07
82F	S	2.48	0.06	14.10	14.10	164.00	224.00	8.56E-04	3.17E-02	1.90	2.37	1.85E-07	115.00	77.20	85.51	14.49	2.43E-07
82F	SA	2.41	0.09	27.30	27.40	652.00	216.00	4.19E-04	3.29E-02	1.45	2.30	1.37E-07	495.00	87.80	81.54	18.46	2.08E-07
82F	SP	2.57	0.07	21.00	21.10	241.00	224.00	8.71E-04	2.76E-02	1.30	2.50	1.15E-07	201.00	83.10	75.87	24.13	1.74E-07

Figure 7.7 Rib Co-variate and Dependent Variable Correlation Matrix with Pearson R

Figure 7.8 Rib Co-variate and Dependent Variable Correlation Matrix Showing Significant P-Values

The correlation matrix of co-variates and dependent variables presents several associations. **Age** is only significantly and moderately correlated with structure separation. However, this finding supports the current model of pores converging with increasing age, such that they reduce the separation between them.

The only aspect of **body size** significantly correlated with rib pore morphometry is height, which is moderately positively correlated with fragmentation index. Developed by Hahn *et al.* (2012) for sections of trabecular bone, this index is also known as trabecular bone pattern factor. It quantifies the relative concavity or convexity of the bone surface – in this case the isolated pore network, rather than trabecular architecture. A lower fragmentation index signifies concavity or the presence of connected "nodes", while a higher fragmentation index suggests convexity or a prevalence of disconnected "struts". Since height is positively correlated with fragmentation index, this interestingly suggests a more disconnected pore network.

BMD has several significant correlations. Continuous total BMD is moderately and significantly negatively correlated with pore density. Logically, a higher density of voids in bone precludes mineralization in those spaces. Continuous total Z-score shows a moderate but significant correlation with pore thickness, and a stronger correlation with its standard deviation, a proxy of the range of local pore thickness. In other words, larger pores are associated with higher demographically matched BMD. This may be an artifact of more excessive

224

resorption in individuals with lower BMD thinning the cortex so much that pores are absorbed into the marrow cavity and artificially decrease pore thickness.

In terms of **cross-sectional geometry,** mean I_{min} is significantly and moderately correlated positively with metrics of pore connectivity (fragmentation index) and network alignment (degree of anisotropy), as is J, of which I_{min} is a component. Imin is also significantly negatively correlated with percentages of open and total porosity. An inverse relationship is seen with mean eccentricity, which is moderately and significantly negatively correlated with degree of anisotropy and moderately and significantly positively correlated with structure thickness. A more eccentric and less circular bone is associated with larger, more prevalent, and less organized pore networks. This points to a potential relationship between porosity-related erosion and changes in cortical shape. Relative cortical volume and cross-sectional thickness are significantly and respectively strongly and moderately negatively correlated with pore connectivity density and pore density. More prevalent and interconnected pores erode the cortex both locally and as a proportion of cross-sectional volume. Relative cortical volume is additionally moderately and significantly positively correlated with pore structure thickness and its standard deviation. The somewhat counter-intuitive positive association of more bone and more space may again be an artifact of less resorbed cortices retaining larger pores that would otherwise be indistinguishable from trabecular spaces.

225

Figure 7.9 Femoral Neck Co-variate and Dependent Variable Correlation Matrix with Pearson R
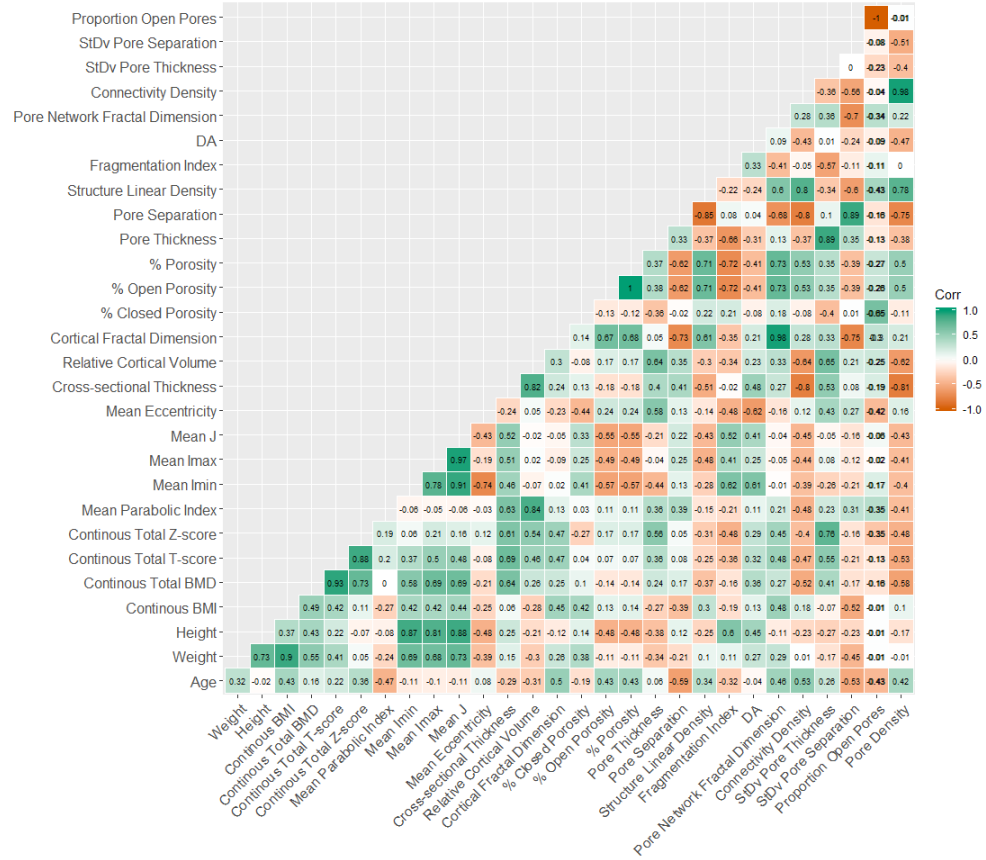
Figure 7.10 Femoral Neck Co-variate and Dependent Variable Correlation Matrix Showing Significant P-Values
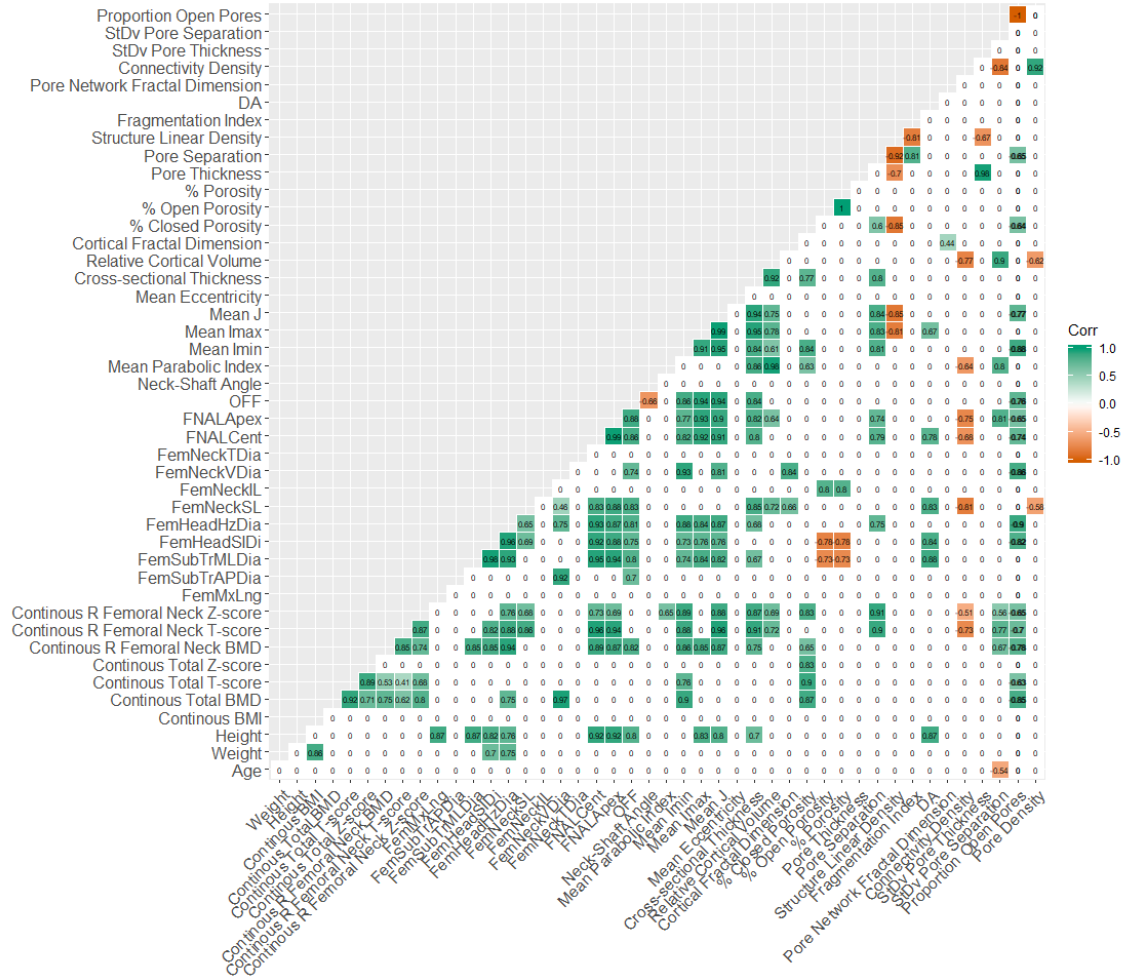
Considering correlations between femoral neck co-variates and pore morphometry, **age** is again significantly and moderately negatively correlated with pore separation, and in this case also pore separation standard deviation.

Height is significantly and strongly positively correlated with pore network organization in the femoral neck, as it is in the rib, but the associated variable is degree of anisotropy rather than fragmentation index.

BMD is also associated with pore prevalence, as it is in the rib, with moderate to strongly significant positive correlations between percent closed porosity and all total and right femoral neck BMD co-variates. All BMD co-variates except continuous total Z score are also moderately to strongly significantly correlated with the proportion of open pores. Again, this appears to be an artifact of cortical thinning absorbing pore networks such that preservation of porosity is actually a signature of reduce relative resorption. Notably, the associations are not with overall percent porosity, but with pores closed off to tissue boundaries, or open to tissue boundaries but not yet fully resorbed. Notably, continuous right femoral neck Z score and T-score are significantly strongly positively correlated with pore separation and moderately to strongly significantly correlated with connectivity density. BMD may be associated with more porosity, but those networks tend to be more distant and separated, rather than converging at tissue margins. Continuous right femoral neck z-score is likely the most representative of these correlated metrics, having significant associations with five distinct pore morphometric variables.

228

The reduced resorption at pore margins is again implied by scarcer, more separated, and less connected pore networks associated with **cross-sectional geometry**. Cross-sectional thickness is significantly and strongly positively correlated with percent closed porosity and pore separation. Relative Cortical Volume and the mean parabolic index are is significantly and moderately to strongly negatively correlated with pore connectivity density but strongly positively correlated with the standard deviation of pore separation. Relative cortical volume is also moderately negatively correlated with pore density. Shape descriptors of Imax, Imin, and J are associated primarily with pore organization metrics, in particular pore separation (strong significant positive) and structure linear density (strong significant negative). Since these correlations all appear to be derived from the geometric configuration of the pores to thin the cortex, cross-sectional thickness is likely the most relative of these correlated co-variates.

Gross geometry correlations with pore metrics reflect this trend of more mineralized and thickened cortices retaining but curbing the expansion of porosity. In general, larger dimensions of the femoral neck produce significant positive correlations with the proportion and percentage of pores open to tissue borders but not resorbed. Femoral neck axial length to the head and apex, femoral head offset, femoral neck vertical diameter, and both vertical and horizontal diameters of the femoral head are significantly and strongly positively correlated with the proportion of open pores. Femoral neck inferior length is similarly strongly and significantly positively correlated with percentages of open and total

229

porosity. However, both ML and AP subtrochanteric shaft diameter are significantly and strongly negatively correlated with open and total porosity percentages. In individuals with larger proximal femur dimensions, significant positive correlations exist with pore separation (head horizontal diameter and femoral neck axial length to head center and apex), and with its standard deviation (femoral neck axial length to head apex). Pores are more aligned larger proportioned individuals, as degree of anisotropy significantly and strongly correlates with ML subtrochanteric shaft diameter and femoral neck vertical head diameter. Finally, a significant and strong negative association exists between pore connectivity density and femoral neck vertical diameter, as well as femoral neck axial length to head apex and center. Femoral neck axial length to head center appears to be the most representative of these relationships, as it has significant and strong positive correlations with pore separation, degree of anisotropy, and proportion of open pores, and a significant moderate negative association with pore connectivity density.

7.3.5. *Significant Effects of Sex on Continuous Co-Variates and Pore Morphometry*

Paired t-tests compared co-variates and dependent variables between males and females, separately in the rib and slightly smaller femoral neck sample.

230

Table 7.26 Paired T-Tests for Sex in the Rib

Variable	p-value
Age	0.688755
Weight*	0.126165
Height* **	0.05906
Continuous BMI*	0.349442
Continuous Total BMD*	0.186207
Continuous Total T-score*	0.927513
Continuous Total Z-score*	0.26613
Mean Parabolic Index	0.088965
Mean Imin	*0.007593*
Mean Imax	0.021042
Mean J	*0.008002*
Mean Eccentricity**	0.2719
Cross-sectional Thickness	0.903722
Relative Cortical Volume	0.135817
Cortical Fractal Dimension	0.47309
% Closed Porosity	0.483675
% Open Porosity	0.113151
% Porosity	0.116291
Pore Thickness	0.168584
Pore Separation	0.909241
Structure Linear Density	0.586336
Fragmentation Index	*0.047597*
DA	0.572011
Pore Network Fractal Dimension	0.457234
Connectivity Density	0.954647
StDv Pore Thickness	0.280641
StDv Pore Separation**	0.5541
Proportion Open Pores**	0.6726
Proportion Closed Pores**	0.6726
Pore Density	0.85868

*39F excluded   **Non-parametric Wilcoxon Signed Rank Test

In the rib, males and females differ significantly in mean Imin and mean Imax. A look at summary statistics indicates that males have a larger Imin and J on average, which can be inferred to correlate with increased stiffness of the rib

231

cross-section, and is likely related to increased body size. Females have a significantly larger pore fragmentation index than males, suggesting that their pore networks are relatively more disconnected and fragmented in the rib.

Table 7.27 Descriptive Statistics of Significant Sex Differences in the Rib

	Mean	SD	Median	Min	Max
Mean Imin (um^4)					
Female	6.13E+13	3.75E+13	5.58E+13	1.91E+13	1.15E+14
Male	1.74E+14	8.42E+13	1.89E+14	8.78E+13	3.33E+14
Mean J (um^4)					
Female	2.19E+14	1.20E+14	2.11E+14	5.52E+13	4.22E+14
Male	4.96E+14	1.91E+14	4.89E+14	2.62E+14	7.35E+14
Pore Fragmentation Index (um^{-1})					
Female	0.034321	0.003438	0.03344	0.03007	0.039157
Male	0.038302	0.003522	0.038239	0.033753	0.044903

Since the modified data set for the femoral neck contains four males and six females, it cannot be truly paired by sex for a t-test. Consequently, Wilcoxon Signed Rank tests were batch processed across the dataset.

Table 7.28 Femoral Neck Continuous Co-Variates

Variable	p-value
Age	1
Weight	0.1779
Height	***0.03977***
Continous BMI	0.7122
Continous Total BMD	0.7133
Continous Total T-score	0.7133
Continous Total Z-score	1
Continous R Femoral Neck BMD	0.1113
Continous R Femoral Neck T-score	0.2187
Continous R Femoral Neck Z-score	0.5403
FemMxLng	0.1116
FemSubTrAPDia	0.3374

FemSubTrMLDia	*0.01421*
FemHeadSIDi	*0.02518*
FemHeadHzDia	*0.03248*
FemNeckSL	0.241
FemNeckIL	0.1098
FemNeckVDia	0.1098
FemNeckTDia	0.1658
FNALCent	*0.01866*
FNALApex	0.06995
OFF	0.241
Neck-Shaft Angle	0.5023
Mean Parabolic Index	0.594
Mean Imin	0.241
Mean Imax	0.1098
Mean J	0.1098
Mean Eccentricity**	0.4555
Cross-sectional Thickness	0.4555
Relative Cortical Volume	0.7491
Cortical Fractal Dimension	0.1939
% Closed Porosity	1
% Open Porosity	*0.01866*
% Porosity	*0.01866*
Pore Thickness	0.3374
Pore Separation	0.594
Structure Linear Density	0.7491
Fragmentation Index	0.6689
DA	*0.01421*
Pore Network Fractal Dimension	1
Connectivity Density	0.9151
StDv Pore Thickness	0.3374
StDv Pore Separation**	0.8307
Proportion Open Pores**	0.1098
Proportion Closed Pores**	0.1098
Pore Density	0.9151

Significant values ($p < 0.05$) are ***bolded***

Table 7.29 Descriptive Statistics of Significant Sex Differences in the Rib

	Mean	SD	Median	Min	Max
Height (m)					
Female	1.68148	0.027824	1.7018	1.651	1.7018
Male	1.77165	0.091287	1.7399	1.7018	1.905
FemSubTrMLDia (mm)					
Female	29.22667	1.899575	28.735	27.3	31.86
Male	35.605	3.094861	34.56	33.19	40.11
FemHeadSIDi (mm)					
Female	44.99833	2.421862	44.215	42.57	49.34
Male	50.83	1.908175	50.335	49.1	53.55
FemHeadHzDia (mm)					
Female	45.48833	2.606203	45.125	42.57	49.65
Male	50.525	1.759972	49.9	49.2	53.1
% Open Porosity					
Female	14.0615	2.591751	14.2845	11.1	18.1
Male	10.135	1.605688	10.85	7.74	11.1
% Porosity					
Female	14.116	2.609509	14.298	11.2	18.2
Male	10.23	1.615632	10.95	7.82	11.2
Degree of Anisotropy					
Female	1.69655	0.179143	1.6634	1.4856	2.0269
Male	2.253825	0.238981	2.205	2.0523	2.553

Females in this smaller sample are significantly shorter than males, and also have significantly smaller dimensions of the femoral head and ML subtrochanteric femoral shaft. Femoral head dimensions are a known correlate of body size (Ruff and Higgens, 2013; Ruff and Larseb, 2014). In terms of pore microstructure, females have significantly more percent porosity than males in the femoral neck (3.8% mean difference). Specifically, they have significantly higher

234

percentages of porosity where the pores open to tissue borders, but not significantly greater closed percent porosity. While rib percent porosity is also greater in females (8.86%) compared to males (6.58%), this difference (2.28%) does not reach statistical significance. Finally, females have a significantly smaller degree of anisotropy in the femoral neck, indicating that the associated pore networks are more isotropic and less consistently oriented than in males.

7.3.6. Selection of Co-variates for Univariate Model Design

The broad list of potential co-variates must be refined to remove highly correlated co-variates. Various aspects of pore morphometry are strongly and significantly correlated with age, sex, BMD metrics, femoral neck gross geometry, and cross-sectional geometry. While BMD is commonly used, in context of porosity it is really just correlating low BMD with the absence of bone tissue in porous voids. Cross-sectional thickness is a better proxy of several categories of co-variates that are strongly and significantly correlated with pore morphometry. It is significantly correlated with BMD and moment of inertia metrics in both the femoral neck and rib. In the femoral neck, cross-sectional thickness is additionally significantly positively correlated with height and metrics of proximal femur gross geometry, a signature of stimulated bone formation and inhibited bone remodeling in response to weight bearing. It also does not show significant variation with sex in the femoral neck or rib. Cross-sectional thickness also has the advantage of avoiding a significant relationship with sex. There are significant sex differences between alternative options such as

235

height, moments of inertia, and femoral neck gross geometry. Most importantly, using cross-sectional thickness as a co-variate is a way to help compensate for elderly individuals who may have lower porosity because it has largely been resorbed through cortical thinning. The final co-variates selected were age, sex, and cross-sectional thickness, which all capture different aspects of pore acquisition without being significantlty correlated with each other.

236

7.3. Univariate Testing of Rib and Femoral Neck Pore Morphometry Differences by Cortical vs. Trabecularized Pore Type

Table 7.30 Cortex Fractal Dimension

	numDF	denDF	F.value	p.value	cohen t	cohen df	cohen d
(Intercept)	1	27	63756.43	0			
bone	1	27	121.1853	*1.74E-11*	5.337676	27	2.054473
type	1	27	441.0138	*0*	20.74415	27	7.984427
age	1	10	3.144897	0.106565	1.422281	10	0.899529
cs.th	1	27	0.034457	0.854125	0.202707	27	0.078022
sex	1	10	0.916481	0.360973	0.201764	10	0.127607
bone:type	1	27	0.050752	0.823457	0.225281	27	0.086711
age:cs.th	1	27	1.223411	0.278451	-0.76685	27	-0.29516
age:sex	1	10	0.344715	0.570138	0.15003	10	0.094887
cs.th:sex	1	27	0.780954	0.384651	-0.35238	27	-0.13563
age:cs.th:sex	1	27	0.020868	0.886213	0.144456	27	0.055601
Marginal R2	0.898028						
Conditional R2	0.928692						
Shapiro-Wilk Normality	0.683256						

Significant values (p < 0.05) are ***bolded***

Table 7.31 Percent Closed Porosity

	numDF	denDF	F.value	p.value	cohen t	cohen df	cohen d
(Intercept)	1	27	124.8039	1.25E-11			
bone	1	27	24.25711	*3.72E-05*	1.475303	27	0.567845
type	1	27	3.186529	0.085488	2.400746	27	0.924048
age	1	10	1.221951	0.294863	1.290419	10	0.816132
cs.th	1	27	1.069395	0.310256	1.016262	27	0.39116
sex	1	10	5.070664	*0.048032*	0.647484	10	0.409505
bone:type	1	27	14.77457	*0.000668*	3.84377	27	1.479468
age:cs.th	1	27	1.571648	0.220715	-0.83219	27	-0.32031
age:sex	1	10	0.151934	0.704867	-0.33717	10	-0.21325
cs.th:sex	1	27	0.062477	0.804514	-0.27357	27	-0.1053
age:cs.th:sex	1	27	0.048401	0.827524	0.220002	27	0.084679
Marginal R2	0.503186						
Conditional R2	0.615638						
Shapiro-Wilk Normality	0.143778						

Significant values (p < 0.05) are ***bolded***

238

Table 7.32 Percent Open Porosity

	numDF	denDF	F.value	p.value	cohen t	cohen df	cohen d
(Intercept)	1	27	382.3867	0			
bone	1	27	28.08021	*1.36E-05*	3.633156	27	1.398402
type	1	27	3.47161	0.073343	-2.34408	27	-0.90224
age	1	10	4.916616	0.050923	-0.60674	10	-0.38374
cs.th	1	27	0.01738	0.896093	-1.73987	27	-0.66968
sex	1	10	8.435479	*0.015715*	2.685884	10	1.698702
bone:type	1	27	9.250512	*0.005189*	-3.04147	27	-1.17066
age:cs.th	1	27	0.00052	0.981968	1.273479	27	0.490162
age:sex	1	10	0.442647	0.520897	-2.58126	10	-1.63253
cs.th:sex	1	27	0.300666	0.587971	-2.75489	27	-1.06036
age:cs.th:sex	1	27	8.85666	*0.006093*	2.976014	27	1.145468
Marginal R2	0.581129						
Conditional R2	0.630007						
Shapiro-Wilk Normality	*0.009267*						

Significant values (p < 0.05) are ***bolded***

239

Table 7.33 Percent Open Porosity: PQL Correction

	Value	Std.Error	DF	t.value	p.value	cohen t	cohen df	cohen d
(Intercept)	1.671993	0.575574	27	2.904917	0.007244			
bone1	0.280841	0.078223	27	3.590265	*0.001294*	3.590265	27	1.381894
type1	-0.09049	0.043743	27	-2.06871	*0.048272*	-2.06871	27	-0.79625
age	0.001539	0.008448	10	0.182174	0.859086	0.182174	10	0.115217
cs.th	-0.00056	0.000495	27	-1.13698	0.265537	-1.13698	27	-0.43762
sex1	1.458508	0.564269	10	2.584773	*0.027193*	2.584773	10	1.634754
bone1:type1	-0.09885	0.043743	27	-2.25991	*0.032102*	-2.25991	27	-0.86984
age:cs.th	3.79E-06	7.07E-06	27	0.53633	0.596122	0.53633	27	0.206434
age:sex1	-0.02183	0.009072	10	-2.40632	*0.036915*	-2.40632	10	-1.52189
cs.th:sex1	-0.00132	0.000509	27	-2.60205	*0.014863*	-2.60205	27	-1.00153
age:cs.th:sex1	2.23E-05	8.19E-06	27	2.71843	*0.011319*	2.71843	27	1.046324
R2	0.621463							

Significant values ($p < 0.05$) are ***bolded***

Table 7.34 Percent Porosity

	numDF	denDF	F.value	p.value	cohen t	cohen df	cohen d
(Intercept)	1	27	396.4588	0			
bone	1	27	35.72855	*2.25E-06*	3.73382	27	1.437148
type	1	27	2.925063	0.098683	-2.13187	27	-0.82056
age	1	10	5.057701	*0.048267*	-0.41992	10	-0.26558
cs.th	1	27	0.000284	0.986669	-1.57511	27	-0.60626
sex	1	10	9.082704	*0.013034*	2.766533	10	1.749709
bone:type	1	27	7.145154	*0.012595*	-2.67304	27	-1.02885
age:cs.th	1	27	0.04903	0.826425	1.143487	27	0.440128
age:sex	1	10	0.356919	0.563505	-2.62913	10	-1.66281
cs.th:sex	1	27	0.337209	0.566261	-2.79548	27	-1.07598
age:cs.th:sex	1	27	9.145056	*0.005416*	3.024079	27	1.163969
Marginal R2	0.603028						
Conditional R2	0.672461						
Shapiro-Wilk Normality	*0.013985*						

Significant values (p < 0.05) are ***bolded***

241

Table 7.35 Percent Porosity: PQL Correction

	Value	Std.Error	DF	t.value	p.value	cohen t	cohen df	cohen d
(Intercept)	1.634859	0.540179	27	3.026517	0.005384			
bone1	0.27532	0.073137	27	3.764424	*0.000823*	3.764424	27	1.448927
type1	-0.07674	0.039798	27	-1.92817	0.064412	-1.92817	27	-0.74215
age	0.002673	0.007958	10	0.335924	0.74387	0.335924	10	0.212457
cs.th	-0.00047	0.000463	27	-1.00851	0.322161	-1.00851	27	-0.38818
sex1	1.430679	0.527738	10	2.710966	*0.021897*	2.710966	10	1.714565
bone1:type1	-0.0732	0.039798	27	-1.8394	0.076877	-1.8394	27	-0.70799
age:cs.th	3.07E-06	6.63E-06	27	0.463684	0.646591	0.463684	27	0.178472
age:sex1	-0.02087	0.008477	10	-2.4623	*0.033544*	-2.4623	10	-1.5573
cs.th:sex1	-0.00126	0.000473	27	-2.6698	*0.012691*	-2.6698	27	-1.02761
age:cs.th:sex1	2.08E-05	7.59E-06	27	2.73853	*0.010793*	2.73853	27	1.054061
R2	0.654886							

Significant values ($p < 0.05$) are ***bolded***

Table 7.36 Pore Thickness

	numDF	denDF	F.value	p.value	cohen t	cohen df	cohen d
(Intercept)	1	27	79.47465	1.57E-09			
bone	1	27	20.31887	***0.000114***	3.115782	27	1.199265
type	1	27	41.52167	***6.63E-07***	-6.45822	27	-2.48577
age	1	10	0.744413	0.408466	-0.69289	10	-0.43822
cs.th	1	27	1.896378	0.179795	-0.77394	27	-0.29789
sex	1	10	2.991127	0.114409	2.267596	10	1.434154
bone:type	1	27	0.394013	0.535471	-0.6277	27	-0.2416
age:cs.th	1	27	0.600593	0.445087	0.343126	27	0.132069
age:sex	1	10	3.32236	0.098337	-2.46763	10	-1.56067
cs.th:sex	1	27	2.477572	0.127127	-2.75882	27	-1.06187
age:cs.th:sex	1	27	10.47669	***0.003191***	3.236772	27	1.245834
Marginal R2	0.633454						
Conditional R2	0.67184						
Shapiro-Wilk Normality	0.000356						

Significant values (p < 0.05) are ***bolded***

243

Table 7.37 Pore Thickness: PQL Correction

	Value	Std.Error	DF	t.value	p.value	cohen t	cohen df	cohen d
(Intercept)	6.671077	1.26717	27	5.264549	1.50E-05			
bone1	0.966576	0.423517	27	2.282261	*0.030574*	2.282261	27	0.878443
type1	-1.02141	0.384598	27	-2.6558	*0.013114*	-2.6558	27	-1.02222
age	-0.02905	0.016293	10	-1.78277	0.104954	-1.78277	10	-1.12752
cs.th	-0.00188	0.001011	27	-1.86181	0.073549	-1.86181	27	-0.71661
sex1	3.240213	0.951424	10	3.405645	*0.006707*	3.405645	10	2.153919
bone1:type1	0.489412	0.384598	27	1.272528	0.214035	1.272528	27	0.489796
age:cs.th	1.60E-05	1.32E-05	27	1.217141	0.234083	1.217141	27	0.468478
age:sex1	-0.0578	0.016388	10	-3.5267	*0.005477*	-3.5267	10	-2.23048
cs.th:sex1	-0.00379	0.000937	27	-4.0429	*0.000395*	-4.0429	27	-1.55611
age:cs.th:sex1	7.06E-05	1.54E-05	27	4.569815	*9.68E-05*	4.569815	27	1.758923
R2	0.718738							

Significant values (p < 0.05) are ***bolded***

244

Table 7.38 Pore Separation (Bone Only)

	numDF	denDF	F.value	p.value	cohen t	cohen df	cohen d
(Intercept)	1	10	651.3251	1.96E-10			
bone	1	5	0.001324	0.972383	-2.12782	5	-1.90318
age	1	10	5.429012	*0.042048*	-1.48488	10	-0.93912
cs.th	1	5	7.28004	*0.042879*	0.902267	5	0.807012
sex	1	10	0.012197	0.914245	1.333679	10	0.843493
age:cs.th	1	5	0.015852	0.904714	0.60606	5	0.542076
age:sex	1	10	3.306205	0.099052	-1.49513	10	-0.94561
cs.th:sex	1	5	0.107502	0.75629	-0.51929	5	-0.46447
age:cs.th:sex	1	5	0.385498	0.56188	0.620884	5	0.555336
Marginal R2	0.437036						
Conditional R2	0.860749						
Shapiro-Wilk Normality	*0.002433*						

Significant values (p < 0.05) are ***bolded***

245

Table 7.39 Pore Separation (Bone Only): PQL Correction

	Value	Std.Error	DF	t.value	p.value	cohen t	cohen df	cohen d
(Intercept)	4.096279	1.027752	10	3.98567	0.002577			
bone1	0.288184	0.126688	5	2.274761	0.072008	2.274761	5	2.034609
age	0.014505	0.015676	10	0.925284	0.376607	0.925284	10	0.585201
cs.th	0.000543	0.000827	5	0.656521	0.540497	0.656521	5	0.587211
sex1	0.875856	1.003476	10	0.872821	0.403232	0.872821	10	0.552021
age:cs.th	-7.63E-06	1.26E-05	5	-0.60806	0.569704	-0.60806	5	-0.54387
age:sex1	-0.01339	0.016034	10	-0.83536	0.423026	-0.83536	10	-0.52833
cs.th:sex1	-0.00101	0.000835	5	-1.20369	0.282583	-1.20369	5	-1.07661
age:cs.th:sex1	1.90E-05	1.36E-05	5	1.395884	0.221565	1.395884	5	1.248516
R2	0.664285							

Significant values (p < 0.05) are ***bolded***

Table 7.40 Pore Network Linear Density

	numDF	denDF	F.value	p.value	cohen t	cohen df	cohen d
(Intercept)	1	27	2.276736	0.142942			
bone	1	27	3.755097	0.063171	-1.33865	27	-0.51525
type	1	27	0.801049	0.37869	-1.05901	27	-0.40761
age	1	10	2.483796	0.146102	-1.1005	10	-0.69602
cs.th	1	27	0.751288	0.393707	-0.51961	27	-0.2
sex	1	10	2.767495	0.127173	-1.17719	10	-0.74452
bone:type	1	27	1.12162	0.298953	-1.05907	27	-0.40763
age:cs.th	1	27	6.758469	*0.014944*	2.063153	27	0.794108
age:sex	1	10	6.25092	*0.031437*	1.660705	10	1.050322
cs.th:sex	1	27	9.076123	*0.00557*	1.734093	27	0.667453
age:cs.th:sex	1	27	6.500713	*0.016775*	-2.54965	27	-0.98136
Marginal R2	0.464729						
Conditional R2	0.487563						
Shapiro-Wilk Normality	*7.11E-09*						

Significant values ($p < 0.05$) are ***bolded***

247

Table 7.41 Pore Network Linear Density: PQL Correction

	Value	Std.Error	DF	t.value	p.value	cohen t	cohen df	cohen d
(Intercept)	22.62195	3.324034	27	6.805571	2.61E-07			
bone1	-0.08647	0.321783	27	-0.26872	0.790188	-0.26872	27	-0.10343
type1	-0.00136	0.144611	27	-0.00937	0.99259	-0.00937	27	-0.00361
age	-0.4884	0.046318	10	-10.5445	*9.76E-07*	-10.5445	10	-6.66894
cs.th	-0.05489	0.005616	27	-9.77324	*2.32E-10*	-9.77324	27	-3.76172
sex1	-28.8242	3.121007	10	-9.23553	*3.28E-06*	-9.23553	10	-5.84106
bone1:type1	-0.6068	0.144611	27	-4.19607	*0.000263*	-4.19607	27	-1.61507
age:cs.th	0.00084	7.38E-05	27	11.38606	*8.17E-12*	11.38606	27	4.382496
age:sex1	0.47461	0.045926	10	10.33418	*1.18E-06*	10.33418	10	6.535911
cs.th:sex1	0.052092	0.005412	27	9.625857	*3.20E-10*	9.625857	27	3.704994
age:cs.th:sex1	-0.00081	7.28E-05	27	-11.1632	*1.27E-11*	-11.1632	27	-4.29673
R2	0.067537							

Significant values ($p < 0.05$) are ***bolded***

Table 7.42 Pore Fragmentation Index

	numDF	denDF	F.value	p.value	cohen t	cohen df	cohen d
(Intercept)	1	27	17.54705	0.000268			
bone	1	27	12.52894	***0.001475***	-3.00059	27	-1.15493
type	1	27	1.816836	0.188892	1.139213	27	0.438483
age	1	10	2.163482	0.172077	0.89284	10	0.564682
cs.th	1	27	0.497251	0.48675	0.99116	27	0.381498
sex	1	10	0.08091	0.781871	-0.17945	10	-0.11349
bone:type	1	27	1.297335	0.264706	-1.13901	27	-0.4384
age:cs.th	1	27	0.058586	0.810575	-0.52726	27	-0.20294
age:sex	1	10	1.033839	0.333227	-0.01522	10	-0.00962
cs.th:sex	1	27	0.877975	0.357063	0.562201	27	0.216391
age:cs.th:sex	1	27	0.116246	0.735781	-0.34095	27	-0.13123
Marginal R2	0.303409						
Conditional R2	0.303409						
Shapiro-Wilk Normality	***0.000185***						

Significant values (p < 0.05) are ***bolded***

Table 7.43 Pore Fragmentation Index: PQL Correction

	Value	Std.Error	DF	t.value	p.value	cohen t	cohen df	cohen d
(Intercept)	17.86731	5966.935	27	0.002994	0.997633			
bone1	-6.86101	5966.912	27	-0.00115	0.999091	-0.00115	27	-0.00044
type1	0.211061	5966.911	27	3.54E-05	0.999972	3.54E-05	27	1.36E-05
age	-0.28145	0.173145	10	-1.6255	0.135118	-1.6255	10	-1.02805
cs.th	-0.038	0.028262	27	-1.34464	0.18993	-1.34464	27	-0.51755
sex1	-24.6391	14.31129	10	-1.72165	0.115864	-1.72165	10	-1.08887
bone1:type1	0.104119	5966.911	27	1.74E-05	0.999986	1.74E-05	27	6.72E-06
age:cs.th	0.000539	0.000332	27	1.625625	0.115647	1.625625	27	0.625703
age:sex1	0.338981	0.173145	10	1.95779	0.078724	1.95779	10	1.238215
cs.th:sex1	0.044749	0.028262	27	1.583357	0.124985	1.583357	27	0.609434
age:cs.th:sex1	-0.00061	0.000332	27	-1.83477	0.07758	-1.83477	27	-0.70621
R2	4.14E-06							

Significant values (p < 0.05) are ***bolded***

Table 7.44 Degree of Anisotropy

	numDF	denDF	F.value	p.value	cohen t	cohen df	cohen d
(Intercept)	1	27	515.1885	0			
bone	1	27	6.619494	*0.015902*	-0.55345	27	-0.21302
type	1	27	50.39212	*1.24E-07*	6.056528	27	2.331159
age	1	10	2.430737	0.150036	-1.6573	10	-1.04817
cs.th	1	27	0.342388	0.563313	-1.2477	27	-0.48024
sex	1	10	0.73116	0.412525	-1.09031	10	-0.68958
bone:type	1	27	32.00783	*5.24E-06*	-5.65755	27	-2.17759
age:cs.th	1	27	3.774854	*0.062524*	1.140821	27	0.439102
age:sex	1	10	4.06569	*0.071413*	0.847692	10	0.536128
cs.th:sex	1	27	0.44828	0.508838	0.324239	27	0.1248
age:cs.th:sex	1	27	0.028195	0.867904	-0.16791	27	-0.06463
Marginal R2	0.653144						
Conditional R2	0.709351						
Shapiro-Wilk Normality	*0.000264*						

Significant values (p < 0.05) are ***bolded***

251

Table 7.45 Degree of Anisotropy: PQL Correction

	Value	Std.Error	DF	t.value	p.value	cohen t	cohen df	cohen d
(Intercept)	1.484689	0.479075	27	3.099074	0.0045			
bone1	-0.00239	0.074717	27	-0.03205	0.974667	-0.03205	27	-0.01234
type1	0.209077	0.030743	27	6.800695	*2.64E-07*	6.800695	27	2.617589
age	-0.01083	0.006757	10	-1.60211	0.140213	-1.60211	10	-1.01326
cs.th	-0.00049	0.000451	27	-1.07697	0.291023	-1.07697	27	-0.41453
sex1	-0.67984	0.409813	10	-1.6589	0.128126	-1.6589	10	-1.04918
bone1:type1	-0.19883	0.030743	27	-6.46736	*6.24E-07*	-6.46736	27	-2.48929
age:cs.th	5.66E-06	6.28E-06	27	0.900552	0.375789	0.900552	27	0.346623
age:sex1	0.009472	0.006803	10	1.392403	0.193985	1.392403	10	0.880633
cs.th:sex1	0.000314	0.000427	27	0.736443	0.467812	0.736443	27	0.283457
age:cs.th:sex1	-3.53E-06	6.73E-06	27	-0.52433	0.604325	-0.52433	27	-0.20182
R2	0.771118							

Significant values ($p < 0.05$) are ***bolded***

Table 7.46 Pore Fractal Dimension

	numDF	denDF	F.value	p.value	cohen t	cohen df	cohen d
(Intercept)	1	27	4491.442	0			
bone	1	27	16.96132	0.000323	2.547305	27	0.980458
type	1	27	23.1989	4.99E-05	4.686011	27	1.803647
age	1	10	0.000171	0.98983	-0.20979	10	-0.13268
cs.th	1	27	0.044176	0.835104	-0.53513	27	-0.20597
sex	1	10	1.976044	0.190109	0.621569	10	0.393115
bone:type	1	27	0.143542	0.707748	-0.37887	27	-0.14583
age:cs.th	1	27	0.017105	0.896915	0.351784	27	0.135402
age:sex	1	10	0.673175	0.43107	-0.28647	10	-0.18118
cs.th:sex	1	27	0.865802	0.360366	-0.80521	27	-0.30993
age:cs.th:sex	1	27	0.352169	0.557827	0.593439	27	0.228415
Marginal R2	0.484792						
Conditional R2	0.484955						
Shapiro-Wilk Normality	1.53E-08						

Significant values ($p < 0.05$) are ***bolded***

253

Table 7.47 Pore Fractal Dimension: PQL Correction

	Value	Std.Error	DF	t.value	p.value	cohen t	cohen df	cohen d
(Intercept)	0.810672	0.197618	27	4.102226	0.000338			
bone1	0.069157	0.027318	27	2.531556	*0.017486*	2.531556	27	0.974396
type1	0.070439	0.015111	27	4.661471	*7.57E-05*	4.661471	27	1.794201
age	-0.0007	0.002965	10	-0.23765	0.816951	-0.23765	10	-0.1503
cs.th	-9.86E-05	0.000182	27	-0.54287	0.591671	-0.54287	27	-0.20895
sex1	0.080837	0.184926	10	0.437129	0.671307	0.437129	10	0.276464
bone1:type1	-0.00972	0.015111	27	-0.6431	0.525581	-0.6431	27	-0.24753
age:cs.th	1.03E-06	2.68E-06	27	0.383025	0.7047	0.383025	27	0.147426
age:sex1	-0.00035	0.003091	10	-0.11268	0.912514	-0.11268	10	-0.07126
cs.th:sex1	-0.00012	0.000182	27	-0.66691	0.510492	-0.66691	27	-0.25669
age:cs.th:sex1	1.33E-06	2.98E-06	27	0.445823	0.65928	0.445823	27	0.171597
R2	0.59102							

Significant values (p < 0.05) are ***bolded***

Table 7.48 Connecitivty Density

	numDF	denDF	F.value	p.value	cohen t	cohen df	cohen d
(Intercept)	1	27	123.1768	1.45E-11			
bone	1	27	0.117974	0.733902	2.666632	27	1.026387
type	1	27	86.78528	***6.35E-10***	9.013103	27	3.469145
age	1	10	2.07244	0.180541	-0.05396	10	-0.03413
cs.th	1	27	6.096346	***0.020163***	-1.80932	27	-0.69641
sex	1	10	0.081874	0.780614	0.673161	10	0.425744
bone:type	1	27	1.070735	0.309959	-1.03476	27	-0.39828
age:cs.th	1	27	0.072017	0.790461	0.450876	27	0.173542
age:sex	1	10	3.354796	0.09692	-0.29616	10	-0.18731
cs.th:sex	1	27	2.135202	0.155493	-1.28338	27	-0.49397
age:cs.th:sex	1	27	0.905144	0.349846	0.951391	27	0.36619
Marginal R2	0.686022						
Conditional R2	0.686022						
Shapiro-Wilk Normality	0.052383						

Significant values (p < 0.05) are ***bolded***

255

Table 7.49 Pore Thickness Standard Deviation

	numDF	denDF	F.value	p.value	cohen t	cohen df	cohen d
(Intercept)	1	27	158.4696	8.23E-13			
bone	1	27	23.79541	*4.23E-05*	1.978448	27	0.761505
type	1	27	23.27984	*4.88E-05*	-5.06266	27	-1.94862
age	1	10	3.300322	0.099314	-0.25959	10	-0.16418
cs.th	1	27	9.816399	*0.004136*	-0.42355	27	-0.16302
sex	1	10	3.607157	0.086729	1.437179	10	0.908952
bone:type	1	27	3.353926	0.078101	-1.83137	27	-0.7049
age:cs.th	1	27	0.240158	0.628051	0.820353	27	0.315754
age:sex	1	10	3.630634	0.085851	-1.69011	10	-1.06892
cs.th:sex	1	27	2.538945	0.12271	-1.92307	27	-0.74019
age:cs.th:sex	1	27	5.720343	*0.023999*	2.391724	27	0.920575
Marginal R2	0.62782						
Conditional R2	0.627821						
Shapiro-Wilk Normality	*6.54E-08*						

Significant values (p < 0.05) are ***bolded***

256

Table 7.50 Pore Thickness Standard Deviation: PQL Correction

	Value	Std.Error	DF	t.value	p.value	cohen t	cohen df	cohen d
(Intercept)	0.810672	0.197618	27	4.102226	0.000338			
bone1	0.069157	0.027318	27	2.531556	*0.017486*	2.531556	27	0.974396
type1	0.070439	0.015111	27	4.661471	*7.57E-05*	4.661471	27	1.794201
age	-0.0007	0.002965	10	-0.23765	0.816951	-0.23765	10	-0.1503
cs.th	-9.86E-05	0.000182	27	-0.54287	0.591671	-0.54287	27	-0.20895
sex1	0.080837	0.184926	10	0.437129	0.671307	0.437129	10	0.276464
bone1:type1	-0.00972	0.015111	27	-0.6431	0.525581	-0.6431	27	-0.24753
age:cs.th	1.03E-06	2.68E-06	27	0.383025	0.7047	0.383025	27	0.147426
age:sex1	-0.00035	0.003091	10	-0.11268	0.912514	-0.11268	10	-0.07126
cs.th:sex1	-0.00012	0.000182	27	-0.66691	0.510492	-0.66691	27	-0.25669
age:cs.th:sex1	1.33E-06	2.98E-06	27	0.445823	0.65928	0.445823	27	0.171597
R2	0.59102							

Significant values (p < 0.05) are ***bolded***

Table 7.51 Pore Separation Standard Deviation

	numDF	denDF	F.value	p.value	cohen t	cohen df	cohen d
(Intercept)	1	10	1090.232	1.53E-11			
bone	1	5	1.221691	0.319356	-0.97161	5	-0.86904
age	1	10	13.70433	*0.004095*	-1.14011	10	-0.72107
cs.th	1	5	0.993978	0.364544	0.945005	5	0.845238
sex	1	10	1.693157	0.222366	1.162552	10	0.735263
age:cs.th	1	5	0.03103	0.867086	0.026492	5	0.023695
age:sex	1	10	11.09406	*0.007608*	-1.36561	10	-0.86368
cs.th:sex	1	5	1.224195	0.31891	-0.01648	5	-0.01474
age:cs.th:sex	1	5	0.08939	0.776983	0.298981	5	0.267417
Marginal R2	0.568277						
Conditional R2	0.574586						
Shapiro-Wilk Normality	0.899029						

Significant values (p < 0.05) are ***bolded***

258

Table 7.52 Proportion Open Pores (Equivalent to Proportion Closed Pores Model)

	numDF	denDF	F.value	p.value	cohen t	cohen df	cohen d
(Intercept)	1	27	8018.862	0			
bone	1	27	16.00398	*0.000442*	-0.50688	27	-0.1951
type	1	27	16.20779	*0.000413*	-4.86511	27	-1.87258
age	1	10	0.824643	0.385188	0.788934	10	0.498965
cs.th	1	27	4.758974	*0.038027*	-0.16572	27	-0.06379
sex	1	10	0.254698	0.624721	0.017727	10	0.011211
bone:type	1	27	28.87102	*1.12E-05*	-5.37318	27	-2.06814
age:cs.th	1	27	0.676499	0.418	-0.83963	27	-0.32317
age:sex	1	10	0.24834	0.629024	-0.27246	10	-0.17232
cs.th:sex	1	27	1.024027	0.320549	-0.17211	27	-0.06625
age:cs.th:sex	1	27	0.190157	0.666253	0.43607	27	0.167843
Marginal R2	0.595037						
Conditional R2	0.595037						
Shapiro-Wilk Normality	0.146757						

Significant values (p < 0.05) are ***bolded***

259

Table 7.53 Pore Density

	numDF	denDF	F.value	p.value	cohen t	cohen df	cohen d
(Intercept)	1	27	113.359	3.64E-11			
bone	1	27	0.471337	0.498227	2.27826	27	0.876903
type	1	27	80.27237	*1.42E-09*	8.521973	27	3.280109
age	1	10	0.536679	0.480631	-0.5808	10	-0.36733
cs.th	1	27	6.926473	0.013869	-2.19512	27	-0.8449
sex	1	10	0.147025	0.709421	0.865949	10	0.547674
bone:type	1	27	3.508848	0.071906	-1.87319	27	-0.72099
age:cs.th	1	27	0.000681	0.979368	0.804807	27	0.30977
age:sex	1	10	3.421783	0.094075	-0.42221	10	-0.26703
cs.th:sex	1	27	3.091476	0.090036	-1.49672	27	-0.57609
age:cs.th:sex	1	27	1.200619	0.282876	1.095728	27	0.421746
Marginal R2	0.67935						
Conditional R2	0.67935						
Shapiro-Wilk Normality	*0.027451*						

Significant values (p < 0.05) are ***bolded***

260

Table 7.54 Pore Density: PQL Correction

	Value	Std.Error	DF	t.value	p.value	cohen t	cohen df	cohen d
(Intercept)	-13.8415	0.848819	27	-16.3068	1.68E-15			
bone1	0.762161	0.467311	27	1.630951	0.114512	1.630951	27	0.627753
type1	1.272482	0.456734	27	2.786043	*0.009641*	2.786043	27	1.072348
age	-0.02447	0.010486	10	-2.33383	*0.041777*	-2.33383	10	-1.47604
cs.th	-0.00365	0.000774	27	-4.71957	*6.47E-05*	-4.71957	27	-1.81656
sex1	1.908894	0.699621	10	2.728471	*0.021249*	2.728471	10	1.725636
bone1:type1	-0.44798	0.456734	27	-0.98084	0.335381	-0.98084	27	-0.37752
age:cs.th	3.01E-05	1.12E-05	27	2.693022	*0.012017*	2.693022	27	1.036545
age:sex1	-0.02344	0.011547	10	-2.02995	0.06981	-2.02995	10	-1.28385
cs.th:sex1	-0.0028	0.000816	27	-3.43372	*0.001936*	-3.43372	27	-1.32164
age:cs.th:sex1	3.70E-05	1.30E-05	27	2.846546	*0.00834*	2.846546	27	1.095636
R2	0.730081							

Significant values (p < 0.05) are ***bolded***

7.4. Interpreting Variation in Rib and Femoral Neck Pore Network Patterning

To begin to make sense of the many univariate models, we can consider both the goodness of fit (R^2) of the model and the effect size (Cohen's d) of the significant fixed factors, co-variates, or interaction terms. Since both bone type and pore type contain only two levels, we can compare means rather than running a post-hoc test. We can also consider the medians of each bone + pore type combination for males and females separately, as some of the pore morphometric variables displayed significant sex differences. Pore morphometry variables in this study fall into three different categories, which describe 1) Pore Prevalence, 2) Pore Size and Spacing, and 3) Pore Connectivity and Network Alignment.

262

7.4.1. Interpreting Pore Prevalence

Table 7.55 Effect Size of Bone Type * Pore Type Factors on Pore Prevalence

Factor	Percent Porosity	Pore Density	Percent Closed Porosity	Percent Open Porosity	Proportion of Open Pores
Bone	**Large** (FN > Rib)		**Medium** (FN>Rib)	**Large** (FN>Rib)	**Small** (FN<Rib)
Pore Type		**Large** (Ct>Tb)		**Medium**	**Large** (FN:Ct<Tb) (Rib:Ct<Tn)
Age		**Large** (Increase)			
Cortical Thickness		**Large** (Decrease)			**Medium**
Sex	**Large** (F>M)	**Large** (F<M)	**Small** (F>M)	**Large** (F>M)	
Bone: Type			**Large** (FN Ct>Tb) (Rib Ct<Tb)	**Large** (FN Ct<Tb) (Rib Ct>Tb)	
age:cs.th		**Large**			
age:sex	**Large**			**Large**	
cs.th:sex	**Large**	**Large**		**Large**	
age:cs.th: sex	**Large**	**Large**		**Large**	
Marginal R^2	65.49%	73.01%	50.32%	62.15%	59.10%

263

Figure 7.11 Significant Interactions in Percent Porosity by Bone Type, Pore Type, and Sex
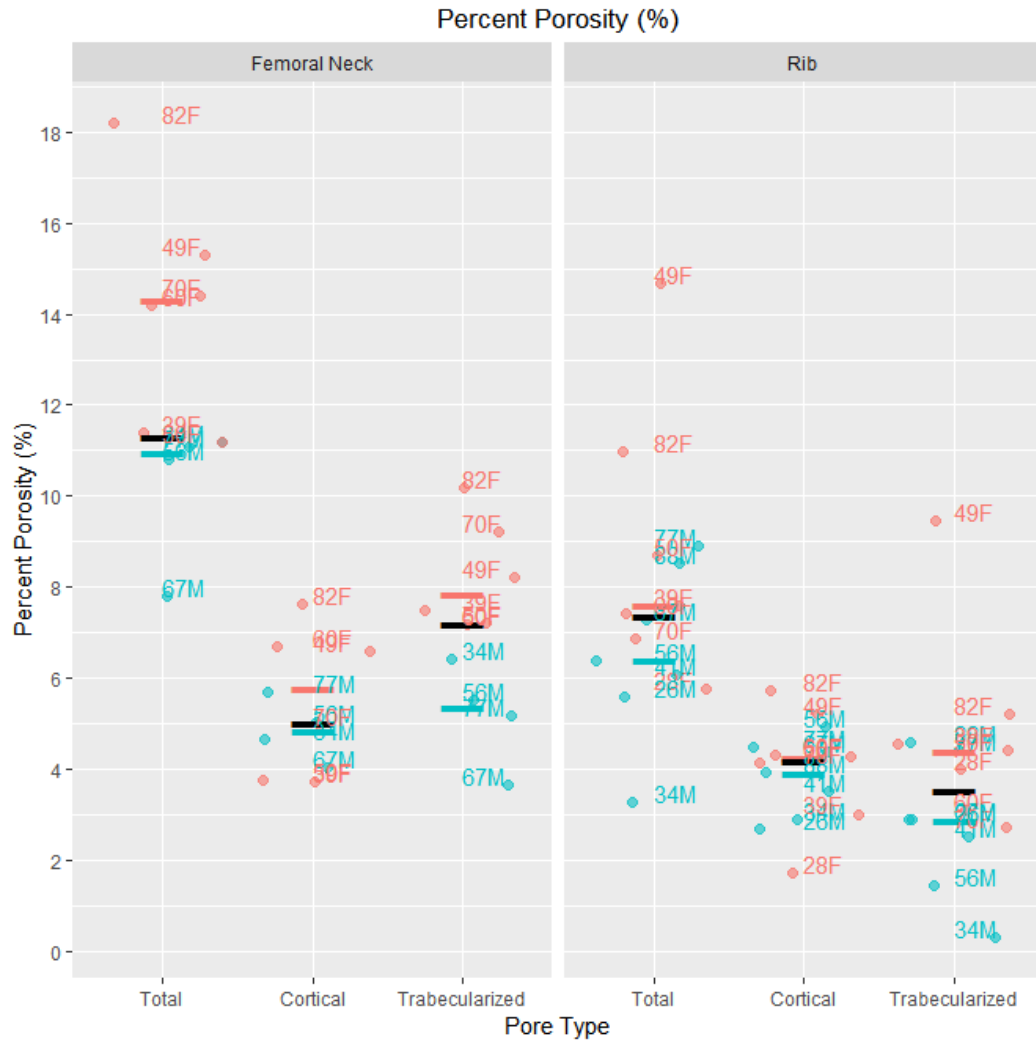
Bars indicate pooled (black), female (red), and male (blue) medians

Significant Differences:

- Femoral Neck > Rib

- Females > Males

Figure 7.12 Significant Interactions in Pore Density by Bone Type, Pore Type, and Sex

Bars indicate pooled (black), female (red), and male (blue) medians

Significant Differences:

- Cortical > Trabecularized

- Males > Females

265

Figure 7.13 Significant Interactions in Pore Density, Age, and Cross-Sectional Thickness by Sex
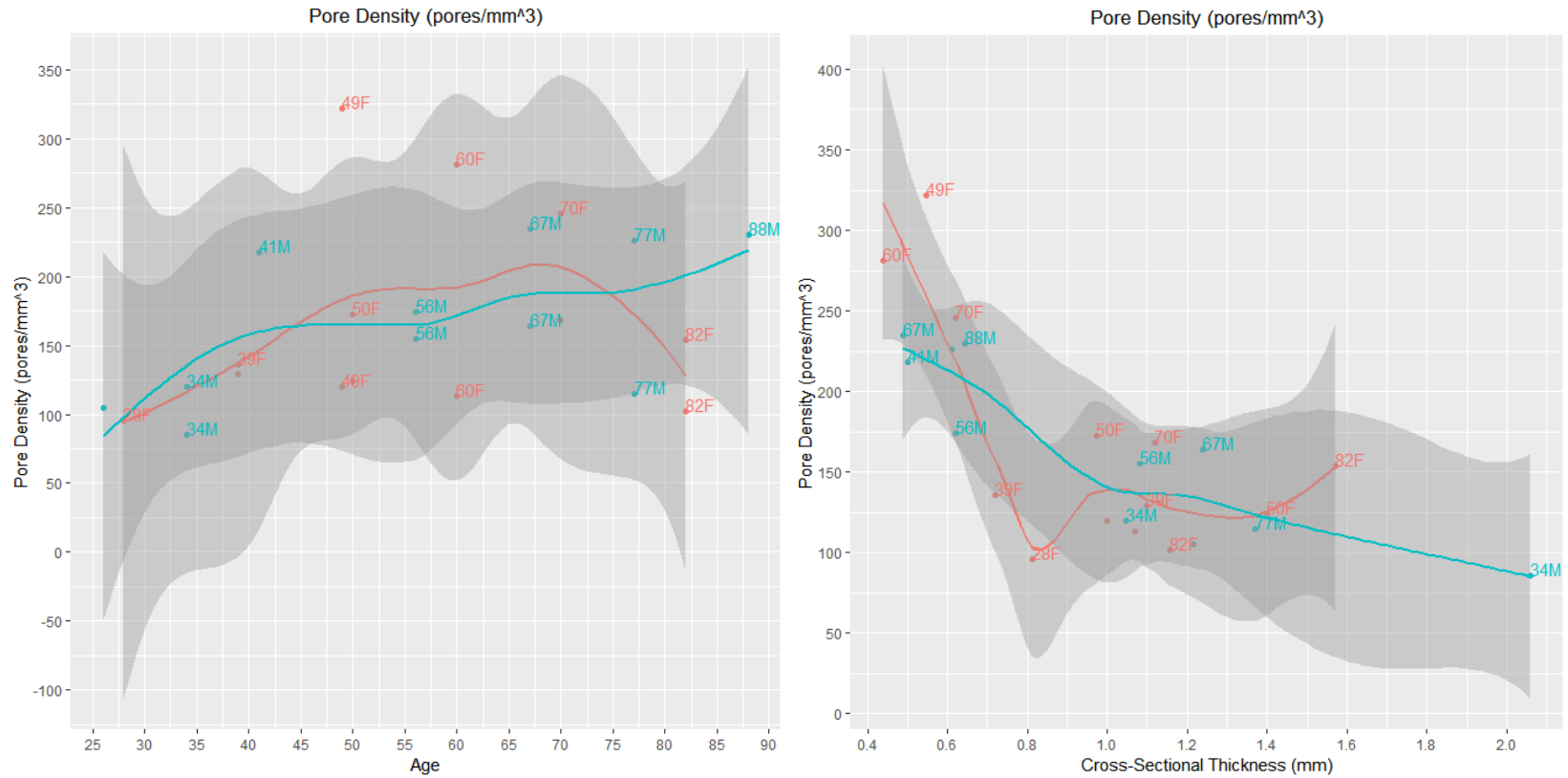
Loess regression line smoothing for smaller observations; Femoral neck and rib values pooled due to lack of significant interaction

Significant Differences: Increases with age, Decreases with cross-sectional thickness

Figure 7.14 Significant Interactions in Percent Closed Porosity by Bone Type, Pore Type, and Sex
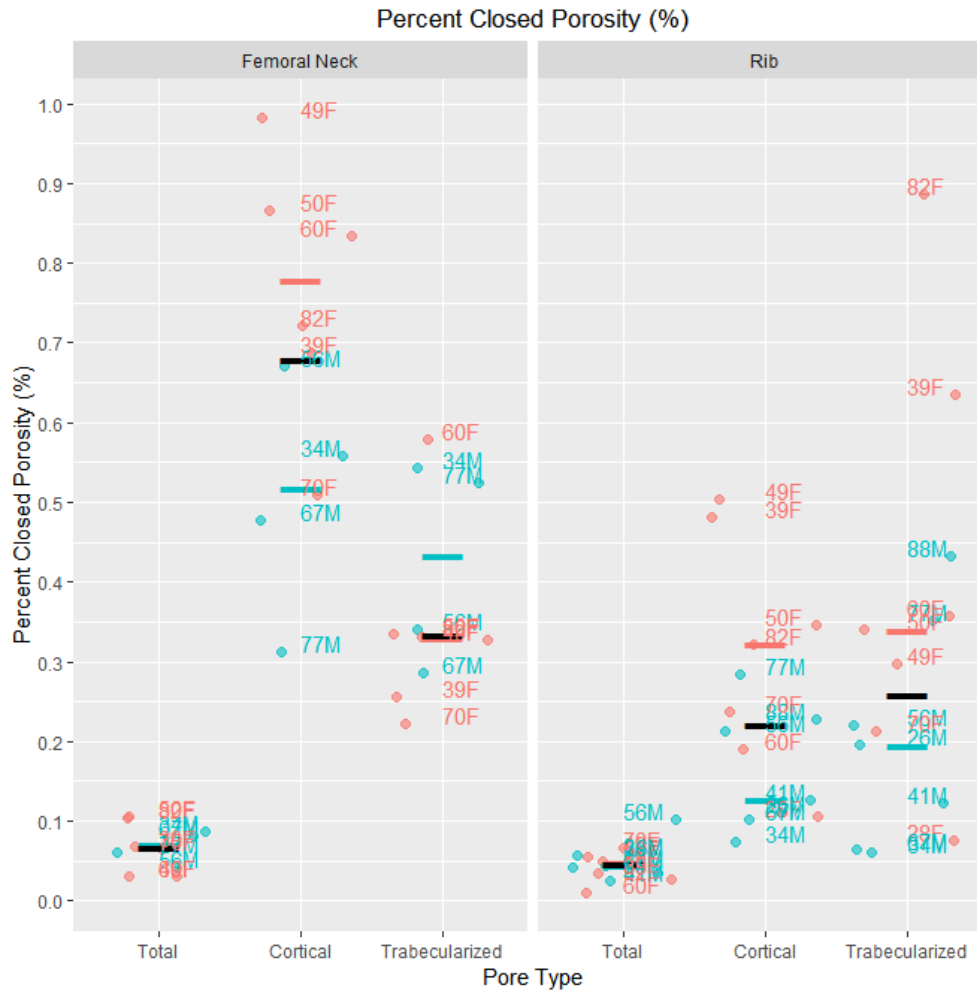
Bars indicate pooled (black), female (red), and male (blue) medians

Significant Differences:

- Femoral Neck > Rib

- Females > Males (small effect)

- Femoral Neck: Cortical > Trabecularized Open Porosity

- Rib: Cortical < Trabecularized Open Porosity

267

Figure 7.15 Significant Interactions in Percent Open Porosity by Bone Type, Pore Type, and Sex

Bars indicate pooled (black), female (red), and male (blue) medians

Significant Differences:

- Femoral Neck > Rib

- Females > Males

- Femoral Neck: Cortical < Trabecularized Open Porosity

- Rib: Cortical > Trabecularized Open Porosity

268

Figure 7.16 Significant Interactions in Percent Open Porosity by Bone Type, Pore Type, and Sex
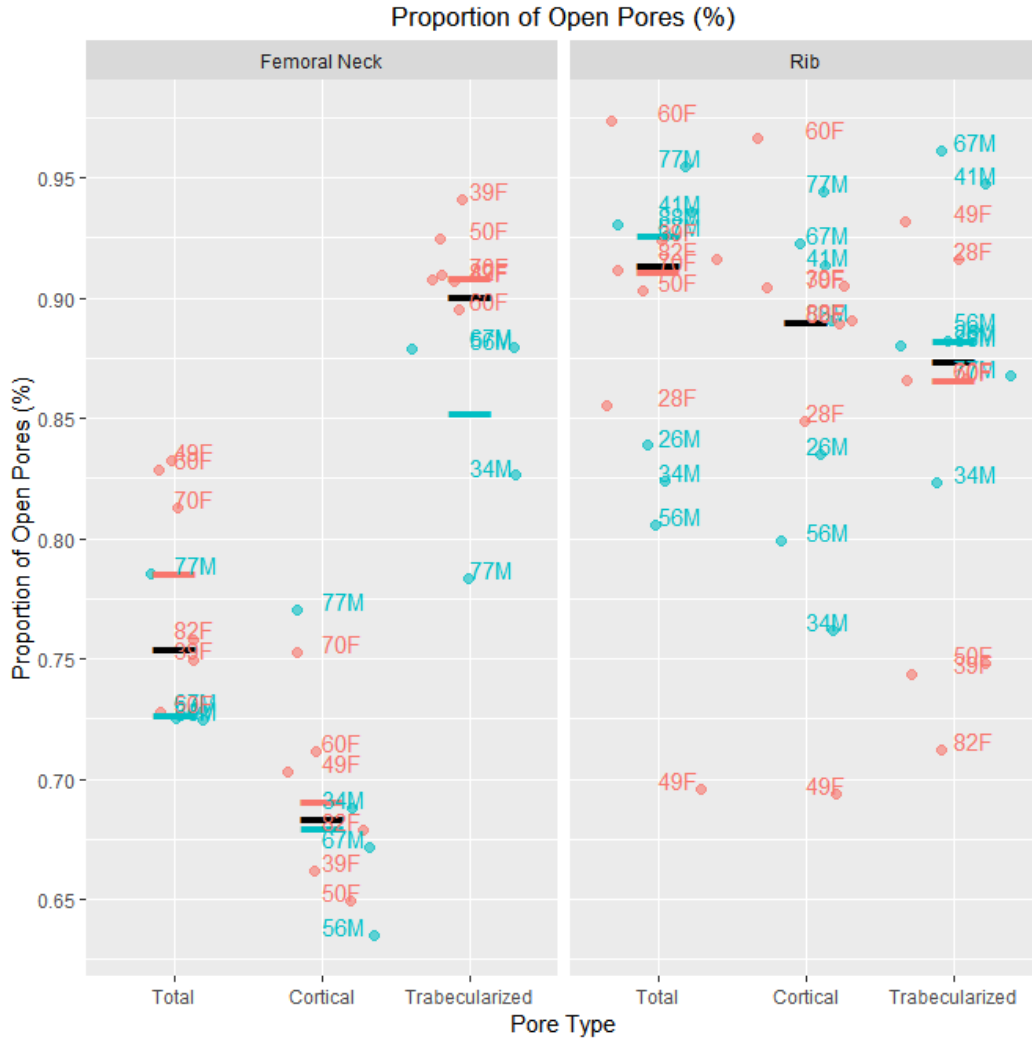
Bars indicate pooled (black), female (red), and male (blue) medians

Significant Differences:

- Femoral Neck < Rib (Small Effect)

- Femoral Neck = More Open Trabecularized Pores

- Rib = More Open Cortical Pores

269

Figure 7.17 Significant Interactions in Proportion of Open Pores and Cross-Sectional Thickness by Sex
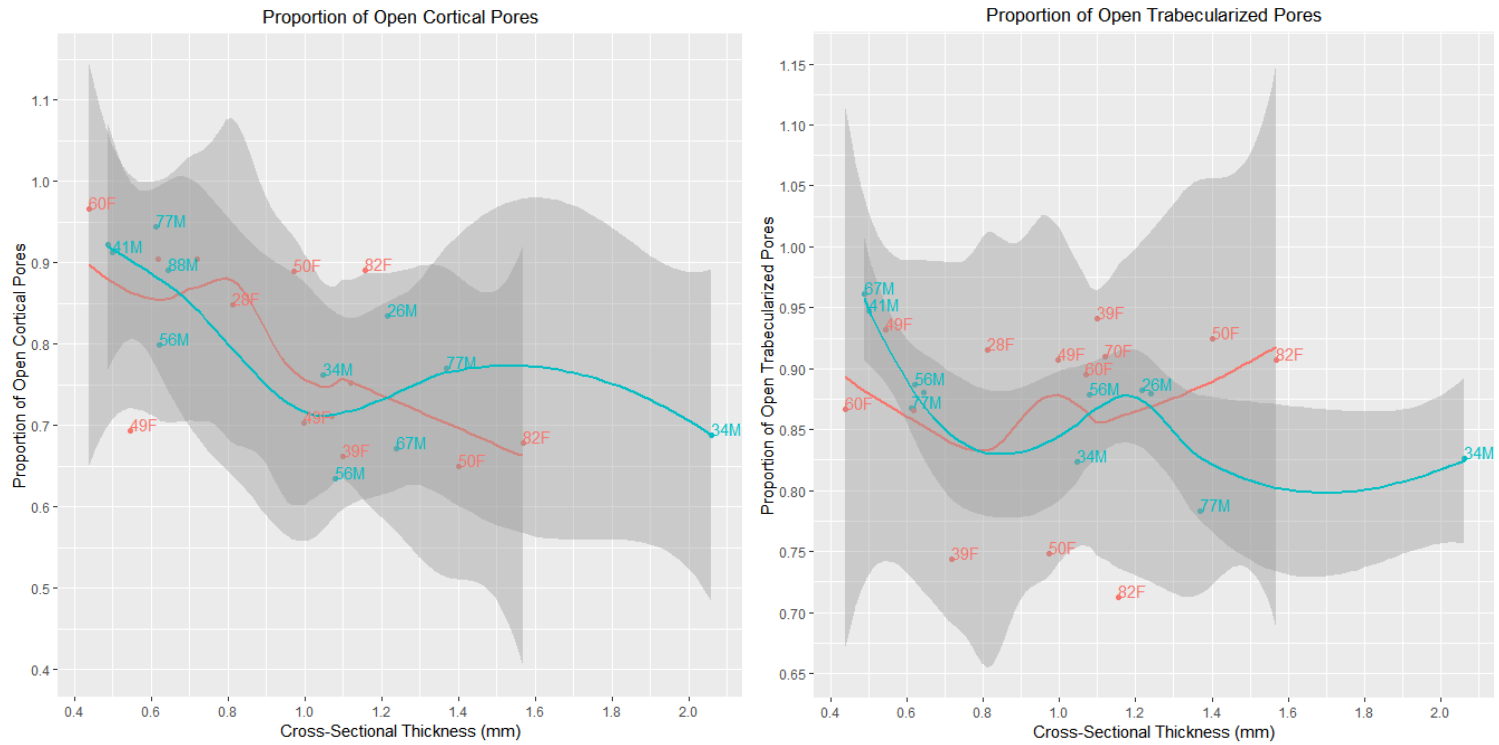
Thicker cortices generally have smaller proportions of pores that open to the cortex, reflecting their reduced trabecularization.

7.4.2. Interpreting Pore Size and Spacing

Table 7.56 Effect Size of Bone Type * Pore Type Factors on Pore Size and Spacing

Factor	Pore Thickness	Pore Separation	St Dv Pore Thickness	St Dv Pore Separation
Bone	Large (FN>Rib)		Large (FN>Rib)	
Pore Type	Large (Ct<Tb)		Large (Ct<Tb)	
Age				Medium (F Only Decrease)
Cortical Thickness				
Sex	Large FN F>M			
Bone: Type				
age:cs.th				
age:sex	Large			Medium
cs.th:sex	Large			
age:cs.th: sex	Large			
Marginal R^2	71.87%	66.43%	59.10%	56.83%

271

Table 7.57 Significant Interactions in Pore Thickness by Bone Type, Pore Type, and Sex

Bars indicate pooled (black), female (red), and male (blue) medians

Significant Differences:

- Femoral neck has relatively larger total, cortical, and trabecularized pores

- Cortical Pores < Trabecularized Pore Size

- Female Pore Size > Male Pore Size in the femoral neck

Table 7.58 Significant Interactions in Standard Deviation of Pore Thickness by Bone Type, Pore Type, and Sex
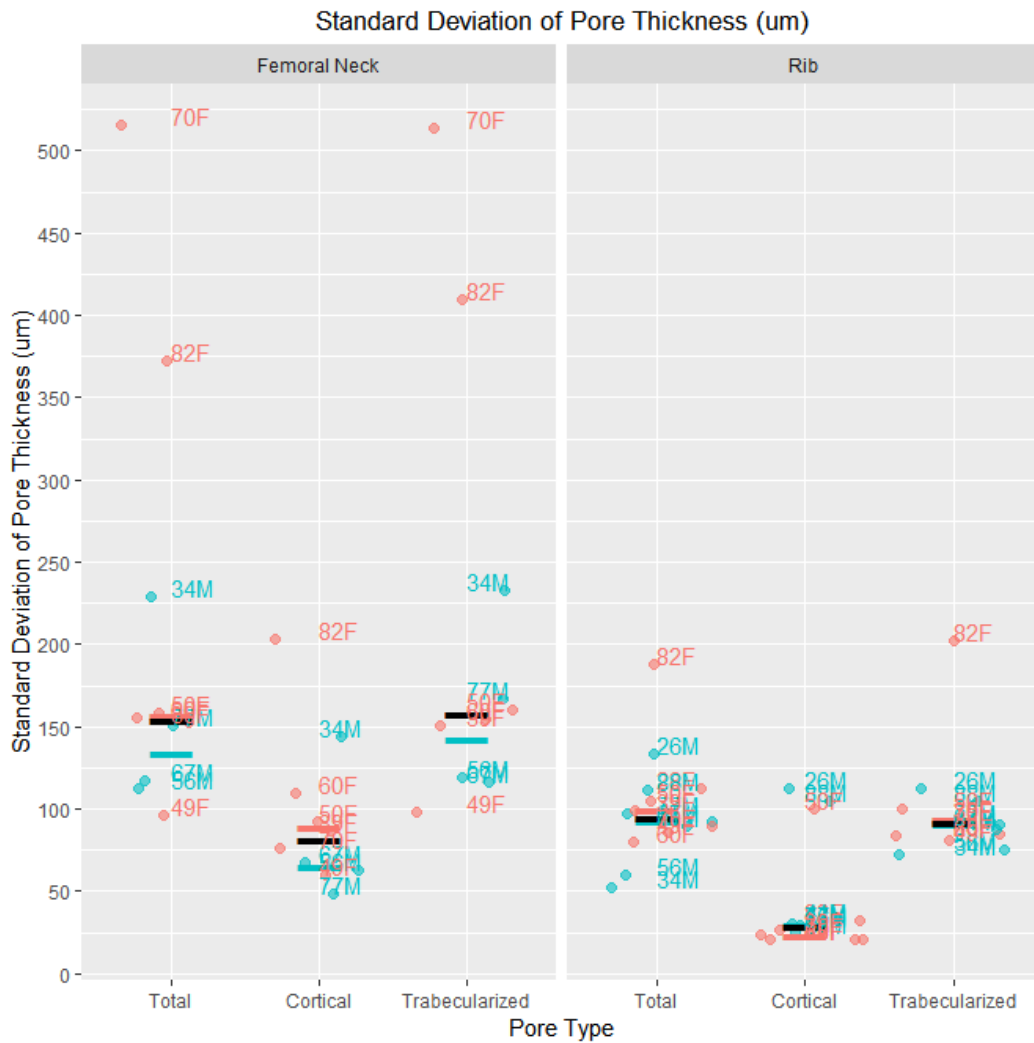
Bars indicate pooled (black), female (red), and male (blue) medians

Significant Differences:

- Femoral neck has a wider range of pore sizes than the rib

- Trabecularized pores have a wider range of pore sizes

273

Table 7.59 Significant Interaction of Age and Standard Deviation of Pore Separation
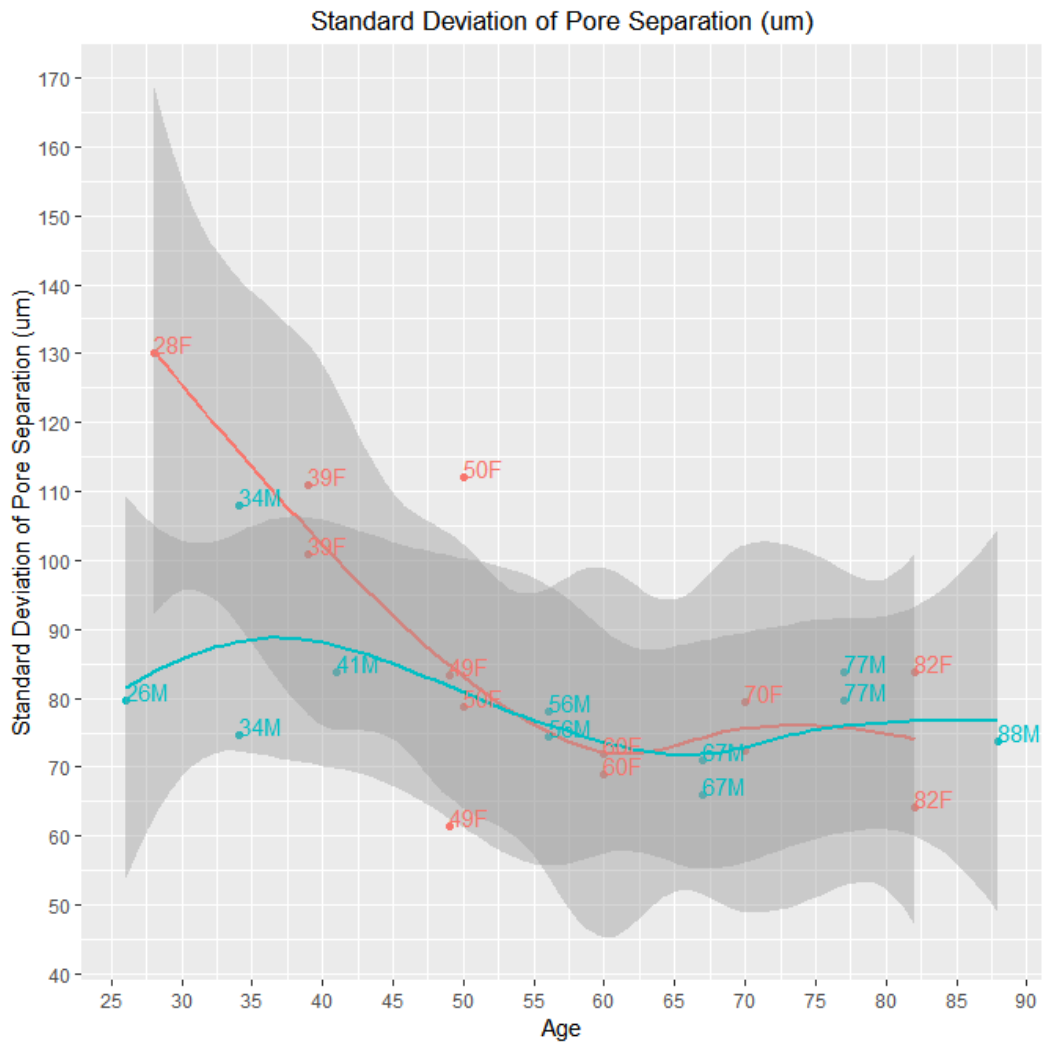
Loess regression line smoothing for smaller observations; Femoral neck and rib

values pooled due to lack of significant interaction

Significant Differences:

- Pores become more uniform in separation with age

- Females decline more than males, but only because they begin with a less

  variable range of pores sizes – equivalence is reached around age 50

274

7.4.3. Interpreting Pore Network Connectivity and Orientation

Table 7.60 Effect Size of Bone Type * Pore Type Factors on Pore Complexity and Network Organization

Pore Factor	Pore Frag Index	Pore Conn. Density	Degree of Anisotropy	Pore Linear Density	Cortex Fractal Dimension	Pore Fractal Dimension
Bone					Large (FN>Rib)	Large (FN>Rib)
Pore Type		Large (Ct>Tb)	Large		Large (Ct>Tb)	Large (CT>Tb)
Age				Large		
Cortical Thickness		Medium Ct Decrease Tb Increase		Large		
Sex				Large		
Bone: Type			Large Rib Only: Ct>FN	Large		
age:cs.th				Large		
age:sex				Large		
cs.th:sex				Large		
age:cs.th: sex				Large		
Marginal R^2	0.000 414%	68.60%	77.11%	6.75% (Poor)	89.8%	59.10%

275

Table 7.61 Significant Interactions in Pore Connectivity Density by Bone Type, Pore Type, and Sex
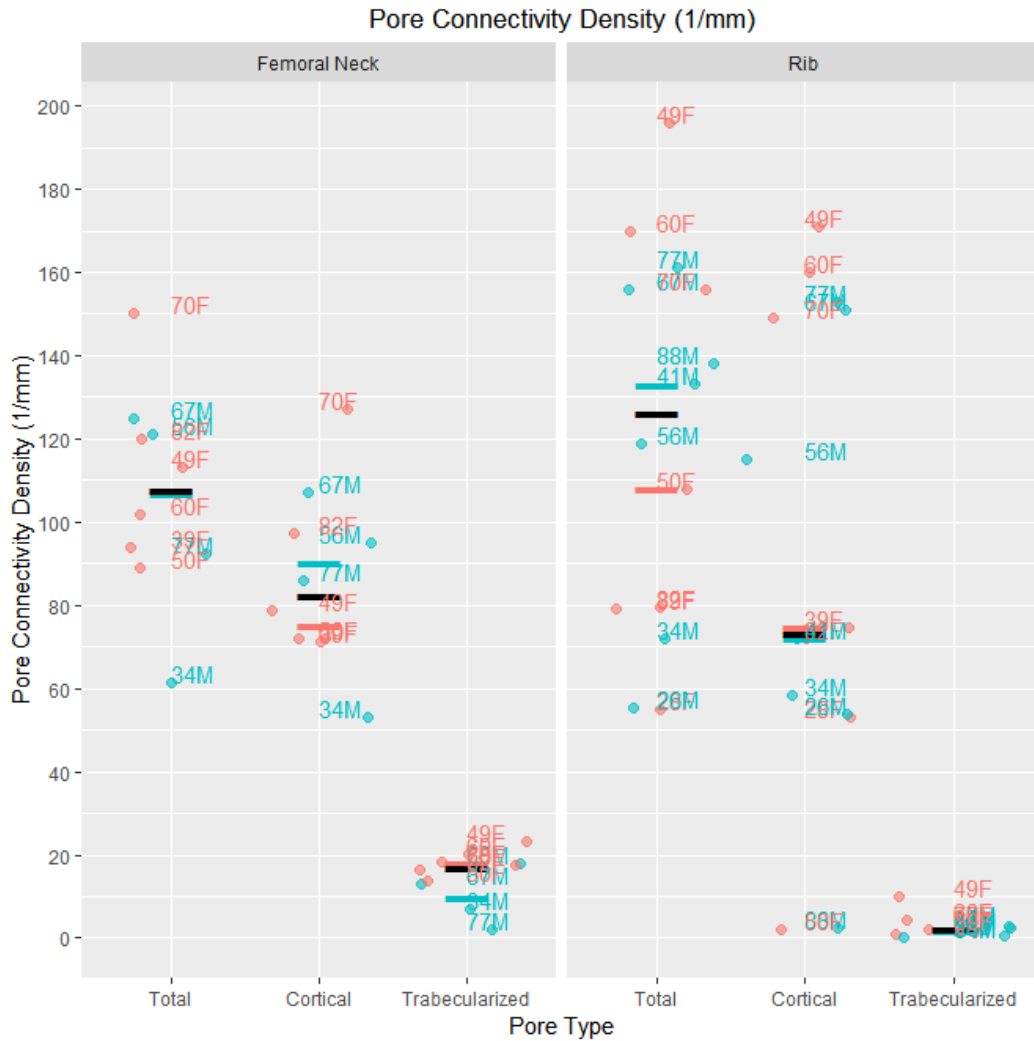
Bars indicate pooled (black), female (red), and male (blue) medians

Significant Differences:

- Cortical pores more densely connected than trabecularized pores

Table 7.62 Significant Interactions in Proportion of Open Pores and Cross-Sectional Thickness by Sex

Significant Differences:

- Cortical pores are more densely connected in thinner cortices

- Trabecularized pores are more densely connected in thicker cortices

277

Table 7.63 Significant Interactions in Degree of Anisotropy by Bone Type, Pore Type, and Sex
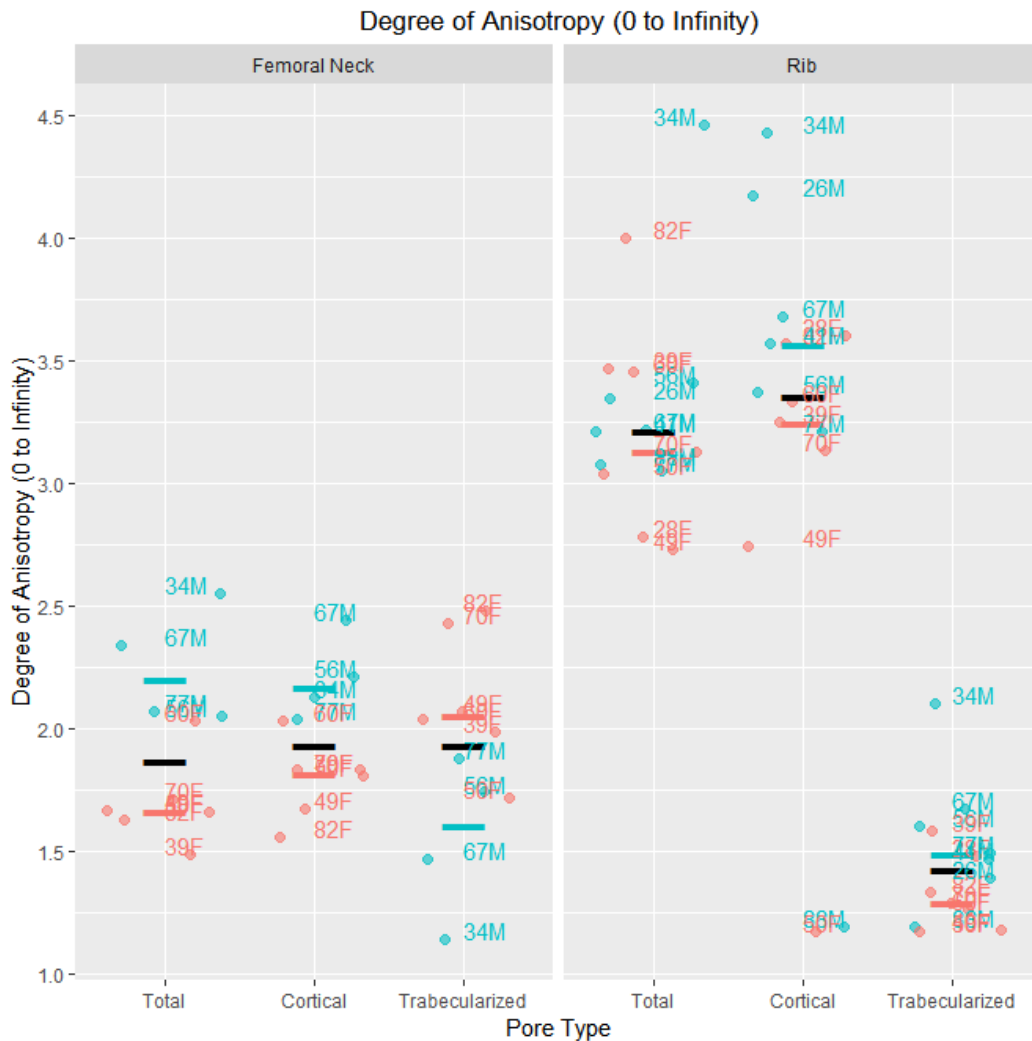
Bars indicate pooled (black), female (red), and male (blue) medians

Significant Differences:

In the rib, cortical pores are significantly more anisotropic (directionally aligned) than trabecularized pores. Femoral neck cortical and trabecularized pores are about equally anisotropic on average.

278

Figure 7.18 Significant Interactions in Cortical Fractal Dimension by Bone Type, Pore Type, and Sex
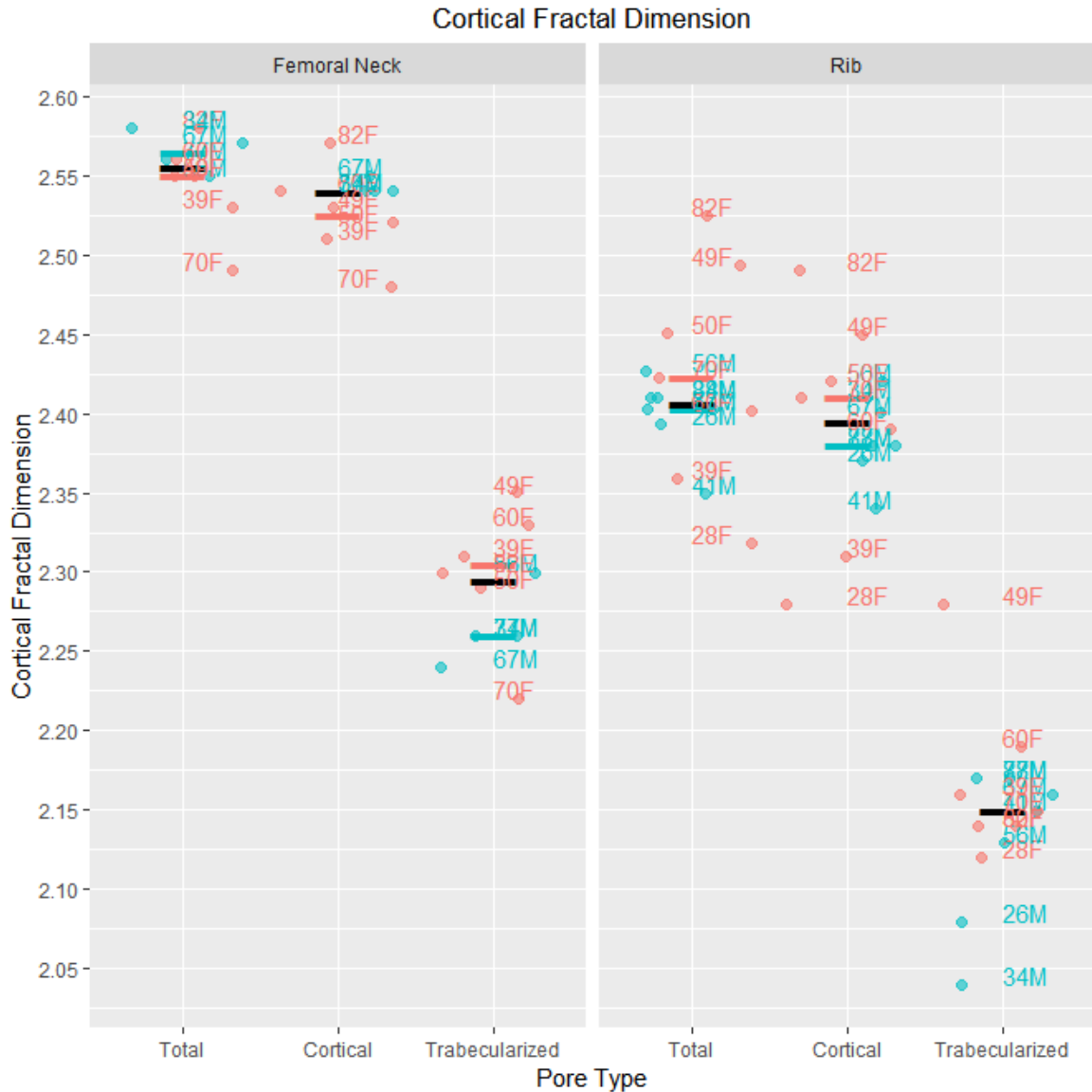
Bars indicate pooled (black), female (red), and male (blue) medians

Significant Differences:

- Femoral neck cortex more complex than the rib

- Cortical porosity has a greater effect on cortical complexity than trabecularized porosity

279

Figure 7.19 Significant Interactions in Cortical Fractal Dimension by Bone Type, Pore Type, and Sex
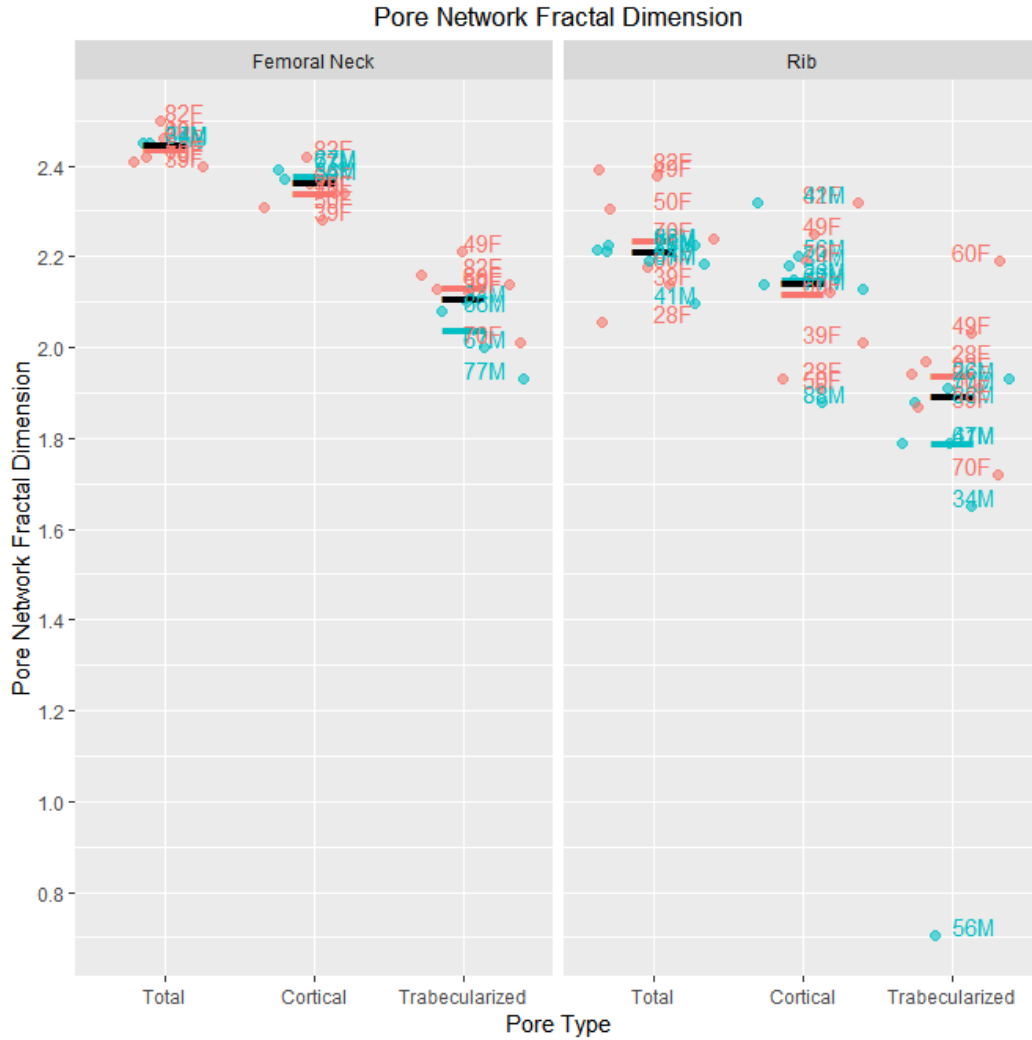
Bars indicate pooled (black), female (red), and male (blue) medians

Significant Differences:
- Femoral neck pore network more complex than rib pore network

- Cortical pore network more complex than trabecularized pore network

280

7.5. Univariate Testing of Regional Distribution in Pore Morphometry in the Femoral Neck

Table 7.64 Cortical Fractal Dimension LMM

	numDF	denDF	F.value	p.value	t	df	d
(Intercept)	1	56	25116.03	0			
age	1	56	0.803209	0.373972	-0.65386	56	-0.17475
cs.th	1	56	0.438511	0.510558	-0.70928	56	-0.18956
sex	1	56	0.246256	0.621666	-0.24595	56	-0.06573
age:cs.th	1	56	0.617983	0.435112	0.663338	56	0.177285
age:sex	1	56	0.045853	0.831221	0.300639	56	0.080349
cs.th:sex	1	56	0.898548	0.347244	0.180838	56	0.048331
age:cs.th:sex	1	56	0.076973	0.782464	-0.27744	56	-0.07415
Octant 1	7	56	3.830889	*0.001814*	-1.03491	56	-0.27659
Octant 2					3.797977	56	1.015052
Octant 3					2.168913	56	0.579666
Octant 4					1.082871	56	0.289409
Octant 5					-0.92631	56	-0.24757
Octant 6					-1.95805	56	-0.52331
Octant 7					-1.30642	56	-0.34916
Marginal R2	0.261242						
Conditional R2	0.509682						
Shapiro-Wilk Normality	0.145739						

Significant values ($p < 0.05$) are ***bolded***

Table 7.65 Cortical Fractal Dimension Post-Hoc

	Lhs	rhs	estimate	std.error	statistic	p.value
1	inferior – anterior	0	0.282962	0.151862	1.863292	1
2	inferioranterior – anterior	0	-0.03843	0.174911	-0.21972	1
3	inferiorposterior – anterior	0	-0.07691	0.178506	-0.43085	1
4	posterior – anterior	0	-0.39884	0.217642	-1.83254	1
5	superior – anterior	0	-0.16584	0.187626	-0.88388	1
6	superioranterior – anterior	0	-0.0162	0.172925	-0.09366	1
7	superiorposterior – anterior	0	0.157212	0.16295	0.964787	1
8	inferioranterior – inferior	0	-0.32139	0.155682	-2.06443	0.935454
9	inferiorposterior – inferior	0	-0.35987	0.15971	-2.25329	0.606028
10	posterior – inferior	0	-0.6818	0.202512	-3.36672	*0.021299*
11	superior – inferior	0	-0.4488	0.169842	-2.64246	0.222228
12	superioranterior – inferior	0	-0.29916	0.153447	-1.94958	1
13	superiorposterior – inferior	0	-0.12575	0.142111	-0.88487	1
14	inferiorposterior - inferioranterior	0	-0.03848	0.181767	-0.21169	1
15	posterior – inferioranterior	0	-0.36041	0.220325	-1.63579	1
16	superior – inferioranterior	0	-0.12741	0.190731	-0.66799	1
17	superioranterior - inferioranterior	0	0.022237	0.17629	0.126136	1
18	superiorposterior - inferioranterior	0	0.195644	0.166516	1.174924	1
19	posterior – inferiorposterior	0	-0.32193	0.223189	-1.4424	1
20	superior – inferiorposterior	0	-0.08893	0.194033	-0.45832	1
21	superioranterior - inferiorposterior	0	0.060714	0.179857	0.337569	1
22	superiorposterior - inferiorposterior	0	0.234121	0.170288	1.374856	1
23	superior – posterior	0	0.232999	0.230548	1.010629	1
24	superioranterior – posterior	0	0.382642	0.218751	1.749209	1
25	superiorposterior – posterior	0	0.556049	0.210954	2.635875	0.222228
26	superioranterior – superior	0	0.149643	0.188912	0.792134	1
27	superiorposterior – superior	0	0.32305	0.179825	1.796469	1
28	superiorposterior - superioranterior	0	0.173407	0.164429	1.054606	1

Significant values (p < 0.05) are ***bolded***

Table 7.66 Radar Plot of Cortical Fractal Dimension Distribution

Table 7.67 Medians of Cortical Fractal Dimension Distribution by Octant

Cortical Fractal Dimension
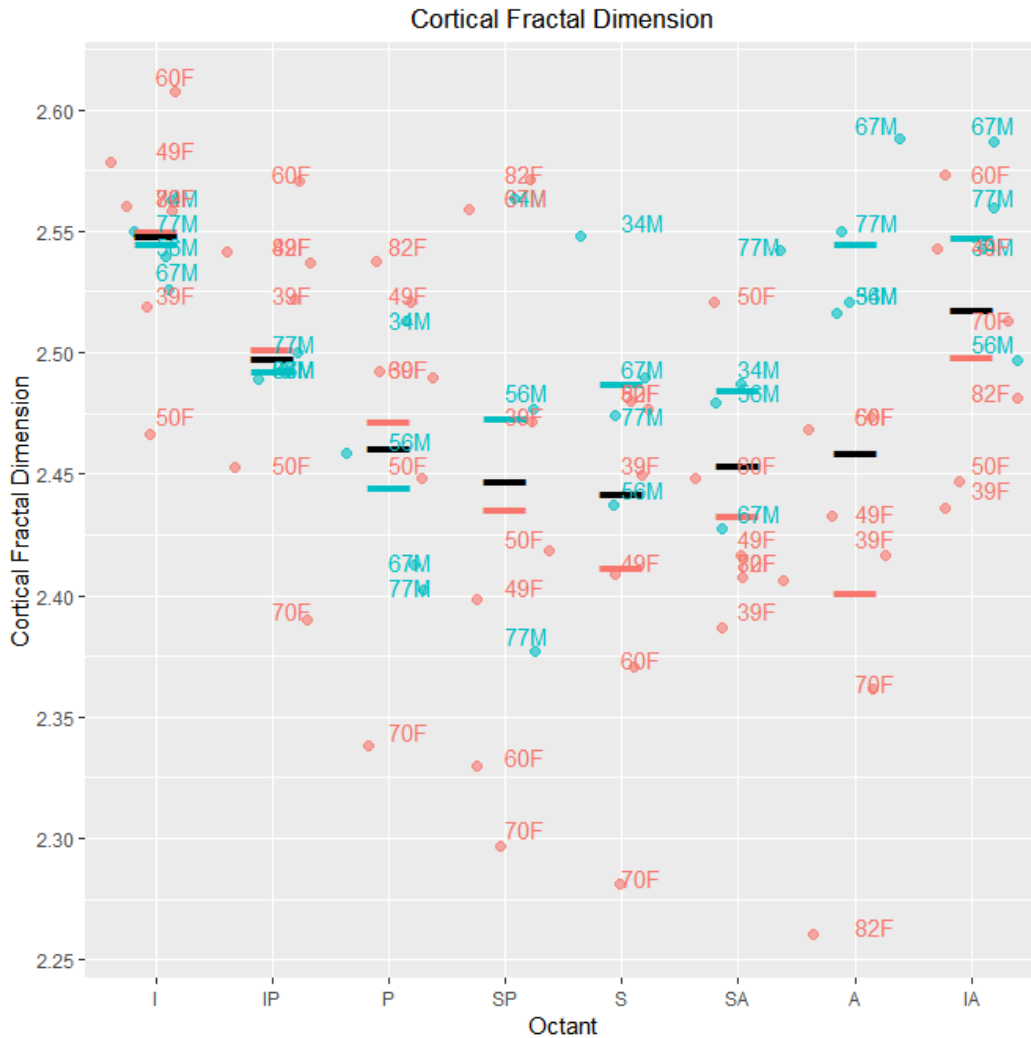
Significant Effect: Note that boxplots in this subsection approximate an inferior
– superior- inferior arc to align the graph with loading environment. Cortical
organizational complexity increases in a superior to inferior gradient, but only
reaches significant differences between posterior and inferior octants. Older
females with extensive osteophyte apposition (70F, 82F) have the lowest cortical
organizational complexity, likely due to these large empty regions.

284

Table 7.68 Percent Closed Porosity LMM

	numDF	denDF	F.value	p.value	t	df	d
(Intercept)	1	56	164.009	0			
age	1	56	0.08915	0.766365	1.490368	56	0.398318
cs.th	1	56	4.570641	*0.036903*	1.745014	56	0.466375
sex	1	56	1.755988	0.190507	1.467882	56	0.392308
age:cs.th	1	56	3.309305	0.074236	-1.52144	56	-0.40662
age:sex	1	56	0.829456	0.366333	-1.56877	56	-0.41927
cs.th:sex	1	56	2.846276	0.097149	-1.33101	56	-0.35573
age:cs.th:sex	1	56	2.264944	0.137951	1.504973	56	0.402221
Octant 1	7	56	2.009272	0.069934	0.029023	56	0.007757
Octant 2					2.771042	56	0.740592
Octant 3					-0.21841	56	-0.05837
Octant 4					-0.43373	56	-0.11592
Octant 5					-2.51909	56	-0.67326
Octant 6					-0.99284	56	-0.26535
Octant 7					0.132518	56	0.035417
Marginal R2	0.355785						
Conditional R2	0.455753						
Shapiro-Wilk Normality	*0.001886*						

Significant values (p < 0.05) are ***bolded***

Table 7.69 Percent Closed Porosity: PQL Corrected

	Value	Std.Error	DF	t.value	p.value	cohen t	cohen df	cohen d
(Intercept)	-15.8033	6.072536	56	-2.60242	0.011824			
octant1	0.033861	0.12694	56	0.266751	0.790641	0.266751	56	0.071292
octant2	0.314656	0.101555	56	3.098378	*0.003041*	3.098378	56	0.828076
octant3	-0.00674	0.13136	56	-0.05132	0.959253	-0.05132	56	-0.01372
octant4	-0.04516	0.135737	56	-0.33273	0.740581	-0.33273	56	-0.08893
octant5	-0.36705	0.180858	56	-2.02947	*0.047173*	-2.02947	56	-0.5424
octant6	-0.13409	0.146634	56	-0.91444	0.364407	-0.91444	56	-0.24439
octant7	0.01557	0.128906	56	0.120786	0.904293	0.120786	56	0.032281
age	0.241083	0.123264	56	1.955828	0.055481	1.955828	56	0.522717
cs.th	0.008178	0.003655	56	2.237292	0.029265	2.237292	56	0.597942
sex1	13.41391	6.068007	56	2.210596	*0.031166*	2.210596	56	0.590807
age:cs.th	-0.00016	8.02E-05	56	-1.98854	0.051647	-1.98854	56	-0.53146
age:sex1	-0.28574	0.123233	56	-2.31872	*0.024085*	-2.31872	56	-0.6197
cs.th:sex1	-0.0076	0.003652	56	-2.0801	0.042105	-2.0801	56	-0.55593
age:cs.th:sex1	0.00018	8.02E-05	56	2.249293	*0.028444*	2.249293	56	0.601149
R2	0.596939							

Significant values (p < 0.05) are ***bolded***

Table 7.70 Percent Closed Porosity Post-Hoc

	Lhs	rhs	estimate	std.error	statistic	p.value
1	inferior – anterior	0	0.282962	0.151862	1.863292	1
2	inferioranterior – anterior	0	-0.03843	0.174911	-0.21972	1
3	inferiorposterior – anterior	0	-0.07691	0.178506	-0.43085	1
4	posterior – anterior	0	-0.39884	0.217642	-1.83254	1
5	superior – anterior	0	-0.16584	0.187626	-0.88388	1
6	superioranterior – anterior	0	-0.0162	0.172925	-0.09366	1
7	superiorposterior – anterior	0	0.157212	0.16295	0.964787	1
8	inferioranterior – inferior	0	-0.32139	0.155682	-2.06443	0.935454
9	inferiorposterior – inferior	0	-0.35987	0.15971	-2.25329	0.606028
10	posterior – inferior	0	-0.6818	0.202512	-3.36672	*0.021299*
11	superior – inferior	0	-0.4488	0.169842	-2.64246	0.222228
12	superioranterior – inferior	0	-0.29916	0.153447	-1.94958	1
13	superiorposterior – inferior	0	-0.12575	0.142111	-0.88487	1
14	inferiorposterior - inferioranterior	0	-0.03848	0.181767	-0.21169	1
15	posterior – inferioranterior	0	-0.36041	0.220325	-1.63579	1
16	superior – inferioranterior	0	-0.12741	0.190731	-0.66799	1
17	superioranterior - inferioranterior	0	0.022237	0.17629	0.126136	1
18	superiorposterior - inferioranterior	0	0.195644	0.166516	1.174924	1
19	posterior – inferiorposterior	0	-0.32193	0.223189	-1.4424	1
20	superior – inferiorposterior	0	-0.08893	0.194033	-0.45832	1
21	superioranterior - inferiorposterior	0	0.060714	0.179857	0.337569	1
22	superiorposterior - inferiorposterior	0	0.234121	0.170288	1.374856	1
23	superior – posterior	0	0.232999	0.230548	1.010629	1
24	superioranterior – posterior	0	0.382642	0.218751	1.749209	1
25	superiorposterior – posterior	0	0.556049	0.210954	2.635875	0.222228
26	superioranterior – superior	0	0.149643	0.188912	0.792134	1
27	superiorposterior – superior	0	0.32305	0.179825	1.796469	1
28	superiorposterior - superioranterior	0	0.173407	0.164429	1.054606	1

Significant values (p < 0.05) are ***bolded***

Figure 7.20 Radar Plot of Percent Closed Porosity Distribution

Figure 7.21 Medians of Cortical Fractal Dimension Distribution by Octant
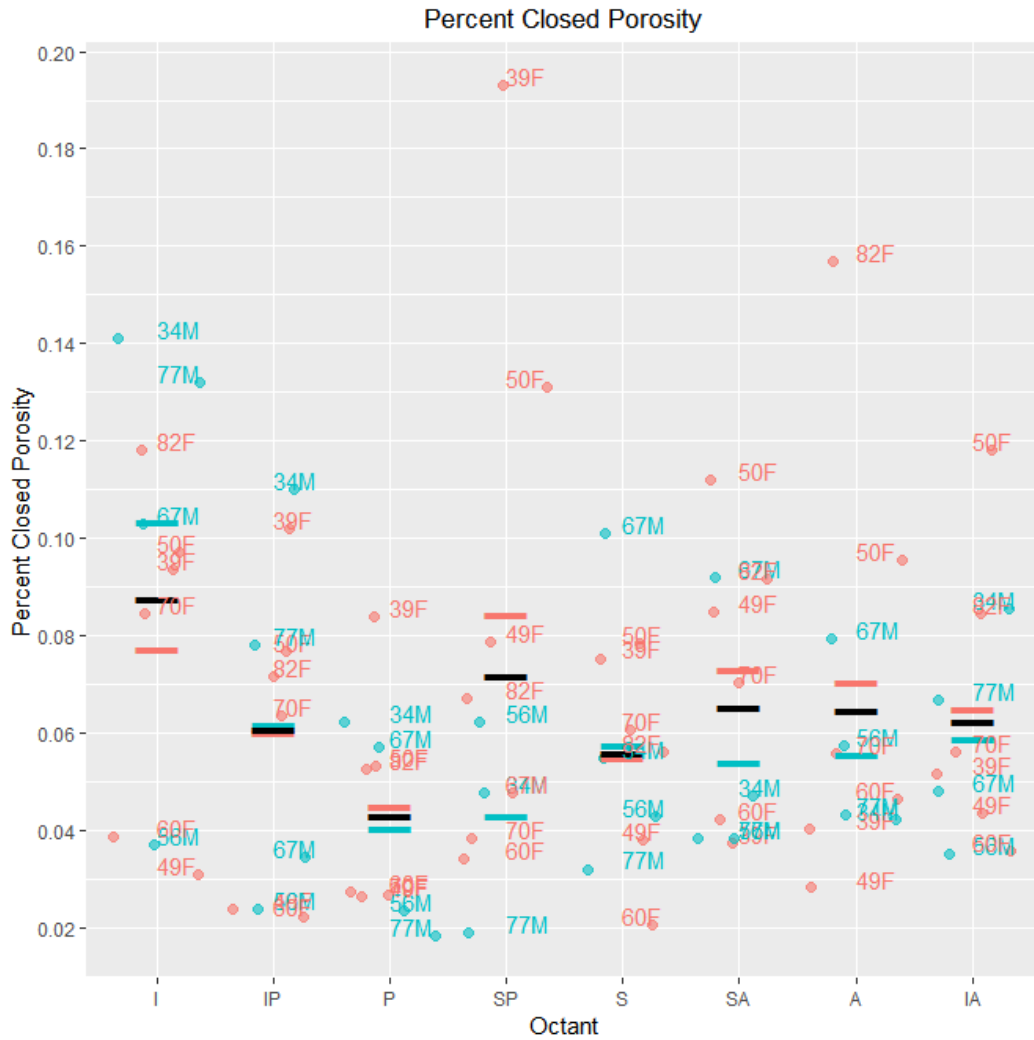
Significant Effects: Closed porosity increases suddenly in inferior regions, reaching significance between posterior and higher inferior percentages of closed porosity.

289

Table 7.71 Percent Open Porosity

	numDF	denDF	F.value	p.value	t	df	d
(Intercept)	1	56	596.9422	0			
age	1	56	5.69933	*0.020372*	-1.37193	56	-0.36666
cs.th	1	56	0.060243	0.807009	-1.58692	56	-0.42412
sex	1	56	14.02876	*0.000427*	-0.98149	56	-0.26231
age:cs.th	1	56	0.052132	0.820225	1.485849	56	0.39711
age:sex	1	56	4.348803	*0.041605*	1.109482	56	0.296522
cs.th:sex	1	56	3.110348	0.083251	0.81881	56	0.218836
age:cs.th:sex	1	56	0.989205	0.324215	-0.99459	56	-0.26581
Octant 1	7	56	5.496395	*7.62E-05*	1.042714	56	0.278677
Octant 2					-2.74748	56	-0.73429
Octant 3					-2.02346	56	-0.54079
Octant 4					-3.05054	56	-0.81529
Octant 5					0.000307	56	8.20E-05
Octant 6					0.68454	56	0.182951
Octant 7					3.71296	56	0.99233
Marginal R2	0.458026						
Conditional R2	0.458027						
Shapiro-Wilk Normality	*0.016615*						

Significant values ($p < 0.05$) are **bolded**

Table 7.72 Percent Open Porosity: PQL Correction

	Value	Std.Error	DF	t.value	p.value	cohen t	cohen df	cohen d
(Intercept)	12.75045	5.9087	56	2.157911	0.035238			
octant1	0.294111	0.075399	56	3.900739	*0.000259*	3.900739	56	1.042516
octant2	-0.37025	0.131851	56	-2.80814	*0.006847*	-2.80814	56	-0.75051
octant3	-0.23315	0.116482	56	-2.00157	0.050185	-2.00157	56	-0.53494
octant4	-0.38422	0.13355	56	-2.87698	*0.005672*	-2.87698	56	-0.76891
octant5	0.0289	0.092916	56	0.311032	0.756931	0.311032	56	0.083127
octant6	0.055311	0.090911	56	0.608416	0.545372	0.608416	56	0.162606
octant7	0.389906	0.070357	56	5.541821	*8.35E-07*	5.541821	56	1.481114
age	-0.2051	0.122652	56	-1.67224	0.100056	-1.67224	56	-0.44692
cs.th	-0.00687	0.00359	56	-1.91217	0.060975	-1.91217	56	-0.51105
sex1	-7.5929	5.902854	56	-1.28631	0.203627	-1.28631	56	-0.34378
age:cs.th	0.000143	8.02E-05	56	1.777353	0.080941	1.777353	56	0.475018
age:sex1	0.176701	0.122579	56	1.44153	0.155004	1.44153	56	0.385265
cs.th:sex1	0.004052	0.003586	56	1.129855	0.263354	1.129855	56	0.301966
age:cs.th:sex1	-0.00011	8.02E-05	56	-1.34363	0.184488	-1.34363	56	-0.3591
R2	0.772303							

Significant values (p < 0.05) are ***bolded***

Table 7.73 Percent Open Porosity Post-Hoc

	Lhs	rhs	estimate	std.error	statistic	p.value
1	inferior – anterior	0	-0.66436	0.147669	-4.49902	*0.000164*
2	inferioranterior - anterior	0	-0.52726	0.132935	-3.9663	*0.001606*
3	inferiorposterior - anterior	0	-0.67833	0.149314	-4.54299	*0.000139*
4	posterior – anterior	0	-0.26521	0.11102	-2.38885	0.219718
5	superior – anterior	0	-0.2388	0.109207	-2.18666	0.34521
6	superioranterior - anterior	0	0.095795	0.091298	1.049257	1
7	superiorposterior - anterior	0	-0.07472	0.097457	-0.76666	1
8	inferioranterior - inferior	0	0.137106	0.174202	0.787055	1
9	inferiorposterior - inferior	0	-0.01397	0.187	-0.07468	1
10	posterior – inferior	0	0.399154	0.158114	2.524467	0.162224
11	superior – inferior	0	0.425566	0.156846	2.713264	0.106599
12	superioranterior - inferior	0	0.76016	0.144948	5.244363	*4.23E-06*
13	superiorposterior - inferior	0	0.589649	0.148904	3.959927	*0.001606*
14	inferiorposterior - inferioranterior	0	-0.15107	0.175598	-0.86033	1
15	posterior - inferioranterior	0	0.262048	0.14445	1.814113	0.675655
16	superior - inferioranterior	0	0.288459	0.143061	2.016343	0.481406
17	superioranterior - inferioranterior	0	0.623054	0.129906	4.796198	*4.2E-05*
18	superiorposterior - inferioranterior	0	0.452542	0.134305	3.369502	*0.015061*
19	posterior - inferiorposterior	0	0.41312	0.159652	2.587631	0.144958
20	superior - inferiorposterior	0	0.439531	0.158396	2.774885	0.093876
21	superioranterior - inferiorposterior	0	0.774126	0.146624	5.279678	*3.62E-06*
22	superiorposterior - inferiorposterior	0	0.603614	0.150536	4.00978	*0.001398*
23	superior – posterior	0	0.026412	0.122965	0.214791	1
24	superioranterior - posterior	0	0.361006	0.107375	3.362098	*0.015061*
25	superiorposterior - posterior	0	0.190495	0.112658	1.690907	0.726836
26	superioranterior - superior	0	0.334594	0.1055	3.171525	*0.027295*
27	superiorposterior - superior	0	0.164083	0.110872	1.479932	0.972239
28	superiorposterior - superioranterior	0	-0.17051	0.093283	-1.82789	0.675655

Significant values (p < 0.05) are ***bolded***

292

Figure 7.22 Radar Plot of Percent Open Porosity

Figure 7.23 Medians of Percent Open Porosity Distribution by Octant
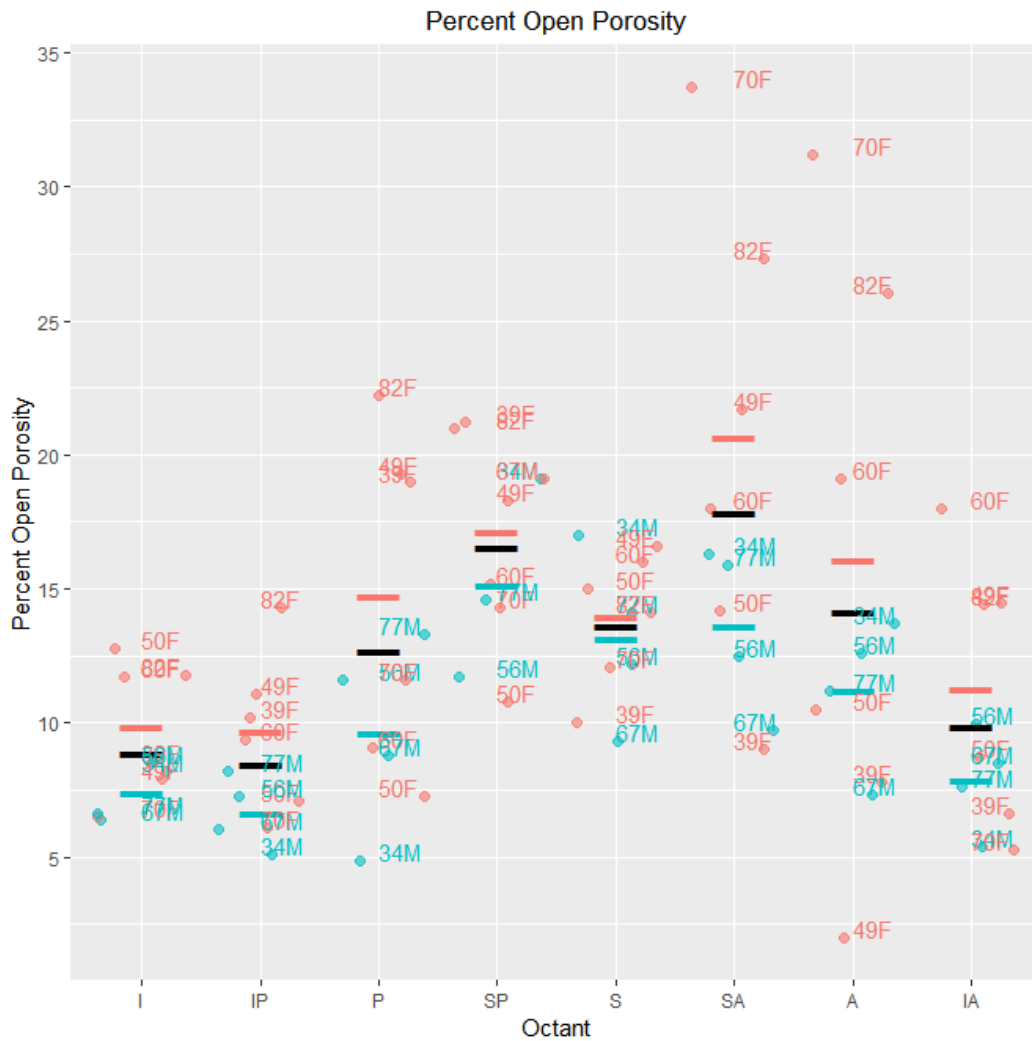
Significant Differences: Open porosity is higher in superior regions and decreases towards inferior regions. Older females with large osteophyte appositions (70F, 82F) have concentrations in superior-anterior and anterior regions.

Table 7.74 Percent Porosity LMM

	numDF	denDF	F.value	p.value	t	df	d
(Intercept)	1	56	728.2182	0			
age	1	56	5.261948	*0.02557*	-1.55842	56	-0.4165
cs.th	1	56	0.049401	0.824918	-1.85659	56	-0.49619
sex	1	56	18.10409	*8.03E-05*	-0.9682	56	-0.25876
age:cs.th	1	56	0.021401	0.884216	1.69232	56	0.452291
age:sex	1	56	5.2321	*0.025973*	1.147498	56	0.306682
cs.th:sex	1	56	6.239214	*0.015459*	0.766149	56	0.204762
age:cs.th:sex	1	56	1.026658	0.315303	-1.01324	56	-0.2708
Octant 1	7	56	7.038049	*5.08E-06*	2.350046	56	0.628076
Octant 2					-3.12652	56	-0.8356
Octant 3					-2.35353	56	-0.62901
Octant 4					-3.46886	56	-0.92709
Octant 5					-0.18073	56	-0.0483
Octant 6					0.560215	56	0.149724
Octant 7					3.866321	56	1.033318
Marginal R2	0.518883						
Conditional R2	0.518883						
Shapiro-Wilk Normality	0.021887						

Significant values (p < 0.05) are ***bolded***

Table 7.75 Percent Porosity: PQL Correction

	Value	Std.Error	DF	t.value	p.value	cohen t	cohen df	cohen d
(Intercept)	12.61345	5.861003	56	2.152097	0.035715			
octant1	0.291593	0.075186	56	3.878295	***0.000279***	3.878295	56	1.036518
octant2	-0.3669	0.130845	56	-2.80406	***0.006923***	-2.80406	56	-0.74942
octant3	-0.23229	0.115859	56	-2.00492	***0.049815***	-2.00492	56	-0.53584
octant4	-0.38349	0.13285	56	-2.88665	***0.005522***	-2.88665	56	-0.77149
octant5	0.027358	0.092604	56	0.295433	0.768755	0.295433	56	0.078958
octant6	0.053635	0.090614	56	0.591904	0.556297	0.591904	56	0.158193
octant7	0.389605	0.070041	56	5.562566	7.73E-07	5.562566	56	1.486658
age	-0.20238	0.121651	56	-1.66364	0.101772	-1.66364	56	-0.44463
cs.th	-0.00677	0.003561	56	-1.90195	0.062325	-1.90195	56	-0.50832
sex1	-7.48504	5.855161	56	-1.27837	0.206394	-1.27837	56	-0.34166
age:cs.th	0.000141	7.96E-05	56	1.768978	0.082343	1.768978	56	0.472779
age:sex1	0.174264	0.121578	56	1.433346	0.157319	1.433346	56	0.383078
cs.th:sex1	0.003995	0.003557	56	1.123138	0.266171	1.123138	56	0.300171
age:cs.th:sex1	-0.00011	7.95E-05	56	-1.33606	0.186933	-1.33606	56	-0.35708
R2	0.772201							

Significant values (p < 0.05) are ***bolded***

Table 7.76 Percent Porosity Post-Hoc

	Lhs	rhs	estimate	std.error	statistic	p.value
1	inferior – anterior	0	-0.65849	0.146689	-4.489	**0.000172**
2	inferioranterior – anterior	0	-0.52388	0.132335	-3.95873	**0.001582**
3	inferiorposterior – anterior	0	-0.67509	0.14863	-4.54207	**0.000139**
4	posterior – anterior	0	-0.26423	0.110729	-2.38632	0.221235
5	superior – anterior	0	-0.23796	0.108931	-2.18448	0.347123
6	superioranterior – anterior	0	0.098012	0.091023	1.076784	1
7	superiorposterior – anterior	0	-0.07111	0.0971	-0.73231	1
8	inferioranterior – inferior	0	0.134609	0.173019	0.777998	1
9	inferiorposterior – inferior	0	-0.0166	0.185779	-0.08933	1
10	posterior – inferior	0	0.394255	0.157111	2.509399	0.169312
11	superior – inferior	0	0.420531	0.155849	2.698321	0.111505
12	superioranterior – inferior	0	0.756501	0.143904	5.256997	3.95E-06
13	superiorposterior – inferior	0	0.587382	0.147822	3.973572	**0.001558**
14	inferiorposterior - inferioranterior	0	-0.15121	0.174667	-0.86567	1
15	posterior – inferioranterior	0	0.259646	0.143801	1.805589	0.685059
16	superior – inferioranterior	0	0.285923	0.142421	2.007581	0.491566
17	superioranterior - inferioranterior	0	0.621893	0.129241	4.811896	**3.89E-05**
18	superiorposterior - inferioranterior	0	0.452773	0.13359	3.389278	**0.014015**
19	posterior – inferiorposterior	0	0.410851	0.158924	2.585202	0.145983
20	superior – inferiorposterior	0	0.437128	0.157677	2.772303	0.094624
21	superioranterior - inferiorposterior	0	0.773098	0.145881	5.299514	**3.25E-06**
22	superiorposterior - inferiorposterior	0	0.603978	0.149748	4.033309	**0.001265**
23	superior – posterior	0	0.026277	0.122606	0.214318	1
24	superioranterior – posterior	0	0.362247	0.107011	3.385128	**0.014015**
25	superiorposterior – posterior	0	0.193127	0.112225	1.72089	0.685059
26	superioranterior – superior	0	0.33597	0.10515	3.195159	**0.025156**
27	superiorposterior – superior	0	0.166851	0.110452	1.510622	0.916194
28	superiorposterior - superioranterior	0	-0.16912	0.092838	-1.82166	0.685059

Significant values (p < 0.05) are **bolded**

297

Figure 7.24 Radar Plot of Percent Porosity

Figure 7.25 Medians of Percent Porosity Distribution By Octant
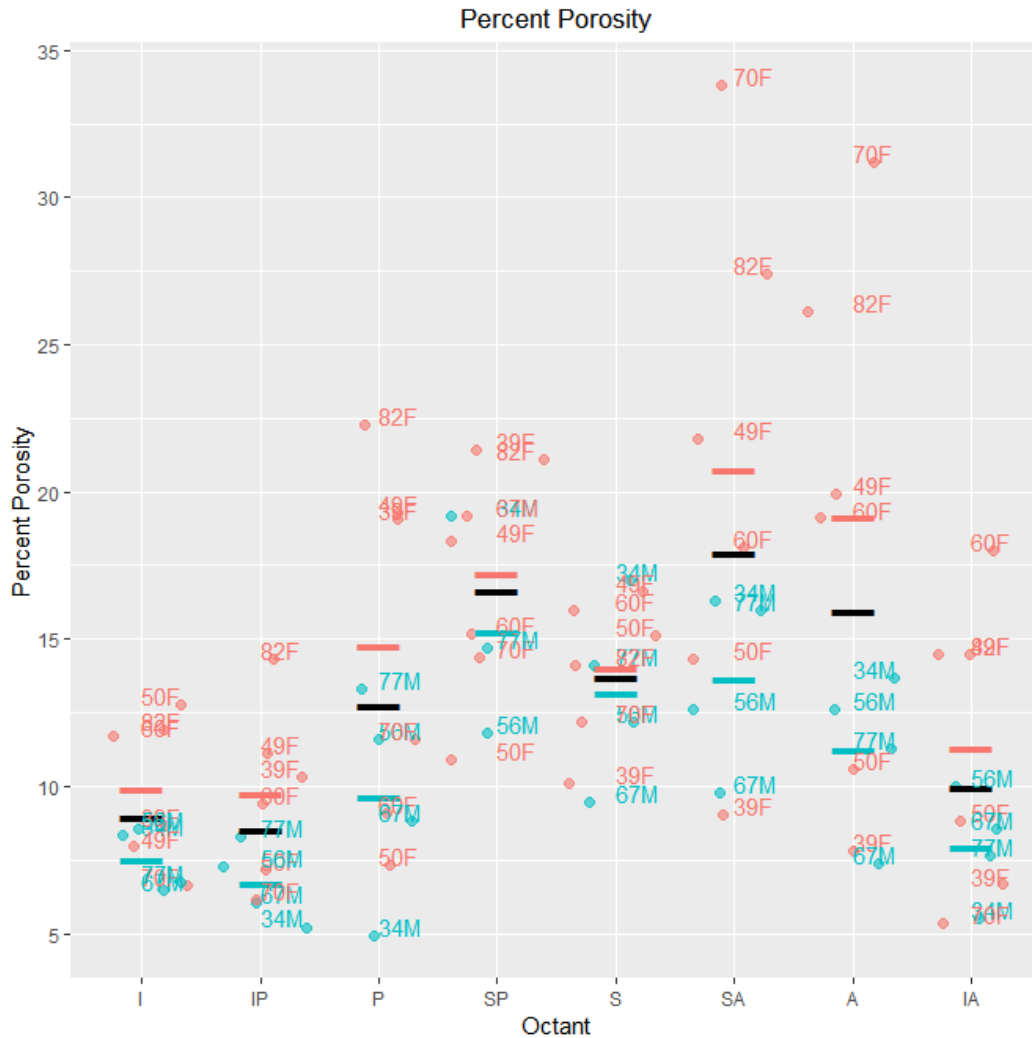
Significant Differences: This graph displays the same smooth superior-to-inferior decrease in percent porosity as seen in percent open porosity. The two oldest females also have high superior-anterior and anterior concentrations of percent porosity due to their osteophyte apposition.

Table 7.77 Pore Thickness LMM

	numDF	denDF	F.value	p.value	t	df	d
(Intercept)	1	56	206.2618	0			
age	1	56	3.568923	0.064052	-0.47513	56	-0.12698
cs.th	1	56	5.369739	*0.02417*	-0.37299	56	-0.09969
sex	1	56	9.611388	*0.003025*	-0.57394	56	-0.15339
age:cs.th	1	56	3.35E-05	0.995402	0.521079	56	0.139264
age:sex	1	56	1.055593	0.30864	0.562674	56	0.150381
cs.th:sex	1	56	0.16399	0.687052	0.561166	56	0.149978
age:cs.th:sex	1	56	0.274849	0.602166	-0.52426	56	-0.14011
Octant 1	7	56	1.580142	0.160369	1.737318	56	0.464318
Octant 2					0.342926	56	0.091651
Octant 3					-0.19896	56	-0.05318
Octant 4					-0.43513	56	-0.11629
Octant 5					-0.53582	56	-0.1432
Octant 6					-1.15216	56	-0.30793
Octant 7					2.115739	56	0.565455
Marginal R2	0.300646						
Conditional R2	0.316153						
Shapiro-Wilk Normality	*1.91E-08*						

Significant values (p < 0.05) are ***bolded***

300

Table 7.78 Pore Thickness: PQL Corrected

	Value	Std.Error	DF	t.value	p.value	cohen t	cohen df	cohen d
(Intercept)	7.5873	9.745405	56	0.778552	0.439521			
octant1	0.338466	0.120915	56	2.799218	*0.007014*	2.799218	56	0.748123
octant2	0.029085	0.154092	56	0.188752	0.850969	0.188752	56	0.050446
octant3	-0.08776	0.170146	56	-0.51576	0.60805	-0.51576	56	-0.13784
octant4	-0.06636	0.167042	56	-0.39725	0.692692	-0.39725	56	-0.10617
octant5	-0.08525	0.169777	56	-0.5021	0.617567	-0.5021	56	-0.13419
octant6	-0.2692	0.199695	56	-1.34807	0.183065	-1.34807	56	-0.36029
octant7	0.502246	0.107913	56	4.654179	*2.04E-05*	4.654179	56	1.243882
age	-0.07499	0.200979	56	-0.37314	0.710454	-0.37314	56	-0.09973
cs.th	-0.00159	0.005898	56	-0.26971	0.788376	-0.26971	56	-0.07208
sex1	-7.08484	9.743733	56	-0.72712	0.470183	-0.72712	56	-0.19433
age:cs.th	5.48E-05	0.000131	56	0.41744	0.677953	0.41744	56	0.111565
age:sex1	0.144907	0.200947	56	0.721123	0.473834	0.721123	56	0.192728
cs.th:sex1	0.004362	0.005896	56	0.739757	0.462537	0.739757	56	0.197708
age:cs.th:sex1	-9.18E-05	0.000131	56	-0.70001	0.486817	-0.70001	56	-0.18709
R2	0.591302							

Significant values (p < 0.05) are ***bolded***

Table 7.79 Pore Thickness: Post-Hoc

	Lhs	rhs	estimate	std.error	statistic	p.value
1	inferior – anterior	0	-0.30938	0.181549	-1.70412	1
2	inferioranterior - anterior	0	-0.42622	0.196467	-2.16943	0.601004
3	inferiorposterior - anterior	0	-0.40482	0.19356	-2.09147	0.656754
4	posterior – anterior	0	-0.42371	0.196121	-2.16046	0.601004
5	superior – anterior	0	-0.60767	0.224585	-2.70574	0.143119
6	superioranterior - anterior	0	0.16378	0.1409	1.162388	1
7	superiorposterior - anterior	0	-0.6997	0.240595	-2.90823	0.083602
8	inferioranterior - inferior	0	-0.11684	0.22019	-0.53063	1
9	inferiorposterior - inferior	0	-0.09544	0.2176	-0.43862	1
10	posterior – inferior	0	-0.11433	0.219881	-0.51996	1
11	superior – inferior	0	-0.29829	0.245606	-1.21449	1
12	superioranterior - inferior	0	0.473161	0.172444	2.743849	0.133592
13	superiorposterior - inferior	0	-0.39032	0.260327	-1.49936	1
14	inferiorposterior - inferioranterior	0	0.021398	0.230194	0.092955	1
15	posterior - inferioranterior	0	0.00251	0.232351	0.010804	1
16	superior - inferioranterior	0	-0.18145	0.25683	-0.70648	1
17	superioranterior - inferioranterior	0	0.590002	0.188086	3.136872	*0.044398*
18	superiorposterior - inferioranterior	0	-0.27348	0.270942	-1.00938	1
19	posterior - inferiorposterior	0	-0.01889	0.229898	-0.08216	1
20	superior - inferiorposterior	0	-0.20284	0.254613	-0.79667	1
21	superioranterior - inferiorposterior	0	0.568604	0.185047	3.072755	0.050902
22	superiorposterior - inferiorposterior	0	-0.29488	0.268841	-1.09686	1
23	superior – posterior	0	-0.18396	0.256566	-0.717	1
24	superioranterior - posterior	0	0.587491	0.187725	3.12954	*0.044398*
25	superiorposterior - posterior	0	-0.27599	0.270691	-1.01959	1
26	superioranterior - superior	0	0.771448	0.217291	3.550306	*0.010389*
27	superiorposterior - superior	0	-0.09204	0.291973	-0.31522	1
28	superiorposterior - superioranterior	0	-0.86348	0.233801	-3.69325	*0.006199*

Significant values (p < 0.05) are ***bolded***

302

Figure 7.26 Radar Plot of Pore Thickness

Figure 7.27 Medians of Pore Thickness Distribution by Octant

Significant Differences: Extreme superior-anterior osteophyte apposition by two elderly females, but fairly consistent throughout other octants

Table 7.80 Pore Separation LMM

	numDF	denDF	F.value	p.value	t	df	d
(Intercept)	1	56	135.1543	1.11E-16			
age	1	56	28.17235	*1.97E-06*	-1.60743	56	-0.4296
cs.th	1	56	0.574409	0.45169	-1.51881	56	-0.40592
sex	1	56	4.856937	*0.031663*	-1.30117	56	-0.34775
age:cs.th	1	56	0.002614	0.959409	1.570817	56	0.419818
age:sex	1	56	0.004519	0.946643	1.409451	56	0.376692
cs.th:sex	1	56	1.432145	0.236457	1.274463	56	0.340615
age:cs.th:sex	1	56	1.968179	0.166161	-1.40292	56	-0.37495
Octant 1	7	56	15.66677	*3.50E-11*	-2.49457	56	-0.6667
Octant 2					6.154495	56	1.644858
Octant 3					3.356268	56	0.897
Octant 4					5.518534	56	1.47489
Octant 5					-0.04612	56	-0.01233
Octant 6					-4.81583	56	-1.28708
Octant 7					-3.6234	56	-0.96839
Marginal R2	0.354756						
Conditional R2	0.950125						
Shapiro-Wilk Normality	0.268178						

Significant values ($p < 0.05$) are ***bolded***

Table 7.81 Pore Separation: Post-Hoc

	Lhs	rhs	estimate	std.error	statistic	p.value
1	inferior – anterior	0	-0.30938	0.181549	-1.70412	1
2	inferioranterior - anterior	0	-0.42622	0.196467	-2.16943	0.601004
3	inferiorposterior - anterior	0	-0.40482	0.19356	-2.09147	0.656754
4	posterior – anterior	0	-0.42371	0.196121	-2.16046	0.601004
5	superior – anterior	0	-0.60767	0.224585	-2.70574	0.143119
6	superioranterior - anterior	0	0.16378	0.1409	1.162388	1
7	superiorposterior - anterior	0	-0.6997	0.240595	-2.90823	0.083602
8	inferioranterior - inferior	0	-0.11684	0.22019	-0.53063	1
9	inferiorposterior - inferior	0	-0.09544	0.2176	-0.43862	1
10	posterior – inferior	0	-0.11433	0.219881	-0.51996	1
11	superior – inferior	0	-0.29829	0.245606	-1.21449	1
12	superioranterior - inferior	0	0.473161	0.172444	2.743849	0.133592
13	superiorposterior - inferior	0	-0.39032	0.260327	-1.49936	1
14	inferiorposterior - inferioranterior	0	0.021398	0.230194	0.092955	1
15	posterior - inferioranterior	0	0.00251	0.232351	0.010804	1
16	superior - inferioranterior	0	-0.18145	0.25683	-0.70648	1
17	superioranterior - inferioranterior	0	0.590002	0.188086	3.136872	*0.044398*
18	superiorposterior - inferioranterior	0	-0.27348	0.270942	-1.00938	1
19	posterior - inferiorposterior	0	-0.01889	0.229898	-0.08216	1
20	superior - inferiorposterior	0	-0.20284	0.254613	-0.79667	1
21	superioranterior - inferiorposterior	0	0.568604	0.185047	3.072755	0.050902
22	superiorposterior - inferiorposterior	0	-0.29488	0.268841	-1.09686	1
23	superior – posterior	0	-0.18396	0.256566	-0.717	1
24	superioranterior - posterior	0	0.587491	0.187725	3.12954	*0.044398*
25	superiorposterior - posterior	0	-0.27599	0.270691	-1.01959	1
26	superioranterior - superior	0	0.771448	0.217291	3.550306	*0.010389*
27	superiorposterior - superior	0	-0.09204	0.291973	-0.31522	1
28	superiorposterior - superioranterior	0	-0.86348	0.233801	-3.69325	*0.006199*

Significant values (p < 0.05) are ***bolded***

306

Figure 7.28 Radar Plot of Pore Separation

Note the almost completely uniform and large distribution of structure separation in 34M, and to a lesser degree in two relatively younger individuals (39F and 50F). Pores are less separated with age in all octants.

Figure 7.29 Medians of Pore Separation Distribution by by Octant
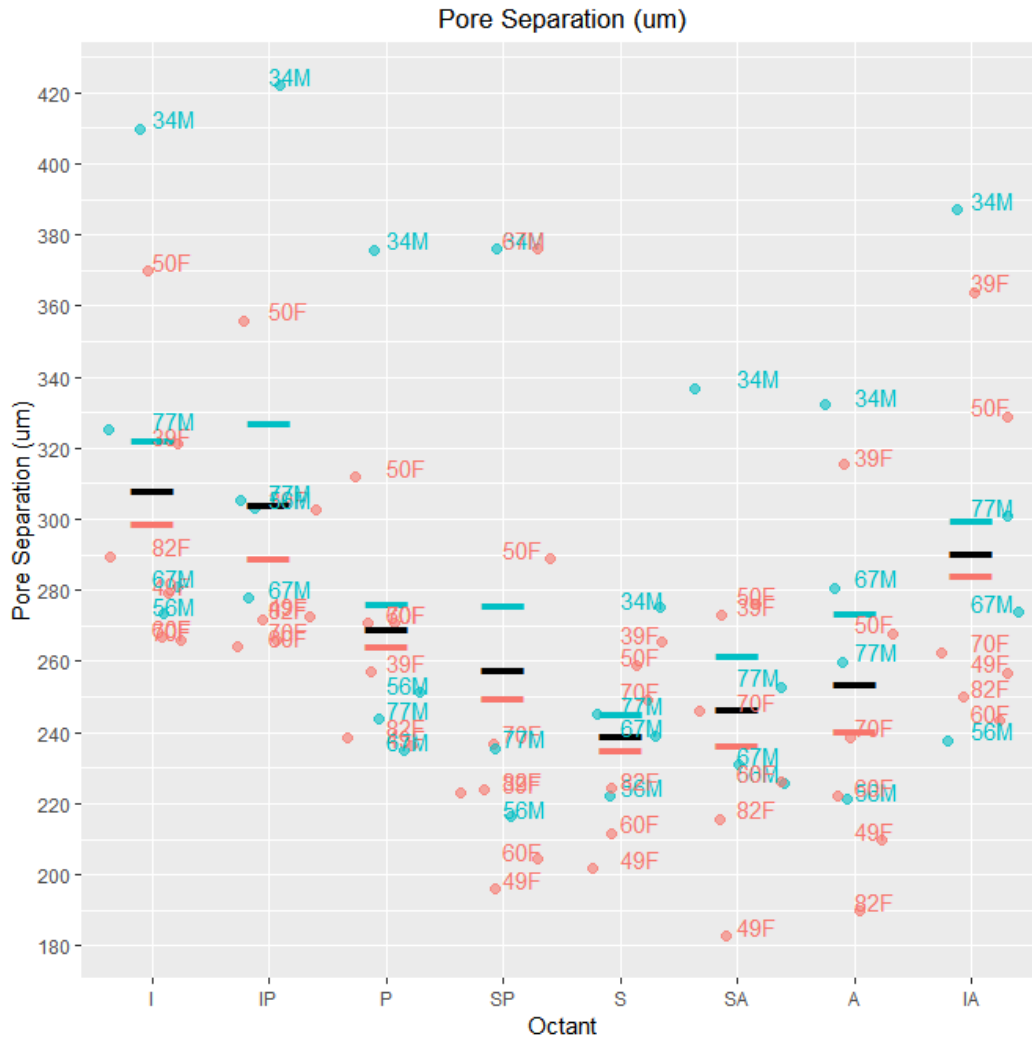
Significant Differences:

The only significant differences are between the superior-anterior region and adjacent superior, superior posterior, posterior, and inferior anterior regions. However, the median plot shows a trend of increasing pore separation along the superior to inferior loading gradient. Additionally, the significant sex effect indicates that males have larger pore separation than females.

308

Table 7.82 Pore Linear Density LMM

	numDF	denDF	F.value	p.value	t	df	d
(Intercept)	1	56	56.73053	4.57E-10			
age	1	56	1.183976	0.281209	0.752881	56	0.201216
cs.th	1	56	0.922886	0.340848	0.613832	56	0.164053
sex	1	56	1.113983	0.29575	0.705178	56	0.188467
age:cs.th	1	56	0.018064	0.893566	-0.7268	56	-0.19425
age:sex	1	56	0.003829	0.950877	-0.72488	56	-0.19373
cs.th:sex	1	56	0.009443	0.922933	-0.71419	56	-0.19088
age:cs.th:sex	1	56	0.529845	0.469705	0.727904	56	0.194541
Octant 1	7	56	8.083045	*9.13E-07*	-2.32079	56	-0.62026
Octant 2					-3.71485	56	-0.99284
Octant 3					-2.0453	56	-0.54663
Octant 4					-2.86016	56	-0.76441
Octant 5					1.212484	56	0.32405
Octant 6					4.04873	56	1.082069
Octant 7					1.932748	56	0.516549
Marginal R2	0.312929						
Conditional R2	0.759024						
Shapiro-Wilk Normality	*3.83E-07*						

Significant values (p < 0.05) are ***bolded***

309

Table 7.83 Pore Linear Density: PQL Correction

	Value	Std.Error	DF	t.value	p.value	cohen t	cohen df	cohen d
(Intercept)	-5.0336	4.906948	56	-1.02581	0.309392			
octant1	-0.19075	0.09013	56	-2.11636	*0.038772*	-2.11636	56	-0.56562
octant2	-0.35834	0.09706	56	-3.69192	*0.000506*	-3.69192	56	-0.98671
octant3	-0.16071	0.088956	56	-1.80665	*0.076191*	-1.80665	56	-0.48285
octant4	-0.2523	0.0926	56	-2.72464	*0.008572*	-2.72464	56	-0.72819
octant5	0.139327	0.078261	56	1.780288	*0.080454*	1.780288	56	0.475802
octant6	0.342815	0.071998	56	4.761426	*1.40E-05*	4.761426	56	1.272545
octant7	0.195054	0.076471	56	2.550705	*0.013511*	2.550705	56	0.681705
age	-0.02204	0.101547	56	-0.21705	0.828961	-0.21705	56	-0.05801
cs.th	-0.00196	0.002999	56	-0.65439	0.515537	-0.65439	56	-0.17489
sex1	0.290426	4.981545	56	0.0583	0.953717	0.0583	56	0.015581
age:cs.th	1.98E-05	6.67E-05	56	0.297587	0.76712	0.297587	56	0.079533
age:sex1	0.001197	0.102508	56	0.011678	0.990724	0.011678	56	0.003121
cs.th:sex1	-0.00047	0.003057	56	-0.15486	0.877485	-0.15486	56	-0.04139
age:cs.th:sex1	2.10E-06	6.74E-05	56	0.031163	0.975251	0.031163	56	0.008329
R2	0.790137							

Significant values (p < 0.05) are ***bolded***

Table 7.84 Pore Linear Density: Post-Hoc

	Lhs	rhs	estimate	std.error	statistic	p.value
1	inferior – anterior	0	-0.16759	0.12965	-1.29262	1
2	inferioranterior - anterior	0	0.030037	0.123191	0.243821	1
3	inferiorposterior - anterior	0	-0.06155	0.126067	-0.48827	1
4	posterior – anterior	0	0.330075	0.11506	2.868729	0.057697
5	superior – anterior	0	0.533563	0.110541	4.826832	*3.47E-05*
6	superioranterior - anterior	0	0.385802	0.113748	3.391723	*0.011807*
7	superiorposterior - anterior	0	0.475653	0.112523	4.227179	*0.000497*
8	inferioranterior - inferior	0	0.197625	0.128769	1.534732	1
9	inferiorposterior - inferior	0	0.106034	0.131523	0.8062	1
10	posterior – inferior	0	0.497664	0.121012	4.112507	*0.000783*
11	superior – inferior	0	0.701152	0.116724	6.006906	*5.29E-08*
12	superioranterior - inferior	0	0.553391	0.119766	4.620604	*8.8E-05*
13	superiorposterior - inferior	0	0.643242	0.118603	5.423507	*1.58E-06*
14	inferiorposterior - inferioranterior	0	-0.09159	0.12516	-0.73179	1
15	posterior - inferioranterior	0	0.300039	0.114065	2.630416	0.110865
16	superior - inferioranterior	0	0.503526	0.109505	4.59819	*9.38E-05*
17	superioranterior - inferioranterior	0	0.355765	0.112742	3.155575	*0.024027*
18	superiorposterior - inferioranterior	0	0.445616	0.111505	3.99637	*0.001222*
19	posterior - inferiorposterior	0	0.39163	0.117165	3.342541	*0.013282*
20	superior - inferiorposterior	0	0.595118	0.112731	5.279091	*3.38E-06*
21	superioranterior - inferiorposterior	0	0.447357	0.115878	3.860598	*0.002036*
22	superiorposterior - inferiorposterior	0	0.537208	0.114675	4.684619	*6.73E-05*
23	superior – posterior	0	0.203488	0.10027	2.0294	0.50901
24	superioranterior - posterior	0	0.055727	0.103795	0.536894	1
25	superiorposterior - posterior	0	0.145578	0.10245	1.420961	1
26	superioranterior - superior	0	-0.14776	0.098762	-1.49613	1
27	superiorposterior - superior	0	-0.05791	0.097348	-0.59487	1
28	superiorposterior - superioranterior	0	0.089851	0.100975	0.889834	1

Significant values (p < 0.05) are ***bolded***

Figure 7.30 Radar Plot of Pore Linear Density
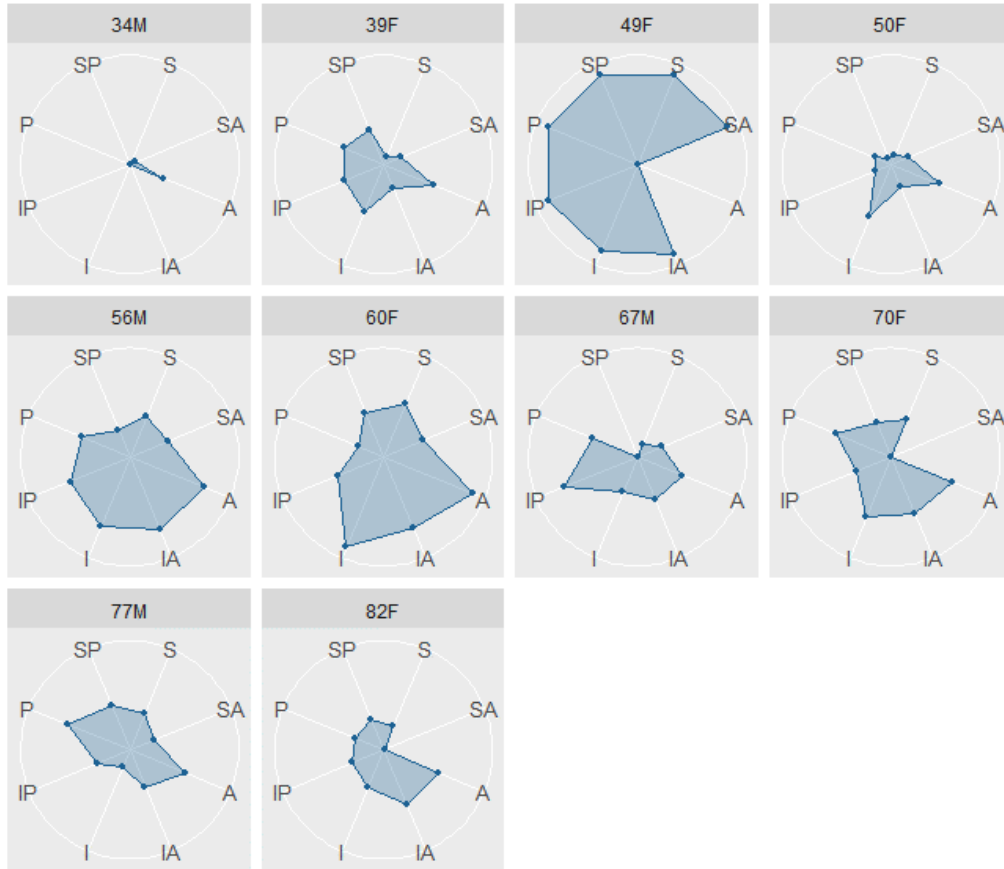
Figure 7.31 Medians of Pore Linear Density Distribution by by Octant
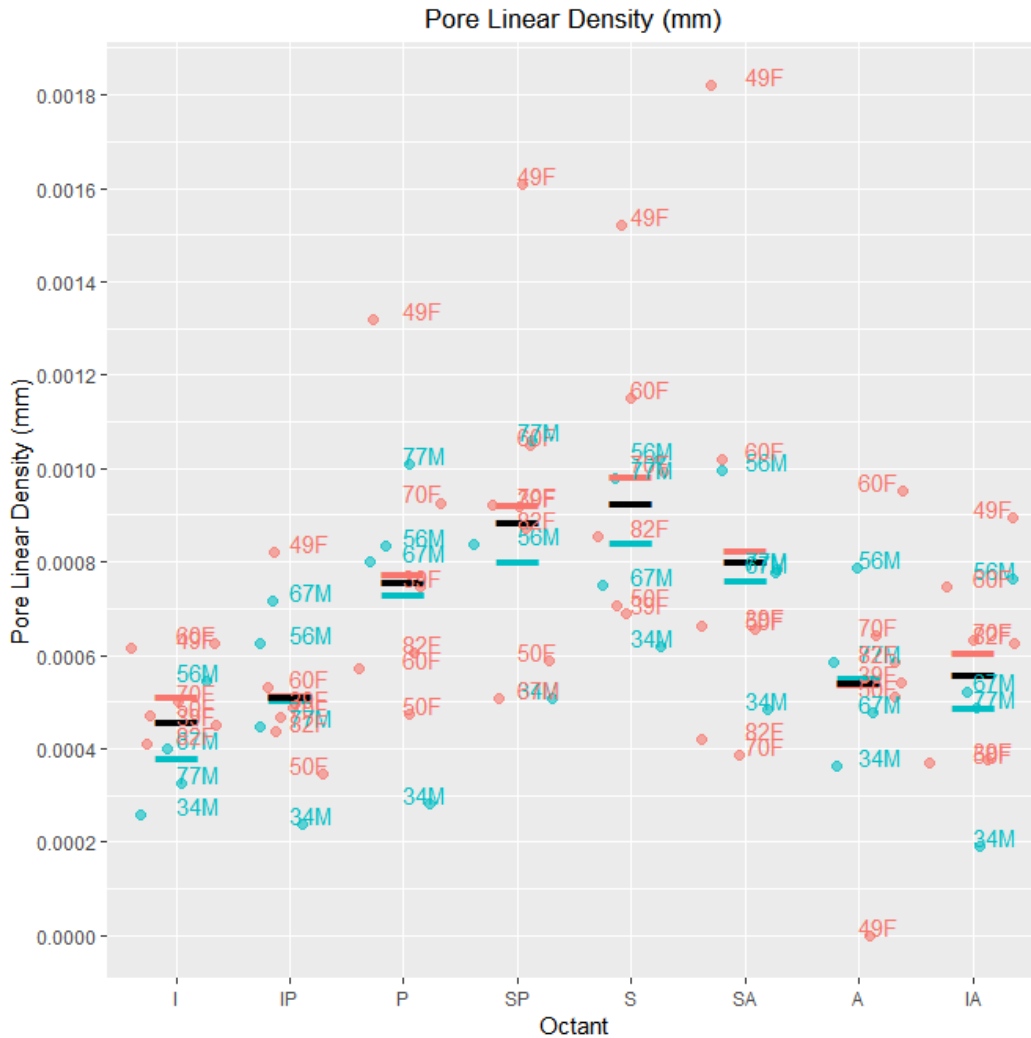
Significant Differences:

Significant differences between more inferior (I, IA, IP) and middle to superior octants (S, P, SA, SP) reinforces this visual trend of decreasing linear pore density along the superior to inferior loading gradient. The anterior octant has significantly less pore linear density than S, SA, and SP given that these points from a single individual compose both extremes of the outliers.

Table 7.85 Pore Fragmentation Index LMM

	numDF	denDF	F.value	p.value	t	df	d
(Intercept)	1	56	806.5607	0			
age	1	56	0.002477	0.960484	0.187293	56	0.050056
cs.th	1	56	0.361308	0.550206	0.282299	56	0.075447
sex	1	56	0.017944	0.89392	0.114594	56	0.030626
age:cs.th	1	56	0.372702	0.544005	-0.22275	56	-0.05953
age:sex	1	56	0.079666	0.778792	-0.18974	56	-0.05071
cs.th:sex	1	56	0.935195	0.337675	-0.09173	56	-0.02452
age:cs.th:sex	1	56	0.036339	0.849507	0.190627	56	0.050947
Octant 1	7	56	4.469632	*0.000523*	0.119461	56	0.031927
Octant 2					3.140959	56	0.839457
Octant 3					1.840444	56	0.491879
Octant 4					2.485812	56	0.664361
Octant 5					-1.07349	56	-0.2869
Octant 6					-2.6478	56	-0.70765
Octant 7					-1.96332	56	-0.52472
Marginal R2	0.232981						
Conditional R2	0.581084						
Shapiro-Wilk Normality	0.195136						

Significant values (p < 0.05) are ***bolded***

Table 7.86 Pore Fragmentation Index: Post Hoc

	Contrast	estimate	SE	df	t.ratio	p.value
1	anterior – inferior	-3.09E-03	0.001545	56	-1.99987	0.4912
2	anterior – inferioranterior	-1.76E-03	0.001545	56	-1.13909	0.945085
3	anterior – inferiorposterior	-2.42E-03	0.001545	56	-1.56624	0.767799
4	anterior – posterior	1.22E-03	0.001545	56	0.789593	0.993023
5	anterior – superior	2.83E-03	0.001545	56	1.831597	0.601913
6	anterior – superioranterior	2.13E-03	0.001545	56	1.378552	0.86304
7	anterior – superiorposterior	2.07E-03	0.001574	56	1.31361	0.889869
8	inferior – inferioranterior	1.33E-03	0.001545	56	0.860786	0.98833
9	inferior – inferiorposterior	6.70E-04	0.001545	56	0.433629	0.999852
10	inferior – posterior	4.31E-03	0.001545	56	2.789464	0.118449
11	inferior – superior	5.92E-03	0.001545	56	3.831468	*0.00733*
12	inferior – superioranterior	5.22E-03	0.001545	56	3.378423	*0.027163*
13	inferior – superiorposterior	5.16E-03	0.001574	56	3.277018	*0.035722*
14	inferioranterior - inferiorposterior	-6.60E-04	0.001545	56	-0.42716	0.999866
15	inferioranterior – posterior	2.98E-03	0.001545	56	1.928678	0.537785
16	inferioranterior – superior	4.59E-03	0.001545	56	2.970682	0.077741
17	inferioranterior - superioranterior	3.89E-03	0.001545	56	2.517637	0.209518
18	inferioranterior - superiorposterior	3.83E-03	0.001574	56	2.431926	0.246678
19	inferiorposterior – posterior	3.64E-03	0.001545	56	2.355835	0.283146
20	inferiorposterior – superior	5.25E-03	0.001545	56	3.397839	*0.025753*
21	inferiorposterior - superioranterior	4.55E-03	0.001545	56	2.944794	0.082716
22	inferiorposterior - superiorposterior	4.49E-03	0.001574	56	2.851295	0.102955
23	posterior – superior	1.61E-03	0.001545	56	1.042004	0.965658
24	posterior – superioranterior	9.10E-04	0.001545	56	0.588959	0.998888
25	posterior – superiorposterior	8.47E-04	0.001574	56	0.538413	0.999379
26	superior – superioranterior	-7.00E-04	0.001545	56	-0.45305	0.999802
27	superior – superiorposterior	-7.63E-04	0.001574	56	-0.48459	0.99969
28	superioranterior - superiorposterior	-6.26E-05	0.001574	56	-0.03981	1

Figure 7.32 Radar Plot of Pore Fragmentation Index

Figure 7.33 Medians of Fragmentation Index Distribution by by Octant

Pore Fragmentation Index (1/um)

Significant Differences: Inferior regions have a significantly lower pore fragmentation index than superior regions, meaning that their networks have more connective "nodes" and fewer disconnected "struts" under increased strain.

Table 7.87 Degree of Anisotropy LMM

	numDF	denDF	F.value	p.value	t	df	d
(Intercept)	1	56	148.3152	0			
age	1	56	0.596876	0.443021	-0.42294	56	-0.11304
cs.th	1	56	0.060253	0.806993	-0.51891	56	-0.13868
sex	1	56	0.807001	0.372855	-0.35207	56	-0.0941
age:cs.th	1	56	1.405834	0.240756	0.436926	56	0.116773
age:sex	1	56	0.051618	0.8211	0.44585	56	0.119159
cs.th:sex	1	56	1.937622	0.169431	0.27288	56	0.07293
age:cs.th:sex	1	56	0.174011	0.678166	-0.41715	56	-0.11149
Octant 1	7	56	1.88942	0.088522	-1.38152	56	-0.36923
Octant 2					2.012699	56	0.537917
Octant 3					1.063823	56	0.284319
Octant 4					1.394008	56	0.372564
Octant 5					0.239881	56	0.064111
Octant 6					-0.35449	56	-0.09474
Octant 7					-2.38777	56	-0.63816
Marginal R2	0.294621						
Conditional R2	0.80466						
Shapiro-Wilk Normality	0.607845						

Significant values (p < 0.05) are ***bolded***

No significant differences between octants in degree of anisotropy.

318

Figure 7.34 Radar Plot of Degree of Anisotropy

Figure 7.35 Medians of Degree of Anisotropy Distribution by Octant

Significant Differences:

The wide dispersion of values reinforces the high influence of the random factor, the individual identity. However, there is a slight trend of increasing anisotropy inferiorly, meaning that pore networks are slightly more consistently aligned under higher strain.

Table 7.88 Pore Fractal Dimension LMM

	numDF	denDF	F.value	p.value	t	df	d
(Intercept)	1	56	45877.31	0			
age	1	56	0.122936	0.727187	-0.19805	56	-0.05293
cs.th	1	56	0.430848	0.514261	-0.38161	56	-0.10199
sex	1	56	0.897426	0.347543	0.152664	56	0.040801
age:cs.th	1	56	0.005272	0.942378	0.250786	56	0.067025
age:sex	1	56	1.219004	0.274278	-0.08326	56	-0.02225
cs.th:sex	1	56	1.959064	0.167129	-0.28862	56	-0.07714
age:cs.th:sex	1	56	0.023239	0.879385	0.152444	56	0.040742
Octant 1	7	56	1.954402	0.077925	-0.56974	56	-0.15227
Octant 2					2.935041	56	0.784423
Octant 3					1.463897	56	0.391243
Octant 4					0.122559	56	0.032755
Octant 5					-0.52648	56	-0.14071
Octant 6					-1.56493	56	-0.41825
Octant 7					-0.78609	56	-0.21009
Marginal R2	0.199099						
Conditional R2	0.254167						
Shapiro-Wilk Normality	0.275213						

Significant values (p < 0.05) are ***bolded***

No significant differences between octants adjusted by co-variates.

Figure 7.36 Radar Plot of Pore Fractal Dimension

Figure 7.37 Medians of Pore Fractal Dimension Distribution by Octant

Significant Differences:

Despite the lack of significant differences, pore fractal dimension trends toward increasing inferiorly, indicating that the pore network is becoming more complex and patterned with increasing strain.

Table 7.89 Pore Connectivity Density LMM

	numDF	denDF	F.value	p.value	t	df	d
(Intercept)	1	56	531.5813	0			
age	1	56	12.12859	*0.000971*	1.250337	56	0.334167
cs.th	1	56	3.214339	0.078397	1.069683	56	0.285885
sex	1	56	0.060636	0.806394	0.883809	56	0.236208
age:cs.th	1	56	0.331647	0.566998	-1.20905	56	-0.32313
age:sex	1	56	2.719872	0.104705	-0.99774	56	-0.26666
cs.th:sex	1	56	1.625834	0.207545	-0.92355	56	-0.24683
age:cs.th:sex	1	56	1.109279	0.296762	1.053223	56	0.281486
Octant 1	7	56	2.275773	*0.041129*	-0.77923	56	-0.20826
Octant 2					-0.91403	56	-0.24428
Octant 3					-0.97371	56	-0.26023
Octant 4					-1.94199	56	-0.51902
Octant 5					-0.26576	56	-0.07103
Octant 6					3.344975	56	0.893982
Octant 7					0.419548	56	0.112129
Marginal R2	0.362962						
Conditional R2	0.402703						
Shapiro-Wilk Normality	*0.006087*						

Significant values (p < 0.05) are ***bolded***

Table 7.90 Pore Connectivity Density: PQL Correction

	Value	Std.Error	DF	t.value	p.value	cohen t	cohen df	cohen d
(Intercept)	-20.4613	3.716117	56	-5.50608	9.52E-07			
octant1	-0.06541	0.094708	56	-0.69064	0.492646	-0.69064	56	-0.18458
octant2	-0.07909	0.095255	56	-0.83033	0.409881	-0.83033	56	-0.22191
octant3	-0.08493	0.095501	56	-0.88929	0.377651	-0.88929	56	-0.23767
octant4	-0.188	0.099825	56	-1.88334	0.064852	-1.88334	56	-0.50334
octant5	-0.01521	0.092723	56	-0.16399	0.870331	-0.16399	56	-0.04383
octant6	0.278692	0.082035	56	3.397244	*0.001259*	3.397244	56	0.907952
octant7	0.047648	0.090292	56	0.52771	0.599786	0.52771	56	0.141036
age	0.102068	0.076718	56	1.330432	0.188768	1.330432	56	0.355573
cs.th	0.002426	0.002281	56	1.063647	0.292054	1.063647	56	0.284272
sex1	3.273695	3.709054	56	0.882623	0.381213	0.882623	56	0.235891
age:cs.th	-6.39E-05	5.05E-05	56	-1.26522	0.211031	-1.26522	56	-0.33814
age:sex1	-0.07854	0.076627	56	-1.02492	0.309807	-1.02492	56	-0.27392
cs.th:sex1	-0.0021	0.002276	56	-0.9217	0.360641	-0.9217	56	-0.24633
age:cs.th:sex1	5.49E-05	5.04E-05	56	1.088066	0.281227	1.088066	56	0.290798
R2	0.630985							

Significant values (p < 0.05) are ***bolded***

Table 7.91 Pore Connectivity Density Post-Hoc

	Lhs	rhs	estimate	std.error	statistic	p.value
1	inferior – anterior	0	-0.01368	0.129954	-0.1053	1
2	inferioranterior – anterior	0	-0.01952	0.130149	-0.14997	1
3	inferiorposterior – anterior	0	-0.1226	0.133618	-0.9175	1
4	posterior – anterior	0	0.050204	0.127955	0.392355	1
5	superior – anterior	0	0.344101	0.119787	2.872619	0.101771
6	superioranterior – anterior	0	0.113057	0.126057	0.896873	1
7	superiorposterior – anterior	0	0.171708	0.12588	1.36406	1
8	inferioranterior – inferior	0	-0.00584	0.13058	-0.04469	1
9	inferiorposterior – inferior	0	-0.10891	0.134038	-0.81254	1
10	posterior – inferior	0	0.063887	0.128394	0.497589	1
11	superior – inferior	0	0.357785	0.120255	2.97521	0.076125
12	superioranterior – inferior	0	0.126741	0.126502	1.001883	1
13	superiorposterior – inferior	0	0.185392	0.126326	1.467562	1
14	inferiorposterior - inferioranterior	0	-0.10308	0.134228	-0.76792	1
15	posterior – inferioranterior	0	0.069723	0.128591	0.542203	1
16	superior – inferioranterior	0	0.36362	0.120466	3.018441	0.068601
17	superioranterior - inferioranterior	0	0.132576	0.126703	1.046353	1
18	superiorposterior - inferioranterior	0	0.191227	0.126527	1.511352	1
19	posterior – inferiorposterior	0	0.172799	0.132101	1.308078	1
20	superior – inferiorposterior	0	0.466697	0.124206	3.757433	***0.004807***
21	superioranterior - inferiorposterior	0	0.235652	0.130264	1.809036	1
22	superiorposterior - inferiorposterior	0	0.294303	0.130093	2.262254	0.54468
23	superior – posterior	0	0.293898	0.118092	2.488713	0.307695
24	superioranterior – posterior	0	0.062853	0.124448	0.505058	1
25	superiorposterior – posterior	0	0.121505	0.124269	0.977754	1
26	superioranterior – superior	0	-0.23104	0.116033	-1.99119	1
27	superiorposterior – superior	0	-0.17239	0.115841	-1.48818	1
28	superiorposterior - superioranterior	0	0.058651	0.122314	0.479513	1

Significant values (p < 0.05) are ***bolded***

Figure 7.38 Radar Plot of Pore Connectivity Density

Figure 7.39 Medians of Pore Connectivity Density Distribution by by Octant

Connectivity Density (1/mm3)

Significant Differences:

Pore connectivity density declines superiorly to inferiorly as loading increases.

However, this only reaches statistical significance for superior vs. inferior

posterior octants.

Table 7.92 Standard Deviation of Pore Thickness LMM

	numDF	denDF	F.value	p.value	t	df	d
(Intercept)	1	56	224.7147	0			
age	1	56	1.684094	0.199701	-0.80457	56	-0.21503
cs.th	1	56	11.05981	*0.001561*	-0.74896	56	-0.20017
sex	1	56	8.216534	*0.005838*	-0.63149	56	-0.16877
age:cs.th	1	56	0.009799	0.921502	0.870455	56	0.232639
age:sex	1	56	2.018984	0.160888	0.678634	56	0.181373
cs.th:sex	1	56	0.333141	0.566129	0.548188	56	0.14651
age:cs.th:sex	1	56	0.369339	0.545821	-0.60773	56	-0.16242
Octant 1	7	56	2.077471	0.061098	1.612817	56	0.431044
Octant 2					0.139286	56	0.037226
Octant 3					-0.03001	56	-0.00802
Octant 4					-0.2013	56	-0.0538
Octant 5					-1.13691	56	-0.30385
Octant 6					-2.34849	56	-0.62766
Octant 7					2.62706	56	0.702111
Marginal R2	0.397775						
Conditional R2	0.453878						
Shapiro-Wilk Normality	9.08E-07						

Significant values ($p < 0.05$) are ***bolded***

329

Table 7.93 Standard Deviation of Pore Thickness PQL Correction

	Value	Std.Error	DF	t.value	p.value	cohen t	cohen df	cohen d
(Intercept)	7.840199	7.356895	56	1.065694	0.291135			
octant1	0.262782	0.096611	56	2.720002	0.008679	2.720002	56	0.726951
octant2	-0.00912	0.120273	56	-0.07584	0.939815	-0.07584	56	-0.02027
octant3	-0.03256	0.122691	56	-0.2654	0.791673	-0.2654	56	-0.07093
octant4	-0.00616	0.119973	56	-0.05137	0.959217	-0.05137	56	-0.01373
octant5	-0.135	0.134045	56	-1.00711	0.318213	-1.00711	56	-0.26916
octant6	-0.41141	0.172002	56	-2.39191	*0.020143*	-2.39191	56	-0.63926
octant7	0.433061	0.085345	56	5.074256	*4.59E-06*	5.074256	56	1.356152
age	-0.08349	0.151494	56	-0.55109	0.583763	-0.55109	56	-0.14729
cs.th	-0.00198	0.004453	56	-0.44562	0.657588	-0.44562	56	-0.1191
sex1	-5.28969	7.353912	56	-0.7193	0.474945	-0.7193	56	-0.19224
age:cs.th	6.13E-05	9.88E-05	56	0.620441	0.537485	0.620441	56	0.16582
age:sex1	0.114572	0.151449	56	0.756508	0.452516	0.756508	56	0.202185
cs.th:sex1	0.003041	0.004451	56	0.683377	0.497187	0.683377	56	0.18264
age:cs.th:sex1	-7.03E-05	9.88E-05	56	-0.71146	0.479755	-0.71146	56	-0.19014
R2	0.686369							

Significant values (p < 0.05) are ***bolded***

Table 7.94 Standard Deviation of Pore Thickness Post-Hoc

	Lhs	rhs	estimate	std.error	statistic	p.value
1	inferior – anterior	0	-0.2719	0.144735	-1.87864	0.964701
2	inferioranterior – anterior	0	-0.29534	0.146916	-2.0103	0.843593
3	inferiorposterior – anterior	0	-0.26894	0.144464	-1.86167	0.964701
4	posterior – anterior	0	-0.39778	0.157297	-2.52885	0.240318
5	superior – anterior	0	-0.67419	0.193202	-3.48959	*0.012094*
6	superioranterior – anterior	0	0.170279	0.11475	1.483907	1
7	superiorposterior – anterior	0	-0.36437	0.15348	-2.37404	0.351892
8	inferioranterior – inferior	0	-0.02344	0.164754	-0.14228	1
9	inferiorposterior – inferior	0	0.002959	0.162572	0.018203	1
10	posterior – inferior	0	-0.12588	0.174075	-0.72312	1
11	superior – inferior	0	-0.40229	0.207091	-1.94258	0.902747
12	superioranterior – inferior	0	0.442183	0.136848	3.231204	*0.028352*
13	superiorposterior – inferior	0	-0.09246	0.170634	-0.54189	1
14	inferiorposterior - inferioranterior	0	0.0264	0.164517	0.160471	1
15	posterior – inferioranterior	0	-0.10244	0.175893	-0.58238	1
16	superior – inferioranterior	0	-0.37885	0.208621	-1.81597	0.971247
17	superioranterior - inferioranterior	0	0.465624	0.139153	3.346133	*0.019667*
18	superiorposterior - inferioranterior	0	-0.06902	0.172488	-0.40016	1
19	posterior – inferiorposterior	0	-0.12884	0.17385	-0.74108	1
20	superior – inferiorposterior	0	-0.40525	0.206902	-1.95866	0.902747
21	superioranterior - inferiorposterior	0	0.439224	0.136562	3.216307	*0.028567*
22	superiorposterior - inferiorposterior	0	-0.09542	0.170404	-0.55998	1
23	superior – posterior	0	-0.27641	0.216057	-1.27935	1
24	superioranterior – posterior	0	0.56806	0.150072	3.785247	*0.004146*
25	superiorposterior – posterior	0	0.033413	0.181412	0.184181	1
26	superioranterior – superior	0	0.844473	0.187366	4.507079	*0.000184*
27	superiorposterior – superior	0	0.309826	0.213295	1.452574	1
28	superiorposterior - superioranterior	0	-0.53465	0.146066	-3.6603	*0.00655*

Significant values (p < 0.05) are ***bolded***

Figure 7.40 Radar Plot of Standard Deviation of Pore Thickness

Figure 7.41 Medians of Standard Deviation of Pore Thickness Distribution by by Octant

Significant Differences: As with pore thickness, there is not a significant trend of the range of pore sizes related to mechanical loading. Significant differences between SA and A and the other octants here are skewed by the large unified osteophyte caviations in 70F and 82F.

Table 7.95 Standard Deivation of Pore Separation LMM

	numDF	denDF	F.value	p.value	t	df	d
(Intercept)	1	56	5495.603	0			
age	1	56	25.80763	*4.49E-06*	-1.47516	56	-0.39425
cs.th	1	56	7.883707	*0.006853*	-0.74738	56	-0.19975
sex	1	56	25.2277	*5.52E-06*	-1.37364	56	-0.36712
age:cs.th	1	56	16.40717	*0.000159*	1.294536	56	0.345979
age:sex	1	56	9.946993	*0.00259*	1.278718	56	0.341752
cs.th:sex	1	56	6.783258	*0.011761*	1.700462	56	0.454467
age:cs.th:sex	1	56	2.116052	0.151344	-1.45467	56	-0.38878
Octant 1	7	56	3.008154	*0.009388*	-0.94374	56	-0.25223
Octant 2					2.292621	56	0.612729
Octant 3					0.515274	56	0.137713
Octant 4					2.69385	56	0.719962
Octant 5					1.012666	56	0.270646
Octant 6					-2.21043	56	-0.59076
Octant 7					-1.76278	56	-0.47112
Marginal R2	0.593265						
Conditional R2	0.593265						
Shapiro-Wilk Normality	*0.000663*						

Significant values (p < 0.05) are ***bolded***

334

Table 7.96 Standard Deivation of Pore Separation PQL Correction

	Value	Std.Error	DF	t.value	p.value	cohen t	cohen df	cohen d
(Intercept)	6.51934	1.692389	56	3.852152	0.000304			
octant1	-0.0351	0.035051	56	-1.00148	0.320903	-1.00148	56	-0.26766
octant2	0.093997	0.031414	56	2.992211	*0.004114*	2.992211	56	0.799702
octant3	0.031337	0.033112	56	0.946392	0.348015	0.946392	56	0.252934
octant4	0.098065	0.031308	56	3.132277	*0.002758*	3.132277	56	0.837136
octant5	0.033705	0.033045	56	1.019975	0.312127	1.019975	56	0.2726
octant6	-0.09513	0.036933	56	-2.57565	*0.012672*	-2.57565	56	-0.68837
octant7	-0.06792	0.036064	56	-1.88344	0.064837	-1.88344	56	-0.50337
age	-0.05519	0.035003	56	-1.57657	0.120526	-1.57657	56	-0.42136
cs.th	-0.00098	0.001028	56	-0.95685	0.342756	-0.95685	56	-0.25573
sex1	-2.32143	1.691376	56	-1.37251	0.175377	-1.37251	56	-0.36682
age:cs.th	3.28E-05	2.29E-05	56	1.429837	0.158319	1.429837	56	0.38214
age:sex1	0.045805	0.034991	56	1.309033	0.195869	1.309033	56	0.349854
cs.th:sex1	0.001695	0.001027	56	1.650505	0.104438	1.650505	56	0.441116
age:cs.th:sex1	-3.34E-05	2.29E-05	56	-1.46012	0.149845	-1.46012	56	-0.39023
R2	0.808657							

Significant values (p < 0.05) are ***bolded***

Table 7.97 Standard Deivation of Pore Separation Post-Hoc

	Lhs	rhs	estimate	std.error	statistic	p.value
1	inferior – anterior	0	0.129099	0.045162	2.858564	0.089368
2	inferioranterior - anterior	0	0.066439	0.046458	1.430101	1
3	inferiorposterior - anterior	0	0.133167	0.045083	2.953859	0.069042
4	posterior – anterior	0	0.068808	0.046406	1.482723	1
5	superior – anterior	0	-0.06002	0.04948	-1.21309	1
6	superioranterior - anterior	0	-0.03282	0.048781	-0.67285	1
7	superiorposterior - anterior	0	-0.02385	0.048388	-0.49283	1
8	inferioranterior - inferior	0	-0.06266	0.043548	-1.43887	1
9	inferiorposterior - inferior	0	0.004068	0.042078	0.096678	1
10	posterior – inferior	0	-0.06029	0.043494	-1.38622	1
11	superior – inferior	0	-0.18912	0.046759	-4.04463	***0.001415***
12	superioranterior - inferior	0	-0.16192	0.046019	-3.51861	***0.010845***
13	superiorposterior - inferior	0	-0.15295	0.045602	-3.35394	***0.018324***
14	inferiorposterior - inferioranterior	0	0.066728	0.043465	1.535203	1
15	posterior - inferioranterior	0	0.002369	0.044837	0.052829	1
16	superior - inferioranterior	0	-0.12646	0.048011	-2.63402	0.160323
17	superioranterior - inferioranterior	0	-0.09926	0.04729	-2.09897	0.60893
18	superiorposterior - inferioranterior	0	-0.09029	0.046885	-1.92569	0.812152
19	posterior - inferiorposterior	0	-0.06436	0.043411	-1.48258	1
20	superior - inferiorposterior	0	-0.19319	0.046682	-4.13845	***0.000979***
21	superioranterior - inferiorposterior	0	-0.16599	0.04594	-3.61316	***0.007865***
22	superiorposterior - inferiorposterior	0	-0.15701	0.045523	-3.44913	***0.013498***
23	superior – posterior	0	-0.12883	0.047962	-2.68613	0.144569
24	superioranterior - posterior	0	-0.10163	0.04724	-2.15135	0.566073
25	superiorposterior - posterior	0	-0.09265	0.046834	-1.97835	0.766225
26	superioranterior - superior	0	0.027202	0.050263	0.541188	1
27	superiorposterior - superior	0	0.036177	0.049882	0.725255	1
28	superiorposterior - superioranterior	0	0.008975	0.049188	0.182469	1

Significant values (p < 0.05) are ***bolded***

Figure 7.42 Radar Plot of Standard Deivation of Pore Separation

Figure 7.43 Medians of Standard Deviation of Pore Separation Distribution by Octant
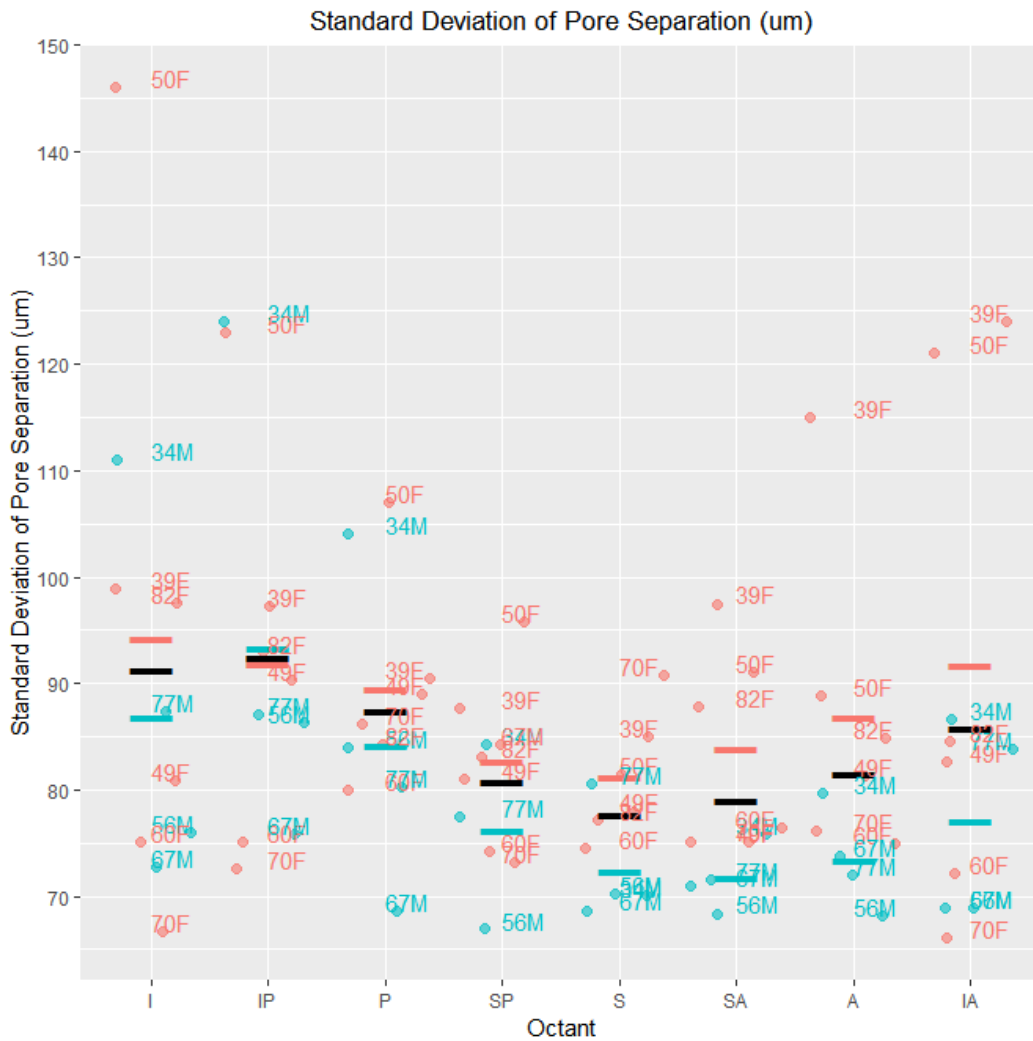
Significant Differences:

Inferior and inferior posterior octants have a significantly larger range of pore sizes than all three superior octants.

Table 7.98 Proportion of Open Pores vs. Closed Pores LMM

	numDF	denDF	F.value	p.value	t	df	d
(Intercept)	1	56	3905.554	0			
age	1	56	0.52628	0.471196	0.065821	56	0.017591
cs.th	1	56	2.128064	0.15021	-0.09212	56	-0.02462
sex	1	56	1.282044	0.262344	0.159058	56	0.04251
age:cs.th	1	56	0.437964	0.510821	0.006119	56	0.001635
age:sex	1	56	0.112294	0.7388	-0.05918	56	-0.01582
cs.th:sex	1	56	1.272566	0.264096	-0.17213	56	-0.046
age:cs.th:sex	1	56	0.003382	0.953834	0.058153	56	0.015542
Octant 1	7	56	4.32035	*0.000697*	-0.77419	56	-0.20691
Octant 2					-3.44094	56	-0.91963
Octant 3					-1.29783	56	-0.34686
Octant 4					0.251231	56	0.067144
Octant 5					3.252916	56	0.869378
Octant 6					2.713408	56	0.725189
Octant 7					-1.26705	56	-0.33863
Marginal R2	0.324359						
Conditional R2	0.636797						
Shapiro-Wilk Normality	0.794887						

Significant values ($p < 0.05$) are ***bolded***

339

Table 7.99 Proportion of Open Pores vs. Closed Pores Post-Hoc

	Contrast	estimate	SE	df	t.ratio	p.value
1	anterior – inferior	0.031921	0.018084	56	1.765089	0.645469
2	anterior - inferioranterior	0.006268	0.018084	56	0.346596	0.999967
3	anterior - inferiorposterior	-0.01227	0.018084	56	-0.67871	0.997255
4	anterior – posterior	-0.0482	0.018084	56	-2.66548	0.155116
5	anterior – superior	-0.04175	0.018084	56	-2.30839	0.3075
6	anterior - superioranterior	0.0059	0.018084	56	0.32622	0.999978
7	anterior - superiorposterior	-0.016	0.018424	56	-0.86838	0.987714
8	inferior - inferioranterior	-0.02565	0.018084	56	-1.41849	0.844889
9	inferior - inferiorposterior	-0.04419	0.018084	56	-2.4438	0.241282
10	inferior – posterior	-0.08012	0.018084	56	-4.43057	***0.001087***
11	inferior – superior	-0.07367	0.018084	56	-4.07348	***0.003463***
12	inferior - superioranterior	-0.02602	0.018084	56	-1.43887	0.835162
13	inferior - superiorposterior	-0.04792	0.018424	56	-2.6009	0.177395
14	inferioranterior - inferiorposterior	-0.01854	0.018084	56	-1.0253	0.96854
15	inferioranterior - posterior	-0.05447	0.018084	56	-3.01208	0.070313
16	inferioranterior - superior	-0.04801	0.018084	56	-2.65499	0.158585
17	inferioranterior - superioranterior	-0.00037	0.018084	56	-0.02038	1
18	inferioranterior - superiorposterior	-0.02227	0.018424	56	-1.20858	0.926023
19	inferiorposterior - posterior	-0.03593	0.018084	56	-1.98677	0.499708
20	inferiorposterior - superior	-0.02947	0.018084	56	-1.62968	0.730596
21	inferiorposterior - superioranterior	0.018174	0.018084	56	1.004929	0.971815
22	inferiorposterior - superiorposterior	-0.00373	0.018424	56	-0.2022	0.999999
23	posterior – superior	0.006458	0.018084	56	0.357093	0.99996
24	posterior - superioranterior	0.054103	0.018084	56	2.991702	0.07389
25	posterior - superiorposterior	0.032204	0.018424	56	1.747919	0.656582
26	superior - superioranterior	0.047645	0.018084	56	2.63461	0.165485
27	superior - superiorposterior	0.025747	0.018424	56	1.397415	0.854621
28	superioranterior - superiorposterior	-0.0219	0.018424	56	-1.18858	0.931897

Significant values (p < 0.05) are ***bolded***

Figure 7.44 Radar Plot of Proportion of Open Pores vs. Closed Pores

Figure 7.45 Medians of Open Pores vs. Closed Pores Distribution by Octant

Significant Differences: Despite the wide spread of individual variation, the inferior octant has a significantly smaller proportion of open pores compaired to superior and posterior octants.

Table 7.100 Pore Density LMM

	numDF	denDF	F.value	p.value	t	df	d
(Intercept)	1	56	685.9644	0			
age	1	56	11.81399	*0.001115*	1.249574	56	0.333963
cs.th	1	56	1.592191	0.212244	1.126062	56	0.300953
sex	1	56	0.030394	0.862228	1.06294	56	0.284083
age:cs.th	1	56	1.856252	0.178513	-1.23172	56	-0.32919
age:sex	1	56	4.527433	*0.037772*	-1.25308	56	-0.3349
cs.th:sex	1	56	4.924428	*0.030548*	-1.09311	56	-0.29214
age:cs.th:sex	1	56	1.731099	0.193632	1.315712	56	0.351639
Octant 1	7	56	1.678735	0.133049	-0.17323	56	-0.0463
Octant 2					-0.86765	56	-0.23189
Octant 3					-1.12219	56	-0.29992
Octant 4					-1.8365	56	-0.49083
Octant 5					-0.68708	56	-0.18363
Octant 6					2.379351	56	0.635908
Octant 7					1.073232	56	0.286833
Marginal R2	0.362713						
Conditional R2	0.38859						
Shapiro-Wilk Normality	*0.036539*						

Significant values (p < 0.05) are ***bolded***

343

Table 7.101 Pore Density PQL Correction

	Value	Std.Error	DF	t.value	p.value	cohen t	cohen df	cohen d
(Intercept)	-20.2147	3.514837	56	-5.75125	3.85E-07			
octant1	-0.00878	0.087116	56	-0.10074	0.920116	-0.10074	56	-0.02692
octant2	-0.07197	0.089513	56	-0.80399	0.424801	-0.80399	56	-0.21488
octant3	-0.0962	0.090454	56	-1.06354	0.292101	-1.06354	56	-0.28424
octant4	-0.16742	0.093295	56	-1.79455	0.078124	-1.79455	56	-0.47961
octant5	-0.05507	0.088867	56	-0.61965	0.538002	-0.61965	56	-0.16561
octant6	0.194564	0.079969	56	2.432998	*0.018193*	2.432998	56	0.650246
octant7	0.095735	0.083341	56	1.148714	0.255557	1.148714	56	0.307007
age	0.100208	0.072665	56	1.379047	0.173363	1.379047	56	0.368566
cs.th	0.002618	0.002156	56	1.214025	0.229833	1.214025	56	0.324462
sex1	3.925361	3.508684	56	1.118756	0.26802	1.118756	56	0.299
age:cs.th	-6.47E-05	4.79E-05	56	-1.35271	0.181584	-1.35271	56	-0.36153
age:sex1	-0.09782	0.072587	56	-1.34763	0.183204	-1.34763	56	-0.36017
cs.th:sex1	-0.00243	0.002152	56	-1.1289	0.263753	-1.1289	56	-0.30171
age:cs.th:sex1	6.72E-05	4.78E-05	56	1.405828	0.165299	1.405828	56	0.375723
R2	0.624109							

Significant values (p < 0.05) are ***bolded***

Table 7.102 Pore Density Post-Hoc

	Lhs	rhs	estimate	std.error	statistic	p.value
1	inferior – anterior	0	-0.06319	0.120602	-0.52397	1
2	inferioranterior - anterior	0	-0.08743	0.12136	-0.72038	1
3	inferiorposterior - anterior	0	-0.15865	0.123668	-1.28284	1
4	posterior – anterior	0	-0.04629	0.120083	-0.38549	1
5	superior – anterior	0	0.20334	0.113103	1.797825	1
6	superioranterior - anterior	0	0.104511	0.115711	0.903211	1
7	superiorposterior - anterior	0	0.117912	0.11689	1.008736	1
8	inferioranterior - inferior	0	-0.02423	0.123235	-0.19664	1
9	inferiorposterior - inferior	0	-0.09545	0.125509	-0.76054	1
10	posterior – inferior	0	0.016902	0.121978	0.138564	1
11	superior – inferior	0	0.266532	0.115113	2.315388	0.535384
12	superioranterior - inferior	0	0.167703	0.117676	1.425123	1
13	superiorposterior - inferior	0	0.181103	0.118836	1.523974	1
14	inferiorposterior - inferioranterior	0	-0.07122	0.126237	-0.56418	1
15	posterior - inferioranterior	0	0.041135	0.122727	0.335175	1
16	superior - inferioranterior	0	0.290765	0.115907	2.508608	0.327261
17	superioranterior - inferioranterior	0	0.191937	0.118453	1.620363	1
18	superiorposterior - inferioranterior	0	0.205337	0.119605	1.716787	1
19	posterior - inferiorposterior	0	0.112356	0.12501	0.898773	1
20	superior - inferiorposterior	0	0.361986	0.118322	3.059342	***0.062111***
21	superioranterior - inferiorposterior	0	0.263157	0.120817	2.178156	0.704222
22	superiorposterior - inferiorposterior	0	0.276557	0.121947	2.267856	0.58345
23	superior – posterior	0	0.24963	0.11457	2.178853	0.704222
24	superioranterior - posterior	0	0.150802	0.117145	1.287312	1
25	superiorposterior - posterior	0	0.164202	0.11831	1.387897	1
26	superioranterior - superior	0	-0.09883	0.109979	-0.89862	1
27	superiorposterior - superior	0	-0.08543	0.111219	-0.76811	1
28	superiorposterior - superioranterior	0	0.0134	0.11387	0.11768	1

Significant values (p < 0.05) are ***bolded***

345

Figure 7.46 Radar Plot of Pore Density
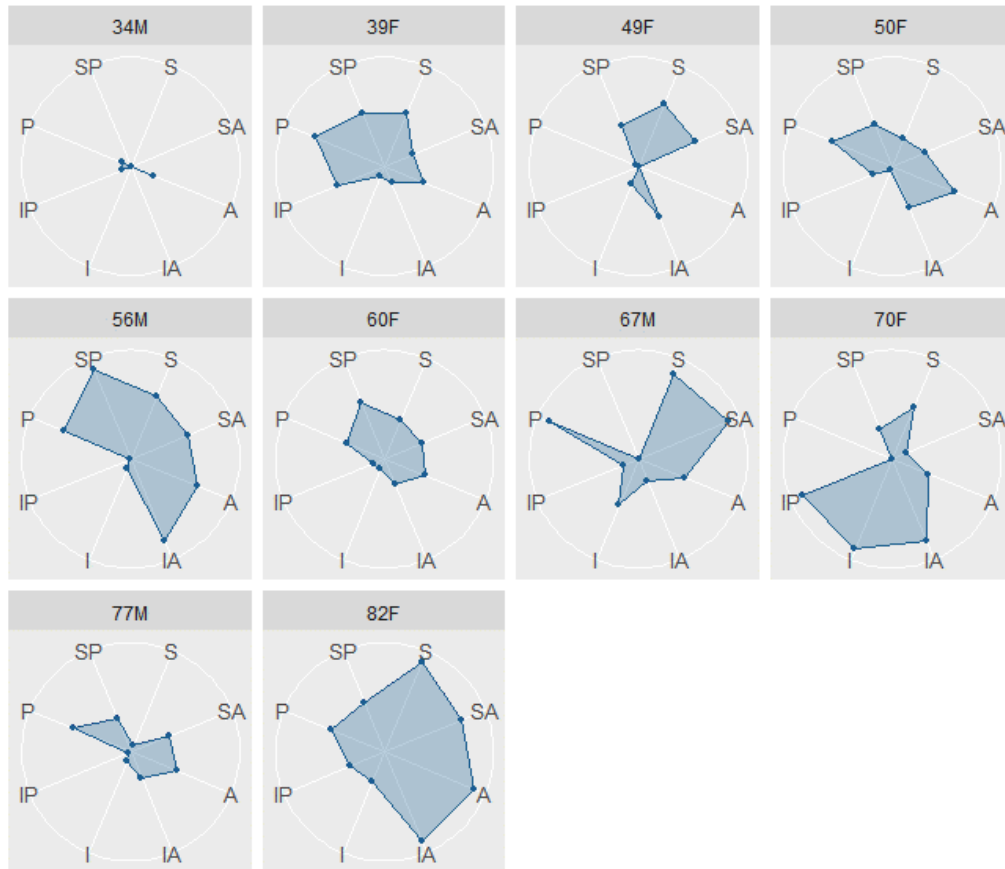
Figure 7.47 Medians of Pore Density Distribution by Octant
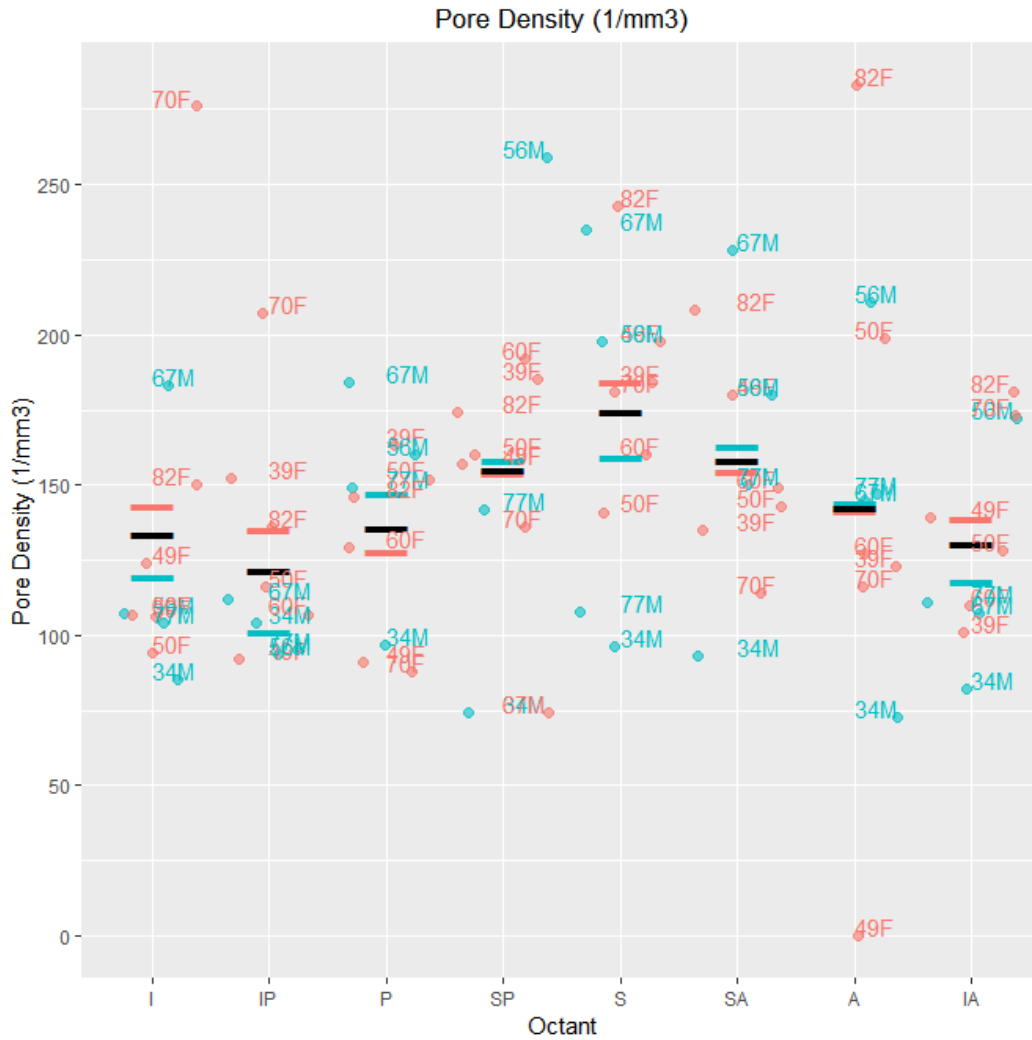
Significant Differences:

Pore density, or the number of pores per square mm, is significantly higher superiorly compared to the inferior posterior octant.

7.6. Univariate Testing of Regional Distribution in Pore Morphometry in the Cutaneous and Pleural Rib Cortices

Table 7.103 Cortical Fractal Dimension LMM

	numDF	denDF	F.value	p.value	cohen t	cohen df	cohen d
(Intercept)	1	39	51776.57	0			
region	1	39	6.248577	*0.016745*	2.499715	39	0.80055
type	1	39	484.1996	*0*	22.00454	39	7.047092
age	1	6	4.486332	0.07849	-0.28285	6	-0.23095
cs.th	1	6	0.039578	0.848879	-0.86797	6	-0.70869
sex	1	6	0.750311	0.419662	0.656596	6	0.536108
region:type	1	39	4.612369	*0.038014*	-2.14764	39	-0.6878
age:cs.th	1	6	0.086751	0.778274	0.573291	6	0.46809
age:sex	1	6	1.076201	0.339537	-0.41481	6	-0.33869
cs.th:sex	1	6	0.697335	0.435663	-0.77417	6	-0.63211
age:cs.th:sex	1	6	0.248881	0.635624	0.49888	6	0.407333
Marginal R2	0.847808						
Conditional R2	0.910905						
Shapiro-Wilk Normality	0.977187						

Significant values (p < 0.05) are ***bolded***

348

Figure 7.48 Medians of Cortical Fractal Dimension Distribution by Cortex

Cortical Fractal Dimension
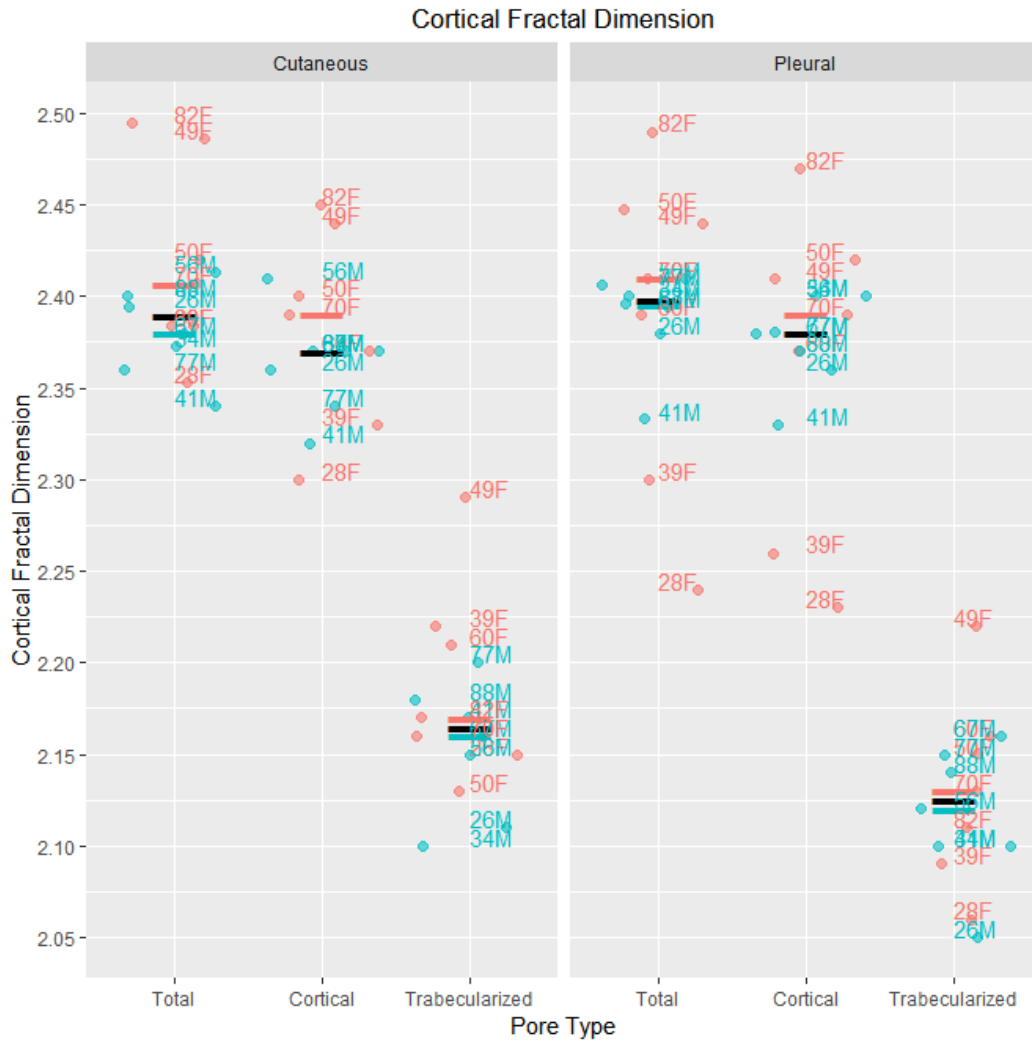
Significant Differences:

- Pleural cortical pore network more complex than cutaneous cortical pore network

- Cutaneous trabecularized pore network more complex than pleural trabecularized pore network

349

Table 7.104 Percent Closed Porosity LMM

	numDF	denDF	F.value	p.value	cohen t	cohen df	cohen d
(Intercept)	1	39	48.31136	2.51E-08			
region	1	39	2.191547	0.146804	1.480387	39	0.474103
type	1	39	2.150873	0.150507	-1.46659	39	-0.46968
age	1	6	2.206996	0.187931	-1.21748	6	-0.99407
cs.th	1	6	0.449919	0.527335	-1.42306	6	-1.16192
sex	1	6	4.653049	0.074375	1.341413	6	1.095259
region:type	1	39	0.129942	0.720437	-0.36047	39	-0.11544
age:cs.th	1	6	0.627032	0.458599	1.369494	6	1.118187
age:sex	1	6	0.518458	0.498577	-0.93107	6	-0.76022
cs.th:sex	1	6	1.667315	0.244131	-1.08394	6	-0.88504
age:cs.th:sex	1	6	0.421827	0.540078	0.649482	6	0.5303
Marginal R2	0.328365						
Conditional R2	0.621947						
Shapiro-Wilk Normality	*0.36457*						

Significant values (p < 0.05) are ***bolded***

No significant differences in percent closed porosity.

Figure 7.49 Medians of Percent Closed Porosity Distribution by Cortex
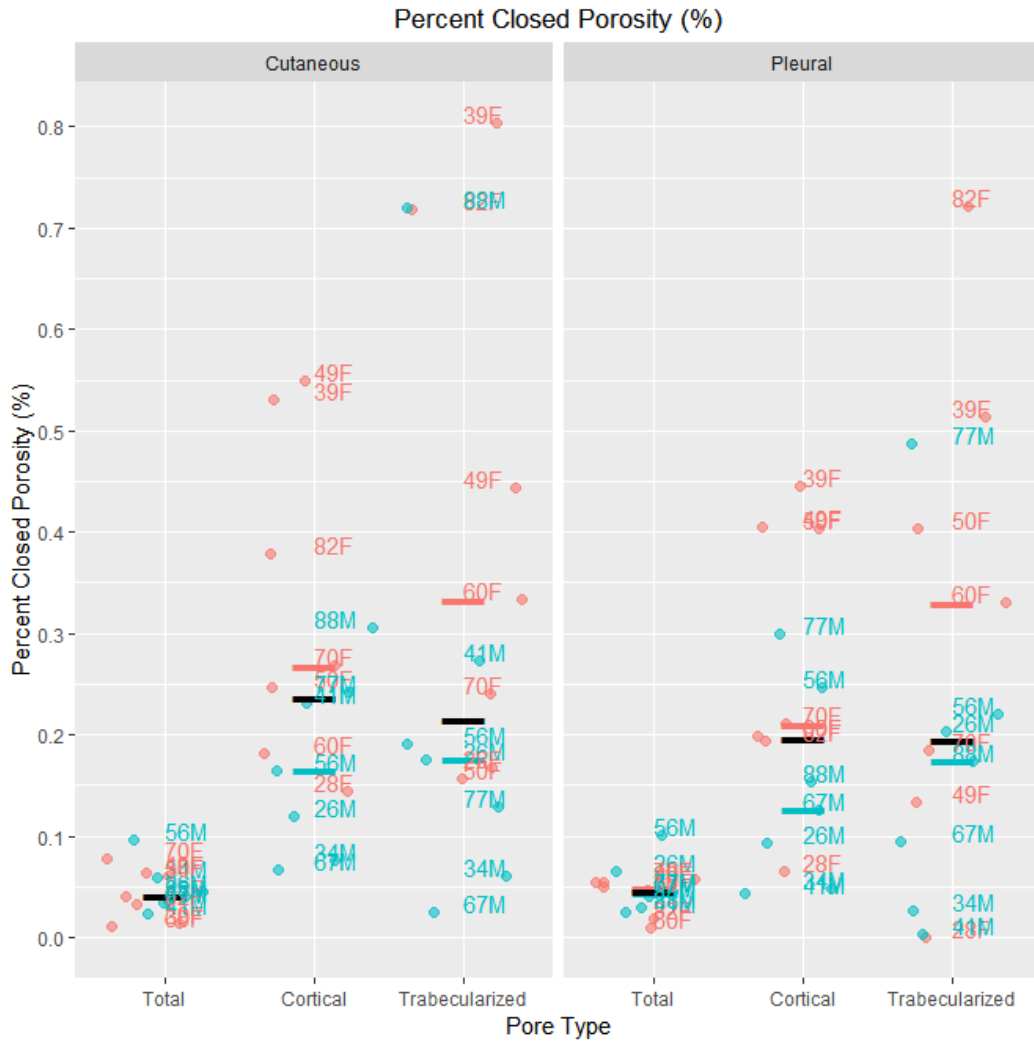
Table 7.105 Percent Open Porosity LMM

	numDF	denDF	F.value	p.value	cohen t	cohen df	cohen d
(Intercept)	1	39	142.2533	1.39E-14			
region	1	39	8.854431	*0.005*	2.97564	39	0.952967
type	1	39	0.253519	0.61744	0.503507	39	0.161251
age	1	6	2.487187	0.16585	-0.59235	6	-0.48365
cs.th	1	6	0.102962	0.759186	-1.11743	6	-0.91237
sex	1	6	2.986794	0.134683	1.806904	6	1.475331
region:type	1	39	3.350268	0.074844	-1.83037	39	-0.58619
age:cs.th	1	6	0.326122	0.588686	0.602302	6	0.491778
age:sex	1	6	0.23494	0.645071	-1.63751	6	-1.33702
cs.th:sex	1	6	0.606924	0.465555	-1.66891	6	-1.36266
age:cs.th:sex	1	6	2.206986	0.187932	1.485593	6	1.212982
Marginal R2	0.313096						
Conditional R2	0.487678						
Shapiro-Wilk Normality	0.298639						

Significant values (p < 0.05) are ***bolded***

Figure 7.50 Medians of Percent Open Porosity Distribution by Cortex
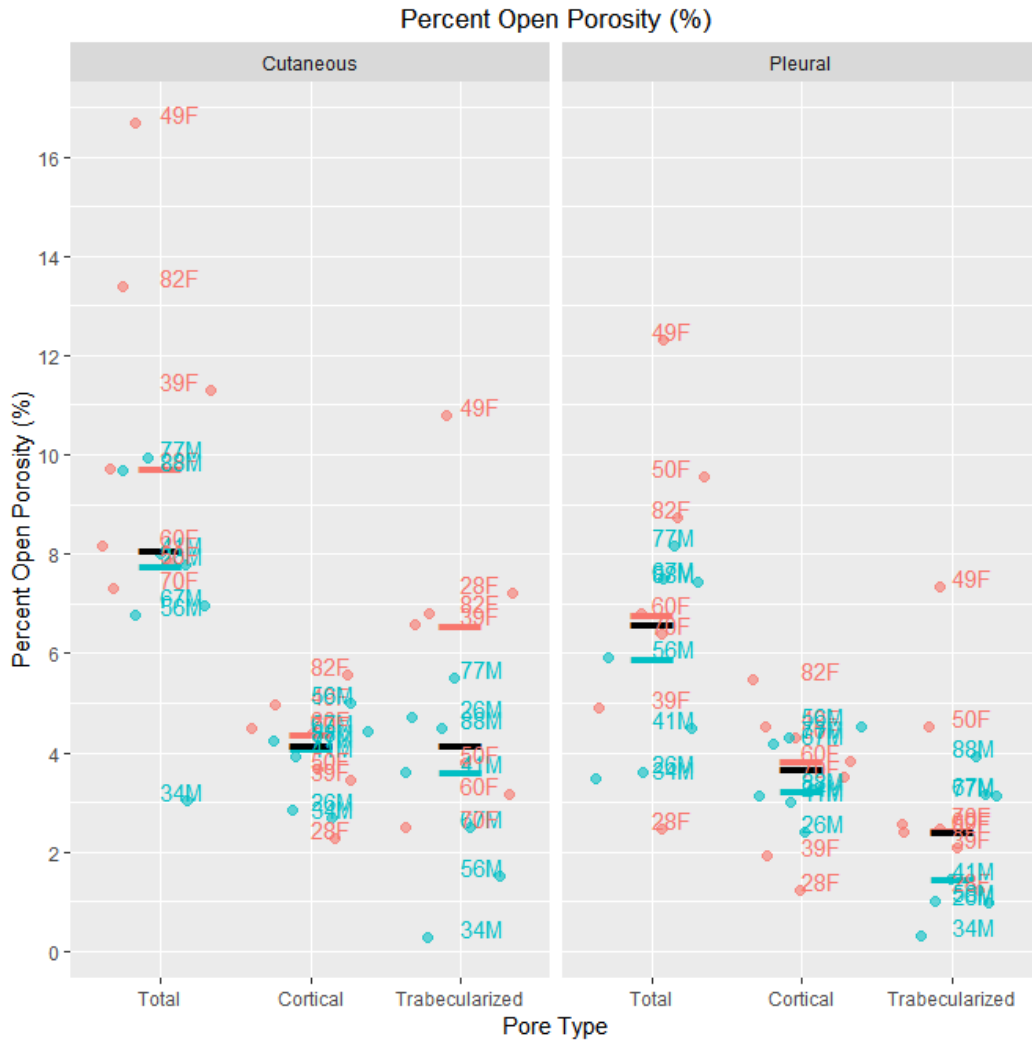
Significant Differences:
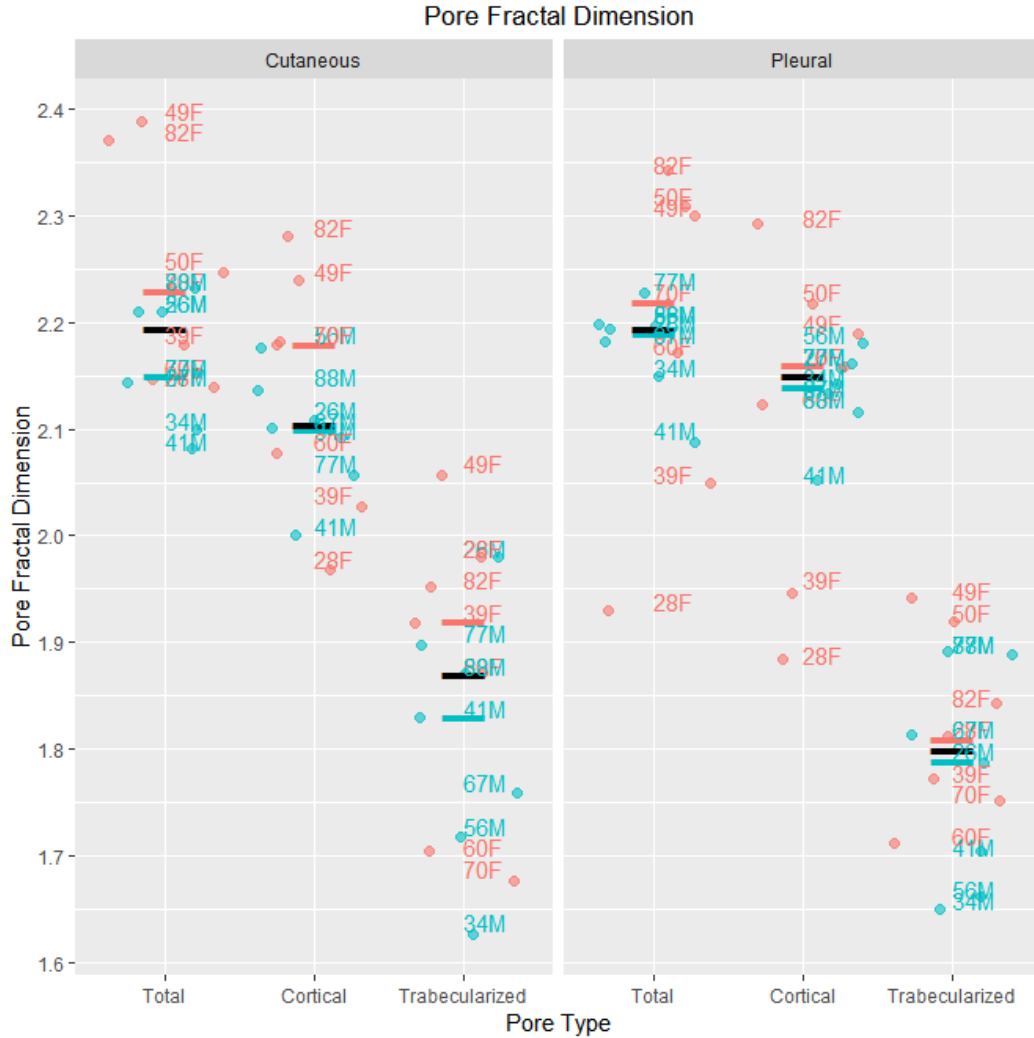
- The cutaneous cortex exceeds the pleural cortex in percent open porosity

- The reduced trabecularized porosity in the pleural cortex in respect to the cutaneous cortex approaches, but does not reach (p = 0.074844) significance

353

Table 7.106 Percent Porosity LMM

	numDF	denDF	F.value	p.value	cohen t	cohen df	cohen d
(Intercept)	1	39	153.9042	4.11E-15			
region	1	39	9.516214	*0.003734*	3.084836	39	0.987938
type	1	39	0.138426	0.711865	0.372057	39	0.119153
age	1	6	2.899828	0.139482	-0.70918	6	-0.57904
cs.th	1	6	0.056688	0.819732	-1.24401	6	-1.01573
sex	1	6	3.702843	0.102656	1.907143	6	1.557176
region:type	1	39	3.415847	0.072167	-1.8482	39	-0.5919
age:cs.th	1	6	0.411663	0.544842	0.736409	6	0.601276
age:sex	1	6	0.300653	0.60326	-1.69661	6	-1.38527
cs.th:sex	1	6	0.812237	0.402185	-1.74464	6	-1.4245
age:cs.th:sex	1	6	2.30471	0.179781	1.518127	6	1.239546
Marginal R2	0.341261						
Conditional R2	0.517941						
Shapiro-Wilk Normality	0.427869						

Significant values (p < 0.05) are ***bolded***

Figure 7.51 Medians of Percent Porosity Distribution by Cortex
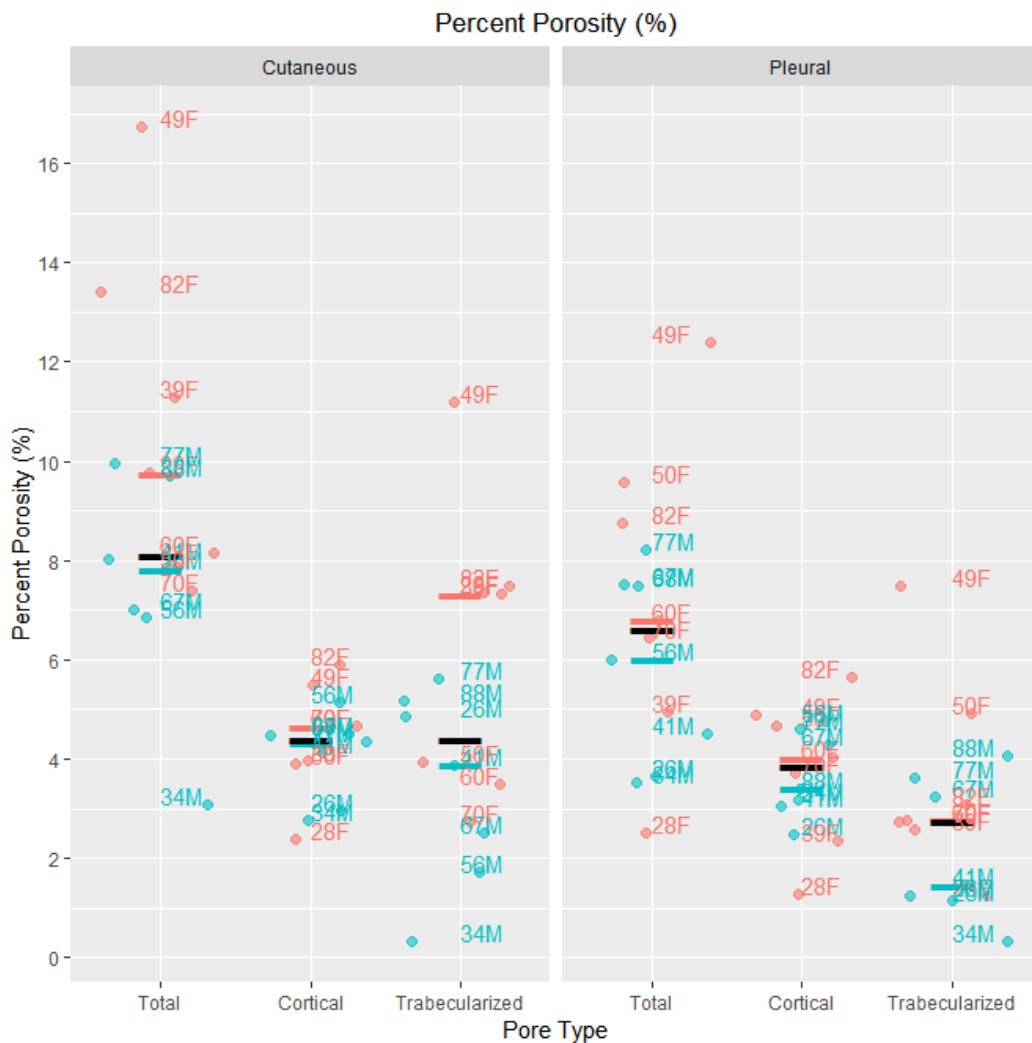
Percent Porosity (%)

Significant Differences:

- The cutaneous cortex exceeds the rib in percent open porosity

- The interaction between region and type, with respect to the reduced trabecularized porosity in the pleural cortex, approaches, but does not reach (p = 0.072167) significance

355

Table 7.107 Pore Thickness LMM

	numDF	denDF	F.value	p.value	cohen t	cohen df	cohen d
(Intercept)	1	39	1095.185	0			
region	1	39	0.493046	0.486742	0.702172	39	0.224875
type	1	39	389.3658	*0*	-19.7324	39	-6.31941
age	1	6	1.097732	0.335124	0.755815	6	0.61712
cs.th	1	6	14.97193	*0.008272*	0.92541	6	0.755594
sex	1	6	0.153521	0.708731	1.355017	6	1.106367
region:type	1	39	0.386133	0.537955	-0.6214	39	-0.19901
age:cs.th	1	6	0.411134	0.545093	-0.75969	6	-0.62029
age:sex	1	6	0.421597	0.540185	-1.78444	6	-1.45699
cs.th:sex	1	6	0.802002	0.404989	-1.36789	6	-1.11688
age:cs.th:sex	1	6	3.362816	0.116374	1.833798	6	1.49729
Marginal R2	0.882092						
Conditional R2	0.882092						
Shapiro-Wilk Normality	*0.001435*						

Significant values (p < 0.05) are ***bolded***

Table 7.108 Pore Thickness: PQL Correction

	Value	Std.Error	DF	t.value	p.value	cohen t	cohen df	cohen d
(Intercept)	3.790804	0.422788	39	8.966207	5.12E-11			
region1	0.019685	0.04141	39	0.475355	0.637185	0.475355	39	0.152236
type1	-0.69853	0.04141	39	-16.8685	*1.63E-19*	-16.8685	39	-5.40225
age	0.011459	0.007809	6	1.467498	0.192613	1.467498	6	1.198207
cs.th	0.000925	0.0005	6	1.847742	0.114147	1.847742	6	1.508675
sex1	0.887128	0.421198	6	2.106205	0.07979	2.106205	6	1.719709
region1:type1	-0.01531	0.04141	39	-0.36963	0.713661	-0.36963	39	-0.11837
age:cs.th	-1.58E-05	1.01E-05	6	-1.56071	0.169614	-1.56071	6	-1.27431
age:sex1	-0.02164	0.007809	6	-2.77169	*0.03235*	-2.77169	6	-2.26307
R2	0.942664	0.0005	6	-2.08961	0.081642	-2.08961	6	-1.70616
age:cs.th:sex1	2.87E-05	1.01E-05	6	2.835875	*0.029728*	2.835875	6	2.315482

Significant values (p < 0.05) are ***bolded***

357

Figure 7.52 Medians of Distribution of Pore Thickness by Cortex
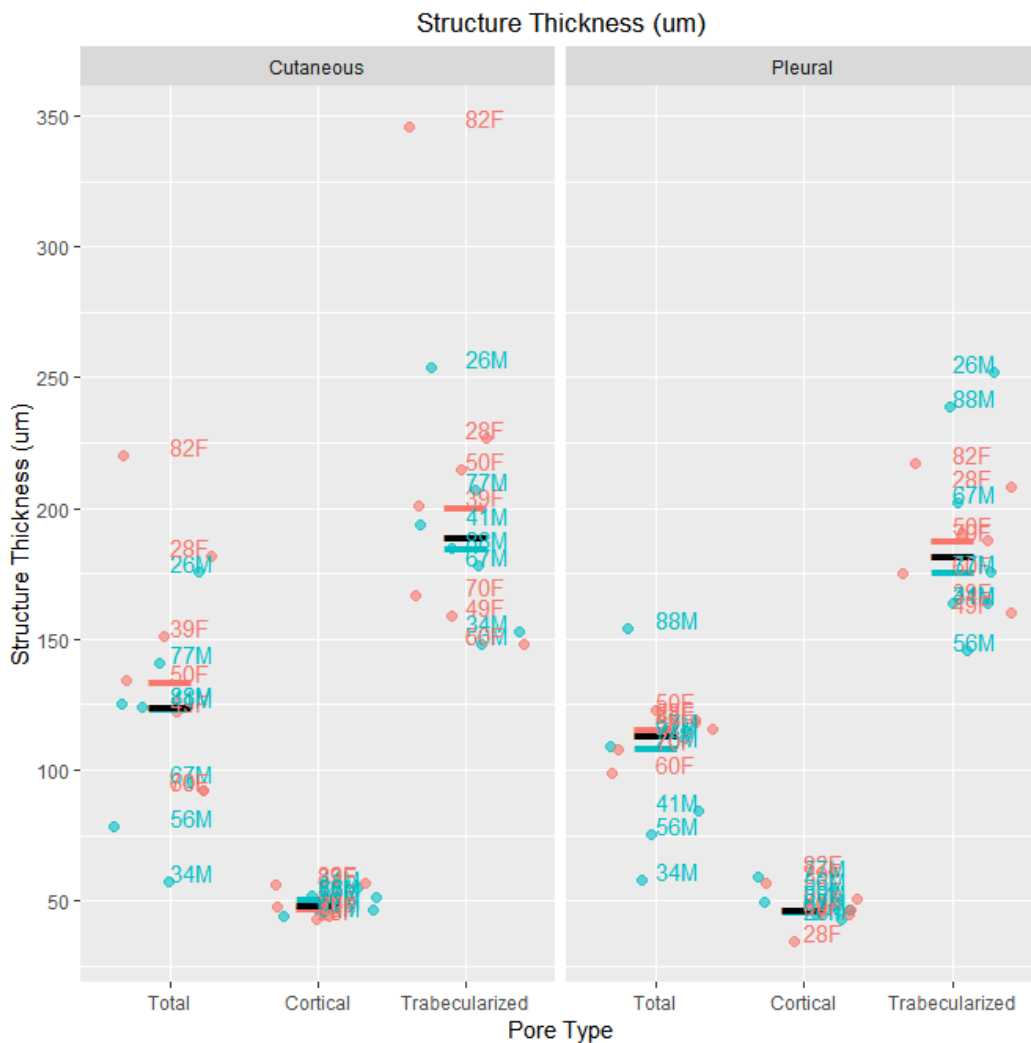
Significant Differences:

Trabecularized porosity has a significantly larger mean pore thickness than cortical porosity. However, the relative sizes of cortical and trabecularized porosity are equivalent between cortices.

Figure 7.53 Effects of Age and Cortical Thickness on Pore Thickness
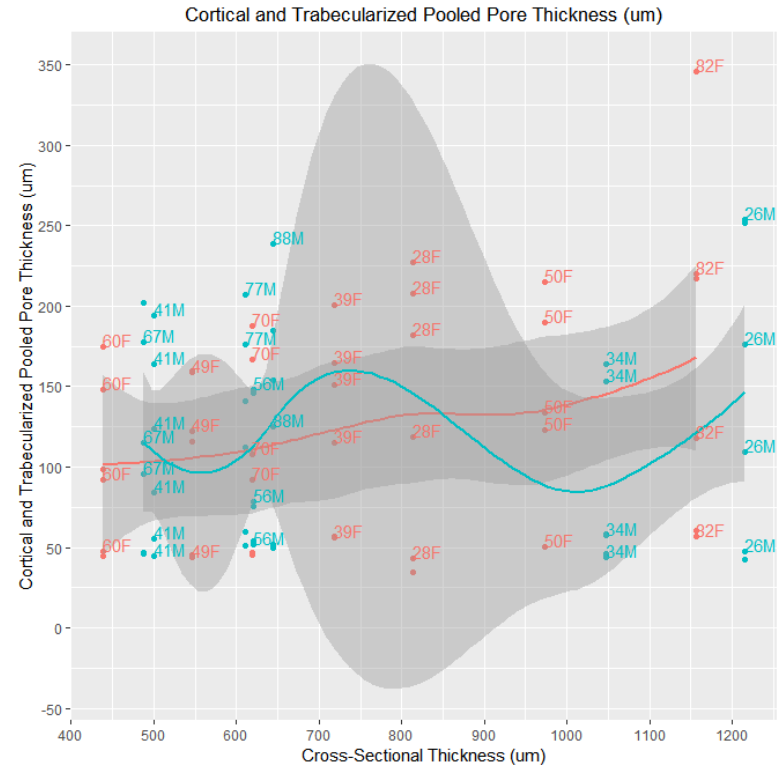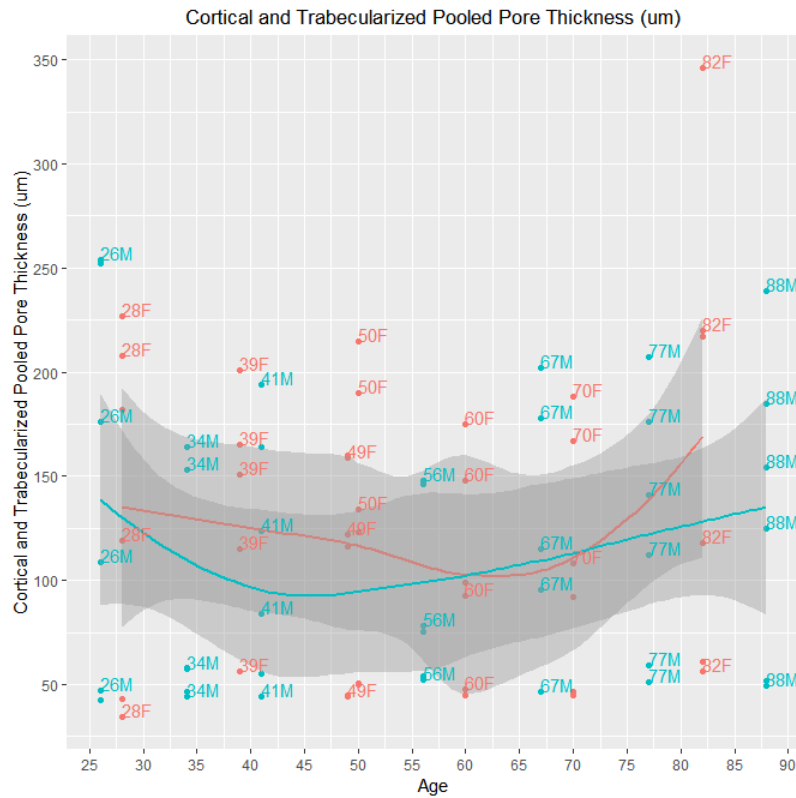
Significant Effects:

Pore thickness increases with age largely due female osteophyte

Driven by highly trabecularized shell of 82F

Table 7.109 Pore Separation (Region Only) LMM

	numDF	denDF	F.value	p.value	cohen t	cohen df	cohen d
(Intercept)	1	13	757.1584	6.57E-13			
region	1	13	8.28265	*0.012944*	-2.87796	13	-1.5964
age	1	6	6.208099	*0.04706*	0.096036	6	0.078413
cs.th	1	6	1.135959	0.327506	0.993915	6	0.811529
sex	1	6	0.000381	0.98507	-0.72419	6	-0.5913
age:cs.th	1	6	0.140763	0.720429	-0.36896	6	-0.30125
age:sex	1	6	3.195277	0.124076	0.588206	6	0.480268
cs.th:sex	1	6	0.544859	0.488281	1.040645	6	0.849683
age:cs.th:sex	1	6	0.680579	0.440945	-0.82497	6	-0.67359
Marginal R2	0.44895						
Conditional R2	0.72405						
Shapiro-Wilk Normality	0.059622						

Significant values (p < 0.05) are ***bolded***

360

Figure 7.54 Medians of Distribution of Pore Separation by Cortex
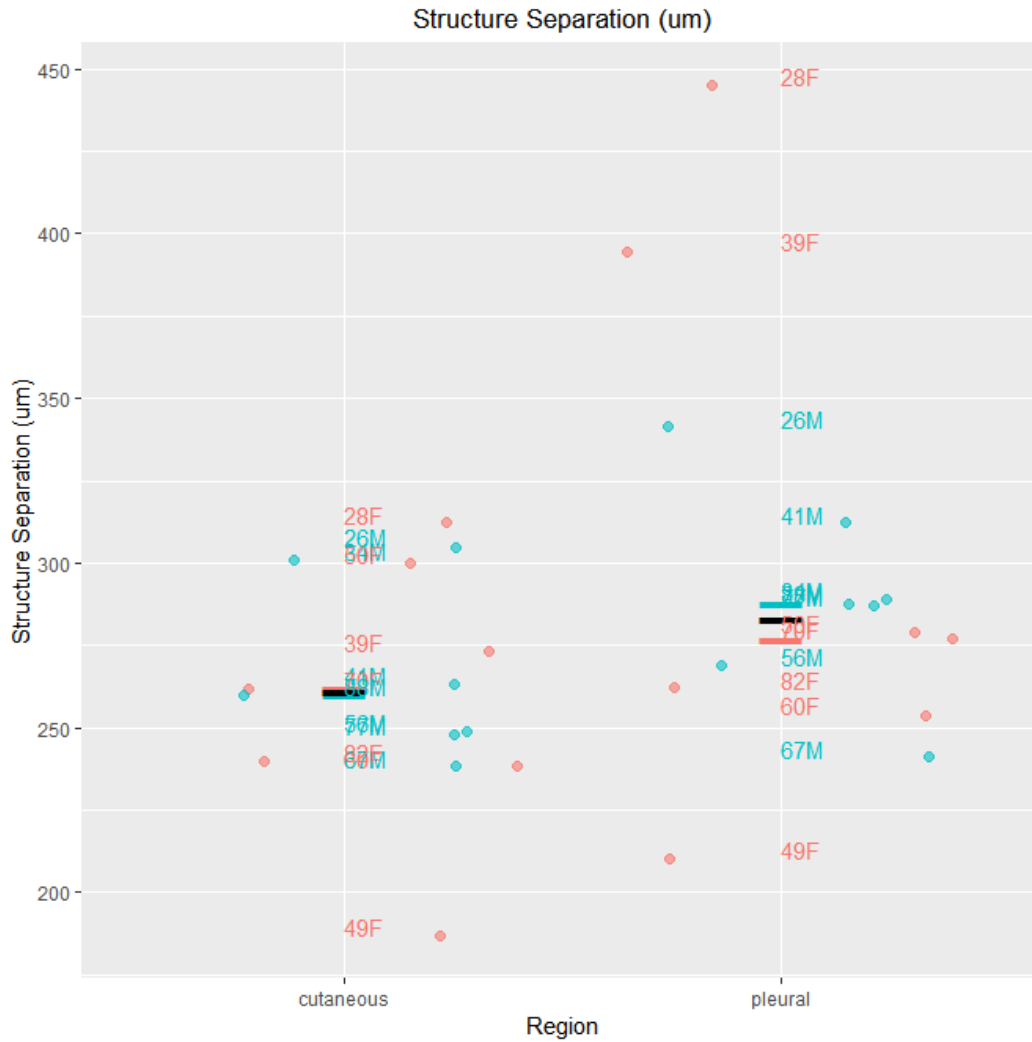
Significant Differences:

Pores are significantly further apart in the pleural cortex.

Figure 7.55 Age Effects on Pore Separation by Cortex
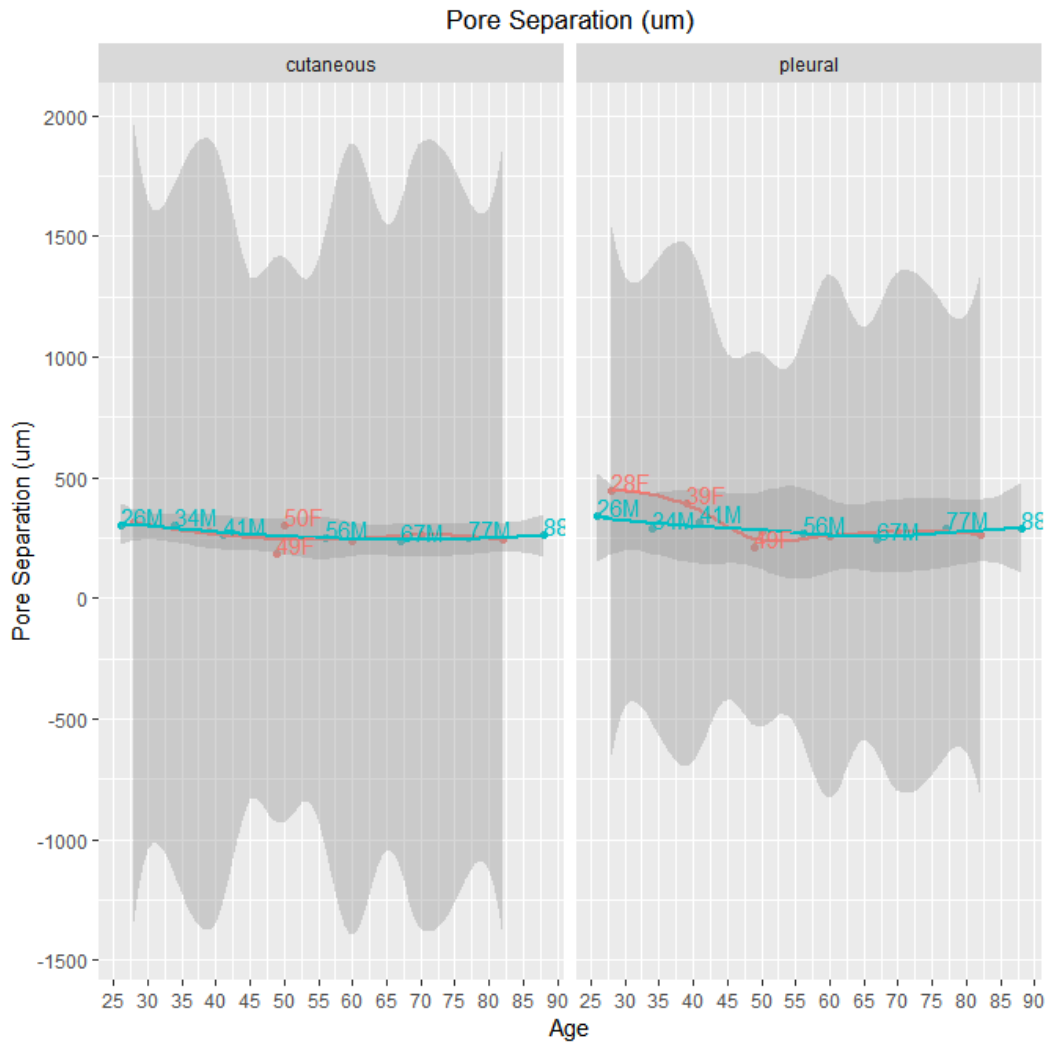
Significance Differences:

Pore separation decreases significantly with age, although the model is weak.

Table 7.110 Pore Linear Density LMM

	numDF	denDF	F.value	p.value	cohen t	cohen df	cohen d
(Intercept)	1	39	191.3686	1.11E-16			
region	1	39	8.786007	*0.005154*	2.96412	39	0.949278
type	1	39	371.9621	*0*	19.28632	39	6.176565
age	1	6	2.71724	0.150366	-0.24693	6	-0.20161
cs.th	1	6	0.981362	0.360116	-0.91135	6	-0.74412
sex	1	6	1.69846	0.240264	1.106645	6	0.903572
region:type	1	39	0.016421	0.898694	0.128144	39	0.041039
age:cs.th	1	6	0.054946	0.822464	0.356777	6	0.291307
age:sex	1	6	0.379124	0.560688	-0.92465	6	-0.75497
cs.th:sex	1	6	0.478464	0.514979	-1.15327	6	-0.94164
age:cs.th:sex	1	6	0.931205	0.371817	0.96499	6	0.787911
Marginal R2	0.785365						
Conditional R2	0.897008						
Shapiro-Wilk Normality	0.956215						

Significant values (p < 0.05) are ***bolded***

363

Figure 7.56 Medians of Distribution of Pore Linear Density by Cortex
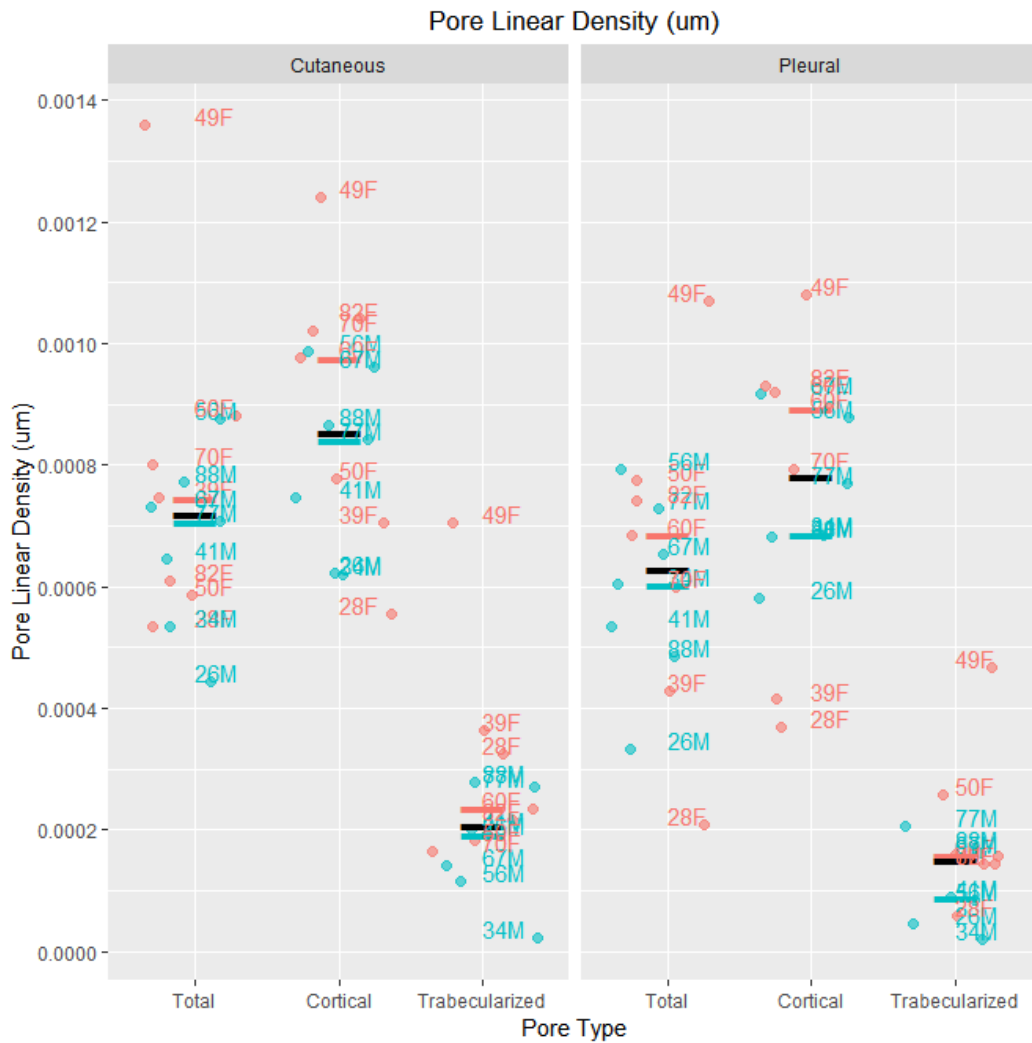
Significant Differences:

- The cutaneous cortex has a significantly higher linear density in regards to both cortical and trabecularized pores.

- Cortical pores have a significantly higher linear density than trabecularized pores.

364

Table 7.111 Pore Fragmentation Index LMM

	numDF	denDF	F.value	p.value	cohen t	cohen df	cohen d
(Intercept)	1	39	2711.267	0			
region	1	39	0.419251	0.521104	-0.6475	39	-0.20736
type	1	39	951.3751	**0**	30.84437	39	9.878103
age	1	6	1.085786	0.337561	-0.6183	6	-0.50484
cs.th	1	6	4.594473	0.075786	-0.69742	6	-0.56944
sex	1	6	0.614621	0.46287	-0.87484	6	-0.7143
region:type	1	39	2.043577	0.160812	-1.42954	39	-0.45782
age:cs.th	1	6	0.64926	0.451122	0.663442	6	0.541698
age:sex	1	6	1.160385	0.322779	1.308103	6	1.068062
cs.th:sex	1	6	1.257086	0.305062	0.787516	6	0.643004
age:cs.th:sex	1	6	1.687376	0.24163	-1.29899	6	-1.06062
Marginal R2	0.93549						
Conditional R2	0.947213						
Shapiro-Wilk Normality	0.453363						

Significant values (p < 0.05) are ***bolded***

Figure 7.57 Medians of Distribution of Pore Fragmentation Index by Cortex

Pore Fragmentation Index (1/um)
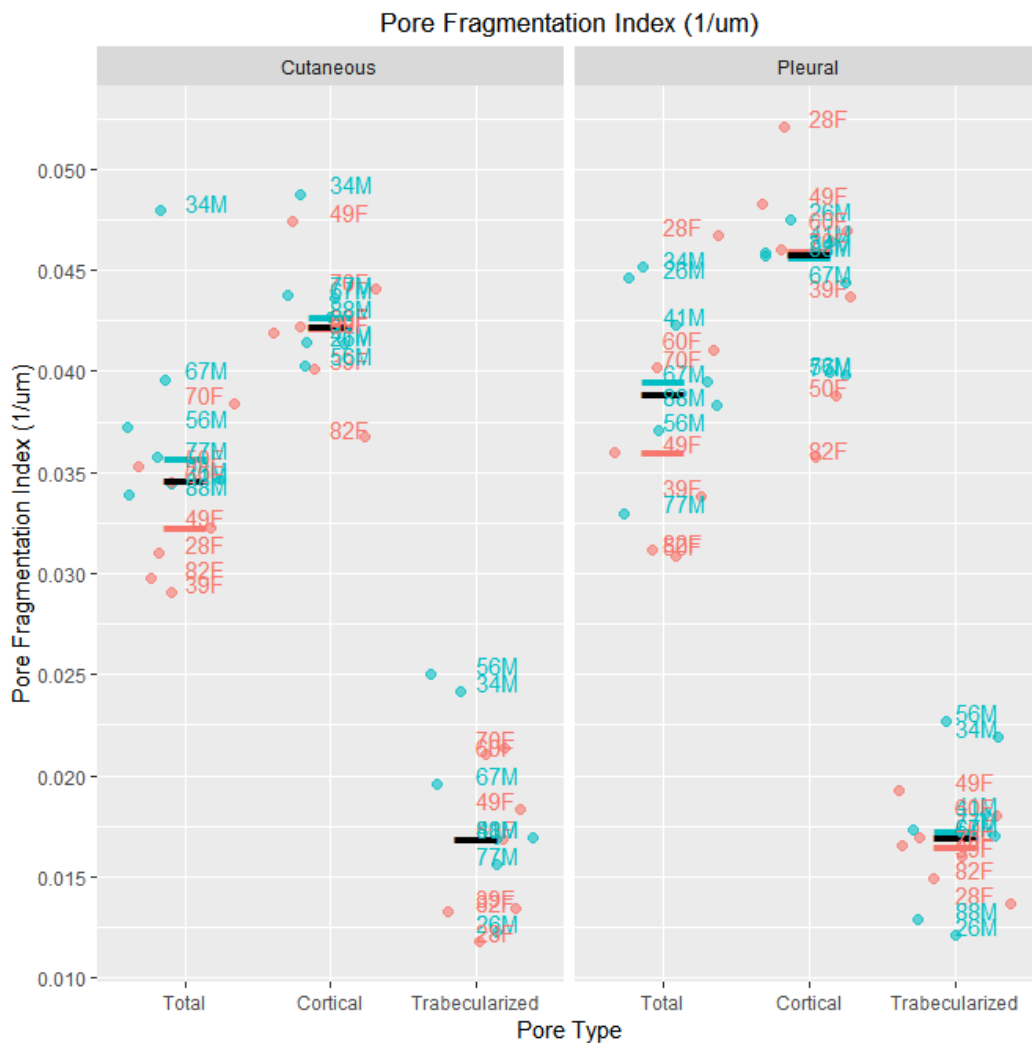
Significant Differences:

Cortical Pores are significantly more separated ("strut-like") than trabecularized

pores ("node-like") in both cortices.

Figure 7.58 Degree of Anisotropy LMM

	numDF	denDF	F.value	p.value	cohen t	cohen df	cohen d
(Intercept)	1	39	1348.759	0			
region	1	39	0.048274	0.82724	-0.21971	39	-0.07036
type	1	39	565.582	*0*	23.78197	39	7.616325
age	1	6	3.35501	0.116718	-0.05435	6	-0.04437
cs.th	1	6	4.107366	0.089074	0.449113	6	0.366699
sex	1	6	5.601499	0.055768	-0.36681	6	-0.2995
region:type	1	39	7.258465	*0.010353*	-2.69415	39	-0.86282
age:cs.th	1	6	0.102168	0.76008	-0.05128	6	-0.04187
age:sex	1	6	0.83933	0.394918	0.335094	6	0.273603
cs.th:sex	1	6	0.048165	0.833564	0.111391	6	0.090951
age:cs.th:sex	1	6	0.043342	0.841969	-0.20819	6	-0.16998
Marginal R2	0.881394						
Conditional R2	0.921242						
Shapiro-Wilk Normality	0.110327						

Significant values (p < 0.05) are ***bolded***

367

Figure 7.59 Medians of Degree of Anistotropy Distribution by Cortex
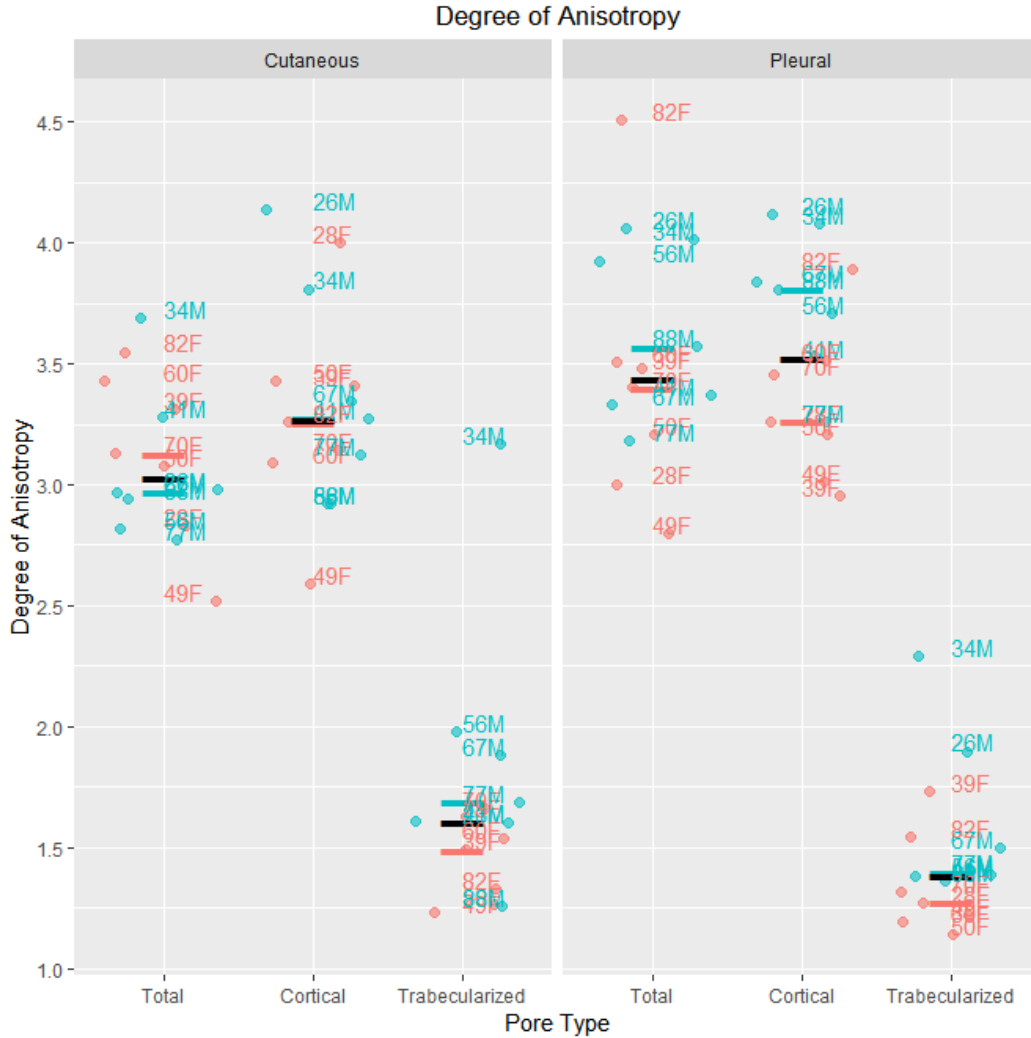
Significant Differences:

Cortical pores are significantly more anisotropic (directionally aligned) than trabecularized pores, and this difference is exacerbated in the pleural cortex.

Table 7.112 Pore Fractal Dimension LMM

	numDF	denDF	F.value	p.value	cohen t	cohen df	cohen d
(Intercept)	1	39	9228.945	0			
region	1	39	0.863007	*0.358613*	0.928982	39	0.297512
type	1	39	164.0388	*1.44E-15*	12.80776	39	4.101767
age	1	6	1.670147	0.243776	0.186437	6	0.152225
cs.th	1	6	2.124879	0.195194	0.013158	6	0.010743
sex	1	6	0.733486	0.424633	1.202813	6	0.982093
region:type	1	39	1.597757	0.213724	-1.26402	39	-0.40481
age:cs.th	1	6	0.001632	0.96909	-0.07826	6	-0.0639
age:sex	1	6	0.09834	0.764446	-1.20346	6	-0.98262
cs.th:sex	1	6	0.039603	0.84883	-1.14149	6	-0.93202
age:cs.th:sex	1	6	1.322931	0.293837	1.150187	6	0.939124
Marginal R2	0.689231						
Conditional R2	0.794916						
Shapiro-Wilk Normality	0.854138						

Significant values (p < 0.05) are *bolded*

369

Figure 7.60 Medians of Pore Fractal Dimension Distribution by Cortex

Significant Differences:

Cortical pores are significantly more complex in their patterning than trabecularized pores. This difference is emphasized in the pleural cortex.

370

Table 7.113 Connectivity Density LMM

	numDF	denDF	F.value	p.value	cohen t	cohen df	cohen d
(Intercept)	1	39	359.5754	0			
region	1	39	4.469038	*0.040962*	2.11401	39	0.677025
type	1	39	325.5514	*0*	18.04304	39	5.778399
age	1	6	12.98312	*0.011323*	0.802422	6	0.655175
cs.th	1	6	18.7464	*0.00493*	-0.58994	6	-0.48168
sex	1	6	0.18057	0.685701	0.223437	6	0.182435
region:type	1	39	3.952848	0.053844	1.988177	39	0.636726
age:cs.th	1	6	0.419867	0.540991	-0.4145	6	-0.33844
age:sex	1	6	1.67295	0.243425	-0.14181	6	-0.11579
cs.th:sex	1	6	0.048277	0.833374	-0.40543	6	-0.33104
age:cs.th:sex	1	6	0.121567	0.73925	0.348665	6	0.284684
Marginal R2	0.870021						
Conditional R2	0.870021						
Shapiro-Wilk Normality	0.646811						

Significant values ($p < 0.05$) are ***bolded***

371

Figure 7.61 Medians of Pore Connectivity Density Distribution by Cortex
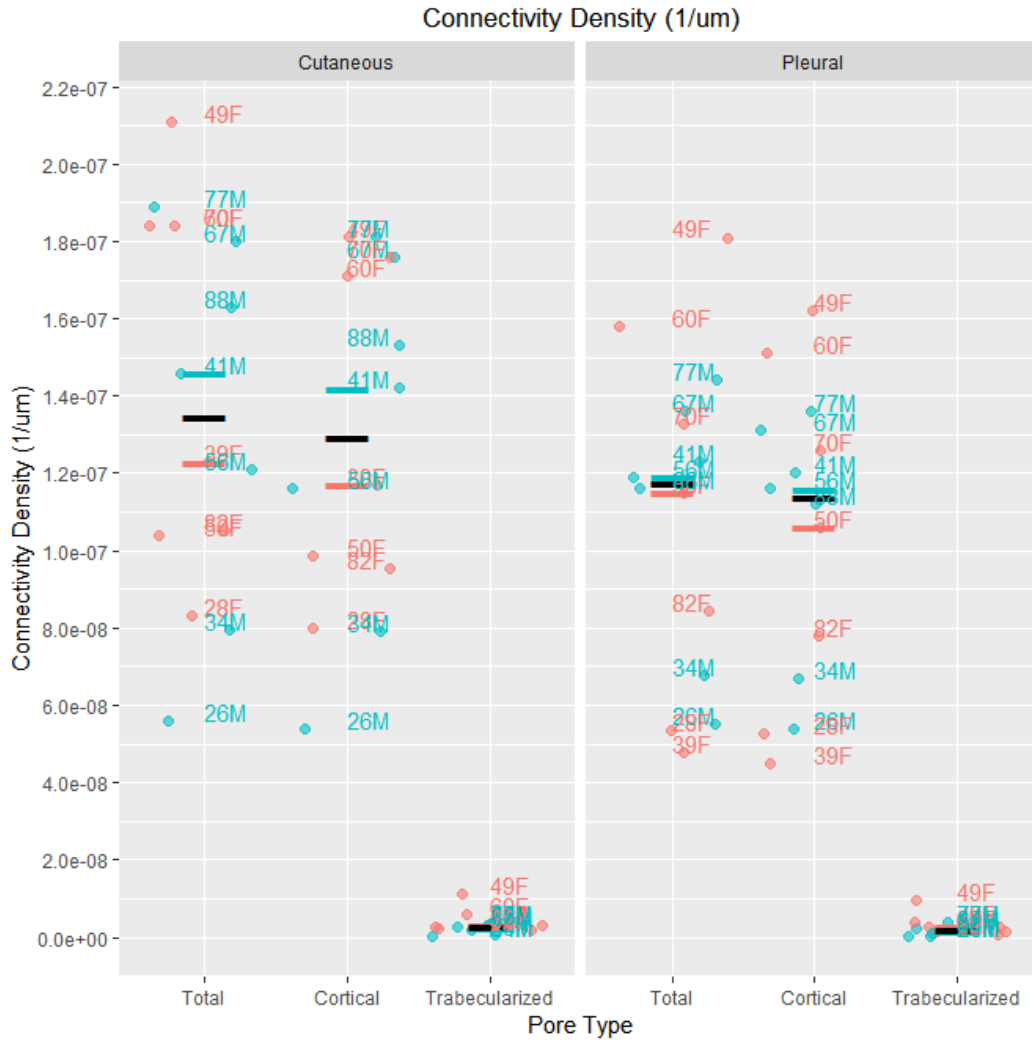
Significant Differences:

The cutaneous cortex has significantly more interconnection than the pleural cortex. Cortical pores have a significantly higher number of connections than trabecularized pores in both cortices. This is logical as trabecularized pores join by merging rather than by sending out transverse connections.

372

Figure 7.62 Pooled Pore Connectivity Density by Age
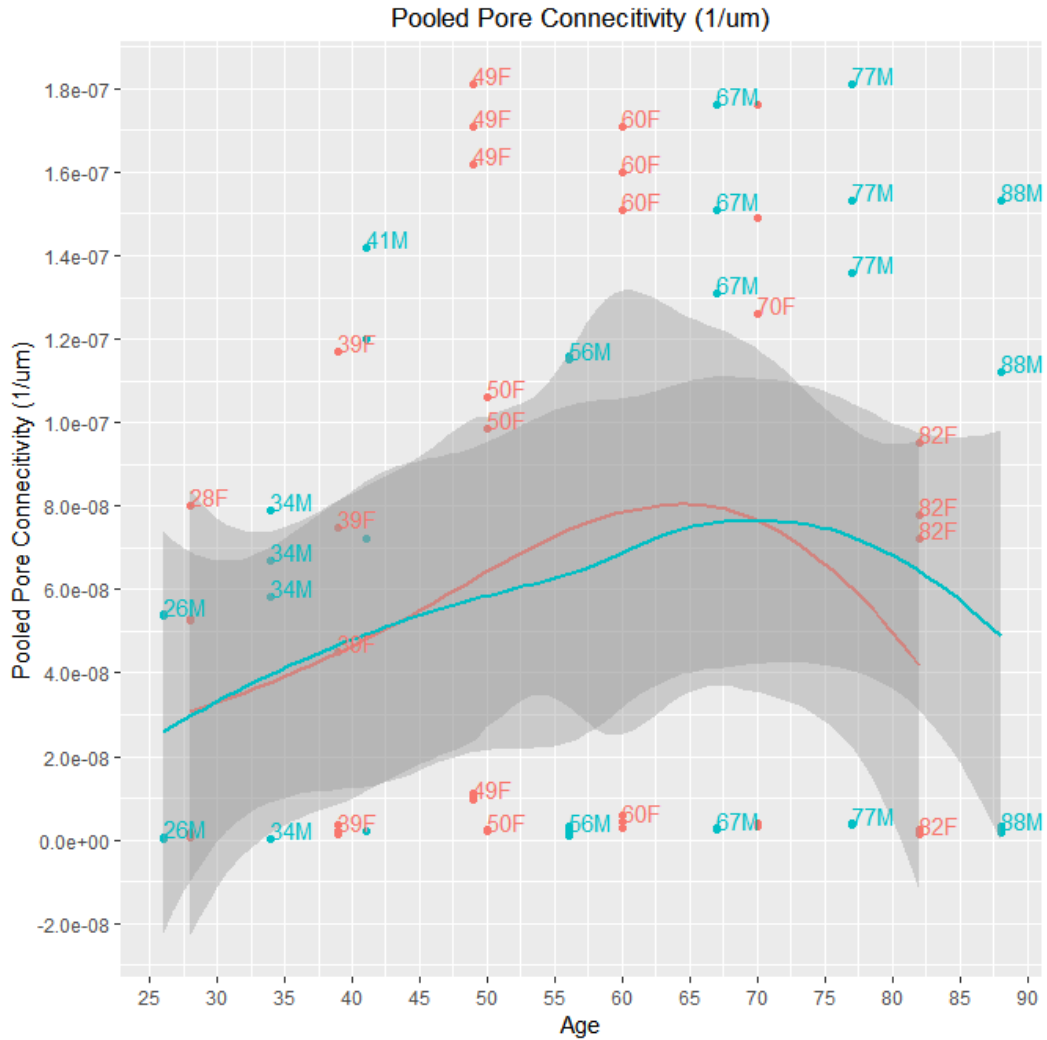
Significant Differences:

Pore connectivity increases in middle age, but then decreases again in old age as the resorbing cortex removes pore connections.

373

Figure 7.63 Pooled Pore Connectivity Density by Cortical Thickness

Pooled Pore Connecitivity (1/um)
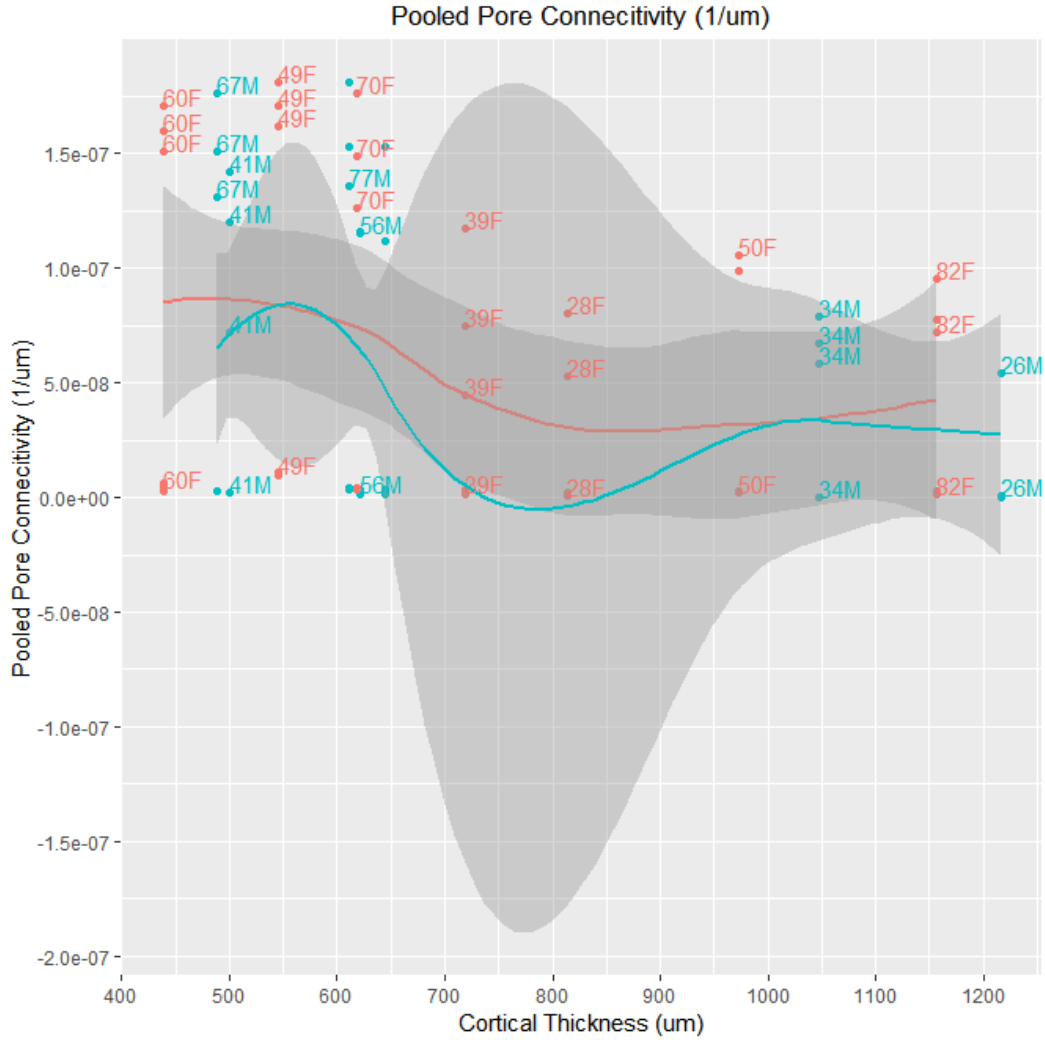
Significant Differences: Pore connectivity is reduced in a thicker cortex, potentially due to the absence of trabecularizing regions. Note the higher connectivity among older individuals with thicker cortices.

374

Table 7.114 Proportion Open Pores

	numDF	denDF	F.value	p.value	cohen t	cohen df	cohen d
(Intercept)	1	39	4558.662	0			
region	1	39	0.269337	0.60671	0.518977	39	0.166206
type	1	39	0.142534	0.707822	0.377536	39	0.120908
age	1	6	0.594301	0.470019	0.833771	6	0.680772
cs.th	1	6	1.669931	0.243803	0.549622	6	0.448764
sex	1	6	1.003764	0.355079	-0.33056	6	-0.2699
region:type	1	39	0.519183	0.475487	-0.72054	39	-0.23076
age:cs.th	1	6	0.003821	0.952717	-0.83688	6	-0.68331
age:sex	1	6	0.000928	0.976692	-0.01994	6	-0.01628
cs.th:sex	1	6	0.939307	0.369885	0.225304	6	0.18396
age:cs.th:sex	1	6	0.021454	0.888347	0.14647	6	0.119593
Marginal R2	0.121985						
Conditional R2	0.306754						
Shapiro-Wilk Normality	0.261907						

Significant values ($p < 0.05$) are ***bolded***

No significant differences are found between cortices or pore types in the proportion of open vs closed pores.

375

Figure 7.64 Medians of Proportion of Open Pores by Cortex
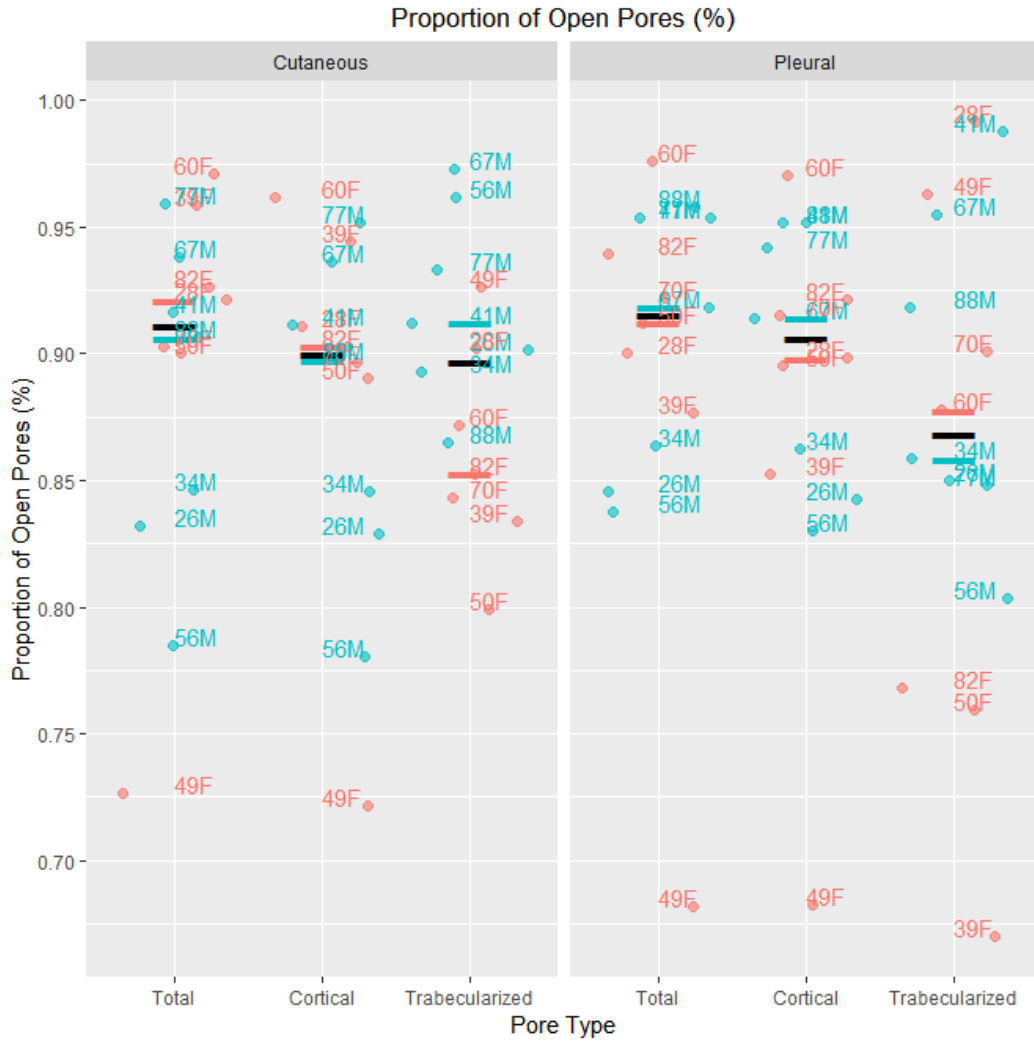
Table 7.115 Pore Density LMM

	numDF	denDF	F.value	p.value	cohen t	cohen df	cohen d
(Intercept)	1	39	207.7976	0			
region	1	39	1.602388	0.213075	1.265855	39	0.405398
type	1	39	315.4434	*0*	17.76073	39	5.687985
age	1	6	4.062506	0.090454	0.157015	6	0.128202
cs.th	1	6	12.08806	*0.013194*	-0.86716	6	-0.70803
sex	1	6	0.662539	0.446757	0.598339	6	0.488542
region:type	1	39	1.239218	0.272436	1.113202	39	0.35651
age:cs.th	1	6	0.627944	0.458288	0.057522	6	0.046967
age:sex	1	6	0.922189	0.373985	-0.30283	6	-0.24726
cs.th:sex	1	6	0.754807	0.41835	-0.66308	6	-0.5414
age:cs.th:sex	1	6	0.133675	0.727196	0.365616	6	0.298524
Marginal R2	0.844657						
Conditional R2	0.867602						
Shapiro-Wilk Normality	0.513587						

Significant values (p < 0.05) are ***bolded***

377

Figure 7.65 Medians of Proportion of Pore Density by Cortex

Significant Differences:

Cortical pores have a significantly higher density than trabecularized pores in both cortices.

378

Figure 7.66 Pooled Pore Density by Cortical Thickness
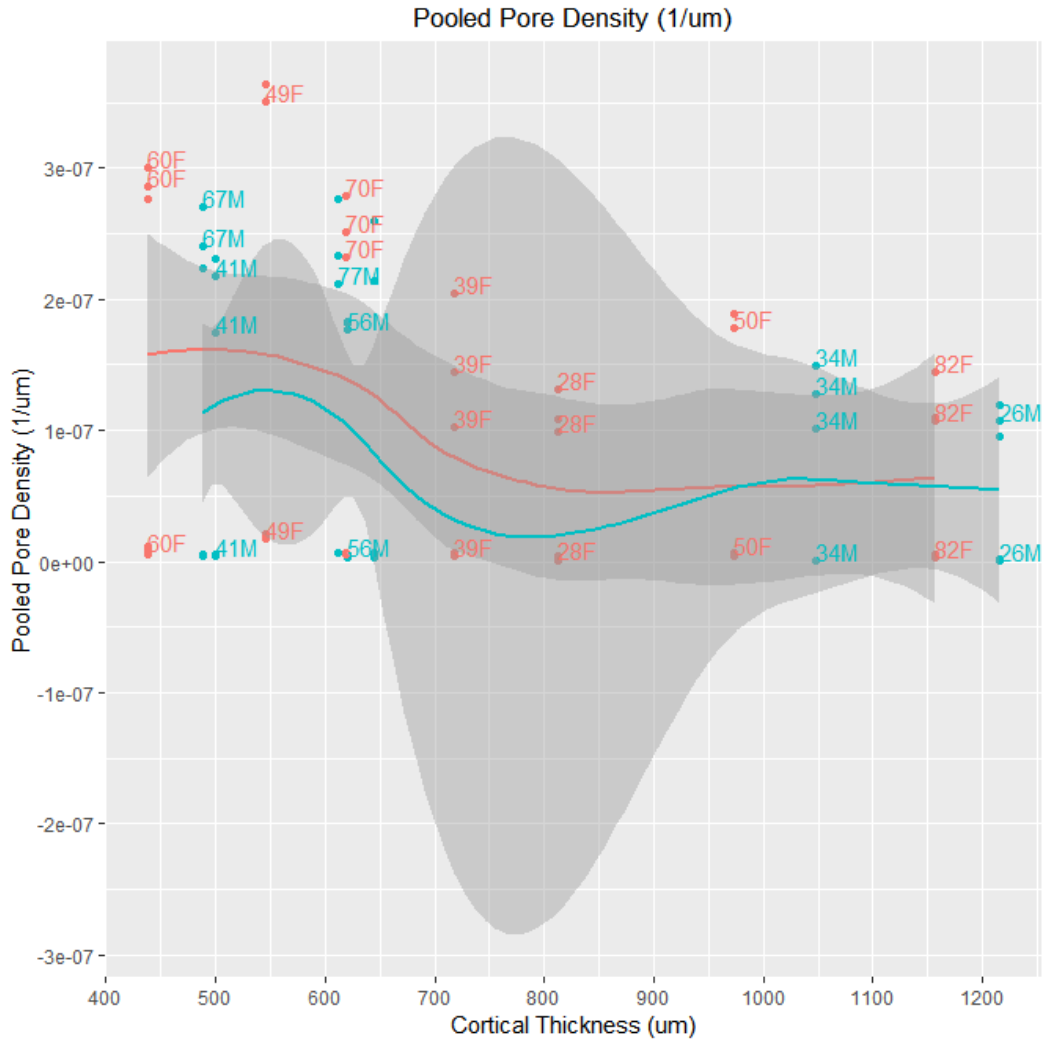
Significant Differences:

Pore density is reduced in a thicker cortex. Thinner cortices are associated with older, more porous individuals.

Table 7.116 Standard Deviation of Pore Separation (Region Only) LMM

	numDF	denDF	F.value	p.value	cohen t	cohen df	cohen d
(Intercept)	1	13	893.7559	2.27E-13			
region	1	13	3.568395	0.081401	-1.88902	13	-1.04784
age	1	6	6.125606	*0.048131*	-0.14434	6	-0.11785
cs.th	1	6	0.006384	0.938916	0.744693	6	0.608039
sex	1	6	0.180618	0.685662	-1.20048	6	-0.98019
age:cs.th	1	6	0.044816	0.839351	-0.12202	6	-0.09963
age:sex	1	6	4.714942	0.072922	1.1191	6	0.913742
cs.th:sex	1	6	0.623998	0.459636	1.622644	6	1.324884
age:cs.th:sex	1	6	2.048792	0.202287	-1.43136	6	-1.1687
Marginal R2	0.440879						
Conditional R2	0.659355						
Shapiro-Wilk Normality	0.07641						

Significant values (p < 0.05) are ***bolded***

Figure 7.67 Medians of Distribution of Pore Separation by Cortex

Significant Differences:

In addition to have significantly more separation between pore systems on average, the pleural cortex has a significantly wider range of distances between networks.

Figure 7.68 Age Effects on Standard Deviation of Pore Separation by Cortex
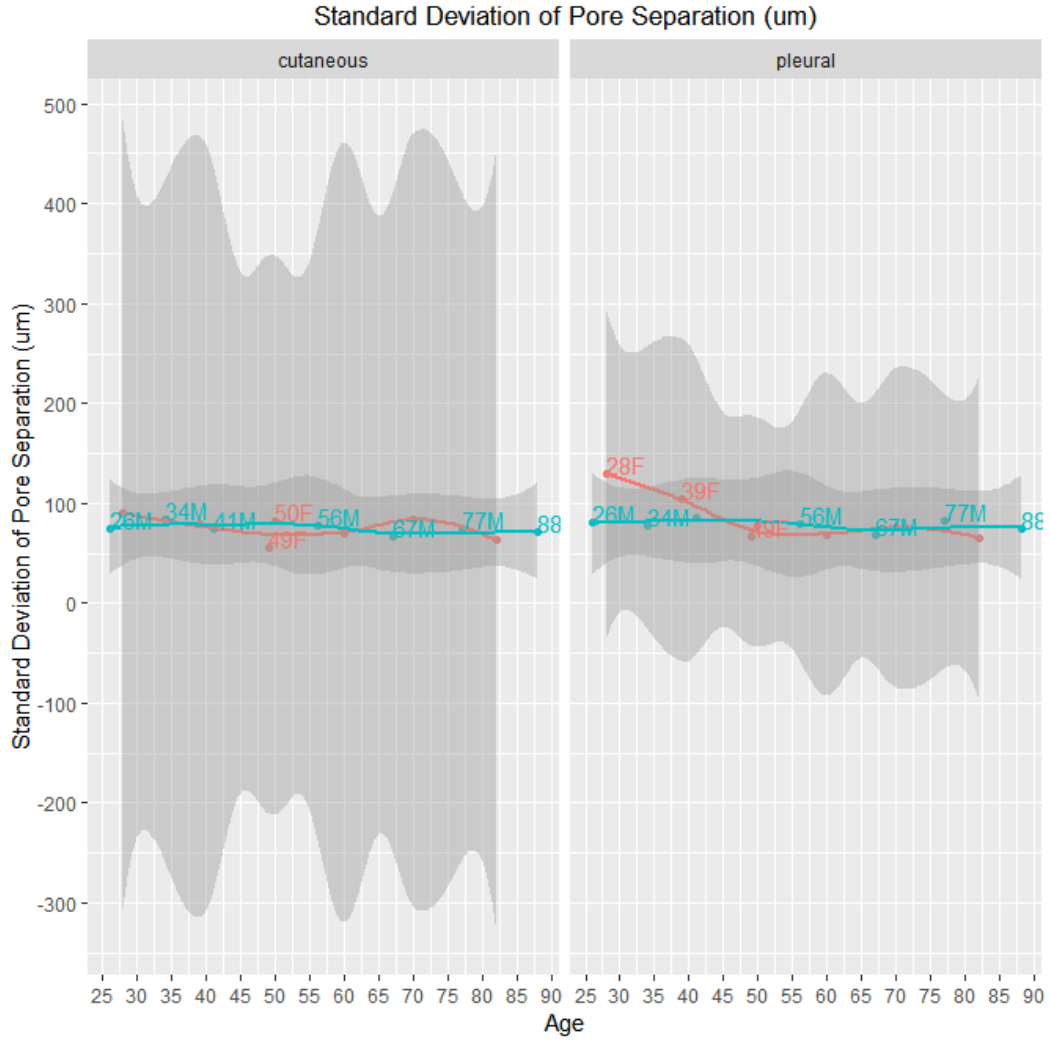
Significant Differences:

The range of distances between pores decreases significantly with age.

382

8. Discussion: The Structure-Strain Model Confirmed

8.1. Methodological Considerations and Limitations

8.1.1. *Sample Size*

The sample size in this study was limited to 14 individuals. Sample movement of one segment of four femoral necks led to the temporary exclusion of four of the femoral necks, reducing the femoral neck subsample to 10 individuals. Therefore, the conclusions in this chapter are generalized from a small group of individuals. However, the trends in pore morphometry displayed by these individuals are consistent with mechanical predictions and with previous findings on related aspects of pore morphometry in the femoral neck. Additionally, linear mixed models were employed as statistical tests, and checked and corrected for normality of residuals, to reduce the potential effects of outliers. These LMM tests are more robust to an unbalanced sample design than the traditional ANCOVA. Thus, it was possible to include unequal numbers of males and females, and of femoral necks and ribs. Future work will seek to expand the sample size by accumulating a wider range of ages, including subadults and more than one male and one female per age group.

383

8.2. Automated Analysis

The automated approach developed for this study is a morphological smoothing routine that isolates large trabecular spaces composing the marrow cavity. The routine then trims the irregular strut-like projections of trabeculae into the marrow space, and clips off the irregular blob-like extensions of trabecularizing pores into the cortex. The same routine is applied uniformly to all samples, including the thresholds of pixel sizes required to remove a trabecular strut or trabecularizing pore.

The only morphological operation on the cortex itself is the initial morphological closing to seal cortical pores and prevent them from being ROI shrink-wrapped with trabecular spaces. The pixel thresholds were developed by the author applying the routine to a substack of all samples in this study, and modifying pixel thresholds until they were sufficient to remove trabecular struts and seal the cortex for all samples. A threshold of 30 pixels for morphological closing was sufficient to visibly seal the cortex for all samples. Another advantage to this routine is that it only smooths protrusions and extensions. The exact topography of adjoining regions of the endocortical border is preserved. Consequently, it is not possible to remove more irregularity than exists. In other words, if one sample has a 10-pixel wide trabecular strut, and another sample has a 20 pixel wide trabecular strut, they will both be equally removed by a morphological closing threshold that closes all gaps up to 30 pixels. The routine will not "cut into" the cortex of the sample with smaller trabeculae, because the

384

morphological operations are being performed on an isolated marrow space. The gaps in very thick linear pore structures that appear on some of the morphological images are spaces where huge trabecularizing pores have physically merged with the marrow cavity. Future refinement of this method might consider machine learning for deciding when to smooth over these regions.

A validation with manual endosteal outlining has not yet been performed for this methodology, although it is planned for immediate extension of the project. At this time, it can be said that comparisons between individuals are consistent, because they are all processed with an identical morphological bounding routine.

8.3. Consideration of Subject Health Complications

While no individuals displayed direct trauma or pathology to the studied right femoral neck or right fourth rib, several individuals had health complications with the potential to affect bone microstructure. The individuals in this sample were randomly selected from the availability of the OSU Body Donation Program, given their match for the required age and sex. The only pathological exclusion conditions were direct trauma or pathology to the right femoral neck. Therefore, any irregularities in the pore network were not known until after sample processing and micro-CT imaging.

Two older individuals (70F and 82F) presented with normal ribs but significant anterior to superior-anterior porosity in the right femoral neck cortex, especially in regions that appeared to be marginal apposition (either osteophyte or enthesophyte). One relatively younger individual (49F) presented with extensive

385

intra-cortical resorption in both the femoral neck and rib, but without bone apposition. This is likely related to her right trans-tibial amputation, as detailed below.

All individuals in this sample were "normal" based on total body DXA scans, but reduced bone mass in the femoral neck specifically was found for 49F (right and left side osteopenia), 60F (right side osteopenia), and 70F (right and left side osteopenia). Although these individuals might have been excluded from the study were a larger sample size available, this would be less representative of a truly random age series. Selecting out individuals with osteoporosis, for example, would exclude the one in three women and one in five men over age 50 who will experience at least one osteoporotic fracture (Melton et al., 1992; Melton et al., 1998; Kanis et al., 2000). Instead, it was decided to leave these individuals in the sample as examples of the range of human variation in bone loss with age. Collection of a larger age-series in future work will increase sample diversity and reduce the effect of these outliers on the "normal" trajectory of porosity changes over the lifespan, which are themelves highly individualized and variable.

Cancer is a cause or contributing factor to death in samples 28F, 60F, and 77M. However, it should be noted that none of these individuals appeared to be significant outliers in metrics of pore morphometry, but were more consistent with non-pathological individuals in their age groups. Breast and prostate cancers combined account for approximately 80% of metastases to bone (Rubens, 1998). Breast cancer (65%-75%) and prostate cancer (68%) are also the most common

386

carcinomas to develop bone metastases (Perez et al., 1990). Lung, kidney, and thyroid cancers develop bone metastases in approximately 30%-40% of cases (Rubens, 1998). Metastatic bone disease is generally osteolytic (bone destroying), including metastases derived from breast, lung, kidney, and thyroid cancers, as well as melanomas (Roudier et al., 2008; Chappard et al., 2011). The exception, prostate cancer, is osteoblastic/osteosclerotic (bone-forming) overall, although it also has an osteolytic presentation at the histological level (Roudier et al., 2008). In response to tissue damage, cellular processes are activated locally in a "regional acceleratory phenomenon" (RAP) (Frost, 1983). Woven bone forms on top of existing osteoid and trabeculae in regions where lamellar bone has been totally resorbed and de novo within the tumor stroma in the marrow cavity. This creates heterogeneous regions with varying degrees of bone resorption and woven bone (Roudier et al., 2008).

In osteolytic cancers, there is still usually local bone formation in an attempt at repair even though the overall effect is destructive (Buijs and van der Pluijm, 2009). For example, in breast cancer at least 15%-20% of cases have predominately osteoblastic lesions (Coleman and Seaman, 2001). Factors released from the bone by osteoclast resorption stimulate osteoblast activity, causing woven bone to form on trabeculae (Chappard et al., 1978). Trabecular destruction and endosteal scalloping (Rubens, 1998) combined with this woven bone formation create a "candelabra" appearance of trabeculae (Chappard et al., 1978). These factors can also diffuse through Haversian canals to reach the periosteum,

387

causing woven bone to form at the periosteum (Wlodarski and Reddi, 1987). Bone formation has also been observed within Haversian canals following this diffusion, especially where they intersect with the bone surface (Anderson et al., 1992).

Cancers where osteolysis predominates (e.g., breast cancer) have a higher fracture risk than cancers that are osteoblastic/osteosclerotic (e.g., prostate cancer), although both types have regions of bone formation and resorption that contribute to fragility (Rubens, 1998). Fractures of long bones, ribs, or vertebrae occur in approximately 50% of all patients with metastases, with most fracture cases resulting from breast carcinoma (53%) and other common sources being kidney (11%), lung (8%), thyroid (4%), lymphoma (4%), and prostate (3%) cancers (Higinbotham and Marcove, 1965). Fractures of long bones occur in ~16% of patients with breast metastases to bone (Coleman and Rubens, 1987). Even though prostate cancer forms new bone, the heterogeneity of osteodense and osteopenic bone may contribute to high bone fragility (Roudier et al., 2008). The amount of bone compromised contributes to fracture risk. Pathological fracture is unusual when below two-thirds of the diameter of a long bone is affected, but occurs in 80% of cases where above two-thirds are affected (Rubens, 1998).

Osteophyte Formation: As mentioned, individuals 70F and 82F presented with significant apposition and erosion of the anterior to superior-anterior cortex. These individuals both match what Bell et al. (1999a,b) identified

388

as an anterior concentration of "giant canals" in females who eventually fracture the femoral neck. In the femoral neck, osteophyte formation is known as "buttressing" and is particularly linked to the inflammation and adhesion of osteoarthritis. Large pockets of osteophyte typically form in such regions of lower strain because they retain more of the cartilaginous articulation, whereas other regions become eroded with age or pathology. If this cartilage becomes revitalized in response to damage or irritation, it can restart endochondral bone formation. This involves vascular invasion and erosion of existing bone, followed by deposition and mineralization of new bone. More rarely, osteophyte results from intramembranous ossification from the synovial membrane of the joint capsule (Resnick 1983).

Individual 70F presents with a superior-anterior pocket of osteophyte, but no additional cortical thickening. Individual 82F presents with extensive cortical thickening and subsequent erosion along the anterior superior-to-inferior gradient, retaining the original anterior cortical wall within this pocket. Individual 70F had a normal T-score in the total body aBMD but was considered osteoporotic in the right and left femoral neck. Surprisingly, individual 82F had a normal T-score in both the total body and femoral neck aBMD. However, this might be associated with her type two diabetes, which generally increases aBMD, as detailed below.

Diabetes mellitus: One individual (88F) also had type 2 diabetes mellitus. This individual did appear to be an outlier on many of the median plots of pore morphometry. While the rib does not appear pathological, examination of the

389

three-dimensional image of the femoral neck reveals a pocket of significant superior-anterior porosity. The irregular extension of this superior anterior region beyond the boundary of the inferior anterior region suggests that this represents marginal new bone apposition (osteophyte), and then subsequent erosion into that new bone. This region is only partially enclosed superior-anteriorly, and more inferiorly it opens to the periosteum and is not included as cortical porosity. Interestingly, this individual was of normal weight and BMI, making it unlikely that excessive weight was a contributor. She also had a normal T-score in both the total body and right femoral neck aBMD, with no dual femoral asymmetry. However, this might be an artifact of her type 2 diabetes mellitus.

Type 2 diabetes mellitus (T2DM) refers to resistance to insulin action and inadequate secretion of insulin to compensate (American Diabetes, 2014). Uncontrolled diabetes mellitus creates an inflammatory response that reduces wound healing, increases bone resorption, and decreases bone formation (Jiao et al., 2015). Type 1 diabetes mellitus (T1DM) rats have reduced or absent bone formation on trabecular, endocortical, and periosteal surfaces (Verhaeghe et al., 1989, 1990a,b). Diabetic rat femoral necks, accordingly, have less cortical bone and an increased core of trabecular bone (Hou et al., 1991). Brittle diabetic bones result from suppression of osteoblast activity (Verhaeghe et al.,1994). Bending stiffness is accordingly increased in diabetic rat femora and tibiae (Reddy et al., 2001; Einhorn et al., 1988). Einhorn et al.'s (1988) study on diabetic rat tibiae

390

also suggests that mineralization is preserved in weight-bearing cortical bone at the expense of trabecular bone.

The risk of skeletal fracture is increased about twofold in diabetic patients (Verhaeghe et al., 1994). Fracture healing is also impaired during the callus mineralization phase (Liuni et al., 2015). For displaced closed fractures of the lower extremity, fracture healing is prolonged by 87% (Loder, 1988), with a 3.4-fold higher risk of complications in fracture union (Folk et al., 1999). Meta-analyses show a trend toward increased fracture risk at most skeletal sites, generally with a higher risk for T1DM compared to T2DM. However, these meta-analyses also indicate that BMD generally decreases for T1DM but increases for T2DM (Vestergaard, 2007; Janghorbani et al., 2007; Thrailkill et al., 2005). Osteopenia and osteoporosis are also frequent complications of T1DM, but are not typically associated with T2DM (Thrailkill et al., 2005). Several explanations have been advanced for why T2DM diabetics have increased fracture risk, despite their increased BMD, compared to nondiabetic controls. First, it is possible that bone resorption actually decreases in T2DM, as some studies have found (El Miedany et al., 1999; Erbagci et al., 2002). Thrailkill et al., (2005) note that T1DM represents insulinopenia, while T2DM represents hyperinsulinemia, with normal or increased concentrations. Hyperinsulinemia may preserve bone mass in T2DM by acting as an anabolic agent. Second, the higher BMI associated with T2DM may increase BMD through mechanical loading (Vestergaard, 2007). Third, comorbidities of T2DM may increase the risk of falls, leading to fracture.

391

These risk factors include impaired vision, peripheral neuropathy, lack of sensation in the lower extremities, and hypoglycemia unawareness or seizures (Janghorbani et al., 2007; Thrailkill et al., 2005). Fourth, T2DM may compromise bone structure in a manner not detected by BMD. In the spine, trabecular BV is lower in T2DM, compromising trabecular bone strength despite higher BMD (Parkinson and Fazzalari, 2003; Strotmeyer et al., 2004).

Bone Unloading: Individual 49F is perhaps the most interesting individual in this study. The femoral neck and rib themselves are extremely gracile, small, and circular. This individual presents with extensive intracortical resorption, but maintains a fairly thick cortex. Resorption is not through marginal erosion of the endosteum, but is occurring fully within the cortical bone. Interestingly, this individual preserves the preferential cutaneous distribution of porosity in the rib, signaling alignment with the structure-strain relationship seen in other individuals. Looking at the DXA results, there is a mild dual femur asymmetry, with a T-score of -2.1 on the right side and -1.2 on the left side, although both would be classified as osteopenic.

The medical history of this individual indicates that they had a right-side trans-tibial amputation. Logically, this individual would tend to shift their weight to the left side of the body to compensate for the lack of lower right-leg stability. This could result in significant unloading of the right femoral neck. Additionally, if the individual was leaning their thoracic cage more heavily on their left side, the cutaneous region of the rib would become particularly tensed and reduced in

392

strain. This unloading might be the source of the unusual intracortical resorption, as this individual might not have advanced far enough into menopause to produce the endocortical resorption and thinning seen in the older females. The individual paralyzed from birth in the Peck and Stout (2007) study, an extreme case of unloading, similarly has very gracile, small, and circular limb and rib bones.

8.4. Intraskeletal Porosity Patterning in the Femoral Neck and Rib

8.3.1. Hypothetical Structure-Strain Pore Morphotypes

The capacity of human bone to respond to a range of mechanical and physiological environments is adaptive for long-lived humans but frustrating for anthropologists to interpret. As discussed in chapter four, remodeling in response to both high and low strain is a confounding factor in studies of pore morphometry, and microstructures derived from remodeling (osteons, osteocytes) more generally. Additionally, bone cell sensitivity to physiological stimuli (diet, stress, inflammation, aging, pathology) alters their predictable responses to mechanical stimuli, and will necessarily become more disregulated with senescence.

Low strain results in "disuse-mode" remodeling, in which bone cells resorb more bone than they eventually replace (Frost, 2003b). Moderate strains result in stochastic remodeling, which is routine bone turnover to replace aging tissue. As stochastic remodeling is not triggered by a specific mechanical event, it is more sensitive to regulation by physiological processes (Martin, 2002, Eriksen,

393

2010). Frost termed this "conservation mode" remodeling, because osteoblasts form bone to replace the resorbed regions (Frost, 1990). High strain represses stochastic remodeling, but it can also produce microcracks that trigger targeted remodeling, which composes an estimated 10% to 30% of all remodeling activity (Burr and Martin, 1993; Li et al., 2001). The cortical pores created by both stochastic and targeted remodeling can themselves become initiation points for microdamage, perpetuating this cycle of stop-gap repairs with eventual consequences (Ebacher et al. 2007).

This study hypothesized that stochastic and targeted remodeling associated with low-strain and high-strain triggers, respectively, can be distinguished through the morphometry of the resulting cortical pores. Stochastic remodeling is permissive, and would allow pores to expand and converge until curbed by mechanical thresholds. Coalescence should also increase the obliqueness of the pore network, as neighboring pores in slightly differing orientations converge, as is seen in osteons (Hennig et al., 2015). Targeted remodeling is responsive, and could be expected to occur only as long as was needed to repair the damage.

The mechanism to produce these morphotypes is inherent in the remodeling cycle. The primary difference in pore size, isolation, and orientation is the extent to which osteoclasts are permitted to resorb the cortex before coupling occurs. As discussed in chapter two, coupling is the switch from osteoclast bone resorption to osteoblast bone formation, which occurs during the reversal stage of remodeling. While osteoblasts are recruited partially by factors released from the

394

resorbed bone, the timing of the coupling period is also regulated by signaling between bone cells. Both osteoclasts and osteoblasts can release factors that promote or inhibit their own activity or the activity of the other cell type (Martin and Sims 2014). Pore morphometry could be regulated not only by the manner in which the remodeling is triggered by osteocytes (strain-induced or damage-induced), but also by cross-talk between all involved cell types and physiological influences.

This model hypothesizes the following structure-strain relationship:

1) High-strain regions accumulate smaller, more isolated, longitudinally oriented pores due to more frequent remodeling; **and**

2) Low-strain regions accumulate larger, more highly connected, obliquely oriented pores due to more frequent disuse-related resorption.

In order to test this hypothesis, this study compared pore morphometry between regions known to experience varying mechanical strain:

A. **Femoral neck** (weight-bearing, dynamically loaded) vs. **rib** (relatively unloaded)

B. **Superior** (low-strain minimum compression) to **Inferior** (high-strain maximum compression) gradient along octants of the femoral neck

After selecting variables that correspond to a structure-strain pore morphotype, this model was used to assess mechanical loading variation in the **cutaneous vs. pleural cortices of the rib**.

395

8.3.2. *Bone Type Attributes*

This study hypothesized that the femoral neck would display a "high strain morphotype" including significantly smaller, more isolated, and more longitudinally oriented pores.

396

Table 8.1 Review of Significant Interactions in Bone Type and Pore Type

Pore Factor	Percent Porosity	Pore Density	Percent Closed Porosity	Percent Open Porosity	Proportion of Open Pores	Pore Thickness	Pore Separation	St Dv Pore Thickness	St Dv Pore Separation	Pore Frag Index	Pore Conn. Density	Degree of Anisotropy	Pore Linear Density	Cortex Fractal Dimension	Pore Fractal Dimension
Bone	L (FN > R)		M (FN>Rib)	L (FN>Rib)	S (FN<Rib)	L (FN>Rib)		L (FN>Rib)						L (FN>R)	L (FN>R)
Pore Type		L (Ct>Tb)		M	L (FN:Ct<Tb) (Rib:Ct<Tn)	L (Ct<Tb)		L (Ct<Tb)			L (Ct>Tb)	L		L (Ct>Tb)	L (CT>Tb)
Age		L ↑								M (F↓)			L		
CS. TH.		L↓			M↓							M Ct ↓Tb↑	L		
Sex	L (F>M)	L (F<M)	S (F>M)	L (F>M)		L FN F>M							L		
Bone: Type			L (FN Ct↑) (R Ct↓)	L (FN↑Tb) (R↓Tb)								L R:Ct>Tb	L		
age:cs.th		L											L		
age:sex	L			L		L			M				L		
cs.th:sex	L	L		L		L							L		
age:cs.th: sex	L	L		L		L							L		
Marginal R²	65.49%	73.01%	50.32%	62.15%	59.10%	71.87%	66.43%	59.10%	56.83%	0.000 414%	68.60%	77.11%	6.75%	89.8%	59.10%

Cohen's d Effect Size: S = 0.2 M = 0.5 L = 0.8

397

Converse to predictions, the femoral neck had significantly higher percentages of total, closed, and open porosity compared to the rib. This was not an effect isolated to old age, or to the individuals with significant cortical (49F) resorption, or osteophyte erosion (70F, 82F). All individuals in this sample had a higher percentage of porosity in the femoral neck compared to the rib, all in excess of 10% porosity, except 67M. Although pore type does not have a significant effect in the model related to percent porosity, based on the median plots this increased porosity seems to be derived from extensive marrow-adjacent (trabecularized) pores in the femoral neck.

The femoral neck and rib do not differ significantly in pore density. However, the rib has a significantly higher proportion (by number) of pores that are open to the tissue borders, despite having a significantly lower percentage of open porosity. That is, individual pore systems are connecting to the tissue borders more frequently in the rib. The femoral neck forms larger intracortical spaces that send more isolated connections to tissue borders. Thus, the entire connected network is an open system.

In terms of proportions, the femoral neck has significantly larger (local thickness) pores, and consistently so for every individual in the sample. Both cortical pores and trabecularized pores are significantly larger in the femoral neck compared to the rib. The femoral neck also has a significantly larger range (standard deviation) of pore thicknesses. However, the mean or range (standard deviation) of local separation between pore systems does not significantly vary

398

between bone types. The femoral neck is forming larger pores, but spacing them approximately the same as the rib.

There are no significant differences involving bone type in pore connectivity (fragmentation index, connectivity density) or orientation (structure linear density, degree of anisotropy). From the median plots, total and cortical mean degree of anisotropy in the rib exceeds the femoral neck, implying that the internal pore networks of the rib are more directionally oriented. However, trabecularized degree of anisotropy is much reduced in the rib, below the femoral neck median, removing significance from the bone type of this hypothesis.

Increased percent porosity in the rib stems from pores that are larger, but not more numerous or more convergent (connected) with other pore systems, compared to the rib. Individual events do not differ significantly from the rib in frequency, spacing, or orientation. This implies that the femoral neck is actually experiencing **more extended resorption during remodeling**, but **<u>not</u>** more **frequent** remodeling.

As a weight-bearing bone, the femoral neck was hypothesized to have more repressed remodeling and consequently fewer, smaller, more isolated pores. Several approaches might explain rejection of this model.

1) The femoral neck is actually remodeling more extensively

Studies calculating remodeling rate from osteon population density generally hold that relatively unloaded bones (e.g., the rib) remodel relatively more frequently than weight-bearing bones (e.g., the femur) (e.g. Hattner and Frost,

399

1963, Frost, 1969, Cho and Stout, 2011, Gocha and Agnew, 2016, Mason et al., 1995, Mulhern, 2000). This is based on the mechanostat model that lower strains are more permissive to stochastic remodeling. However, some studies have found higher remodeling rates the femur compared to the rib, which could be linked to increased targeted remodeling to repair more frequent microdamage (Robling and Stout, 2003, Mason et al., 1995, Zedda et al., 2015, Mayya et al., 2013). In this case, more extensive remodeling in the femoral neck could be due to increased targeting of microdamage. However, as was found in the comparison of femoral neck octants, porosity is concentrated in the lower strain superior regions, not the higher strain inferior regions more prone to microdamage. This does not necessarily disqualify the increased remodeling option. In their study of regional pore distribution in the femoral mid-diaphysis, Thomas et al. (2005) found high porosity in the posterior octant of young individuals, an unexpected result given the relatively higher strain in this region compared to other regions of the femoral midshaft cross-section. This region is highly strained by muscle attachments at the linea aspera. They suggested that bone turnover is higher in an area of muscle attachment.

This option is complicated by the femoral neck's non-significant difference in pore density compared to the rib. It should be noted that pore frequency or density is not a proxy of remodeling rate or OPD, because it excludes evidence of fragmentary osteons that mark occluded remodeling events. However, some correspondence might be expected between increased remodeling rate and

400

increased pore frequency in the femoral neck. Even though the model is not significant, median plots show that the rib trends towards a higher pore frequency, the opposite of what would be expected in this model.

2) The more extensive porosity of the rib has already been resorbed

A second option is that evidence of higher porosity in the rib has been removed through more extensive endocortical resorption. If a bone is highly trabecularized to the extent that the former cortical regions are fully resorbed, percent porosity and associated metrics will be artificially reduced. For example, Villanueva et al. (1966) found normal intracortical porosity in osteoporotic ribs, but a thinned cortex and expanded marrow cavity. Again, this option is complicated by the presence of high relative percentages of femoral neck porosity in young individuals, who should not have an excessively resorbed rib cortex.

3) Large pores reflect a localized low-strain mechanical effect

Unlike the rib, which preferentially distributes trabecularized porosity in the cutaneous cortex, the femoral neck consistently displayed a "ring" of trabecularized pores adjacent to the entire circumferenceof the endosteum. This is especially evident in the Absolute LUT (look up table) images that remove the smaller pore networks. These pores are large enough and close enough to the marrow cavity to be categorized as "trabecularized," but they are typically separated from the marrow by the continuous cortical wall. This is reflected statistically in the femoral neck's larger percentage of open porosity, but lower proportion of individual pores that open to issue borders. During the 1 cm length

401

of the sampled femoral neck, from the distal (trochanter adjacent) end to the

proximal (head adjacent) end, the cortex rapidly thins and becomes more circular.

Trabecularized pores that previously composed only a small boundary fraction of

cortical thickness may now subsume its entire breadth, without having

substantially altered their size. This difference is exacerbated in individuals with

age-associated or pathological resorption in intra-cortical regions. Trabecularized

pores in these regions are vulnerable to coalescence into "huge" pores, especially

more proximally.

Figure 8.1 Trabecularized "ring" in distal 67M
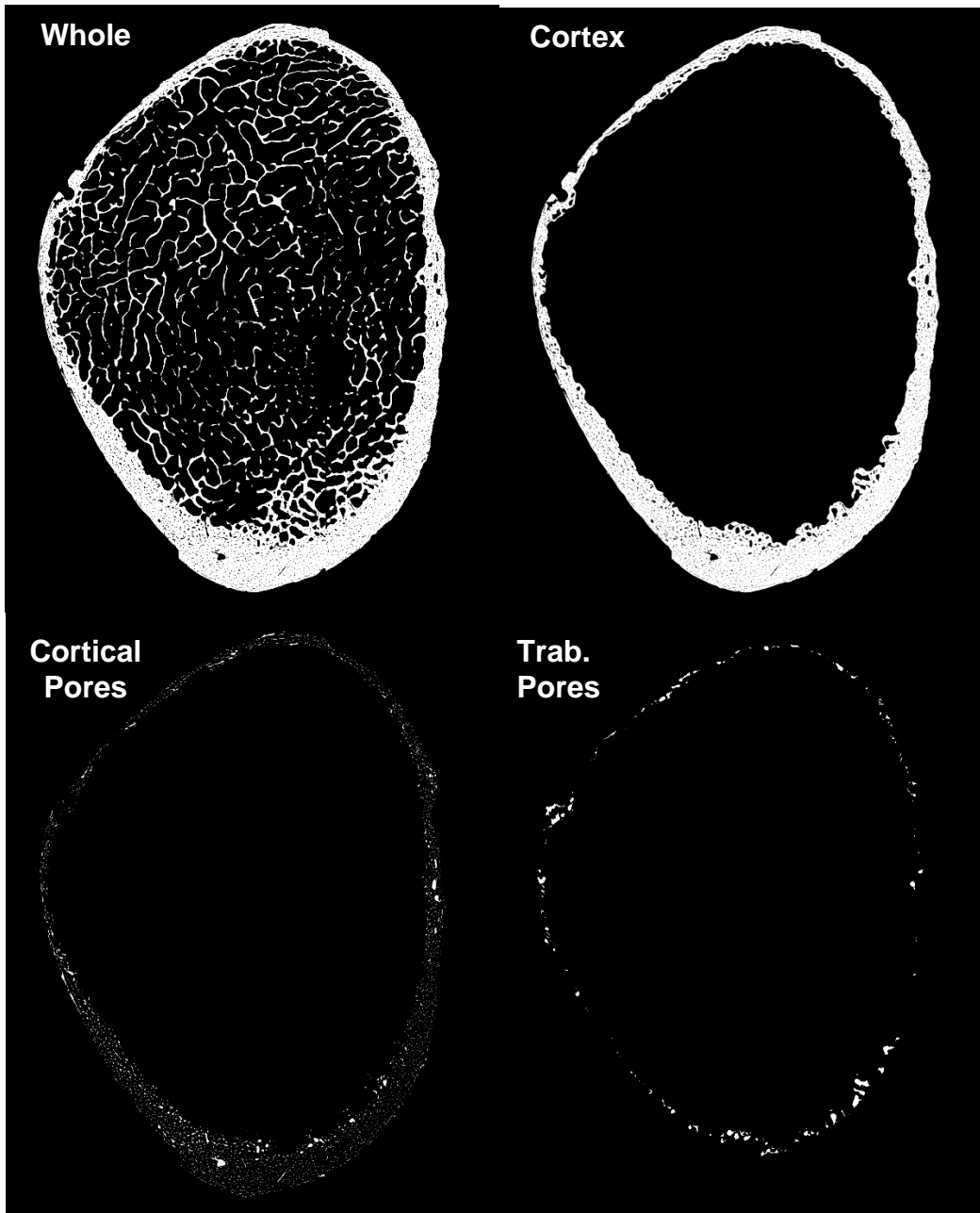
Figure 8.2 Trabecularized "ring" in proximal 67M

404
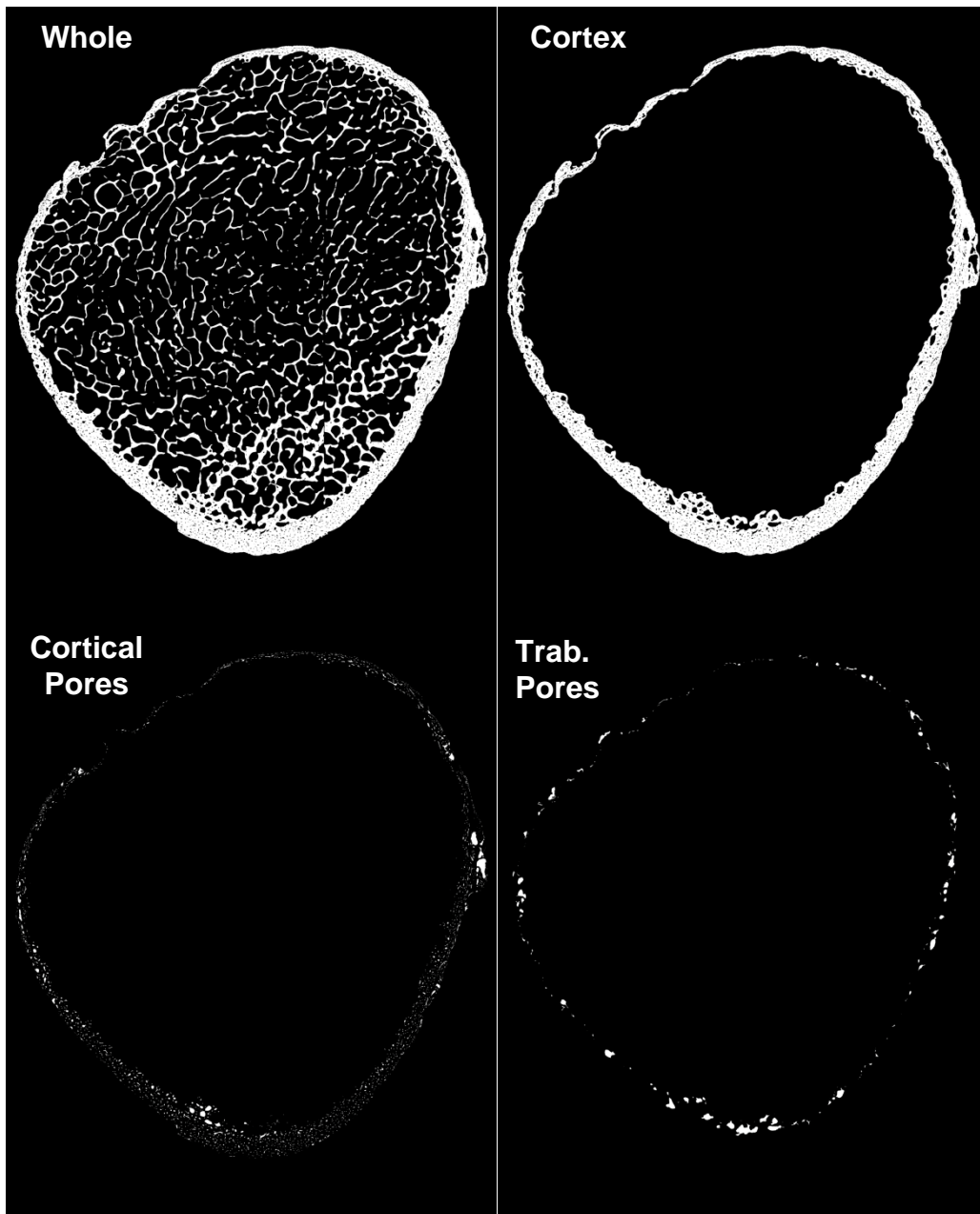
Figure 8.3 Trabecularized "ring" convergence in distal 82F
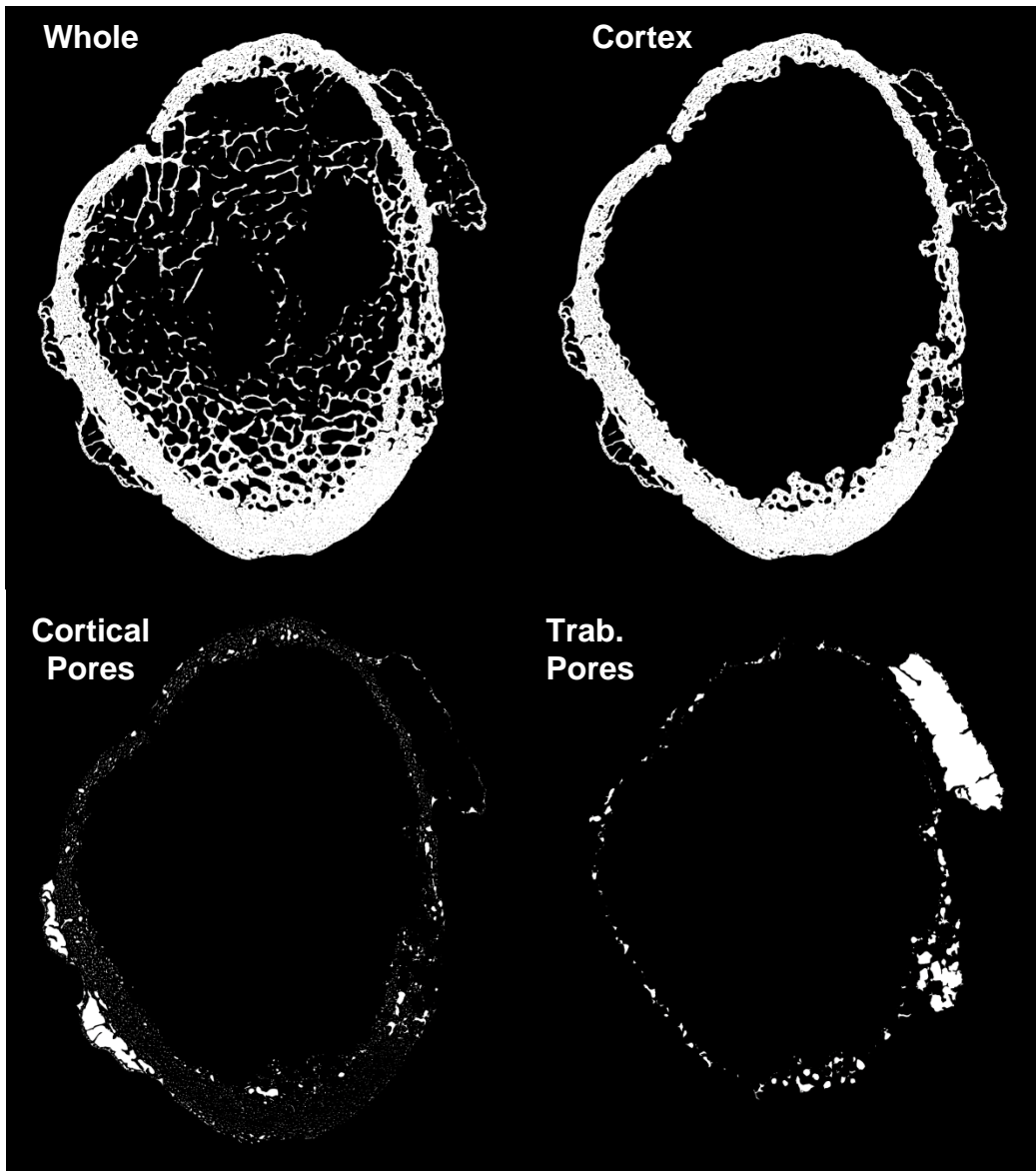
Figure 8.4 Trabecularized "ring" convergence in proximal 82F
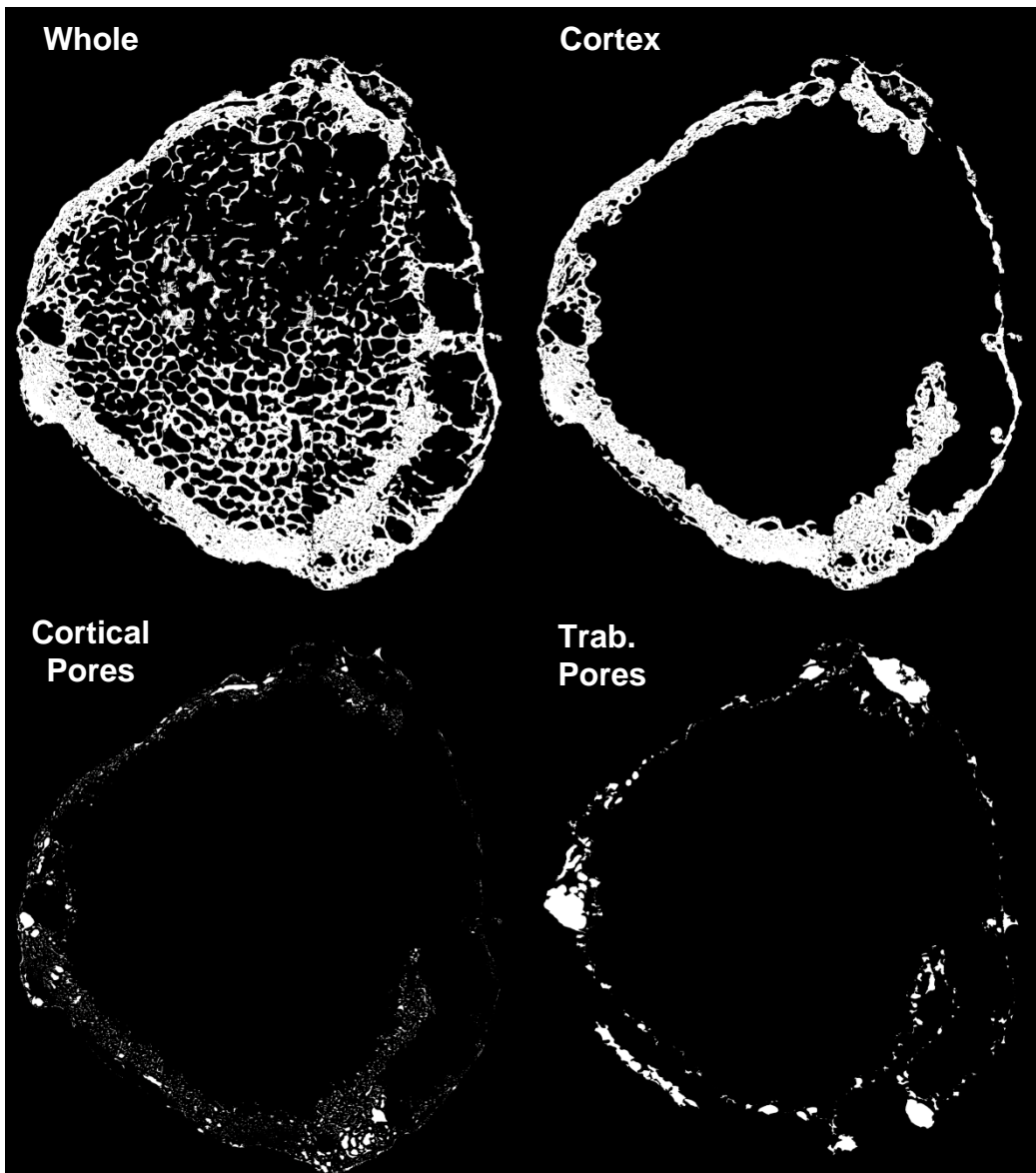
The source of this trabecularized ring is likely the superior-to-inferior strain gradient within the femoral neck. Strain is lowest at the endosteum, closest to the neutral axis. Thus,trabecularized pores form unformly around its circumference (Martin, 1993; Thomas et al., 2005). However, since the cortex is thicker inferiorly, trabecularized pores (and porosity in general) composes a smaller percentage of the cortex regionally. Conversely, in the rib, trabecularized pores are localized in the cutaneous cortex due to opposing loading modes between the two cortices. This effect can be seen in the three-dimensional images in the appendix, and will be statistically discussed below. This unbalanced apposition allows the relatively thicker pleural cortex to preserve its endosteal cortical bone. Therefore, while the femoral neck may be more loaded overall by weight-bearing and dynamic activity, it may exhibit broader endosteal regions that are locally low in strain and permissive to trabecularization. As endosteal resorption accelerates with aging and menopause, the regressing endosteum encounters these existing trabecularized voids, and can converge with them to accelerate cortical thinning. This may be one contributor to the fragility of the femoral neck and its prominenance as a fracture site.

The frequency, rate, and extent of remodeling is intraskeletally sensitive to mechanical loading variation, as well as localized physiological influences. Unless mechanical strain can be directly measured, comparing two separate elements of "known" mechanical variation within an individual is likely not the best approach to defining the mechanical sensitivity of microstructural

407

morphometry. The pitfalls of this common approach can be seen in the frequency with which different skeletal elements disagree regarding the morphometry of porosity, osteon population density, osteon size and shape, and osteon lacunae (Table 1.1). Instead, structure-strain patterns in morphometry should be derived from regional comparisons within cross-sections, which hold the localized physiological environment and whole-bone loading factors constant.

Previous two-dimensional studies of intracortical porosity variation have not found significant differences in percent porosity between the distal radius, midshaft rib, and midshaft femur of the same individuals (Hunter and Agnew 2016) or midshafts of the femur, tibia, and rib of the same individuals (Cole and Stout 2015). Consideration of the whole volume of these structures shows that significant intraskeletal differences in percent porosity do exist, but that the distribution and characterization of these differences is complex. This reinforces the importance of three-dimensional imaging in understanding why and how microstructures adopt differing morphological configurations within a given bone.

8.3.3. Pore Type Attributes

Cortical pores are significantly smaller and more complex (fractal dimension) than trabecularized pores. They also have a higher connectivity density, in the sense that they have more discrete transverse connections. This is the difference between connectivity and convergence. Somewhat paradoxically, trabecularized pores can reduce their connectivity by merging with one another. They are more *connected*, but they have fewer discrete *connections*.

408

8.3.4. Age Attributes

Although percent porosity does increase with age, there is no significant interaction with closed, open, or total percentage of porosity. Individuals are too variable in the progression of cortical thickness. This is not unprecedented, as Stein et al. (1999) found that age explains only 12.1% of the variation in porosity between individuals, even when controlled for height, weight, and sex. A larger sample size might be able to detect stronger trends by grouping individuals by age category and compensating for outliers. Pore density does increase significantly with age in both males and females, although females decline in older age as their cortex is more extensively thinned. Pore density is the number of individual pore structures per total cortical shell volume, so this indicates an increase in the number of isolated remodeling events, either due to increased unfinished remodeling, or increased targeted remodeling of microdamage to brittle bones.

From the correlation matrix, it was known that age is only significantly and moderately negatively correlated with pore separation. This implies that pores are expanding and converging, consistent with existing data (Bell et al., 1999a, b, Bousson et al., 2001; Cooper et al. 2007a; Chen et al., 2010; Chen and Kubo, 2014; Milovanovic et al., 2014).

The range (standard deviation) of pore separation decreases with age, but this can be attributed to female changes. Females decline more than males, but only because they begin with a less variable range of pores sizes – equivalence is

409

reached around age 50. Males have a fairly consistent range of pore separation throughout life.

8.3.5. Sex Attributes

Females had significantly more percent open, closed, and total porosity compared to males. However, males had a significantly higher pore density. This suggests that the convergence of pores is a major driver of increased porosity in females, as has also been found in other studies of the femoral neck (Bell et al., 2001; Cooper et al., 2007a; Chen et al., 2010). Females had significantly larger pores than males in the femoral neck, but not in the rib.

8.3.6. Cortical Thickness Attributes

Pore density decreases as cortical thickness increases. This reflects the central role that increasing porosity plays in endocortical erosion. Trabecularized pores are more densely connected in thicker cortices, likely because they have not yet fully converged with each other and the endosteum, and are still sending out transverse connections. Cortical pores are more densely connected in thinner cortices, likely because trabecularized pores have already been resorbed.

8.5. Regional Porosity Patterning in the Femoral Neck

Unlike intraskeletal comparisons, femoral neck regional patterning of porosity significantly aligned with the hypothetical structure-strain pore morphotype. All pore morphotype variables except pore thickness and its standard deviation showed either significant differences or a visual trend of octant medians between

410

more superior (SP, S, SA) and more inferior (IP, I, IA) octants of the femoral neck. Scatterplots of octants with their medians were plotted in order to reflect the anatomical orientation of the femoral neck in an arc from inferior, to superior, and back to inferior regions, as follows: I, IP, P, SP, S, SA, A, IA. Pore morphotype values plotted in this manner consistently displayed a parabolic or inverted parabolic distributing, signifying that values were respectively decreasing S→I (parabolic) or increasing S→I (inverted parabolic). Regional comparisons revealed a secondary trend of the coalescence of pores in the superior-anterior octant, with significant variation in pore morphotypes related to size and convergence from adjacent and more inferior regions. This effect was largely due to extensive intracortical resorption in 49F, and osteophyte apposition, subchondral resorption, and subsequent erosion of the new bone in 70F and 82F.

Table 8.2 Alignment of Pore Morphometry with Strain Gradients in the Femoral Neck

ID	Cortex Fractal Dimension	%Closed Porosity	%Open Porosity	%Porosity	Pore Thickness	Pore Separation	Pore Linear Density	Fragmentation Index	Degree of Anisotrooy	Pore Fractal Dimension	Connectivity Density	StDv PoreThickness	StDv Pore Separation	Proportion Open Pores	Pore Density
Superior (High Strain) to Inferior (Low Strain) Trend	↑ I more complex	↑ P to I Strain closes off pores	↓ SA, A, SP more porous than IA, I, IP	↓ SA, A, SP more porous than IA, I, IP		Trend ↑	↓ I less dense	↓ I fewer struts	Trend ↑	Trend ↑	↓ S to IP		↑ S, SA, SP to I, IP	↓ S and P to I	↓ S to IP
Superior Anterior Convergence					SA > IA, IP, P, S	SA> SP, S, P, IA	SA< SP, S, P, IA					SA> I, IA, IP, P, S, SP S<A			
Marginal R²	26.12%	59.59%	77.23%	77.22%	59.13%	35.47%	79.01%	23.29%	29.46%	68.63%	63.09%	68.83%	80.86%	32.44%	62.41%

412

8.4.1. Refining the Structure-Strain Model for Pore Morphometry

Regional patterning of pore morphotypes in the femur confirmed that increased mechanical strain predicts reduced pore prevalence, increased pore isolation, and increased longitudinal orientation. These are all indicators that pores are produced largely by targeted remodeling or briefer strain-repressed stochastic remodeling. Increased strain did not significantly predict a reduction in mean pore size (thickness), and the median scatterplots also do not indicate a strain-related trend. Thickness variation is instead localized to the superior-anterior cortex in individuals with medical complications (amputation, osteoporosis, type II diabetes mellitus).

Percent porosity does not strictly reflect remodeling frequency. More frequent but less extensive targeted remodeling could result in overall lower percentages of porosity. However, this study finds that high-strain inferior regions are reduced both in the number of individual pores per unit volume (pore density), and overall percentages of open and total porosity. This suggests that remodeling is not only less extensive, but also less frequent, under high strain. Such a model agrees with studies of osteon population density finding reduced remodeling rates in skeletal elements and cross-sectional regions under high strain (Hattner and Frost, 1963; Frost, 1964; Portigliatti et al., 1983; Mason et al., 1995; Skedros et al., 1996; Mulhern and Van Gerven, 1997; Mulhern, 2000; Cho and Stout, 2011; Gocha and Agnew, 2016).

413

Multiple pore morphometric measurements captured the confirmed model concepts of pore prevalence, isolation, and orientation, as detailed in the following table.

Table 8.3 Pore Morphometry Predictors of Regional Mechanical Strain

High-Strain Pore Morphotype	Measurement Variable Prediction
Reduced Pore Prevalence by Number	Pore Linear Density ↓ Fragmentation Index ↓ Pore Density ↓
Reduced Pore Prevalence by Volume	% Total, Open Porosity ↓ % Closed Porosity ↑
Decreased Pore Convergence	Pore Separation and StDv ↑ Cortex/Pore Fractal Dimension ↑ Connectivity Density↓ Proportion Open Pores ↓
Longitudinal Pore Alignment	Degree of Anisotropy ↑

Several of these morphometric indicators are less obvious. Fragmentation index refers to the degree to which a structure is "strut-like" or "node-like." The trabecular equivalent is trabecular pattern factor (Tb.Pf). Inferior regions have a lower fragmentation index, indicating that they are more node-like. This does not mean that highly strained pores are convergent, since they also have decreased connectivity density and increased pore separation. Rather, the presence of a more "strut-like" organization in low-strain superior regions likely corresponds to the higher pore density and pore linear density of individual pore networks.

While connectivity density did significantly decrease with in highly strained inferior regions, it should be used with caution when detecting pore convergence. Comparisons of cortical and trabecularized porosity in the femoral

neck and rib indicated that cortical pores are significantly more connected than trabecularized pores. Since trabecularized pores ultimately converge through resorption of their interstitial spaces, they do not need to connect using more numerous, discrete transverse canals. A region with more prevalent cortical porosity may be less convergent but have a greater density of discrete connections. Pore separation, cortex or pore fractal dimension, and the proportion of open pores can help interpret connectivity density in respect to pore convergence.

8.4.2. Age and Sex Effects

The only pore morphotype variable significantly influenced by co-variates (age and sex) was pore separation, which is also the only strong and significant correlation with age for both the femoral neck and the rib. Age significantly decreased separation between pores ($p = 1.97 \times 10^{-6}$) with a medium effect size (Cohen's d = -0.4296), indicating that pore separation is decreasing as age increases. Sex significantly ($p = 0.031663$) altered pore separation with a medium effect size (Cohen's d = -0.34775). The median scatterplot indicates that females had significantly less pore separation than males. Aging has been associated with pore convergence in the femur (Bousson et al. 2001; Cooper et al. 2007a) and in the femoral neck specifically by numerous studies (Chen and Kubo, 2014; Milovanovic et al., 2014). Pore separation has also previously be shown to be exacerbated in women at menopause due to declining estrogen levels that increase bone resorption (Chen and Kubo, 2014). As in the comparison with the rib, the

415

highly individualized progression of porosity expansion with respect to chronological age limits consistent correlations or significant effects with other pore morphometric variables.

8.4.3. *Superior Anterior Convergence*

Variation in pore size (local thickness and its standard deviation) is localized to the superior-anterior cortex in respect to adjoining and more inferior cortices. Three individuals with medical complications (amputation, osteoporosis, type II diabetes mellitus) have the most significant superior-anterior cortical erosion, and are often outliers on median scatterplots. Previously studies have found that abnormal pore localization is associated with increased bone fragility. Bell et al. (2001) indentified "giant" coalesced canals (>385 µm in diameter) in the femoral necks of individuals older than 75 years. These enlarged cavities composed 27% of total femoral neck porosity, but only 1% of femoral neck pore number. Bell et al. (1999a, b) also found that porosity increases as much as 41% in the anterior cortex of women with femoral neck fractures. They identified a doubling of pore coalescence into "giant canals" (>385 µm) in this region. They attribute this localization to reduced loading of the anterior cortex by hip extension and adduction, as aging individuals decline in physical activity and mobility. Individuals with anteriorly localized coalescence are particularly vulnerable to femoral neck fracture during a sideways fall, as the deformation will occur along the inferoanterior to superoposterior axis. This essentially crushes the weakened anterior to superior regions. Similarly, large canals that typically

416

concentrate at the endosteum can also occur at the periosteum in elderly women (Chen et al. 2010). This matches the abnormal intracortical resorption without significant endosteal resorption seen in 49F.

8.6. Matching Pore Morphometry to the Structure-Strain Model in the Rib

After refining the structure-strain model for pore morphometry, the model was applied to the morphometry of cortical and trabecularized porosity in the cutaneous and pleural cortices of the rib. This analysis is intended to support their differentiation as to loading mode. As discussed in the study design section, in the simplified "bucket handle" model of thoracic cage expansion, lower ribs (7-10) are bent inwards as they move laterally and superiorly. The cutaneous cortex (lateral) is tensed, experiencing relatively lower strain, while the pleural cortex (medial) is compressed, experiencing relatively higher strain (Agnew and Stout, 2012). However, the upper ribs are actually bent slightly outwards, as their sternal end moves superiorly and anteriorly in a "pump handle" motion. Additionally, both lateral and anterior-posterior expansion of the thoracic cage occur during forced inspiration (Moore et al., 2014). Thus it is uncertain whether the cutaneous cortex of a mid-level (4th – 7th) rib is actually experiencing lower mechanical strain at the midshaft (Hunter and Agnew 2016; Dominguez and Agnew, 2014).

417

Table 8.4 Review of Significant Interactions in Rib Region and Pore Type

Pore Factor	Percent Porosity	Pore Density	Percent Closed Porosity	Percent Open Porosity	Proportion Open Pores	Pore Thickness	Pore Separation	St Dv Pore Thickness	St Dv Pore Separation	Pore Frag Index	Pore Conn. Density	Degree of Anisotropy	Pore Linear Density	Cortex Fractal Dimension	Pore Fractal Dimension
Region	L (Cu>Pl)		L (Cu>Pl)				L (Pl>Cu)		M (Pl>Cu)		M (Cu>Pl)		L (Cu>Pl)	L (Cu<Pl)	S (Cu Diff < Pl Diff)
Pore Type		L (Ct>Tb)		L (Ct<Tb)						L (Ct>Tb)	L (Ct>Tb)	L (Ct>Tb)	L (Ct>Tb)	M (Ct>Tb)	L (Ct >Tb)
Age							M↓		S↓		M↑ →↓				
CS. TH.		M↓									S↓				
Sex															
Bone: Type												L (Cu Type< Pl Type)			
age:cs.th															
age:sex						L F↑									
cs.th:sex															
age:cs.th: sex						L↑									
Marginal R²	34.13%	84.46%	32.38%	31.30%	12.20%	94.26%	44.8%	59.10%	44.08%	93.55%	87.00%	88.14%	78.53%	89.8%	68.92%

Cohen's d Effect Size: S = 0.2 M = 0.5 L = 0.8

Table 8.5 Alignment of Pleural Cortex Pore Morphometry with High-Strain Morphotype

High-Strain Morphotype	High Strain Predictor	Pleural Cortex	Confounding Effects
Reduced Pore Prevalence by Number	Pore Linear Density ↓	**Yes**	
	Fragmentation Index ↓	Not significant	Ct>Tb
	Pore Density ↓	Not significant	CS.TH ↓
Reduced Pore Prevalence by Volume	% Total ↓	**Yes**	
	% Open Porosity ↓	**Yes**	
	% Closed Porosity ↑	Not significant	
Decreased Pore Convergence	Pore Separation ↑	**Yes**	Age↓
	Pore Separation StDv↑	**Yes**	Age↓
	Cortex/Pore Fractal Dimension ↑	**Yes**	
	Connectivity Density↓	**Yes**	Ct>Tb Age↑then↓ CS.TH ↓
	Proportion Open Pores ↓	Not significant	
Longitudinal Pore Alignment	Degree of Anisotropy ↑	**Yes**	Ct>Tb

Overall, the pleural cortex does align with a high-strain morphotype at the midshaft fourth rib, using metrics derived from the known strain gradient of the femoral neck. The increased percent porosity seen in the cutaneous cortex in two-dimensional studies (Agnew and Stout 2012, Cole and Stout 2015, Dominguez and Agnew 2016) is a real three-dimensional volumetric effect, and not an artifact of pore orientation or sectioning angle.

419

The primary exception to this high-strain model seems to be that the pleural cortex does not have a significantly smaller pore density or proportion of open pores. The cutaneous and pleural cortices may remodel equally, with the pleural cortex merely less permissive to the extent of that remodeling. Inclusion of a differentiation in pore type, which was not included in femoral neck octant analysis, may complicate the equivalence of this metric. Pore type data has been collected for femoral neck octants, but was not analyzed due to time constraints. It will be incorporated in future refinement of the pore morphotype structure-strain model. Additionally, the rib appears more sensitive to confounding factors of age and cortical thickness, which could obscure regional mechanical variation. In the rib, aging significantly increases pore thickness (in females), separation, and connectivity. Porosity is also less expansive in individuals with a thicker cortex, who display significantly lower pore density and pore connectivity. Frost (1963) suggests that ribs reflect physiological effects of age and disease ealier than appendicular bones, due to their high remodeling rate. This may explain the relative absence of co-variate interactions in regional comparisons of the femoral neck.

8.5.1. *Pore Type Effects*

The reduced trabecularized porosity in the pleural cortex is primarily due to reduced trabecularization, although the region:type interaction does not reach significance ($p = 0.074844$). This complemenets my earlier finding from two-dimensional histological sections that the high porosity of the cutaneous cortex is

420

only significant in regards to trabecularized porosity. Cortical pores are significantly more complex in their patterning than trabecularized pores. This difference is emphasized in the pleural cortex.

Several morphometric trends are implied by the formative processes of cortical (remodeling) and trabecularized (resorption / convergence). **Prevalence:** Cortical pores have a significantly higher pore density than trabecularized pores in both cortices. Cortical pores also have a significantly higher fragmentation index ("strut-like") than trabecularized pores ("node-like") in both cortices. **Convergence:** Cortical pores have a significantly higher number of connections than trabecularized pores in both cortices. This is logical as trabecularized pores join by merging rather than by sending out transverse connections. **Size:** Trabecularized porosity has a significantly larger mean pore thickness than cortical porosity, as could be hypothesized from its convergent nature. However, the relative sizes of cortical and trabecularized porosity are equivalent between pleural and cutaneous cortices. **Directionality:** Cortical pores are significantly more anisotropic (directionally aligned) than trabecularized pores, and this difference is exacerbated in the pleural cortex.

8.7. Hypotheses Revisited

This study fundamentally asked whether the three-dimensional geometry of pore networks is **morphologically optimized** to resist local mechanical strain. The positive overarching finding is that such an optimized relationship does exist in the femoral neck, where the strain patterning is known, and is also implied in

421

the rib, where the strain patterning fits a hypothesized model. Pores in higher-strain regions are morphologically resistant to the initiation and propagation of microcracking because they are significantly less prevalent, less expansive, less convergent, and more longitudinally oriented than pores in lower-strain regions. As porosity is not a significant risk factor for microcracking under low-strain, such as tension (Ebacher et al,, 2007), these regions are responsive to permissive remodeling and resorption. This creates the opposing low-strain pore morphotype of increased prevalence, increased percent porosity, more convergence, and more oblique orientation. Despite this overarching finding, there was variation in confirmation of several adjoining research questions and hypotheses:

[RQ1]: Does three-dimensional pore volume, connectivity, and orientation significantly vary between high strain and low strain regions?

[H1A] The femoral neck will display a high-strain morphotype (significantly smaller, less connected, more longitudinal pores) compared to the matched rib of an individual.

> **[H1A] Reject:** The femoral neck has a complex configuration of increased percentages and larger sizes and size ranges of porosity. However, it is equivalent in pore density, spacing, connectivity, and orientation to the rib. Imaging suggests that this reflects a broader and more uniform endocortical ring of localized low strains adjacent to the endosteum, which are repressed in the thickened pleural cortex of the rib.

[H2A] Within a given cross-section, three-dimensional morphometry will significantly vary between anatomical divisions that describe strain distribution: superior-to-inferior femoral neck octants, and pleural/cutaneous rib halves.

> **[H2A]: Accept:** All morphometric aspects of femoral neck porosity align with the superior-to-inferior strain gradient, except those related to pore thickness. Inferior regions under higher strain have 1) reduced pore prevalence by number, 2) reduced pore prevalence by volume, 3) decreased pore convergence, and 4) longitudinal pore alignment. The pleural cortex of the rib displays all of these high-strain morphotypes except reduced pore prevalence by number. This suggests that the pleural cortex does experience higher strain at the midshaft, at least in the region visualized in this study.

[RQ2]: Does dynamic loading result in significantly more variation between individuals in patterns of strain, and associated pore structure?

[H2A]: In the femoral neck, compared to the rib, body weight and physical activity will produce significantly larger inter-individual variability in three-dimensional pore morphometry in a given anatomical region.

> **[H2A] Reject:** Age, sex, and cross-sectional thickness co-variates had a significant effect on multiple pore morphometric measurements in the rib, but only on pore separation and its standard deviation in the femoral neck. Consistency of loading in the femoral neck appears to reduce inter-

423

individual variation, compared to the rib, which is more sensitive to physiological perturbations.

[H2B] In the femoral neck, compared to the rib, body weight and physical activity will produce larger effect sizes for co-variates related to physical size.

> **[H2B] Reject:** Cross-sectional thickness as a proxy of cross-sectional geometry, BMD, and gross femoral neck geometry did not have a significant effect on any pore morphometric variable. In the rib, cortical thickness significantly decreased both pore density (medium effect size) and pore connective density (small effect size).

[RQ3]: Does bone maintain a structure-strain relationship with age?

[H3A]: With age, pores in high-strain regions will increasingly resemble low-strain morphology.

> **[H3A]: Accept:** As found in previous studies, individual variation obscures much of the significant patterning associated with age. However, aging did have a significant effect on pore separation and its standard deviation (proxy of range) in all levels of analysis (femoral neck vs rib, femoral neck octants, rib cortices). In low-strain regions, pores are less separated on average due to convergence. This suggests that aging causes pores to converge throughout femoral neck and rib cortices, beyond what is mechanically advantageous for specific regional conditions. In the rib, aging additionally significantly increased pore connectivity density, and

then decreased this connectivity as the trabecularized regions were fully resorbed.

[H3B]: This change will be more significant in women, compared to men.

> **[H3B] Accept:** Sex has a significant interaction with age in the intraskeletal comparison between the femoral neck and rib. Aging females had significantly more percent open, closed, and total porosity compared to males. However, males had a significantly higher pore density. Females had significantly larger pores than males in the femoral neck, but not in the rib. This suggests that the convergence of pores is a major driver of increased porosity in females, as has also been found in other studies of the femoral neck. Females showed a significant decrease in pore separation of pooled femoral neck and rib, around the time of menopause (~50), but actually just receded to already lower male levels. In the regional analysis of the femoral neck, aging females were shown to decline significantly below males in pore separation. In the regional analysis of the rib, aging females accumulated significantly larger (thicker) pores than males.

 [H3C]: The rib will show these changes earlier because it remodels more frequently than the femoral neck.

> **[H3C] Reject:** The femoral neck has a consistently higher percent porosity and larger mean pore size across the lifespan, compared to this

425

rib. This appears to be the consequence of localized low-strain resorption at the femoral neck endosteum.

8.8. Future Directions

8.7.1. Validate Marrow Bounding Method

The methodology for automatically drawing the endocortical boundary should be validated and refined through comparisons with traditional manual segmentation. Ideally, this comparison will incorporate multiple skilled bone histologisists for inter-observer error. One option for this manual-automated comparative analysis would be the open source tool EvaluateSegmentation, developed by Taha and Hanbury (2015). This tool assesses 2D and 3D segmentation of medical images and compares two segmentations of the same image over 20 pair-counting metrics.

8.7.2. Improve Sample Representation

All femoral neck octants have already been three-dimensional morphometrically analyzed by pore type. These individuals will be statistically processed to refine the structure-strain model with pore type differentiation. The four femoral neck sections excluded from analysis will also be either rescued through image processing or re-scaned to improve sample size.

426

8.7.3. *Additional Morphological Analysis on Current Images*

In addition to cross-sectional geometry and pore geometry, the marrow bounding protocol also generates an unused 1) image stack of all spaces (cortical and marrow), 2) image stack of isolated trabecular architecture, and 3) image stack of isolated trabecular spaces. These data sets will be processed to quantify trabecular morphometry in relationship to cortical pore indicators of regional strain. Since the femoral neck is physically cut during analysis, pre-cutting micro-CT scans were performed on each intact, 1 cm thick femoral neck at a trabecular analysis resolution of 35 µm. Trabecular analysis will be able to compare results from the high-resolution, uncut rib, the high-resolution, cut femoral neck, and the relatively low-resolution, uncut rib. Additionally, the image stacks of all spaces and trabecular spaces will be analyzed to quantify whether trabecular and cortical spaces are complementary in their association with regional strain.

8.7.4. *Volumetric Bone Mineral Density (vBMD)*

In collaboration with the OSU Wright Center of Innovation in Biomedical Imaging, volumetric bone mineral density, all femoral neck samples were scanned to prepare for analysis of volumetric bone mineral density (vBMD) with a bone mineral density phantom in a Phillips Vereos digital PET/CT. Vereos scans were repeated while femoral neck samples were intact in the proximal femur and after extraction of the neck. All HeliScan micro-CT scans of the femoral neck and rib included a bone mineral density phantom and water standard for vBMD

427

calibration. This data will be analyzed in the future to assess the predictive capacity of vBMD for pore morphometry, and to determine how vBMD is affected by sample processing stage and CT/micro-CT imaging resolution.

8.7.5. *Skeletonization for Individualized Network Connectivity*

Many three-dimensional imaging packages, including Dragonfly, Avizo, Amira, and even ImageJ, have routines for skeletonizing networks for connectivity analysis. This approach thins a network to its smallest dimension and quantifies the number and length of branches and nodes. The current study quantified connectivity in terms of the mean of the overall pore network (e.g. pore linear density, degree of anisotropy, connectivity density). Future approaches will asses variation in the branching morphometry of individual pore networks in relation to mechanical loading and other co-variates. Preliminary skeletonization analysis of a subset of ribs from this study in Avizo indicate that essentially all pores in the rib are connected in a single network, allowing efficient communication around the circumference of the bone.

428

Figure 8.5 Pore Segment Length Decreases with Age in Rib Skeletonization Subsample
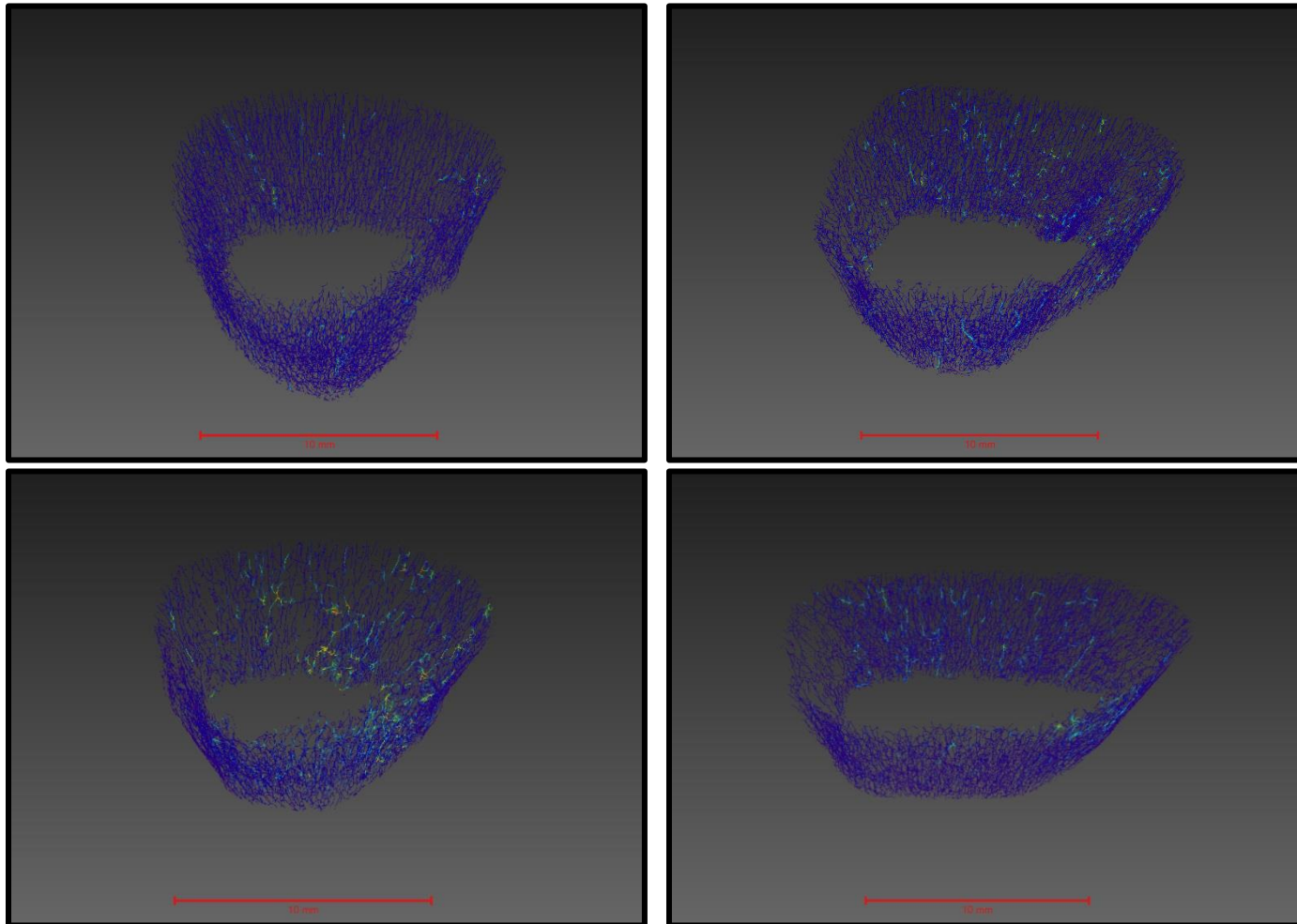
8.7.6. *Incorporate Three-dimensional Histological Analysis*

Ideally, this study will represent the beginning of a larger sample of micro-CT visualizations of pore networks throughout the human skeletal system. More immediately, the author has collected histological serial sections of all ribs in this study using decalcification and cryosectioning along a 1 mm length. This length represents 1/10th of the volume of the micro-CT reconstructions used in this study, but ten times the thickness of a traditional histological section (~100 µm). The author has also developed a methodology for automatically extracting pore boundaries from histological serial sections, and interpolating these ROIs from the 34 adjacent slices (each 30 µm thick) in each 1 mm length to reconstruct a three-dimensional volume (Cole et al., 2017; Cole et al., 2018). This serial section sample includes 26 additional individuals (total n = 40), with at least two males and two females per age group, including teenaged subadults. In immediately future work, the author will analyze these smaller three-dimensional volumes to compare to the conclusions about rib pore morphometry from this study. Moreover, the histological nature of these slides provides an opportunity to associate three-dimensional pore morphometry with patterning in osteon population density, osteon size and shape, osteocyte lacunar density, and collagen fiber orientation for osteon strain morphotypes.

430

9.   Conclusions

Research often approaches cortical porosity as an adversary, hungrily resorbing the cortex and setting traps for microcracks to spontaneously fracture the aged. Yet porosity is so much more than a rouge artifact of the remodeling process. It is the architecture of the vascular "super highway" that nourishes trapped osteocytes and transports osteoclasts and osteoblasts to sites requiring repair or turnover. Sites in need of repair can quickly receive a branch from the highly interconnected and complex pore network. Without retaining this vascular connection, distant regions of the cortex would starve their osteocytes and become cracked and brittle.

All microstructural features that protect and repair bone have consequences when cells begin to uncouple from their mechanical and physiological regulation. Severe bone loss is merely a more common pathology than diseases that trigger erratic woven bone formation or osteocytic osteolysis. This is because excessive bone loss stems not from doing the wrong thing (tissue malformation), but from doing the right thing (tissue turnover) in the wrong proportions or location.

The purpose of this study was to determine whether cortical porosity morphologically adapts to localized mechanical conditions, in order to reduce the probability of microcrack propagation and spontaneous fracture. Specifically, this

431

study proposed a structure-strain model of pore morphotypes, in which remodeling in high-strain regions adapted pore geometry to reduce the risk of microcracking. Three-dimensional imaging and analysis of the human femoral neck and rib confirmed and refined the morphometric quantification of this relationship. The cellular mechanism of this morphometric differentiation is probably signaling based control of the "coupling" period of reversal, where osteoclasts turn over remodeling to osteoblasts. The existing stimulatory and inhibiatory signaling cascades between osteocytes, osteoclasts, and osteoblasts inherent in this process would allow for fine control of the size, shape, orientation, and convergence of pore networks.

This structure-strain relationship detereoriates with age, as pores become significantly more convergent in the femoral neck and rib. This decay is accelerated in females due to the loss of endosteum-preserving estrogen at menopause. There are also significant interactions with cortical thickness, and with broader demographic co-variates that represent body size, bone mineral density, femoral neck gross geometry, and cross-sectional mass and shape.

Methodologically, this study produced broadly applicable, open-source code for many applications in processing micro-CT images of bone tissue for morphometric analysis. Specifically, these utilities include brightness-contrast thresholding (ImageJ), automated pore extraction (CT-Analyser) and batch process lateral merging of large cut samples (ImageJ). Additionally, a morphological marrow bounding routine was developed to automatically estimate

432

the endocortical boundary (CT-Analyser). The output of this routine is a series of image stacks of the filled cortical shell, isolated cortical bone with retained pores, isolated pore network, isolated trabecular architecture, all spaces, and all trabecular spaces. The pore network is further morphologically modified by code for separating cortical and trabecularized pore types (ImageJ) and quantifying cross-sectional geometry and bone mass metrics (ImageJ). Finally, regional differentiation routines (ImageJ) use the major axis to automatically divide the rib image stack into cutaneous and pleural cortices and the femoral neck image stack into octants based on the geometry of each individual slice.

More conceptually, this study cautions that presumed "unloaded" and "loaded" intraskeletal elements will not necessarily produce "low strain" and "high strain" morphometry results. Unless the local mechanical loading conditions are extremely well defined, structure-strain relationships should be extracted from regional cross-sectional variation in strain, where the bone controls for its own local mechanical and physiological condtions. Cortical bone does indeed "optimize bone loss across the lifespan" by retaining protective structure-strain patterning in high-risk regions even in older individuals, and limiting the influence of co-variates in the vital femoral neck. While time and change are inevitable, bone tissue makes the most of what it has left, until the very end.

433

References

Chapter 1: Statement of the Problem

Amstadter AB, Zajac K, Strachan M, Hernandez MA, Kilpatrick DG, Acierno R. 2011. Prevalence and correlates of elder mistreatment in South Carolina: The South Carolina Elder Mistreatment Study. J Interpers Violence. 26:2947–2972.

Acierno R, Hernandez MA, Amstadter AB, Resnick HS, Steve K, Muzzy W, Kilpatrick DG. 2010. Prevalence and correlates of emotional, physical, sexual, and financial abuse and potential neglect in the United States: The National Elder Mistreatment Study. Am J Public Health 100:292–297

Agarwal, AM. 2008. Light and broken bones: examining and interpreting bone loss and osteoporosis in past populations. In: Sanders, S.R., Katzenberg, M.A. (Eds.), Biological Anthropology of the Human Skeleton. Wiley-Liss, New York, pp. 387–410.

Agnew AM, Murach MM, Dominguez VM, Sreedhar A, Misicka E, Harden A, Bolte JH, Stammen J, Moorhouse K, Kang Y-S. 2018. Sources of variability in structural bending response of pediatric and adult human ribs in dynamic frontal impacts. Stapp Car Crash Journal. Vol. 62, 119-192.

Agnew, A.M., Moorhouse, K., Kang, Y.S., Donnelly, B.R., Pfefferle, K., Manning, A.X., et al., 2013. The response of pediatric ribs to quasi-static loading: mechanical properties and microstructure. Ann. Biomed. Eng. 41, 2501–2504.

Agnew AM and Stout, SD. 2012. Brief Communication: Reevaluating osteoporosis in human ribs: The role of intracortical porosity. Am. J. Phys. Anthropol. 148: 462-466

Beauchesne, P., Agarwal, S.C., 2014. Age-related cortical bone maintenance and loss in an Imperial Roman population. Int. J. Osteoarchaeol. 24 (1), 15–30.

Bell KL, Loveridge N, Power J, Garrahan N, Meggitt BF, Reeve J. 1999a. Regional differences in cortical porosity in the fractured femoral neck. Bone 24:57–64.

Bell KL, Loveridge N, Power J, Garrahan N, Stanton M, Lunt M, Meggitt BF, Reeve J. 1999b. Structure of the femoral neck in hip fracture: Cortical bone loss in the inferoanterior to superoposterior axis. J Bone Miner Res 14:111–119.

Bellemare F, Jeanneret A, Couture J. 2003. Sex differences in thoracic dimensions and configuration. Am J Respir Crit Care Med 168:305–312.

Bousson V, Meunier A, Bergot C. 2001. Distribution of intracortical porosity in the human middle cortex by age and gender. J. Bone. Miner. Res. 16:1308–1317

Britz, H.M., Thomas, C.D.L., Clement, J.G., Cooper, D.M.L., 2009. The relation of femoral osteon geometry to age, sex, height and weight. Bone 45 (1), 77–83.

Brown A, Cole ME, Stout SD. 2015. A preliminary study of cortical and trabecularized porosity distribution in human and quadruped ribs. The 84th Annual Meeting of the American Association of Physical Anthropologists, St. Louis, MO.

Burr, D.B., 2011. Why bones bend but don't break. J. Musculoskelet Neuronal Interact 11(4), 270–285.

Burr DB and Akkus O. 2014. Bone Morphology and Organization. In: Basic and Applied Bone Biology. David B. Burr and Matthew R. Allen, eds. London, UK: Academic Press. pp 3- 25.

Burr DB and Martin RB. 1993. Calculating the probability that microcracks initiate resorption spaces. J Biomech 26:613–616

Burnes D, Pillemer K, Caccamise PL, Mason A, Henderson CR Jr, Berman J, Cook AM, Shukoff D, Brownell P, Powell M, Salamone A, Lachs MS. 2015. Prevalence of and risk factors for elder abuse and neglect in the community: A population-based study. J Am Geroatr Soc 63(9):1906-12

Chen H and Kubo KY. 2014. Bone three-dimensional microstructural features of the common osteoporotic fracture sites. World J Orthop. 5(4):486-95

Cho, H., Stout, S.D., 2003. Bone remodeling and age-associated bone loss in the past: a histomorphometric analysis of the imperial roman skeletal population of Isola Sacra. In: Agarwal, S.C., Stout, S.D. (Eds.), Bone Loss and Osteoporosis: An Anthropological Perspective. Kluwer Academic/Plenum, New York, pp. 207–228

Crescimanno, A., Stout, S.D., 2012. Differentiating fragmented human and nonhuman long bone using osteon circularity. J. Forensic Sci. 57 (2), 287–294.

Cole ME, Stout SD. 2015. A semi-automatic method for intracortical porosity quantification with application to intraskeletal variability. The 84th Annual Meeting of the American Association of Physical Anthropologists, St. Louis, MO. American Journal of Physical Anthropology 156(S60):108

Cole ME, Stout SD. 2017. Three-dimensional reconstruction of vascular pore networks in the human rib from two-dimensional serial sections. The 86th Annual Meeting of the American Association of Physical Anthropologists, New Orleans, LA. American Journal of Physical Anthropology 162(S64):147

Cole ME, Stout SD, Agnew AM. 2018. Automated extraction of two-dimensional cortical porosity descriptors from histological and micro-computed tomography serial sections. American Journal of Physical Anthropology 165(S66):51-52

Currey, JD. 2003. The many adaptations of bone. Journal of Biomechanics 36(10):1487-1495.

Dolinak D. 2008. Review of the significance of various low force fractures in the elderly. Am J Forensic Med Pathol 29(2):99-105.

Dominguez VM, Agnew AM. 2016. Examination of factors potentially influencing osteon size in the human rib. Anat Rec (Hoboken). 299(3):313-24

Ebacher, V., Tang, C., McKay, H., Oxland, T.R., Guy, P., Wang, R., 2007. Strain redistribution and cracking behavior of human bone during bending. Bone 40 (5), 1265–1275.

Gilligan I, Chandraphak S, Mahakkanukrauh P. 2013. Femoral neck-shaft angle in humans: variation relating to climate, clothing, lifestyle, sex, age and side. J Anat 223(2):133-51

Gocha, T.P., Agnew, A.M., 2016. Spatial variation in osteon population density at the human femoral midshaft: histomorphometric adaptations to habitual load environment. J. Anat. 28 (5), 733–745.

Goliath, J.R., Stewart, M.C., Stout, S.D., 2016. Variation in osteon histomorphometrics and their impact on age-at-death estimation in older individuals. Forensic Sci. Int. 262, 282.e1–6.

Gullberg B, Johnell O, Kanis JA. 1997. World-wide projections for hip fracture. Osteoporos Int 7:407.

Frost, H.M., 1969. Tetracycline-based histological analysis of bone remodeling. Calcif. Tissue Res. 3 (3), 211–237.

Frost HM. 2003. Bone's mechanostat: a 2003 update. Anat. Rec. A. Discov. Mol. Cell. Evol. Biol. 275(2): 1081 – 1101.

Hattner, R., Frost, H.M., 1963. Mean skeletal age: its meaning and a method of calculation. Henry Ford Hosp. Med. Bull. 11, 201–216

Holzer G, von Skrbensky G, Holzer LA, Pichl W. 2009. Hip fractures and the contribution of cortical versus trabecular bone to femoral neck strength. J Bone Miner Res 24(3):468-74

Hunt, K.J., Skedros, J.G., 2001. The role of osteocyte lacunae populations in interpreting loading history of bone. Am. J. Phys. Anthropol. 32 (Suppl.), 83.

Hunter, R.L., Agnew, A.M., 2016. Intraskeletal variation in human cortical osteocyte lacunar density: implications for bone quality assessment. Bone Rep. 5, 252–261.

Kanis JA, Johnell O, Oden A, Sembo I, Redlund-Johnell I, Dawson A, De Laet C, Jonsson B. 2000. Long-term risk of osteoporotic fracture in Malmo. Osteoporos Int 11:669.

Kannus P, Parkkari J, Koskinen S, Niemi S, Palvanen M, Järvinen M, Vuori I.1999. Fall-induced injuries and deaths among older adults. JAMA. 281:1895–1899

Komori T. 2013. Functions of the osteocyte network in the regulation of bone mass. Cell Tissue Res 352:191-198

Lanyon LD, Baggott DG. 1976. Mechanical function as an influence on the structure and form of bone. J Bone Joint Surg.58-B:436–443

Laumann EO, Leitsch SA, Waite LJ. 2008. Elder mistreatment in the United States: Prevalence estimates from a nationally representative study. J Gerontol B Psychol Sci Soc Sci 63B:S248–SS254.

Lovejoy CO. 1988. Evolution of human walking. Sci Am 259:118–125

Li, J., Mashiba, T., and Burr, D. B. 2001. Bisphosphonate treatment suppresses targeted repair of microdamage. Trans Orthop Res Soc 26:320.

Martin, R.B., 1993. Aging and strength of bone as a structural material. Calcif. Tissue Int. 53 (Suppl. 1), S34–S39.

Mason, M.W., Skedros, J.G., Bloebaum, R.D., 1995. Evidence of strain-mode-related cortical adaptation in the diaphysis of the horse radius. Bone 17 (3), 229–237.

Mayya A, Banerjee A, Rajesh R (2013) Mammalian cortical bone in tension is non-Haversian. Nat Sci Rep 3, 2533.

Meeusen RA, Christensen AM, Hefner JT. 2015. The use of femoral neck axis length to Estimate sex and ancestry. J Forensic Sci 60(5):1300-4

Melton LJ 3rd, Chrischilles EA, Cooper C, Lane AW, Riggs BL. 1992. Perspective. How many women have osteoporosis? J Bone Miner Res 7:1005.

Melton LJ 3rd, Atkinson EJ, O'Connor MK, O'Fallon WM, Riggs BL. 1998. Bone density and fracture risk in men. J Bone Miner Res 13:1915.

Milovanovic P, Djonic D, Marshall RP, Hahn M, Nikolic S, Zivkovic V, Amling M, Djuric M. 2012. Micro-structural basis for particular vulnerability of the superolateral neck trabecular bone in the postmenopausal women with hip fractures. Bone 50(1):63-8.

Mulhern, D.M., 2000. Rib remodeling dynamics in a skeletal population from Kulubnarti, Nubia. Am. J. Phys. Anthropol. 111 (4), 519–530.

Mulhern, D.M., Van Gerven, D.P., 1997. Patterns of bone remodeling dynamics in a medieval Nubian population. Am. J. Phys. Anthropol. 104 (1), 133–146.

Nalla, R.K., Kruzic, J.J., Kinney, J.H., Ritchie, R.O., 2005. Mechanistic aspects of fracture and r-curve behavior in human cortical bone. Biomaterials 26, 217–231.

Ohman JC, Krochta TJ, Lovejoy CO, Mensforth RP, Latimer B. 1997. Cortical bone distribution in the femoral neck of hominoids: implications for the locomotion of Australopithecus afarensis. Am J Phys Anthropol 104:117–131.

Pearson, O.M., Lieberman, D.E., 2004. The aging of Wolff's "law:" ontogeny and responses to mechanical loading in cortical bone. Yearb. Phys. Anthropol. Suppl. 39, 63–99.

Pfeiffer, S., 1998. Variability in osteon size in recent human populations. Am. J. Phys. Anthropol. 106 (2), 219–227.

Pfeiffer, S., Crowder, C., Harrington, L., Brown, M., 2006. Secondary osteon and Haversian canal dimensions as behavioral indicators. Am. J. Phys. Anthropol. 131 (4), 460–468.

Portigliatti Barbos, M., Bianco, P., Ascenzi, A., 1983. Distribution of osteonic and interstitial components in the human femoral shaft with reference to structure, calcification and mechanical properties. Acta Anat. 115 (2), 178–186.

Plotkin LI and Bivi N. Local regulation of bone cell function. In: Basic and Applied Bone Biology. David B. Burr and Matthew R. Allen, eds. London, UK: Academic Press. pp. 47 – 73.

Pratt IV, Johnston JD, Walker E, Cooper DML. 2018. Interpreting the three-dimensional orientation of vascular canals and cross-sectional geometry of cortical bone in birds and bats. J Anat, 14(Pt 5), p.S13.

Qu X, He Z, Qiao H, Zhai Z, Mao Z, Yu Z, Dai K. 2018. Serum copper levels are associated with bone mineral density and total fracture. J Orthop Translat. 14:34-44.

Reilly GC and Currey JD. 2000. The effects of damage and microcracking on the impact strength of bone. J. Biomech., 33: 337–343

Robling AG, Fuchs RK, Burr DB. 2014. Mechanical Adaptation. In: Basic and Applied Bone Biology. David B. Burr and Matthew R. Allen, eds. London, UK: Academic Press. pp 175

Robling, A.G., Stout, S., 2003. Histomorphology, geometry, and mechanical loading in past populations. In: Agarwal, S.C., Stout, S.D. (Eds.), Bone Loss and Osteoporosis: An Anthropological Perspective. Kluwer Academic/Plenum, New York, pp. 189–203.

Rondanelli M, Opizzi A, Perna S, Faliva MA. 2013. Update on nutrients involved in maintaining healthy bone. Endocrinol Nutr. 60(4):197-210.

Ruff, C., Holt, B., Trinkaus, E., 2006. Who's afraid of the big bad Wolff?: "Wolff's law" and bone functional adaptation. Am. J. Phys. Anthropol. 129 (4), 484–498.

Ruff CB and Higgins R. 2013. Femoral neck structure and function in early hominins. Am. J. Phys. Anthropol. 150:512–525

Sjogren H, Bjornstig U. 1989. Unintentional injuries among elderly people: incidence, causes, severity, and costs. Accid Anal Prev. 21:233–242.

Skedros, J.G., Bloebaum, R.D., Mason, M.W., Bramble, D.M., 1994a. Analysis of a tension/compression skeletal system: possible strain-specific differences in the hierarchical organization of bone. Anat. Rec. 239 (4), 396–404.

Skedros, J.G., Mason, M.W., Bloebaum, R., 1994b. Differences in osteonal micromorphology between tensile and compressive cortices of a bending skeletal system: indications of potential strain-specific differences in bone microstructure. Anat. Rec. 239 (4), 405–413.

Skedros JG, Mendenhall SD, Kiser CJ, Winet H. 2009. Interpreting cortical bone adaptation and load history by quantifying osteon morphotypes in circularly polarized light images. Bone 44(3): 392 – 403

Skedros, J.G., Su, S.C., Bloebaum, R.D., 1997. Biomechanical implications of mineral content and microstructural variations in cortical bone of horse, elk and sheep calcanei. Anat. Rec. 249 (3), 297–316.

Skedros, J.G., Sybrowsky, C.L., Dayton, M.R., Bloebaum, R.D., Bachus, K.N., 2003. The role of osteocyte lacuna population density on the mechanical properties of cortical bone. Trans. Orthop. Res. Soc. 28, 414.

Skedros, J.G., Hunt, K.J., Bloebaum, R.D., 2004. Relationships of loading history and structural and material characteristics of bone: development of the mule deer calcaneus. J. Morphol. 259 (3), 281–307.

Skedros, J.G., Grunander, T.R., Hamrick, M.W., 2005. Spatial distribution of osteocyte lacunae in equine radii and third metacarpals: considerations for cellular communication, microdamage detection and metabolism. Cells Tissues Organs 180 (4), 215–236.

Wang, R., Gupta, H.S., 2011. Deformation and fracture mechanisms of bone and nacre. Ann. Rev. Mater. Res. 41 (1), 41–73

Weaver, CM. 2013. Potassium and Health. Adv Nutr. 2013 May; 4(3): 368S–377S.

Weinbaum S, Cowin SC, Zeng Y. 1994. A model for the excitation of osteocytes by mechanical loading-induced bone fluid shear stresses. J Biomech 27(3): 339- 360

Yeni, Y.N., Brown, C.U., Wang, Z., Norman, T.L., 1997. The influence of bone morphology on fracture toughness of the human femur and tibia. Bone 21 (5), 453–459.

Zedda M, Lepore G, Biggio GP, Gadau S, Mura E, Farina V. 2015. Morphology, morphometry, and spatial distribution of secondary osteons in equine femur. Anat Histol Embryol 44, 328–332.

Chapter 2: Cellular Basis of Bone Formation and Resorption

Addison WN, Nakano Y, Loisel T, Crine P, McKee MD. 2008. MEPE-ASARM Peptides Control Extracellular Matrix Mineralization by Binding to Hydroxyapatite: An Inhibition Regulated by PHEX Cleavage of ASARM. J Bone Miner Res 23(10):1638 – 1649.

Afzal F, Pratap J, Ito K, Ito Y, Stein JL, van Wijnen AJ, Stein GS, Lian JB, Javed A. 2005. Smad function and intranuclear targeting share a Runx2 motif required for osteogenic lineage induction and BMP2 responsive transcription. J Cell Physiol 204:63–72.

Akiyama H, Chaboissier MC, Martin JF, Schedl A & de Crombrugghe B 2002 The transcription factor Sox9 has essential roles in successive steps of the chondrocyte differentiation pathway and is required for expression of Sox5 and Sox6. Genes and Development 16 2813–2828.

Allan EH, Häusler KD, Wei T, Gooi JH, Quinn JM, Crimeen-Irwin B, Pompolo S, Sims NA, Gillespie MT, Onyia JE, Martin TJ.. 2008. EphrinB2 regulation by PTH and PTHrP revealed by molecular profiling in differentiating osteoblasts. J BoneMiner Res 23:1170–1181.

Alliston T, Choy L, Ducy P, Karsenty G, Derynck R. 2001 TGF-betainduced repression of CBFA1 by Smad3 decreases cbfa1 and osteocalcin expression and inhibits osteoblast differentiation. EMBO J 20:2254–72.

Alnaeeli M, Penninger JM, Teng YT. 2006. Immune interactions with CD4þ T cells promote the development of functional osteoclasts from murine CD11cþ dendritic cells. J Immunol 177:3314–3326.

Ambrosetti D, Holmes G, Mansukhani A, Basilico C. 2008. Fibroblast growth factor signaling uses multiple mechanisms to inhibit Wnt-induced transcription in osteoblasts. Mol Cell Biol. 28:4759–4771.

Amizuka N, Warshawsky H, Henderson JE, Goltzman D, Karaplis AC. 1994. Parathyroid hormonerelated peptide-depleted mice show abnormal epiphyseal cartilage development and altered endochondral bone formation. J. Cell. Biol. 126: 1611–1623.

Aubin JE, Liu F. 1996. The osteoblast lineage. In: Bilezikian JP, Raisz, LG, Rodan GA, editors. The principles of bone biology. Toronto: Academic Press. p 51–67.

Bae KS, Park JB, Kim HS, Kim DS, Park DJ, Kang SJ. 2011. Neuron-like differentiation of bone marrow-derived mesenchymal stem cells. Yonsei Med 52(3):401-412.

Bandyopadhyay A, Tsuji K, Cox K, Harfe BD, Rosen V, Tabin CJ. 2006. Genetic analysis of the roles of BMP2, BMP4, and BMP7 in limb patterning and skeletogenesis. PLoS Genet 2: e216.

Bakker AD, Klein-Nulend J, Tanck E, Albers GH, Lips P, Burger EH. 2005. Additive effects of estrogen and mechanical stress on nitric oxide and prostaglandin E2 production by bone cells from osteoporotic donors. Osteoporos Int. 16(8):983-9

Bellido T, Plotkin LI, Bruzzaniti A. 2014. Bone cells. In: Basic and Applied Bone Biology. David B. Burr and Matthew R. Allen, eds. London, UK: Academic Press. pp. 27 – 46.

Bellido T and Gallant KMH. 2014. Hormal effects on bone cells. In: Basic and Applied Bone Biology. David B. Burr and Matthew R. Allen, eds. London, UK: Academic Press. pp. 299 – 314

Bivi N, Condon KW, Allen MR, Farlow N, Passeri G, Brun LR, Rhee Y, Bellido T, Plotkin LI 2012. Cell autonomous requirement of connexin 43 for osteocyte survival: consequences for endocortical resorption and periosteal bone formation. J Bone Miner Res 27:374–389

Borton A, Frederick J, Datto M, Wang X-F, Weinstein R. 2001. The loss of SMAD3 results in lower rate of bone formation and osteopenia through dysregulation of osteoblast differentiation and apoptosis. J Bone Miner Res 16:1754–1764.

Bougeret C1, Mansur IG, Dastot H, Schmid M, Mahouy G, Bensussan A, Boumsell L.. 1992. Increased surface expression of a newly identified 150-kDa dimer early after human T lymphocyte activation. J Immunol 48:318–323.

Burr DB and Akkus O. Bone Morphology and Organization. 2014. In: Basic and Applied Bone Biology, David B. Burr and Matthew R. Allen, eds. Elsevier: London. pp. 3 – 26.

Burr, D. B. and Martin, R. B. Calculating the probability that microcracks initiate resorption spaces. J Biomech 26:613–616; 1993.

Burr, D. B., Martin, R. B., Schaffler, M. B., and Radin, E. L. 1985. Bone remodeling in response to in vivo fatigue microdamage. J Biomech 18:189–200

Burton, P., Nyssen-Behets, C., Dhem, A., 1989. Haversian bone remodeling in the human fetus. Acta Anatomica 135, 171–175.

Brotto M and Johnson ML. 2014. Endocrine crosstalk between muscle and bone. Curr Osteoporos Rep 12(2):135-141.

Cabrita, G. J. M., B. S. Ferreira, C. L. da Silva, R. Goncalves, G. Almeida-Porada, J. M. S. Cabral. 2003. Hematopoietic stem cells: from the bone to the bioreactor. Trends Biotechnol. 21(5):233–240

438

Callewaert F, Sinnesael M, Gielen E, Boonen S, Vanderschueren D. 2010a. Skeletal sexual dimorphism: relative contribution of sex steroids, GH-IGF1, and mechanical loading. 207(2):127-34

Callewaert F, Boonen S and Vanderschueren D. 2010b Sex steroids and the male skeleton: a tale of two hormones. Trends in Endocrinology and Metabolism 21 89–95.

Callewaert F, Venken K, Kopchick J, Torcasio A, van Lenthe GH, Boonen S and Vanderschueren D. 2010c Sexual dimorphism in cortical bone size and strength but not density is determined by independent and time-specific actions of sex steroids and IGF-I: evidence from pubertal mouse models. Journal of Bone and Mineral Research 25 617–626.

Callewaert F, Bakker A, Schrooten J, VanMeerbeek B, VerhoevenG, Boonen S and Vanderschueren D 2010d. Androgen receptor disruption increases the osteogenic response to mechanical loading in male mice. Journal of Bone and Mineral Research 25 124–131

Caplan AI, Pechak DG. 1987. The cellular and molecular embryology of bone formation. In Bone and mineral research (ed. Peck WA), Vol. 5, pp. 117–183. Elsevier, New York.

Campbell PG, Novak JF, Yanosick TB, McMaster JH. 199.2. Involvement of the plasmin system in dissociation of the insulin-like growth factor-binding protein complex. Endocrinology 130:1401–1412.

Canalis E, Centrella M, Burch W, McCarthy TL. 1989. Insulin-like growth factor I mediates selective anabolic effects of parathyroid hormone in bone cultures. J Clin Invest. Jan; 83(1):60-5.

Celil A.B. and Campbell P.G. 2005. BMP-2 and insulin-like growth factor-I mediate Osterix (Osx) expression in human mesenchymal stem cells via the MAPK and protein kinase D signaling pathways. J. Biol. Chem. 280, 31353-31359

Cenci S, Weitzmann MN, Roggia C, Namba N, Novack D, Woodring J, Pacifici R. 2000. Estrogen deficiency induces bone loss by enhancing T-cell production of TNF-alpha. J Clin Invest 106:1229–1237.

Chan GK, Miao D, Deckelbaum R, Bolivar I, Karaplis A, Goltzman D. Parathyroid hormone-related peptide interacts with bone morphogenetic protein 2 to increase osteoblastogenesis and decrease adipogenesis in pluripotent C3H10T 1/2 mesenchymal cells. Endocrinology. 144(12):5511-20.

Chau JFL, Leong WF, Li B. 2009. Signaling pathways governing osteoblast proliferation, differentiation and function. Histol Histopathol 24:1593-1606

Chen G, Deng C, LI T. 2012. TGF-β and BMP Signaling in Osteoblast Differentiation and Bone Formation. Int J Biol Sci 8(2):272-288

Cheung WY, Simmons CA, You L. 2012 Osteocyte apoptosis regulates osteoclast precursor adhesion via osteocytic IL-6 secretion and endothelial ICAM-1 expression. Bone 50:104–110

Choi JY, Pratap J, Javed A, Zaidi SK, Xing L, Balint E, Dalamangas S, Boyce B, van Wijnen AJ, Lian JB, Stein JL, Jones SN, Stein GS. 2001. Subnuclear targeting of Runx/Cbfa/AML factors is essential for tissue-specific differentiation during embryonic development. Proc Natl Acad Sci 98: 8650–8655.

Choi YH, Jeong HM, Jin YH, Li H, Yeo CY, Lee KY. Akt phosphorylates and regulates the osteogenic activity of Osterix. Biochem Biophys Res Commun. 2011; 411:637-41.

Cirmanova V, Bayer M, Starka L, Zajickova K. 2008. The effect of leptin on bone: an evolving concept of action. Physiol Res 57, Suppl 1: S143–S151

Correa D, Hesse E, Seriwatanachai D, Kiviranta R, Saito H, Yamana K, Neff L, Atfi A, Coillard L, Sitara D et al. 2010 Zfp521 is a target gene and key effector of parathyroid hormone-related peptide signaling in growth plate chondrocytes. Developmental Cell 19 533–546.

Currey, John D. 2003. The many adaptations of bone. Journal of Biomechanics 36(10):1487-1495.

Datta NS, Chen C, Berry JE, McCauley LK. 2005. PTHrP signaling targets cyclin D1 and induces osteoblastic cell growth arrest. J Bone Miner Res. 20(6):1051-64.

Datta NS, Pettway GJ, Chen C, Koh AJ, McCauley LK. 2007. Cyclin D1 as a target for the proliferative effects of PTH and PTHrP in early osteoblastic cells. J Bone Miner Res. 22(7):951-64.

Datta NS, Abou-Samra AB. PTH and PTHrP signaling in osteoblasts. Cell Signal 21(8):1245-1254

Day TF, Guo X, Garrett-Beal L, Yang Y. 2005. Wnt/b-catenin signaling in mesenchymal progenitors controls osteoblast and chondrocyte differentiation during vertebrate skeletogenesis. Dev Cell 8: 739–750.

de Crombrugghe B, Lefebvre V, Behringer RR, BiW,Murakami S, Huang W. 2000. Transcriptional mechanisms of chondrocyte differentiation. Matrix Biol 19: 389–394.

DeChiara TM, Robertson EJ & Efstratiadis A 1991 Parental imprinting of the mouse insulin-like growth factor II gene. Cell 64 849–859.

DiGirolamo DJ, Mukherjee A, Fulzele K, Gan Y, Cao X, Frank SJ, Clemens TL. 2007. Mode of growth hormone action in osteoblasts. J. Biol. Chem. 282, 31666–31674

Dobnig H, Turner RT. 1995 Evidence that intermittent treatment with parathyroid hormone increases bone formation in adult rats by activation of bone lining cells. Endocrinology.136:3632–3638.

Eferl R, Hoebertz A, Schilling AF, Rath M,Karreth F,Kenner L, Amling M, Wagner EF. 2004. The Fos-related antigen Fra-1 is an activator of bone matrix formation. EMBO J 23: 2789–2799.

Einhorn TA. 1992. Bone strength: the bottom line. Calcif Tissue Int. 51:333–339

Eriksen EF. 2010. Cellular mechanisms of bone remodeling. Rev Endocr Metab Disord 11:219-227.

Eswarakumar VP,Monsonego-Ornan E, Pines M, Antonopoulou I,Morriss- Kay GM, Lonai P. 2002. The IIIc alternative of Fgfr2 is a positive regulator of bone formation. Development 129: 3783–3793.

Eswarakumar VP, Horowitz MC, Locklin R, Morriss-Kay GM, Lonai P. 2004. A gain-of-function mutation of Fgfr2c demonstrates the roles of this receptor variant in osteogenesis. Proc Natl Acad Sci 101: 12555–12560.

Fakhry A, Ratisoontorn C, Vedhachalam C, Salhab I, Koyama E, Leboy P, Pacifici M, Kirschner RE, Nah HD. 2005. Effects of FGF-2/-9 in calvarial bone cell cultures: differentiation stage-dependent mitogenic effect, inverse regulation of BMP-2 and noggin, and enhancement of osteogenic potential. Bone. 36:254-66.

Feik S, Thomas C, Bruns R, Clement J. 2000. Regional variations in cortical modeling in the femoral mid-shaft: sex and age differences. Am. J. Phys. Anthropol. 112:191–205

Ferretti JL, Capozza RF, Cointry GR, Garcia SL, Plotkin H, Alvarez Filgueira ML, Zanchetta JR. 1998. Gender-related differences in the relationship between densitometric values of whole-body bone mineral content and lean body mass in humans between 2 and 87 years of age. Bone 22:683–690.

Ferretti, M., M.A. Muglia, F. Remaggi, V. Canè, C. Palumbo. 1999. Histomorphometric study on the osteocyte lacuno-canalicular network in animals of different species. 2. Parallel-fi bered and lamellar bones. Ital J Anat Embryol 104: 121–131.

Ferron M, Wei J, Yoshizawa T, Del Fattore A, DePinho RA, Teti A, Ducy P, Karsenty G. 2010. Insulin signaling in osteoblasts integrates bone remodeling and energy metabolism. Cell 142, 296–308.

Fogelholm G, Sievänen H, Kukkonen-Harjula T, Pasanen M. 2001. Bone mineral density during reduction, maintenance, and regain of body weight in premenopausal, obese women. Osteoporos Int 12:199–206

Frost HM. 1983. The regional acceleratory phenomenon: a review. Henry Ford Hosp Med J. 31(1):3-9.

Frost HM. 1987. Bone mass and the mechanostat. A proposal. Anat. Rec. 219:1-9

Frost HM. 1990. Skeletal structural adaptations to mechanical usage(SATMU): 2. Redefining Wolff's Law: the remodeling problem. Anat. Rec. 226:414–422.

Frost HM. 1992. The role of changes in mechanical usage set points in the pathogenesis of osteoporosis. J Bone Miner Res 7:253-261.

Frost HM. 2003a. Bone's mechanostat: a 2003 update. Anat. Rec. A. Discov. Mol. Cell. Evol. Biol. 275(2): 1081 – 1101.

Frost HM. 2003b. On changing view about age-related bone loss. In: Bone Loss and Osteoporosis: An anthropological perspective. Agarwal SC and Stout SD, eds. New York: Spring Science + Business Media. pp 19 – 31)

Fuentealba LC, Eivers E, Ikeda A, Hurtado C, Kuroda H, Pera EM, De Robertis EM. 2007. Integrating patterning signals: Wnt/GSK3 regulates the duration of the BMP/Smad1 signal. Cell. 131:980–993.

Fukumoto S, Allan EH, Yee JA, Gelehrter TD, Martin TJ. 1992. Plasminogen activator regulation inosteoblasts: parathyroid hormone inhibition of type-1 plasminogen activator inhibitor and its mRNA. J Cell Physiol 152:346–355.

440

Fukumoto S, Allan EH, Martin TJ. 1994. Regulation of plasminogen activator inhibitor-1 (PAI-1) expression by 1,25-dihydroxyvitamin D-3 in normal and malignant rat osteoblasts. Biochim Biophys Acta 1201:223–228

Jee WS. 2000. Principles in bone physiology. J Musculoskeletal Interactions 1:9-11

Galvard H, Elmstahl S, Elmstahl B et al (1996) Differences in body composition between female geriatric hip fracture patients and healthy controls: body fat is more important as an explanatory factor for the fracture than body weight and lean body mass. Aging Clin Exp Res 8:282–286

Goldman, Haviva M., Shannon C. McFarlin, David M.L. Cooper, C. David L. Thomas, and John G. Clement. 2009. Ontogenetic patterning of cortical bone microstructure and geometry at the human mid-shaft femur. The Anatomical Record 292: 48-64.

Gurkan UA and Akkus O. 2008. The mechanical environment of bone marrow: a review. Ann. Biomed. Engng. 36, 1978- 1991.

Gluhak-Heinrich J, Ye L, Bonewald LF, Feng JQ, MacDougallmM, Harris SE, Pavlin D. 2003. Mechanical loading stimulates dentin matrix protein 1 (DMP1) expression in osteocytes in vivo. J Bone Miner Res. 18:807-17.

Hall BK, Miyake T. 2000. All for one and one for all: Condensations and the initiation of skeletal development. Bioessays 22: 138–147.

Han ZH, Palnitkar S, Rao DS, Nelson D, Parfitt AM. 1997. Effects of ethnicity and age or menopause on the remodeling and turnover of iliac bone: implications for mechanisms of bone loss. J Bone Miner Res 12:498–508.

Harris WH, Heaney RP. 1969. Skeletal renewal and metabolic bone disease. N Engl J Med 280:193–202.

Harris SE, Gluhak-Heinrich J, Harris MA, Yang W, Bonewald LF, Riha D, Rowe PS, Robling AG, Turner CH, Feng JQ, McKee MD, Nicollela D. 2007. DMP1 and MEPE expression are elevated in osteocytes after mechanical loading in vivo: theoretical role in controlling mineral quality in the perilacunar matrix. J Musculoskelet Neuronal Interact 7:313-5.

Hauge EM, Qvesel D, Eriksen EF, Mosekilde L, Melsen F. 2001. Cancellous bone remodeling occurs in specialized compartments lined by cells expressing osteoblastic markers. J Bone Miner Res. 16(9):1575-82.

Heaney, R.P., Abrams, S., Dawson-Hughes, B., Looker, A., Looker, A., Marcus, R., et al., 2000. Peak bone mass. Osteoporos. Int. 11 (12), 985-1009.

Henriksen K, Andreassen KV, Thudium CS, Gudmann KN, Moscatelli I, Crüger-Hansen CE, Schulz AS, Dziegiel MH, Richter J, Karsdal MA, Neutzsky-Wulff AV. 2012. A specific subtype of osteoclasts secretes factors inducing nodule formation by osteoblasts. Bone 2012;51:353–361.

Herman BC, Laudier DM, Cardoso L, Zhu L-L, Li Y, Majeska RJ, Sun HB, Schaffler MB. 2007. Acute osteocyte response to fatigue microdamage: production of HIF-1α and VEGF-A. Orthop Trans 32:118.

Hill TP, Spater D, Taketo MM, Birchmeier W, Hartmann C. 2005. Canonical Wnt/b-catenin signaling prevents osteoblasts from differentiating into chondrocytes. Dev Cell 8: 727–738.

Hilton MJ, Tu X, Cook J, Hu H, Long F. 2005. Ihh controls cartilage development by antagonizing Gli3, but requires additional effectors to regulate osteoblast and vascular development. Development 132: 4339–4351.

Holloway WR, Collier FM, Aitken CJ, Myers DE, Hodge JM, Malakellis M, Gough TJ, Collier GR, Nicholson GC. 2002. Leptin inhibits osteoclast generation. J Bone Miner Res 17: 200–209

Horne WC , Sanjay A , Bruzzaniti A , Baron R . 2005 . The role(s) of Src kinase and Cbl proteins in the regulation of osteoclast differentiation and function . Immunol Rev 208 : 106 – 125 .

Horwood NJ, Kartsogiannis V, Quinn JM, Romas E, Martin TJ, Gillespie MT. 1999. Activated T lymphocytes support osteoclast formation in vitro. Biochem Biophys Res Commun 265:144–150.

Hu H, Hilton MJ, Tu X, Yu K, Ornitz DM, Long F. 2005. Sequential roles of Hedgehog and Wnt signaling in osteoblast development. Development 132: 49–60.

Huang W, Chung UI, Kronenberg HM & de Crombrugghe B 2001 The chondrogenic transcription factor Sox9 is a target of signaling by the parathyroid hormone-related peptide in the growth plate of endochondral bones. PNAS 98 160–165.

Hurley MM, Tetradis S, Huang YF, Hock J, Kream BE, Raisz LG, Sabbieti MG. 1999. Parathyroid hormone regulates the expression of fibroblast growth factor-2 mRNA and fibroblast growth factor receptor mRNA in osteoblastic cells. J Bone Miner Res. 14(5):776-83.

Ireland P, Fordtran JS. 1973. Effect of dietary calcium and age on jejunal calcium absorption in humans studied by intestinal perfusion. J Clin Invest 52(11): 2672 – 2681.

Irie N, Takada Y, Watanabe Y, Matsuzaki Y, Naruse C, Asano M, Iwakura Y, Suda T, Matsuo K.. 2009. Bidirectional signaling through ephrinA2-EphA2 enhances osteoclastogenesis and suppresses osteoblastogenesis. J Biol Chem 284:14637–14644.

Isakova T, Gutiérrez OM, Smith K, Epstein M, Keating LK, Jüppner H, Wolf M.2011. Pilot study of dietary phosphorus restriction and phosphorus binders to target fibroblast growth factor 23 in patients with chronic kidney disease. Nephrol. Dial. Transplant. 26, 584-591.

Iuliano-Burns S, Hopper J & Seeman E 2009 The age of puberty determines sexual dimorphism in bone structure: a male/female co-twin control study. Journal of Clinical Endocrinology and Metabolism 94 1638–1643.

Jonason JH, Xiao G, Zhang M, Xing L, Chen D. 2009. Post-translational Regulation of Runx2 in Bone and Cartilage. J Dent Res. 88:693-703.

Jacob AL, Smith C, Partanen J, Ornitz DM. 2006. Fibroblast growth factor receptor 1 signaling in the osteo-chondrogenic cell lineage regulates sequential steps of osteoblast maturation. Dev Biol 296: 315–328.

Joeng KS and Long F 2009 The Gli2 transcriptional activator is a crucial effector for Ihh signaling in osteoblast development and cartilage vascularization.

Development 136 4177–4185.

Jeong HM, Jin YH, Kim YJ, Yum J, Choi YH, Yeo CY, Lee KY. 2011. Akt phosphorylates and regulates the function of Dlx5. Biochem Biophys Res Commun. ; 409:681-6.

Jochum W, David JP, Elliott C,Wutz A, PlenkHJr, Matsuo K,Wagner EF. 2000. Increased bone formation and osteosclerosis in mice overexpressing the transcription factor Fra-1. Nat Med 6: 980–984.

Joldersma M, Klein-Nulend J, Oleksik AM, Heyligers IC, Burger EH. 2001. Estrogen enhances mechanical stress-induced prostaglandin production by bone cells from elderly women. Am J Physiol Endocrinol Metab. 280(3):E436-42.

Justesen J1, Stenderup K, Ebbesen EN, Mosekilde L, Steiniche T, Kassem M. 2001. Adipocyte tissue volume in bone marrow is increased with aging and in patients with osteoporosis. Biogerontology 2:165–171

Kajiya M, Giro G, Taubman MA, Han X, Mayer MP, Kawai T. 2010. Role of periodontal pathogenic bacteria in RANKL-mediated bone destruction in periodontal disease. J Oral Microbiol 8:2.

Kawano Y and Kypta R. 2003. Secreted antagonists of the Wnt signaling pathways. J Cell Science 116:2627-2634

Kennedy OD, Laudier D, Fealey D, Majeska RJ, Schaffler MB. 2011. Response to bone fatigue in vivo involves apoptosis and active pro-osteoclastogenic signaling by distinct osteocyte cell populations. Trans Orthop Res Soc No. 461.

Kim BJ, Lee YS, Lee SY, Park SY, Dieplinger H, Ryu SH, Yea K, Choi S, Lee SH, Koh JM, Kim GS. 2012. Afamin secreted from nonresorbing osteoclasts acts as a chemokine for preosteoblasts via the Akt-signaling pathway. Bone 51:431–440.

Kim GS, Hong JS, Kim SW, Koh JM, An CS, Choi JY, Cheng SL. 2003. Leptin induces apoptosis via ERK/cPLA2/Cytochrome c pathway in human bone marrow stromal cells. J Biol Chem 278:21920–21929

Klaus, H.D. 2014. Frontiers in the Bioarchaeology of Stress and Disease: Cross-Disciplinary Perspectives From Pathophysiology, Human Biology, and Epidemiology. Am. J. Phys. Anthropol. 155: 294 – 308

Komori T, Yagi H, Nomura S, Yamaguchi A, Sasaki K, Deguchi K, Shimizu Y, Bronson RT, Gao YH, Inada M, Sato M, Okamoto R, Kitamura Y, Yoshiki S, Kishamoto T. 1997. Targeted disruption of

Cbfa1 results in a complete lack of bone formation owing to maturational arrest of osteoblasts. Cell 89: 755–764.

Kronenberg HM 2006 PTHrP and skeletal development. Annals of the New York Academy of Sciences 1068 1–13.

Kristensen HB, Andersen TL, Marcussen N, Rolighed L, Delaisse JM. 2013. Increased presence of capillaries next to remodeling sites in adult human cancellous bone. J Bone Miner Res 28:574–585.

Kubota K, Sakikawa C, Katsumata M, Nakamura T, Wakabayashi K. 2002. Platelet-derived growth factor BB secreted from osteoclasts acts as an osteoblastogenesis inhibitory factor. J Bone Miner Res 17:257–265.

Kulkarni NH, Halladay DL, Miles RR, Gilbert LM, Frolik CA, Galvin RJ, Martin TJ, Gillespie MT, Onyia JE. Effects of parathyroid hormone on Wnt signaling pathway in bone. J Cell Biochem. 95(6):1178-90.

Komori T. 2013. Functions of the osteocyte network in the regulation of bone mass. Cell Tissue Res 352:191-198

Kveiborg M, Sabatakos G, Chiusaroli R, Wu M, Philbrick WM, Horne WC, Baron R. 2004. DFosB induces osteosclerosis and decreases adipogenesis by two independent cell-autonomous mechanisms. Mol Cell Biol 24: 2820–2830.

Kreja L, Brenner RE, Tautzenberger A, Liedert A, Friemert B, Ehrnthaller C, Huber-Lang M, Ignatius A. 2010. Nonresorbing osteoclasts induce migration and osteogenic differentiation of mesenchymal stem cells. J Cell Biochem 109:347–355.

Li, J., Mashiba, T., and Burr, D. B. 2001. Bisphosphonate treatment suppresses targeted repair of microdamage. Trans Orthop Res Soc 26:320.

Liu S, Tang W, Zhou J, Stubbs JR, Luo Q, Pi M, Quarles LD. 2006. Fibroblast growth factor 23 is a counter-regulatory phosphaturic hormone for vitamin D. J. Am. Soc. Nephrol. 17, 1305-1315.

Lee KS, Kim HJ, Li QL, Chi XZ, Ueta C, Komori T, Wozney JM, Kim E, Choi J, Ryoo H, Bae S. 2000. Runx2 is a common target of transforming growth factor beta1 and bone morphogenetic protein 2, and cooperation between Runx2 and Smad5 induces osteoblast-specific gene expression in the pluripotent mesenchymal precursor cell line C2C12. Mol Cell Biol. 20:8783-92.

Lee KS, Hong SH, Bae SC. 2002. Both the Smad and p38 MAPK pathways play a crucial role in Runx2 expression following induction by transforming growth factor-beta and bone morphogenetic protein. Oncogene. 21:7156-63.

Lee MH, Kwon TG, Park HS, Wozney JM, Ryoo HM. 2003. BMP-2-induced Osterix expression is mediated by Dlx5 but is independent of Runx2. Biochem Biophys Res Commun. 309:689-94.

Lee SW, Choi KY, Cho JY, Jung SH, Song KB, Park EK, Choi J, Shin H, Kim S, Woo K, Baek J, Nam S, Kim J, Kim J, Ryoo H. 2006, TGF-beta2 stimulates cranial suture closure through activation of the Erk-MAPK pathway. J Cell Biochem. 98:981-91.

Lee K, Lanske B, Karaplis AC, Deeds JD, Kohno H, Nissenson RA, Kronenberg HM & Segre GV 1996 Parathyroid hormone-related peptide delays terminal differentiation of chondrocytes during endochondral bone development. Endocrinology 137 5109–5118.

Lian JB, Stein GS, Javed A, van Wijnen AJ, Stein JL, Montecino M, Hasan MQ, Gaur T,

Lengner CJ, Young DW. 2006. Networks and hubs for the transcriptional control of osteoblastogenesis. Rev Endocr Metab Disord. 7:1–16.

Leung KC, Johannsson G, Leong GM, Ho KK. 2004. Estrogen regulation of growth hormone action. Endocr Rev 25(5): 693 - 721

Lin C, Jiang X, Dai Z, Guo X, Weng T, Wang J, Li Y, Feng G, Gao X, He L 2009. Sclerostin mediates bone response to mechanical unloading through antagonizing Wnt/β-catenin signaling. J Bone Miner Res 24:1651–1661

Lin GL and Hankenson KD. 2011. Integration of BMP, Wnt, and Notch signaling pathways in osteoblast differentiation. J Cell Biochem 112(12):3491-3501

Linkhart TA, Mohan S. 1989. Parathyroid hormone stimulates release of insulin-like growth factor-I (IGF-I) and IGF-II from neonatal mouse calvaria in organ culture. Endocrinology. 125(3):1484-91.

443

Logan CY, Nusse R. 2004. The Wnt signaling pathway in development and disease. Ann Rev Cell Dev Biol. 20:781–810

Long F, Chung UI, Ohba S,McMahon J, Kronenberg HM,McMahon AP. 2004. Ihh signaling is directly required for the osteoblast lineage in the endochondral skeleton. Development 131: 1309–1318.

Long, F., 2012. Building strong bones: molecular regulation of the osteoblast lineage. Nat. Rev. Mol. Cell Biol. 13, 27-38.

Long F and Ornitz DM. 2013. Development of the Endochondral Skeleton. Cold Spring Harb Perspect Biol 2013 ;5:a008334

Mackie EJ, Tatarczuch L, Mirams M. 2011. The skeleton: a multi-functional complex organ. The growth plate chondrocyte and endochondral ossification. Journal of Endocrinology 211, 109–121

Martin TJ, Sims NA. 2005. Osteoclast-derived activity in the coupling of bone formation to resorption. Trends Mol Med 11:76–81.

Maes C, Kobayashi T, Selig MK, Torrekens S, Roth SI, Mackem S, Carmeliet G, Kronenberg HM. 2010. Osteoblast precursors, but not mature osteoblasts, move into developing and fractured bones along with invading blood vessels. Dev Cell 19: 329–344

Maggiano Isabel S., Corey M. Maggiano, Vera Tiesler, Horst Kierdorf, Samuel D. Stout, and Michael Schultz. 2011. A distinct region of microarchitectural variation in femoral compact bone: histomorphology of the endosteal lamellar pocket. International Journal of Osteoarchaeology 21(6):743-750.

Maeda K, Kobayashi Y, Udagawa N, Uehara S, Ishihara A, Mizoguchi T, Kikuchi Y, Takada I, Kato S, Kani S, Nishita M, Marumo K, Martin TJ, Minami Y,Takahashi N. 2012. Wnt5a-Ror2 signaling between osteoblast-lineage cells and osteoclast precursors enhances osteoclastogenesis. Nat Med 18:405–412.

Mansukhani A, Ambrosetti D, Holmes G, Cornivelli L, Basilico C. 2005. Sox2 induction by FGF and FGFR2 activating mutations inhibits Wnt signaling and osteoblast differentiation. J Cell Biol. 168:1065–1076.

Mantzoros CS, Moschos S, Avramopoulos I, Kaklamani V, Liolios A,Doulgerakis DE, Griveas I, Katsilambros N, Flier S. 1997. Leptin concentrations in relation to body mass index and the tumor necrosis factor-alpha system in humans. J Clin Endocrinol Metab 82: 3408–3413

Mao B, Wu W, Davidson G, Marhold J, Li M, Mechler BM, Delius H, Hoppe D, Stannek P, Walter C, Glinka A, Niehrs C. 2002. Kremen proteins are Dickkopf receptors that regulate Wnt/beta-catenin signalling. Nature 417,664 -667.

Martin RB. 2003a. Fatigue damage, remodeling, and the minimization of skeletal weight. Journal of Theoretical Biology 220: 271 – 276.

Martin RB. 2003b. Functional adaptation and fragility of the skeleton. In: Agarwal SC and Stout SD. 2003. Bone Loss and Osteoporosis: An anthropological perspective. New York: Spring Science + Business Media. pp. 121- 137

Matsuguchi T, Chiba N, Bandow K, Kakimoto K, Masuda A, Ohnishi T. 2009. JNK activity is essential for Atf4 expression and late-stage osteoblast differentiation. J Bone Miner Res 24:398–410.

McGill GG, Horstmann M, Widlund HR, Du J, Motyckova G, Nishimura EK, Lin YL, Ramaswamy S, Avery W, Ding HF, Jordan SA, Jackson IJ, Korsmeyer SJ,Golub TR, Fisher DE. 2002. Bcl2 regulation by the melanocyte master regulator Mitf modulates lineage survival and melanoma cell viability. Cell 109, 707–718.

Meazzini MC, Toma CD, Schaffer JL, Gray ML, Gerstenfeld LC. 1998. Osteoblast cytoskeletal modulation in response to mechanical strain in vivo. J. Orthop. Res. 16: 170–180.

Merciris D, Marty C, Collet C, de Vernejoul MC, Geoffroy V. 2007. Overexpression of the transcriptional factor Runx2 in osteoblasts abolishes the anabolic effect of parathyroid hormone in vivo. Am J Pathol. 170(5):1676-85.

Miao D, Tong X, Chan GK, Panda D, McPherson PS, Goltzman D. 2001. Parathyroid Hormone-related Peptide Stimulates Osteogenic Cell Proliferation through Protein Kinase C Activation of the Ras/Mitogen-activated Protein Kinase Signaling Pathway. J Biol Chem 276: 32204-32218

Mirosavljevic D, Quinn JM, Elliott J, Horwood NJ, Martin TJ, Gillespie MT. 2003. T-cells mediate an inhibitory effect of interleukin-4 on osteoclastogenesis. J Bone Miner Res 18: 984–993.

Moriishi T, Fukuyama R, Ito M, Miyazaki T, Maeno T, Kawai Y, Komori H, Komori T. 2012. Osteocyte network; a negative regulatory system for bone mass augmented by the induction of rankl in osteoblasts and sost in osteocytes at unloading. PLoS One 7:e40143

Mori, S. and Burr, D. B. 1993. Increased intracortical remodeling following fatigue damage. Bone 14:103–109.

Mulcahy LE, Taylor D, Lee TC, Duffy GP. 2011. RANKL and OPG activity is regulated by injury size in networks of osteocyte-like cells. Bone 48:182-188.

Nakashima K, Zhou X, Kunkel G, Zhang Z, Deng JM, Behringer RR, de Crombrugghe B. 2002. The novel zinc finger-containing transcription factor Osterix is required for osteoblast differentiation and bone formation. Cell 108: 17–29.

Otto F, Thornell AP, Crompton T, Denzel A, Gilmour KC, Rosewell IR, StampGW, Beddington RS,Mundlos S, Olsen BR, et al. 1997. Cbfa1, a candidate gene for cleidocranial dysplasia syndrome, is essential for osteoblast differentiation and bone development. Cell 89: 765–771.

Naganawa T, Xiao L, Coffin JD, Doetschman T, Sabbieti MG, Agas D, Hurley MM. Reduced expression and function of bone morphogenetic protein-2 in bones of Fgf2 null mice. J Cell Biochem. 2008; 103:1975-88.

Negishi-Koga T, Shinohara M, Komatsu N, Bito H, Kodama T, Friedel RH, Takayanagi H. 2011. Suppression of bone formation by osteoclastic expression of semaphorin 4D. Nat Med 2011;17:1473–1480.

Niger C, Herbert C, Stains JP. 2010. Interaction of connexin43 and protein kinase C-delta during FGF2 signaling. BMC Biochem. 11:14

Niger C, Luciotti MA, Buo AM, Hebert C, Ma V, Stains JP. 2013. The regulation of runt-related transcription factor 2 by fibroblast growth factor-2 and connexin43 requires the inositol polyphosphate/protein kinase Cδ cascade. J Bone Miner Res 28(6):1468-1477

Nilsson O, Marino R, De Luca F, Phillip M and Baron J 2005 Endocrine regulation of the growth plate. Hormone Research 64 157–165.

Noel D, Gazit D, Bouquet C, Apparailly F, Bony C, Plence P, Millet V, Turgeman G, Perricaudet M, Sany J, Jorgensen C. 2004. Short-term BMP-2 expression is sufficient for in vivo osteochondral differentiation of mesenchymal stem cells. Stem Cells. 22:74-85.

Parfitt AM, Kleerekoper M, Villanueva AR. 1987. Increased bone age: mechanisms and consequences. In: Osteoporosis. Osteopress ApS: Copenhagen. Pp. 301 – 308.

Parfitt AM. 1990. Bone-forming cells in clinical conditions. In: Hall BK, editor. Bone, Vol. 1: the osteoblast and osteocyte. Boca Raton, FL: Telford Press and CRC Press. p 351–429.

Parfitt AM. 2010. Skeletal heterogeneity and the purposes of bone remodeling: implications for the understanding of osteoporosis. In: Marcus R, Feldman D, Nelson DA, Rosen CJ, editors. Fundamentals of osteoporosis. San Diego: Academic Press. p 35–54

Pajevic PD. 2013. Recent Progress in Osteocyte Research. Endocrinology and Metabolism 28:255-261

Petley T, Graff K, Jiang W, Yang H, Florini J. 1999. Variation among cell types in the signaling pathways by which IGF-I stimulates specific cellular responses. Hormone and Metabolic Research 31 70–76.

Pizette S, Niswander L. 2000. BMPs are required at two steps of limb chondrogenesis: Formation of prechondrogenic condensations and their differentiation into chondrocytes. Dev Biol 219: 237–249.

Pierroz D, Baldock PA, Bouxsein ML, Ferrari S. 2006. Low cortical bone mass in mice lacking beta 1 and beta 2 adrenergic receptors is associated with low bone formation and circulating IGF-1. J Bone Min Res 21(Suppl. 1):S26

Plotkin LI and Bivi N. Local regulation of bone cell function. In: Basic and Applied Bone Biology. David B. Burr and Matthew R. Allen, eds. London, UK: Academic Press. pp. 47 – 73.

Poole AR. 1991. The growth plate: Cellular physiology, cartilage assembly and mineralization. In Cartilage: Molecular aspects (ed. Hall BK, Newman SA), pp. 179–212. CRC Press, Boca Raton, FL.

445

Price JS, Sugiyama T, Galea GL, Meakin LB, Sunters A, Lanyon LE. 2011. Role of endocrine and paracrine factors in the adaptation of bone to mechanical loading. Curr Osteoporos Rep 9(2):76-82.

Qin L., Li X., Ko J.K. and Partridge N.C. 2005. Parathyroid hormone uses multiple mechanisms to arrest the cell cycle progression of osteoblastic cells from G1 to S phase. J. Biol. Chem. 280, 3104-3111.

Qiu S, Rao DS, Palnitkar S, Parfitt AM. 2010. Dependence of bone yield (volume of bone formed per unit of cement surface area) on resorption cavity size during osteonal remodeling in human rib: implications for osteoblast function and the pathogenesis of age-related bone loss. J Bone Miner Res 25:423–430.

Quinn JM, Itoh K, Udagawa N, Hausler K, Yasuda H, Shima N, Mizuno A, Higashio K, Takahashi N, Suda T, Martin TJ, Gillespie MT. 2001. Transforming growth factor beta affects osteoclast differentiation via direct and indirect actions. J Bone Miner Res 16:1787–1794.

Quarles, L.D., 2012. Skeletal secretion of FGF-23 regulates phosphate and vitamin D metabolism. Nat. Rev. Endocrinol. 8, 276-286

Rauch F, Schoenau E. 2001.The developing bone: slave or master of its cells and molecules? Pediatric Research 50: 309–314.

Reeve J. 1978. The turnover time of calcium in the exchangeable pools of bone in man and the long-term effect of a parathyroid hormone fragment. Clin Endocrinol 8: 445-455

Retting KN, Song B, Yoon BS, Lyons KM. 2009. BMP canonical Smad signaling through Smad1 and Smad5 is required for endochondral bone formation. Development 136: 1093–1104

Reid I, Ames R, Evans M, Sharpe S, Gamble G, France J, Lim T, Cundy T. 1992. Determinants of total body and regional bone mineral density in normal postmenopausal women-a key role for fat mass. J Clin Endocrinol Metab 75:45–51

Robling AG, Hinant FM, Burr DB, Turner CH. 2002. Improved bone structure and strength after long-term mechanical loading is greatest if loading is separated into short bouts. J Bone Miner Res 17:1545–1554.

Robling AG, Niziolek PJ, Baldridge LA, Condon KW, Allen MR, Alam I, Mantila SM, Gluhak-Heinrich J, Bellido TM, Harris SE, Turner CH. 2008. Mechanical stimulation of bone
in vivo reduces osteocyte expression of Sost/sclerostin. J
Biol Chem 283:5866-75.

Robling AG, Fuchs RK, Burr DB. 2014. Mechanical adaptation. In: Basic and Applied Bone Biology. David B. Burr and Matthew R. Allen, eds. London, UK: Academic Press. pp 175 – 203.

Rodda SJ,McMahon AP. 2006. Distinct roles for Hedgehog and canonical Wnt signaling in specification, differentiation and maintenance of osteoblast progenitors. Development 133: 3231–3244.

Ross, F. 2013. Osteoclast Biology and Bone Resorption. In: Primer on the Metabolic Bone Diseases and Disorders of Mineral Metabolism. 8th ed. Clifford J. Rosen, ed. John Wiley and Sons, Inc. pp. 25 - 33

Ross FP and Teitelbaum SL. 2005. αvβ3 and macrophage colony-stimulating factor: partners in osteoclast biology. Immunol. Rev. 208: 88–105

Rowe, P.S., 2012. Regulation of bone-renal mineral and energy metabolism: The PHEX, FGF23, DMP-1, MEPE ASARM pathway. Crit. Rev. Eukaryot. Gene Expr. 22, 61-86.

Rubinacci A, Covini M, Bisogni C, Villa I, Galli M, Palumbo C, Ferretti M, Muglia MA, Marotti G. 2000. Bone as an ion exchange system: evidence for a link between mechanotransduction and metabolic needs. Am J Physiol Endocrinol Metab. 282(4):E851-64.

Ruff CB and W.C. Hayes. 1983. Cross-sectional geometry of Pecos Pueblo femora and tibiae-a biomechanical investigation. I: method and general patterns of variation. Am. J. Phys. Anthropol., 60:383–400.

Sabatakos G, Sims NA, Chen J, Aoki K, Kelz MB, Amling M, Bouali Y, Mukhopadhyay K, Ford K, Nestler EJ, Baron R. 2000. Overexpression of DFosB transcription factor(s) increases bone formation and inhibits adipogenesis. Nat Med 6: 985–990.

Sanchez-Fernandez MA, Gallois A, Riedl T, Jurdic P, Hoflack B. 2003. Osteoclasts control
osteoblast chemotaxis via PDGF-BB/PDGF receptor beta signaling. PLoS One 3:e3537

Sanders EJ, Parker E, Harvey S 2006 Retinal ganglion cell survival in development: mechanisms of retinal growth hormone action. Experimental Eye Research 83 1205–1214.

Sasaki T, Ito Y, Bringas P, Jr., Chou S, Urata MM, Slavkin H, Chai Y.TGFbeta-mediated FGF signaling is crucial for regulating cranial neural crest cell proliferation during frontal bone development. Development. 2006; 133:371-81

Saxon LK and Turner CH 2006 Low-dose estrogen treatment suppresses periosteal bone formation in response to mechanical loading. Bone 39 1261–1267.

Schoenwolf GC, Bleyl SB, Brauer PR, Francis-West PH. Development of the limbs. In: Larsen's Human Embryology, 4th ed. Churchill Livngstone Elsevier: Philidelphia, PA. pp. 619-645.

Seeman E and Delmas PD. 2006. Bone quality – The material and structural basis of bone strength and fragility. N Engl J Med 354:2250 – 61

Skedros JG, Grunander TR, Hamrick MW. 2005. Spatial distribution of osteocyte lacunae in equine radii and third metacarpals: Considerations for cellular communication, microdamage detection and metabolism. Cells Tissues Organs 180: 215 – 236.

Skedros JG, Knight AN, Gunnar CC, Crowder CM, Dominguez VM, Qiu Shijing, Mulhern DM, Donahue SW, Busse B, Hulsey BI, Zedda M, Sorenson SM. 2013. Scaling of Haversian Canal Surface Area to Secondary Osteon Bone Volume in Ribs and Limb Bones. Am. J. Phys. Anthropol. 151: 230 – 244.

Sims NA, Martin TJ. 2014. Coupling the activities of bone formation and resorption: a multitude of signals within the basic multicellular unit. BoneKEy Reports 3, 481;1-10.

Sims NA, Brennan K, Spaliviero J, Handelsman DJ and Seibel MJ 2006 Perinatal testosterone surge is required for normal adult bone size but not for normal bone remodeling. American Journal of Physiology. Endocrinology and Metabolism 290 E456–E462.

Sims NA, Jenkins BJ, Quinn JM, Nakamura A, Glatt M, Gillespie MT, Ernst M, Martin TJ. 2004. Glycoprotein 130 regulates bone turnover and bone size by distinct downstream signaling pathways. J Clin Invest 2004;113:379–389

Sowa H, Kaji H, Iu MF, Tsukamoto T, Sugimoto T, Chihara K. 2003. Parathyroid hormone-Smad3 axis exerts anti-apoptotic action and augments anabolic action of transforming growth factor beta in osteoblasts. J Biol Chem. 278(52):52240–52252.

Shandala T, Shen Ng Y, Hopwood B, Yip YC, Foster BK, Xian CJ. 2012. The role of osteocyte apoptosis in cancer chemotherapyinduced bone loss. J Cell Physiol 227:2889–2897

Shimoaka T, Kamekura S, Chikuda H, et al. Impairment of bone healing by insulin receptor substrate-1 deficiency. J Biol Chem. 2004;279(15):15314–22.

Seeman E 2002 Pathogenesis of bone fragility in women and men. Lancet 359 1841–1850

Sevetson B, Taylor S, Pan Y. 2004. Cbfa1/RUNX2 directs specific expression of the sclerosteosis gene (SOST). J Biol Chem 279:13849–58

Singhatanadgit W, Salih V, Olsen I. Up-regulation of bone morphogenetic protein receptor IB by growth factors enhances BMP-2-induced human bone cell functions. J Cell Physiol. 2006; 209:912-22.

Skedros JG, Hunt KJ, Bloebaum RD. 2004. Relationships of loading history and structural and material characteristics of bone: Development of the Mule Deer calcaneus. J. Morph. 259: 281 – 307.

Skedros JG. 2012. Interpreting Load History in Limb-Bone Diaphyses: Important Considerations and Their Biomechanical Foundations. Chapter 7, In: Bone Histology, An Anthropological Perspective. Eds. S. Stout and C. Crowder. CRC Press, Boca Raton Florida, 417 pgs.

Sutton AL, Zhang X, Dowd DR, Kharode YP, Komm BS, Macdonald PN. 2008. Semaphorin 3B is a 1,25-dihydroxyvitamin D3-induced gene in osteoblasts that promotes osteoclastogenesis and induces osteopenia in mice. Mol Endocrinol 22:1370–1381

Stadler HS, Higgins KM, Capecchi MR. 2001. Loss of Eph-receptor expression correlates with loss of cell adhesion and chondrogenic capacity in Hoxa13 mutant limbs. Development 128: 4177–4188.

Takada I, Mihara M, Suzawa M, Ohtake F, Kobayashi S, Igarashi M, Youn MY, Takeyama K, Nakamura T, Mezaki Y, Takezawa S, Yogiashi Y, Kitagawa H,Yamada G, Takada S, Minami Y, Shibuya H, Matsumoto K, Kato S. 2007. A histone lysine methyltransferase activated by non-canonical Wnt signalling suppresses PPAR-γ transactivation. Nature Cell Biol. 9, 1273–1285

447

Takayanagi, H. 2007. Osteoimmunology: shared mechanisms and crosstalk between the immune and bone systems. Nat. Rev. Immunol. 7(4): 292 – 304

Takeshita S1, Fumoto T, Matsuoka K, Park KA, Aburatani H, Kato S, Ito M, Ikeda K. 2013. Osteoclast-secreted

CTHRC1 in the coupling of bone resorption to formation. J Clin Invest 123:3914–3924.

Talmage RV, Lester GE, Hirsch PF. 2000. Parathyroid hormone and plasma calcium control: an editorial. J Musculoskel Neuron Interact 1:. 121–126

Tami AE, Nasser P, Verborgt O, Schaffler MB, Knothe Tate ML. 2002. The role of interstitial fluid flow in the remodeling response to fatigue loading. J Bone Miner Res 17:2030–7.

Tang Y, Wu X, Lei W, Pang L, Wan C, Shi Z, Zhao L, Nagy TR, Peng X, Hu J, Feng X, Van Hul W, Wan M, Cao X.. 2009. TGF-beta1-induced migration of bone mesenchymal stem cells couples bone resorption with formation. Nat Med 15:757–765.

Thomas T, Gori F, Khosla S, Jensen MD, Burguera B, Riggs BL.. 1999. Leptin acts on human marrow stromal cells to enhance differentiation to osteoblasts and to inhibit differentiation to adipocytes. Endocrinology 140: 1630–1638

Trotter M, Hixon BB 1974 Sequential changes in weight, density, and percentage ash weight of human skeletons from an early fetal period through old age. Anat Rec 179:1–18

Tsuji K, Bandyopadhyay A, Harfe BD, Cox K, Kakar S, Gerstenfeld L, Einhorn T, Tabin CJ, Rosen V.. BMP2 activity, although dispensable for bone formation, is required for the initiation of fracture healing. Nat Genet. 2006; 38:1424-9.

Tsuji K, Cox K, Gamer L, Graf D, Economides A, Rosen V. 2010. Conditional deletion of BMP7 from the limb skeleton does not affect bone formation or fracture repair. J Orthop Res. 28:384-9.

Tu X, Joeng KS, Nakayama KI, Nakayama K, Rajagopal J, Carroll TJ, McMahon AP, Long F. 2007. Noncanonical Wnt signaling through G protein-linked PKCd activation promotes bone formation. Dev Cell 12: 113–127.

Turner TC. 2006. Bone Strength: Current Concepts. Ann. NY Acad. Sci 1068: 429 – 446.

Turner N, Grose R. 2010. Fibroblast growth factor signalling: From development to cancer. Nat Rev Cancer 10: 116–129.

Vanderschueren D, van Herck E, Nijs J, Ederveen AG, De Coster R and Bouillon R 1997 Aromatase inhibition impairs skeletal modeling and decreases bone mineral density in growing male rats. Endocrinology 138 2301–2307.

Valverde-Franco G, Liu H, Davidson D, Chai S, Valderrama-Carvajal H, Goltzman D, Ornitz DM, Henderson JE. 2004. Defective bone mineralization and osteopenia in young adult FGFR3– / – mice. Hum Mol Genet 13: 271–284.

Verborgt O, Gibson GJ, Schaffler MB. 2000. Loss of osteocyte integrity in association with microdamage and bone remodeling after fatigue in vivo. J Bone Miner Res 15:60-7.

Vidal O, Lindberg MK, Hollberg K, Baylink DJ, Andersson G, Lubahn DB, Mohan S, Gustafsson JA and Ohlsson C 2000 Estrogen receptor specificity in the regulation of skeletal growth and maturation in male mice. PNAS 97 5474–5479.

von Essen MR, Kongsbak M, Schjerling P, Olgaard K, OdumN,Geisler C. 2010. Vitamin D controls T cell antigen receptor signaling and activation of human T cells. Nat Immunol 11: 344–349.

Vortkamp A, Lee K, Lanske B, Segre GV, Kronenberg HM & Tabin CJ 1996 Regulation of rate of cartilage differentiation by Indian hedgehog and PTH-related protein. Science 273 613–622.

Vu TH, Shipley JM, Bergers G, Berger JE, Helms JA, Hanahan D, Shapiro SD, Senior RM,Werb Z. 1998. MMP-9/gelatinase B is a key regulator of growth plate angiogenesis and apoptosis of hypertrophic chondrocytes. Cell 93: 411–422.

Walker E, McGregor N, Poulton I, Pompolo S, Allan E, Quinn J et al. 2008. Cardiotrophin-1 is an osteoclast-derived stimulus of bone formation required for normal bone remodeling. J Bone Miner Res 23:2025–2032.

Weaver CM and Fuchs RK. Skeletal growth and development. In: Basic and Applied Bone Biology. David B. Burr and Matthew R. Allen, eds. London, UK: Academic Press. pp. 245 – 260.

Weber, T. J., Liu, S., Indridason, O. S. and Quarles, L. D. 2003. Serum FGF23 levels in normal and disordered phosphorus homeostasis. J. Bone Miner. Res. 18, 1227-1234,

Weinbaum S, Cowin SC, Zeng Y. 1994. A model for the excitation of osteocytes by mechanical loading-induced bone fluid shear stresses. J Biomech 27(3): 339- 360

Winkler IG, Sims NA, Pettit AR, Barbier V, Nowlan B, Helwani F, Poulton IJ, van Rooijen N, Alexander KA, Raggatt LJ, Lévesque JP. 2010. Bone marrow macrophages maintain hematopoietic stem cell (HSC) niches and their depletion mobilizes HSCs. Blood 116:4815–4828.

Winkler IG1, Pettit AR, Raggatt LJ, Jacobsen RN, Forristal CE, Barbier V, Nowlan B, Cisterne A, Bendall LJ, Sims NA, Lévesque JP. 2012. Hematopoietic stem cell mobilizing agents G-CSF, cyclophosphamide or AMD3100 have distinct mechanisms of action on bone marrow HSC niches and bone formation. Leukemia 26:1594–1601.

Wodarz A,Nusse R. 1998. Mechanisms of Wnt signaling in development. Annu Rev Cell Dev Biol 14: 59–88.

Wu XB and Tao R. Hepatocyte differentiation of mesenchymal stem cells. Hepatobiliary Pancreat Dis Int 11(4): 360 – 271

Wysolmerski JJ. 2012. Osteocytic osteolysis: time for a second look? Bonekey Rep 1:229.

Wyshak G, Frisch RE. 1994. Carbonated beverages, dietary calcium, the dietary calcium/phosphorus ratio, and bone fractures in girls and boys. J AdolescHealth 15:210–5.

Xian L, Wu X, Pang L, Lou M, Rosen CJ, Qiu T, Crane J, Frassica F, Zhang L, Rodriguez JP, Xiaofeng Jia, Shoshana Yakar, Shouhong Xuan, Argiris Efstratiadis, Mei Wan, Xu Cao. 2012. Matrix IGF-1 maintains bone mass by
activation of mTOR in mesenchymal stem cells. Nat Med 18:1095–1101.

Xiong J, Onal M, Jilka RL, Weinstein RS, Manolagas SC, O'Brien CA. 2011. Matrix-embedded cells control osteoclast formation. Nat Med 17: 1235–1241

Yamamoto T., Kambe F., Cao X., Lu X., Ishiguro N. and Seo H. 2007. Parathyroid hormone activates phosphoinositide 3-kinase-Akt-Bad cascade in osteoblast-like cells. Bone 40, 354-359.

Yamashita J., Datta N.S., Chun Y.H., Yang D.Y., Carey A.A., Kreider, J.M., Goldstein S.A. and McCauley L.K. 2008. Role of Bcl2 in osteoclastogenesis and PTH anabolic actions in bone. J. Bone Miner. Res. 23, 621-632.

Yamashita S, Andoh M, Ueno-Kudoh H, Sato T, Miyaki S & Asahara H 2009 Sox9 directly promotes Bapx1 gene expression to repress Runx2 in chondrocytes. Experimental Cell Research 315 2231–2240.

Yang X., Matsuda K., Bialek P., Jacquot S., Masuoka H.C., Schinke T., Li L., Brancorsini S., Sassone-Corsi P., Townes T.M., Hanauer A. and Karsenty G. 2004. ATF4 is a substrate of RSK2 and an essential regulator of osteoblast biology; implication for Coffin-Lowry Syndrome. Cell 117, 387-398.

Yee JA, Yan L, Dominguez JC, Allan EH, Martin TJ. 1993. Plasminogen-dependent activation of latent transforming growth factor beta (TGF beta) by growing cultures of osteoblast-like cells. J Cell Physiol 157:528–534.

Yeh CR, Chiu JJ, Lee CI, et al. Estrogen augments shear stressinduced signaling and gene expression in osteoblast-like cells via estrogen receptor-mediated expression of β1-integrin. J Bone Miner Res. 2010;25:627–39.

Yoon BS, Ovchinnikov DA, Yoshii I, Mishina Y, Behringer RR, Lyons KM. 2005. Bmpr1a and Bmpr1b have overlapping functions and are essential for chondrogenesis in vivo. Proc Natl Acad Sci 102: 5062– 5067.

You J, Reilly GC, Zhen X, Yellowley CE, Chen Q, Donahue HJ, Jacobs CR. 2001. Osteopontin gene regulation by oscillatory fluid flow via intracellular calcium mobilization and activation of mitogen-activated protein kinase in MC3T3-E1 osteoblasts. J. Biol. Chem. 276: 13365–13371

Yu K, Xu J, Liu Z, Sosic D, Shao J, Olson EN, Towler DA, Ornitz DM. 2003. Conditional inactivation of FGF receptor 2 reveals an essential role for FGF signaling in the regulation of osteoblast function and bone growth. Development 130: 3063–3074

Yu, V. W. Ambartsoumian G, Verlinden L, Moir JM, Prud'homme J, Gauthier C, Roughley PJ, St-Arnaud R. 2005. FIAT represses ATF4-mediated transcription to regulate bone mass in transgenic mice. J. Cell Biol. 169: 591–601

449

Yu K, Ornitz DM. 2008. FGF signaling regulates mesenchymal differentiation and skeletal patterning along the limb bud proximodistal axis. Development 135: 483–491.

Zhang M, Xuan S, Bouxsein ML, von Stechow D, Akeno N, Faugere MC, Malluche H, Zhao G, Rosen CJ, Efstratiadis A, Clemens TL. 2002. Osteoblast-specific knockout of the insulin-like growth factor (IGF) receptor gene reveals an essential role of IGF signaling in bone matrix mineralization. J. Biol. Chem. 277, 44005–44012

Zhao G, Monier-Faugere MC, Langub MC, Geng Z, Nakayama T, Pike JW, Chernausek SD, Rosen CJ, Donahue LR, Malluche HH, Fagin JA, Clemens TL. 2000.Targeted overexpression of insulin-like growth factor I to osteoblasts of transgenic mice: increased trabecular bone volume without increased osteoblast proliferation. Endocrinology 141, 2674–2682

Zhao C, Irie N, Takada Y, Shimoda K, Miyamoto T, Nishiwaki T, Suda T, Matsuo K. 2006. Bidirectional ephrinB2- EphB4 signaling controls bone homeostasis. Cell Metab 4:111–121.

Zhou S. 2011. TGF-beta regulates beta-catenin signaling and osteoblast differentiation in human mesenchymal stem cells. J Cell Biochem. 112:1651-60

Zou W , Kitaura H , Reeve J , Long F , Tybulewicz VLJ , Shattil SJ , Ginsberg MH , Ross FP , Teitelbaum SL . 2007 . Syk, c-Src, the avp3 integrin, and ITAM immunoreceptors, in concert, regulate osteoclastic bone resorption . J Cell Biol 877–88 .

Chapter 3/4: Mechanical Basis and Predictions

Abbasi, A.A., Rudman, D., Wilson, C.R., Drinka, P.J., Basu, S.N., Mattson, D.E., Richardson, T.J., 1995. Observations on nursing home residents with a history of hip fracture. Am J Med Sci. 310(6):229-34.

Abbott, S., Trinkaus, E., Burr, D.B., 1996. Dynamic bone remodeling in later Pleistocene fossil hominids. Am J Phys Anthropol 99(4):585–601.

Adler, C-P., 2000. Bone Tumors. In: Adler, C-P (Ed.) Bone Diseases: Macroscopic, Histological, and Radiological Diagnosis of Structural Changes in the Skeleton. Springer, Berlin Heidelberg, pp. 207-421.

Agnew, A.M., Moorhouse, K., Kang, Y.S., Donnelly, B.R., Pfefferle, K., Manning, A.X., Litsky, A.S., Herriott, R., Abdel-Rasoul, M., Bolte, J.H., 2013. The response of pediatric ribs to quasi-static loading: mechanical properties and microstructure. Ann Biomed Eng 41:2501–4.

Agnew, A.M., Dominguez, V.M., Sciulli, P.W., Stout, S.D., 2017. Variability of in vivo linear microcrack accumulation in the cortex of elderly human ribs. Bone Rep 6:60-3.

Agnew, A.M., Schafman, M., Moorhouse, K., White, S.E., Kang, Y.S., 2015. The effect of age on the structural properties of human ribs. J Mech Behav Biomed Mater 41:302-314

Agnew, A.M., Stout, S.D., 2012. Brief Communication: Reevaluating osteoporosis in human ribs: The role of intracortical porosity. Am J Phys Anthropol 148(3):462-6.

Akkus, O., Polyakova-Akkus, A., Adar, F., Schaffler, M.B., 2003. Aging of microstructural compartments in human compact bone. J Bone Miner Res 18(6):1012-9.

Albert, C., Jameson, J., Smith, P., Harris, G., 2014. Reduced diaphyseal strength associated with high intracortical vascular porosity within long bones of children with osteogenesis imperfecta. Bone 66:121-30.

Allen, M.R., Burr., 2008. Skeletal microdamage: less about biomechanics and more about remodeling. Clin Rev Bone Miner Metab 6:24-30.

Armstrong, D.W., Rue, J.P.H.,Wilckens, J.H., Frassica, F.J., 2004. Stress fracture injury in young military men and women. Bone 35(3):806-16.

Ascenzi, A. 1955. Some histochemical properties of the organic substance in Neandertalian bone. Am J Phys Anthropol 13(4):557-66.

Ascenzi, A., Bonucci, E., 1972. The shearing properties of single osteons. Anat Rec 172(3):499-510.

Atkinson, P.J., 1965. Changes in resorption spaces in femoral cortical bone with age. J Path Bacteriol 89:173-8.

Aubin, J.E., Liu, F., 1996. The Osteoblast Lineage. In: Bilezikian JP, Raisz LG, Rodan GA (Eds.) Principles of Bone Biology. Academic Press, San Diego, pp. 51–67.

Bacabac, R.G., Mizuno, D., Schmidt, C.F., Mackintosh, F.C., van Loon, J.J.W.A., Klein-Nulend, J., Smit, T.H., 2008. Round versus flat: bone cell morphology, elasticity, and mechanosensing. J Biomech 41(7):1590–8.

Bach-Gansmo, F.L., Brüel, A., Jensen, M.V., Ebbesen, E.N., Birkedal, H., Thomsen, J.S., 2016. Osteocyte lacunar properties and cortical microstructure in human iliac crest as a function of age and sex. Bone 91:11–9.

Bala, Y., Farlay, D., Boivin, G., 2013. Bone mineralization: from tissue to crystal in normal and pathological contexts. Osteoporosis Int. 24:2153–66.

Bala, Y., Farlay, D., Chapurlat, R., Boivin, G., 2011. Modifications of bone material properties in postmenopausal osteoporotic women long-term treated with alendronate. Eur J Endocrinol 165:647– 55.

Banks, W.J., 1974. The ossification process of the developing antler in the white-tailed deer (Odocoileus virginianus). Calc Tissue Res 14(1):257-74.

Bassett, J.H., Williams, G.R., 2003. The molecular actions of thyroid hormone in bone.
Trends Endocrinol Metab 14(8):356-64.

Bart, Z.R., Hammond, M.A., Wallace, J.M., 2014. Multi-scale analysis of bone chemistry, morphology and mechanics in the oim model of osteogenesis imperfecta. Connect Tissue Res 55(Suppl 1):4–8.

Beddoe, A.H., 1977. Measurements of the microscopic structure of cortical bone. Phys Med Biol 22(2):298-308.

Bell, L.S., Kayser, M., Jones, C., 2008. The mineralized osteocyte: A living fossil. Am J Phys Anthropol 137(4):449-56.

Bell, K.L., Loveridge, N., Power, J., Garrahan, N., Meggitt, B.F., Reeve, J., 1999. Regional differences in cortical porosity in the fractured femoral neck. Bone 24(1):57–64.

Bell, K.L., Loveridge, N., Power, J., Garrahan, N., Stanton, M., Lunt, M., Meggitt, B.F., Reeve, J., 1999. Structure of the femoral neck in hip fracture: Cortical bone loss in the inferoanterior to superoposterior axis. J Bone Miner Res 14(1):111-9.

Bell, K.L., Loveridge, N., Reeve, J., Thomas, C.D., Feik, S.A., Clement, J.G., 2001 Super-osteons (remodeling clusters) in the cortex of the femoral shaft: influence of age and gender. Anat Rec 264(4):378-86.

Bellemare, F., Jeanneret, A., Couture, J., 2003. Sex differences in thoracic dimensions and configuration. Am J Respir Crit Care Med 168(3):305-12.

Biewener, A.A., Bertram, J.E.A., 1993. Mechanical loading and bone growth in vivo. In: Hall BK (Ed.) Bone Growth B, vol. 7. CRC Press, Nova Scotia, pp. 1-36.

Black, J., Mattson, R., Korostoff, E., 1974. Haversian osteons: size, distribution, internal structure, and orientation. J Biomed Mater Res 8(5):299-319.

Bleuze M. 2012. Proximal femoral diaphyseal cross-sectional geometry in Orrorin tugenensis. Homo 63(3):153-66.

Borah, B., Dufresne, T.E., Ritman, E.L., Jorgensen, S.M., Liu, S., Chmielewski, P.A., Phipps, R.J., Zhou, X., Sibonga, J.D., Turner, R.T., 2006. Long-term risedronate treatment normalizes mineralization and continues to preserve trabecular architecture: sequential triple biopsy studies with micro-computed tomography. Bone 39:345–52.

Boivin, G.Y., Bala, Y., Doublier, A., Farlay, D., Ste-Marie, L.G., Meunier, P.J., Delmas, P.D., 2008. The role of mineralization and organic matrix in the microhardness of bone tissue from controls and osteoporotic patients. Bone 43(3):532-8.

Boivin, G.Y., Chavassieux, P.M., Santora, A.C., Yates, J., Meunier, P.J., 2000. Alendronate increases bone strength by increasing the mean degree of mineralization of bone tissue in osteoporotic women. Bone 27:687–94.

Boivin, G., Meunier, P.J., 2002. Changes in bone remodeling rate influence the degree of mineralization of bone. Connect Tissue Res 43(2-3):535-7.

Bonewald, L.F., 2017. The role of the osteocyte in bone and nonbone disease. Endocrinol Metab Clin N Am 46(1):1-18.

Bonucci, E., Gherardi, G., 1977. Osteocyte ultrastructure in renal osteodystrophy. Virchows Arch A Pathol Anat Histol 373(3):213-31.

451

Bonucci, E., Gherardi, G., Faraggiana, T., 1976. Bone changes in hemodialyzed uremic subjects. Comparative light and electron microscope investigations. Virchows Arch A Pathol Anat Histol. 371(3):183-98.

Bonucci, E., Lo Cascio, V., Adami, S. Cominacini, L., Galvanini, G., Scuro, A., 1978. The ultrastructure of bone cells and bone matrix in human primary hyperparathyroidism. Virchows Arch A Path Anat and Histol 379(1):11-23.

Boskey, A.L., Marks, S.C. Jr., 1985. Mineral and matrix alterations in the bones of incisors-absent (ia/ia) osteopetrotic rats. Calcif Tissue Int 37:287–292.

Boskey, A.L., Spevak, L., Weinstein, R.S., 2009. Spectroscopic markers of bone quality in alendronate-treated postmenopausal women. Osteoporos Int 20:793–800.

Bourdel, A., Mahoudeau, J.A., Guaydier-Soquieres, G., Leymarie, P., Sabatier, J.P., Loyau, G., 1989. Etude de la function gonadique au cours de l'osteoporose masculine en apparence primitive. La Presse Med 18:1691-5

Bousson, V., Meunier, A., Bergot, C., 2001. Distribution of intracortical porosity in the human middle cortex by age and gender. J Bone Miner Res 16(7):1308-17.

Boyce, T.M., Fyhrie, D.P., Glotkowski, M.C., Radin, E.L., Schaffler, M.B., 1998. Damage type and strain mode associations in human compact bone bending fatigue. J Orthop Res 16(3): 322-9.

Bressot, C., Meunier, P., Chapuy, M., Lejeune, E., Edouard, C., Darby, A. 1979. Histomorphometric profile, pathophysiology and reversibility of corticosteroid-induced osteoporosis. Metab Bone Dis Relat Res 1(4)303-11.

Britz, H.M., Thomas, C.D.L., Clement, J.G., Cooper, D.M.L., 2009. The relation of femoral osteon geometry to age, sex, height and weight. Bone 45(1):77-83.

Brown, T.D., Ferguson, A.B. Jr., 1978. The development of a computational stress analysis of the femoral head. J Bone Jt Surg 60(5):619-29.

Burstein, A.H., Reilly, D.T., Martens, M.J., 1976. Aging of bone tissue: mechanical properties. J Bone Jt Surg 58(1):82-6.

Burr, D.B., 1992. Estimated intracortical bone turnover in the femur of growing macaques: implications for their use as models in skeletal pathology. Anat Rec 232(2):180-9.

Burr, D.B., 2011. Why bones bend but don't break. J. Musculoskelet Neuronal Interact 11(4): 270–85.

Burr, D.B., Akkus, O., 2014. Bone Morphology and Organization. In: Burr DB, Allen Mr (Eds.) Basic and Applied Bone Biology. Elsevier, London, pp. 3-26.

Burr, D.B., Martin, R.B., 1983. The effects of composition, structure and age on the torsional properties of the human radius. J Biomech 16(8):603-8.

Burr, D.B., Martin, R.B., 1993. Calculating the probability that microcracks initiate resorption spaces. J Biomech 26:613-6.

Burr, D.B., Ruff, C.B., Thompson, D.D., 1990. Patterns of skeletal histologic change through time: comparison of an archaic native American population with modern populations. Anat Rec 226(3):307-13.

Burr, D.B., Turner, C.H., Naick, P., Forwood, M.R., Ambrosius, W., Hasan, M.S., Pidaparti, R. 1998. Does microdamage accumulation affect the mechanical properties of bone? J Biomech. 31(4):337–45.

Burton, P., Nyssen-Behets, C., Dhem, A., 1989. Haversian bone remodeling in human fetus. Acta Anat 135(2):171-5.

Busse, B., Djonic, D., Milovanovic, P., Hahn, M., Puschel, K., Ritchie, R.O., Djuric, M., Amling, M., 2010. Decrease in the osteocyte lacunar density accompanied by hypermineralized lacunar occlusion reveals failure and delay of remodeling in aged human bone. Aging Cell. 9(6):1065–75.

Caler W.E., Carter, D.R., 1989. Bone creep-fatigue damage accumulation. J Biomech 22(6-7):625-35.

Carter, D.R., Hayes, W.C., 1977. Compact bone fatigue damage-I. Residual strength and stiffness. J Biomech. 10(5-6):325–37.

Carter, Y., Thomas, C.D., Clement, J.G., Cooper, D.M., 2013a. Femoral osteocyte lacunar density, volume and morphology in women across the lifespan. J Struct Biol 183(3):519–26.

Carter, Y., Thomas, C.D., Clement, J.G., Peele, A.G., Hannah, K., Cooper, D.M., 2013b. Variation in osteocyte lacunar morphology and density in the human femur – a synchrotron radiation micro-CT study. Bone 52(1):126–32.

452

Carter, Y., Suchorab, J.L., Thomas, C.D., Clement, J.G., Cooper, D.M., 2014. Normal variation in cortical osteocyte lacunar parameters in healthy young males. J Anat 225(3):328-36.

Center, J.R., Nguyen, T.V., Sambrook, P.N., Eisman, J.A., 1999. Hormonal and biochemical parameters in the determination of osteoporosis in elderly men. J Clin Endocrinol Metab 84(10):3626-35.

Chappard, D., Laurent, J.L., Bousquet, G., Riffat, G., Odelin, M.F., 1978. Mean osteoplastic surface in zones of plexiform neo-osteogenesis compared with mean osteoplastic surface measured on the fetal bone. Bull Assoc Anat (Nancy) 62(179):389-99.

Chavassieux, P.M., Seeman, E., Delmas, P.D., 2007. Insights into material and structural basis of bone fragility from diseases associated with fractures: how determinants of the biomechanical properties of bone are compromised by disease. Endocr Rev 28:151–164.

Chen, H., Kubo, K., 2010. Bone three-dimensional microstructural features of the common osteoporotic fracture sites. World J Orthop 5(4):486-95.

Chen, H., Zhou, Z., Shoumura, S., Emura, S., Bunai, Y., 2010. Age- and gender-dependent changes in three-dimensional microstructure of cortical and trabecular bone at the human femoral neck. Osteoporos Int 21(4):627–36.

Cho, H., Stout, S.D., 2011. Age-associated bone loss and intraskeletal variability in the Imperial Romans. J Anthropol Sci. 89:109-25.

Ciarelli, T.E., Fyhrie, D.P., Parfitt, A.M., 2003. Effects of vertebral bone fragility and bone formation rate on the mineralization levels of cancellous bone from white females. Bone 32(3):311-5.

Cohen, J., Harris, W.H., 1958. The three-dimensional anatomy of haversian systems. J Bone Joint Surg, 40-A(2):419-34.

Cole, M.E., Stout S.D., 2015. A semi-automatic method for intracortical porosity quantification with application to intraskeletal variability. Am J Phys Anthropol 156(Suppl 60):108

Cole, M.E., Stout S.D., 2016. Identification of osteoporosis with the parabolic index varies based on the method of adjustment for porosity. Am J Phys Anthropol 159(Suppl 62):119.

Cooper, C., Atkinson, E.J., O'Fallon, W.M., Melton, L.J. 3rd., 1992. Incidence of clinically diagnosed vertebral fractures: a population-based study in Rochester, Minnesota, 1985-1989. J Bone Miner Res 7(2):221-7.

Cooper, D.M., Erickson, B., Peele, A.G., Hannah, K., Thomas, C.D., Clement, J.G., 2011. Visualization of 3D osteon morphology by synchrotron radiation micro-CT. J Anat. 219(4):481-9.

Cooper, D.M., Matyas, J.R., Katzenberg, M.A., Hallgrimsson, B., 2004. Comparison of microcomputed tomographic and microradiographic measurements of cortical bone porosity. Calcif Tissue Int 74(5):437-47.

Cooper, D.M., Thomas, C.D., Clement, J.G., Hallgrimsson, B., 2006. Three-dimensional microcomputed tomography imaging of basic multicellular unit-related resorption spaces in human cortical bone. Anat Rec A Discov Mol Cell Evol Biol 288(7):806-16.

Cooper, D.M., Thomas, C.D., Clement J.G., Turinsky, A.L., Sensen, C.W., Hallgrímsson, B., 2007a. Age-dependent change in the 3D structure of cortical porosity at the human femoral midshaft. Bone 40(4):957-65.

Cooper, D.M., Turinsky, A., Sensen, C., Hallgrimsson, B., 2007b. Effect of voxel size on 3D micro-CT analysis of cortical bone porosity. Calcif Tissue Int 80(3):211-9.

Cooper, D.M., Turinsky, A.L., Sensen, C.W., Hallgrímsson, B., 2003. Quantitative 3D analysis of the canal network in cortical bone by micro-computed tomography. Anat Rec B New Anat 274(1):169-79.

Cooper, R.R., Milgram, J.W., Robinson, R.A., 1966. Morphology of the osteon. J Bone Joint Surg Am 48(7):1239-71.

Congiu, T., Pazzaglia, U.E., 2011. The sealed osteons of cortical diaphyseal bone. Early observations revisited with scanning electron microscopy. Anat Rec 294(2):193-8.

Cramer, S.F., Fried, L., Carter, K.J., 1981. The cellular basis of metastatic bone disease in patients with lung cancer. Cancer 48(12):2649-60.

Crescimanno, A., Stout, S.D., 2012. Differentiating fragmented human and nonhuman long bone using osteon circularity. J Forensic Sci 57(2):287-94.

Currey, J.D., 1962. Stress concentrations in bone. J Cell Sci s3-103:111-33.

Currey, J.D., 1964. Some effects of ageing in human Haversian systems. J Anat 98(1):69-75.

453

Currey, J.D., 1999. What determines the bending strength of compact bone? J Exp Biol 202(18):2495-503.

Dallas, S.L., Prideaux, M., Bonewald, L.F., 2013. The osteocyte: An endocrine cell…and more. Endocr Rev 34(5): 658–690.

Dalle Carbonare, L, Arlot, M.E., Chavassieux, P.M., Roux, J.P., Portero, N.R, Meunier, P.J., 2001. Comparison of trabecular bone microarchitecture and remodeling in glucocorticoid-induced and postmenopausal osteoporosis. J Bone Miner Res. 16(1): 97-103.

Dalle Carbonare, L., Bertoldo, F., Valenti, M.T., Zenari, S., Zanatta, M., Sella, S., Giannini, S., Cascio, V.L., 2005. Histomorphometric analysis of glucocorticoid-induced osteoporosis

Micron, 36(7-8):645-52.

Dechow, P.C., Dong, H.C., Bolouri, M., 2008. Relationship Between Three-Dimensional Microstructure and Elastic Properties of Cortical Bone in the Human Mandible and Femur. In: Vinyard C, Ravosa MJ, Wall C (Eds.) Primate Craniofacial Function and Biology. Springer Science + Business Media, New York, pp. 265-93.

Del Fattore, A., Cappariello, A., Teti, A., 2008. Genetics, pathogenesis and complications of osteopetrosis. Bone 42(1):19-29.

Delling, G. 1973. Age-related bone changes. Histomorphometric investigation of the structure of human cancellous bone. Curr Top Pathol 58:117-47.

Diab, T., Vashishth, D., 2005. Effects of damage morphology on cortical bone fragility. Bone 37(1):96-102.

Diab, T., Vashishth, D., 2007. Morphology, localization and accumulation of in vivo microdamage in human cortical bone. Bone. 40(3):612–8.

Diab, T., Sit, S., Kim, D., Rho, J., Vashishth, D., 2005. Age-dependent fatigue behaviour of human cortical bone. Eur J Morphol. 42(1-2):53–9.

Dominguez, V.M., Agnew, A.M., 2014. Patterns in resorptive spaces in elderly rib cortices. Am Phys Anthropol 153(Suppl 58):107

Dominguez, V.M., Crowder, C., 2015. Sex differences in measures of bone remodeling. In: Proceedings of the 67th Annual Scientific Meeting of the American Academy of Forensic Sciences. Orlando. p 185–186.

Dominguez ,V.M., Kang, Y.-S., Murach, M.M., Crowe, N., Agnew, A.M., 2016. Bone area vs cortical area: Considering intracortical porosity when predicting rib structural properties. 2016 International Research Council on Biomechanics of Injury (IRCOBI) Conference Proceedings

Dong, P., Haupert, S., Hesse, B., Langer, M., Gouttenoire, P.-J., Bousson, V., Peyrin, F., 2014.

3D osteocyte lacunar morphometric properties and distributions in human femoral cortical bone using synchrotron radiation micro-CT images. Bone 60:172–85.

Dunstan, C.R., Somers, N.M., Evans, R.A., 1993. Osteocyte death and hip fracture. Calcif Tissue Int 53(suppl. 1):S113-7.

Ebacher, V., Tang, C., McKay, H., Oxland, T.R., Guy, P., Wang, R., 2007. Strain redistribution and cracking behavior of human bone during bending. Bone 40(5):1265–75.

Ebeling, P.R., 2008. Osteoporosis in men. N Engl J Med 358(14):1474-82.

El Miedany, Y.M., el Gaafary, S., el Baddini, M.A., 1999. Osteoporosis in older adults with non-insulin-dependent diabetes mellitus: is it sex related? Clin Exp Rheumatol 17(5):561-7.

Epker, B.N., Frost, H.M., 1965. The direction of transverse drift of actively forming osteons in the human rib cortex. J Bone Joint Surg 47:1211-5.

Epker, B.N., Kelin, M., Frost, H., 1965. Magnitude and location of cortical bone loss in human rib with aging. Clin Orthop 41:198-203.

Epker, B.N., Frost, H.M., 1964. The parabolic index: A proposed index of the degree of osteoporosis in ribs. J Gerontol 19(4):469-73.

Einhorn, T.A., 1992. Bone strength: The bottom line. Calcif Tissue Int. 51:333–39.

Einhorn, T.A., Boskey, A.L., Gundberg, C.M. Vigorita, V.J., Devlin, V.J., Beyer, M.M., 1988. The mineral and mechanical properties of bone in chronic experimental diabetes. J Othorp Res 6(3):317-23.

Erbagci, A.B., Araz, M., Erbagci, A., Tarakcioglu, M., Namidaru, E.S., 2002. Serum prolidase activity as a marker of osteoporosis in type 2 diabetes mellitus. Clin Biochem 35(4):263-8.

454

Ericksen, M.F., 1991. Histologic estimation of age at death using the anterior cortex of the femur. Am J Phys Anthropol 84(2):171-9.

Evans, F.G., 1976. Mechanical properties and histology of cortical bone from younger and older men. Anat Rec 185(1):1-11.

Feik, S., Thomas, C., Bruns, R., Clement, J., 2000. Regional variations in cortical modeling in the femoral mid-shaft: sex and age differences. Am J Phys Anthropol 112(2):191-205.

Ferretti, J.L., Capozza, R.F., Cointry, G.R., Garcia, S.L., Plotkin, H., Alvarez Filgueira, M.L., Zanchetta, J.R., 1998. Gender-related differences in the relationship between densitometric values of whole-body bone mineral content and lean body mass in humans between 2 and 87 years of age. Bone 22(6):683-90.

Filogamo, G., 1946. La forme et la taille des osteones chez quelques Mammiferes. Arch Biol 57: 137-43.

Frost, H.M., 1960a. In vivo osteocyte death. J Bone Jt Surg 42-A:138-143.

Frost, H.M., 1960b. Micropetrosis. J Bone Joint Surg Am. 42-A:144–50.

Frost, H.M., 1960c. Presence of microscopic cracks in vivo in bone. Henry Ford Hosp Med Bull 8:25–35.

Frost, H.M., 1963. Bone remodelling dynamics. Charles C Thomas, Springfield, IL, pp. 3-115.

Frost, H.M., 1969. Tetracycline-based histological analysis of bone remodeling. Calc Tiss Res 3(3):211-37.

Frost, H.M., 1987. Bone "mass" and the "mechanostat": a proposal. Anat Rec 219(1):1-9.

Frost, H.M., 1990. Skeletal structural adaptations to mechanical usage(SATMU): 2. Redefining Wolff's Law: the remodeling problem. Anat Rec 226(4):414–22.

Frost, H.M., 1992. The role of changes in mechanical usage set points in the pathogenesis of osteoporosis. J Bone Miner Res 7(3):253-61.

Frost, H.M., 2003. On changing view about age-related bone loss. In: Agarwal SC, Stout SD (Eds.) Bone Loss and Osteoporosis: An Anthropological Perspective. Kluwer Academic/Plenum, New York, pp. 19-31.

Galante, J., Rostoker, W., Ray, R.D., 1970. Physical properties of trabecular bone. Calcif Tissue Res 5:236-46.

Gennari, L., Merlotti, D., Martini, G., Gonnelli, S., Franci, B., Campagna, S., Lucani, B., Canto, N.D., Valenti, R., Gennari, C., Nuti, R., 2003. Longitudinal association between sex hormone levels, bone loss, and bone turnover in elderly men. J Clin Endocrinol Metab 88(11):5327-33.

Gocha, T.P., Agnew A.M., 2016. Spatial variation in osteon population density at the human femoral midshaft: histomorphometric adaptations to habitual load environment. J Anat 28(5):733-45.

Goldman, H.M., Mcfarlin, S.C., Cooper, D.M.L., Thomas, C.D.L., Clement, J.G., 2009. Ontogenetic Patterning of Cortical Bone Microstructure and Geometry at the Human Mid-Shaft Femur. Anat Rec 292(1):48-64.

Goliath, J.R., Stewart, M.C., Stout, S.D., 2016. Variation in osteon histomorphometrics and their impact on age-at-death estimation in older individuals. Forensic Sci Int 262:282.e1–6.

Green, J.O., Wang, J., Diab, T., Vidakovic, B., Guldberg, R.E., 2011. Age-related differences in the morphology of microdamage propagation in trabecular bone. J Biomech 44(15):2659–66.

Greendale, G.A., Edelstein, S., Barrett-Connor, E., 1997 Endogenous sex steroids and bone mineral density in older women and men: The Rancho Bernardo study. J Bone Miner Res 12(11):1833-43.

Gruss, L.T., 2007. Limb length and locomotor biomechanics in the genus Homo: an experimental study. Am J Phys Anthropol 134(1):106-16.

Han, Z.H., Palnitkar, S., Rao, D.S., Nelson, D., Parfitt, A.M., 1997. Effects of ethnicity and age or menopause on the remodeling and turnover of iliac bone: implications for mechanisms of bone loss. J Bone Miner Res 12:498-508.

Han, Z.H., Palnitkar, D., Rao, S., Nelson, D., Parfitt, A.M., 1996. Effect of ethnicity and age or menopause on the structure and geometry of iliac bone. J Bone Miner Res 11(12):1967–1975.

Hannah, K.M., Thomas, C.D., Clement, J.G., De Carlo, F., Peele, A.G., 2010. Bimodal distribution of osteocyte lacunar size in the human femoral cortex as revealed by micro-CT. Bone 47(5):866–71.

Hansen, S., Beck Jensen, J.E., Rasmussen, L., Hauge, E.M., Brixen, K. 2010. Effects on bone geometry, density, and microarchitecture in the distal radius but not the tibia in women with primary hyperparathyroidism: A case-control study using HR-pQCT. J Bone Miner Res 25(9):1941-7.

Hattner, R., Frost, H.M. 1963. Mean skeletal age: Its meaning and a method of calculation. Henry Ford Hospital Med Bull 11:201-16.

Havill, L.M., 2004. Osteon remodeling dynamics in Macaca mulatta: normal variation with regard to age, sex, and skeletal maturity. Calcif Tissue Int 74(1):95-102.

Heaney, R.P., Abrams, S., Dawson-Hughes, B., Looker, A., Marcus, R., Matkovic, V., Weaver C., 2000. Peak bone mass. Oseoporos Int 11(12):985-1009.

Hennig C., Thomas C.D.L., Clement, J.G., Cooper D.M.L., 2015. Does 3D orientation account for variation in osteon morphology assessed by 2D histology? J Anat 227(4):497-505.

Henrie, T.R., Dalton, M., Skedros, J.G., 2014. Sealed osteons: a pathological consequence or natural circumstance of extensive remodeling? Am J Phys Anthropol 153(Suppl 58):140.

Herman, B.C., Cardoso, L., Majeska, R.J., Jepsen, K.J., Schaffler, M.B., 2010. Activation of bone remodeling after fatigue: Differential response to linear microcracks and diffuse damage. Bone 47(4):766-72.

Himeno-Ando, A., Izumi, Y., Yamaguchi, A., Iimura, T., 2012. Structural differences in the osteocyte network between the calvaria and long bone revealed by three-dimensional fluorescence morphometry, possibly reflecting distinct mechano-adaptations and sensitivities. Biochem Biophys Res Commun. 417(2):765-70.

Hofstaetter, J.G., Roschger, A., Puchner, S.E., Dominkus, M., Sulzbacher, I., Windhager, R., Klaushofer, K., Roschger, P. 2013. Altered matrix mineralization in a case of a sclerosing osteosarcoma. Bone 53(2):409-13.

Hou, J.C., Zernicke, R.F., Barnard, R.J., 1991. Experimental diabetes, insulin treatment, and femoral neck morphology and biomechanics in rats. Clin Orthop Relat Res 264:278-85.

Hunt, K.J., Skedros, J.G., 2001. The role of osteocyte lacunae populations in interpreting loading history of bone. Am J Phys Anthropol 32(Suppl):83.

Hunter, R.L., Agnew, A.M., 2016. Intraskeletal variation in human cortical osteocyte lacunar density: Implications for bone quality assessment. Bone Rep. 5:252-261

Iwamoto, S., Oonuki, E., Konishi, M., 1978. Study on the age-related changes of the compact bone and the age estimation 2. On the humerus. Acta Med Kinki Univ 3:203-8.

Jackson, S.A., Tenenhouse, A., Robertson, L., 2000. Vertebral fracture definition from population-based data: preliminary results from the Canadian Multicenter Osteoporosis Study (CaMos). Osteoporos Int 11:680-7.

Janghorbani, M., Van Dam, R.M., Willett, W.C., Hu, F.B., 2007. Systematic review of type 1 and type 2 diabetes mellitus and risk of fracture. Am J Epidemiol 166(5):495–505.

Jepsen, K.J., Evans, R., Negus, C.H., Gagnier, J.J., Centi, A., Erlich, T., Hadid, A., Yanovich, R., Moran, D.S., 2013. Variation in tibial functionality and fracture susceptibility among healthy, young adults arises from the acquisition of biologically distinct sets of traits. J Bone Miner Res. 28(6):1290-300.

Jiao, H., Xiao, E., Graves, D.T., 2015. Diabetes and its effect on bone and fracture healing. Curr Osteoporos Rep 13(5):327-35.

Jilka, R.L., Noble, B., Weinstein, R.S., 2013. Osteocyte apoptosis. Bone 54(2):264–71.

Jilka, R.L., O'Brien, C.A., 2016. The role of osteocytes in age-related bone loss. Curr Osteoporos Rep 14(1):16-25.

Johnell, O., Kanis, J.A., 2006. An estimate of the worldwide prevalence and disability associated with osteoporotic fractures. Osteoporos Int 17(12):1726-33.

Johnson, L.C., 1964. Morphologic analysis of pathology. In: Frost HM (Ed.) Bone Biodynamics. Little, Brown. & Co., Boston, pp. 543–654.

Jowsey, J., 1960. Age changes in human bone. Clin Orthop Rel Res 17:210-19.

Jowsey, J., 1964. Variation in bone mineralization with age and disease. In: Frost HM (Ed.) Bone Biodynamics. Little, Brown. & Co., Boston, pp. 461-71.

Juvinall, R.C., Marshek, K.M., 1991. Fundamentals of Machine Component Design. 2nd ed. John Wiley, New York.

Kafantari, H., Kounadi, E., Fatouros, M., Milonakis, M., Tzaphlidou, M., 2000. Structural alterations in rat skin and bone collagen fibrils induced by ovariectomy. Bone 26(4):349-53.

Kalender, W.A., Felsenberg, D., Louis, O., Lopez, P., Klotz, E., Osteaux, M., Fraga, J., 1989 Reference values for trabecular and cortical vertebral bone density in single and dual-energy quantitative computed tomography. Eur J Radiol 9(2):75-80.

Kanis, J.A., Johnell, O., Oden, A., Sembo, I., Redlund-Johnell, I., Dawson, A., De Laet, C., Jonsson, B., 2000. Long-term risk of osteoporotic fracture in Malmo. Osteoporos Int 11(8):669-74.

Kannus, P., Parkkari, J., Koskinen, S., Niemi, S., Palvanen, M., Järvinen, M., Vuori, I., 1999. Fall-induced injuries and deaths among older adults. JAMA. 281(20):1895-9.

Kennedy, O.D., Laudier, D.M., Majeska, R.J., Sun, H.B., Schaffler, M.B., 2014. Osteocyte apoptosis is required for production of osteoclastogenic signals following bone fatigue in vivo. Bone 64:132-7.

Khosla, S., Melton, L.J. 3rd, Atkinson, E.J., O'Fallon, W.M., 2001. Relationship of serum sex steroid levels to longitudinal changes in bone density in young versus elderly men. J Clin Endocrinol Metab 86(8):3555-61.

Khosla, S., Melton, L.J. 3rd, Robb, R.A., Camp, J.J., Atkinson, E.J., Oberg, A.L., Rouleau, P.A., Riggs, B.L., 2005 Relationship of volumetric BMD and structural parameters at different skeletal sites to sex steroid levels in men. J Bone Miner Res 20(5):730-40.

Khosla, S., Melton, L.J. 3rd, Atkinson, E.J., O'Fallon, W.M., Klee, G.G., Riggs, B.L., 1998, Relationship of serum sex steroid levels and bone turnover markers with bone mineral density in men and women: A key role for bioavailable estrogen. J Clin Endocrinol Metab 83(7):2266-74.

Klenerman, L., Swanson, S.A.V., Freeman, M.A.R. 1967. A method for the clinical estimation of the strength of a bone. Proc. Royal Society of Medicine 60:1-4.

Koltze,H., 1951. Studie zur ausseren Form der Osteone. Z Anat Entwicklungsgesch 115:584-96.

Komatsubara, S., Mori, S., Mashiba, T., Ito, M., Li, J., Kaji, Y., Akiyama, T., Miyamoto, K., Cao, Y., Kawanishi, J., Norimatsu, H.. 2003. Long-term treatment of incadronate disodium accumulates microdamage but improves the trabecular bone microarchitecture in dog vertebra. J Bone Miner Res 18(3):512-20.

Komori, T., 2013. Functions of the osteocyte network in the regulation of bone mass. Cell Tissue Res 352(2):191-8.

Koszyca, B., Fazzalari, N. L., Vernon-Roberts, B., 1989. Trabecular microfractures. Nature and distribution in the proximal femur. Clin Orthop Rel Res 244:208-16.

Kuo, T.T., Davis, C.P., 1981. Osteopetrosis: a scanning electron microscopic study. Hum Pathol 12(4):376-9.

Lane, N.E., Yao, W., Balooch, M., Nalla, R.K., Balooch, G., Habelitz, S., Kinney, J.H., Bonewald, L.F., 2006. Glucocorticoid-treated mice have localized changes in trabecular bone material properties and osteocyte lacunar size that are not observed in placebo-treated or estrogen-deficient mice. J Bone Miner Res 21(3):466-76.

Lanyon, L.D., Baggott, D.G., 1976. Mechanical function as an influence on the structure and form of bone. J Bone Joint Surg.58-B(4):436–43.

Lanyon, L.E., Goodship, A.E., Pye, C.J., MacFie, J.H., 1982. Mechanically adaptive bone remodelling. J Biomech 15(3):141-54.

Lai, X., Price, C., Modla, S., Thompson, W.R., Caplan, J., Kirn-Safran, C.B., Wang, L., 2015. The dependences of osteocyte network on bone compartment, age, and disease. Bone Research 3:15009

Logan, A., Lindau, T.R., 2008. The management of distal ulnar fractures in adults: a review of the literature and recommendations for treatment. Strategies Trauma Limb Reconstr. 3(2):49–56.

Lovejoy, C.O., Trinkaus, E., 1980. Strength and robusticity of the Neandertal tibia. Am J Phys Anthropol 53(4):465-70.

Maeda, H., Koizumi, M., Yoshimura, K., Yamauchi, T., Kawai, T., Ogata, E., Correlation between bone metabolic markers and bone scan in prostatic cancer. J Urol 157(2):539-43.

Maggiano, I.S., Maggiano, C.M., Clement, J.G., Thomas, C.D., Carter, Y., Cooper, D.M.,2016. Three-dimensional reconstruction of Haversian systems in human cortical bone using synchrotron radiation-based micro-CT: morphology and quantification of branching and transverse connections across age. J Anat 228(5):719-32.

457

Maggiano, I.S., Maggiano, C.M., Tiesler, V., Kierdorf, H., Stout, S.D., Schultz, M. 2011. A distinct region of microarchitectural variation in femoral compact bone: histomorphology of the endosteal lamellar pocket. Int J Osteoarchaeol 21(6):743-750.

Maggiano C, Dupras T.., Schultz M., Biggerstaff J. 2006. Spectral and photobleaching analysis using confocal laser scanning microscopy: a comparison of modern and archaeological bone fluorescence. Molecular and Cellular Probes 20(3-4):154-62

Maggiano, C., Dupras, Z.T., Schultz, M., Biggerstaff, J., 2009. Confocal laser scanning microscopy: a flexible tool for simultaneous polarization and three-dimensional fluorescence imaging of archaeological compact bone. J Arch Science 36: 2392-401.

Makhluf, H., Mueller, S., Mizuno, S., Glowacki, J., 2000. Age-related decline in osteoprotegerin expression by human bone marrow cells cultured in three-dimensional collagen sponges. Biochem Biophys Res Commun 268:669–72.

Mankin, H.F., 1992 Nontraumatic necrosis of bone (osteonecrosis). N Engl J Med 326(22): 1473-9.

Marotti, G., 1990. The original contributions of the scanning electron microscope to the knowledge of bone structure. In: Bonucci E, Motta P (Eds.) Ultrastructure of Skeletal Tissues: Bone and Cartilage in Health and Disease. Kluwer Academic Publishers, Norwell, MA, pp. 19 – 41.

Marotti, G., Muglia, M.A., Zaffe, D., 1985. A SEM study of osteocyte orientation in alternately structured osteons. Bone 6(5):331-4.

Martin, R.B., 1993. Aging and strength of bone as a structural material. Calcified Tissue International 53(Suppl 1):S34-9.

Martin, R.B., 2003. Functional adaptation and fragility of the skeleton. In: Agarwal SC and Stout SD (Eds.) Bone Loss and Osteoporosis: An Anthropological Perspective. Kluwer Academic/Plenum, New York, pp. 121-36.

Martin, R.B., Burr, D.B., 1984a. Mechanical implications of porosity distribution in bone of the appendicular skeleton. Orthop Trans 8:342-343.

Martin, R.B., Burr, D.B., 1984b. Non-invasive measurement of long bone cross-sectional moment of inertia by photon absorptiometry. J Biomech 17(3):195-201.

Martin, R.B., Burr, D.B., 1989. The Microscopic Structure of Bone. In: Martin RB, Burr DB (Eds.) The Structure, Function, and Adaptation of Compact Bone. Raven Press, New York, pp. 18-56.

Martin, R.B., Atkinson, P.J., 1977. Age- and sex-related changes in the structure and strength of the human femoral shaft. J Binmech 10(4):223-231

Martin, R.B., Gibson, V.A., Stover, S.M., Gibleling, J.C., Griffin, L.V., 1997. Residual strength of equine bone is not reduced by intense fatigue loading: implications for stress fracture. J Biomech 30(2):109-14.

Martin, R.B., Pickett, J.C., Zinaich, S., 1980. Studies of skeletal remodeling in aging men. Clin Orthop Relat Res 149:268-82

Mashiba, T., Hirano, T., Turner, C.H., Forwood, M.R., Johnston, C.C., Burr, D.B., 2000. Suppressed bone turnover by bisphosphonates increases microdamage accumulation and reduces some biomechanical properties in dog rib. J Bone Miner Res. 15(4):613–20.

Mashiba, T., Turner, C.H., Hirano, T., Forwood, M.R., Johnston, C.C., Burr, D.B., 2001. Effects of suppressed bone turnover by bisphosphonates on microdamage accumulation and biomechanical properties in clinically relevant skeletal sites in beagles. Bone 28(5):524–31.

Mason, M.W., Skedros, J.G., Bloebaum, R.D., 1995. Evidence of strain-mode-related cortical adaptation in the diaphysis of the horse radius. Bone 17(3): 229–37.

McCalden, R.W., McGeough, J.A., Barker, M.B., Court-Brown, C.M., 1993. Age-related changes in the tensile properties of cortical bone. The relative importance of changes in porosity, mineralisation and microstructure. J Bone Joint Surg 75(8):1193-205.

McCarthy, E.F., 2016. The histology of metabolic bone disease. Diagn Histopathol 22(10):378-83.

McCreadie, B.R., Hollister, S.J., Schaffler, M.B., Goldstein, S.A., 2004. Osteocyte lacuna size and shape in women with and without osteoporotic fracture. J Biomech 37(4):563-72.

Meena, S., Sharma, P., Sambharia, A.K., Dawar, A., 2014. Fractures of distal radius: an overview. J Family Med Prim Care. 3(4):325-32.

Meier, D.E., Orwoll, E.S., Jones, J.M., 1984. Marked disparity between trabecular and cortical bone loss with age in healthy men. Ann Intern Med 101(5):605–612.

Melton, L.J. 3rd, Atkinson, E.J., O'Connor, M.K., O'Fallon, W.M., Riggs, B.L., 1998. Bone density and fracture risk in men. J Bone Miner Res 13(12):1915-23.

Melton, L.J. 3rd, Lane, A.W., Cooper, C., Eastell, R., O'Fallon, W.M., Riggs, B.L., 1993. Prevalence and incidence of vertebral deformities. Osteoporos Int 3(3):113-9.

Melton, L.J. 3rd, Chat, E.Y.S., Lane, J.M., 1988. Biomechanical aspects of fractures. In: Riggs BL, Melton LJ 3rd (Eds) Osteoporosis: etiology, diagnosis and management. Raven Press, New York, pp. 111-31.

Milovanovic, P., Zimmermann, E.A., Hahn, M., Djonic, D., Puschel, K., Djuric, M., Amling, M., Busse, B., 2013. Osteocytic canalicular networks: morphological implications for altered mechanosensitivity. ACS Nano 7(9):7542-51.

Milovanovic, P., Rakocevic, Z., Djonic, D., Zivkovic, V., Hahn, M., Nikolic, S., Amling, M., Busse, B., Djuric, M., 2014. Nano-structural, compositional and micro-architectural signs of cortical bone fragility at the superolateral femoral neck in elderly hip fracture patients vs. healthy aged controls. Exp Gerontol 55:19-28.

Mori, S., Harruff, R., Ambrosius, W., Burr, D.B., 1997. Trabecular bone volume and microdamage accumulation in the femoral heads of women with and without femoral neck fractures. Bone 21(6):521–6.

Mosekilde, L., Mosekilde, L., 1990. Sex differences in age-related changes in vertebral body size, density and biomechanical competence in normal individuals. Bone 11(2):67-73.

Mulhern, D.M., 2000. Rib remodeling dynamics in a skeletal population from Kulubnarti, Nubia. Am J Phys Anthropolropol 111(4):519-30.

Mulhern, D.M., Van Gerven, D.P., 1997. Patterns of bone remodeling dynamics in a medieval Nubian population. Am J Phys Anthropol 104(1):133-46.

Mullender, M.G., van der Meer, D.D., Huiskes, R., Lips, P., 1996. Osteocyte density changes in aging and osteoporosis. Bone 18(2):109-13.

Murach, M.M., Kang, Y.S., Goldman, S.D., Schafman, M.A., Schlecht, S.H., Moorhouse, K., Bolte, J.H. 4th, Agnew, A.M., 2017. Rib geometry explains variation in dynamic structural response: Potential implications for frontal impact fracture risk. Ann Biomed Eng 45(9):2159-73.

Nalla, R.K., Kruzic, J.J., Kinney, J.H., Ritchie, R.O., 2005. Mechanistic aspects of fracture and r-curve behavior in human cortical bone. Biomaterials 26:217–31.

Nishida, S., Endo, N., Yamigiwa, H., Tanizawa, T., Takahashi, H., 1999. Number of osteoprogenitor cells in human bone marrow markedly decreases after skeletal maturation. J Bone Miner Metab 17:171–7.

Noble, B.S., Stevens, H., Loveridge, N., Reeve, J., 1997. Identification of apoptotic changes in osteocytes in normal and pathological human bone. Bone 20(3):273–82.

Norman, T.L., Wang, Z., 1997. Microdamage of human cortical bone: incidence and morphology in long bones. Bone 20(4):375-9.

Olsen, G.A., 1956. Strength of Materials. Prentice-Hall, Inc., New York.

O'Neill, T.W., Felsenberg, D., Varlow, J., Cooper, C., Kanis, K.A., Silman, A.J., 1996. The prevalence of vertebral deformity in European men and women: the European Vertebral Osteoporosis Study. J Bone Miner Res 11:1010-8.

Ortner, D.J., 1975. Aging effects on osteon remodeling. Calc Tiss Res 18(1):27-36.

Parfitt, A.M., Mathews, C.H.E., Villaneuva, A.R., Kleerekoper, M., Frame, B., Rao, D.S., 1983. Relationships between surface, volume, and thickness of iliac trabecular bone in aging and in osteoporosis. J Clin Invest 72(4):1396-409.

Parkinson, I.H., Fazzalari, N.L., 2003. Interrelationships between structural parameters of cancellous bone reveal accelerated structural change at low bone volume. J Bone Miner Res 18(12):2200-5

Paschalis, E.P., Glass, E.V., Donley, D.W., Eriksen, E.F., 2005. Bone mineral and collagen quality in iliac crest biopsies of patients given teriparatide: new results from the fracture prevention trial. J Clin Endocrinol Metab 90(8):4644-9.

Pattin, C.A., Caler, W.E., Carter, D.R., 1996. Cyclic mechanical property degradation during fatigue loading of cortical bone. J Biomech 29(1):69-79.

Pazzaglia, U.E., Congiu, T., Pienazza, A., Zakaria, M., Gnecchi, M., Dell'orbo, C., 2013. Morphometric analysis of osteonal architecture in bones from healthy young human male subjects using scanning electron microscopy. J Anat 223(3):242-54.

Pearson, O.M., Lieberman, D.E., 2004. The aging of Wolff 's ''law:'' ontogeny and responses to mechanical loading in cortical bone. Yrbk Phys Anthropol Suppl 39:63–99.

Peck, J., Stout, S.D., 2007. Intraskeletal variability in bone mass. Am J Phys Anthropol 132(1):89-97.

Pfeiffer, S., 1998. Variability in osteon size in recent human populations. Am J Phys Anthropol 106(2):219–27.

Pfeiffer, S., Crowder, C., Harrington, L., Brown, M. 2006. Secondary osteon and Haversian canal dimensions as behavioral indicators. Am J Phys Anthropol 131(4):460–8.

Pietschmann, P., Kudlacek, S., Grisar, J., Spitzauer, S., Woloszczuk, W., Willvonseder, R., Peterlik, M., 2001. Bone turnover markers and sex hormones in men with idiopathic osteoporosis. Eur J Clin Invest 31(5):444-51.

Popov, E.P., 1952. Mechanics of Materials. Prentice-Hall, Inc., New York.

Portigliatti Barbos, M., Bianco, P., Ascenzi, A., 1983. Distribution of osteonic and interstitial components in the human femoral shaft with reference to structure, calcification and mechanical properties. Acta Anat 115(2):178-86.

Power, J., Loveridge, N., Lyon, A., Rushton, N., Parker, M., Reeve, J. 2004. Osteoclastic cortical erosion as a determinant of subperiosteal osteoblastic bone formation in the femoral neck's response to BMU imbalance: effects of stance-related loading and hip fracture. Osteoporos Int. 16(9):1049-56.

Qing, H., Bonewald, L.F., 2009. Osteocyte remodeling of the perilacunar and pericanalicular matrix. Int J Oral Sci 1(2):59–65.

Qing, H., Ardeshirpour, L., Pajevic, P.D., Dusevich, V., Jähn, K., Kato, S., Wysolmerski, J., Bonewald, L.F., 2012. Demonstration of osteocytic perilacunar/canalicular remodeling in mice during lactation. J Bone Miner Res 27(5):1018-29.

Qiu, S., Rao, D.S., Fyhrie, D.P., Palnitkar, S., Parfitt, A.M., 2005. The morphological association between microcracks and osteocyte lacunae in human cortical bone. Bone 37:10-5.

Qiu, S., Rao, D.S., Palnitkar, S., Parfitt, A.M., 2002. Age and distance from the surface but not menopause reduce osteocyte density in human cancellous bone. Bone 31(2):313-18.

Qiu, S., Rao, D.S., Palnitkar, S., Parfitt, A.M., 2003. Reduced iliac cancellous osteocyte density in patients with osteoporotic vertebral fracture. J Bone Miner Res 18(9):1657-63.

Rauch, F., Schoenau E. 2001.The developing bone: slave or master of its cells and molecules? Pediatr Res 50(3):309-14.

Rauch, F., Travers, R., Parfitt, A.M., Glorieux, F.H., 2000. Static and dynamic bone histomorphometry in children with osteogenesis imperfecta. Bone 26: 581–89.

Reilly, D.T., Burstein, A.H., 1974. The mechanical properties of cortical bone. J Bone Jt Surg 56(5):1001-21.

Reilly, D.T., Burstein, A.H., 1975. The elastic and ultimate properties of compact bone tissue. J Biomech 8(6):393-405.

Recker, R., Lappe, J., Davies, K., Heaney, R., 2004. Bone remodeling increases substantially in the years after menopause and remains increased in older osteoporosis patients. J Bone Miner Res 19:1628–33.

Reilly, D.T., Burstein, A.H., 1974. The mechanical properties of cortical bone. J Bone Joint Surg Am 56(5):1001-22.

Reilly, G.C., Currey, J.D., 1999. The development of microcracking and failure in bone depends on the loading mode to which it is adapted. J Exp Biol 202(5):543–52.

Reilly, G.C., Currey, J.D., 2000. The effects of damage and microcracking on the impact strength of bone. J. Biomech., 33(3):337-43.

Riggs, B.L., Melton, L.J., Robb, R.A., Camp, J.J., Atkinson, E.J., McDaniel, L., Amin, S., Rouleau, P.A., Khosla, S., 2008. A population-based assessment of rates of bone loss at multiple skeletal sites:

evidence for substantial trabecular bone loss in young adult women and men. J Bone Miner Res 23(2):205-14.

Riggs, B.L., Melton, L.J., Robb, R.A., Camp, J.J., Atkinson, E.J., Peterson, J.M., Rouleau, P.A., McCollough, C.H., Bouxsein, M.L., Khosla, S., 2004 Population-based study of age and sex differences in bone volumetric density, size, geometry, and structure at different skeletal sites. J Bone Miner Res 19(12):1945-54.

Ritchie, R.O., 2011. The conflicts between strength and toughness. Nature Materials 10:817–22.

Robling, A.G., Fuchs, R.K., Burr, D.B., 2014. Mechanical adaptation. In: Burr DB, Allen MR (Eds.) Basic and Applied Bone Biology. Academic Press, London, pp. 175-203.

Robling, A.G., Stout, S., 1999. Morphology of the drifting osteon. Cells Tissues Organs 164(4):192-204.

Robling, A.G., Stout, S., 2003. Histomorphology, geometry, and mechanical loading in past populations. In: Agarwal SC, Stout SD (Eds.) Bone Loss and Osteoporosis: An Anthropological Perspective. Kluwer Academic/Plenum, New York, pp. 189-203.

Robling, A.G., Turner, C.H., 2002. Mechanotransduction in bone: genetic effects on mechanosensitivity in mice. Bone 31(5):562-9.

Roschger, P., Dempster, D.W., Zhou, H., Paschalis, E.P., Silverberg, S.J., Shane, E., Bilezikian, J.P., Klaushofer, K., 2007. New observations on bone quality in mild primary hyperparathyroidism as determined by quantitative backscattered electron imaging. J Bone Miner Res 22(5):717-23.

Ruff CB. 1999. Skeletal structure and behavioral patterns of prehistoric Great Basin populations. In: Hemphill BE, Larsen CS (Eds.) Prehistoric lifeways in the Great Basin wetlands: bioarchaeological reconstruction and interpretation. University of Utah Press, Salt Lake City, pp. 290-320.

Ruff, C.B., 2009. Relative limb strength and locomotion in Homo habilis. Am J Phys Anthropol 138(1):90-100.

Ruff, C.B., Hayes, W.C., 1983. Cross-sectional geometry of Pecos Pueblo femora and tibiae-a biomechanical investigation. I: method and general patterns of variation. Am J Phys Anthropol 60(3):383–400.

Ruff, C.B., Hayes, W.C., 1988. Sex differences in age-related remodeling of the femur and tibia. J Orthop Res 6(6):886-96.

Ruff, C.B., Larsen, C.S., 2014. Long bone structural analyses and the reconstruction of past mobility: a historical review. In: Carlson KJ, Marchi D (Eds.) Reconstructing mobility: Environmental, behavioral, and morphological determinants. Springer, New York, pp. 13-29.

Ruff, C.B., McHenry, H.M, Thackeray, J.F., 1999. Cross-sectional morphology of the SK 82 and 97 proximal femora. Am J Phys Anthropol 109(4):509-21.

Ruff, C., Holt, B., Trinkaus, E., 2006. Who's afraid of the big bad Wolff?: "Wolff's law" and bone functional adaptation. Am J Phys Anthropol 129(4):484-98.

Ruppel, M.E., Miller, L.M., Burr, D.B., 2008. The effect of the microscopic and nanoscale structure on bone fragility. Osteoporos Int 19(9):1251-65.

Sedlin, E.D., Frost, H.M., Villanueva, A.R., 1963. Age changes in resorption in the human rib cortex. J Gerontol 18:345–349.

Schaffler, M.B., Choi, K., Milgrom, C., 1995. Aging and matrix microdamage accumulation in human compact bone. Bone 17(6):521-5.

Schlecht, S.H., Bigelow, E.M., Jepsen, K.J., 2014. Mapping the natural variation in whole bone stiffness and strength across skeletal sites. Bone 67:15–22.

Schlecht, S.H., Bigelow, E., Jepsen, K.J., 2015. How does bone strength compare across sex, site, and ethnicity? Clin Orthop Relat Res 473(8):2540-7.

Schlecht, S.H., Pinto, D.C., Agnew, A.M., Stout, S.D., 2012. Brief communication: the effects of disuse on the mechanical properties of bone: what unloading tells us about the adaptive nature of skeletal tissue. Am J Phys Anthropol 149(4):599–605.

Schultz, M., 2011. Light Microscopic Analysis of Macerated Pathologically Changed Bones. In: Stout SD, Crowder C (Eds.) Bone Histology: An Anthropological Perspective. CRC Press, Boca Raton Florida, pp 253-296.

461

Seeman, E., 2013. Age- and menopause-related bone loss compromise cortical and trabecular microstructure. J Gerontol A Biol Sci Med Sci 68(1):1218-25.

Seeman, E., Delmas, P.D., 2006. Bone quality – The material and structural basis of bone strength and fragility. N Engl J Med 354:2250-61.

Seitz, S., Priemel, M., Zustin, J., Beil, F.T., Semler, J., Minne, H., Schinke, T., Amling, M., 2009. Paget's disease of bone: histologic analysis of 754 patients. J Bone Miner Res 24(1):62-9.

Semba, I., Ishigami, T., Sugihara, K., Kitano, M., 2000. Higher osteoclastic demineralization and highly mineralized cement lines with osteocalcin deposition in a mandibular cortical bone of autosomal dominant osteopetrosis type II: ultrastructural and undecalcified histological investigations. Bone 27(3):389-95.

Seref-Ferlengez, Z., Kennedy, O.D., Schaffler, M.B., 2015. Bone microdamage, remodeling and bone fragility: how much damage is too much damage? BoneKEy Reports 4(644)

Shapiro, F., Glimcher, M.J., Holtrop, M.E., Tashjian, A.H., Brickley-Parsons, D., Kenzora, J.E., 1981. Human osteopetrosis. A histological, ultrastructural and biochemical study. J Bone Joint. Surg. 62(3):384-99.

Sillence, D.O., Rimoin, D.L., 1978. Classification of osteogenesis imperfect. Lancet 1(8072):1041-2.

Silva, M.J., Gibson, L.J. 1997. Modeling the mechanical behavior of vertebral trabecular bone: Effects of agerelated changes in microstructure. Bone 21(2):191-9.

Simmons, E.D., Pritzker, K.P.H., Grynpas, M.D., 1991. Age-related changes in the human femoral cortex. J Orthop Res 9(2):155-67.

Singh, I.J., Gunberg, D.L., 1970. Estimation of age at death in human males from quantitative histology of bone fragments. Am J Phys Anthropol 33(3):373-81.

Singh, I.J., Gunberg, D.L., 1971. Quantitative histology of changes with age in rat bone cortex. J Morphol 133(2):241-51.

Sjögren, H., Björnstig, U., 1989. Unintentional injuries among elderly people: incidence, causes, severity, and costs. Accid Anal Prev 21(3):233-42.

Skedros, J.G., 2011. Bone Remodeling, Histomorphology, and Histomorphometry. In: Stout SD, Crowder C (Eds.) Bone Histology: An Anthropological Perspective. CRC Press, Boca Raton Florida, pp 153-221.

Skedros JG, Hunt KJ, Bloebaum RD. 2004. Relationships of loading history and structural and material characteristics of bone: Development of the Mule Deer calcaneus. J. Morph. 259: 281 – 307.

Skedros, J.G., Bloebaum, R.D., Mason, M.W., Bramble, D.M., 1994a. Analysis of a tension/compression skeletal system: possible strain-specific differences in the hierarchical organization of bone. Anat Rec 239(4):396–404.

Skedros, J.G., Grunander, T.R., Hamrick, M.W., 2005a. Spatial distribution of osteocyte lacunae in equine radii and third metacarpals: considerations for cellular communication, microdamage detection and metabolism. Cells Tissues Organs 180(4):215-36.

Skedros, J.G., Hunt, K.J., Bloebaum, R.D., 2004. Relationships of loading history and structural and material characteristics of bone: Development of the mule deer calcaneus. J. Morph. 259(3): 281-307.

Skedros, J.G., Mason, M.W., Bloebaum, R., 1994b. Differences in osteonal micromorphology between tensile and compressive cortices of a bending skeletal system: indications of potential strain-specific differences in bone microstructure. Anat Rec 239(4):405-13.

Skedros, J.G., Mason, M.W., Bloebaum, R.D., 2001. Modeling and remodeling in a developing artiodactyl calcaneus: a model for evaluating Frost's Mechanostat hypothesis and its corollaries. Anat Rec 263(2):167-85.

Skedros, J.G., Mason, M.W., Nelson, M.C., Bloebaum, R.D., 1996. Evidence of structural and material adaptation to specific strain features in cortical bone. Anat Rec 246:47–63.

Skedros, J.G., Sybrowsky, C.L., Dayton, M.R., Bloebaum, R.D., Bachus, K.N., 2003. The role of osteocyte lacuna population density on the mechanical properties of cortical bone. Trans. Orthop. Res. Soc. 28:414

Skedros, J.G., Su, S.C., Bloebaum, R.D., 1997. Biomechanical implications of mineral content and microstructural variations in cortical bone of horse, elk and sheep calcanei. Anat Rec 249(3):297-316.

Sladek, V., Berner, M., Sailer, R., 2006. Mobility in central European Late Eneolithic and Early Bronze Age: Tibial cross-sectional geometry. J Archaeol Sci 33(4):470-82.

Slemenda, C.W., Longcope, C., Zhou, L., Hui, S.L., Peacock, M., Johnston, C., 1997. Sex steroids and bone mass in older men: Positive associations with serum estrogens and negative associations with androgens. J Clin Invest 100(7):1755-9.

Stein, M.S., Feik, S.A., Thomas, C.D., Clement, J.G., Wark, J.D., 1999. An automated analysis of intracortical porosity in human femoral bone across age. J Bone Miner Res 14(4):624-32.

Stewart, M.C., Goliath, J.R., Stout, S.D., Hubbe, M. 2015. Intraskeletal Variability of Relative Cortical Area in Humans. Anat Rec 298(9):1635-43.

Strotmeyer, E.S., Cauley, J.A., Schwartz, A.V., Nevitt, M.C., Resnick, H.E., Zmuda, J.M., Bauer, D.C., Tylavsky, F.A., de Rekeneire, N., Harris, T.B., Newman, A.B. 2004. Diabetes is associated independently of body composition with BMD and bone volume in older white and black men and women: The Health, Aging, and Body Composition Study. J Bone Miner Res 19(7): 1084-91.

Stout, S.D., Brunsden, B.S., Hildebolt, C.F., Commean, P.K., Smith, K.E., Tappen, N.C., 1999. Computer assisted 3D reconstruction of serial sections of cortical bone to determine the 3D structure of osteons. Calcif Tissue Int 65(4):280-4.

Stout, S.D., Lueck, R., 1995. Bone remodeling rates and skeletal maturation in three archaeological skeletal populations. Am J Phys Anth 98(2):600-4.

Stout, S.D., Crowder, C., 2011. Bone Remodeling, Histomorphology, and Histomorphometry. In: Stout SD, Crowder C (Eds.) Bone Histology: An Anthropological Perspective. CRC Press, Boca Raton Florida. pp 1 – 22.

Streeter, M., 2011. Histological Age-at-Death Estimation. In: Stout SD, Crowder C (Eds.) Bone Histology: An Anthropological Perspective. CRC Press, Boca Raton Florida. pp .135-152

Szulc, P., Munoz, F., Claustrat, B., Garnero, P., Marchand, F., 2001 Bioavailable estradiol may be an important determinant of osteoporosis osteoporosis in men: The MINOS study. J Clin Endocrinol Metab 86(1):192-9.

Takahashi, H., Frost, H.M., 1965. Age and sex related changes in the amount of cortex of normal human ribs. Acta Orthopaedica Scandinavia 37(2):122-30.

Takahashi, H., Epker, B., Frost, H.M., 1965. Relation between age and size of osteons in man. Henry Ford Hosp Med Bull 13:25-31.

Tami, A.E., Nasser, P., Verborgt, O., Schaffler, M.B., Knothe Tate, M.L., 2002. The role of interstitial fluid flow in the remodeling response to fatigue loading. J Bone Miner Res 17(11):2030-7.

Tappen, N.C., 1977. Three-dimensional studies of resorption spaces and developing osteons. Am J Anat 149(2):301–32.

Taylor, D., Lee, T.C., 1998. Measuring the shape and size of microcracks in bone. J Biomech 31(12):1177-80.

Tazawa, K., Hoshi, K., Kawamoto, S., Tanaka, M., Ejiri, S., Ozawa, H., 2004. Osteocytic osteolysis observed in rats to which parathyroid hormone was continuously administered.
J Bone Miner Metab 22(6):524-9.

Thomas, C.D., Feik, S.A., Clement, J.G., 2005. Regional variation of intracortical porosity in the midshaft of the human femur: age and sex differences. J Anat 206:115–25.

Thompson, D.D. 1980. Age changes in bone mineralization, cortical thickness, and Haversian canal area. Calcif Tissue Int 31(1):5-11.

Thompson, D.D., Galvin, C.A., 1983. Estimation of age at death by tibial osteon remodeling in an autopsy series. Forensic Sci Int 22(2-3):203-11.

Thrailkill, K.M., Lumpkin, C.K., Jr., Bunn, R.C., Kemp, S.F., Fowlkes, J.L., 2005. Is insulin an anabolic agent in bone? Dissecting the diabetic bone for clues. Am J Physiol Endocrinol Metab 289(5):E735-45.

463

Torres-Lagares, D., Tulasne, J.F., Pouget, C., Llorens, A., Saffar, J.L., Lesclous, P., 2010. Structure and remodelling of the human parietal bone: an age and gender histomorphometric study. J Craniomaxillofac Surg 38(5):325–30.

Traub, W., Arad, T., Vetter, U., Weiner, S., 1994. Ultrastructural studies of bones from patients with osteogenesis imperfecta. Matrix Biol 14(4):337-45.

Trinkaus, E., Churchill, S.E., Ruff, C.B., 1994. Postcranial robusticity in Homo. II: Humeral bilateral asymmetry and bone plasticity. Am J Phys Anthropol 93(1):1-34.

Trinkaus, E., Churchill, S.E., Ruff, C.B., Vandermeersch, B.,1998. Locomotion and body proportions of the Saint-Cesaire 1 Chatelperronian Neandertal. Proc Natl Acad Sci USA 95:5836-40.

Trinkaus, E., Churchill, S.E., Ruff, C.B., Vandermeersch, B., 1999. Long bone shaft robusticity and body proportions of the Saint-Césaire 1 Châtelperronian Neandertal. J Archaeol Sci 26(7):753-73.

Trinkaus, E., Ruff, C.B., 1989. Diaphyseal cross-sectional geometry and biomechanics of the Fond-de-Forêt 1 femur and the Spy 2 femur and tibia. Bulletin de la Societé Royale Belge d'Anthropologie et de Préhistoire 100:33–42.

Trinkaus E, Ruff CB., 1999a. Diaphyseal cross-sectional geometry of Near
Eastern Middle Palaeolithic humans: the femur. J Archaeol Sci 26(4):409–24.

Trinkaus, E. and Ruff, C.B. 1999b Diaphyseal cross-sectional geometry of Near Eastern Middle Paleolithic humans: The tibia. Journal of Archaeological Science 26(10):1289-300.

Trotter, M., Hixon, B.B., 1974. Sequential changes in weight, density, and percentage ash weight of human skeletons from an early fetal period through old age. Anat Rec 179(1):1-18.

Turner, T.C., 2006. Bone strength: Current concepts. Ann NY Acad Sci 1068:429-46.

Unnanuntana, A., Rebolledo, B.J., Michael Khair, M., DiCarlo, E.F., Lane, J.M., 2011. Diseases affecting bone quality: Beyond osteoporosis. Clin Orthop Relat Res 469(8):2194-206.

Ural, A., Vashishth, D., 2007. Effects of intracortical porosity on fracture toughness in aging human bone: a microCT-based cohesive finite element study. J Biomech Eng, 129(5):625-31.

van Doorn, L., Lips, P., Netelenbos, J.C., Hackeng, W.H., 1993. Bone histomorphometry and serum concentrations of intact parathyroid hormone (PTH(1-84)) in patients with primary hyperparathyroidism. Bone Miner 23(3):233-42.

van Hove, R.P., Nolte, P.A., Vatsa, A., Semeins, C.M., Salmon, P.L., Smit, T.H., Klein-Nulend, J., 2009. Osteocyte morphology in human tibiae of different bone pathologies with different bone mineral density--is there a role for mechanosensing? Bone 45(2):321-9.

van Oers, R., Rulmerman, R., van Reitbergen, B., Hilbers, A., Huiskes, R., 2008. Relating osteon diameter to strain. Bone 43(3):476-82.

van Pottelbergh, I., Goemaere, S., Kaufman, J.M., 2003. Bioavailable estradiol and an aromatase gene polymorphism are determinants of bone mineral density changes in men over 70 years of age. J Clin Endocrinol Metab 88(7):3075-81.

Vashishth, D., Gibson, G., Kimura, J., Schaffler, M.B., Fyhrie, D.P., 2002. Determination of bone volume by osteocyte population. Anat Rec 267(4):292-5.

Vashishth, D., Gibson, G.J., Fyhrie, D.P., 2005. Sexual dimorphism and age dependence of osteocyte lacunar density for human vertebral cancellous bone. Anat Rec A: Discov Mol Cell Evol Biol 282A(2):157–62.

Vashishth, D., Verborgt, O., Divine, G., Schaffler, M.B., Fyhrie, D.P., 2000. Decline in osteocyte lacunar density in human cortical bone is associated with accumulation of microcracks with age. Bone 26(4), 375–80.

Vedi, S., Elkin, S.L., Compston, J.E., 2005. A histomorphometric study of cortical bone of the iliac crest in patients treated with glucocorticoids. Calcif Tissue Int 77(2):79-83

Verborgt, O., Gibson, G.J., Schaffler, M.B., 2000. Loss of osteocyte integrity in association with microdamage and bone remodeling after fatigue in vivo. J Bone Miner Res 15(1):60-7.

Verhaeghe, J., Suiker, A.M., Einhorn, T.A., Geusens, P., Visser, W.J., Van Herck, E., Van Bree, R., Magitsky, S., Bouillon, R., 1994. Brittle bones in spontaneously diabetic female rats cannot be predicted by bone mineral measurements: studies in diabetic and ovariectomized rats. J Bone Miner Res 9(10):1657-67.

464

Verhaeghe, J., Suiker, A.M., Nyomba, B.L., Visser, W.J., Einhorn, T.A., Dequek, J., Bouillon, R., 1989. Bone mineral homeostasis in spontaneously diabetic BB rats. II. Impaired bone turnover and decreased osteocalcin synthesis. Endocrinology 124(2):573-82.

Verhaeghe, J., van Herck, E., Visser, W.J., Suiker, A.M., Thomasset, M., Einhorn, T.A., Faierman, T.A., Bouillon, R., 1990a. Bone and mineral metabolism in BB rats with long-term diabetes. Decreased bone turnover and osteoporosis. Diabetes 39(4):477-82.

Verhaeghe, J., Visser, W.J., Einhorn, T.A., Bouillon, R., 1990b. Osteoporosis and diabetes: lessons from the diabetic BB rat. Horm Res 34(5-6):245-8.

Vestergaard, P., 2007. Discrepancies in bone mineral density and fracture risk in patients with type 1 and type 2 diabetes – a meta-analysis. Osteoporosis International 18(4):427–444.

Villanueva, A., Frost, H., Ilnicki, L., Frame, B., Smith, R., Arnstein, R., 1966. Cortical bone dynamics measured by means of tetracycline labeling in 21 cases of osteoporosis. J Lab Clin Med 68(4):599-616.

Vincentelli, R., Grigorov, M.. 1985. The effect of haversian remodeling on the tensile properties of human cortical bone. J Biomech 18(3):201-7.

Vogel, M., Hahn, M., Delling, G. 1993. Relation between 2- and 3-dimensional architecture of trabecular bone in the human spine. Bone 14(3):199-203.

Volkmann, R., 1863. Zur Histologie der Karies und Ostitis. Arch f Klin Chir, iv, 437.

Vu, T.D., Wang, X.F., Wang, Q., Cusano, N.E., Irani, D., Silva, B.C., Ghasem-Zadeh, A., Udesky, J., Romano, M.E., Zebaze, R., Jerums, G., Boutroy, S. Bilezikian, J.P., Seeman, E., 2013. New insights into the effects of primary hyperparathyroidism on the cortical and trabecular compartments of bone. Bone 55(1):57–63.

Wang, R., Gupta, H.S., 2011. Deformation and fracture mechanisms of bone and nacre. Ann Rev Mater Res 41(1):41-73.

Ward, L.M., Rauch, F., Travers, R., Chabot, G., Azouz, E.M., Lalic, L., Roughley, P.J., Glorieux, F.H., 2002. Osteogenesis imperfecta type VII: an autosomal recessive form of brittle bone disease. Bone 31(1):12-8.

Wasserman, N., Yerramshetty, J., Akkus, O., 2005. Microcracks colocalize within highly mineralized regions of cortical bone tissue. Eur J Morphol 42(1-2):43-51.

Watanabe, Y., Konishi, M., Shimada, M., Oharaa, H., Iwamotob, S., 1998. Estimation of age from the femur of Japanese cadavers. Forensic Sci Int 98(1-2):55-65.

Weaver, C.M., Fuchs, R.K., 2014. Skeletal growth and development. In: Burr DB, Allen Mr (Eds.) Basic and Applied Bone Biology. Elsevier, London, pp. 245-260.

Weinstein, R.S., Jilka, R.L., Parfitt, A.M., Manolagas, S.C., 1998. Inhibition of osteoblastogenesis and promotion of apoptosis of osteoblasts and osteocytes by glucocorticoids: Potential mechanisms of their deleterious effects on bone. J Clin Invest 102(2):274-82.

Weinstein, R.S., Nicholas, R.W., Manolagas, S.C. 2000. Apoptosis of osteocytes in glucocorticoid-induced osteonecrosis of the hip. J Clin Endocrinol Metab 85(8):2907-12.

Williams, E.D., Barr, W.T., Rajan, K.T., 1981. Relative vitamin D deficiency in Paget's disease. Lancet 372(8216):384–5.

Wlodarski, K.H., Reddi, H.A., 1987. Tumor cells stimulate in vivo periosteal bone formation. Bone Miner 2(3):185-92.

Wong, S.Y.P., Kariks, J., Evans, R.A., Dunstan, C.R., Hills, E., 1985. The effect of age on bone composition and viability in the femoral head. J Bone Jt Surg 67(2):274-83.

Wong, S.Y.P., Evans, R.A., Needs, C., Dunstan, C.R., Hills, E., Garvan, J., 1987. The pathogenesis of osteoarthritis of the hip. Clin Orthop Rel Res 214:305-12.

Wood, K.B., Li, W., Lebl, D.S., Ploumis, A., 2014. Management of thoracolumbar spine fractures. Spine J 14:145–64.

Wright, P.H., Jowsey, J.O., Robb, R.A., 1978. Osteocyte lacunar area in normal bone, hyperparathyroidism, renal disease, and osteoporosis. Surg Forum 29:558-9.

Wysolmerski, J.J., 2012. Osteocytic osteolysis: time for a second look? BoneKEy Reports 1(229):1-7

Yeni, Y.N., Brown, C.U., Wang, Z., Norman, T.L., 1997. The influence of bone morphology on fracture toughness of the human femur and tibia. Bone 21(5):453-9.

Yoshino, M., Imaizumi, K., Miyasaka, S., Seta, S., 1994. Histological estimation of age at death using microradiographs of humeral compact bone. Forensic Sci Int 64(2-3):191-8.

Yu, W., Qin, M., Xu, L., van Kuijk, C., Meng, X., Xing, X., Cao, J., Genant, H.K., 1999. Normal changes in spinal bone mineral density in a Chinese population: Assessment by quantitative computed tomography and dual-energy x-ray absorptiometry. Osteoporos Int 9(2):179-87.

Zebaze, R.M., Seeman, E., 2015. Cortical bone: A challenging geography. J Bone Miner Res 30(1)24-9.

Zebaze, R.M., Ghasem-Zadeha, A., Bohte, A., Iuliano-Burnsa, S., Mackiea, E. Seemanb, E. 2009. Age-related bone loss: The effect of neglecting intracortical porosity. Bone 44(Suppl 1):S99-120.

Zebaze, R.M., Ghasem-Zadeha, A., Bohte, A., Iuliano-Burnsa, S., Mirams, M., Price, R.I., Mackie, E.J., Seeman, E., 2010. Intracortical remodelling and porosity in the distal radius and post-mortem femora of women: a cross-sectional study. Lancet 375(9727):1729-36.

Zioupos, P., Currey, J., 1994. The extent of microcracking and the morphology of microcracks in damaged bone. J Mater Sci 29(4):978–86.

Chapter 5/6: Methods

Agnew AM. 2011. Histomorphometry of the elderly rib: A methodological approach with implications for biomechanics, function, and fracture risk. [Doctoral dissertation]. Retrieved from OhioLINK Electronic Theses & Dissertation Center. (Accession No. osu1305558389)

Bass, W. M. (1995) Human Osteology. A Laboratory and Field Manual. Missouri Archaeological Society, Special Publication No. 2. Fourth edition. Columbia, Missouri.

Bellemare F, Jeanneret A, Couture J. 2003. Sex differences in thoracic dimensions and configuration. Am J Respir Crit Care Med 168:305–312.

Binkley N, Kiebzak GM, Lewiecki EM, Krueger D, Gangnon RE, Miller PD, Shepherd JA, Drezner MK. 2005. Recalculation of the NHANES database SD improves T-score agreement and reduces osteoporosis prevalence. J Bone Miner Res. 20(2):195-201.

Buikstra, J. E. and Ubelaker, D. H. (eds.) (1994). Standards for Data Collection from Human Skeletal Remains. Arkansas Archaeological Survey Research Series 44.

Buie HR, Campbell GM, Klinck RJ, MacNeil JA, Boyd SK. 2007. Automatic segmentation of cortical and trabecular compartments based on a dual threshold technique for in vivo micro-CT bone analysis. Bone. 41(4):505-15.

Cohen, J. 1977. Statistical power analysis for the behavioral sciencies. Routledge.

Cole ME, Stout SD, Agnew AM. 2017. Three-dimensional reconstruction of vascular pore networks in the human rib from two-dimensional serial sections. The 86th Annual Meeting of the American Association of Physical Anthropologists, New Orleans, LA. American Journal of Physical Anthropology 162(S64):147

Cole ME, Stout SD, Agnew AM. 2018. Automated extraction of two-dimensional cortical porosity descriptors from histological and micro-computed tomography serial sections. The 87th Annual Meeting of the American Association of Physical Anthropologists, Austin, TX. American Journal of Physical Anthropology 165(S66):51-52

Cooper D, Turinsky A, Sensen C, Hallgrimsson B. Effect of voxel size on 3D micro-CT analysis of cortical bone porosity. Calcif Tissue Int. 2007;80:211–219

DiMichele D and Hunt DR. 2015. Robert J. Terry Anatomical Skeletal Collection Postcranial Osteometric Database. Retrieved from [https://naturalhistory.si.edu/research/anthropology]

Doube M, Kłosowski MM, Arganda-Carreras I, Cordeliéres F, Dougherty RP, Jackson J, Schmid B, Hutchinson JR, Shefelbine SJ. 2010. BoneJ: free and extensible bone image analysis in ImageJ. Bone 47:1076-9

Gregory JS, Aspden RM. 2008. Femoral geometry as a risk factor for osteoporotic hip fracture in men and women. Med Eng Phys. 30(10):1275-86

Kruger C, Tian L. 2004. A comparison of the general linear mixed model and repeated measures ANOVA using a dataset with multiple missing data points. Biol Res Nurs. 2004 Oct;6(2):151-7.

Lovejoy CO. 1988. Evolution of human walking. Sci Am 259:118–125

Ohman JC, Krochta TJ, Lovejoy CO, Mensforth RP, Latimer B. 1997. Cortical bone distribution in the femoral neck of hominoids: implications for the locomotion of Australopithecus afarensis. Am J Phys Anthropol 104:117–131.

Martin, R. Saller, K. 1957. Lehrbuch der Anthropologie. Vol. 1 and Vol. 2, Gustav Fisher Verlag, Stuttgart.

Martín-Badosa E, Elmoutaouakkil A, Nuzzo S, Amblard D, Vico L, Peyrin F. 2003. A method for the automatic characterization of bone architecture in 3D mice microtomographic images. Comput Med Imaging Graph. 27(6):447-58

Meeusen R, Duclos M, Foster C, Fry A, Gleeson M, Nieman D, Raglin J, Rietjens G, Steinacker J, Urhausen A. 2013. Prevention, diagnosis, and treatment of the overtraining syndrome: joint consensus statement of the European College of Sport Science and the American College of Sports Medicine. Med Sci Sports Exerc. 45(1):186-205

Michelotti J, Clark J. 1999, Femoral neck length and hip fracture risk. J Bone Miner Res. 14(10):1714-20.

Moore KL, Dalley AF, Agur AMR. 2014. Clinically Oriented Anatomy. 7th ed. Baltimore, MD: Lippincott Williams & Wilkins

Murlimanju BV, Prabhu LV, Pai MM, Buraje MK, Dhananjaya KVN, Prashanth KU. 2012. Osteometric study of the upper end of femur and its clinical applications. European Journal of Orthopaedic Surgery & Traumatology 22(3): 227–230

Nakagawa S, Schielzeth H. 2013. A general and simple method for obtaining R2 from generalized linear mixed-effects models. Methods In Ecology And Evolution 4(2): 133-142.

NMNH Physical Anthropology Laboratory Manual 1995. Repatriation Office, National Museum of Natural History, Smithsonian Institution, Washington D.C.

Pearson, K. 1917. A study of the long bones of the English skeleton. I: The femur. University of London, University College, Department of Applied Statistics, Company Research, Memoirs, Biometric Series X, Chapters 1-4 (1917-1919).

Pratt, J. W. 1959. Remarks on zeros and ties in the Wilcoxon signed rank procedures. Journal of the American Statistical Association 54(287), 655--667. 10.1080/01621459.1959.10501526

Robling, A.G., Stout, S., 2003. Histomorphology, geometry, and mechanical loading in past populations. In: Agarwal, S.C., Stout, S.D. (Eds.), Bone Loss and Osteoporosis: An Anthropological Perspective. Kluwer Academic/Plenum, New York, pp. 189–203.

Resnick D. 1983. Osteophytosis of the femoral head and neck. Arthritis and Rheumatism 26(7): 908-913

Rüedi TP, Murphy WM (eds). 2000. AO Principles of Fracture Management. Stuttgart, Thieme 683–684

Ruff CB and Higgins R. 2013. Femoral neck structure and function in early hominins. Am. J. Phys. Anthropol. 150:512–525

Schneider P, Voide R, Stampanoni M, Donahue LR, Müller R. 2013. The importance of the intracortical canal network for murine bone mechanics. Bone. 53(1):120-8.

Taha AA and Hanbury A. 2015. Metrics for evaluating 3D medical image segmentation: analysis, selection, and tool. BMC Med Imaging 15: 29.

Zoebeck, T. S. 1983. Postcraniometric Variation Among the Arikara. Unpublished Ph.D. Dissertation. University of Tennessee, Knoxville.

Appendix A: Image Processing Macros

Batch Process Histogram (ImageJ)

```
macro "BatchHistogram"{
          setBatchMode(true);
//Open the directory with the raw images
dir1= getDirectory("SelectInput");
list1= getFileList(dir1);
//Select directory for output images
dir2= getDirectory("SelectOutput");
list2= getFileList(dir2);
//Set the number of 8-bit bins to 0-255
nBins = 256;
run("Clear Results");
setOption("ShowRowNumbers", false);
//Create the data table with an empty column for Summed Pixel Count
for(i=0; i<nBins; i++){
   setResult("Index", nResults, nResults);
   setResult("Pixel Count", i, 0);}
//Get the value bins from the middle image (though they should all be the same)
midpoint=floor(lengthOf(list1)/2);
open(dir1+list1[midpoint]);
run("Enhance Contrast...", "saturated=0.3 normalize");
getHistogram(values, counts, nBins);
Table.setColumn("Bin Start",values);
close();
//Loop through each image, enhance contrast, get histogram, get pixel counts, add to existing pixel counts
for (i=0; i<lengthOf(list1); i++) {
          open(dir1+list1[i]);
          run("Enhance Contrast...", "saturated=0.3 normalize");
          getHistogram(values, counts, nBins);
          Table.setColumn("Temp Pixel Count",counts);
          for (n=0; n<nResults; n++ ) {
                    old=getResult("Pixel Count",n);
                    new=getResult("Temp Pixel Count",n);
                    setResult("Pixel Count",n,old+new);}
//Close the open image
close();}
//Delete the final image's temporary pixel column
Table.deleteColumn("Temp Pixel Count")
//**Find the lowest point between the black (first) peak and white (second) peak to include maximum white
pixel values
pixelcount=Table.getColumn("Pixel Count");
//Remove last white peak representing pure white
```

468

```
pixelcrop=Array.slice(pixelcount, 0, pixelcount.length-1);
//Reverse the array to work backwards from white to black
pixelreverse=Array.reverse(pixelcrop);
//Work backwards until you find the second largest peak, representing the majority of whitish pixels
for (i=0; i<pixelreverse.length; i++ ) {
        if (pixelreverse[i]>pixelreverse[i+1])
        {break;}
        secondpeak=pixelreverse[i+1];
        secondpeaknum=i+1;}
//Clip the array above the second peak
pixelclip=Array.slice(pixelreverse, secondpeaknum, pixelreverse.length);
//Work backwards until you find the lowest point between the second peak and first peak, representing the
beginning of the ascent to the second white peak
for (i=0; i<pixelclip.length; i++ ) {
        if (pixelclip[i]<pixelclip[i+1])
        {break;}
        valley=pixelclip[i+1];
        valleynum=i+1;}
//The valley position accounts for its position after the second peak, the second peak distance from the end,
the 255 value, and the 0 start point
valleyposition=pixelcount.length-valleynum-secondpeaknum-2
//Match the valley's position to the bin start
minbin=getResult("Bin Start",valleyposition);
rminbin=floor(minbin)
//Append information to table and save in output directory
setResult("Notes",valleyposition,"Minimum Bin Start");
saveAs("results", dir2+"Histogram.xls");
//Open images individually, normalize histogram, and set the minimum value for the pixels
for (i=0; i<lengthOf(list1); i++) {
        open(dir1+list1[i]);
        currentimg=list1[i];
        selectImage(currentimg);
        run("Enhance Contrast...", "saturated=0.3 normalize");
        run("Brightness/Contrast...");
        setMinAndMax(rminbin,65535);
        run("Apply LUT");
        saveAs("tiff", dir2 + list1[i]);
        close(currentimg);}}
```

Slice Histogram (ImageJ)

```
macro "SliceHistogram"{
        setBatchMode(true);
//Open the directory with the raw images
dir1= getDirectory("SelectInput");
list1= getFileList(dir1);
//Select directory for output images
dir2= getDirectory("SelectOutput");
run("Clear Results");
setOption("ShowRowNumbers", false);
//Create the data table that will hold the summed results
title1 = "Slice Pixel Minima";
title2 = "["+title1+"]";
f=title2;
run("New... ", "name="+title2+" type=Table");
print(f,"\\Headings:Slice\tPixel Minima");
//Loop through each image, enhance contrast, get histogram, get values and their corresponding pixel
counts
for (a=0; a<lengthOf(list1); a++) {
//Close any images
while (nImages>0) {
        selectImage(nImages);
        close(); }
//Clear variables and results
run("Clear Results");
values=0;
counts=0;
//Open next image
        open(dir1+list1[a]);
        currentimg=list1[a];
        imgname=getTitle();
        nBins = 256;
        selectImage(currentimg);
//Reset brightness and contrast from last loop
resetMinAndMax();
// Enhance contrast and apply Auto brightness contrast to shrink the histogram to visible pixel values
run("Enhance Contrast...", "saturated=0.3 normalize");
//Run Auto Threshold macro from http://imagej.1557.x6.nabble.com/Auto-Brightness-Contrast-and-
setMinAndMax-td4968628.html
AUTO_THRESHOLD = 5000;
 getRawStatistics(pixcount);
 limit = pixcount/10;
 threshold = pixcount/AUTO_THRESHOLD;
 getHistogram(values, histA, nBins);
 i = -1;
 found = false;
 do { counts = histA[++i];
     if (counts > limit) counts = 0;
     found = counts > threshold;  } while ((!found) && (i < histA.length-1))
 hmin = values[i];
 i = histA.length;
 do {counts = histA[--i];
```

```
        if (counts > limit) counts = 0;
        found = counts > threshold;
  } while ((!found) && (i > 0))
  hmax = values[i];
  setMinAndMax(hmin, hmax);
//print(hmin, hmax);
  run("Apply LUT");
//Convert the histogram to a table
//Histogram table code based on the ImageJ StackHistogramLister.txt inherent macro
  row = 0;
  getHistogram(values, counts, nBins);
  for (i=0; i<nBins; i++) {
     setResult("Values", row, values[i]);
     setResult("Counts", row, counts[i]);
     row++;
  }
  updateResults();
//Extract maximum pixel counts in the array
//Typically these correspond to three peaks: black, gray, and white pixel counts
//The 1 setting excludes edges (0 and 255 peaks)
//Tolerance=1000 means points must differ by 1000 pixels to qualify as a peak
  values=Table.getColumn("Values");
  counts=Table.getColumn("Counts");
  //Array.print(values);
  //Array.print(counts);
  tolerance=1000;
  maxcounts= Array.findMaxima(counts, tolerance, 1);
//The output is the index position of the three maximum peaks, which corresponds to their 8-bit (0-255)
value
//Sometimes only two peaks may be displayed, so the code must extract the first and last peaks
  maxcountsort=Array.sort(maxcounts);
  endpeakpos=maxcountsort.length-1;
//Match to the index positions (0-255) of the last two peaks
  firstpeakindex=maxcountsort[0];
  endpeakindex=maxcountsort[endpeakpos];
//Now clip the array of pixel counts between the index positions of the two peaks
  countsclip=Array.slice(counts, firstpeakindex, endpeakindex);
//Find the minimum pixel count (valley) between these two peaks by sorting the counts array
//This position will exclude the maximum gray pixels (e.g. parafilm wrapping, soft tissue) and include the
maximum bone
  countsclipsort=Array.sort(countsclip);
//Extract the pixel count valley from the front of the sorted array
  countsvalley=countsclipsort[0];
//Find the index position of the pixel count valley in the histogram table by looping through pixel counts
until a match
//This corresponds to its 8-bit (0-255) bin value
//Countsvalleynum, if called as a variable, is the index position (starts at 0), not the table position (starts at
one)
  for (i=0; i<counts.length; i++ ) {
        if (counts[i]==countsvalley)
        {break;}
        countsvalleynum=i+1;}
//Find the 16-bit pixel brightness value corresponding to this index position and round
```

```
minbin=values[countsvalleynum];
rminbin=floor(minbin);
//Set the minimum pixel value to the bin start
        selectWindow(currentimg);
        setMinAndMax(rminbin,65535);
        run("Apply LUT");
        saveAs("tiff", dir2 + imgname);
        close();
//Print pixel minima to the table
print(f, imgname + "\t" + rminbin);}
//Save the completed pixel minima table to the output file
selectWindow("Slice Pixel Minima");
saveAs("Text", dir2+"Slice Pixel Minima"+".xlsx");
run("Close");
selectWindow("Results");
run("Close");
}
```

MergeFemora (ImageJ)

```
macro "Merge Femora"{
  setBatchMode(false);
  dir1= getDirectory("SelectAnterior");
  list1= getFileList(dir1);
  dir2= getDirectory("SelectMiddle");
        list2= getFileList(dir2);
        dir3= getDirectory("SelectPosterior");
        list3= getFileList(dir3);
  dir4 = getDirectory("SelectOutput");
  for (i=0; i<lengthOf(list1); i++) {
         open(dir1+list1[i]);
   open(dir2+list2[i]);
   open(dir3+list3[i]);
          anterior=list1[i];
          middle=list2[i];
          posterior=list3[i];
          run("Paste Control...");
          setPasteMode("Transparent-zero");
         //Get image heights and widths for pasting
         selectImage(anterior);
         ah=getHeight();
         aw=getWidth();
         selectImage(middle);
         mh=getHeight();
         selectImage(posterior);
         ph=getHeight();
         pw=getWidth();
         //Manually enter upper left paste coordinates from Macro Recorder
         //Anterior
         ax=;
         ay=;
         //Posterior
         px=;
         py=;
  selectImage(middle); run("Canvas Size...", "width=6000 height=mh position=Center");
  selectImage(anterior); run("Copy"); close();
  selectImage(middle); makeRectangle(ax, ay, aw, ah); run ("Paste");
  selectImage(posterior); run("Copy"); close();
  selectImage(middle); makeRectangle(px, py, pw, ph); run ("Paste");
  //Crop image at maximum of paste borders
         //Crop x (upper left corner) = posterior x
         cx=px;
  //Crop y = 0 so no height is clipped
  cy=0;
  //Crop height is height of middle image - reselect in case it has changed with paste
  selectImage(middle);
         ch=getHeight();
  //Crop width is the posterior width, plus the anterior width
  //Plus the middle space between them [(px+pw)+aw]
  cw=pw+(ax-(px+pw)+aw);
  makeRectangle(cx, cy, cw,= ch);
```

473

```
run("Crop");
//Save image
saveAs("bmp", dir4 + list2[i]);
close();}
```

Marrow Bounding (CT-Analyser)

Thresholding
Mode, Global
Lower grey threshold, 1
Upper grey threshold, 255

ROI shrink-wrap
Mode : Shrink-wrap (2D space)

Morphological operations
Type: Closing (2D space)
Kernel: Round
Radius: 60
Apply to: Region of Interest

Despeckle
Type: Remove pores (2D space)
Detected by: by image borders
Apply to: Region of Interest

Bitwise operations
<Clipboard> = COPY <Image>

Despeckle
Type: Remove inner objects (2D space)
Detected by: by image borders
Apply to: Image

Morphological operations
Type: Closing by reconstruction (2D space)
Kernel: Round
Radius: 30
Apply to: Image

Morphological operations
Type: Erosion (2D space)
Kernel: Round
Radius: 2
Apply to: Region of Interest

Bitwise operations
<Image> = NOT <Image>

Bitwise operations
<Image> = <Image> AND <Region of Interest>

ROI shrink-wrap
Mode : Adaptive (2D space)
Stretch over holes with a diameter in 20 pixels

Despeckle
Type: Sweep (3D space)

475

Remove: all exept the largest object
Apply to: Region of Interest

Morphological operations
Type: Erosion (2D space)
Kernel: Round
Radius: 30
Apply to: Region of Interest

Morphological operations
Type: Dilation (2D space)
Kernel: Round
Radius: 30
Apply to: Region of Interest

Despeckle
Type: Sweep (3D space)
Remove: all exept the largest object
Apply to: Region of Interest

Morphological operations
Type: Dilation (2D space)
Kernel: Round
Radius: 30
Apply to: Region of Interest

Morphological operations
Type: Closing (2D space)
Kernel: Round
Radius: 30
Apply to: Region of Interest

Morphological operations
Type: Erosion (2D space)
Kernel: Round
Radius: 30
Apply to: Region of Interest

Despeckle
Type: Remove pores (2D space)
Detected by: by image borders
Apply to: Region of Interest

Despeckle
Type: Sweep (3D space)
Remove: all exept the largest object
Apply to: Region of Interest

Morphological operations
Type: Dilation (2D space)
Kernel: Round
Radius: 1
Apply to: Region of Interest

476

```
-----------------------------------------------------------
Save bitmaps(only ROI):
Destination folder: E:\7438 Femoral\7438 Merge Output To Bound\2\Marrow
File format: bmp
-----------------------------------------------------------
Bitwise operations
<Image> = COPY <Clipboard>
-----------------------------------------------------------
Save bitmaps(image inside ROI):
Destination folder: E:\7438 Femoral\7438 Merge Output To Bound\2\Trabecular Bone
File format: bmp
Resize to the ROI bounds: Off
-----------------------------------------------------------
Bitwise operations
<Region of Interest> = NOT <Region of Interest>
-----------------------------------------------------------
Save bitmaps(image inside ROI):
Destination folder: E:\7438 Femoral\7438 Merge Output To Bound\2\Cortical Bone Unsealed
File format: bmp
Resize to the ROI bounds: Off
-----------------------------------------------------------
Bitwise operations
<Clipboard> = COPY <Region of Interest>
-----------------------------------------------------------
ROI shrink-wrap
Mode : Adaptive (2D space)
-----------------------------------------------------------
Morphological operations
Type: Closing (2D space)
Kernel: Round
Radius:  60
Apply to: Region of Interest
-----------------------------------------------------------
Despeckle
Type: Remove pores (2D space)
Detected by: by image borders
Apply to: Region of Interest
Despeckle done
-----------------------------------------------------------
Morphological operations
Type: Erosion (2D space)
Kernel: Round
Radius:   2
Apply to: Region of Interest
-----------------------------------------------------------
Bitwise operations
<Image> = NOT <Image>
-----------------------------------------------------------
Save bitmaps(image inside ROI):
Destination folder: E:\7438 Femoral\7438 Merge Output To Bound\2\All Spaces
File format: bmp
Resize to the ROI bounds: Off
-----------------------------------------------------------
```

477

Bitwise operations
<Region of Interest> = <Region of Interest> AND <Clipboard>

Save bitmaps(only ROI):
Destination folder: E:\7438 Femoral\7438 Merge Output To Bound\2\Cortical Mask Sealed
File format: bmp

Save bitmaps(image inside ROI):
Destination folder: E:\7438 Femoral\7438 Merge Output To Bound\2\Cortical Pores Sealed
File format: bmp
Resize to the ROI bounds: Off

Bitwise operations
<Region of Interest> = SWAP <Clipboard>

Bitwise operations
<Region of Interest> = NOT <Region of Interest>

Save bitmaps(image inside ROI):
Destination folder: E:\7438 Femoral\7438 Merge Output To Bound\2\Trabecular Spaces Sealed
File format: bmp
Resize to the ROI bounds: Off

Pore Type Differentiation (ImageJ)

```
macro "Pore Type"{
setBatchMode(true);
dir1= getDirectory("Select_Binarized_Pores");
list1= getFileList(dir1);
dir2= getDirectory("Select_Marrow");
list2= getFileList(dir2);
//Make an output directory for cortical and trabecularized pores
dir3= getDirectory("Select_Output");
totdir=dir3+"/Cortical Pores Sealed Binary/";
File.makeDirectory(totdir);
cordir=dir3+"/Cortical/";
File.makeDirectory(cordir);
tradir=dir3+"/Trabecularized/";
File.makeDirectory(tradir);
//Clear any past results
run("Clear Results");
//Set 32 bit for EDM map
run("Options...", "edm=32-bit");
//Create the data table for summed total pore measurements, including min and max gray values
setOption("ShowRowNumbers", false);
tot="[Total Pore Measurements]";
run("New... ", "name="+tot+" type=Table");
print(tot,"\\Headings:Slice\tSlice Name\tPore\tArea\tMin Gray\tMax Gray\tCentroid X\tCentroid
Y\tPerimeter\tEllipse Major Axis\tEllipse Minor Axis\tEllipse Axis Angle\tCircularity\tMax Feret
Diameter\tMax Feret X\tMax Feret Y\tFeret Angle\tMin Feret Diameter (um)\tMin Feret Diameter
(pixel)\tAspect Ratio\tRoundness\tSolidity\t");
//Create the data table for summed cortical pore measurements
cor="[Cortical Pore Measurements]";
```

478

```
run("New... ", "name="+cor+" type=Table");
print(cor,"\\Headings:Slice\tSlice Name\tPore\tArea\tCentroid X\tCentroid Y\tPerimeter\tEllipse Major
Axis\tEllipse Minor Axis\tEllipse Axis Angle\tCircularity\tMax Feret Diameter\tMax Feret X\tMax Feret
Y\tFeret Angle\tMin Feret Diameter\tAspect Ratio\tRoundness\tSolidity\t");
//Create the data table for summed trabecularized pore measurements
trab="[Trabecularized Pore Measurements]";
run("New... ", "name="+trab+" type=Table");
print(trab,"\\Headings:Slice\tSlice Name\tPore\tArea\tCentroid X\tCentroid Y\tPerimeter\tEllipse Major
Axis\tEllipse Minor Axis\tEllipse Axis Angle\tCircularity\tMax Feret Diameter\tMax Feret X\tMax Feret
Y\tFeret Angle\tMin Feret Diameter\tAspect Ratio\tRoundness\tSolidity\t");
//**Beginning of image-by-image processing**
for (i=0; i<lengthOf(list1); i++){
//Open the pore image
        open(dir1+list1[i]);
        pores=list1[i];
        imgname=getTitle();
        imgnum=i+1;
//Set scale for pore measurements to 1 pixel / 6.409749671 um or 0.15601233298 pixel/um
        run("Set Scale...", "distance=0.15601233298 known=1 unit=um global");
        getPixelSize(unit, pw, ph);
//**Fill Holes in Pores**
        selectImage(pores);
        run("Invert");
        run("Dilate");
        run("Close-");
        run("Fill Holes");
        run("Erode");
        run("Invert");
        selectWindow(pores);
        run("8-bit");
        setAutoThreshold("Default dark");
        run("Threshold...");
        setThreshold(1,255);
        setOption("BlackBackground", true);
        run("Convert to Mask");
        saveAs("bmp", totdir + imgname);
        rename("Total Pores");
        pores="Total Pores";
//Duplicate the pore image for cortical and trabecular differentiation
        selectImage(pores); run("Duplicate...", "title=[CorTemp]");
        cortemp="CorTemp";
        selectImage(pores); run("Duplicate...", "title=[TrabTemp]");
        trabtemp="TrabTemp";
//**Total Pore Analysis**
//Convert pores to ROIs
        run("Set Measurements...", "area min centroid perimeter fit shape feret's redirect=None
decimal=3");
        selectImage(pores);
        setAutoThreshold("Default dark");
        run("Threshold...");
        setThreshold(1,255);
        setOption("BlackBackground", false);
        run("Convert to Mask");
```

479

```
        run("Analyze Particles...", "display clear add");
//**Pore Differentiation**
//Close the results table and pore image
    run("Clear Results");
        close(pores);
        open(dir2+list2[i]);
        marrow=list2[i];
        selectImage(marrow); run("Distance Map"); rename("EDM"); close(marrow);
        EDM="EDM";
//Run measurements for the pore ROIs superimposed on the EDM of the marrow.
//Increasing minimum gray values on the EDM = increasing minimum distance from the marrow cavity
//Trabecularized if diameter (minferet) is greater than or equal to distance from the marrow (min gray
value)
        selectImage(EDM); roiManager("Show All");
//Save values to total pore table
roiManager("Measure");
Area=Table.getColumn("Area");
Min=Table.getColumn("Min");
Max=Table.getColumn("Max");
X=Table.getColumn("X");
Y=Table.getColumn("Y");
Perim=Table.getColumn("Perim.");
Major=Table.getColumn("Major");
Minor=Table.getColumn("Minor");
Angle=Table.getColumn("Angle");
Circ=Table.getColumn("Circ.");
Feret=Table.getColumn("Feret");
FeretX=Table.getColumn("FeretX");
FeretY=Table.getColumn("FeretY");
FeretAngle=Table.getColumn("FeretAngle");
MinFeret=Table.getColumn("MinFeret");
AR=Table.getColumn("AR");
Round=Table.getColumn("Round");
Solidity=Table.getColumn("Solidity");
MinFeretPixel=newArray(lengthOf(MinFeret));
for (z=0; z<lengthOf(MinFeret); z++)
{MinFeretPixel[z]=(MinFeret[z]/pw);}
for (c=0; c<nResults; c++)
    print(tot, imgnum +"\t"+ imgname +"\t"+ (c+1) +"\t"+
    Area[c] +"\t"+ Min[c] +"\t"+ Max[c] +"\t"+ X[c] +"\t"+ Y[c] +"\t"+
        Perim[c] +"\t"+ Major[c] +"\t"+ Minor[c] +"\t"+ Angle[c] +"\t"+
        Circ[c]+"\t"+ Feret[c] +"\t"+ FeretX[c] +"\t"+ FeretY[c] +"\t"+
        FeretAngle[c] +"\t"+ MinFeret[c] +"\t"+ MinFeretPixel[c] +"\t"+ AR[c] +"\t"+ Round[c] +"\t"+
Solidity[c] +"\t");
run("Clear Results");
//Convert measurement scale to pixels
        run("Set Scale...", "distance=0 known=0 pixel=1 unit=pixel global");
        n = roiManager("count");
        for (a = n - 1; a >= 0; a--) {
    roiManager("select", a);
    run("Clear Results");
    roiManager("select", a);
    run("Measure");
```

480

```
        mindistancepx=getResult("Min");
        minferetpx=getResult("MinFeret");
                    if(mindistancepx<=minferetpx)
                            roiManager("delete");else
                            roiManager("rename","cortical");}
            close(EDM);
            run("Clear Results");
//Delete retained cortical pore ROIs from duplicate pore image to obtain trabecularized pores
            roiManager("deselect");
            roiManager("Set Fill Color", "black");
            selectWindow(trabtemp);
            roiManager("Show All without Labels");
            run("Flatten");
            selectWindow("TrabTemp-1");
            rename("Trabecularized Pores");
            close(trabtemp);
            trabfin="Trabecularized Pores";
//Subtract trabecularized pore image from duplicate pore image to obtain cortical pores
            imageCalculator("Subtract create", "CorTemp","Trabecularized Pores");
            rename("Cortical Pores");
            close(cortemp);
            corfin="Cortical Pores";
//Save final cortical and trabecularized pore images in output directory
//Trabecularized pore image must be thresholded after flattening
            selectWindow(trabfin);
            run("8-bit");
            setAutoThreshold("Default dark");
            run("Threshold...");
            setThreshold(1,255);
            setOption("BlackBackground", true);
            run("Convert to Mask");
            saveAs("bmp", tradir + imgname);
            rename("Trabecularized Pores");
            trabfin="Trabecularized Pores";
            selectWindow(corfin);
            run("8-bit");
            saveAs("bmp", cordir + imgname);
            rename("Cortical Pores");
            corfin="Cortical Pores";
//**Trabecularized Pore Analysis**
//Clear ROI manager
if (isOpen("ROI Manager")) {
    selectWindow("ROI Manager");
    run("Close");
 }
//Clear Results Table
            run("Clear Results");
//Set scale for pore measurements to 1 pixel / 6.409749671 um or 0.15601233298 pixel/um
//Remove gray level measurement
            run("Set Scale...", "distance=0.15601233298 known=1 unit=um global");
            run("Set Measurements...", "area centroid perimeter fit shape feret's redirect=None decimal=3");
//Analyze particles for trabecularized pores
            selectImage(trabfin);
```

481

```
            setAutoThreshold("Default dark");
            run("Threshold...");
            setThreshold(1,255);
            setOption("BlackBackground", false);
            run("Convert to Mask");
            run("Analyze Particles...", "display clear add");
//Add pore measurements to trabecularized pore table
Area=Table.getColumn("Area");
X=Table.getColumn("X");
Y=Table.getColumn("Y");
Perim=Table.getColumn("Perim.");
Major=Table.getColumn("Major");
Minor=Table.getColumn("Minor");
Angle=Table.getColumn("Angle");
Circ=Table.getColumn("Circ.");
Feret=Table.getColumn("Feret");
FeretX=Table.getColumn("FeretX");
FeretY=Table.getColumn("FeretY");
FeretAngle=Table.getColumn("FeretAngle");
MinFeret=Table.getColumn("MinFeret");
AR=Table.getColumn("AR");
Round=Table.getColumn("Round");
Solidity=Table.getColumn("Solidity");
for (c=0; c<nResults; c++)
    print(trab, imgnum +"\t"+ imgname +"\t"+ (c+1) +"\t"+
    Area[c] +"\t"+ X[c] +"\t"+ Y[c] +"\t"+
            Perim[c] +"\t"+ Major[c] +"\t"+ Minor[c] +"\t"+ Angle[c] +"\t"+
            Circ[c]+"\t"+ Feret[c] +"\t"+ FeretX[c] +"\t"+ FeretY[c] +"\t"+
            FeretAngle[c] +"\t"+ MinFeret[c] +"\t"+ AR[c] +"\t"+ Round[c] +"\t"+ Solidity[c] +"\t");
run("Clear Results");
//Clear ROI manager
if (isOpen("ROI Manager")) {
    selectWindow("ROI Manager");
    run("Close");}
//Clear Results Table and trabecularized image
            run("Clear Results");
//**Cortical Pore Analysis**
//Analyze particles for cortical pores
            selectImage(corfin);
            setAutoThreshold("Default dark");
            run("Threshold...");
            setThreshold(1,255);
            setOption("BlackBackground", false);
            run("Convert to Mask");
            run("Analyze Particles...", "display clear add");
//Add pore measurements to cortical pore table
Area=Table.getColumn("Area");
X=Table.getColumn("X");
Y=Table.getColumn("Y");
Perim=Table.getColumn("Perim.");
Major=Table.getColumn("Major");
Minor=Table.getColumn("Minor");
Angle=Table.getColumn("Angle");
```

482

```
Circ=Table.getColumn("Circ.");
Feret=Table.getColumn("Feret");
FeretX=Table.getColumn("FeretX");
FeretY=Table.getColumn("FeretY");
FeretAngle=Table.getColumn("FeretAngle");
MinFeret=Table.getColumn("MinFeret");
AR=Table.getColumn("AR");
Round=Table.getColumn("Round");
Solidity=Table.getColumn("Solidity");
for (c=0; c<nResults; c++)
    print(cor, imgnum +"\t"+ imgname +"\t"+ (c+1) +"\t"+
    Area[c] +"\t"+ X[c] +"\t"+ Y[c] +"\t"+
            Perim[c] +"\t"+ Major[c] +"\t"+ Minor[c] +"\t"+ Angle[c] +"\t"+
            Circ[c]+"\t"+ Feret[c] +"\t"+ FeretX[c] +"\t"+ FeretY[c] +"\t"+
            FeretAngle[c] +"\t"+ MinFeret[c] +"\t"+ AR[c] +"\t"+ Round[c] +"\t"+ Solidity[c] +"\t");
run("Clear Results");
//Clear ROI manager
if (isOpen("ROI Manager")) {
    selectWindow("ROI Manager");
    run("Close");}
//Clear Results Table and all pore images
        run("Clear Results");
        while (nImages>0) {
    selectImage(nImages);
    close(); }}
selectWindow("Total Pore Measurements");
saveAs("Text", dir3+"Total Pore Measurements"+".csv");
run("Close");
selectWindow("Cortical Pore Measurements");
saveAs("Text", dir3+"Cortical Pore Measurements"+".csv");
run("Close");
selectWindow("Trabecularized Pore Measurements");
saveAs("Text", dir3+"Trabecularized Pore Measurements"+".csv");
run("Close");
selectWindow("Results");
run("Close");
}
```

Rib Regional Bounding (ImageJ)

```
macro "Rib Regions"{
setBatchMode(true);
//Clear any past results
run("Clear Results");
//Set background color to black for filling regions
setBackgroundColor(0, 0, 0);
//Set input and output directories
dir1= getDirectory("Select_Cortical_Mask");
list1= getFileList(dir1);
//Make an output directory for both regions
dir2= getDirectory("Select_Output");
region1dir=dir2+"/Region 1/";
File.makeDirectory(region1dir);
```

483

```
region2dir=dir2+"/Region2/";
File.makeDirectory(region2dir);
for (i=0; i<lengthOf(list1); i++){
//Open the cortical mask image
        open(dir1+list1[i]);
        orig=list1[i];
        imgname=getTitle();
        imgnum=i+1;
//Convert measurement scale to um and get pixel size
run("Set Scale...", "distance=0.15601233298 known=1 unit=um global");
getPixelSize(unit, pw, ph);
//Run BoneJ Slice Geometry
run("Slice Geometry", "bone=unknown bone_min=1 bone_max=255 slope=0.0000 y_intercept=1.8000");
//Get image width and height - these are in pixels regardless of scale
w = getWidth();
h = getHeight();
//Pull variables from BoneJ results table and divide by pixel size
cX= getResult("X cent. (µm)",i)/pw;
cY = getResult("Y cent. (µm)",i)/pw;
th = getResult("Theta (rad)",i);
rMin = getResult("R1 (µm)",i)/pw;
rMax = getResult("R2 (µm)",i)/pw;
thPi = th + PI / 2;
//Get image width and height - these are in pixels regardless of scale
w = getWidth();
h = getHeight();
//Pull variables from BoneJ results table and divide by pixel size
cX= getResult("X cent. (µm)",i)/pw;
cY = getResult("Y cent. (µm)",i)/pw;
th = getResult("Theta (rad)",i);
rMin = getResult("R1 (µm)",i)/pw;
rMax = getResult("R2 (µm)",i)/pw;
thPi = th + PI / 2;
//Define major axis - this will be vertical for a long image, and horizontal for a short image
x1 = floor(cX - cos(-th) * 2 * rMax);
y1 = floor(cY + sin(-th) * 2 * rMax);
x2 = floor(cX + cos(-th) * 2 * rMax);
y2 = floor(cY - sin(-th) * 2 * rMax);
//Majoraxis is drawLine(x1, y1, x2, y2);
//Define minor axis
//x1 = floor(cX - cos(thPi) * 2 * rMin);
//y1 = floor(cY - sin(thPi) * 2 * rMin);
//x2 = floor(cX + cos(thPi) * 2 * rMin);
//y2 = floor(cY + sin(thPi) * 2 * rMin);
//Minor axis is drawLine(x1, y1, x2, y2);
//Duplicate image
selectImage(orig); run("Duplicate...", "title=[Region1]");
region1="Region1";
selectImage(orig); run("Duplicate...", "title=[Region2]");
region2="Region2";
//Determine how the image is oriented with the long dimension of the rib
//Vertically (height > width) or horizontally (width>height)
//Note: The axis drawn by the BoneJ macro is incorrect and extends the major axis beyond image bounds
```

484

```
//This corrected axis drawing will not match BoneJ macro axis output
if (w>=h){
//Draw the top polygon on the horizontally oriented image
//x1,0 is the top left corner
//x1,0 is the top right corner
selectImage(region1);
makePolygon(x1,0,x2,0,x2,y2,x1,y1);
run("Clear");
saveAs("bmp", region1dir + imgname);
//Draw the bottom polygon on the horizontally oriented image
//x1,h is the bottom left corner
//x2,h is the bottom right corner
selectImage(region2);
makePolygon(x1,h,x2,h,x2,y2,x1,y1);
run("Clear");
saveAs("bmp", region2dir + imgname);}else
{//Draw the left polygon on the vertically oriented image
//0,y1 is upper left corner
//0,y2 is lower left corner
selectImage(region1);
makePolygon(0,y1,0,y2,x2,y2,x1,y1);
run("Clear");
saveAs("bmp", region1dir + imgname);
//Draw the right polygon on the vertically oriented image
//w,y1 is upper right corner
//w,y2 is lower right corner
selectImage(region2);
makePolygon(w,y1,w,y2,x2,y2,x1,y1);
run("Clear");
saveAs("bmp", region2dir + imgname);}
close();
close();
close();}
//Save compiled results
selectWindow("Results");
slice=newArray(lengthOf(list1));
for (x=0; x<nResults; x++){
        setResult("Slice",x,x+1);}
        updateResults();
for (x=0; x<nResults; x++){
        setResult("Bone Code",x,"Rib");}
        updateResults();
saveAs("Text", dir2+"Cross-Sectional Geometry"+".xls");
selectWindow("Results"); run("Close");}
```

Femoral Octant Bounding (ImageJ)

```
macro "Octant Regions"{
setBatchMode(true);
//Clear any past results
run("Clear Results");
//Set background color to black for clearing regions
setBackgroundColor(0, 0, 0);
```

485

```
//Set input directories
dir1= getDirectory("Select_Cortical_Mask");
list1= getFileList(dir1);
//dir2= getDirectory("Select_Marrow");
//list2= getFileList(dir2);
dir3=getDirectory("Select_Total_Pores");
list3= getFileList(dir3);
dir4=getDirectory("Select_Cortical_Pores");
list4= getFileList(dir4);
dir5=getDirectory("Select_Trabecularized_Pores");
list5= getFileList(dir5);
//Make an output directory
dir6= getDirectory("Select_Output");
//Make table for exporting slice geometry values
slicegeo="[Slice Geometry]";
run("New... ", "name="+slicegeo+" type=Table");
print(slicegeo,"\\Headings:Slice\tLabel\tCSA (µm²)\tX center (µm)\tY center (µm)\tTheta (rad)\tR1
(µm)\tR2 (µm)\tImin (µm^4)\tImax (µm^4)\tIpm (µm^4)\tZmax (µm³)\tZmin (µm³)\tZpol (µm³)\tFeretMin
(µm)\tFeretMax (µm)\tFeretAngle (rad)\tPerimeter (µm)\t");
//Make table for collecting octant coordinates and maximum crop values
oct="[Octant Bounding]";
run("New... ", "name="+oct+" type=Table");
print(oct,"\\Headings:Slice\tcX\tcY\to2x\to2y\to3x\to3y\to4x\to4y\to5x\to5y\to6x\to6y\to7x\to7y\to8x\to8y
\to9x\to9y\tBX1\tBY1\tWidth1\tHeight1\tBX1end\tBY1end\tBX2\tBY2\tWidth2\tHeight2\tBX2end\tBY2e
nd\tBX3\tBY3\tWidth3\tHeight3\tBX3end\tBY3end\tBX4\tBY4\tWidth4\tHeight4\tBX4end\tBY4end\tBX
5\tBY5\tWidth5\tHeight5\tBX5end\tBY5end\tBX6\tBY6\tWidth6\tHeight6\tBX6end\tBY6end\tBX7\tBY7
\tWidth7\tHeight7\tBX7end\tBY7end\tBX8\tBY8\tWidth8\tHeight8\tBX8end\tBY8end");
//Make output directories
//Stack of drawn regional divisions
regiondraw=dir6+"/Drawn Octants/";
File.makeDirectory(regiondraw);
//Superior octant
region1dir=dir6+"/Superior/";
File.makeDirectory(region1dir);
maskregion1dir=region1dir+"/Superior Mask/";
File.makeDirectory(maskregion1dir);
totregion1dir=region1dir+"/Superior Total Pores/";
File.makeDirectory(totregion1dir);
corregion1dir=region1dir+"/Superior Cortical Pores/";
File.makeDirectory(corregion1dir);
trabregion1dir=region1dir+"/Superior Trabecularized Pores/";
File.makeDirectory(trabregion1dir);
//Superior anterior octant
region2dir=dir6+"/Superior Anterior/";
File.makeDirectory(region2dir);
maskregion2dir=region2dir+"/Superior Anterior Mask/";
File.makeDirectory(maskregion2dir);
totregion2dir=region2dir+"/Superior Anterior Total Pores/";
File.makeDirectory(totregion2dir);
corregion2dir=region2dir+"/Superior Anterior Cortical Pores/";
File.makeDirectory(corregion2dir);
trabregion2dir=region2dir+"/Superior Anterior Trabecularized Pores/";
File.makeDirectory(trabregion2dir);
```

486

```
//Anterior octant
region3dir=dir6+"/Anterior/";
File.makeDirectory(region3dir);
maskregion3dir=region3dir+"/Anterior Mask/";
File.makeDirectory(maskregion3dir);
totregion3dir=region3dir+"/Anterior Total Pores/";
File.makeDirectory(totregion3dir);
corregion3dir=region3dir+"/Anterior Cortical Pores/";
File.makeDirectory(corregion3dir);
trabregion3dir=region3dir+"/Anterior Trabecularized Pores/";
File.makeDirectory(trabregion3dir);
//Inferior Anterior Octant
region4dir=dir6+"/Inferior Anterior/";
File.makeDirectory(region4dir);
maskregion4dir=region4dir+"/Inferior Anterior Mask/";
File.makeDirectory(maskregion4dir);
totregion4dir=region4dir+"/Inferior Anterior Total Pores/";
File.makeDirectory(totregion4dir);
corregion4dir=region4dir+"/Inferior Anterior Cortical Pores/";
File.makeDirectory(corregion4dir);
trabregion4dir=region4dir+"/Inferior Anterior Trabecularized Pores/";
File.makeDirectory(trabregion4dir);
//Inferior Octant
region5dir=dir6+"/Inferior/";
File.makeDirectory(region5dir);
maskregion5dir=region5dir+"/Inferior Mask/";
File.makeDirectory(maskregion5dir);
totregion5dir=region5dir+"/Inferior Total Pores/";
File.makeDirectory(totregion5dir);
corregion5dir=region5dir+"/Inferior Cortical Pores/";
File.makeDirectory(corregion5dir);
trabregion5dir=region5dir+"/Inferior Trabecularized Pores/";
File.makeDirectory(trabregion5dir);
//Inferior Posterior Octant
region6dir=dir6+"/Inferior Posterior/";
File.makeDirectory(region6dir);
maskregion6dir=region6dir+"/Inferior Posterior Mask/";
File.makeDirectory(maskregion6dir);
totregion6dir=region6dir+"/Inferior Posterior Total Pores/";
File.makeDirectory(totregion6dir);
corregion6dir=region6dir+"/Inferior Posterior Cortical Pores/";
File.makeDirectory(corregion6dir);
trabregion6dir=region6dir+"/Inferior Posterior Trabecularized Pores/";
File.makeDirectory(trabregion6dir);
//Posterior Octant
region7dir=dir6+"/Posterior/";
File.makeDirectory(region7dir);
maskregion7dir=region7dir+"/Posterior Mask/";
File.makeDirectory(maskregion7dir);
totregion7dir=region7dir+"/Posterior Total Pores/";
File.makeDirectory(totregion7dir);
corregion7dir=region7dir+"/Posterior Cortical Pores/";
File.makeDirectory(corregion7dir);
```

487

```
trabregion7dir=region7dir+"/Posterior Trabecularized Pores/";
File.makeDirectory(trabregion7dir);
//Superior Posterior Octant
region8dir=dir6+"/Superior Posterior/";
File.makeDirectory(region8dir);
maskregion8dir=region8dir+"/Superior Posterior Mask/";
File.makeDirectory(maskregion8dir);
totregion8dir=region8dir+"/Superior Posterior Total Pores/";
File.makeDirectory(totregion8dir);
corregion8dir=region8dir+"/Superior Posterior Cortical Pores/";
File.makeDirectory(corregion8dir);
trabregion8dir=region8dir+"/Superior Posterior Trabecularized Pores/";
File.makeDirectory(trabregion8dir);
//Process images individually - first loop to obtain the crop values
for (i=0; i<lengthOf(list1); i++){
//Open the cortical mask image
        open(dir1+list1[i]);
        orig=list1[i];
        imgname=getTitle();
//Convert measurement scale to um and get pixel size
run("Set Scale...", "distance=0.15601233298 known=1 unit=um global");
getPixelSize(unit, pw, ph);
//Run BoneJ Slice Geometry
run("Slice Geometry", "bone=unknown bone_min=1 bone_max=255 slope=0.0000 y_intercept=1.8000");
//Save slice geometry values to print to the table
Slice=i+1;
Label= getResultLabel(0);
CSA=getResult("CSA (µm²)",0);
Xcent=getResult("X cent. (µm)",0);
Ycent=getResult("Y cent. (µm)",0);
Theta = abs(getResult("Theta (rad)",0));
R1 = getResult("R1 (µm)",0);
R2 = getResult("R2 (µm)",0);
Imin= getResult("Imin (µm^4)",0);
Imax= getResult("Imax (µm^4)",0);
Ipm=getResult("Ipm (µm^4)",0);
Zmax= getResult("Zmax (µm³)",0);
Zmin= getResult("Zmin (µm³)",0);
Zpol= getResult("Zpol (µm³)",0);
FeretMin= getResult("Feret Min (µm)",0);
FeretMax= getResult("Feret Max (µm)",0);
FeretAngle= getResult("Feret Angle (rad)",0);
Perimeter= getResult("Perimeter (µm)",0);
print(slicegeo,Slice+"\t"+Label+"\t"+CSA+"\t"+Xcent+"\t"+Ycent+"\t"+Theta+"\t"+R1+"\t"+R2+"\t"+Imin+"\t"+Imax+
"\t"+Ipm+"\t"+Zmax+"\t"+Zmin+"\t"+Zpol+"\t"+FeretMin+"\t"+FeretMax+"\t"+FeretAngle+"\t"+Perimeter+"\t");
//Get image width and height - these are in pixels regardless of scale
w = getWidth();
h = getHeight();
//Pull variables from BoneJ results table and divide by pixel size to obtain pixel coordinates
cX= getResult("X cent. (µm)",0)/pw;
cY = getResult("Y cent. (µm)",0)/pw;
```

488

```
th = abs(getResult("Theta (rad)",0));
rMin = getResult("R1 (µm)",0)/pw;
rMax = getResult("R2 (µm)",0)/pw;
thPi = th + PI / 2;
//Define major axis - this will be vertical for a long image, and horizontal for a short image
Majorx1 = floor(cX - cos(-th) * 1.5 * rMax);
Majory1 = floor(cY + sin(-th) * 1.5 * rMax);
Majorx2 = floor(cX + cos(-th) * 1.5 * rMax);
Majory2 = floor(cY - sin(-th) * 1.5 * rMax);
//Majoraxis is drawLine(x1, y1, x2, y2);
//Define minor axis
Minorx1 = floor(cX - cos(thPi) * 2 * rMin);
Minory1 = floor(cY - sin(thPi) * 2 * rMin);
Minorx2 = floor(cX + cos(thPi) * 2 * rMin);
Minory2 = floor(cY + sin(thPi) * 2 * rMin);
//Select the more vertical axis
if (Majory1<Minory1){
        x1 = Majorx1;
        y1= Majory1;
        x2 = Majorx2;
        y2 = Majory2;}else{
        x1 = Minorx1;
        y1 = Minory1;
        x2 = Minorx2;
        y2 = Minory2;}
//Rotate the major axis to the start position of all octants on the original image
selectImage(orig);
makeLine(x1, y1, x2, y2);
//Rotate major axis right to top of octant 2
run("Rotate...", "  angle=22.5");
//Get coordinates for opposing lines 2 and 6
getSelectionCoordinates(x, y);
o2x=x[0];
o2y=y[0];
o6x=x[1];
o6y=y[1];
//Rotate major axis right 45 degrees to top of octant 3
run("Rotate...", "  angle=45");
//Get coordinates for opposing lines 3 and 7
getSelectionCoordinates(x, y);
o3x=x[0];
o3y=y[0];
o7x=x[1];
o7y=y[1];
//Rotate major axis right 45 degrees to top of octant 4
run("Rotate...", "  angle=45");
//Get coordinates for opposing lines 4 and 8
getSelectionCoordinates(x, y);
o4x=x[0];
o4y=y[0];
o8x=x[1];
o8y=y[1];
//Rotate major axis right 45 degrees to top of octant 5
```

489

```
run("Rotate...", "  angle=45");
//Get coordinates for opposing lines 5 and 9
getSelectionCoordinates(x, y);
o5x=x[0];
o5y=y[0];
o9x=x[1];
o9y=y[1];
//Duplicate image for drawing all octants on the slice
selectImage(orig); run("Duplicate...", "title=[Drawn]");
drawoct="Drawn";
selectImage(drawoct);
makePolygon(o9x,o9y,o2x,o2y,cX,cY);
run("Draw");
makePolygon(o2x,o2y,o3x,o3y,cX,cY);
run("Draw");
makePolygon(o3x,o3y,o4x,o4y,cX,cY);
run("Draw");
makePolygon(o4x,o4y,o5x,o5y,cX,cY);
run("Draw");
makePolygon(o5x,o5y,o6x,o6y,cX,cY);
run("Draw");
makePolygon(o6x,o6y,o7x,o7y,cX,cY);
run("Draw");
makePolygon(o7x,o7y,o8x,o8y,cX,cY);
run("Draw");
makePolygon(o8x,o8y,o9x,o9y,cX,cY);
run("Draw");
saveAs("bmp", regiondraw + imgname);
close();
//Remove um scale for polygon operations in pixel scale
run("Set Scale...", "distance=0 known=0 pixel=1 unit=pixel global");
//Set measurements to bounding rectangle only
run("Set Measurements...", "bounding redirect=None decimal=3");
//Measure Octant 1
selectImage(orig); run("Duplicate...", "title=[Temp Octant]");
tempoct="Temp Octant";
selectImage(tempoct);
makePolygon(o9x,o9y,o2x,o2y,cX,cY);
setBackgroundColor(0, 0, 0);
run("Clear Outside");
setAutoThreshold("Default dark");
run("Threshold...");
setThreshold(1,255);
setOption("BlackBackground", true);
run("Convert to Mask");
//Octant 1 Bounding
//Counts particle(s), if multiple ROIs combines them in a single ROI and deletes individual ROIs
//Then finds the bounding rectangle for the ROI set
run("Clear Results");
selectImage(tempoct);
run("Analyze Particles...", "display clear add");
roicount=roiManager("Count");
//Combine multiple ROIs for fragmented cortex region
```

490

```
if (roicount>1){
roiManager("show all without labels");
roiManager("Combine");
roiManager("Add");
newcount=roiManager("Count")-1;
deleteroi=Array.getSequence(newcount);
roiManager("Select", deleteroi);
roiManager("Delete");
roiManager("Select", 0);}
//Or select single ROI for non-fragmented cortex region
else
{roiManager("Select", 0);}
run("Clear Results");
roiManager("Measure");
BX1 = getResult("BX",0);
BY1 = getResult("BY",0);
Width1 = getResult("Width",0);
Height1 = getResult("Height",0);
BX1end=BX1+Width1;
BY1end=BY1+Height1;
roiManager("Deselect");
roiManager("Delete");
selectImage(tempoct);
close();
//Measure Octant 2
selectImage(orig); run("Duplicate...", "title=[Temp Octant]");
tempoct="Temp Octant";
selectImage(tempoct);
makePolygon(o2x,o2y,o3x,o3y,cX,cY);
setBackgroundColor(0, 0, 0);
run("Clear Outside");
setAutoThreshold("Default dark");
run("Threshold...");
setThreshold(1,255);
setOption("BlackBackground", true);
run("Convert to Mask");
//Octant 2 Bounding
//Counts particle(s), if multiple ROIs combines them in a single ROI and deletes individual ROIs
//Then finds the bounding rectangle for the ROI set
run("Clear Results");
run("Analyze Particles...", "display clear add");
roicount=roiManager("Count");
//Combine multiple ROIs for fragmented cortex region
if (roicount>1){
roiManager("show all without labels");
roiManager("Combine");
roiManager("Add");
newcount=roiManager("Count")-1;
deleteroi=Array.getSequence(newcount);
roiManager("Select", deleteroi);
roiManager("Delete");
roiManager("Select", 0);}
//Or select single ROI for non-fragmented cortex region
```

491

```
else
{roiManager("Select", 0);}
run("Clear Results");
roiManager("Measure");
BX2 = getResult("BX",0);
BY2 = getResult("BY",0);
Width2 = getResult("Width",0);
Height2 = getResult("Height",0);
BX2end=BX2+Width2;
BY2end=BY2+Height2;
roiManager("Deselect");
roiManager("Delete");
selectImage(tempoct);
close();
//Measure Octant 3
selectImage(orig); run("Duplicate...", "title=[Temp Octant]");
tempoct="Temp Octant";
selectImage(tempoct);
makePolygon(o3x,o3y,o4x,o4y,cX,cY);
setBackgroundColor(0, 0, 0);
run("Clear Outside");
setAutoThreshold("Default dark");
run("Threshold...");
setThreshold(1,255);
setOption("BlackBackground", true);
run("Convert to Mask");
//Octant 3 Bounding
//Counts particle(s), if multiple ROIs combines them in a single ROI and deletes individual ROIs
//Then finds the bounding rectangle for the ROI set
run("Clear Results");
run("Analyze Particles...", "display clear add");
roicount=roiManager("Count");
//Combine multiple ROIs for fragmented cortex region
if (roicount>1){
roiManager("show all without labels");
roiManager("Combine");
roiManager("Add");
newcount=roiManager("Count")-1;
deleteroi=Array.getSequence(newcount);
roiManager("Select", deleteroi);
roiManager("Delete");
roiManager("Select", 0);}
//Or select single ROI for non-fragmented cortex region
else
{roiManager("Select", 0);}
run("Clear Results");
roiManager("Measure");
BX3 = getResult("BX",0);
BY3 = getResult("BY",0);
Width3 = getResult("Width",0);
Height3 = getResult("Height",0);
BX3end=BX3+Width3;
BY3end=BY3+Height3;
```

492

```
roiManager("Deselect");
roiManager("Delete");
selectImage(tempoct);
close();
//Measure Octant 4
selectImage(orig); run("Duplicate...", "title=[Temp Octant]");
tempoct="Temp Octant";
selectImage(tempoct);
makePolygon(o4x,o4y,o5x,o5y,cX,cY);
setBackgroundColor(0, 0, 0);
run("Clear Outside");
setAutoThreshold("Default dark");
run("Threshold...");
setThreshold(1,255);
setOption("BlackBackground", true);
run("Convert to Mask");
//Octant 4 Bounding
//Counts particle(s), if multiple ROIs combines them in a single ROI and deletes individual ROIs
//Then finds the bounding rectangle for the ROI set
run("Clear Results");
run("Analyze Particles...", "display clear add");
roicount=roiManager("Count");
//Combine multiple ROIs for fragmented cortex region
if (roicount>1){
roiManager("show all without labels");
roiManager("Combine");
roiManager("Add");
newcount=roiManager("Count")-1;
deleteroi=Array.getSequence(newcount);
roiManager("Select", deleteroi);
roiManager("Delete");
roiManager("Select", 0);}
//Or select single ROI for non-fragmented cortex region
else
{roiManager("Select", 0);}
run("Clear Results");
roiManager("Measure");
BX4 = getResult("BX",0);
BY4 = getResult("BY",0);
Width4 = getResult("Width",0);
Height4 = getResult("Height",0);
BX4end=BX4+Width4;
BY4end=BY4+Height4;
roiManager("Deselect");
roiManager("Delete");
selectImage(tempoct);
close();
//Measure Octant 5
selectImage(orig); run("Duplicate...", "title=[Temp Octant]");
tempoct="Temp Octant";
selectImage(tempoct);
makePolygon(o5x,o5y,o6x,o6y,cX,cY);
setBackgroundColor(0, 0, 0);
```

493

```
run("Clear Outside");
setAutoThreshold("Default dark");
run("Threshold...");
setThreshold(1,255);
setOption("BlackBackground", true);
run("Convert to Mask");
//Octant 5 Bounding
//Counts particle(s), if multiple ROIs combines them in a single ROI and deletes individual ROIs
//Then finds the bounding rectangle for the ROI set
run("Clear Results");
run("Analyze Particles...", "display clear add");
roicount=roiManager("Count");
//Combine multiple ROIs for fragmented cortex region
if (roicount>1){
roiManager("show all without labels");
roiManager("Combine");
roiManager("Add");
newcount=roiManager("Count")-1;
deleteroi=Array.getSequence(newcount);
roiManager("Select", deleteroi);
roiManager("Delete");
roiManager("Select", 0);}
//Or select single ROI for non-fragmented cortex region
else
{roiManager("Select", 0);}
run("Clear Results");
roiManager("Measure");
BX5 = getResult("BX",0);
BY5 = getResult("BY",0);
Width5 = getResult("Width",0);
Height5 = getResult("Height",0);
BX5end=BX5+Width5;
BY5end=BY5+Height5;
roiManager("Deselect");
roiManager("Delete");
selectImage(tempoct);
close();
//Measure Octant 6
selectImage(orig); run("Duplicate...", "title=[Temp Octant]");
tempoct="Temp Octant";
selectImage(tempoct);
makePolygon(o6x,o6y,o7x,o7y,cX,cY);
setBackgroundColor(0, 0, 0);
run("Clear Outside");
setAutoThreshold("Default dark");
run("Threshold...");
setThreshold(1,255);
setOption("BlackBackground", true);
run("Convert to Mask");
//Octant 6 Bounding
//Counts particle(s), if multiple ROIs combines them in a single ROI and deletes individual ROIs
//Then finds the bounding rectangle for the ROI set
run("Clear Results");
```

494

```
run("Analyze Particles...", "display clear add");
roicount=roiManager("Count");
//Combine multiple ROIs for fragmented cortex region
if (roicount>1){
roiManager("show all without labels");
roiManager("Combine");
roiManager("Add");
newcount=roiManager("Count")-1;
deleteroi=Array.getSequence(newcount);
roiManager("Select", deleteroi);
roiManager("Delete");
roiManager("Select", 0);}
//Or select single ROI for non-fragmented cortex region
else
{roiManager("Select", 0);}
run("Clear Results");
roiManager("Measure");
BX6 = getResult("BX",0);
BY6 = getResult("BY",0);
Width6 = getResult("Width",0);
Height6 = getResult("Height",0);
BX6end=BX6+Width6;
BY6end=BY6+Height6;
roiManager("Deselect");
roiManager("Delete");
selectImage(tempoct);
close();
//Measure Octant 7
selectImage(orig); run("Duplicate...", "title=[Temp Octant]");
tempoct="Temp Octant";
selectImage(tempoct);
makePolygon(o7x,o7y,o8x,o8y,cX,cY);
setBackgroundColor(0, 0, 0);
run("Clear Outside");
setAutoThreshold("Default dark");
run("Threshold...");
setThreshold(1,255);
setOption("BlackBackground", true);
run("Convert to Mask");
//Octant 7 Bounding
//Counts particle(s), if multiple ROIs combines them in a single ROI and deletes individual ROIs
//Then finds the bounding rectangle for the ROI set
run("Clear Results");
run("Analyze Particles...", "display clear add");
roicount=roiManager("Count");
//Combine multiple ROIs for fragmented cortex region
if (roicount>1){
roiManager("show all without labels");
roiManager("Combine");
roiManager("Add");
newcount=roiManager("Count")-1;
deleteroi=Array.getSequence(newcount);
roiManager("Select", deleteroi);
```

495

```
roiManager("Delete");
roiManager("Select", 0);}
//Or select single ROI for non-fragmented cortex region
else
{roiManager("Select", 0);}
run("Clear Results");
roiManager("Measure");
BX7 = getResult("BX",0);
BY7 = getResult("BY",0);
Width7 = getResult("Width",0);
Height7 = getResult("Height",0);
BX7end=BX7+Width7;
BY7end=BY7+Height7;
roiManager("Deselect");
roiManager("Delete");
selectImage(tempoct);
close();
//Measure Octant 8
selectImage(orig); run("Duplicate...", "title=[Temp Octant]");
tempoct="Temp Octant";
selectImage(tempoct);
makePolygon(o8x,o8y,o9x,o9y,cX,cY);
setBackgroundColor(0, 0, 0);
run("Clear Outside");
setAutoThreshold("Default dark");
run("Threshold...");
setThreshold(1,255);
setOption("BlackBackground", true);
run("Convert to Mask");
//Octant 8 Bounding
//Counts particle(s), if multiple ROIs combines them in a single ROI and deletes individual ROIs
//Then finds the bounding rectangle for the ROI set
run("Clear Results");
run("Analyze Particles...", "display clear add");
roicount=roiManager("Count");
//Combine multiple ROIs for fragmented cortex region
if (roicount>1){
roiManager("show all without labels");
roiManager("Combine");
roiManager("Add");
newcount=roiManager("Count")-1;
deleteroi=Array.getSequence(newcount);
roiManager("Select", deleteroi);
roiManager("Delete");
roiManager("Select", 0);}
//Or select single ROI for non-fragmented cortex region
else
{roiManager("Select", 0);}
run("Clear Results");
roiManager("Measure");
BX8 = getResult("BX",0);
BY8 = getResult("BY",0);
Width8 = getResult("Width",0);
```

496

```
Height8 = getResult("Height",0);
BX8end=BX8+Width8;
BY8end=BY8+Height8;
roiManager("Deselect");
roiManager("Delete");
selectImage(tempoct);
close();
//Print all results to string
print(oct,imgname+"\t"+cX+"\t"+cY+"\t"+o2x+"\t"+o2y+"\t"+o3x+"\t"+o3y+
"\t"+o4x+"\t"+o4y+"\t"+o5x+"\t"+o5y+"\t"+o6x+"\t"+o6y+"\t"+o7x+"\t"+o7y+
"\t"+o8x+"\t"+o8y+"\t"+o9x+"\t"+o9y+"\t"
+BX1+"\t"+BY1+"\t"+Width1+"\t"+Height1+"\t"+BX1end+"\t"+BY1end+"\t"
+BX2+"\t"+BY2+"\t"+Width2+"\t"+Height2+"\t"+BX2end+"\t"+BY2end+"\t"
+BX3+"\t"+BY3+"\t"+Width3+"\t"+Height3+"\t"+BX3end+"\t"+BY3end+"\t"
+BX4+"\t"+BY4+"\t"+Width4+"\t"+Height4+"\t"+BX4end+"\t"+BY4end+"\t"
+BX5+"\t"+BY5+"\t"+Width5+"\t"+Height5+"\t"+BX5end+"\t"+BY5end+"\t"
+BX6+"\t"+BY6+"\t"+Width6+"\t"+Height6+"\t"+BX6end+"\t"+BY6end+"\t"
+BX7+"\t"+BY7+"\t"+Width7+"\t"+Height7+"\t"+BX7end+"\t"+BY7end+"\t"
+BX8+"\t"+BY8+"\t"+Width8+"\t"+Height8+"\t"+BX8end+"\t"+BY8end+"\t");
//Close original slice
close();
//Clear results table to make way for slice geometry in next loop
run("Clear Results");}
selectWindow("Results");
run("Close");
selectWindow("Octant Bounding");
saveAs("Text", dir6+"Octant Bounding"+".csv");
run("Close");
selectWindow("Slice Geometry");
saveAs("Text", dir6+"Slice Geometry"+".csv");
run("Close");
//**TABLE MODIFICATION FOR CROPPING**
//Find maximum crop coordinates for each octant
open(dir6+"Octant Bounding.csv");
oct="Octant Bounding.csv";
selectWindow(oct);
//Octant 1 Universal Crop Window
//Find the minimum X coordinate of all slices
BX1=Table.getColumn("BX1",oct);
BX1rank= Array.rankPositions(BX1);
BX1rankpos= Array.rankPositions(BX1rank);
if (BX1rankpos[0]==0)
{BX1minpos=0;}
else{for (i=0; i<BX1rankpos.length; i++ ) {
if (BX1rankpos[i]==0) {break;}BX1minpos=i+1;}}
BX1min=BX1[BX1minpos];
//Find the maximum X coordinate of all slices
BX1end=Table.getColumn("BX1end",oct);
BX1endrank= Array.rankPositions(BX1end);
BX1endrankpos= Array.rankPositions(BX1endrank);
if (BX1endrankpos[0]==(BX1endrankpos.length-1))
{BX1maxpos=0;}
else{for (i=0; i<BX1endrankpos.length-1; i++ ) {
```

497

```
if (BX1endrankpos[i]==(BX1endrankpos.length-1)){break;}BX1maxpos=i+1;}}
BX1max=BX1end[BX1maxpos];
//Crop width is maximum X value - minimum X value, since the width is measured from the upper left
hand corner
Cropwidth1=BX1max-BX1min;
//Find the minimum Y coordinate of all slices
selectWindow(oct);
BY1=Table.getColumn("BY1",oct);
BY1rank= Array.rankPositions(BY1);
BY1rankpos= Array.rankPositions(BY1rank);
if (BY1rankpos[0]==0)
{BY1minpos=0;}
else{for (i=0; i<BY1rankpos.length; i++ ) { if (BY1rankpos[i]==0){break;}BY1minpos=i+1;}}
BY1min=BY1[BY1minpos];
//Find the maximum Y coordinate of all slices
BY1end=Table.getColumn("BY1end",oct);
BY1endrank= Array.rankPositions(BY1end);
BY1endrankpos= Array.rankPositions(BY1endrank);
if (BY1endrankpos[0]==(BY1endrankpos.length-1))
{BY1maxpos=0;}
else {for (i=0; i<BY1endrankpos.length-1; i++ ) { if (BY1endrankpos[i]==(BY1endrankpos.length-1))
{break;}BY1maxpos=i+1;}}
BY1max=BY1end[BY1maxpos];
//Crop height is maximum Y value - minimum Y value, since the height is measured from the upper left
hand corner
Cropheight1=BY1max-BY1min;
//Octant 2 Universal Crop Window
//Find the minimum X coordinate of all slices
BX2=Table.getColumn("BX2",oct);
BX2rank= Array.rankPositions(BX2);
BX2rankpos= Array.rankPositions(BX2rank);
if (BX2rankpos[0]==0)
{BX2minpos=0;}
else{for (i=0; i<BX2rankpos.length; i++ ) {
if (BX2rankpos[i]==0){break;}BX2minpos=i+1;}}
BX2min=BX2[BX2minpos];
//Find the maximum X coordinate of all slices
BX2end=Table.getColumn("BX2end",oct);
BX2endrank= Array.rankPositions(BX2end);
BX2endrankpos= Array.rankPositions(BX2endrank);
if (BX2endrankpos[0]==(BX2endrankpos.length-1))
{BX2maxpos=0;}
else{for (i=0; i<BX2endrankpos.length-1; i++ ) {
if (BX2endrankpos[i]==(BX2endrankpos.length-1)){break;}BX2maxpos=i+1;}}
BX2max=BX2end[BX2maxpos];
//Crop width is maximum X value - minimum X value, since the width is measured from the upper left
hand corner
Cropwidth2=BX2max-BX2min;
//Find the minimum Y coordinate of all slices
selectWindow(oct);
BY2=Table.getColumn("BY2",oct);
BY2rank= Array.rankPositions(BY2);
BY2rankpos= Array.rankPositions(BY2rank);
```

498

```
if (BY2rankpos[0]==0)
{BY2minpos=0;}
else{for (i=0; i<BY2rankpos.length; i++ ) { if (BY2rankpos[i]==0){break;}BY2minpos=i+1;}}
BY2min=BY2[BY2minpos];
//Find the maximum Y coordinate of all slices
BY2end=Table.getColumn("BY2end",oct);
BY2endrank= Array.rankPositions(BY2end);
BY2endrankpos= Array.rankPositions(BY2endrank);
if (BY2endrankpos[0]==(BY2endrankpos.length-1))
{BY2maxpos=0;}
else {for (i=0; i<BY2endrankpos.length-1; i++ ) { if (BY2endrankpos[i]==(BY2endrankpos.length-1))
{break;}BY2maxpos=i+1;}}
BY2max=BY2end[BY2maxpos];
//Crop height is maximum Y value - minimum Y value, since the height is measured from the upper left
hand corner
Cropheight2=BY2max-BY2min;
//Octant 3 Universal Crop Window
//Find the minimum X coordinate of all slices
BX3=Table.getColumn("BX3",oct);
BX3rank= Array.rankPositions(BX3);
BX3rankpos= Array.rankPositions(BX3rank);
if (BX3rankpos[0]==0)
{BX3minpos=0;}
else{for (i=0; i<BX3rankpos.length; i++ ) { if (BX3rankpos[i]==0){break;}BX3minpos=i+1;}}
BX3min=BX3[BX3minpos];
//Find the maximum X coordinate of all slices
BX3end=Table.getColumn("BX3end",oct);
BX3endrank= Array.rankPositions(BX3end);
BX3endrankpos= Array.rankPositions(BX3endrank);
if (BX3endrankpos[0]==(BX3endrankpos.length-1))
{BX3maxpos=0;}
else{for (i=0; i<BX3endrankpos.length-1; i++ ) { if (BX3endrankpos[i]==(BX3endrankpos.length-1))
{break;}BX3maxpos=i+1;}}
BX3max=BX3end[BX3maxpos];
//Crop width is maximum X value - minimum X value, since the width is measured from the upper left
hand corner
Cropwidth3=BX3max-BX3min;
//Find the minimum Y coordinate of all slices
selectWindow(oct);
BY3=Table.getColumn("BY3",oct);
BY3rank= Array.rankPositions(BY3);
BY3rankpos= Array.rankPositions(BY3rank);
if (BY3rankpos[0]==0)
{BY3minpos=0;}
else{for (i=0; i<BY3rankpos.length; i++ ) {if (BY3rankpos[i]==0){break;}BY3minpos=i+1;}}
BY3min=BY3[BY3minpos];
//Find the maximum Y coordinate of all slices
BY3end=Table.getColumn("BY3end",oct);
BY3endrank= Array.rankPositions(BY3end);
BY3endrankpos= Array.rankPositions(BY3endrank);
if (BY3endrankpos[0]==(BY3endrankpos.length-1))
{BY3maxpos=0;}
```

499

else {for (i=0; i<BY3endrankpos.length-1; i++) { if (BY3endrankpos[i]==(BY3endrankpos.length-1)) {break;}BY3maxpos=i+1;}}
BY3max=BY3end[BY3maxpos];
//Crop height is maximum Y value - minimum Y value, since the height is measured from the upper left hand corner
Cropheight3=BY3max-BY3min;
//Octant 4 Universal Crop Window
//Find the minimum X coordinate of all slices
BX4=Table.getColumn("BX4",oct);
BX4rank= Array.rankPositions(BX4);
BX4rankpos= Array.rankPositions(BX4rank);
if (BX4rankpos[0]==0)
{BX4minpos=0;}
else{for (i=0; i<BX4rankpos.length; i++) { if (BX4rankpos[i]==0)
{break;}BX4minpos=i+1;}}
BX4min=BX4[BX4minpos];
//Find the maximum X coordinate of all slices
BX4end=Table.getColumn("BX4end",oct);
BX4endrank= Array.rankPositions(BX4end);
BX4endrankpos= Array.rankPositions(BX4endrank);
if (BX4endrankpos[0]==(BX4endrankpos.length-1))
{BX4maxpos=0;}
else{for (i=0; i<BX4endrankpos.length-1; i++) { if (BX4endrankpos[i]==(BX4endrankpos.length-1))
{break;}BX4maxpos=i+1;}}
BX4max=BX4end[BX4maxpos];
//Crop width is maximum X value - minimum X value, since the width is measured from the upper left hand corner
Cropwidth4=BX4max-BX4min;
//Find the minimum Y coordinate of all slices
selectWindow(oct);
BY4=Table.getColumn("BY4",oct);
BY4rank= Array.rankPositions(BY4);
BY4rankpos= Array.rankPositions(BY4rank);
if (BY4rankpos[0]==0)
{BY4minpos=0;}
else{for (i=0; i<BY4rankpos.length; i++) { if (BY4rankpos[i]==0){break;}BY4minpos=i+1;}}
BY4min=BY4[BY4minpos];
//Find the maximum Y coordinate of all slices
BY4end=Table.getColumn("BY4end",oct);
BY4endrank= Array.rankPositions(BY4end);
BY4endrankpos= Array.rankPositions(BY4endrank);
if (BY4endrankpos[0]==(BY4endrankpos.length-1))
{BY4maxpos=0;}
else {for (i=0; i<BY4endrankpos.length-1; i++) { if (BY4endrankpos[i]==(BY4endrankpos.length-1)) {break;}BY4maxpos=i+1;}}
BY4max=BY4end[BY4maxpos];
//Crop height is maximum Y value - minimum Y value, since the height is measured from the upper left hand corner
Cropheight4=BY4max-BY4min;
//Octant 5 Universal Crop Window
//Find the minimum X coordinate of all slices
BX5=Table.getColumn("BX5",oct);
BX5rank= Array.rankPositions(BX5);

500

```
BX5rankpos= Array.rankPositions(BX5rank);
if (BX5rankpos[0]==0)
{BX5minpos=0;}
else{for (i=0; i<BX5rankpos.length; i++ ) { if (BX5rankpos[i]==0){break;}BX5minpos=i+1;}}
BX5min=BX5[BX5minpos];
//Find the maximum X coordinate of all slices
BX5end=Table.getColumn("BX5end",oct);
BX5endrank= Array.rankPositions(BX5end);
BX5endrankpos= Array.rankPositions(BX5endrank);
if (BX5endrankpos[0]==(BX5endrankpos.length-1))
{BX5maxpos=0;}
else{for (i=0; i<BX5endrankpos.length-1; i++ ) { if (BX5endrankpos[i]==(BX5endrankpos.length-1))
{break;}BX5maxpos=i+1;}}
BX5max=BX5end[BX5maxpos];
//Crop width is maximum X value - minimum X value, since the width is measured from the upper left
hand corner
Cropwidth5=BX5max-BX5min;
//Find the minimum Y coordinate of all slices
selectWindow(oct);
BY5=Table.getColumn("BY5",oct);
BY5rank= Array.rankPositions(BY5);
BY5rankpos= Array.rankPositions(BY5rank);
if (BY5rankpos[0]==0)
{BY5minpos=0;}
else{for (i=0; i<BY5rankpos.length; i++ ) { if (BY5rankpos[i]==0){break;}BY5minpos=i+1;}}
BY5min=BY5[BY5minpos];
//Find the maximum Y coordinate of all slices
BY5end=Table.getColumn("BY5end",oct);
BY5endrank= Array.rankPositions(BY5end);
BY5endrankpos= Array.rankPositions(BY5endrank);
if (BY5endrankpos[0]==(BY5endrankpos.length-1))
{BY5maxpos=0;}
else {for (i=0; i<BY5endrankpos.length-1; i++ ) { if (BY5endrankpos[i]==(BY5endrankpos.length-1))
{break;}BY5maxpos=i+1;}}
BY5max=BY5end[BY5maxpos];
//Crop height is maximum Y value - minimum Y value, since the height is measured from the upper left
hand corner
Cropheight5=BY5max-BY5min;
//Octant 6 Universal Crop Window
//Find the minimum X coordinate of all slices
BX6=Table.getColumn("BX6",oct);
BX6rank= Array.rankPositions(BX6);
BX6rankpos= Array.rankPositions(BX6rank);
if (BX6rankpos[0]==0)
{BX6minpos=0;}
else{for (i=0; i<BX6rankpos.length; i++ ) {if (BX6rankpos[i]==0){break;}BX6minpos=i+1;}}
BX6min=BX6[BX6minpos];
//Find the maximum X coordinate of all slices
BX6end=Table.getColumn("BX6end",oct);
BX6endrank= Array.rankPositions(BX6end);
BX6endrankpos= Array.rankPositions(BX6endrank);
if (BX6endrankpos[0]==(BX6endrankpos.length-1))
{BX6maxpos=0;}
```

501

```
else{for (i=0; i<BX6endrankpos.length-1; i++ ) { if (BX6endrankpos[i]==(BX6endrankpos.length-
1)){break;}BX6maxpos=i+1;}}
BX6max=BX6end[BX6maxpos];
//Crop width is maximum X value - minimum X value, since the width is measured from the upper left
hand corner
Cropwidth6=BX6max-BX6min;
//Find the minimum Y coordinate of all slices
selectWindow(oct);
BY6=Table.getColumn("BY6",oct);
BY6rank= Array.rankPositions(BY6);
BY6rankpos= Array.rankPositions(BY6rank);
if (BY6rankpos[0]==0)
{BY6minpos=0;}
else{for (i=0; i<BY6rankpos.length; i++ ) { if (BY6rankpos[i]==0){break;}BY6minpos=i+1;}}
BY6min=BY6[BY6minpos];
//Find the maximum Y coordinate of all slices
BY6end=Table.getColumn("BY6end",oct);
BY6endrank= Array.rankPositions(BY6end);
BY6endrankpos= Array.rankPositions(BY6endrank);
if (BY6endrankpos[0]==(BY6endrankpos.length-1))
{BY6maxpos=0;}
else {for (i=0; i<BY6endrankpos.length-1; i++ ) { if (BY6endrankpos[i]==(BY6endrankpos.length-
1)){break;}BY6maxpos=i+1;}}
BY6max=BY6end[BY6maxpos];
//Crop height is maximum Y value - minimum Y value, since the height is measured from the upper left
hand corner
Cropheight6=BY6max-BY6min;
//Octant 7 Universal Crop Window
//Find the minimum X coordinate of all slices
BX7=Table.getColumn("BX7",oct);
BX7rank= Array.rankPositions(BX7);
BX7rankpos= Array.rankPositions(BX7rank);
if (BX7rankpos[0]==0)
{BX7minpos=0;}
else{for (i=0; i<BX7rankpos.length; i++ ) { if (BX7rankpos[i]==0){break;}BX7minpos=i+1;}}
BX7min=BX7[BX7minpos];
//Find the maximum X coordinate of all slices
BX7end=Table.getColumn("BX7end",oct);
BX7endrank= Array.rankPositions(BX7end);
BX7endrankpos= Array.rankPositions(BX7endrank);
if (BX7endrankpos[0]==(BX7endrankpos.length-1))
{BX7maxpos=0;}
else{for (i=0; i<BX7endrankpos.length-1; i++ ) { if (BX7endrankpos[i]==(BX7endrankpos.length-
1)){break;}BX7maxpos=i+1;}}
BX7max=BX7end[BX7maxpos];
//Crop width is maximum X value - minimum X value, since the width is measured from the upper left
hand corner
Cropwidth7=BX7max-BX7min;
//Find the minimum Y coordinate of all slices
selectWindow(oct);
BY7=Table.getColumn("BY7",oct);
BY7rank= Array.rankPositions(BY7);
BY7rankpos= Array.rankPositions(BY7rank);
```

502

```
if (BY7rankpos[0]==0)
{BY7minpos=0;}
else{for (i=0; i<BY7rankpos.length; i++ ) { if (BY7rankpos[i]==0){break;}BY7minpos=i+1;}}
BY7min=BY7[BY7minpos];
//Find the maximum Y coordinate of all slices
BY7end=Table.getColumn("BY7end",oct);
BY7endrank= Array.rankPositions(BY7end);
BY7endrankpos= Array.rankPositions(BY7endrank);
if (BY7endrankpos[0]==(BY7endrankpos.length-1))
{BY7maxpos=0;}
else {for (i=0; i<BY7endrankpos.length-1; i++ ) { if (BY7endrankpos[i]==(BY7endrankpos.length-
1)){break;}BY7maxpos=i+1;}}
BY7max=BY7end[BY7maxpos];
//Crop height is maximum Y value - minimum Y value, since the height is measured from the upper left
hand corner
Cropheight7=BY7max-BY7min;
//Octant 8 Universal Crop Window
//Find the minimum X coordinate of all slices
BX8=Table.getColumn("BX8",oct);
BX8rank= Array.rankPositions(BX8);
BX8rankpos= Array.rankPositions(BX8rank);
if (BX8rankpos[0]==0)
{BX8minpos=0;}
else{for (i=0; i<BX8rankpos.length; i++ ) { if (BX8rankpos[i]==0){break;}BX8minpos=i+1;}}
BX8min=BX8[BX8minpos];
//Find the maximum X coordinate of all slices
BX8end=Table.getColumn("BX8end",oct);
BX8endrank= Array.rankPositions(BX8end);
BX8endrankpos= Array.rankPositions(BX8endrank);
if (BX8endrankpos[0]==(BX8endrankpos.length-1))
{BX8maxpos=0;}
else{for (i=0; i<BX8endrankpos.length-1; i++ ) { if (BX8endrankpos[i]==(BX8endrankpos.length-
1)){break;}BX8maxpos=i+1;}}
BX8max=BX8end[BX8maxpos];
//Crop width is maximum X value - minimum X value, since the width is measured from the upper left
hand corner
Cropwidth8=BX8max-BX8min;
//Find the minimum Y coordinate of all slices
selectWindow(oct);
BY8=Table.getColumn("BY8",oct);
BY8rank= Array.rankPositions(BY8);
BY8rankpos= Array.rankPositions(BY8rank);
if (BY8rankpos[0]==0)
{BY8minpos=0;}
else{for (i=0; i<BY8rankpos.length; i++ ) { if (BY8rankpos[i]==0){break;}BY8minpos=i+1;}}
BY8min=BY8[BY8minpos];
//Find the maximum Y coordinate of all slices
BY8end=Table.getColumn("BY8end",oct);
BY8endrank= Array.rankPositions(BY8end);
BY8endrankpos= Array.rankPositions(BY8endrank);
if (BY8endrankpos[0]==(BY8endrankpos.length-1))
{BY8maxpos=0;}
```

503

```
else {for (i=0; i<BY8endrankpos.length-1; i++ ) { if (BY8endrankpos[i]==(BY8endrankpos.length-1)){break;}BY8maxpos=i+1;}}
BY8max=BY8end[BY8maxpos];
//Crop height is maximum Y value - minimum Y value, since the height is measured from the upper left hand corner
Cropheight8=BY8max-BY8min;
//Save crop window as a separate table for the dataset
croptable="[Octant Crop Window]";
run("New... ", "name="+croptable+" type=Table");
print(croptable,"\\Headings:Octant Number\tAnatomical Name\tX\tY\tWidth\tHeight");
print(croptable,"1"+"\t"+"Superior"+"\t"+BX1min+"\t"+BY1min+"\t"+Cropwidth1+"\t"+Cropheight1);
print(croptable,"2"+"\t"+"Superior
Anterior"+"\t"+BX2min+"\t"+BY2min+"\t"+Cropwidth2+"\t"+Cropheight2);
print(croptable,"3"+"\t"+"Anterior"+"\t"+BX3min+"\t"+BY3min+"\t"+Cropwidth3+"\t"+Cropheight3);
print(croptable,"4"+"\t"+"Inferior
Anterior"+"\t"+BX4min+"\t"+BY4min+"\t"+Cropwidth4+"\t"+Cropheight4);
print(croptable,"5"+"\t"+"Inferior"+"\t"+BX5min+"\t"+BY5min+"\t"+Cropwidth5+"\t"+Cropheight5);
print(croptable,"6"+"\t"+"Inferior
Posterior"+"\t"+BX6min+"\t"+BY6min+"\t"+Cropwidth6+"\t"+Cropheight6);
print(croptable,"7"+"\t"+"Posterior"+"\t"+BX7min+"\t"+BY7min+"\t"+Cropwidth7+"\t"+Cropheight7);
print(croptable,"8"+"\t"+"Superior
Posterior"+"\t"+BX8min+"\t"+BY8min+"\t"+Cropwidth8+"\t"+Cropheight8);
selectWindow("Octant Crop Window");
saveAs("Text", dir6+"Octant Crop Window"+".csv");
run("Close");
//**CORTICAL MASK MODIFICATION LOOP**
for (i=0; i<lengthOf(list1); i++){
//Open the cortical mask image
open(dir1+list1[i]);
orig=list1[i];
imgname=getTitle();
//Get octant bounding values from table
selectWindow(oct);
cX=Table.get("cX",i);
cY=Table.get("cY",i);
o2x=Table.get("o2x",i);
o2y=Table.get("o2y",i);
o3x=Table.get("o3x",i);
o3y=Table.get("o3y",i);
o4x=Table.get("o4x",i);
o4y=Table.get("o4y",i);
o5x=Table.get("o5x",i);
o5y=Table.get("o5y",i);
o6x=Table.get("o6x",i);
o6y=Table.get("o6y",i);
o7x=Table.get("o7x",i);
o7y=Table.get("o7y",i);
o8x=Table.get("o8x",i);
o8y=Table.get("o8y",i);
o9x=Table.get("o9x",i);
o9y=Table.get("o9y",i);
//Draw Octant 1
selectImage(orig);
```

504

```
run("Duplicate...", "title=[Temp Octant]");
tempoct="Temp Octant";
selectImage(tempoct);
makePolygon(o9x,o9y,o2x,o2y,cX,cY);
setBackgroundColor(0, 0, 0);
run("Clear Outside");
setAutoThreshold("Default dark");
run("Threshold...");
setThreshold(1,255);
setOption("BlackBackground", true);
run("Convert to Mask");
//Crop Octant 1 Mask
selectImage(tempoct);
makeRectangle(BX1min,BY1min,Cropwidth1,Cropheight1);
run("Crop");
saveAs("bmp", maskregion1dir + imgname);
close();
//Draw Octant 2
selectImage(orig);
run("Duplicate...", "title=[Temp Octant]");
tempoct="Temp Octant";
selectImage(tempoct);
makePolygon(o2x,o2y,o3x,o3y,cX,cY);
setBackgroundColor(0, 0, 0);
run("Clear Outside");
setAutoThreshold("Default dark");
run("Threshold...");
setThreshold(1,255);
setOption("BlackBackground", true);
run("Convert to Mask");
//Crop Octant 2 Mask
selectImage(tempoct);
makeRectangle(BX2min,BY2min,Cropwidth2,Cropheight2);
run("Crop");
saveAs("bmp", maskregion2dir + imgname);
close();
//Draw Octant 3
selectImage(orig);
run("Duplicate...", "title=[Temp Octant]");
tempoct="Temp Octant";
selectImage(tempoct);
makePolygon(o3x,o3y,o4x,o4y,cX,cY);
setBackgroundColor(0, 0, 0);
run("Clear Outside");
setAutoThreshold("Default dark");
run("Threshold...");
setThreshold(1,255);
setOption("BlackBackground", true);
run("Convert to Mask");
//Crop Octant 3 Mask
selectImage(tempoct);
makeRectangle(BX3min,BY3min,Cropwidth3,Cropheight3);
run("Crop");
```

505

```
saveAs("bmp", maskregion3dir + imgname);
close();
//Draw Octant 4
selectImage(orig);
run("Duplicate...", "title=[Temp Octant]");
tempoct="Temp Octant";
selectImage(tempoct);
makePolygon(o4x,o4y,o5x,o5y,cX,cY);
setBackgroundColor(0, 0, 0);
run("Clear Outside");
setAutoThreshold("Default dark");
run("Threshold...");
setThreshold(1,255);
setOption("BlackBackground", true);
run("Convert to Mask");
//Crop Octant 4 Mask
selectImage(tempoct);
makeRectangle(BX4min,BY4min,Cropwidth4,Cropheight4);
run("Crop");
saveAs("bmp", maskregion4dir + imgname);
close();
//Draw Octant 5
selectImage(orig);
run("Duplicate...", "title=[Temp Octant]");
tempoct="Temp Octant";
selectImage(tempoct);
makePolygon(o5x,o5y,o6x,o6y,cX,cY);
setBackgroundColor(0, 0, 0);
run("Clear Outside");
setAutoThreshold("Default dark");
run("Threshold...");
setThreshold(1,255);
setOption("BlackBackground", true);
run("Convert to Mask");
//Crop Octant 5 Mask
selectImage(tempoct);
makeRectangle(BX5min,BY5min,Cropwidth5,Cropheight5);
run("Crop");
saveAs("bmp", maskregion5dir + imgname);
close();
//Draw Octant 6
selectImage(orig);
run("Duplicate...", "title=[Temp Octant]");
tempoct="Temp Octant";
selectImage(tempoct);
makePolygon(o6x,o6y,o7x,o7y,cX,cY);
setBackgroundColor(0, 0, 0);
run("Clear Outside");
setAutoThreshold("Default dark");
run("Threshold...");
setThreshold(1,255);
setOption("BlackBackground", true);
run("Convert to Mask");
```

506

```
//Crop Octant 6 Mask
selectImage(tempoct);
makeRectangle(BX6min,BY6min,Cropwidth6,Cropheight6);
run("Crop");
saveAs("bmp", maskregion6dir + imgname);
close();
//Draw Octant 7
selectImage(orig);
run("Duplicate...", "title=[Temp Octant]");
tempoct="Temp Octant";
selectImage(tempoct);
makePolygon(o7x,o7y,o8x,o8y,cX,cY);
setBackgroundColor(0, 0, 0);
run("Clear Outside");
setAutoThreshold("Default dark");
run("Threshold...");
setThreshold(1,255);
setOption("BlackBackground", true);
run("Convert to Mask");
//Crop Octant 7 Mask
selectImage(tempoct);
makeRectangle(BX7min,BY7min,Cropwidth7,Cropheight7);
run("Crop");
saveAs("bmp", maskregion7dir + imgname);
close();
//Draw Octant 8
selectImage(orig);
run("Duplicate...", "title=[Temp Octant]");
tempoct="Temp Octant";
selectImage(tempoct);
makePolygon(o9x,o9y,o8x,o8y,cX,cY);
setBackgroundColor(0, 0, 0);
run("Clear Outside");
setAutoThreshold("Default dark");
run("Threshold...");
setThreshold(1,255);
setOption("BlackBackground", true);
run("Convert to Mask");
//Crop Octant 8 Mask
selectImage(tempoct);
makeRectangle(BX8min,BY8min,Cropwidth8,Cropheight8);
run("Crop");
saveAs("bmp", maskregion8dir + imgname);
close();
//Close original mask
selectImage(orig);
close();}
//**TOTAL PORE WINDOW MODIFICATION LOOP**
for (i=0; i<lengthOf(list3); i++){
//Open the total pore image
open(dir3+list3[i]);
orig=list3[i];
imgname=getTitle();
```

507

```
//Duplicate and crop to Octant 1
selectImage(orig);
run("Duplicate...", "title=[Temp Octant]");
tempoct="Temp Octant";
selectImage(tempoct);
makeRectangle(BX1min,BY1min,Cropwidth1,Cropheight1);
run("Crop");
saveAs("bmp", totregion1dir + imgname);
close();
//Duplicate and crop to Octant 2
selectImage(orig);
run("Duplicate...", "title=[Temp Octant]");
tempoct="Temp Octant";
selectImage(tempoct);
makeRectangle(BX2min,BY2min,Cropwidth2,Cropheight2);
run("Crop");
saveAs("bmp", totregion2dir + imgname);
close();
//Duplicate and crop to Octant 3
selectImage(orig);
run("Duplicate...", "title=[Temp Octant]");
tempoct="Temp Octant";
selectImage(tempoct);
makeRectangle(BX3min,BY3min,Cropwidth3,Cropheight3);
run("Crop");
saveAs("bmp", totregion3dir + imgname);
close();
//Duplicate and crop to Octant 4
selectImage(orig);
run("Duplicate...", "title=[Temp Octant]");
tempoct="Temp Octant";
selectImage(tempoct);
makeRectangle(BX4min,BY4min,Cropwidth4,Cropheight4);
run("Crop");
saveAs("bmp", totregion4dir + imgname);
close();
//Duplicate and crop to Octant 5
selectImage(orig);
run("Duplicate...", "title=[Temp Octant]");
tempoct="Temp Octant";
selectImage(tempoct);
makeRectangle(BX5min,BY5min,Cropwidth5,Cropheight5);
run("Crop");
saveAs("bmp", totregion5dir + imgname);
close();
//Duplicate and crop to Octant 6
selectImage(orig);
run("Duplicate...", "title=[Temp Octant]");
tempoct="Temp Octant";
selectImage(tempoct);
makeRectangle(BX6min,BY6min,Cropwidth6,Cropheight6);
run("Crop");
saveAs("bmp", totregion6dir + imgname);
```

508

```
close();
//Duplicate and crop to Octant 7
selectImage(orig);
run("Duplicate...", "title=[Temp Octant]");
tempoct="Temp Octant";
selectImage(tempoct);
makeRectangle(BX7min,BY7min,Cropwidth7,Cropheight7);
run("Crop");
saveAs("bmp", totregion7dir + imgname);
close();
//Duplicate and crop to Octant 8
selectImage(orig);
run("Duplicate...", "title=[Temp Octant]");
tempoct="Temp Octant";
selectImage(tempoct);
makeRectangle(BX8min,BY8min,Cropwidth8,Cropheight8);
run("Crop");
saveAs("bmp", totregion8dir + imgname);
close();
//Close original total pore image
selectImage(orig);
close();}
//**CORTICAL PORE WINDOW MODIFICATION LOOP**
for (i=0; i<lengthOf(list4); i++){
//Open the cortical pore image
open(dir4+list4[i]);
orig=list4[i];
imgname=getTitle();
//Duplicate and crop to Octant 1
selectImage(orig);
run("Duplicate...", "title=[Temp Octant]");
tempoct="Temp Octant";
selectImage(tempoct);
makeRectangle(BX1min,BY1min,Cropwidth1,Cropheight1);
run("Crop");
saveAs("bmp", corregion1dir + imgname);
close();
//Duplicate and crop to Octant 2
selectImage(orig);
run("Duplicate...", "title=[Temp Octant]");
tempoct="Temp Octant";
selectImage(tempoct);
makeRectangle(BX2min,BY2min,Cropwidth2,Cropheight2);
run("Crop");
saveAs("bmp", corregion2dir + imgname);
close();
//Duplicate and crop to Octant 3
selectImage(orig);
run("Duplicate...", "title=[Temp Octant]");
tempoct="Temp Octant";
selectImage(tempoct);
makeRectangle(BX3min,BY3min,Cropwidth3,Cropheight3);
run("Crop");
```

509

```
saveAs("bmp", corregion3dir + imgname);
close();
//Duplicate and crop to Octant 4
selectImage(orig);
run("Duplicate...", "title=[Temp Octant]");
tempoct="Temp Octant";
selectImage(tempoct);
makeRectangle(BX4min,BY4min,Cropwidth4,Cropheight4);
run("Crop");
saveAs("bmp", corregion4dir + imgname);
close();
//Duplicate and crop to Octant 5
selectImage(orig);
run("Duplicate...", "title=[Temp Octant]");
tempoct="Temp Octant";
selectImage(tempoct);
makeRectangle(BX5min,BY5min,Cropwidth5,Cropheight5);
run("Crop");
saveAs("bmp", corregion5dir + imgname);
close();
//Duplicate and crop to Octant 6
selectImage(orig);
run("Duplicate...", "title=[Temp Octant]");
tempoct="Temp Octant";
selectImage(tempoct);
makeRectangle(BX6min,BY6min,Cropwidth6,Cropheight6);
run("Crop");
saveAs("bmp", corregion6dir + imgname);
close();
//Duplicate and crop to Octant 7
selectImage(orig);
run("Duplicate...", "title=[Temp Octant]");
tempoct="Temp Octant";
selectImage(tempoct);
makeRectangle(BX7min,BY7min,Cropwidth7,Cropheight7);
run("Crop");
saveAs("bmp", corregion7dir + imgname);
close();
//Duplicate and crop to Octant 8
selectImage(orig);
run("Duplicate...", "title=[Temp Octant]");
tempoct="Temp Octant";
selectImage(tempoct);
makeRectangle(BX8min,BY8min,Cropwidth8,Cropheight8);
run("Crop");
saveAs("bmp", corregion8dir + imgname);
close();
//Close original cortical pore image
selectImage(orig);
close();}
//**TRABECULARIZED PORE WINDOW MODIFICATION LOOP**
for (i=0; i<lengthOf(list5); i++){
//Open the trabecularized pore image
```

510

```
open(dir5+list5[i]);
orig=list5[i];
imgname=getTitle();
//Duplicate and crop to Octant 1
selectImage(orig);
run("Duplicate...", "title=[Temp Octant]");
tempoct="Temp Octant";
selectImage(tempoct);
makeRectangle(BX1min,BY1min,Cropwidth1,Cropheight1);
run("Crop");
saveAs("bmp", trabregion1dir + imgname);
close();
//Duplicate and crop to Octant 2
selectImage(orig);
run("Duplicate...", "title=[Temp Octant]");
tempoct="Temp Octant";
selectImage(tempoct);
makeRectangle(BX2min,BY2min,Cropwidth2,Cropheight2);
run("Crop");
saveAs("bmp", trabregion2dir + imgname);
close();
//Duplicate and crop to Octant 3
selectImage(orig);
run("Duplicate...", "title=[Temp Octant]");
tempoct="Temp Octant";
selectImage(tempoct);
makeRectangle(BX3min,BY3min,Cropwidth3,Cropheight3);
run("Crop");
saveAs("bmp", trabregion3dir + imgname);
close();
//Duplicate and crop to Octant 4
selectImage(orig);
run("Duplicate...", "title=[Temp Octant]");
tempoct="Temp Octant";
selectImage(tempoct);
makeRectangle(BX4min,BY4min,Cropwidth4,Cropheight4);
run("Crop");
saveAs("bmp", trabregion4dir + imgname);
close();
//Duplicate and crop to Octant 5
selectImage(orig);
run("Duplicate...", "title=[Temp Octant]");
tempoct="Temp Octant";
selectImage(tempoct);
makeRectangle(BX5min,BY5min,Cropwidth5,Cropheight5);
run("Crop");
saveAs("bmp", trabregion5dir + imgname);
close();
//Duplicate and crop to Octant 6
selectImage(orig);
run("Duplicate...", "title=[Temp Octant]");
tempoct="Temp Octant";
selectImage(tempoct);
```

511

```
makeRectangle(BX6min,BY6min,Cropwidth6,Cropheight6);
run("Crop");
saveAs("bmp", trabregion6dir + imgname);
close();
//Duplicate and crop to Octant 7
selectImage(orig);
run("Duplicate...", "title=[Temp Octant]");
tempoct="Temp Octant";
selectImage(tempoct);
makeRectangle(BX7min,BY7min,Cropwidth7,Cropheight7);
run("Crop");
saveAs("bmp", trabregion7dir + imgname);
close();
//Duplicate and crop to Octant 8
selectImage(orig);
run("Duplicate...", "title=[Temp Octant]");
tempoct="Temp Octant";
selectImage(tempoct);
makeRectangle(BX8min,BY8min,Cropwidth8,Cropheight8);
run("Crop");
saveAs("bmp", trabregion8dir + imgname);
close();
//Close original trabecularized pore image
selectImage(orig);
close();}}
```

512

Relative Cortical Area and Parabolic Index (ImageJ)

```
macro "RCA"{
setBatchMode(true);
//Clear any past results
run("Clear Results");
//Set input and output directories
dir1= getDirectory("Select_Marrow");
list1= getFileList(dir1);
dir2= getDirectory("Select_Cortical_Mask");
list2= getFileList(dir2);
dir3= getDirectory("Select_Output");
dir3tot=dir3+"/Filled Cortex/";
File.makeDirectory(dir3tot);
//Make table for exporting slice geometry values
rca="[Relative Cortical Area]";
run("New... ", "name="+rca+" type=Table");
print(rca,"\\Headings:Slice\tLabel\tTotal Area (µm²)\tMarrow Area (µm)\tCortical Area (µm)\tRelative
Cortical Area (%)\tParabolic Index (Y)\tOsteoporotic (Y<0.19)\t");

//Begin loop
for (i=0; i<lengthOf(list1); i++){
//Open the marrow and measure its area
open(dir1+list1[i]);
marrow=list1[i];
imgname=getTitle();
rename("Marrow");
marrow="Marrow";
run("Set Scale...", "distance=0.15601233298 known=1 unit=um global");
run("Set Measurements...", "area redirect=None decimal=3");
run("Clear Results");
selectWindow(marrow);
run("Analyze Particles...", "display clear add");
//Combine any fragmented regions
roicount=roiManager("Count");
if (roicount>1){
roiManager("show all without labels");
roiManager("Combine");
roiManager("Add");
newcount=roiManager("Count")-1;
deleteroi=Array.getSequence(newcount);
roiManager("Select", deleteroi);
roiManager("Delete");
roiManager("Select", 0);}
//Or select single ROI for non-fragmented cortex region
else
{roiManager("Select", 0);}
run("Clear Results");
roiManager("Measure");
//Measure marrow area (MA)
MA=getResult("Area");
//Add the cortical mask to marrow to acquire total area
open(dir2+list2[i]);
```

513

```
mask=list2[i];
rename("Mask");
mask="Mask";
imageCalculator("Add create", "Mask", "Marrow");
total="Result of Mask";
selectWindow(marrow);
close();
selectWindow(mask);
close();
selectWindow(total);
saveAs("bmp", dir3tot + imgname);
rename("Total");
total="Total";
//Measure total area from marrow+mask image
run("Clear Results");
selectWindow(total);
run("Analyze Particles...", "display clear add");
//Combine any fragmented regions
roicount=roiManager("Count");
if (roicount>1){
roiManager("show all without labels");
roiManager("Combine");
roiManager("Add");
newcount=roiManager("Count")-1;
deleteroi=Array.getSequence(newcount);
roiManager("Select", deleteroi);
roiManager("Delete");
roiManager("Select", 0);}
//Or select single ROI for non-fragmented cortex region
else
{roiManager("Select", 0);}
run("Clear Results");
roiManager("Measure");
TA=getResult("Area");
//Compute table calculations
Slice=i+1;
CA=TA-MA;
RCA=(CA/TA)*100;
Para=(CA*MA)/(TA*TA);
//Diagnose parabolic index
if (Para>=0.19)
        Paracode="No";
        else
        Paracode="Yes";
//Print to table
print(rca,Slice+"\t"+imgname+"\t"+TA+"\t"+MA+"\t"+CA+"\t"+RCA+"\t"+Para+"\t"+Paracode+"\t");
//Close marrow, mask, and filled mask images
close();}
selectWindow("Relative Cortical Area");
saveAs("Text", dir3+"Relative Cortical Area"+".csv");
run("Close");
selectWindow("Results");
run("Close");}
```

514

Appendix B: R Statistical Code

Packages and Libraries

```
library(dplyr)
library(ggpubr)
library(lmerTest)
library(reshape)
library(psycho)
library(dlookr)
library(memisc)
library(lme4)
library(sjPlot)
library(sjmisc)
library(sjlabelled)
library(MuMIn)
library(broom)
library(purrr)
library(coin)
library(Hmisc)
library(corrplot)
library(ggcorrplot)
library(psych)
library(nlme)
library(piecewiseSEM)
library(EMAtools)
library(r2glmm)
library(fmsb)
library (ggplot2)
library (ggiraph)
library (plyr)
library (reshape2)
library (moonBook)
library (sjmisc)
library (ggiraphExtra)
```

Test for Co-Variate and Total Pore Morphometry Normality

```
#Set working directory
setwd("G:/Dissertation Storage/Analysis Tables/Base Tables for R Modification/Finished Tables")
#Read in whole pore data set
ribdat <- read.csv(file="rib_base_numeric_pores_whole_load.csv", stringsAsFactors=TRUE)
femdat <- read.csv(file="femoral_base_numeric_pores_whole_only.csv", stringsAsFactors=TRUE)
##Rename pore variables for rib
colnames(ribdat)[colnames(ribdat)=="sex"] <- "Sex"
colnames(ribdat)[colnames(ribdat)=="age"] <- "Age"
colnames(ribdat)[colnames(ribdat)=="weight"] <- "Weight"
colnames(ribdat)[colnames(ribdat)=="height"] <- "Height"
colnames(ribdat)[colnames(ribdat)=="BMI_con"] <- "Continous BMI"
colnames(ribdat)[colnames(ribdat)=="BMD_total_con"] <- "Continous Total BMD"
colnames(ribdat)[colnames(ribdat)=="T_total_con"] <- "Continous Total T-score"
colnames(ribdat)[colnames(ribdat)=="Z_total_con"] <- "Continous Total Z-score"
colnames(ribdat)[colnames(ribdat)=="pi_mean_slice"] <- "Mean Parabolic Index"
colnames(ribdat)[colnames(ribdat)=="imin_mean_ctan"] <- "Mean Imin CTan"
colnames(ribdat)[colnames(ribdat)=="imax_mean_ctan"] <- "Mean Imax Ctan"
colnames(ribdat)[colnames(ribdat)=="j_mean_ctan"] <- "Mean J Ctan"
colnames(ribdat)[colnames(ribdat)=="imin_mean_bonej"] <- "Mean Imin BoneJ"
colnames(ribdat)[colnames(ribdat)=="imax_mean_bonej"] <- "Mean Imax BoneJ "
colnames(ribdat)[colnames(ribdat)=="j_mean_bonej"] <- "Mean J BoneJ "
colnames(ribdat)[colnames(ribdat)==" rca_mean_slice"] <- "Mean RCA by Slice"
colnames(ribdat)[colnames(ribdat)==" rca_mean_stack"] <- "Mean RCA by Stack"
colnames(ribdat)[colnames(ribdat)=="ecc"] <- "Mean Eccentricity"
colnames(ribdat)[colnames(ribdat)=="cs.th"] <- "Cross-sectional Thickness"
colnames(ribdat)[colnames(ribdat)=="rcv"] <- "Relative Cortical Volume"
colnames(ribdat)[colnames(ribdat)=="fractal_dimension_cortex"] <- "Cortical Fractal Dimension"
colnames(ribdat)[colnames(ribdat)=="percent_closed_porosity"] <- "% Closed Porosity"
colnames(ribdat)[colnames(ribdat)=="percent_open_porosity"] <- "% Open Porosity"
colnames(ribdat)[colnames(ribdat)=="percent_porosity"] <- "% Porosity"
colnames(ribdat)[colnames(ribdat)=="structure_thickness"] <- "Pore Thickness"
colnames(ribdat)[colnames(ribdat)=="structure_separation"] <- "Pore Separation"
colnames(ribdat)[colnames(ribdat)=="structure_linear_density"] <- "Structure Linear Density"
colnames(ribdat)[colnames(ribdat)=="fragmentation_index"] <- "Fragmentation Index"
colnames(ribdat)[colnames(ribdat)=="fractal_dimension_pores"] <- "Pore Network Fractal Dimension"
colnames(ribdat)[colnames(ribdat)=="connectivity_density"] <- "Connectivity Density"
colnames(ribdat)[colnames(ribdat)=="stdv_structure_thickeness"] <- "StDv Pore Thickness"
colnames(ribdat)[colnames(ribdat)=="stdv_structure_separation"] <- "StDv Pore Separation"
colnames(ribdat)[colnames(ribdat)=="percent_open_pores"] <- "Proportion Open Pores"
colnames(ribdat)[colnames(ribdat)=="percent_closed_pores"] <- "Proportion Closed Pores"
colnames(ribdat)[colnames(ribdat)=="pore_density"] <- "Pore Density"
ribnorm<-normality(ribdat)
write.csv(ribnorm,file="rib_pore_normality.csv")
#Rename pore variables for femoral neck
colnames(femdat)[colnames(femdat)=="age"] <- "Age"
colnames(femdat)[colnames(femdat)=="weight"] <- "Weight"
colnames(femdat)[colnames(femdat)=="height"] <- "Height"
colnames(femdat)[colnames(femdat)=="BMI_con"] <- "Continous BMI"
colnames(femdat)[colnames(femdat)=="BMD_total_con"] <- "Continous Total BMD"
colnames(femdat)[colnames(femdat)=="T_total_con"] <- "Continous Total T-score"
colnames(femdat)[colnames(femdat)=="Z_total_con"] <- "Continous Total Z-score"
```

```
colnames(femdat)[colnames(femdat)=="BMD_neck_con"] <- "Continous R Femoral Neck BMD"
colnames(femdat)[colnames(femdat)=="T_neck_con"] <- "Continous R Femoral Neck T-score"
colnames(femdat)[colnames(femdat)=="Z_neck_con"] <- "Continous R Femoral Neck Z-score"
colnames(femdat)[colnames(femdat)=="fem_mx_lng"] <- "FemMxLng"
colnames(femdat)[colnames(femdat)=="fem_sub_tr_ap_dia"] <- "FemSubTrAPDia"
colnames(femdat)[colnames(femdat)=="fem_sub_tr_ml_dia"] <- "FemSubTrMLDia"
colnames(femdat)[colnames(femdat)=="fem_head_si_dia"] <- "FemHeadSIDi"
colnames(femdat)[colnames(femdat)=="fem_neck_sl"] <- "FemNeckSL"
colnames(femdat)[colnames(femdat)=="fem_head_hz_dia"] <- "FemHeadHzDia"
colnames(femdat)[colnames(femdat)=="fem_neck_sl"] <- "FemNeckSL"
colnames(femdat)[colnames(femdat)=="fem_neck_il"] <- "FemNeckIL"
colnames(femdat)[colnames(femdat)=="fem_neck_v_dia"] <- "FemNeckVDia"
colnames(femdat)[colnames(femdat)=="fem_neck_t_dia"] <- "FemNeckTDia"
colnames(femdat)[colnames(femdat)=="fnal_cent"] <- "FNALCent"
colnames(femdat)[colnames(femdat)=="fnal_apex"] <- "FNALApex"
colnames(femdat)[colnames(femdat)=="off"] <- "OFF"
colnames(femdat)[colnames(femdat)=="neck_shaft_angle"] <- "Neck-Shaft Angle"
colnames(femdat)[colnames(femdat)=="pi_mean_slice"] <- "Mean Parabolic Index"
colnames(femdat)[colnames(femdat)=="imin_mean_ctan"] <- "Mean Imin CTan"
colnames(femdat)[colnames(femdat)=="imax_mean_ctan"] <- "Mean Imax Ctan"
colnames(femdat)[colnames(femdat)=="j_mean_ctan"] <- "Mean J Ctan"
colnames(femdat)[colnames(femdat)=="imin_mean_bonej"] <- "Mean Imin BoneJ"
colnames(femdat)[colnames(femdat)=="imax_mean_bonej"] <- "Mean Imax BoneJ "
colnames(femdat)[colnames(femdat)=="j_mean_bonej"] <- "Mean J BoneJ "
colnames(femdat)[colnames(femdat)==" rca_mean_slice"] <- "Mean RCA by Slice"
colnames(femdat)[colnames(femdat)==" rca_mean_stack"] <- "Mean RCA by Stack"
colnames(femdat)[colnames(femdat)=="ecc"] <- "Mean Eccentricity"
colnames(femdat)[colnames(femdat)=="cs.th"] <- "Cross-sectional Thickness"
colnames(femdat)[colnames(femdat)=="rcv"] <- "Relative Cortical Volume"
colnames(femdat)[colnames(femdat)=="fractal_dimension_cortex"] <- "Cortical Fractal Dimension"
colnames(femdat)[colnames(femdat)=="percent_closed_porosity"] <- "% Closed Porosity"
colnames(femdat)[colnames(femdat)=="percent_open_porosity"] <- "% Open Porosity"
colnames(femdat)[colnames(femdat)=="percent_porosity"] <- "% Porosity"
colnames(femdat)[colnames(femdat)=="structure_thickness"] <- "Pore Thickness"
colnames(femdat)[colnames(femdat)=="structure_separation"] <- "Pore Separation"
colnames(femdat)[colnames(femdat)=="structure_linear_density"] <- "Structure Linear Density"
colnames(femdat)[colnames(femdat)=="fragmentation_index"] <- "Fragmentation Index"
colnames(femdat)[colnames(femdat)=="fractal_dimension_pores"] <- "Pore Network Fractal Dimension"
colnames(femdat)[colnames(femdat)=="connectivity_density"] <- "Connectivity Density"
colnames(femdat)[colnames(femdat)=="stdv_structure_thickeness"] <- "StDv Pore Thickness"
colnames(femdat)[colnames(femdat)=="stdv_structure_separation"] <- "StDv Pore Separation"
colnames(femdat)[colnames(femdat)=="percent_open_pores"] <- "Proportion Open Pores"
colnames(femdat)[colnames(femdat)=="percent_closed_pores"] <- "Proportion Closed Pores"
colnames(femdat)[colnames(femdat)=="pore_density"] <- "Pore Density"
femnorm<-normality(femdat)
write.csv(femnorm,file="fem_pore_normality.csv")
```

Test Variation in Cross-Sectional Geometry Calculation Method

```
#Reshape RCA data for aov comparison
ribrcadat<-melt(ribdat, id.vars = "ID", measure.vars = c("rca_mean_slice", "rca_mean_stack", "rcv"),
variable_name = "rib_rca_opts")
#Rib RCA LMM
ribrcaout<-lmer(value ~ rib_rca_opts + (1|ID), data=ribrcadat, REML=F)
tab_model(ribrcaout)
a<-anova(ribrcaout)
ar2<-r.squaredGLMM(ribrcaout)
a$R2marginal<-ar2[1,1]
a$R2conditional<-ar2[1,2]
write.csv(as.matrix(a), file = "MyANOVA2.csv", na = "")
#Femoral neck RCA LMM
femrcadat<-melt(femdat, id.vars = "ID", measure.vars = c("rca_mean_slice", "rca_mean_stack", "rcv"),
variable_name = "fem_rca_opts")
femrcaout<-lmer(value ~ fem_rca_opts + (1|ID), data=femrcadat, REML=F)
tab_model(femrcaout)
a<-anova(femrcaout)
ar2<-r.squaredGLMM(femrcaout)
a$R2marginal<-ar2[1,1]
a$R2conditional<-ar2[1,2]
write.csv(as.matrix(a), file = "MyANOVA2.csv", na = "")
#Moments of inertia t-tests - rib
t1<-t.test(ribdat$imin_mean_bonej, ribdat$imin_mean_ctan, paired=TRUE, conf.level=0.95)
t2<-t.test(ribdat$imax_mean_bonej, ribdat$imax_mean_ctan, paired=TRUE, conf.level=0.95)
t3<-t.test(ribdat$j_mean_bonej, ribdat$j_mean_ctan, paired=TRUE, conf.level=0.95)
tab <- map_df(list(t1, t2, t3), tidy)
write.csv(as.matrix(tab), file = "Ttest.csv", na = "")
#Moments of inertia t-tests - femoral neck
t1<-t.test(femdat$imin_mean_bonej, femdat$imin_mean_ctan, paired=TRUE, conf.level=0.95)
t2<-t.test(femdat$j_mean_bonej, femdat$j_mean_ctan, paired=TRUE, conf.level=0.95)
#Wilcoxon signed rank with symmetry problem (tie) test due to non-normal imax_mean_ctan
wilcox.test(femdat$imax_mean_bonej ~ femdat$imax_mean_ctan,
        alternative = "two.sided",
        mu = 0, paired = TRUE, exact = FALSE, correct = TRUE,
        conf.int = TRUE, conf.level = 0.95)
tab <- map_df(list(t1, t2), tidy)
write.csv(as.matrix(tab), file = "Ttest.csv", na = "")
```

Correlation Matrices for Rib and Femoral Neck Co-variates

```
#Correlation matrix: rib
#Remove non-numeric vars
ribdatcor<-subset(ribdat, select = -c(ID,newID,sex,BMI_cat,T_total_cat,
rca_mean_stack,rca_mean_slice,imin_mean_bonej,j_mean_bonej, imax_mean_bonej))
#Create a named version of data set
colnames(ribdatcor)[colnames(ribdatcor)=="age"] <- "Age"
colnames(ribdatcor)[colnames(ribdatcor)=="weight"] <- "Weight"
colnames(ribdatcor)[colnames(ribdatcor)=="height"] <- "Height"
colnames(ribdatcor)[colnames(ribdatcor)=="BMI_con"] <- "Continous BMI"
colnames(ribdatcor)[colnames(ribdatcor)=="BMD_total_con"] <- "Continous Total BMD"
colnames(ribdatcor)[colnames(ribdatcor)=="T_total_con"] <- "Continous Total T-score"
colnames(ribdatcor)[colnames(ribdatcor)=="Z_total_con"] <- "Continous Total Z-score"
colnames(ribdatcor)[colnames(ribdatcor)=="pi_mean_slice"] <- "Mean Parabolic Index"
colnames(ribdatcor)[colnames(ribdatcor)=="imin_mean_ctan"] <- "Mean Imin"
colnames(ribdatcor)[colnames(ribdatcor)=="imax_mean_ctan"] <- "Mean Imax"
colnames(ribdatcor)[colnames(ribdatcor)=="j_mean_ctan"] <- "Mean J"
colnames(ribdatcor)[colnames(ribdatcor)=="ecc"] <- "Mean Eccentricity"
colnames(ribdatcor)[colnames(ribdatcor)=="cs.th"] <- "Cross-sectional Thickness"
colnames(ribdatcor)[colnames(ribdatcor)=="rcv"] <- "Relative Cortical Volume"
#Run correlation matrix
rib.cor<-cor(ribdatcor, use = "complete.obs")
write.csv(as.matrix(rib.cor), file = "RibCovariateCorrelations.csv", na = "")
#Get p-values
rib.cor.p<-cor_pmat(ribdatcor)
write.csv(as.matrix(rib.cor.p), file = "RibCovariateCorrelationsPvalue.csv", na = "")


#Correlation matrix in situ
ggcorrplot(rib.cor,hc.order = FALSE,
          outline.col = "white",
          ggtheme = ggplot2::theme_gray,
           colors = c("#D55E00", "white", "#009E73"),
           lab = TRUE, type = "lower")
#Correlation matrix re-ordered
ggcorrplot(rib.cor,hc.order = TRUE,
          outline.col = "white",
          ggtheme = ggplot2::theme_gray,
           colors = c("#D55E00", "white", "#009E73"),
          lab = TRUE,type = "lower")
#Non-significant correlation blanked out for non-sig p values
ggcorrplot(rib.cor,hc.order = FALSE,
          outline.col = "white",
          ggtheme = ggplot2::theme_gray,
           colors = c("#D55E00", "white", "#009E73"),
          lab = TRUE,type = "lower", p.mat=rib.cor.p,insig = "blank")
#Correlation matrix: femoral neck
#Remove non-numeric vars
femdatcor<-subset(femdat, select = -c(ID,newID,sex,BMI_cat,T_total_cat,T_neck_cat,
rca_mean_stack,rca_mean_slice,imin_mean_bonej,j_mean_bonej, imax_mean_bonej))
#Create a named version of data set
colnames(femdatcor)[colnames(femdatcor)=="age"] <- "Age"
colnames(femdatcor)[colnames(femdatcor)=="weight"] <- "Weight"
```

```r
colnames(femdatcor)[colnames(femdatcor)=="height"] <- "Height"
colnames(femdatcor)[colnames(femdatcor)=="BMI_con"] <- "Continous BMI"
colnames(femdatcor)[colnames(femdatcor)=="BMD_total_con"] <- "Continous Total BMD"
colnames(femdatcor)[colnames(femdatcor)=="T_total_con"] <- "Continous Total T-score"
colnames(femdatcor)[colnames(femdatcor)=="Z_total_con"] <- "Continous Total Z-score"
colnames(femdatcor)[colnames(femdatcor)=="BMD_neck_con"] <- "Continous R Femoral Neck BMD"
colnames(femdatcor)[colnames(femdatcor)=="T_neck_con"] <- "Continous R Femoral Neck T-score"
colnames(femdatcor)[colnames(femdatcor)=="Z_neck_con"] <- "Continous R Femoral Neck Z-score"
colnames(femdatcor)[colnames(femdatcor)=="fem_mx_lng"] <- "FemMxLng"
colnames(femdatcor)[colnames(femdatcor)=="fem_sub_tr_ap_dia"] <- "FemSubTrAPDia"
colnames(femdatcor)[colnames(femdatcor)=="fem_sub_tr_ml_dia"] <- "FemSubTrMLDia"
colnames(femdatcor)[colnames(femdatcor)=="fem_head_si_dia"] <- "FemHeadSIDi"
colnames(femdatcor)[colnames(femdatcor)=="fem_neck_sl"] <- "FemNeckSL"
colnames(femdatcor)[colnames(femdatcor)=="fem_head_hz_dia"] <- "FemHeadHzDia"
colnames(femdatcor)[colnames(femdatcor)=="fem_neck_sl"] <- "FemNeckSL"
colnames(femdatcor)[colnames(femdatcor)=="fem_neck_il"] <- "FemNeckIL"
colnames(femdatcor)[colnames(femdatcor)=="fem_neck_v_dia"] <- "FemNeckVDia"
colnames(femdatcor)[colnames(femdatcor)=="fem_neck_t_dia"] <- "FemNeckTDia"
colnames(femdatcor)[colnames(femdatcor)=="fnal_cent"] <- "FNALCent"
colnames(femdatcor)[colnames(femdatcor)=="fnal_apex"] <- "FNALApex"
colnames(femdatcor)[colnames(femdatcor)=="off"] <- "OFF"
colnames(femdatcor)[colnames(femdatcor)=="neck_shaft_angle"] <- "Neck-Shaft Angle"
colnames(femdatcor)[colnames(femdatcor)=="pi_mean_slice"] <- "Mean Parabolic Index"
colnames(femdatcor)[colnames(femdatcor)=="imin_mean_ctan"] <- "Mean Imin"
colnames(femdatcor)[colnames(femdatcor)=="imax_mean_ctan"] <- "Mean Imax"
colnames(femdatcor)[colnames(femdatcor)=="j_mean_ctan"] <- "Mean J"
colnames(femdatcor)[colnames(femdatcor)=="ecc"] <- "Mean Eccentricity"
colnames(femdatcor)[colnames(femdatcor)=="cs.th"] <- "Cross-sectional Thickness"
colnames(femdatcor)[colnames(femdatcor)=="rcv"] <- "Relative Cortical Volume"
#Run correlation matrix
fem.cor<-cor(femdatcor, use = "complete.obs")
write.csv(as.matrix(fem.cor), file = "femCovariateCorrelations.csv", na = "")
#Get p-values
fem.cor.p<-cor_pmat(femdatcor)
write.csv(as.matrix(rib.cor.p), file = "femCovariateCorrelationsPvalue.csv", na = "")
#Correlation matrix in situ
ggcorrplot(fem.cor,hc.order = FALSE,
        outline.col = "white",
        ggtheme = ggplot2::theme_gray,
         colors = c("#D55E00", "white", "#009E73"),
         lab = TRUE, type = "lower",lab_size = 2.8)
#Correlation matrix re-ordered
ggcorrplot(fem.cor,hc.order = TRUE,
        outline.col = "white",
        ggtheme = ggplot2::theme_gray,
         colors = c("#D55E00", "white", "#009E73"),
        lab = TRUE,type = "lower",lab_size = 2.8)
#Non-significant correlation blanked out for non-sig p values
ggcorrplot(fem.cor,hc.order = FALSE,
        outline.col = "white",
        ggtheme = ggplot2::theme_gray,
         colors = c("#D55E00", "white", "#009E73"),
        lab = TRUE,type = "lower", p.mat=fem.cor.p,insig = "blank",lab_size = 2.8)
```

520

Correlation Matrices Between Co-Variates and Total Pore Morphometry Variables in the Rib

```
#Read in whole pore data set
ribdat <- read.csv(file="rib_base_numeric_pores_whole_load.csv", stringsAsFactors=TRUE)
femdatvar <- read.csv(file="femoral_base_numeric_pores_whole_only.csv", stringsAsFactors=TRUE)
##Pore Dependent Variable Correlation Matrix – Rib
#Remove non-numeric vars
ribdatcor<-subset(ribdat, select = -c(ID,newID,region,regioncode,type,sex,BMI_cat,T_total_cat,
rca_mean_stack,rca_mean_slice,imin_mean_bonej,j_mean_bonej, imax_mean_bonej))
sapply(ribdatcor, class)
#Create a named version of data set
colnames(ribdatcor)[colnames(ribdatcor)=="age"] <- "Age"
colnames(ribdatcor)[colnames(ribdatcor)=="weight"] <- "Weight"
colnames(ribdatcor)[colnames(ribdatcor)=="height"] <- "Height"
colnames(ribdatcor)[colnames(ribdatcor)=="BMI_con"] <- "Continous BMI"
colnames(ribdatcor)[colnames(ribdatcor)=="BMD_total_con"] <- "Continous Total BMD"
colnames(ribdatcor)[colnames(ribdatcor)=="T_total_con"] <- "Continous Total T-score"
colnames(ribdatcor)[colnames(ribdatcor)=="Z_total_con"] <- "Continous Total Z-score"
colnames(ribdatcor)[colnames(ribdatcor)=="pi_mean_slice"] <- "Mean Parabolic Index"
colnames(ribdatcor)[colnames(ribdatcor)=="imin_mean_ctan"] <- "Mean Imin"
colnames(ribdatcor)[colnames(ribdatcor)=="imax_mean_ctan"] <- "Mean Imax"
colnames(ribdatcor)[colnames(ribdatcor)=="j_mean_ctan"] <- "Mean J"
colnames(ribdatcor)[colnames(ribdatcor)=="ecc"] <- "Mean Eccentricity"
colnames(ribdatcor)[colnames(ribdatcor)=="cs.th"] <- "Cross-sectional Thickness"
colnames(ribdatcor)[colnames(ribdatcor)=="rcv"] <- "Relative Cortical Volume"
colnames(ribdatcor)[colnames(ribdatcor)=="fractal_dimension_cortex"] <- "Cortical Fractal Dimension"
colnames(ribdatcor)[colnames(ribdatcor)=="percent_closed_porosity"] <- "% Closed Porosity"
colnames(ribdatcor)[colnames(ribdatcor)=="percent_open_porosity"] <- "% Open Porosity"
colnames(ribdatcor)[colnames(ribdatcor)=="percent_porosity"] <- "% Porosity"
colnames(ribdatcor)[colnames(ribdatcor)=="structure_thickness"] <- "Pore Thickness"
colnames(ribdatcor)[colnames(ribdatcor)=="structure_separation"] <- "Pore Separation"
colnames(ribdatcor)[colnames(ribdatcor)=="structure_linear_density"] <- "Structure Linear Density"
colnames(ribdatcor)[colnames(ribdatcor)=="fragmentation_index"] <- "Fragmentation Index"
colnames(ribdatcor)[colnames(ribdatcor)=="fractal_dimension_pores"] <- "Pore Network Fractal
Dimension"
colnames(ribdatcor)[colnames(ribdatcor)=="connectivity_density"] <- "Connectivity Density"
colnames(ribdatcor)[colnames(ribdatcor)=="stdv_structure_thickeness"] <- "StDv Pore Thickness"
colnames(ribdatcor)[colnames(ribdatcor)=="stdv_structure_separation"] <- "StDv Pore Separation"
colnames(ribdatcor)[colnames(ribdatcor)=="percent_open_pores"] <- "Proportion Open Pores"
colnames(ribdatcor)[colnames(ribdatcor)=="percent_closed_pores"] <- "Proportion Closed Pores"
colnames(ribdatcor)[colnames(ribdatcor)=="pore_density"] <- "Pore Density"
#Run correlation matrix
rib.cor<-cor(ribdatcor, use = "p")
write.csv(as.matrix(rib.cor), file = "RibCovariateCorrelations.csv", na = "")
#Get p-values
rib.cor.p<-cor_pmat(ribdatcor)
write.csv(as.matrix(rib.cor.p), file = "RibCovariateCorrelationsPvalue.csv", na = "")

#Correlation matrix in situ
ggcorrplot(rib.cor,hc.order = FALSE,
```

```
            outline.col = "white",
            ggtheme = ggplot2::theme_gray,
             colors = c("#D55E00", "white", "#009E73"),
            lab = TRUE, type = "upper", lab_size = 2.3)
#Correlation matrix re-ordered
ggcorrplot(rib.cor,hc.order = TRUE,
            outline.col = "white",
            ggtheme = ggplot2::theme_gray,
             colors = c("#D55E00", "white", "#009E73"),
            lab = TRUE,type = "lower")
#Non-significant correlation blanked out for non-sig p values
ggcorrplot(rib.cor,hc.order = FALSE,
            outline.col = "white",
            ggtheme = ggplot2::theme_gray,
             colors = c("#D55E00", "white", "#009E73"),
            lab = TRUE,type = "lower", p.mat=rib.cor.p,insig = "blank")
##Pore Dependent Variable Correlation Matrix – Femoral Neck
#Remove non-numeric vars
femdatcor<-subset(femdatvar, select = -c(region,type,ID,newID,sex,BMI_cat,T_total_cat,T_neck_cat,
rca_mean_stack,rca_mean_slice,imin_mean_bonej,j_mean_bonej, imax_mean_bonej))
sapply(femdatcor, class)
#Create a named version of data set
colnames(femdatcor)[colnames(femdatcor)=="age"] <- "Age"
colnames(femdatcor)[colnames(femdatcor)=="weight"] <- "Weight"
colnames(femdatcor)[colnames(femdatcor)=="height"] <- "Height"
colnames(femdatcor)[colnames(femdatcor)=="BMI_con"] <- "Continous BMI"
colnames(femdatcor)[colnames(femdatcor)=="BMD_total_con"] <- "Continous Total BMD"
colnames(femdatcor)[colnames(femdatcor)=="T_total_con"] <- "Continous Total T-score"
colnames(femdatcor)[colnames(femdatcor)=="Z_total_con"] <- "Continous Total Z-score"
colnames(femdatcor)[colnames(femdatcor)=="BMD_neck_con"] <- "Continous R Femoral Neck BMD"
colnames(femdatcor)[colnames(femdatcor)=="T_neck_con"] <- "Continous R Femoral Neck T-score"
colnames(femdatcor)[colnames(femdatcor)=="Z_neck_con"] <- "Continous R Femoral Neck Z-score"
colnames(femdatcor)[colnames(femdatcor)=="fem_mx_lng"] <- "FemMxLng"
colnames(femdatcor)[colnames(femdatcor)=="fem_sub_tr_ap_dia"] <- "FemSubTrAPDia"
colnames(femdatcor)[colnames(femdatcor)=="fem_sub_tr_ml_dia"] <- "FemSubTrMLDia"
colnames(femdatcor)[colnames(femdatcor)=="fem_head_si_dia"] <- "FemHeadSIDi"
colnames(femdatcor)[colnames(femdatcor)=="fem_neck_sl"] <- "FemNeckSL"
colnames(femdatcor)[colnames(femdatcor)=="fem_head_hz_dia"] <- "FemHeadHzDia"
colnames(femdatcor)[colnames(femdatcor)=="fem_neck_sl"] <- "FemNeckSL"
colnames(femdatcor)[colnames(femdatcor)=="fem_neck_il"] <- "FemNeckIL"
colnames(femdatcor)[colnames(femdatcor)=="fem_neck_v_dia"] <- "FemNeckVDia"
colnames(femdatcor)[colnames(femdatcor)=="fem_neck_t_dia"] <- "FemNeckTDia"
colnames(femdatcor)[colnames(femdatcor)=="fnal_cent"] <- "FNALCent"
colnames(femdatcor)[colnames(femdatcor)=="fnal_apex"] <- "FNALApex"
colnames(femdatcor)[colnames(femdatcor)=="off"] <- "OFF"
colnames(femdatcor)[colnames(femdatcor)=="neck_shaft_angle"] <- "Neck-Shaft Angle"
colnames(femdatcor)[colnames(femdatcor)=="pi_mean_slice"] <- "Mean Parabolic Index"
colnames(femdatcor)[colnames(femdatcor)=="imin_mean_ctan"] <- "Mean Imin"
colnames(femdatcor)[colnames(femdatcor)=="imax_mean_ctan"] <- "Mean Imax"
colnames(femdatcor)[colnames(femdatcor)=="j_mean_ctan"] <- "Mean J"
colnames(femdatcor)[colnames(femdatcor)=="ecc"] <- "Mean Eccentricity"
colnames(femdatcor)[colnames(femdatcor)=="cs.th"] <- "Cross-sectional Thickness"
colnames(femdatcor)[colnames(femdatcor)=="rca_vol"] <- "Relative Cortical Volume"
```

```
colnames(femdatcor)[colnames(femdatcor)=="fractal_dimension_cortex"] <- "Cortical Fractal Dimension"
colnames(femdatcor)[colnames(femdatcor)=="percent_closed_porosity"] <- "% Closed Porosity"
colnames(femdatcor)[colnames(femdatcor)=="percent_open_porosity"] <- "% Open Porosity"
colnames(femdatcor)[colnames(femdatcor)=="percent_porosity"] <- "% Porosity"
colnames(femdatcor)[colnames(femdatcor)=="structure_thickness"] <- "Pore Thickness"
colnames(femdatcor)[colnames(femdatcor)=="structure_separation"] <- "Pore Separation"
colnames(femdatcor)[colnames(femdatcor)=="structure_linear_density"] <- "Structure Linear Density"
colnames(femdatcor)[colnames(femdatcor)=="fragmentation_index"] <- "Fragmentation Index"
colnames(femdatcor)[colnames(femdatcor)=="fractal_dimension_pores"] <- "Pore Network Fractal
Dimension"
colnames(femdatcor)[colnames(femdatcor)=="connectivity_density"] <- "Connectivity Density"
colnames(femdatcor)[colnames(femdatcor)=="stdv_structure_thickeness"] <- "StDv Pore Thickness"
colnames(femdatcor)[colnames(femdatcor)=="stdv_structure_separation"] <- "StDv Pore Separation"
colnames(femdatcor)[colnames(femdatcor)=="percent_open_pores"] <- "Proportion Open Pores"
colnames(femdatcor)[colnames(femdatcor)=="percent_closed_pores"] <- "Proportion Closed Pores"
colnames(femdatcor)[colnames(femdatcor)=="pore_density"] <- "Pore Density"


#Run correlation matrix
fem.cor<-cor(femdatcor , use = "complete.obs")
write.csv(as.matrix(fem.cor), file = "FemPoreCovariateCorrelations.csv", na = "")
#Get p-values
fem.cor.p<-cor_pmat(femdatcor)
write.csv(as.matrix(rib.cor.p), file = "femCovariateCorrelationsPvalue.csv", na = "")
#Correlation matrix in situ
ggcorrplot(fem.cor,hc.order = FALSE,
          outline.col = "white",
          ggtheme = ggplot2::theme_gray,
           colors = c("#D55E00", "white", "#009E73"),
           lab = TRUE, type = "lower",lab_size = 2)


#Correlation matrix re-ordered
ggcorrplot(fem.cor,hc.order = TRUE,
          outline.col = "white",
          ggtheme = ggplot2::theme_gray,
           colors = c("#D55E00", "white", "#009E73"),
          lab = TRUE,type = "lower",lab_size = 2)
#Non-significant correlation blanked out for non-sig p values
ggcorrplot(fem.cor,hc.order = FALSE,
          outline.col = "white",
          ggtheme = ggplot2::theme_gray,
           colors = c("#D55E00", "white", "#009E73"),
          lab = TRUE,type = "lower", p.mat=fem.cor.p,insig = "blank",lab_size = 2)
```

T-Test for Sex Differences in Co-Variates and Pore Morphometry

```
## T-test for Sex
#Remove non-numeric variables
ribdatnum<-subset(ribdat, select = -c(ID,newID,region,regioncode,type,sex,BMI_cat,T_total_cat,
rca_mean_stack,rca_mean_slice,imin_mean_bonej,j_mean_bonej, imax_mean_bonej))
colnames(ribdatnum)[colnames(ribdatnum)=="sex"] <- "Sex"
colnames(ribdatnum)[colnames(ribdatnum)=="age"] <- "Age"
colnames(ribdatnum)[colnames(ribdatnum)=="weight"] <- "Weight"
colnames(ribdatnum)[colnames(ribdatnum)=="height"] <- "Height"
colnames(ribdatnum)[colnames(ribdatnum)=="BMI_con"] <- "Continous BMI"
colnames(ribdatnum)[colnames(ribdatnum)=="BMD_total_con"] <- "Continous Total BMD"
colnames(ribdatnum)[colnames(ribdatnum)=="T_total_con"] <- "Continous Total T-score"
colnames(ribdatnum)[colnames(ribdatnum)=="Z_total_con"] <- "Continous Total Z-score"
colnames(ribdatnum)[colnames(ribdatnum)=="pi_mean_slice"] <- "Mean Parabolic Index"
colnames(ribdatnum)[colnames(ribdatnum)=="imin_mean_ctan"] <- "Mean Imin"
colnames(ribdatnum)[colnames(ribdatnum)=="imax_mean_ctan"] <- "Mean Imax"
colnames(ribdatnum)[colnames(ribdatnum)=="j_mean_ctan"] <- "Mean J"
colnames(ribdatnum)[colnames(ribdatnum)=="ecc"] <- "Mean Eccentricity"
colnames(ribdatnum)[colnames(ribdatnum)=="cs.th"] <- "Cross-sectional Thickness"
colnames(ribdatnum)[colnames(ribdatnum)=="rcv"] <- "Relative Cortical Volume"
colnames(ribdatnum)[colnames(ribdatnum)=="fractal_dimension_cortex"] <- "Cortical Fractal Dimension"
colnames(ribdatnum)[colnames(ribdatnum)=="percent_closed_porosity"] <- "% Closed Porosity"
colnames(ribdatnum)[colnames(ribdatnum)=="percent_open_porosity"] <- "% Open Porosity"
colnames(ribdatnum)[colnames(ribdatnum)=="percent_porosity"] <- "% Porosity"
colnames(ribdatnum)[colnames(ribdatnum)=="structure_thickness"] <- "Pore Thickness"
colnames(ribdatnum)[colnames(ribdatnum)=="structure_separation"] <- "Pore Separation"
colnames(ribdatnum)[colnames(ribdatnum)=="structure_linear_density"] <- "Structure Linear Density"
colnames(ribdatnum)[colnames(ribdatnum)=="fragmentation_index"] <- "Fragmentation Index"
colnames(ribdatnum)[colnames(ribdatnum)=="fractal_dimension_pores"] <- "Pore Network Fractal
Dimension"
colnames(ribdatnum)[colnames(ribdatnum)=="connectivity_density"] <- "Connectivity Density"
colnames(ribdatnum)[colnames(ribdatnum)=="stdv_structure_thickeness"] <- "StDv Pore Thickness"
colnames(ribdatnum)[colnames(ribdatnum)=="stdv_structure_separation"] <- "StDv Pore Separation"
colnames(ribdatnum)[colnames(ribdatnum)=="percent_open_pores"] <- "Proportion Open Pores"
colnames(ribdatnum)[colnames(ribdatnum)=="percent_closed_pores"] <- "Proportion Closed Pores"
colnames(ribdatnum)[colnames(ribdatnum)=="pore_density"] <- "Pore Density"
sext <- data.frame(p.value= sapply(ribdatnum[,1:ncol(ribdatnum)], function(i) t.test(i ~ ribdat$sex, na.rm =
TRUE)$p.value))
write.csv(as.matrix(sext), file = "RibCovariatesMorphometrySex.csv", na = "")
##Sex
#Calculate for variables without NA for 39F
sext <- data.frame(p.value= sapply(ribdatnum[,8:ncol(ribdatnum)], function(i) t.test(i ~ ribdat$sex, na.rm =
TRUE,  paired = TRUE, alternative = "two.sided")$p.value))
write.csv(as.matrix(sext), file = "RibCovariatesMorphometrySex.csv", na = "")
#Manually pull remaining variables with NA for 39F
sextNA <- data.frame(p.value= sapply(ribdatnum[1:12,1:7], function(i) t.test(i ~ ribdat[1:12,]$sex, na.rm =
TRUE,  paired = TRUE, alternative = "two.sided")$p.value))
write.csv(as.matrix(sextNA), file = "RibCovariatesMorphometrySexNA.csv", na = "")
#Wilcoxon test for non-normal variables
ribdatf <- subset(ribdat, sex == "F")
ribdatm <- subset(ribdat, sex == "M")
wilcox.test(ribdatf[1:13,]$height, ribdatm[1:13,]$height,
```

524

```
        mu = 0, paired = TRUE, exact = FALSE, correct = TRUE,
        conf.int = TRUE, conf.level = 0.95, alternative = "two.sided",)
wilcox.test(ribdatf$ecc, ribdatm$ecc,
        mu = 0, paired = TRUE, exact = FALSE, correct = TRUE,
        conf.int = TRUE, conf.level = 0.95,  alternative = "two.sided",)
femdat <- read.csv(file="femoral_base_numeric_pores_whole_only.csv", stringsAsFactors=TRUE)
## T-test for Sex - Femoral Neck
#Remove non-numeric variables
femdatnum<-subset(femdat, select = -c(ID,newID,region,type,sex,BMI_cat,T_total_cat, T_neck_cat,
rca_mean_stack,rca_mean_slice,imin_mean_bonej,j_mean_bonej, imax_mean_bonej))
colnames(femdatnum)[colnames(femdatnum)=="sex"] <- "Sex"
colnames(femdatnum)[colnames(femdatnum)=="age"] <- "Age"
colnames(femdatnum)[colnames(femdatnum)=="weight"] <- "Weight"
colnames(femdatnum)[colnames(femdatnum)=="height"] <- "Height"
colnames(femdatnum)[colnames(femdatnum)=="BMI_con"] <- "Continous BMI"
colnames(femdatnum)[colnames(femdatnum)=="BMD_total_con"] <- "Continous Total BMD"
colnames(femdatnum)[colnames(femdatnum)=="T_total_con"] <- "Continous Total T-score"
colnames(femdatnum)[colnames(femdatnum)=="Z_total_con"] <- "Continous Total Z-score"
colnames(femdatnum)[colnames(femdatnum)=="fem_mx_lng"] <- "FemMxLng"
colnames(femdatnum)[colnames(femdatnum)=="fem_sub_tr_ap_dia"] <- "FemSubTrAPDia"
colnames(femdatnum)[colnames(femdatnum)=="fem_sub_tr_ml_dia"] <- "FemSubTrMLDia"
colnames(femdatnum)[colnames(femdatnum)=="fem_head_si_dia"] <- "FemHeadSIDi"
colnames(femdatnum)[colnames(femdatnum)=="fem_neck_sl"] <- "FemNeckSL"
colnames(femdatnum)[colnames(femdatnum)=="fem_head_hz_dia"] <- "FemHeadHzDia"
colnames(femdatnum)[colnames(femdatnum)=="fem_neck_sl"] <- "FemNeckSL"
colnames(femdatnum)[colnames(femdatnum)=="fem_neck_il"] <- "FemNeckIL"
colnames(femdatnum)[colnames(femdatnum)=="fem_neck_v_dia"] <- "FemNeckVDia"
colnames(femdatnum)[colnames(femdatnum)=="fem_neck_t_dia"] <- "FemNeckTDia"
colnames(femdatnum)[colnames(femdatnum)=="fnal_cent"] <- "FNALCent"
colnames(femdatnum)[colnames(femdatnum)=="fnal_apex"] <- "FNALApex"
colnames(femdatnum)[colnames(femdatnum)=="off"] <- "OFF"
colnames(femdatnum)[colnames(femdatnum)=="neck_shaft_angle"] <- "Neck-Shaft Angle"
colnames(femdatnum)[colnames(femdatnum)=="pi_mean_slice"] <- "Mean Parabolic Index"
colnames(femdatnum)[colnames(femdatnum)=="imin_mean_ctan"] <- "Mean Imin"
colnames(femdatnum)[colnames(femdatnum)=="imax_mean_ctan"] <- "Mean Imax"
colnames(femdatnum)[colnames(femdatnum)=="j_mean_ctan"] <- "Mean J"
colnames(femdatnum)[colnames(femdatnum)=="ecc"] <- "Mean Eccentricity"
colnames(femdatnum)[colnames(femdatnum)=="cs.th"] <- "Cross-sectional Thickness"
colnames(femdatnum)[colnames(femdatnum)=="rcv"] <- "Relative Cortical Volume"
colnames(femdatnum)[colnames(femdatnum)=="fractal_dimension_cortex"] <- "Cortical Fractal
Dimension"
colnames(femdatnum)[colnames(femdatnum)=="percent_closed_porosity"] <- "% Closed Porosity"
colnames(femdatnum)[colnames(femdatnum)=="percent_open_porosity"] <- "% Open Porosity"
colnames(femdatnum)[colnames(femdatnum)=="percent_porosity"] <- "% Porosity"
colnames(femdatnum)[colnames(femdatnum)=="structure_thickness"] <- "Pore Thickness"
colnames(femdatnum)[colnames(femdatnum)=="structure_separation"] <- "Pore Separation"
colnames(femdatnum)[colnames(femdatnum)=="structure_linear_density"] <- "Structure Linear Density"
colnames(femdatnum)[colnames(femdatnum)=="fragmentation_index"] <- "Fragmentation Index"
colnames(femdatnum)[colnames(femdatnum)=="fractal_dimension_pores"] <- "Pore Network Fractal
Dimension"
colnames(femdatnum)[colnames(femdatnum)=="connectivity_density"] <- "Connectivity Density"
colnames(femdatnum)[colnames(femdatnum)=="stdv_structure_thickeness"] <- "StDv Pore Thickness"
colnames(femdatnum)[colnames(femdatnum)=="stdv_structure_separation"] <- "StDv Pore Separation"
```

525

```
colnames(femdatnum)[colnames(femdatnum)=="percent_open_pores"] <- "Proportion Open Pores"
colnames(femdatnum)[colnames(femdatnum)=="percent_closed_pores"] <- "Proportion Closed Pores"
colnames(femdatnum)[colnames(femdatnum)=="pore_density"] <- "Pore Density"
#Wilcoxon Test Across Table
lapply(femdatnum, function(x) wilcox.test(x ~ femdat$sex, alternative="two.sided", exact = FALSE,
correct = TRUE,
        conf.int = TRUE, conf.level = 0.95,  data=femdatnum))
#Call summary statistics for sex differences, such as:
sexstat<-data.frame(describeBy(ribdat$"% Porosity",  ribdat$Sex, mat = TRUE))
write.csv(as.matrix(sexstat), file = "Sexstat.csv", na = "")
```

Sample Linear Mixed Model Code with R_2 and Cohen's d

```
#Purpose: Assessing Influence of Bone Type and Pore Type on Pore Morphometry
#Set working directory
setwd("G:/Temp Dissertation Storage/Analysis Tables/Base Tables for R Modification/Finished Tables")
df <- read.csv(file="allpores.csv", stringsAsFactors=TRUE)
#Set type III anova contrasts
options(contrasts=c("contr.sum", "contr.poly"))
#Extract whole, total porosity for rib and femoral neck
dftot <- filter(df, region=="whole" & type!="total")
#Drop unused levels
dftot$type<-droplevels(dftot)$type
dftot$bone<-droplevels(dftot)$bone
#Linear model for repeated measures
a<-lme(fractal_dimension_cortex ~ bone + type + age * cs.th * sex, random = ~ 1 | ID, data = dftot, method
= "REML", na.action = na.exclude)
#Associated ANOVA
csva<-data.frame(anova(a))
#Cohen's D for effect size
cohen<-lme.dscore(a,dftot,"nlme")
cohent<-c(NA,cohen$t)
cohendf<-c(NA,cohen$df)
cohend<-c(NA,cohen$d)
#Add to matrix
csva$"cohen t"<-cohent
csva$"cohen df"<-cohendf
csva$"cohen d"<-cohend
#pseudo R2, with AIC corrected for small sample size
csvr<-rsquared(a)
csva[10,1]<-csvr$Marginal
csva[11,1]<-csvr$Conditional
rownames(csva)[10]<-"Marginal R2"
rownames(csva)[11]<-"Conditional R2"
#Test residuals for normality
qqnorm(resid(a))
qqline(resid(a))
norm<-shapiro.test(resid(a))
csva[12,1]<-norm$p.value
rownames(csva)[12]<-"Shapiro-Wilk Normality"
write.csv(as.matrix(csva), file = "anova.csv", na = "")
```

Sample PQL General Linear Mixed Model with R_2 and Cohen's d

#Purpose: Assessing Influence of Bone Type and Pore Type on Pore Morphometry when residuals from LMM fail Shapiro-Wilk Normality Test

```
PQL <- glmmPQL(percent_open_porosity ~ bone * type + age * cs.th * sex, ~1 | ID, family = gaussian(link = "log"),
    data = dftot, verbose = FALSE)
a<-summary(PQL)
csva<-data.frame(a$tTable)

#Cohen's D for effect size
cohen<-lme.dscore(PQL,dftot,"nlme")
cohent<-c(NA,cohen$t)
cohendf<-c(NA,cohen$df)
cohend<-c(NA,cohen$d)
#Add to matrix
csva$"cohen t"<-cohent
csva$"cohen df"<-cohendf
csva$"cohen d"<-cohend
#pseudo R2 for glmmPQL models
r2<-r2beta(PQL, partial=TRUE)
csva[12,1]<-r2$Rsq[1]
rownames(csva)[12]<-"R2"
write.csv(as.matrix(csva), file = "PQL.csv", na = "")
```

Calculate Pore Morphotype Medians Across Table

```
setwd("G:/Temp Dissertation Storage/Analysis Tables/Base Tables for R Modification/Finished Tables")
df <- read.csv(file="allpores_clipped.csv", stringsAsFactors=TRUE)
#Filter whole pores
#Whole rib and femoral neck
ribtot <-filter(df, bone=="rib" & type=="total" & region =="whole")
ribtotM <- filter(df, bone=="rib" & type=="total" & region =="whole" & sex =="M")
ribtotF <- filter(df, bone=="rib" & type=="total" & region =="whole" & sex =="F")
femtot <-filter(df, bone=="femoralneck" & type=="total" & region =="whole")
femtotM <- filter(df, bone=="femoralneck" & type=="total" & region =="whole" & sex =="M")
femtotF <- filter(df, bone=="femoralneck" & type=="total" & region =="whole" & sex =="F")
#Whole rib + cort
ribC  <-filter(df, bone=="rib" & type=="cortical" & region =="whole")
ribCM <- filter(df, bone=="rib" & type=="cortical" & region =="whole" & sex =="M")
ribCF <- filter(df, bone=="rib" & type=="cortical" & region =="whole" & sex =="F")
#Whole rib + trab
ribT <- filter(df, bone=="rib" & type=="trabecularized" & region =="whole")
ribTM <- filter(df, bone=="rib" & type=="trabecularized" & region =="whole" & sex =="M")
ribTF <- filter(df, bone=="rib" & type=="trabecularized" & region =="whole" & sex =="F")
#Whole fem + cort
femC <- filter(df, bone=="femoralneck" & type=="cortical" & region =="whole")
femCM <- filter(df, bone=="femoralneck" & type=="cortical" & region =="whole" & sex =="M")
femCF<- filter(df, bone=="femoralneck" & type=="cortical" & region =="whole" & sex =="F")
#Whole fem + trab
femT <- filter(df, bone=="femoralneck" & type=="trabecularized" & region =="whole")
femTM <- filter(df, bone=="femoralneck" & type=="trabecularized" & region =="whole" & sex =="M")
femTF <- filter(df, bone=="femoralneck" & type=="trabecularized" & region =="whole" & sex =="F")
mdf <- data.frame(Date=as.Date(character()),
          File=character(),
          User=character(),
          stringsAsFactors=FALSE)
a<-dplyr::summarise_each(ribtot, funs(mean))
b<-dplyr::summarise_each(ribtotM, funs(mean))
c<-dplyr::summarise_each(ribtotF, funs(mean))
d<-dplyr::summarise_each(ribC, funs(mean))
e<-dplyr::summarise_each(ribCM, funs(mean))
f<-dplyr::summarise_each(ribCF, funs(mean))
g<-dplyr::summarise_each(ribT, funs(mean))
h<-dplyr::summarise_each(ribTM, funs(mean))
i<-dplyr::summarise_each(ribTF, funs(mean))
j<-dplyr::summarise_each(femtot, funs(mean))
k<-dplyr::summarise_each(femtotM, funs(mean))
l<-dplyr::summarise_each(femtotF, funs(mean))
m<-dplyr::summarise_each(femC, funs(mean))
n<-dplyr::summarise_each(femCM, funs(mean))
o<-dplyr::summarise_each(femCF, funs(mean))
p<-dplyr::summarise_each(femT, funs(mean))
q<-dplyr::summarise_each(femTM, funs(mean))
r<-dplyr::summarise_each(femTF, funs(mean))
out<-rbind(a,b,c,d,e,f,g,h,i,j,k,l,m,n,o,p,q,r)
write.csv(as.matrix(out), file = "bonemedians.csv", na = "")
```

529

Sample Plots for Bone Type vs. Pore Type

```r
setwd("G:/Temp Dissertation Storage/Analysis Tables/Base Tables for R Modification/Finished Tables")
df <- read.csv(file="allpores_clipped.csv", stringsAsFactors=TRUE)
dfw<-filter(df, region =="whole")
#Rename levels
dfw$type <- factor(dfw$type, levels = c("total","cortical","trabecularized"))
levels(dfw$type) <- c("Total","Cortical","Trabecularized")
dfw$bone<-droplevels(dfw)$bone
levels(dfw$bone) <- c("Femoral Neck", "Rib")
#Categorical
var<-"Pore Network Fractal Dimension"
g<-ggplot(dfw, aes(x = type, y = fractal_dimension_pores, color = sex)) +
geom_jitter(size = 2, alpha = 0.6)
g + stat_summary(fun.y = median,  geom = "point", aes(group = interaction(type, sex)), shape = 95, size =
12, show.legend = F)+
stat_summary(fun.y = median,  geom = "point", aes(group = type), shape = 95, size = 12, show.legend =
F)+
facet_grid(.~bone ) +
labs(title = var, fill = "Sex", x = "Pore Type", y = var) +
geom_text(aes(label=newID),hjust=0, vjust=0)+
theme(legend.position = "none")+
theme(plot.title = element_text(hjust = 0.5))+
scale_y_continuous(breaks = scales::pretty_breaks(n = 10))
#Age Effects
setwd("G:/Temp Dissertation Storage/Analysis Tables/Base Tables for R Modification/Finished Tables")
df <- read.csv(file="allpores_clipped.csv", stringsAsFactors=TRUE)
dfw2<-filter(df, region =="whole" & type=="total")
var<-"Standard Deviation of Pore Separation (um)"
g <- ggplot(dfw2, aes(x=age, y=stdv_structure_separation, color=sex)) + geom_point(shape=16) +
geom_smooth(method=loess)
g+labs(title = var, fill = "Sex", x = "Age", y = var) +
geom_text(aes(label=newID),hjust=0, vjust=0,check_overlap = TRUE)+
theme(legend.position = "none")+
theme(plot.title = element_text(hjust = 0.5))+
scale_y_continuous(breaks = scales::pretty_breaks(n = 10))+
scale_x_continuous(breaks = scales::pretty_breaks(n = 10))
#Cortical Thickness Effects
dfw2<-filter(df, region =="whole" & type=="cortical")
dfw$type<-droplevels(dfw)$type
dfw2$cs.th_mm<-dfw2$cs.th/1000
var<-"Connectivity Density (1/um) of Cortical Pores"
g <- ggplot(dfw2, aes(x=cs.th_mm, y=pore_connectivit, color=sex)) + geom_point(shape=16) +
geom_smooth(method=loess)
g+labs(title = var, fill = "Sex", x = "Cross-Sectional Thickness (mm)", y = var) +
geom_text(aes(label=newID),hjust=0, vjust=0,check_overlap = TRUE)+
theme(legend.position = "none")+
theme(plot.title = element_text(hjust = 0.5))+
scale_y_continuous(breaks = scales::pretty_breaks(n = 10))+
scale_x_continuous(breaks = scales::pretty_breaks(n = 10))
```

530

Sample Linear Mixed Model for Femoral Neck Octant Comparisons with Posthoc

```
setwd("G:/Temp Dissertation Storage/Analysis Tables/Base Tables for R Modification/Finished Tables")
df <- read.csv(file="allpores_clipped.csv", stringsAsFactors=TRUE)
#Isolate octants dataset
oct<-filter(df, region =="octant")
oct$octant<-droplevels(oct)$octant

#Linear model for repeated measures
a<-lme(fractal_dimension_pores ~ octant + age * cs.th * sex, random = ~ 1 | ID, data = oct, method =
"REML", na.action = na.exclude)
#Associated ANOVA
csva<-data.frame(anova(a))
#Cohen's D for effect size
cohen<-lme.dscore(a,oct,"nlme")
#Bind to lower half of data frame
csva.sub<-csva[c(1,3:9),]
cohen.sub<-cohen[8:14,]
empty<-c(NA,NA,NA)
cohen.bind<-rbind(empty,cohen.sub)
bind<-cbind(csva.sub,cohen.bind)
#Bind octant terms
csva.top<-csva[2,]
csva.top[2:7,]<-NA
cohen.top<-cohen[1:7,]
bind2<-cbind(csva.top,cohen.top)
out<-rbind(bind,bind2)
rownames(out)[9]<-"Octant 1"
rownames(out)[10]<-"Octant 2"
rownames(out)[11]<-"Octant 3"
rownames(out)[12]<-"Octant 4"
rownames(out)[13]<-"Octant 5"
rownames(out)[14]<-"Octant 6"
rownames(out)[15]<-"Octant 7"
#pseudo R2, with AIC corrected for small sample size
csvr<-rsquared(a)
out[16,1]<-csvr$Marginal
out[17,1]<-csvr$Conditional
rownames(out)[16]<-"Marginal R2"
rownames(out)[17]<-"Conditional R2"
#Test residuals for normality
# plot & test the residual
qqnorm(resid(a))
qqline(resid(a))
norm<-shapiro.test(resid(a))
out[18,1]<-norm$p.value
rownames(out)[18]<-"Shapiro-Wilk Normality"
write.csv(as.matrix(out), file = "unianova.csv", na = "")
#Associated posthoc
post<-emmeans(a, "octant")
pairs<-pairs(post)
out<-data.frame(summary(pairs))
write.csv(as.matrix(out), file = "unianovaposthoc.csv", na = "")
```

Sample PQL General Linear Mixed Model for Correcting Non-Normal Residuals

```
PQL <- glmmPQL(connectivity_density~ octant + age * cs.th * sex, ~1 | ID, family = gaussian(link =
"log"),
    data = oct, verbose = FALSE)

a<-summary(PQL)
csva<-data.frame(a$tTable)

#Cohen's D for effect size
cohen<-lme.dscore(PQL,dfbone,"nlme")

cohent<-c(NA,cohen$t)
cohendf<-c(NA,cohen$df)
cohend<-c(NA,cohen$d)
#Add to matrix
csva$"cohen t"<-cohent
csva$"cohen df"<-cohendf
csva$"cohen d"<-cohend
#pseudo R2, with AIC corrected for small sample size
r2<-r2beta(PQL, partial=TRUE)
csva[16,1]<-r2$Rsq[1]
rownames(csva)[16]<-"R2"
write.csv(as.matrix(csva), file = "UniPQL.csv", na = "")
#Associated posthoc
out<-tidy(summary(glht(PQL, linfct = mcp(octant = "Tukey")), test = adjusted("holm")))
summary(glht(PQL, mcp(octant="Tukey")))
write.csv(as.matrix(out), file = "UniPQLposthoc.csv", na = "")
```

Radar Plot for Comparing Octant Distribution of Pore Morphometry

```
setwd("G:/Temp Dissertation Storage/Analysis Tables/Base Tables for R Modification/Finished Tables")
df <- read.csv(file="allpores_clipped.csv", stringsAsFactors=TRUE)
#Isolate octants dataset
oct<-filter(df, region =="octant")
#Select pore morphotype and reshape columns with octants as column names
myvars <- c("newID", "octant", "connectivity_density")
oct2 <- oct[myvars]
oct3<-oct2 %>% spread(octant, connectivity_density, fill = NA, convert = FALSE)
#Order data for clockwise rotation
oct4<-
oct3[,c("newID","superior","superioranterior","anterior","inferioranterior","inferior","inferiorposterior","po
sterior","superiorposterior")]
oct5<-rename(oct4,
c("superior"="S","superiorposterior"="SP","posterior"="P","inferiorposterior"="IP","inferior"="I","inferior
anterior"="IA","anterior"="A","superioranterior"="SA"))
##Based on design from Matthias Döring at https://www.datascienceblog.net/post/data-visualization/radar-
plot/
mycolor <- "#1c6193"
p <- ggRadar(oct5, aes(group = newID),
   rescale = TRUE, legend.position = "none",
   size = 1, interactive = FALSE, use.label = TRUE, scales="free") +
   facet_wrap(~newID) +
   scale_y_discrete(breaks = NULL) + # don't show ticks
  theme(axis.text.x = element_text(size = 10)) + # larger label sizes
  # adjust colors of radar charts to uniform colors
  scale_fill_manual(values = rep(mycolor, nrow(oct5))) +
  scale_color_manual(values = rep(mycolor, nrow(oct5))) +
   ggtitle("")
print(p)
```

Sample Plots for Octant vs. Pore Morphometry by Sex

```
setwd("G:/Temp Dissertation Storage/Analysis Tables/Base Tables for R Modification/Finished Tables")
df <- read.csv(file="allpores_clipped.csv", stringsAsFactors=TRUE)
#Isolate octants dataset
oct<-filter(df, region =="octant")
var<-"Percent Porosity"
octplot<-oct
octplot$octant<-droplevels(octplot)$octant
octplot$octant<-reorder(octplot$octant, new.order=c("inferior","inferiorposterior",
"posterior","superiorposterior","superior","superioranterior","anterior","inferioranterior"))
levels(octplot$octant) <- c("I","IP","P","SP","S","SA","A","IA")
g<-ggplot(octplot, aes(x = octant, y = percent_porosity, color = sex)) +
geom_jitter(size = 2, alpha = 0.6)
g + stat_summary(fun.y = mean,  geom = "point", aes(group = (sex)), shape = 95, size = 12, show.legend =
F)+
stat_summary(fun.y = mean,  geom = "point", aes(group = octant), shape = 95, size = 12, show.legend =
F)+
labs(title = var, x = "Octant", y = var) +
geom_text(aes(label=newID),hjust=0, vjust=0)+
theme(legend.position = "none")+
theme(plot.title = element_text(hjust = 0.5))+
scale_y_continuous(breaks = scales::pretty_breaks(n = 10))
```

Appendix C: 3D Images of Femoral Neck Samples

The three-dimensional structural thickness morphometry implemented by CT-Analyser generates a grayscale image of each slice in a stack. The local thickness of a pore is represented by a grayscale pixel brightness value. Brighter grayscale values correspond to thicker structures. The three-dimensional image visualization software AvizoFire 8.1 can interpolate the slices in a stack as a three-dimensional image, assigning a look up table (LUT) color value to each discrete grayscale value. The scale for the LUT was determined by the largest mean pore thickness value in the sample, associated with the osteophyte of 70F.

All femoral neck three-dimensional visualizations are viewed from the distal trochanter-adjacent face and are oriented as follows:

Superior

Posterior   **Anterior**

Inferior

Additionally, three-dimensional visualizations were tilted so that the inferior octant appeared closest to the camera. This view facilitates an inferior-to-superior view of pore morphometry along the sample thickness.

535

Correspondance Between Pixel Brightness and Pore Thickness

Gray Level	Thickness Range (um)	Gray Level	Thickness Range (um)	Gray Level	Thickness Range (um)
1	1.2819E+001 - <3.8458E+001	23	5.7688E+002 - <6.0252E+002	45	1.1409E+003 - <1.1666E+003
2	3.8458E+001 - <6.4097E+001	24	6.0252E+002 - <6.2816E+002	46	1.1666E+003 - <1.1922E+003
3	6.4097E+001 - <8.9736E+001	25	6.2816E+002 - <6.5379E+002	47	1.1922E+003 - <1.2179E+003
4	8.9736E+001 - <1.1538E+002	26	6.5379E+002 - <6.7943E+002	48	1.2179E+003 - <1.2435E+003
5	1.1538E+002 - <1.4101E+002	27	6.7943E+002 - <7.0507E+002	49	1.2435E+003 - <1.2691E+003
6	1.4101E+002 - <1.6665E+002	28	7.0507E+002 - <7.3071E+002	50	1.2691E+003 - <1.2948E+003
7	1.6665E+002 - <1.9229E+002	29	7.3071E+002 - <7.5635E+002	51	1.2948E+003 - <1.3204E+003
8	1.9229E+002 - <2.1793E+002	30	7.5635E+002 - <7.8199E+002	52	1.3204E+003 - <1.3460E+003
9	2.1793E+002 - <2.4357E+002	31	7.8199E+002 - <8.0763E+002	53	1.3460E+003 - <1.3717E+003
10	2.4357E+002 - <2.6921E+002	32	8.0763E+002 - <8.3327E+002	54	1.3717E+003 - <1.3973E+003
11	2.6921E+002 - <2.9485E+002	33	8.3327E+002 - <8.5891E+002	55	1.3973E+003 - <1.4230E+003
12	2.9485E+002 - <3.2049E+002	34	8.5891E+002 - <8.8455E+002	56	1.4230E+003 - <1.4486E+003
13	3.2049E+002 - <3.4613E+002	35	8.8455E+002 - <9.1018E+002	57	1.4486E+003 - <1.4742E+003
14	3.4613E+002 - <3.7177E+002	36	9.1018E+002 - <9.3582E+002	58	1.4742E+003 - <1.4999E+003
15	3.7177E+002 - <3.9740E+002	37	9.3582E+002 - <9.6146E+002	59	1.4999E+003 - <1.5255E+003
16	3.9740E+002 - <4.2304E+002	38	9.6146E+002 - <9.8710E+002	60	1.5255E+003 - <1.5512E+003
17	4.2304E+002 - <4.4868E+002	39	9.8710E+002 - <1.0127E+003	61	1.5512E+003 - <1.5768E+003
18	4.4868E+002 - <4.7432E+002	40	1.0127E+003 - <1.0384E+003	62	1.5768E+003 - <1.6024E+003
19	4.7432E+002 - <4.9996E+002	41	1.0384E+003 - <1.0640E+003	63	1.6024E+003 - <1.6281E+003
20	4.9996E+002 - <5.2560E+002	42	1.0640E+003 - <1.0897E+003	64	1.6281E+003 - <1.6537E+003
21	5.2560E+002 - <5.5124E+002	43	1.0897E+003 - <1.1153E+003	65	1.6537E+003 - <1.6794E+003
22	5.5124E+002 - <5.7688E+002	44	1.1153E+003 - <1.1409E+003	66	1.6794E+003 - <1.7050E+003
				67	1.7050E+003 - <1.7306E+003
				68	1.7306E+003 - <1.7563E+003

34M Distal Face View

12 um   885 um   1756 um

10 mm

537

34M Tilted Distal View

12 um   885 um   1756 um

10 mm

538

39F Distal Face View

12 um   885 um   1756 um

5 mm

539
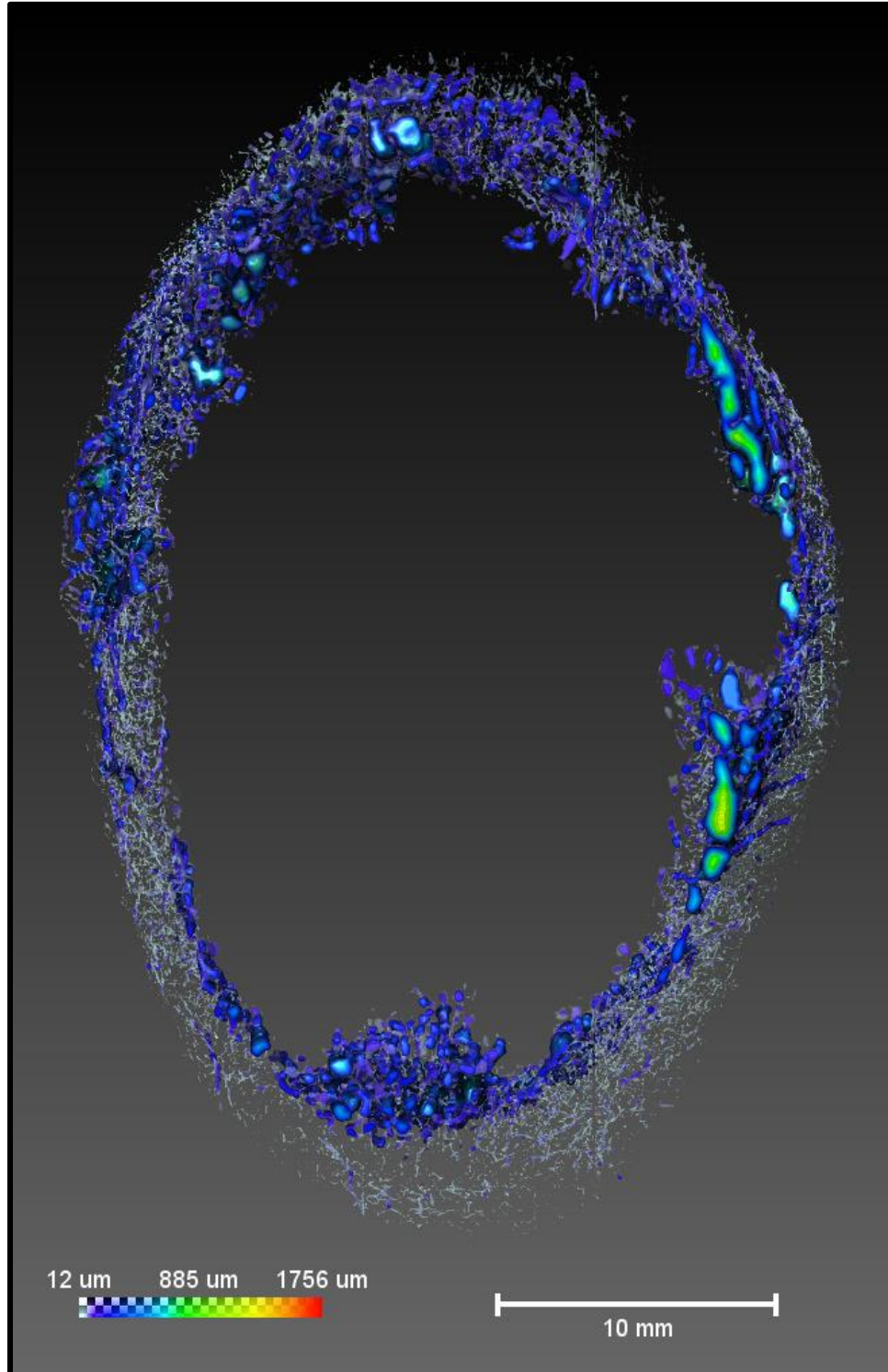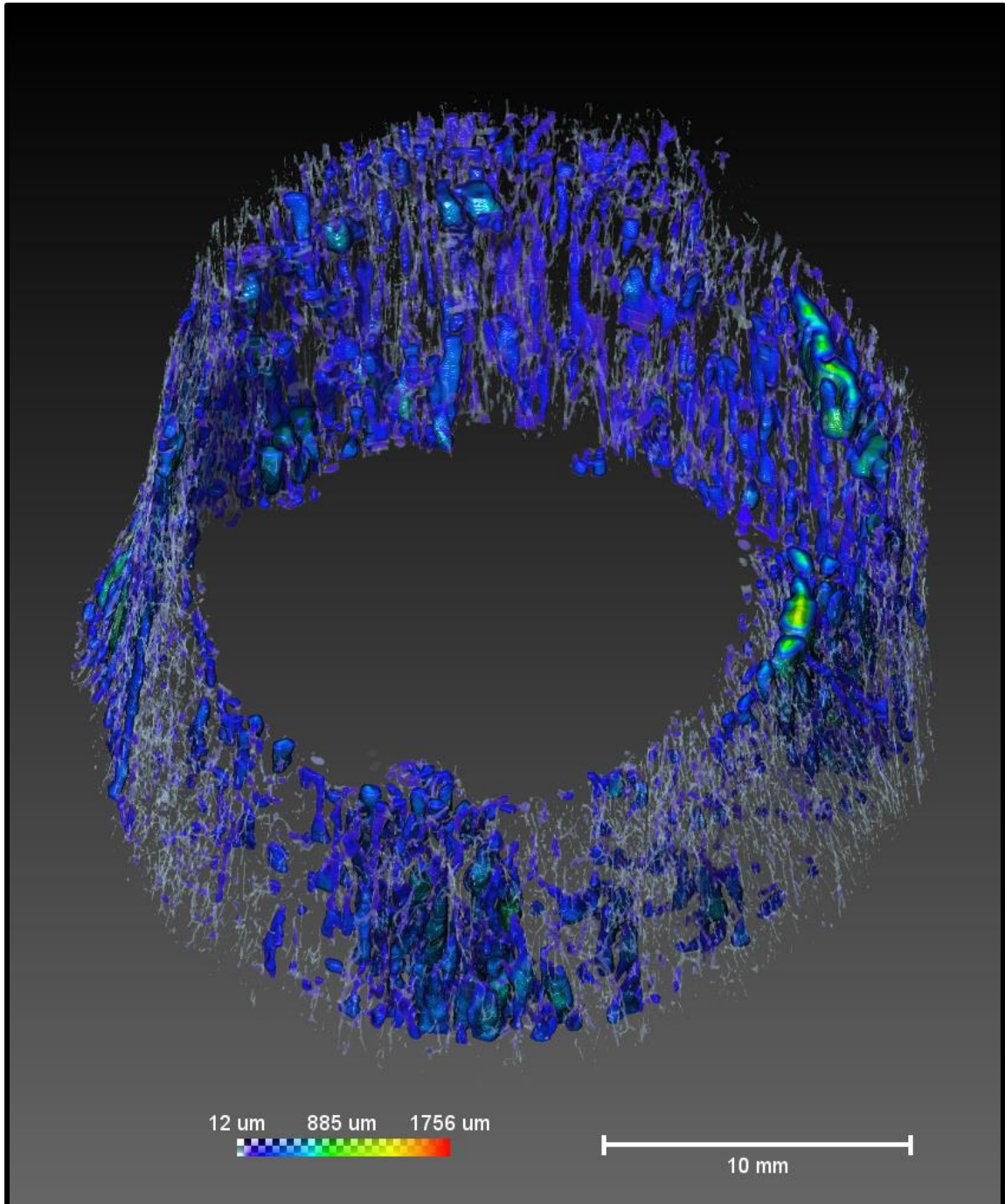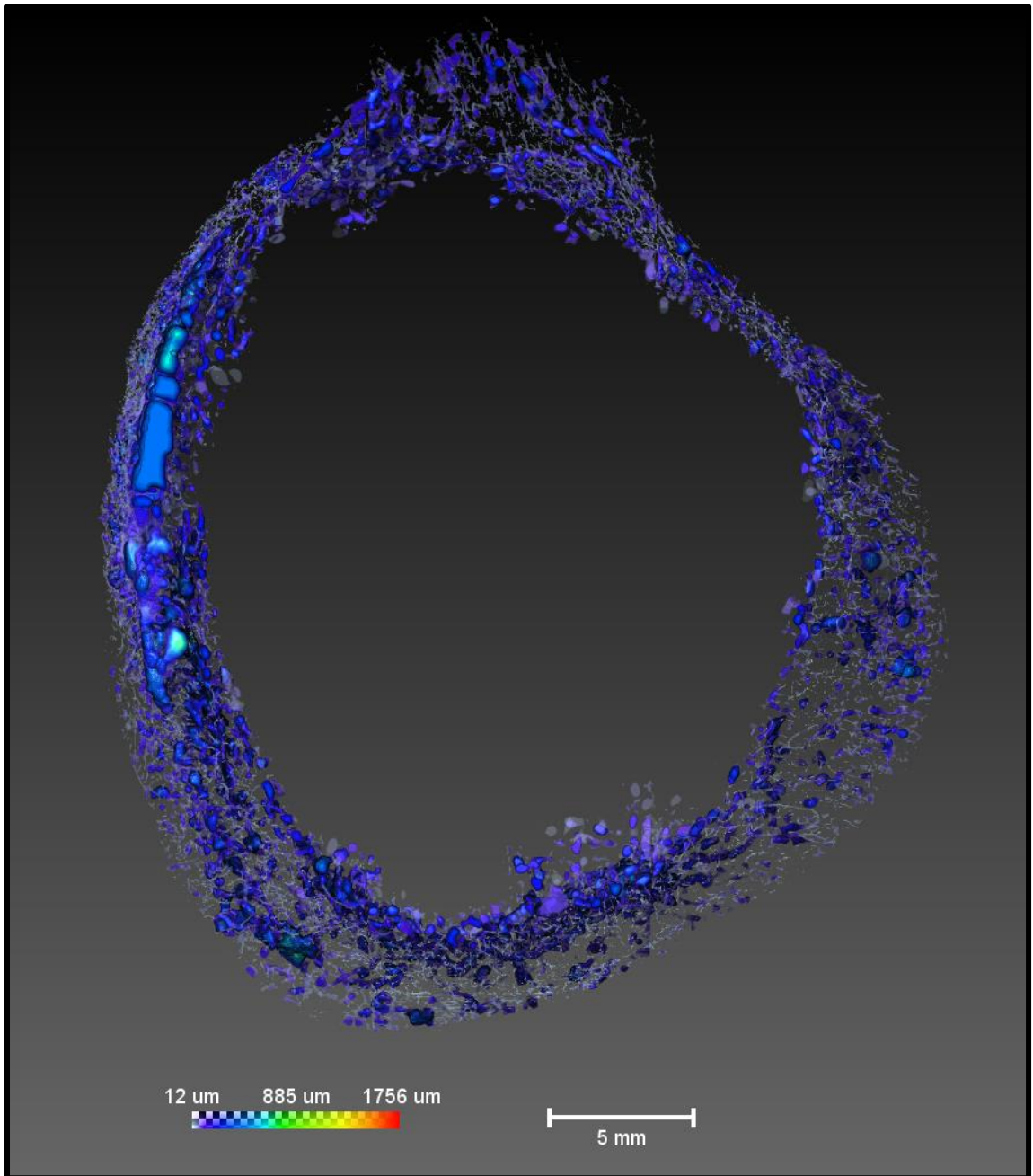
39F Tilted Distal View

49F Distal Face View

12 um   885 um   1756 um

10 mm

541

49F Tilted Distal View

12 um   885 um   1756 um

10 mm

542
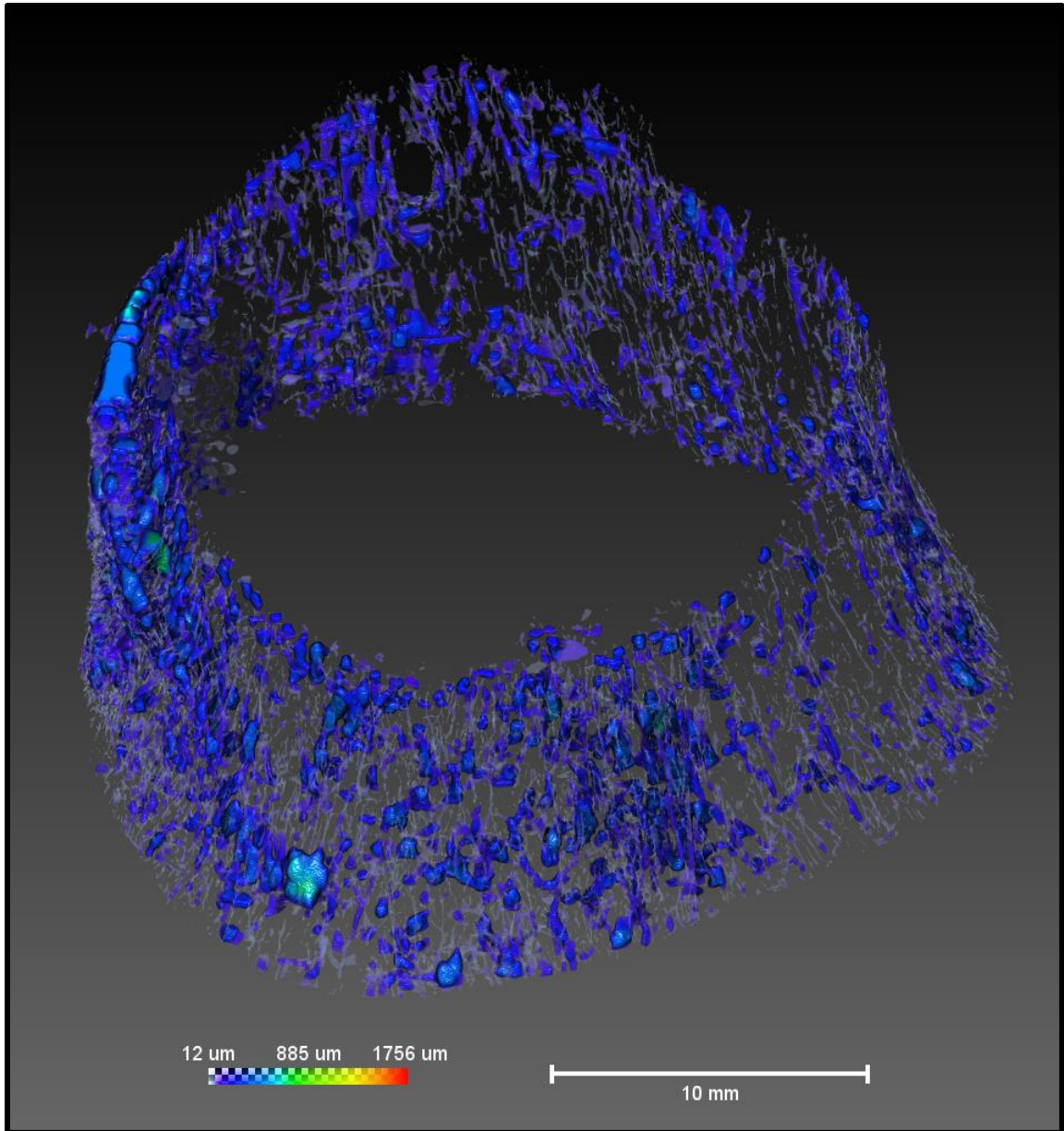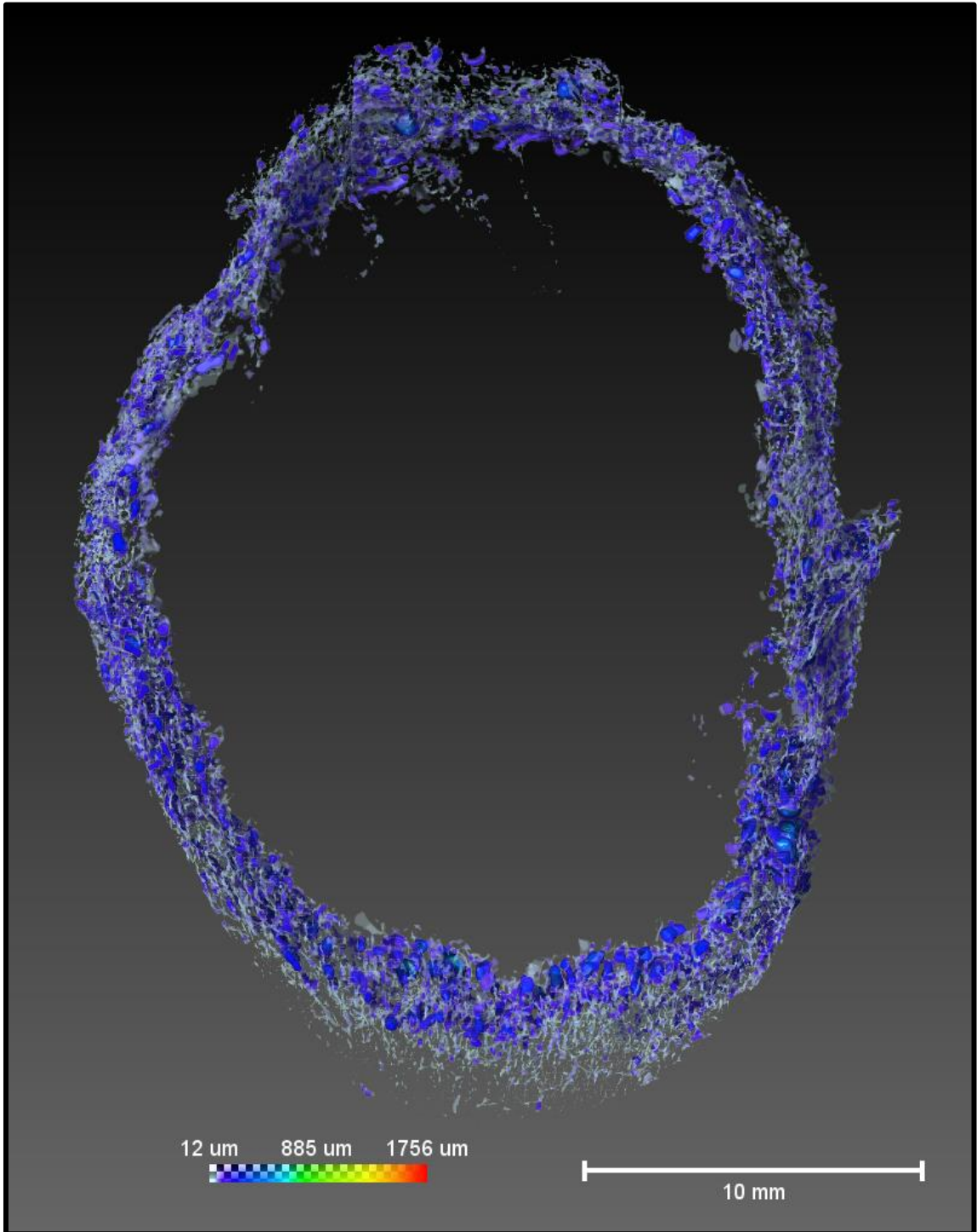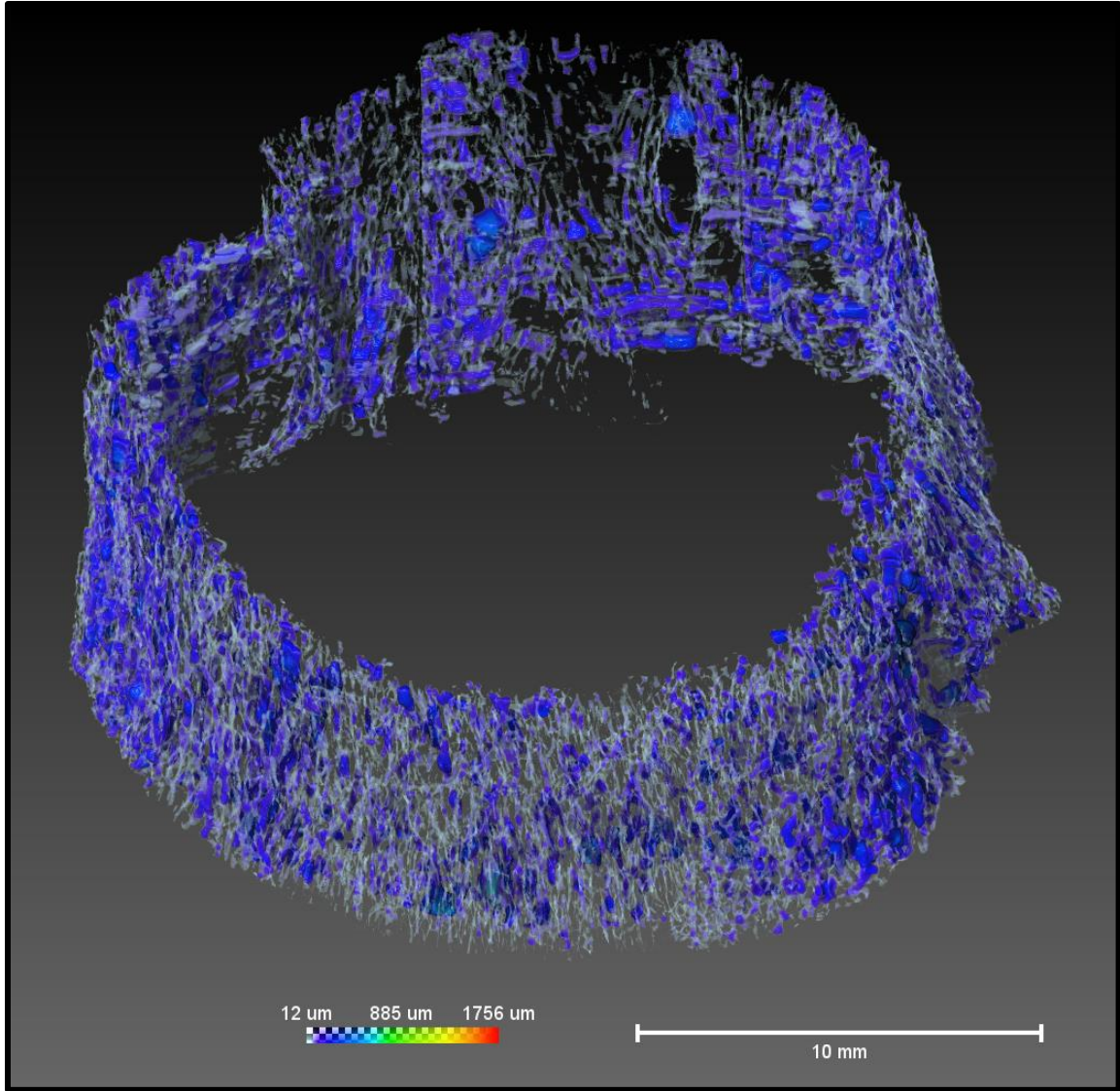
50F Distal Face View

50F Tilted Distal View

12 um 885 um 1756 um

10 mm

544
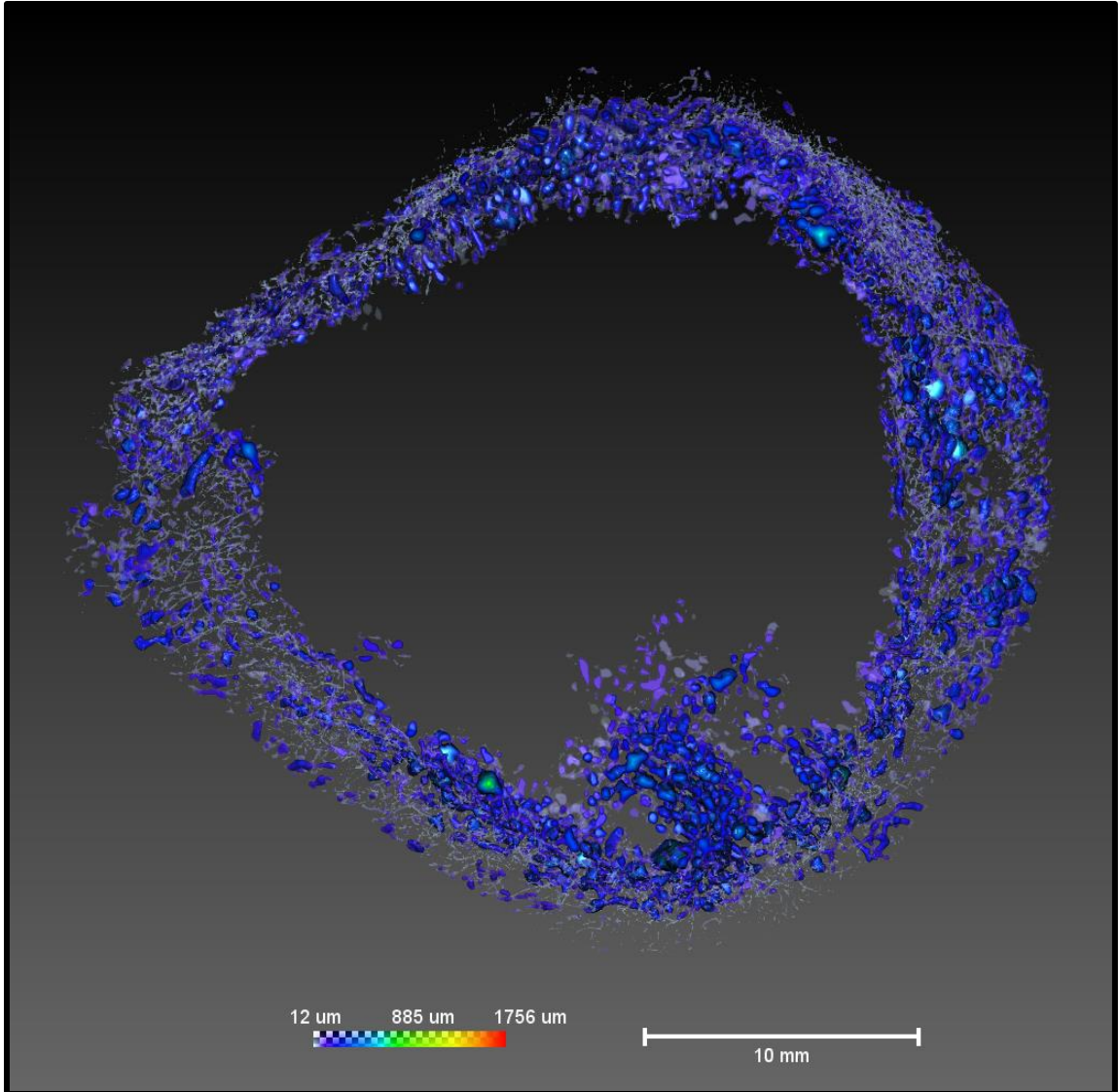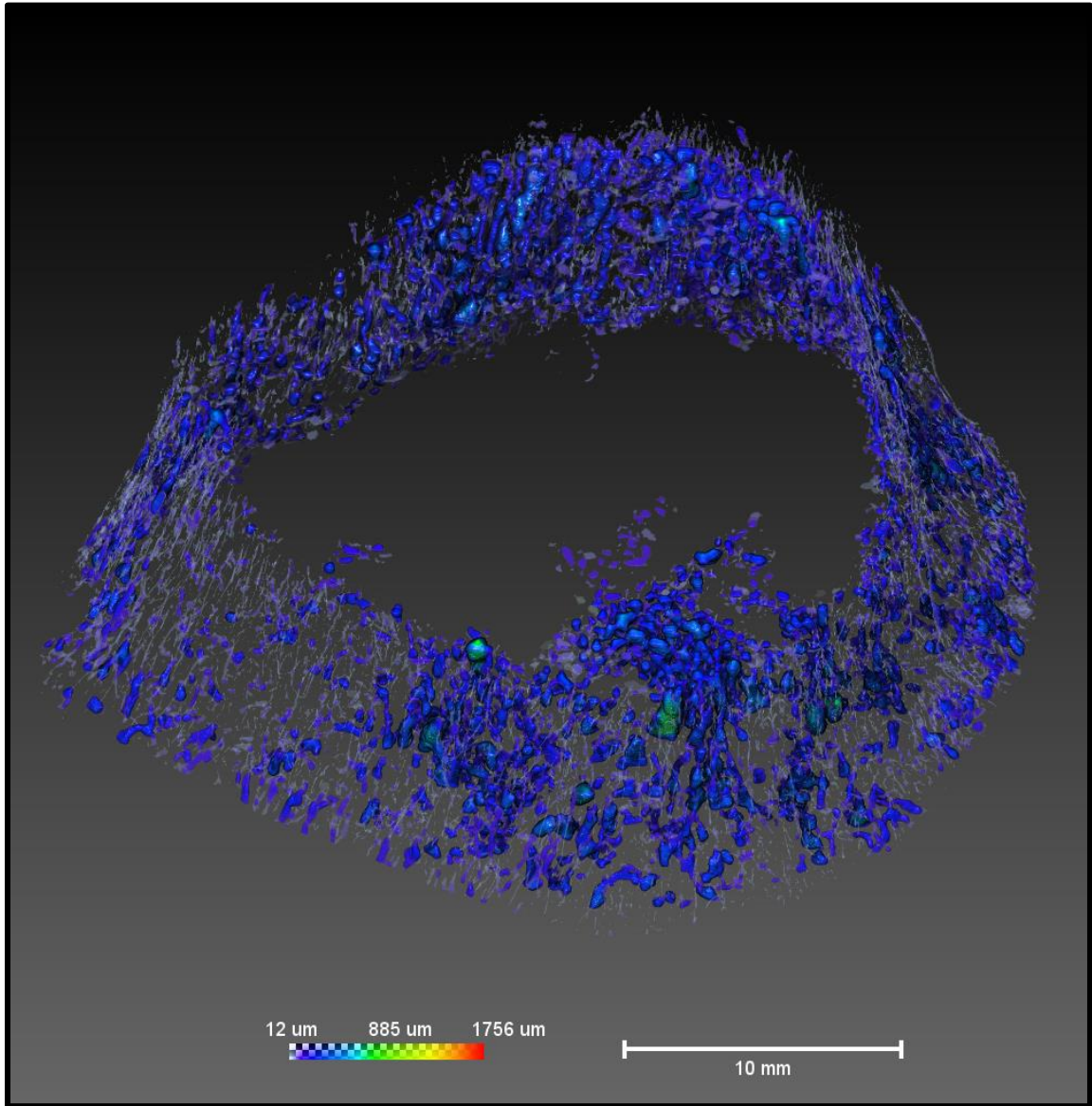
56M Distal Face View

56M Tilted Distal View

546

60F Distal Face View

12 um   885 um   1756 um

10 mm

547
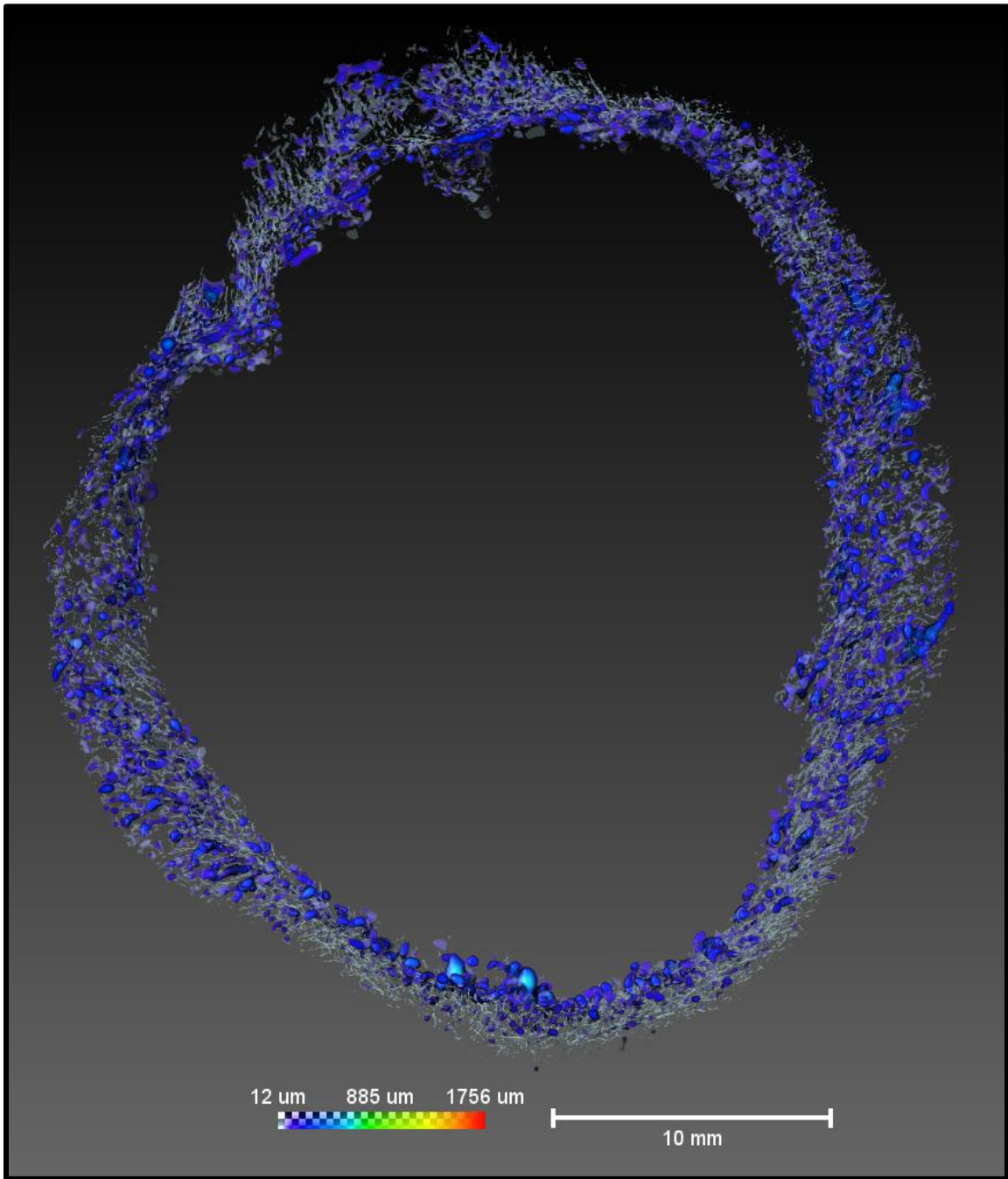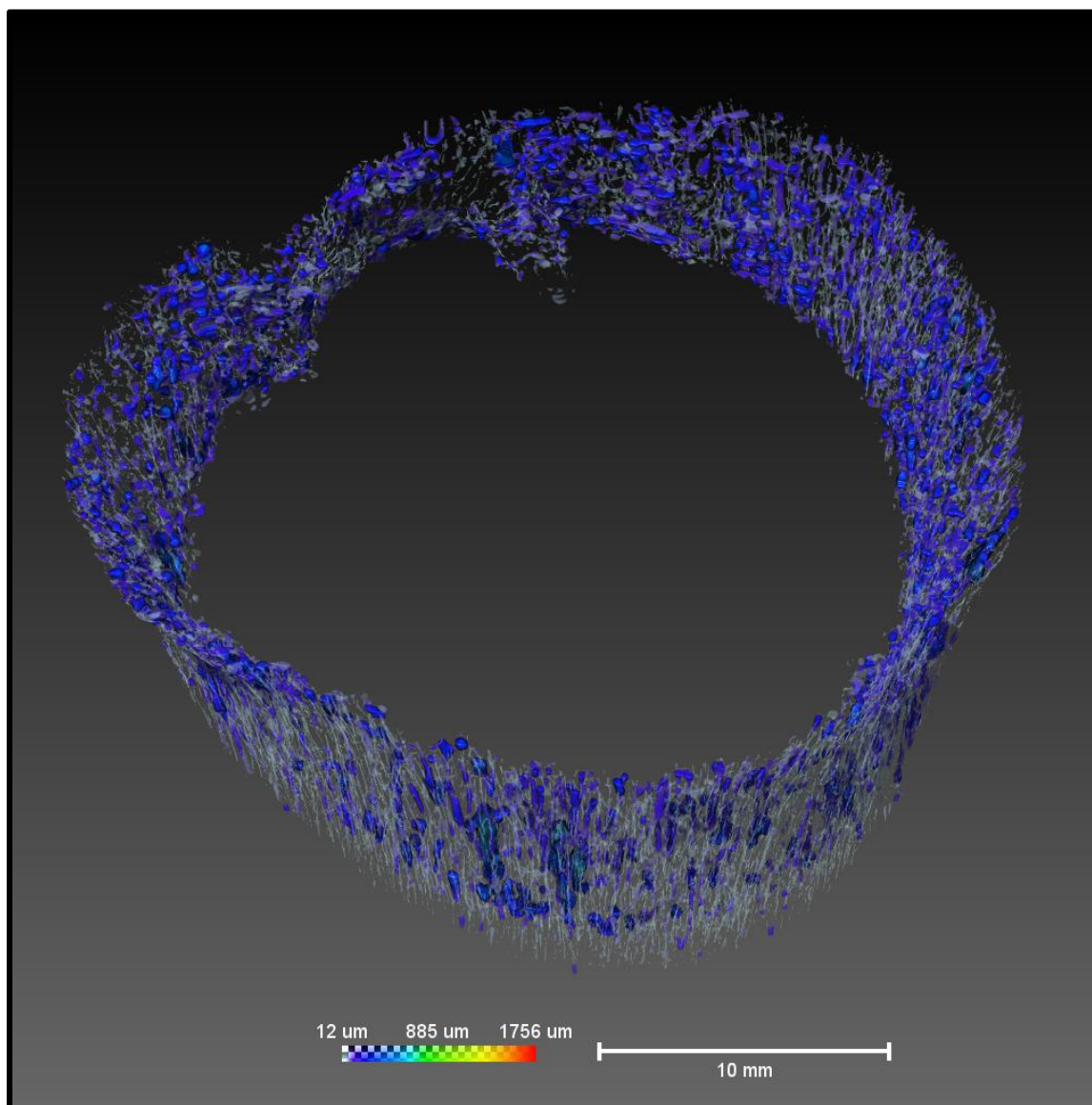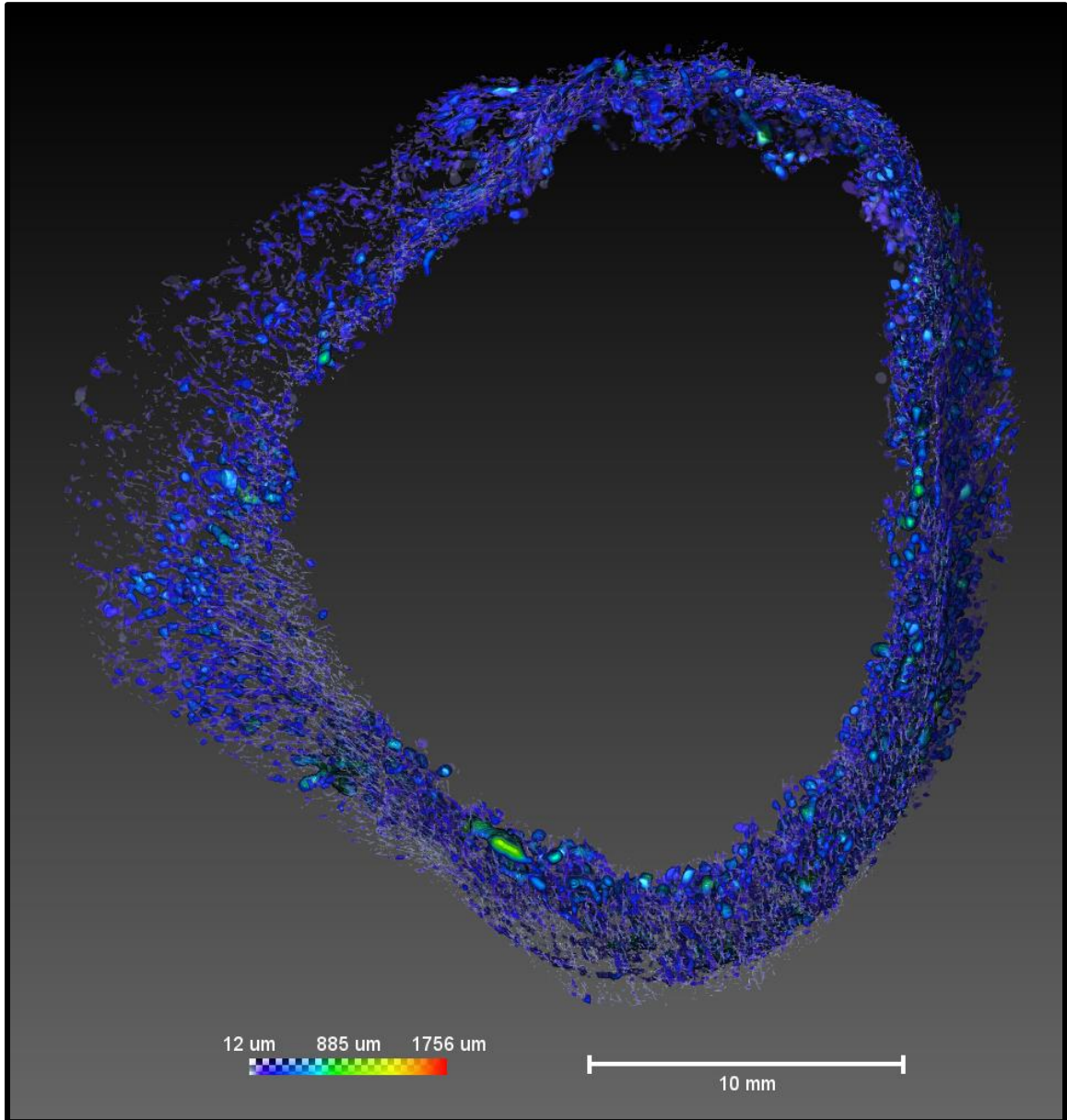
60F Tilted Distal View

67M Distal Face View
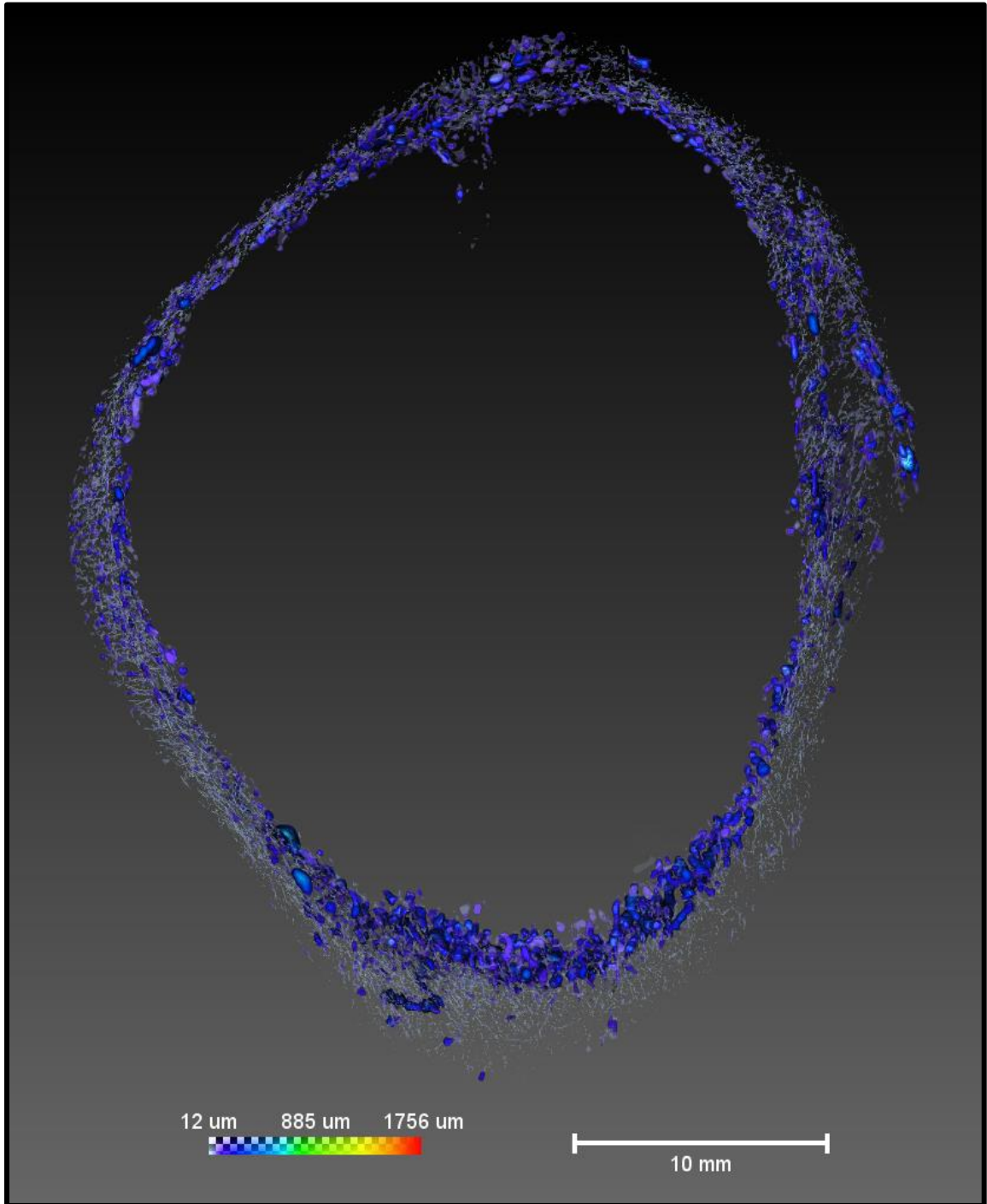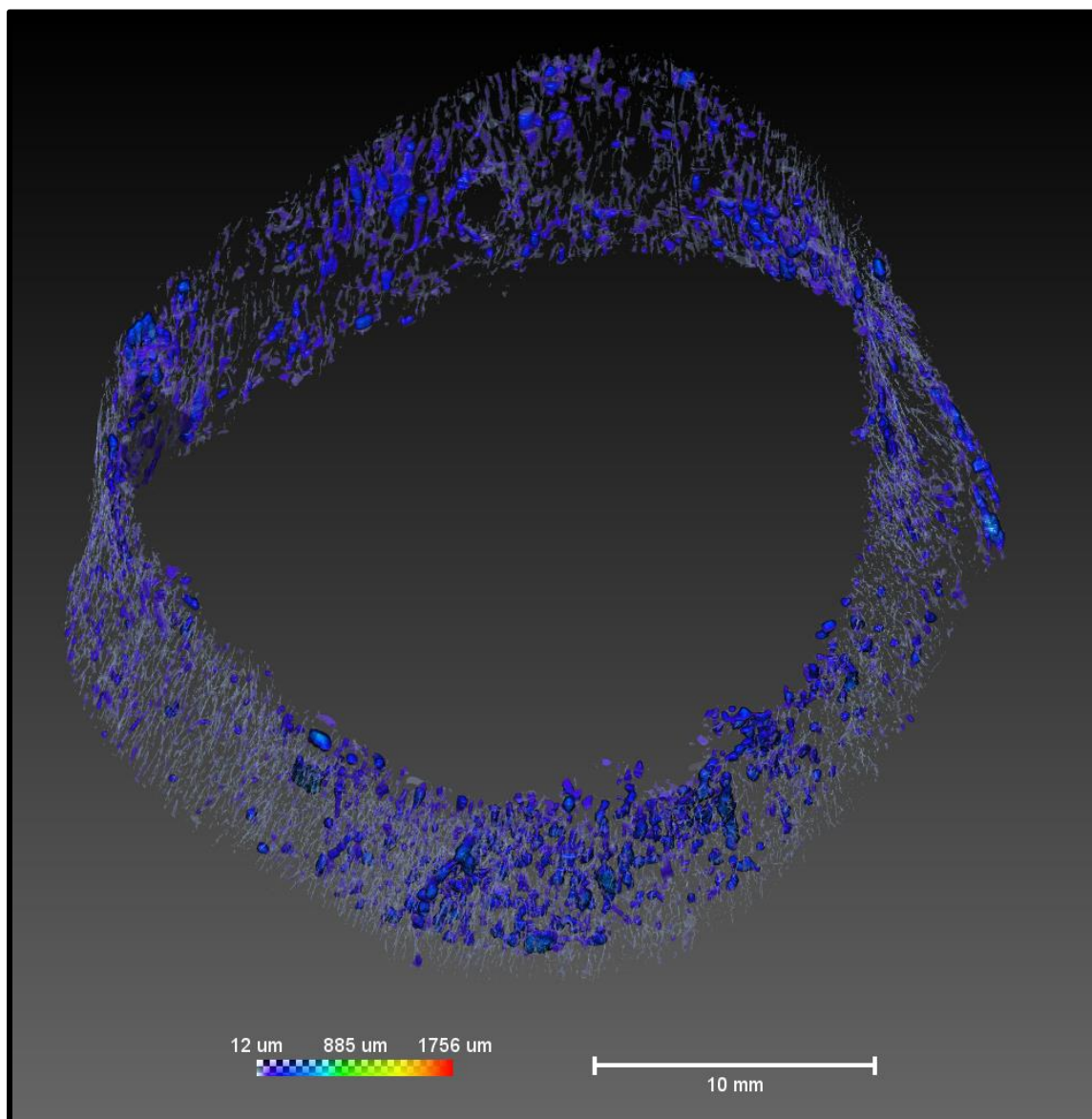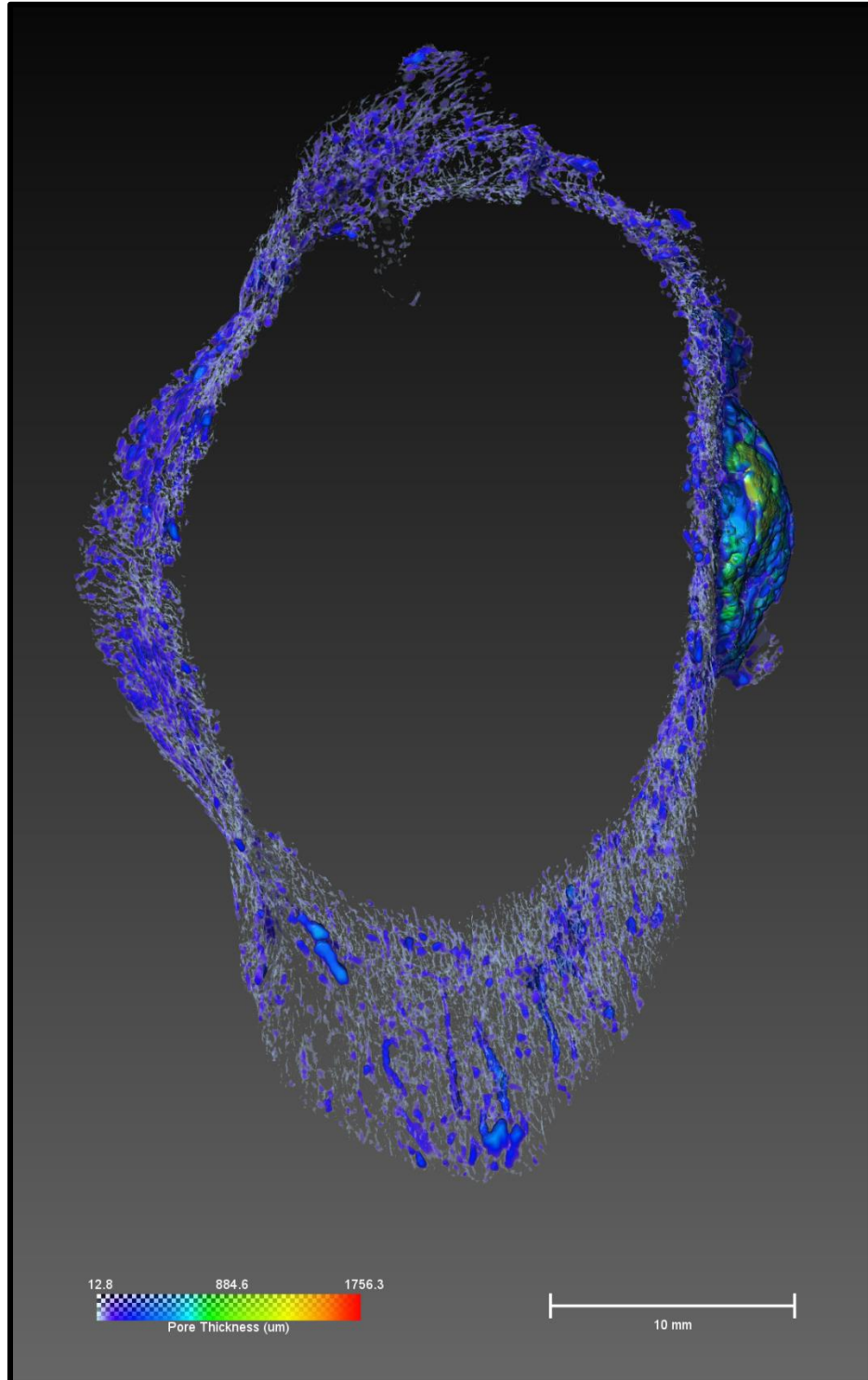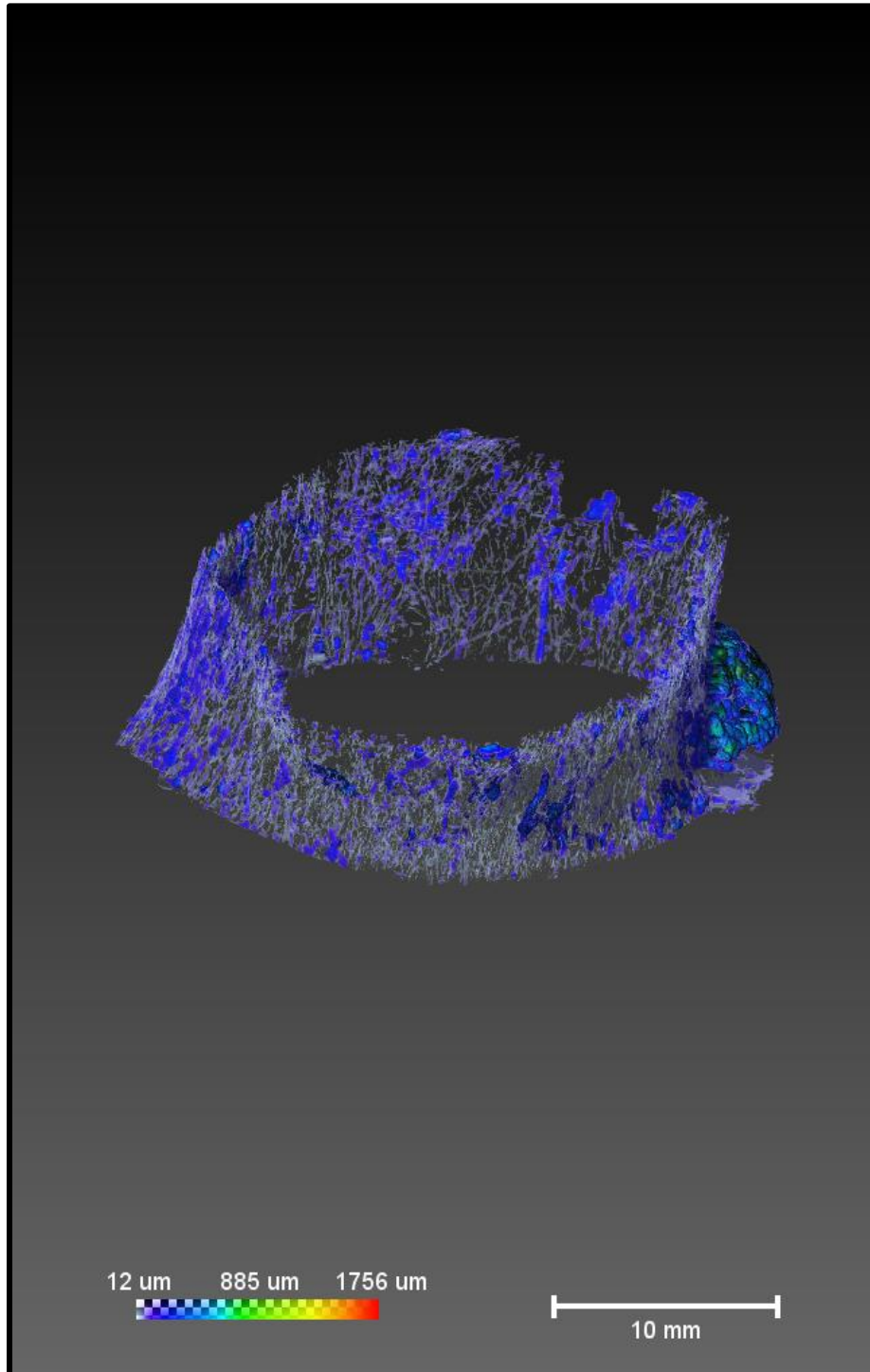
12 um   885 um   1756 um

10 mm

549

67M Tilted Distal View

550

70F Distal Face View

551

70F Tilted Distal View

552

77M Distal Face View

12 um   885 um   1756 um

10 mm

553

77M Tilted Distal View

12 um   885 um   1756 um

10 mm

82F Tilted Distal View

12 um   885 um   1756 um

10 mm

556
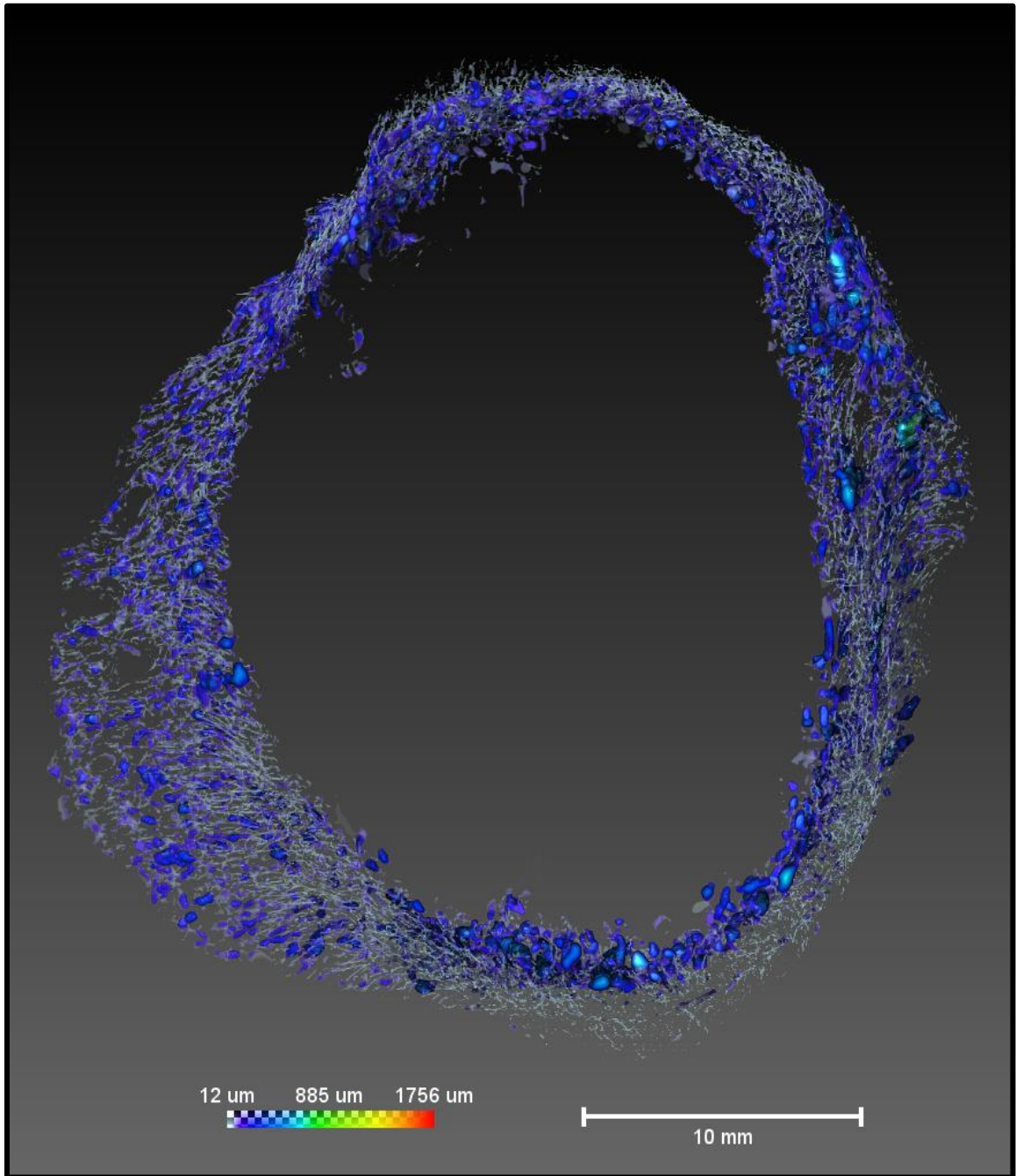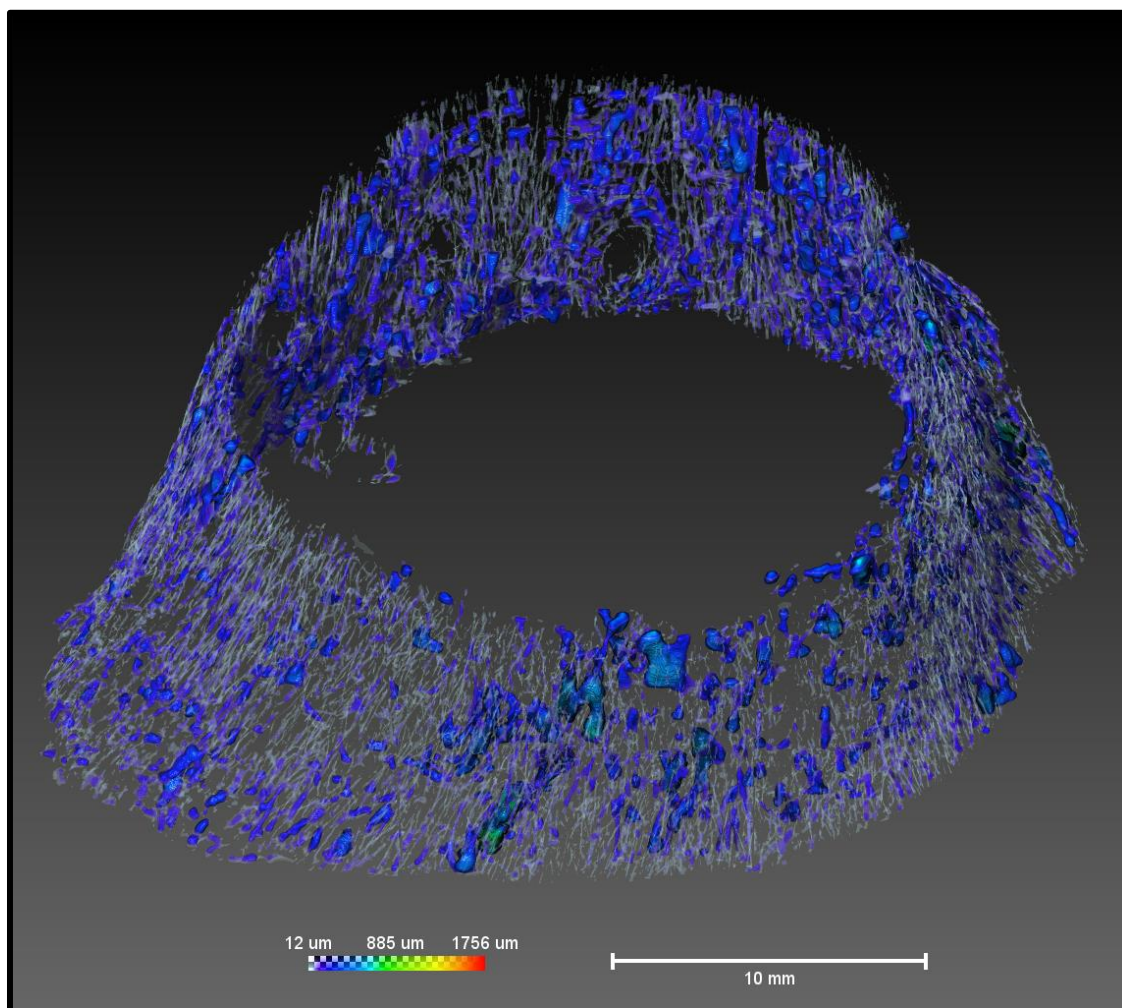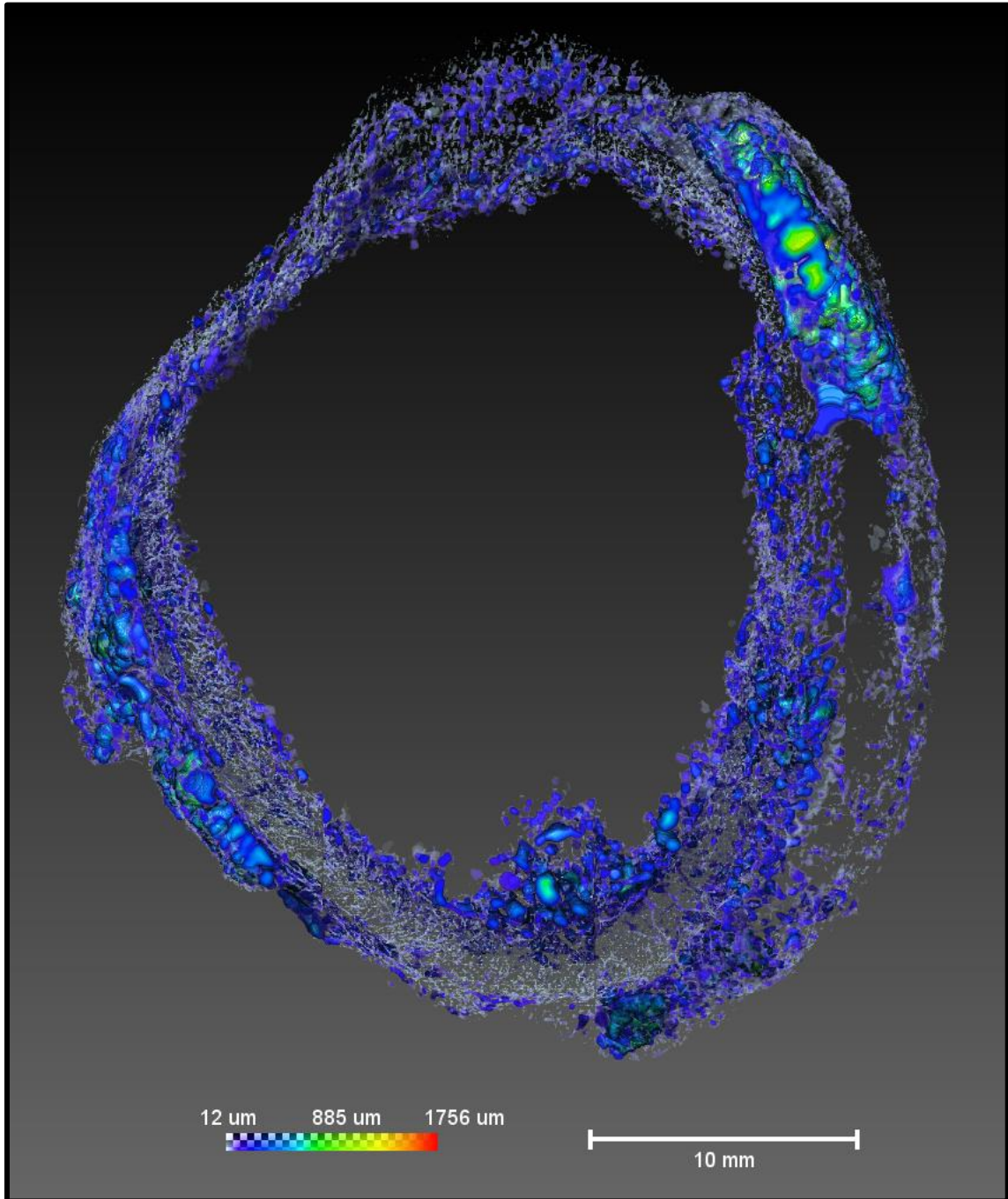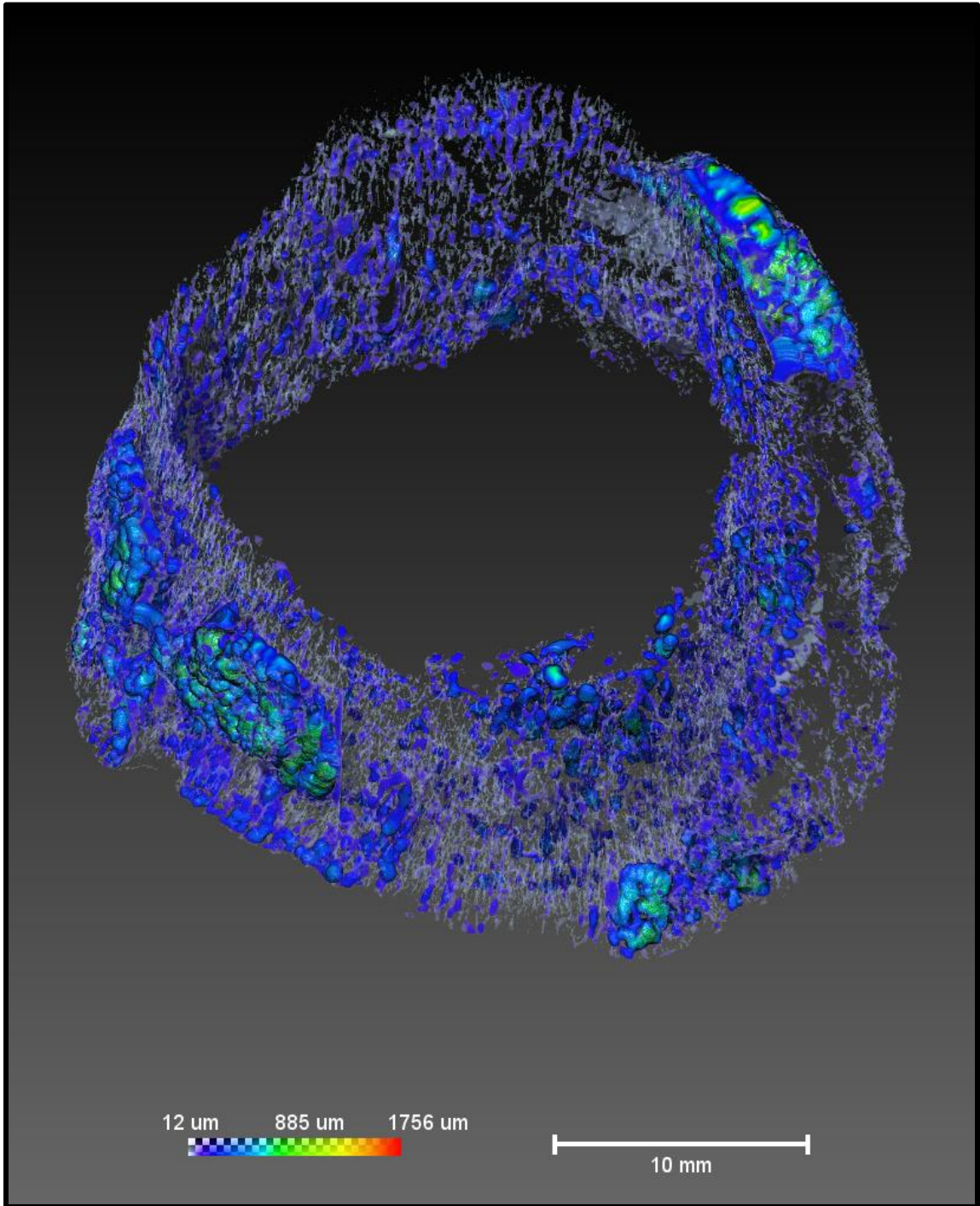
Appendix D: 3D Images of Rib Samples

Like the femoral neck, rib samples are grayscale stacks of pore thickness cross-sections, visualized in AvizoFire 8.1. All femoral neck three-dimensional visualizations are viewed from the vertebral face with the **cutaneous cortex** on the top and the **pleural cortex** on the bottom. Samples are visualized with a slight tilt of the pleural wall towards the camera, from the top, and from the side. Samples are oriented as follows:

Superior

Medial   **Lateral**

Inferior

557

26M Vertebral Tilt View
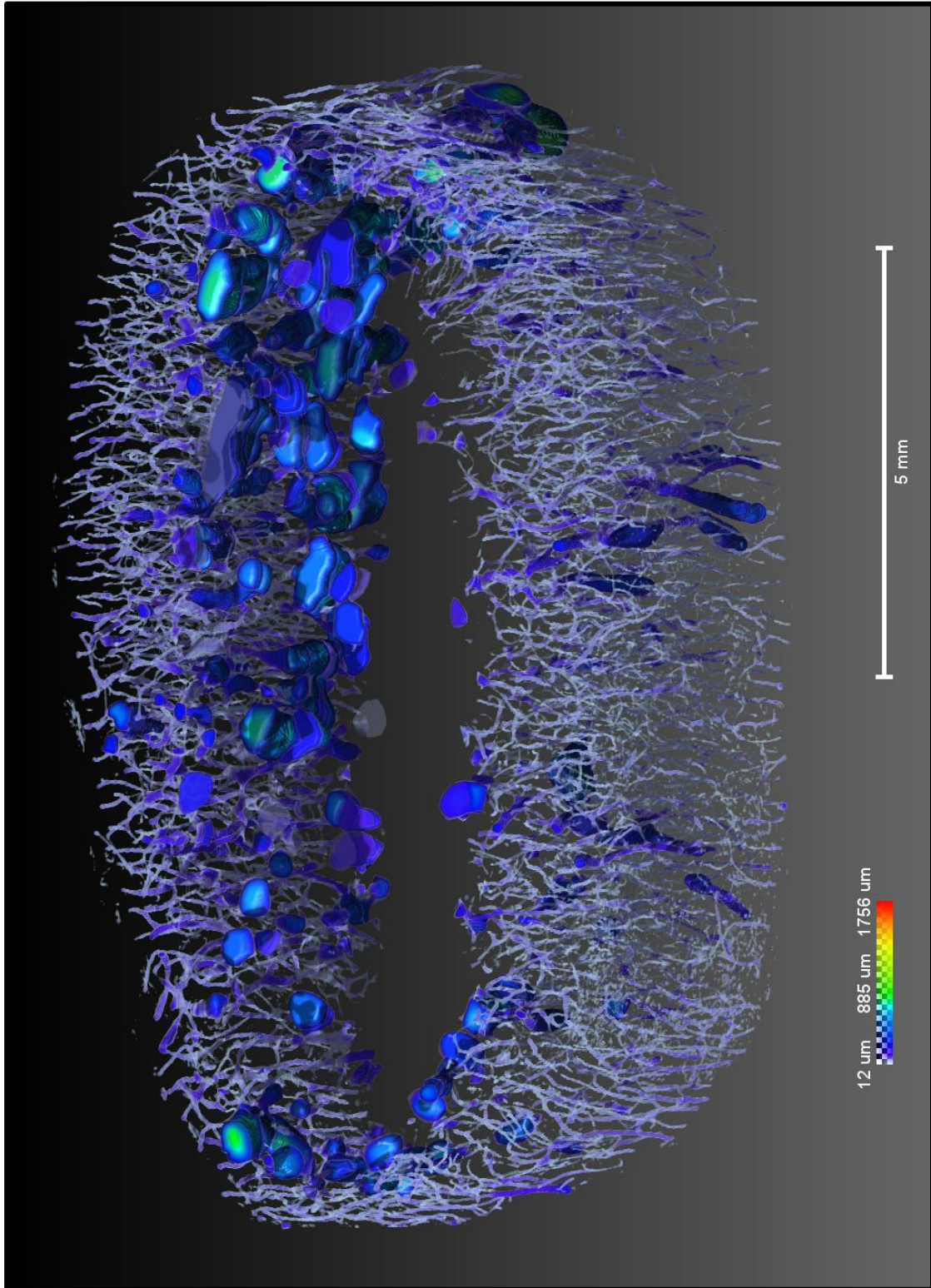
558

26M Vertebral Top and Side View

559
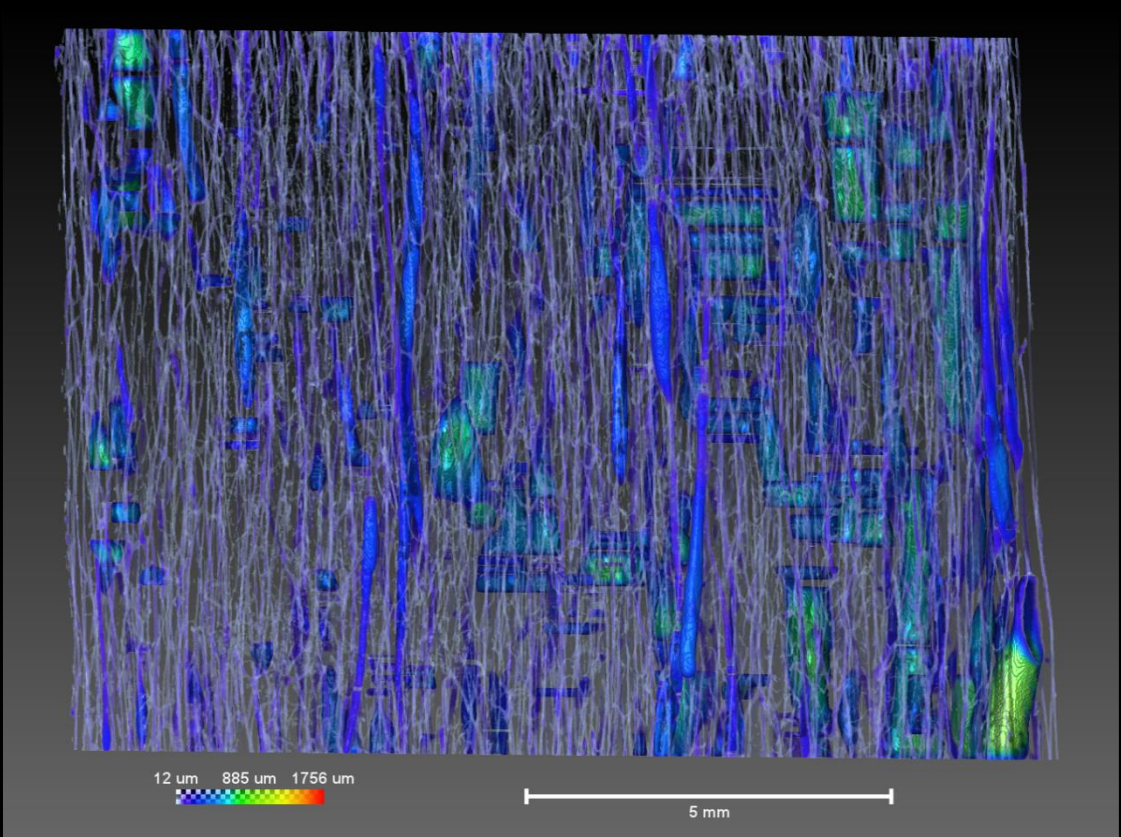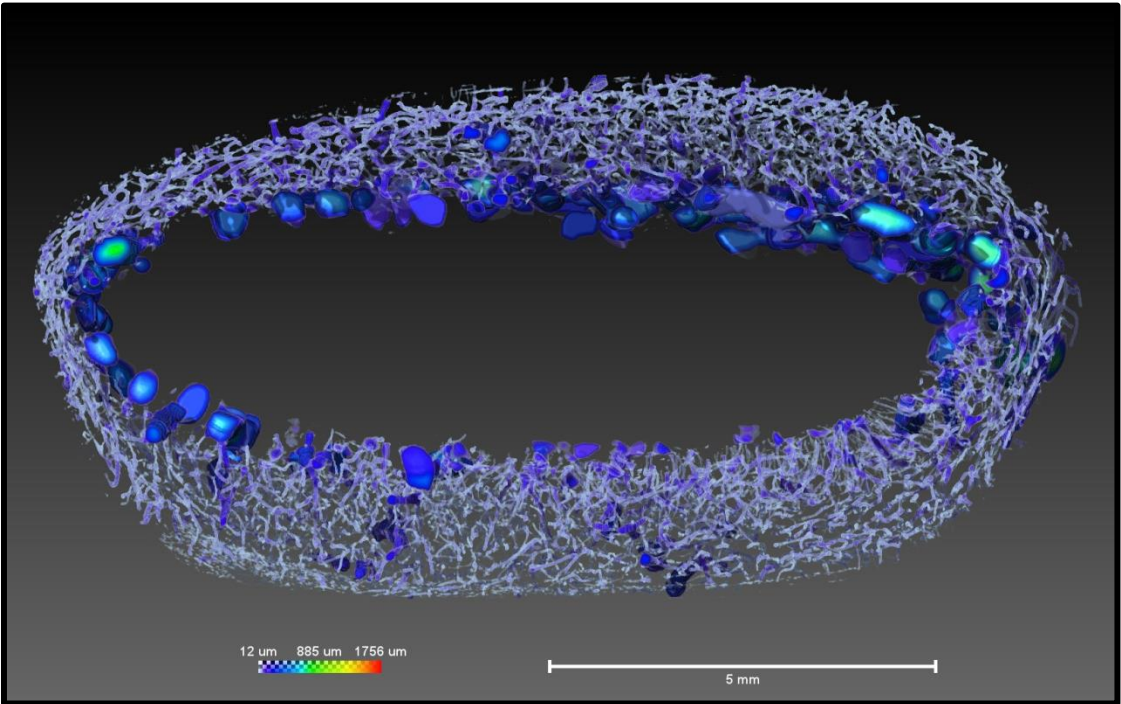
28F Vertebral Tilt View
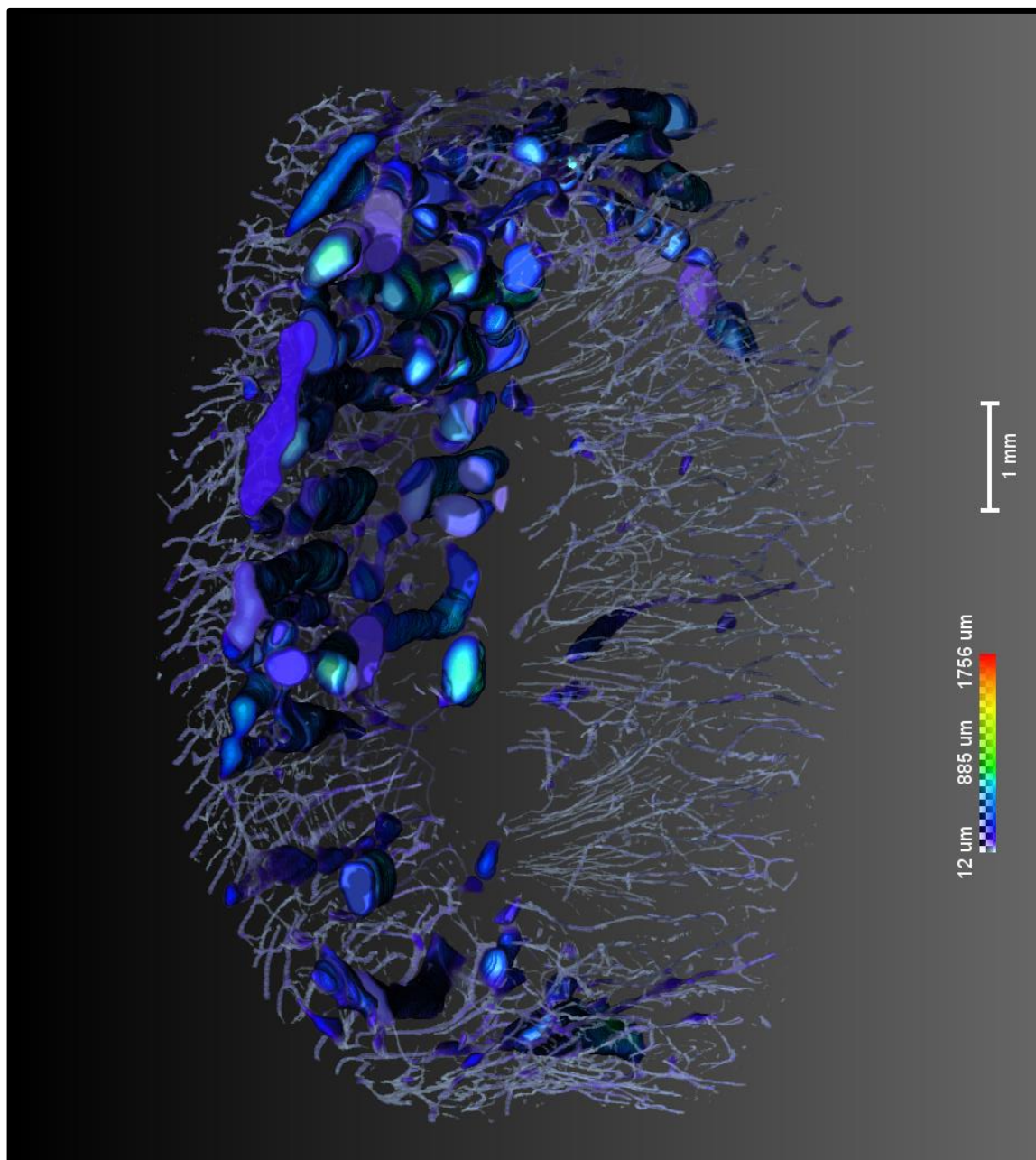
28F Vertebral Top and Side View
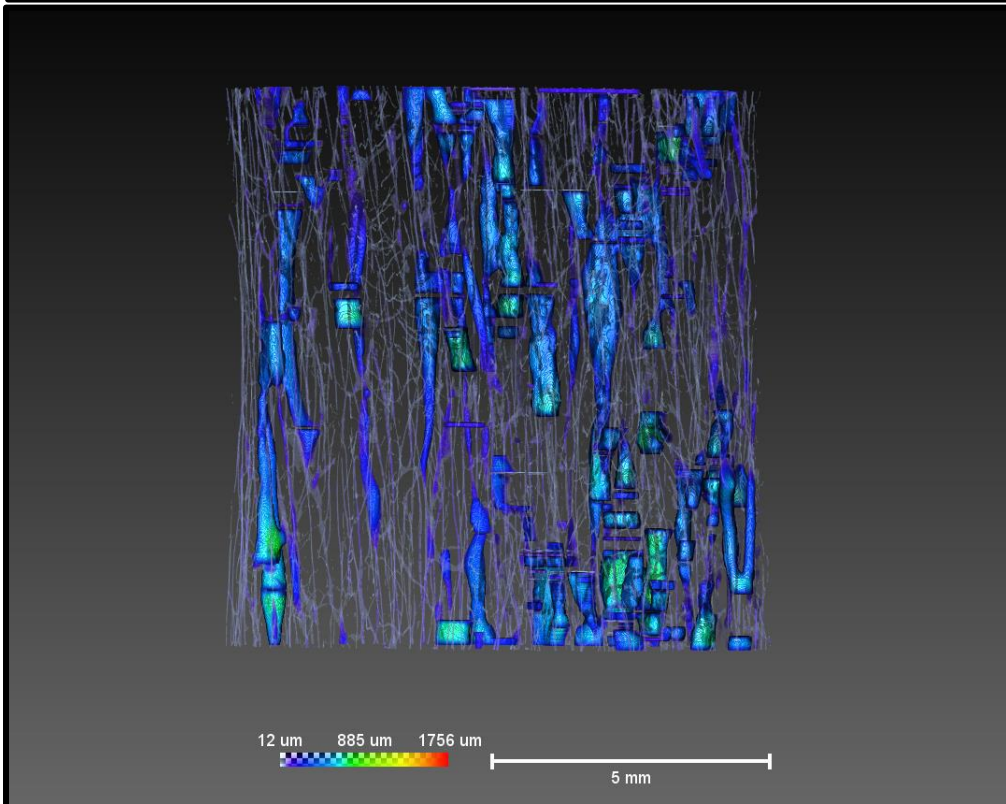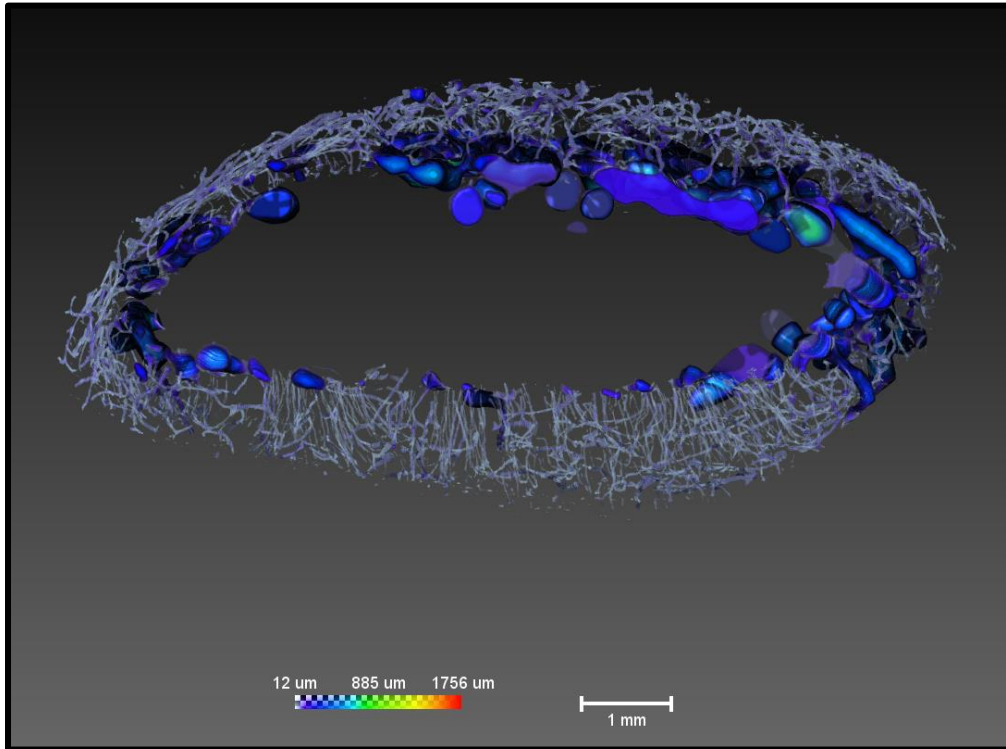
561

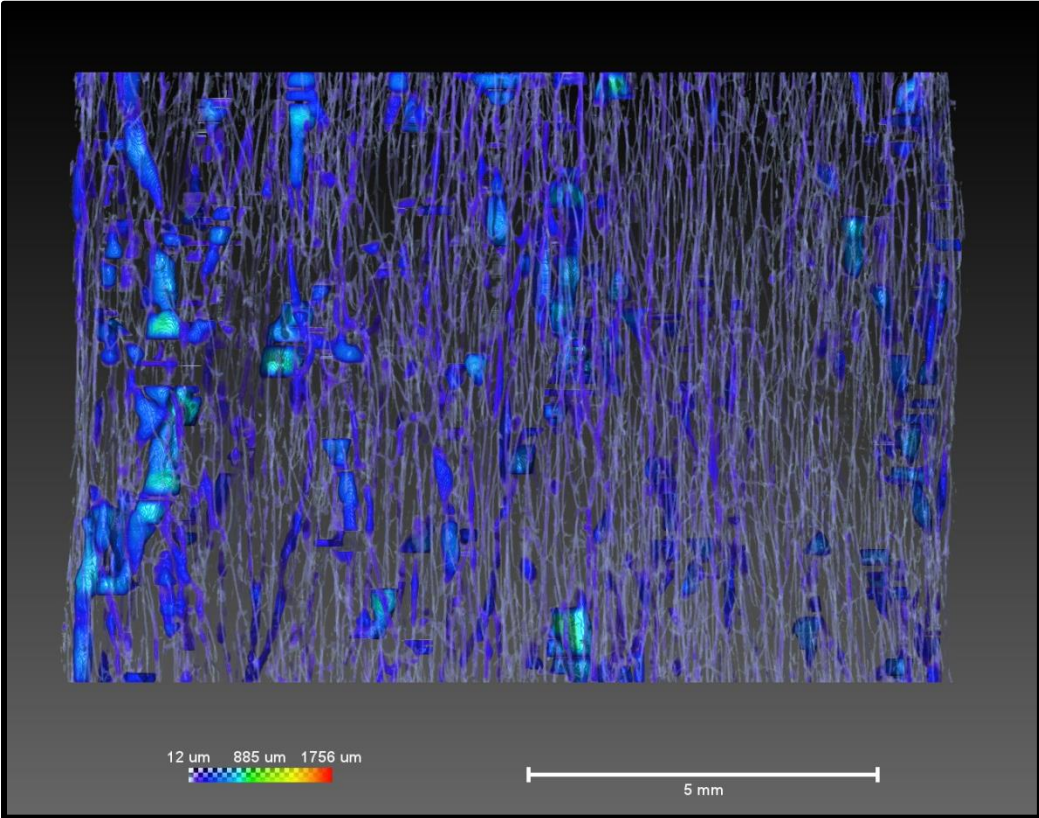# 34M Vertebral Tilt View
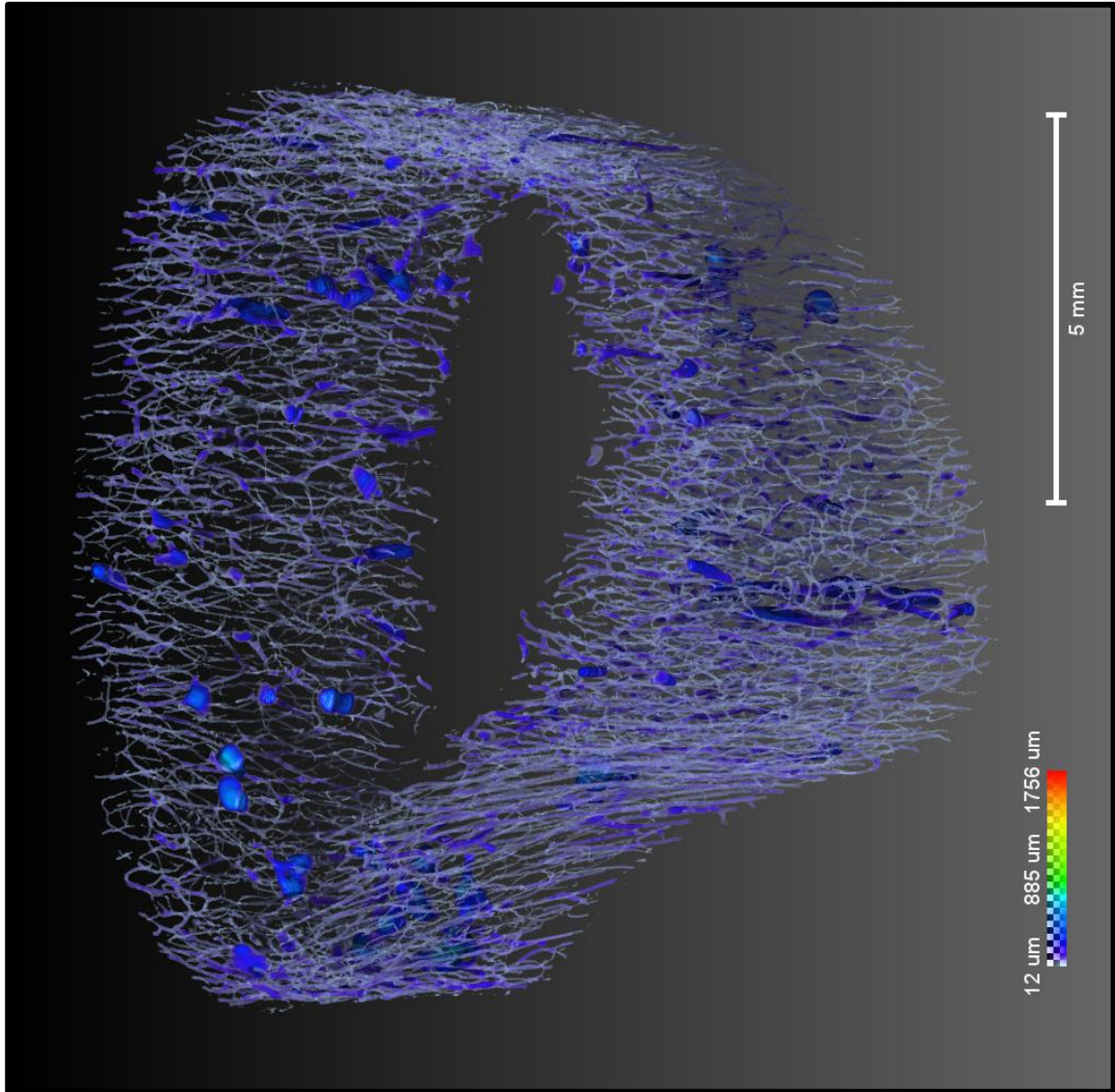
34M Vertebral Top and Side View

563
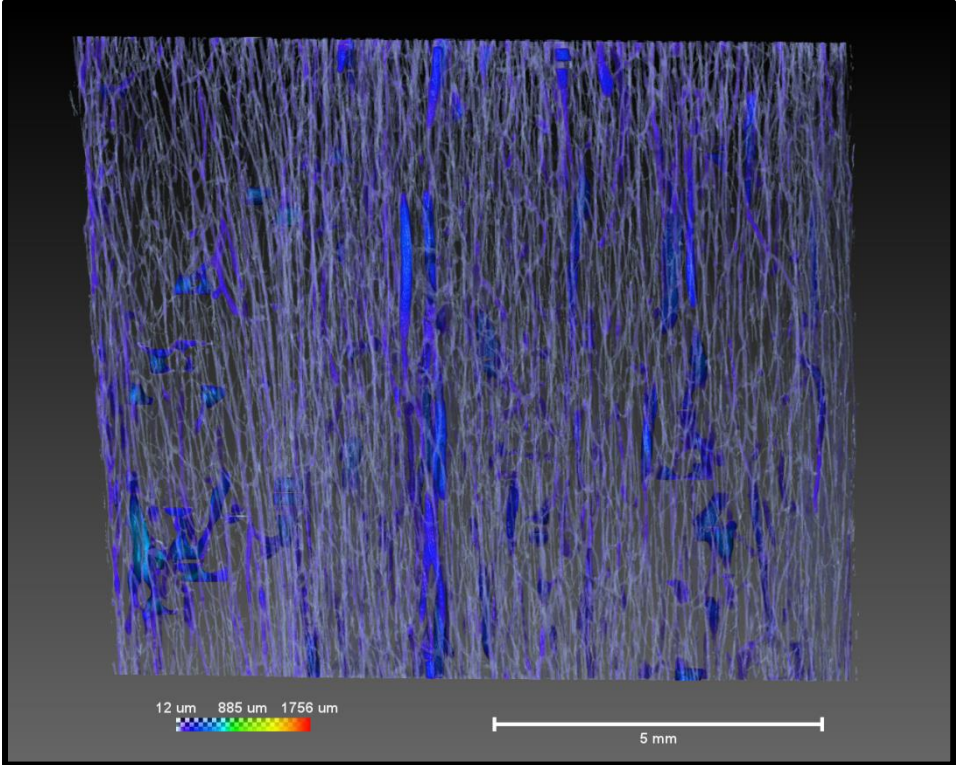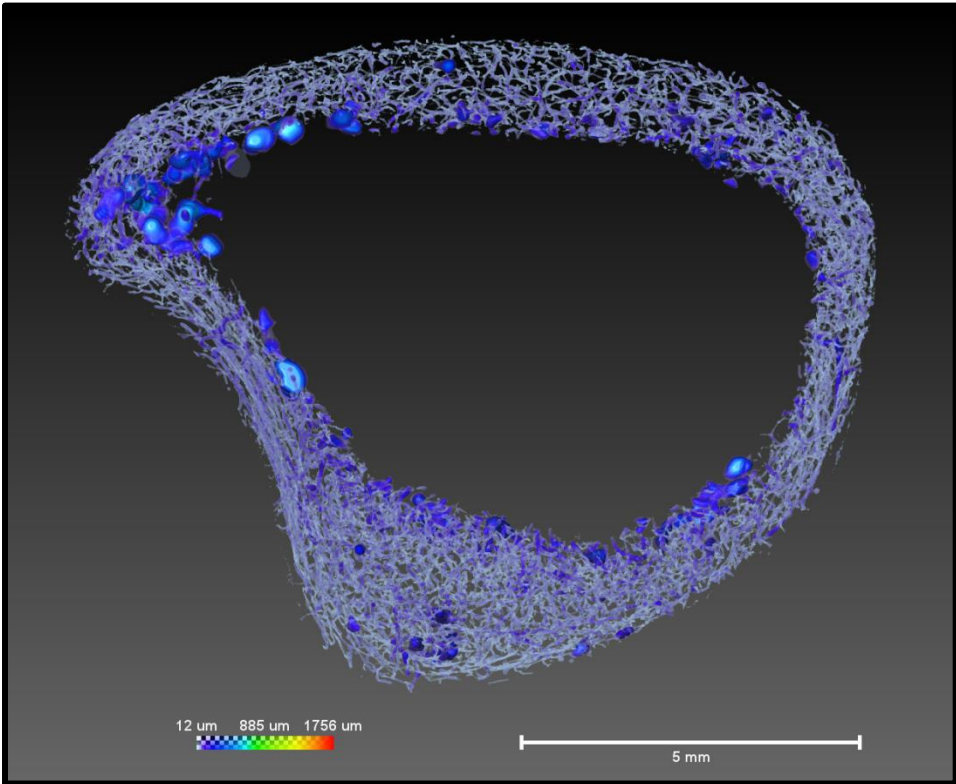
39F Vertebral Tilt View

564
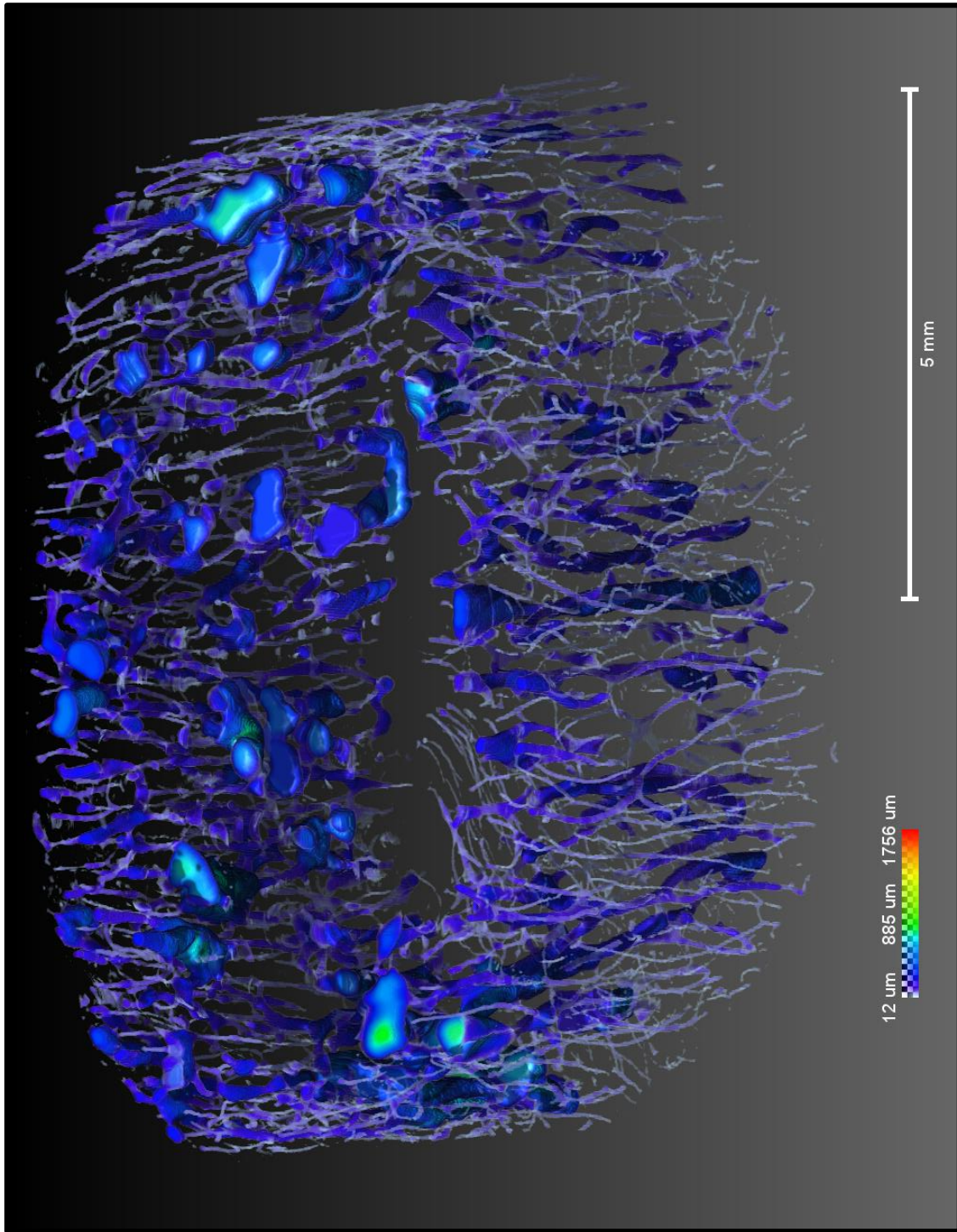
39F Vertebral Top and Side View

565
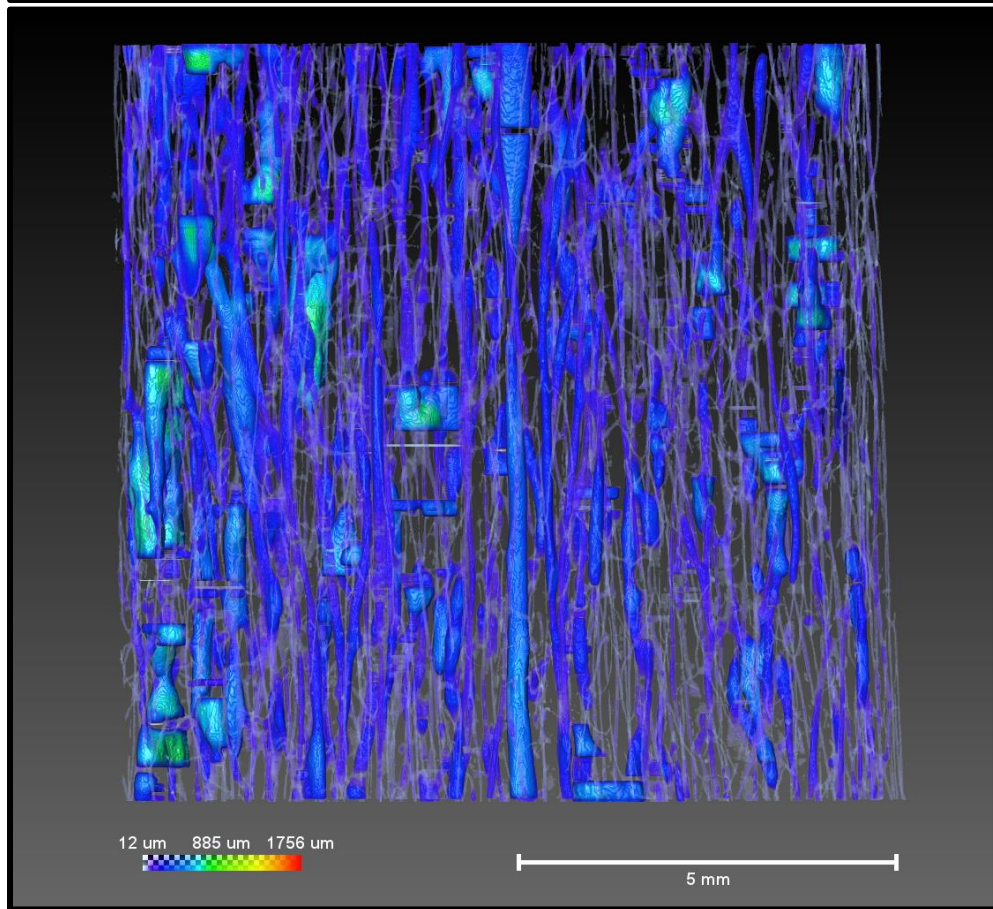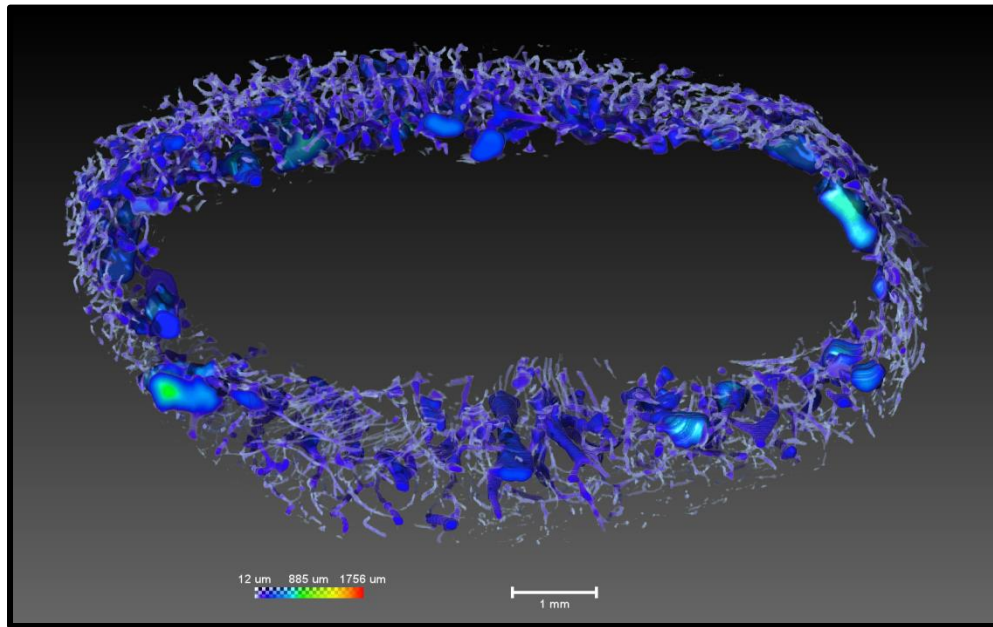
49F Vertebral Tilt View

566
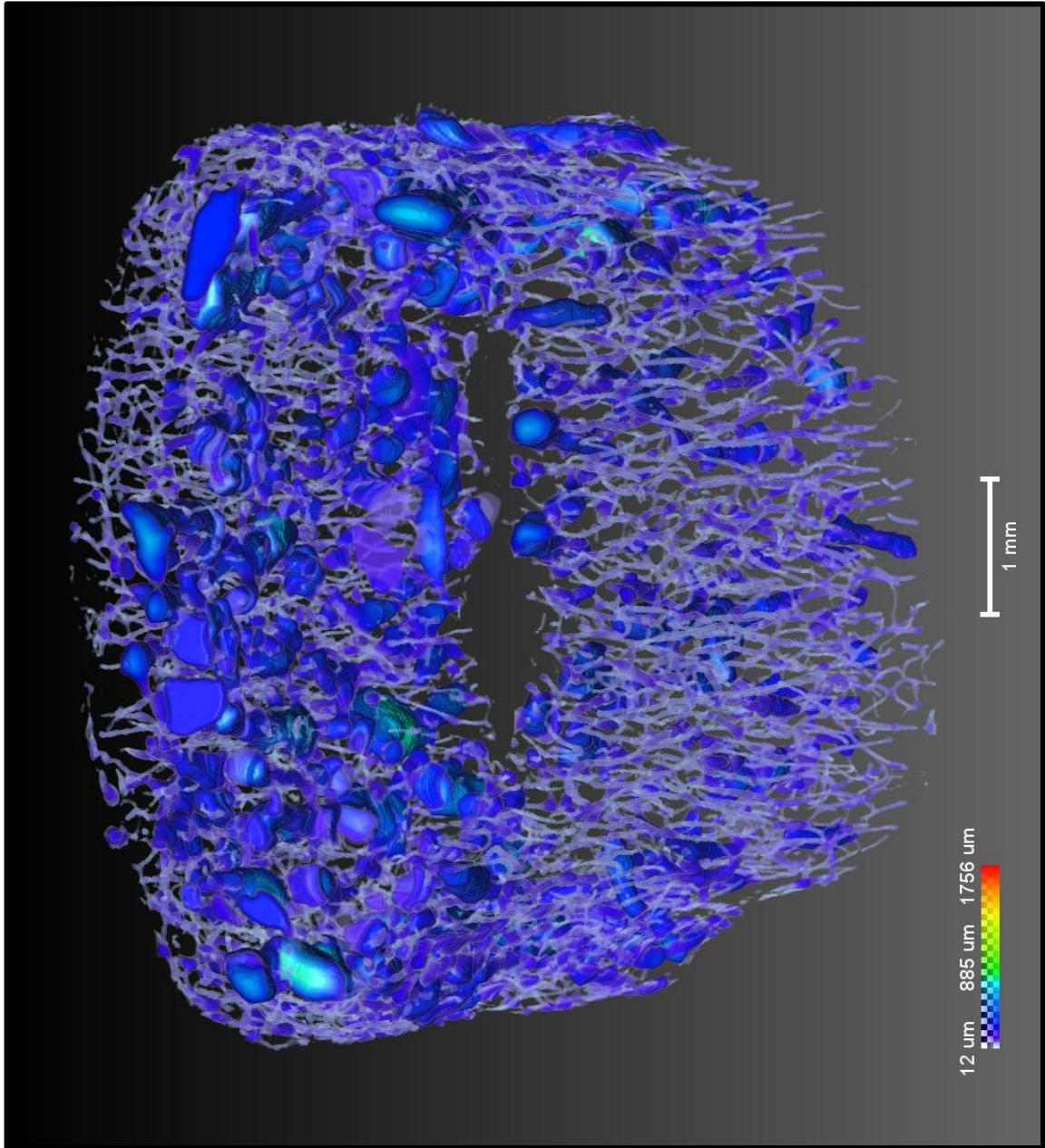
49F Vertebral Top and Side View
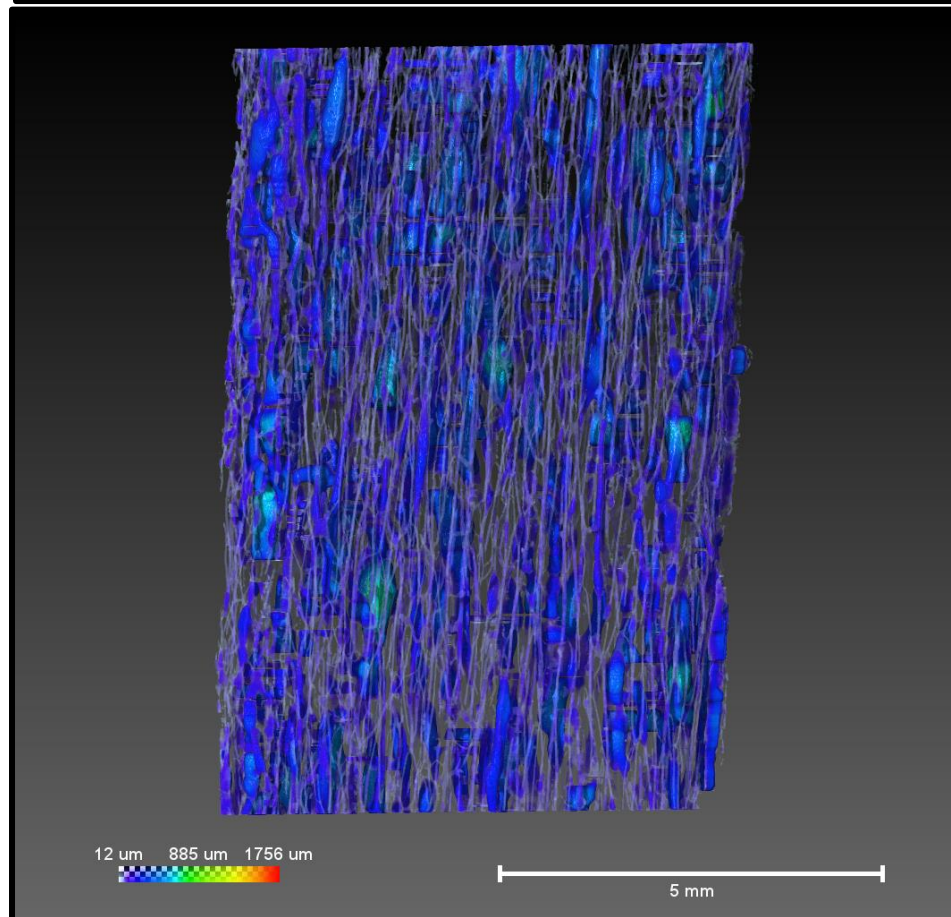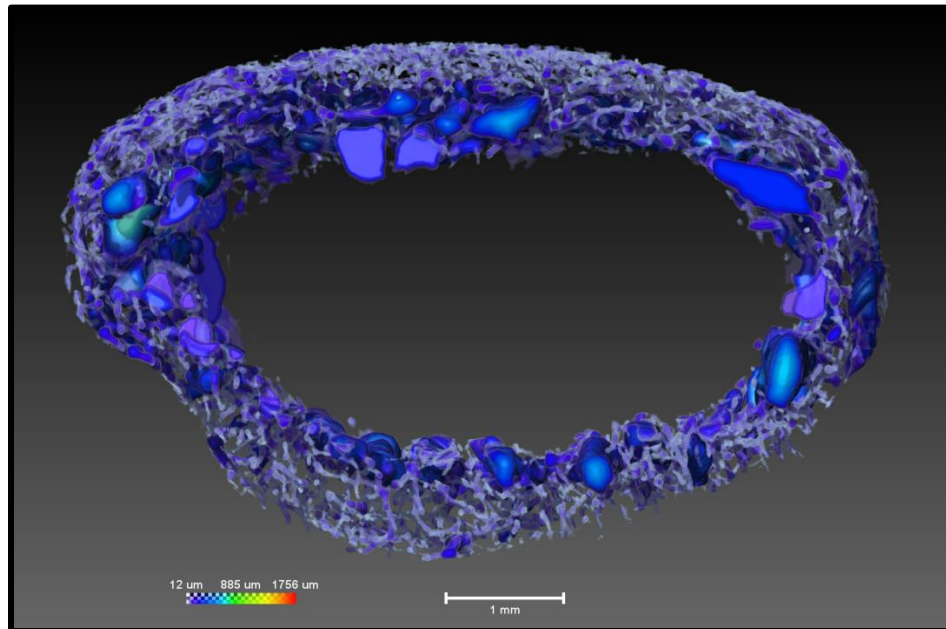
567

41M Vertebral Tilt View

568
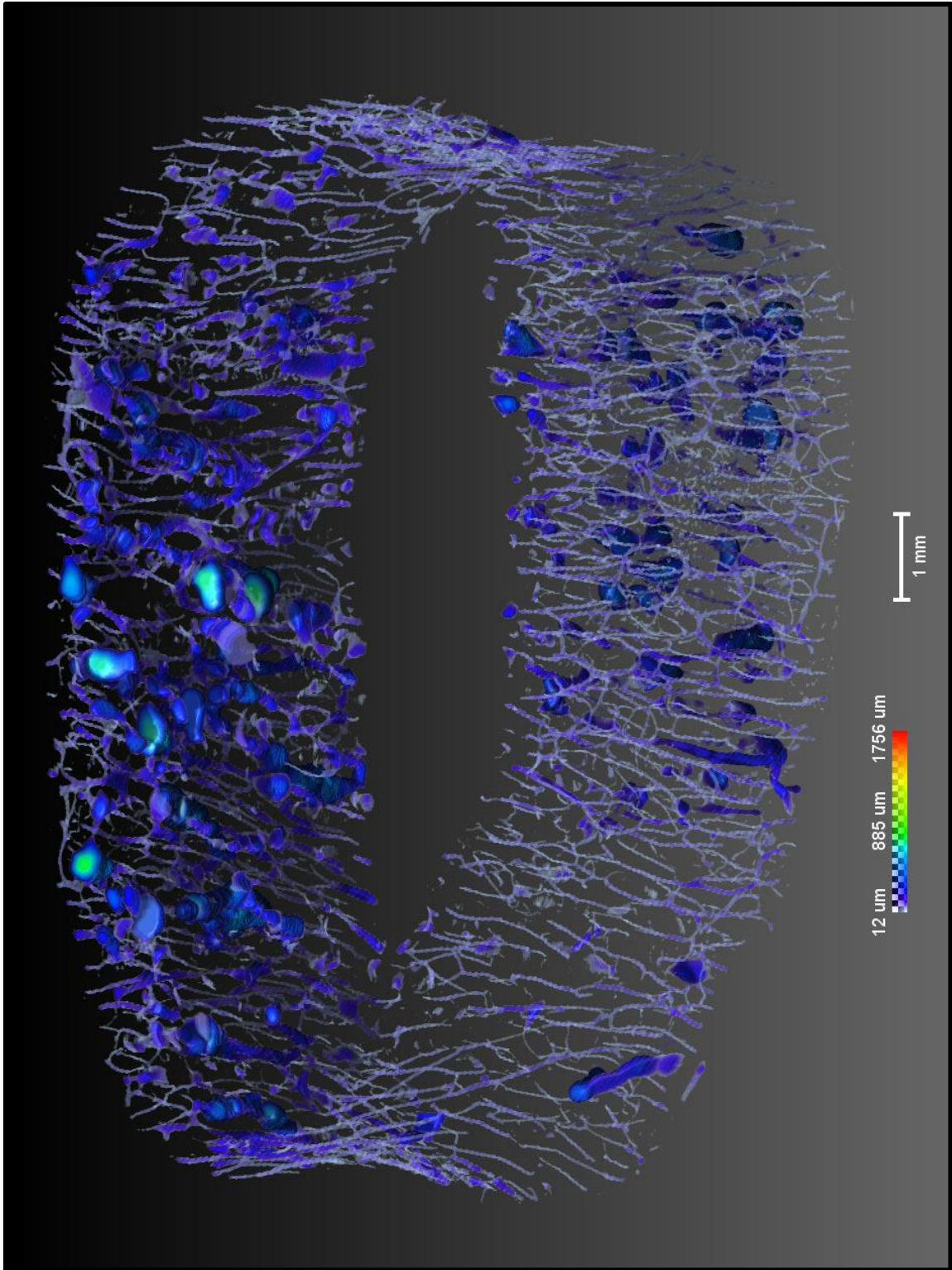
41M Vertebral Top and Side View


569
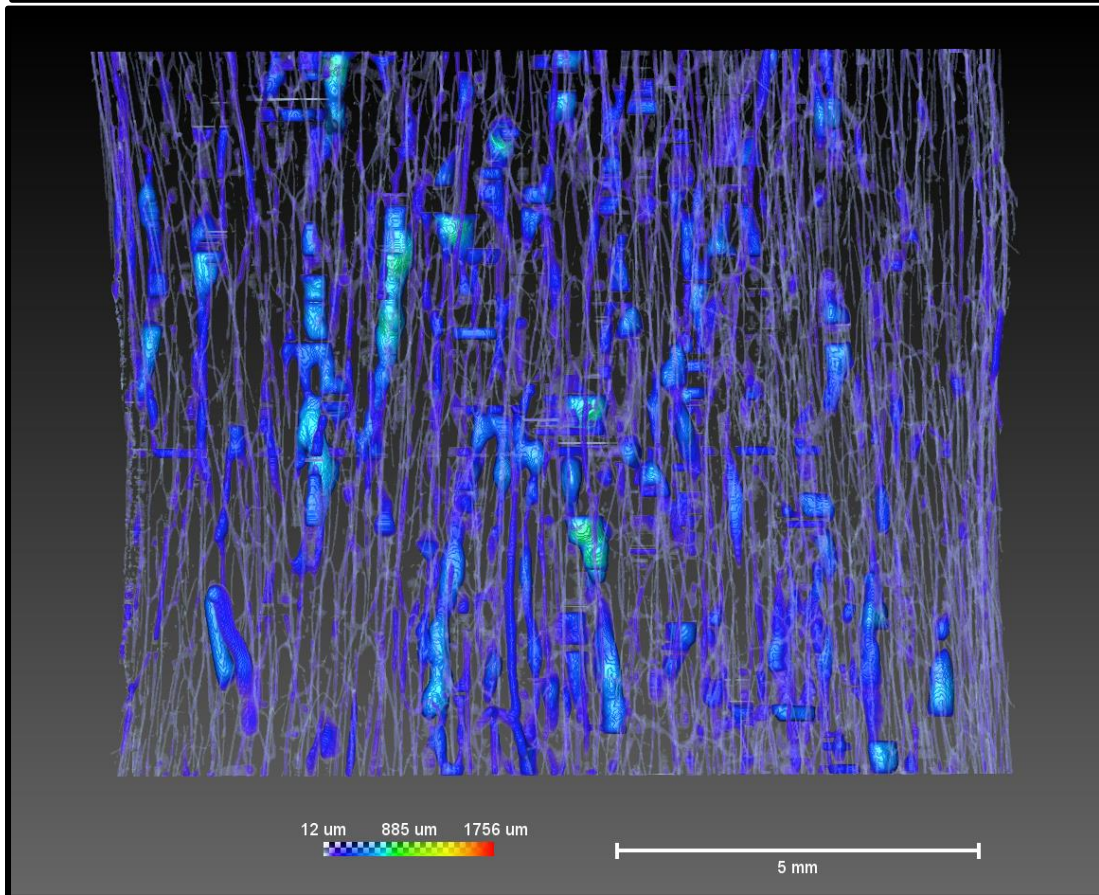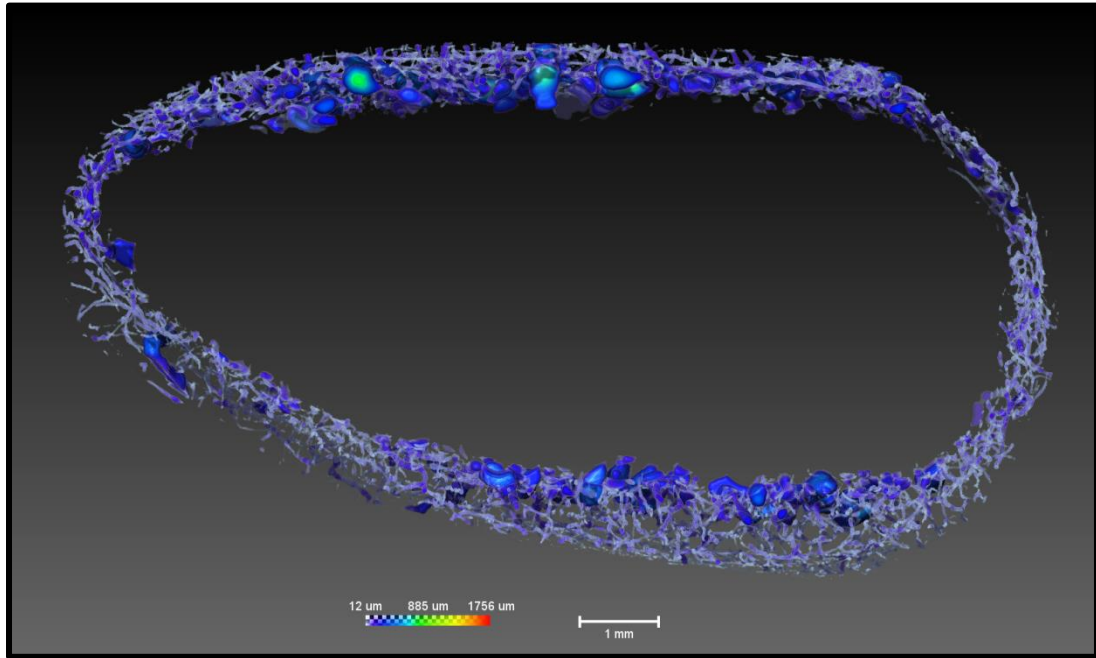
50F Vertebral Tilt View
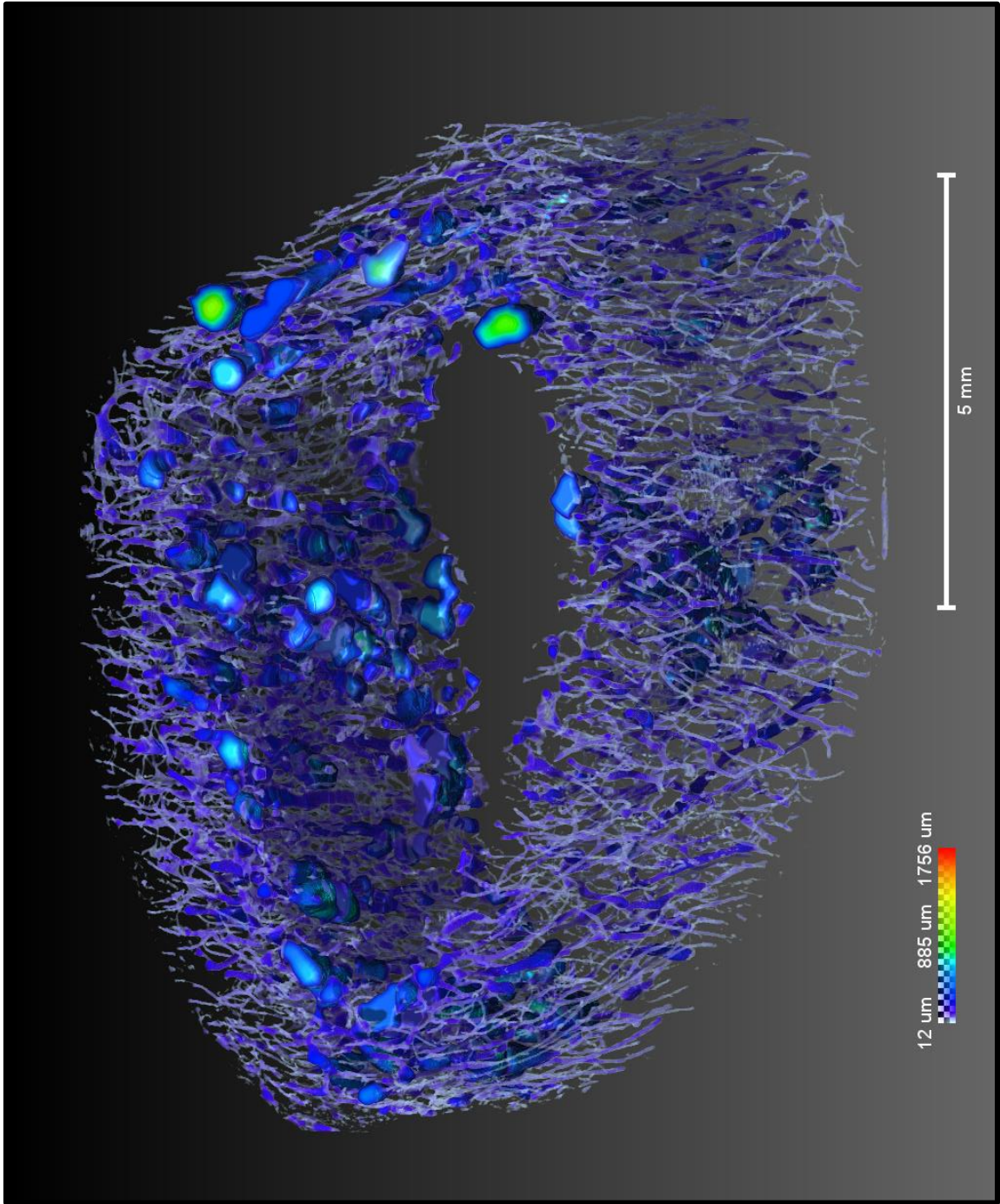
50F Vertebral Top and Side View
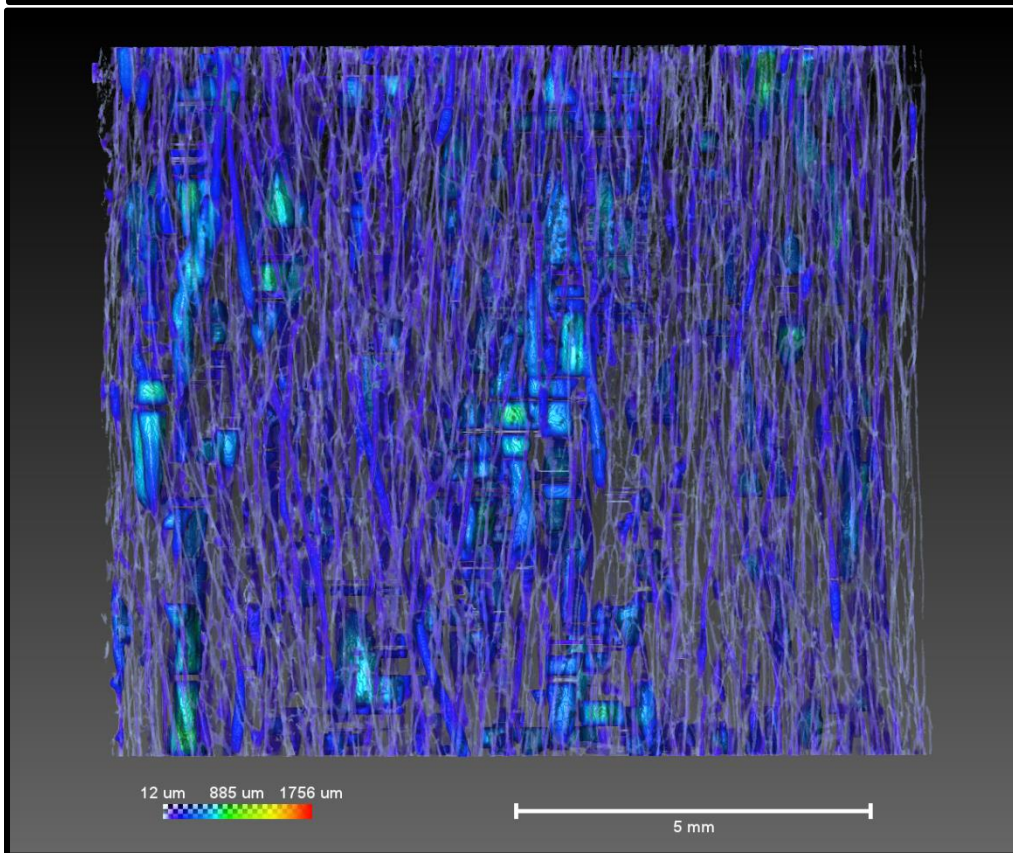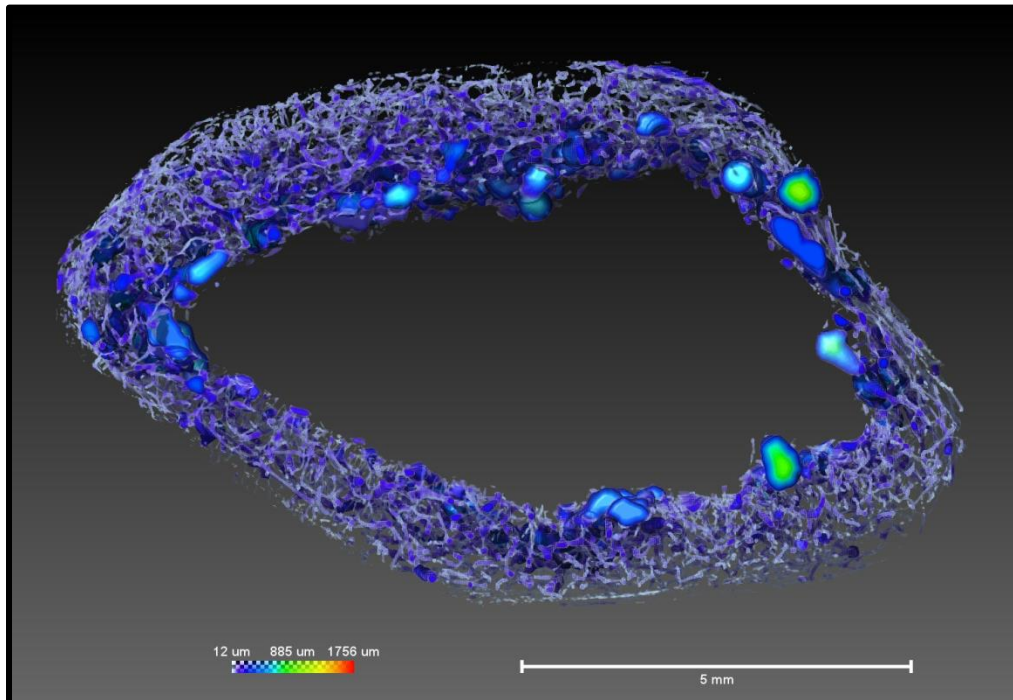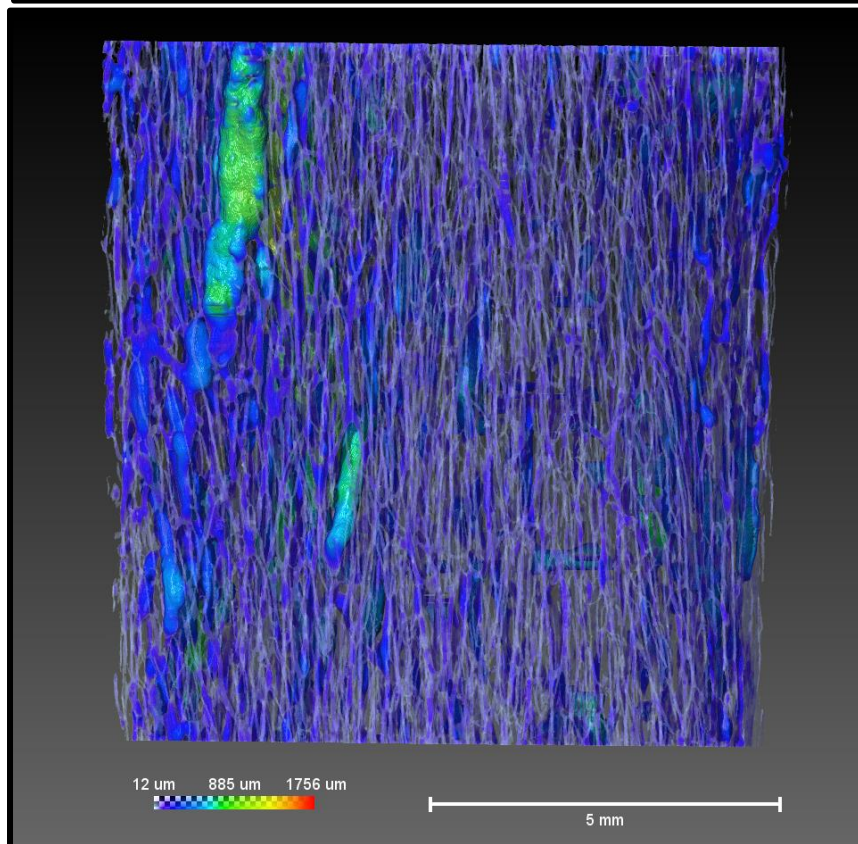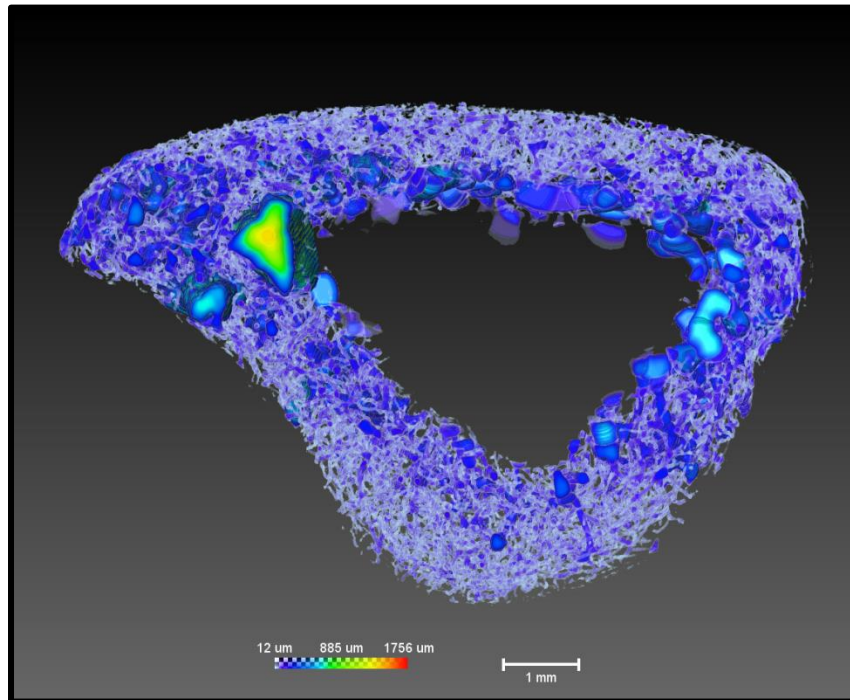

571

56M Vertebral Tilt View

572
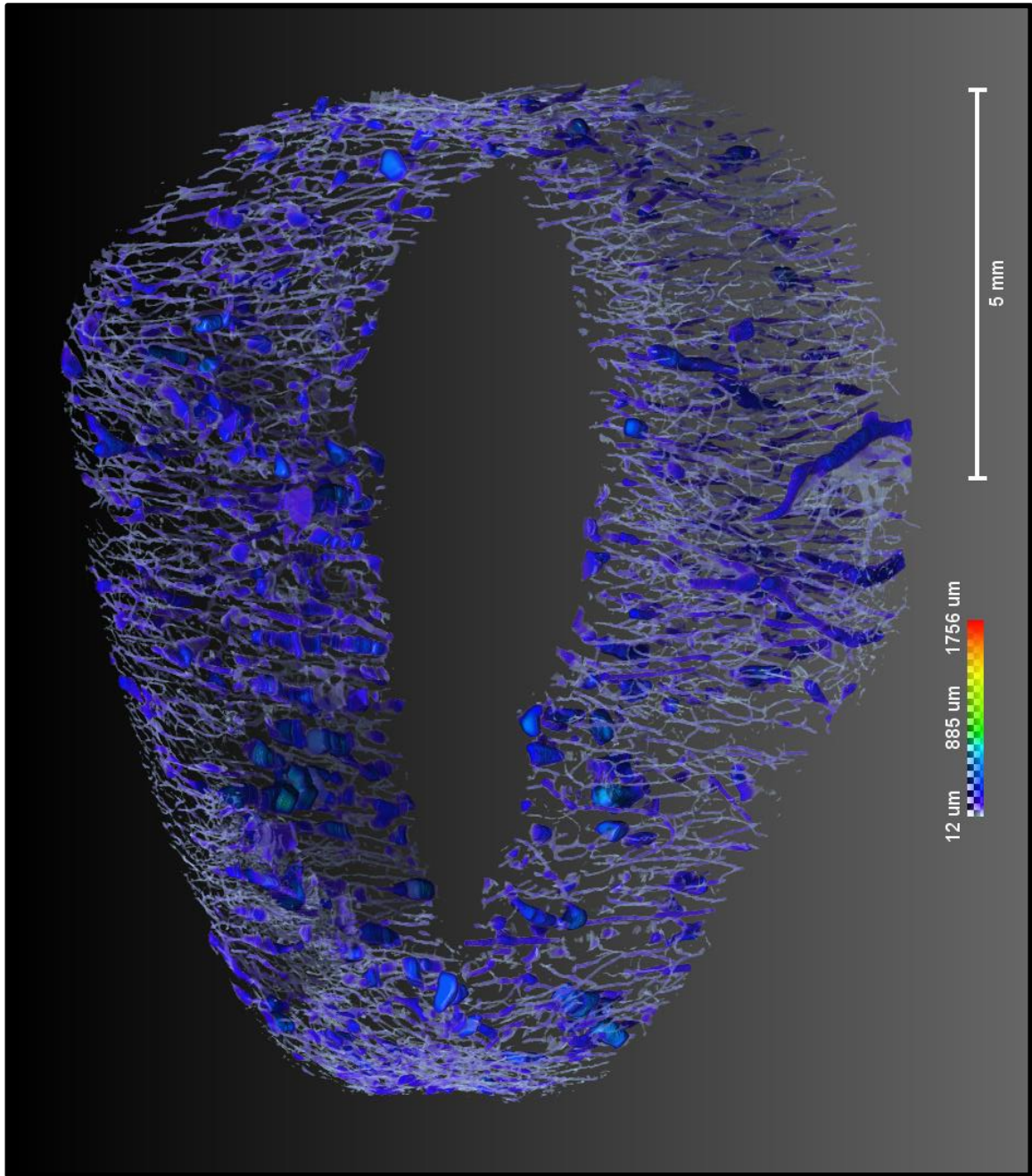
56M Vertebral Top and Side View
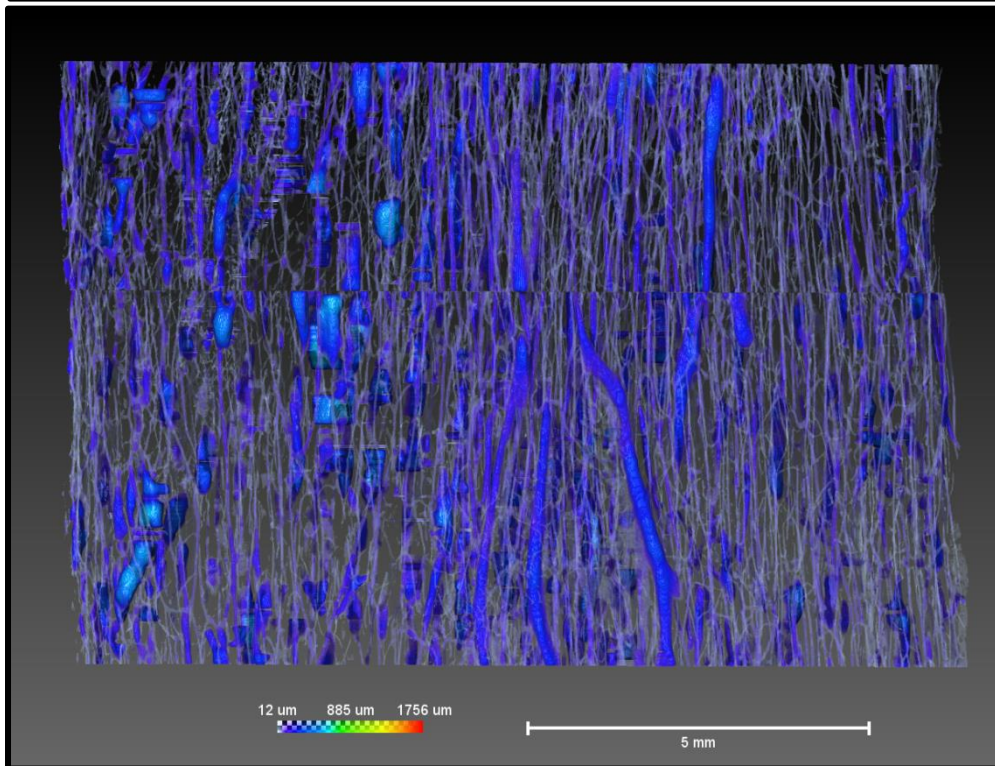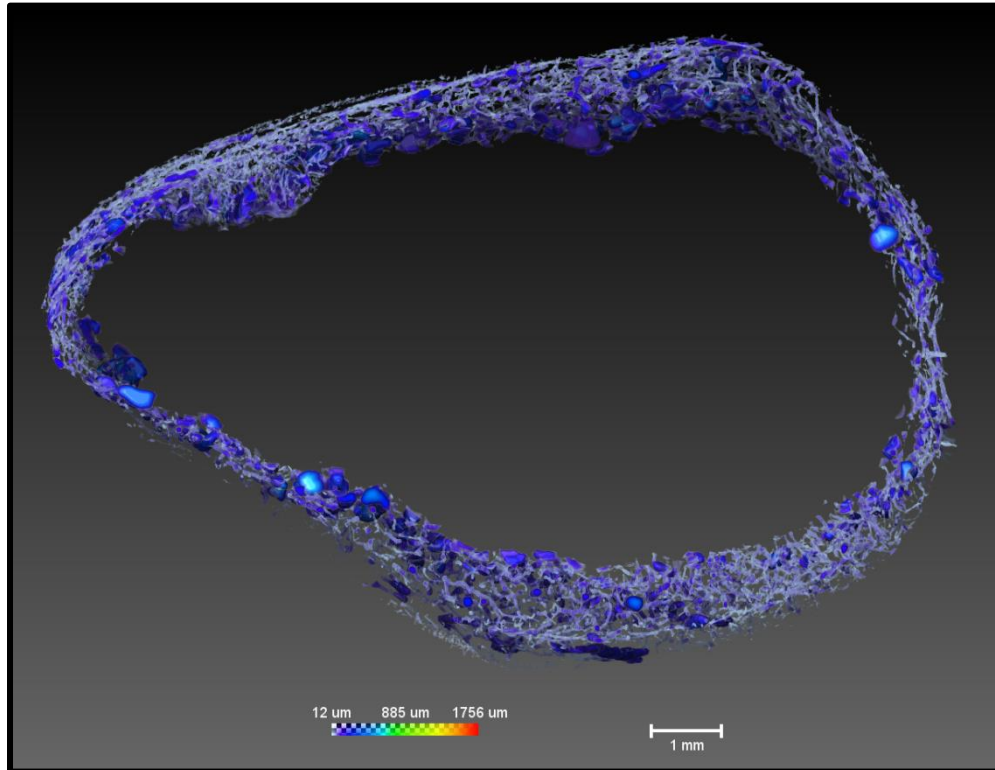
573

60F Vertebral Tilt View

1 mm

1756 um

885 um
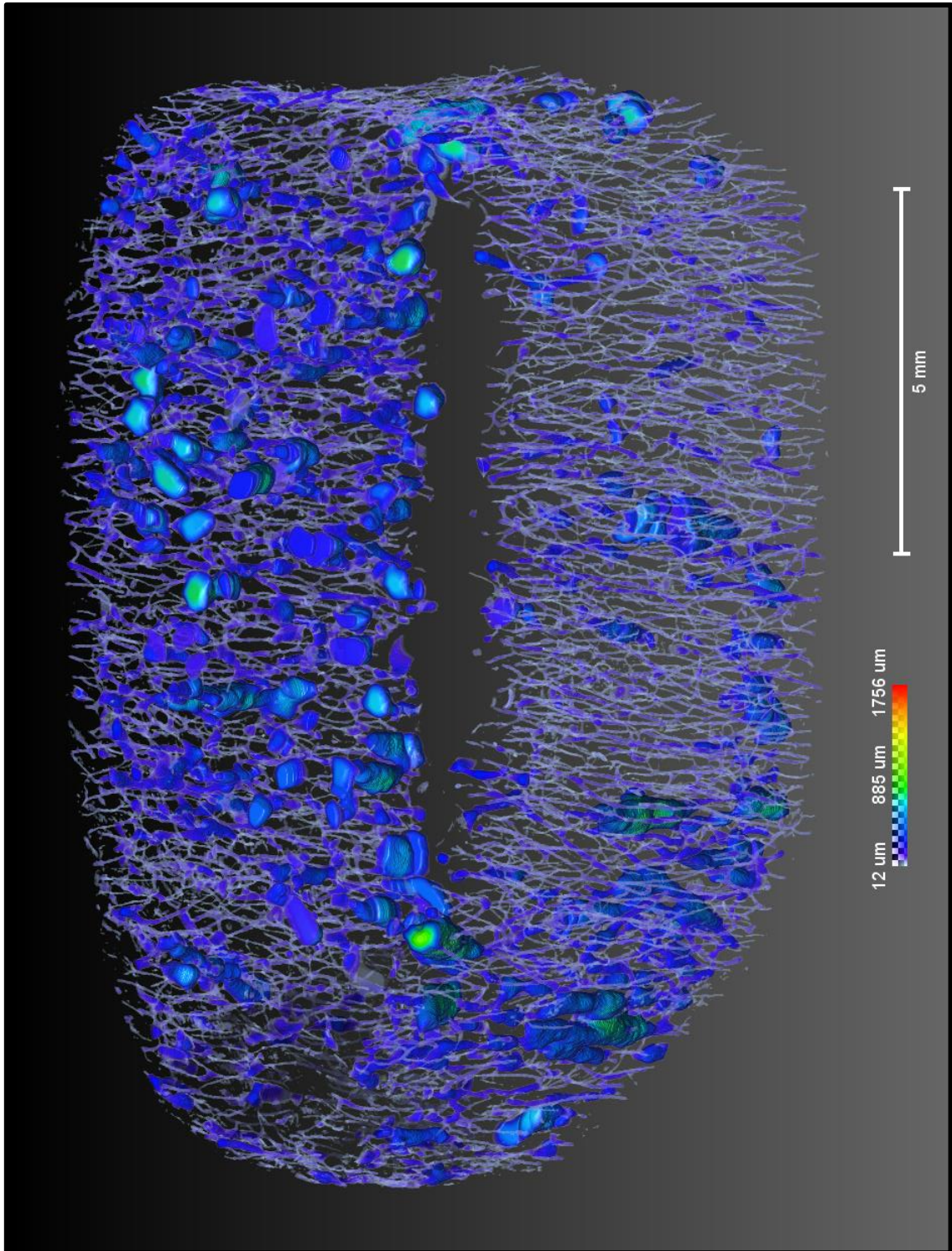
12 um

574
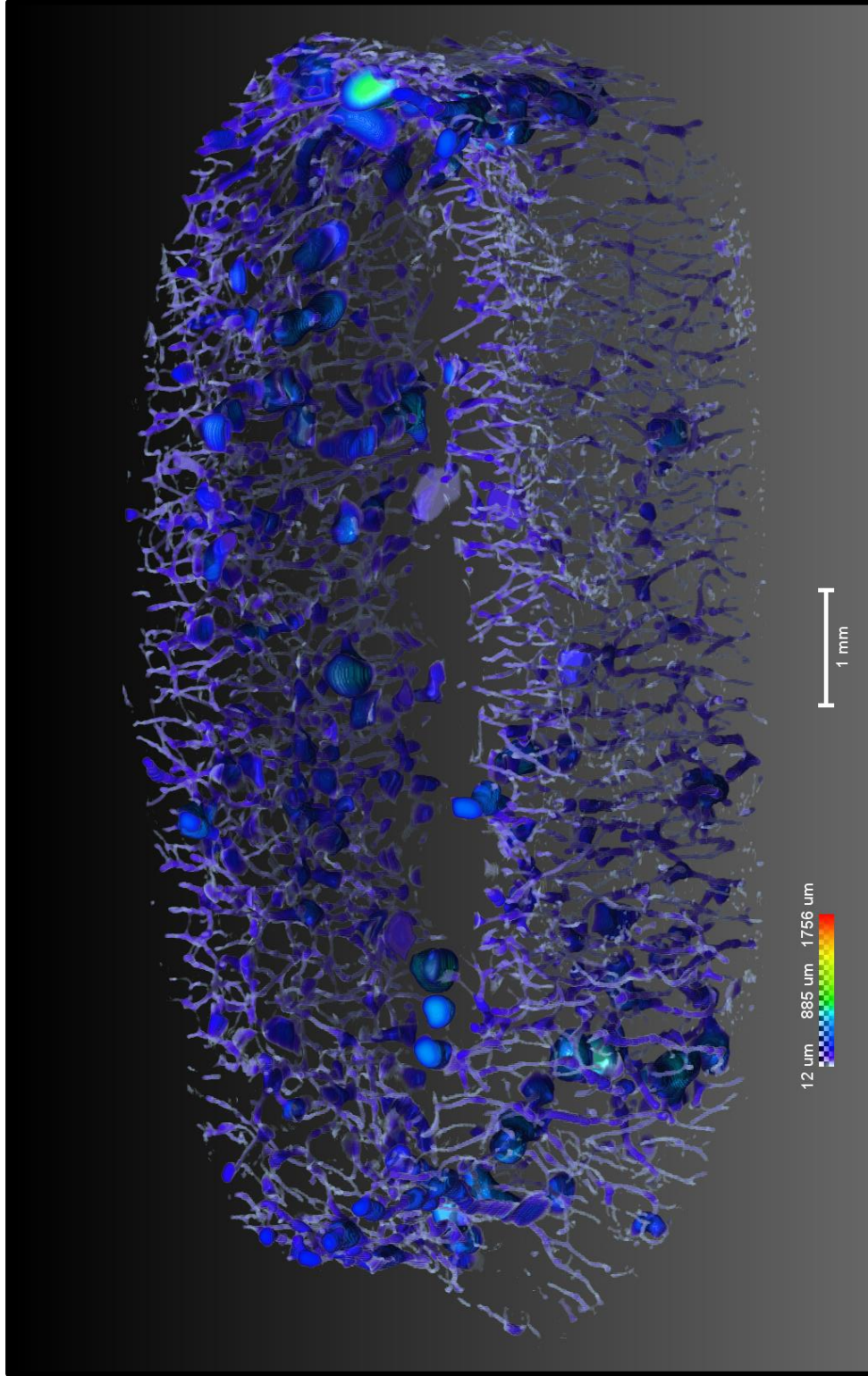
60F Vertebral Top and Side View

576
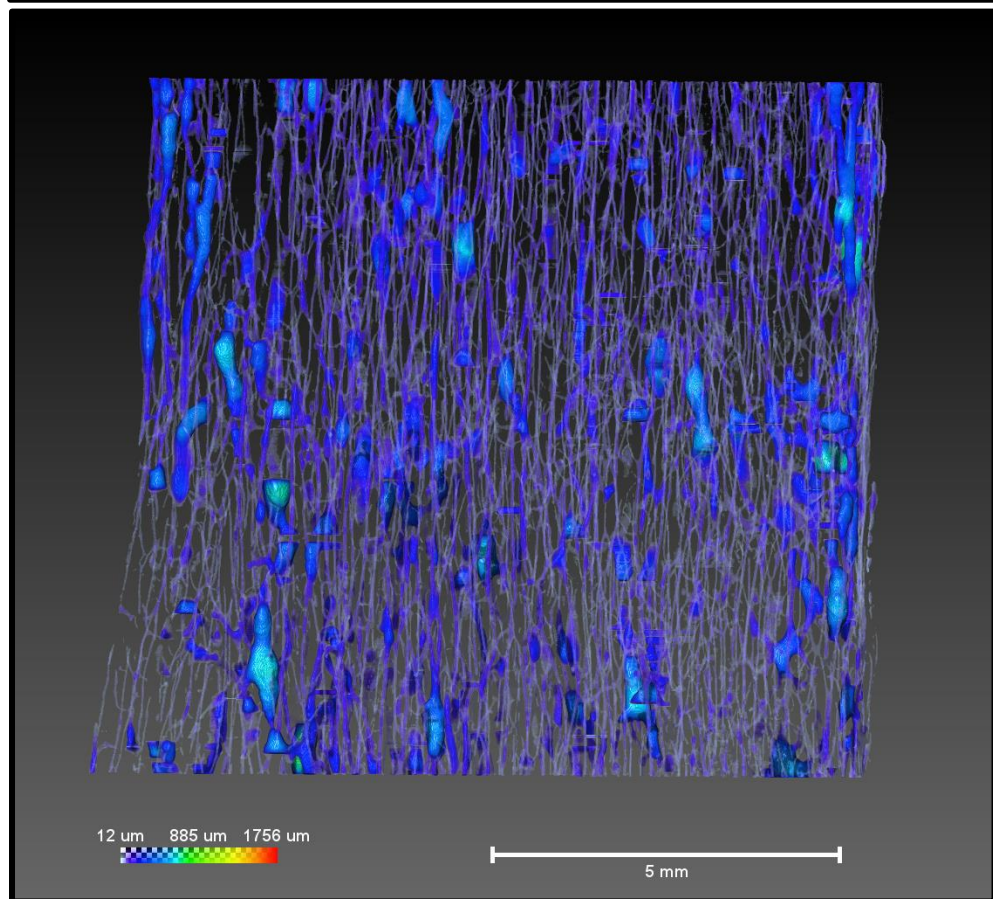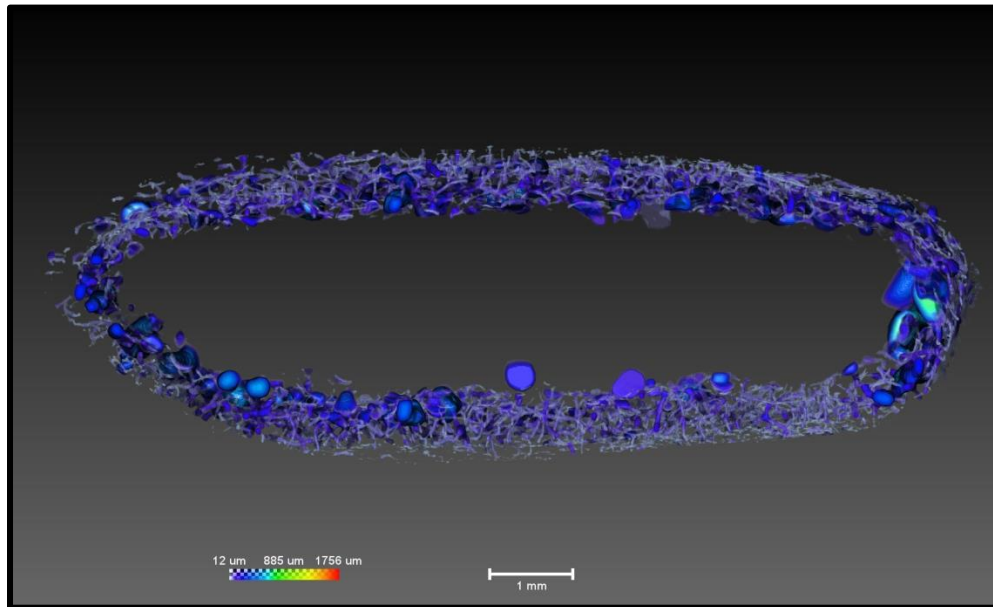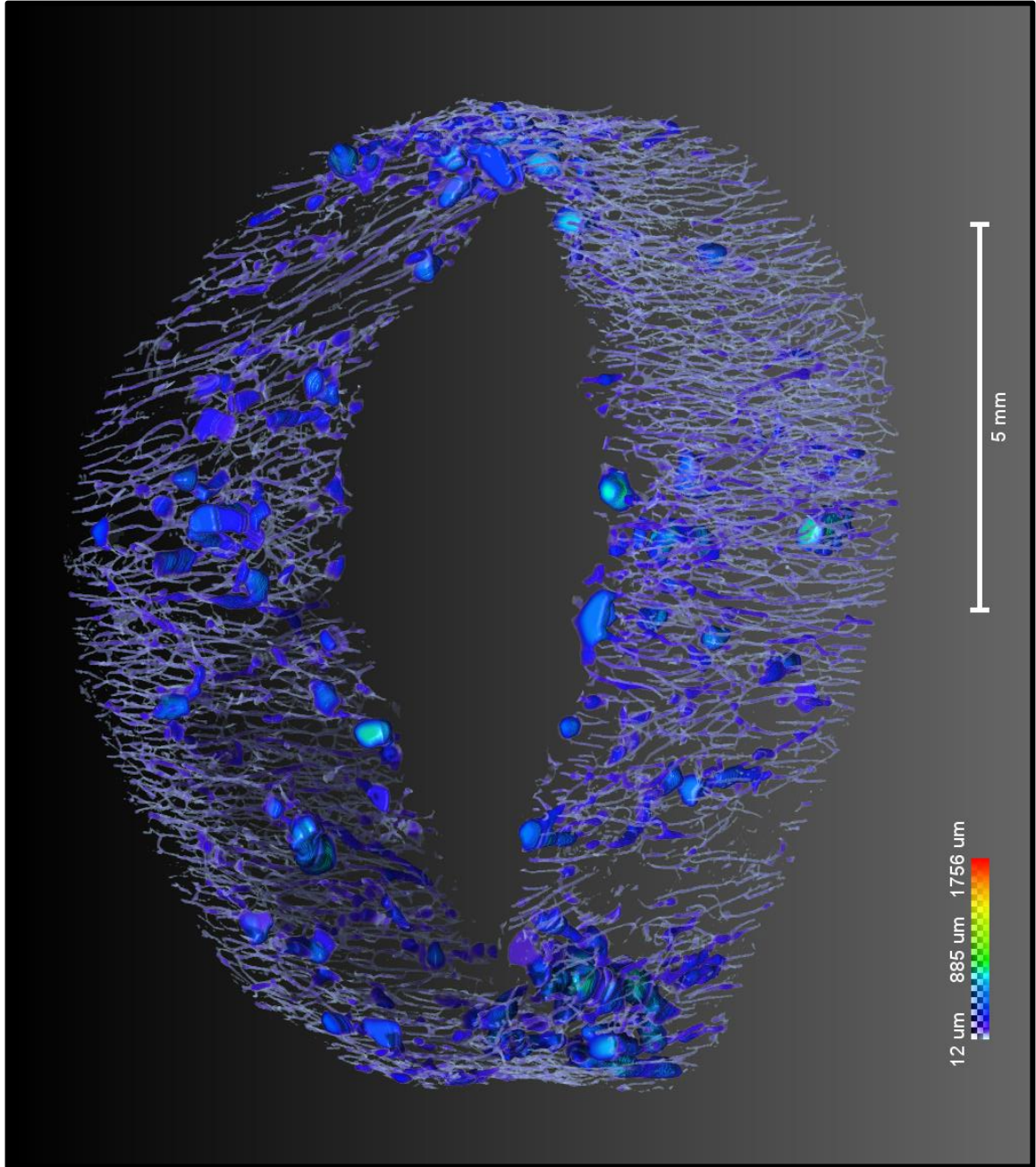
67M Vertebral Top and Side View
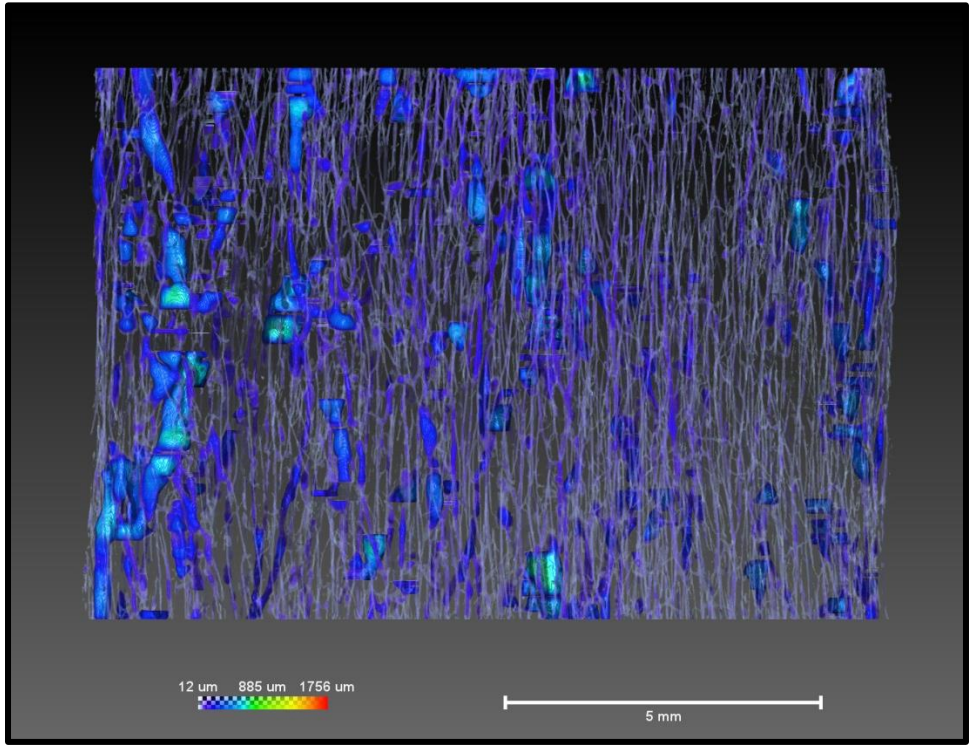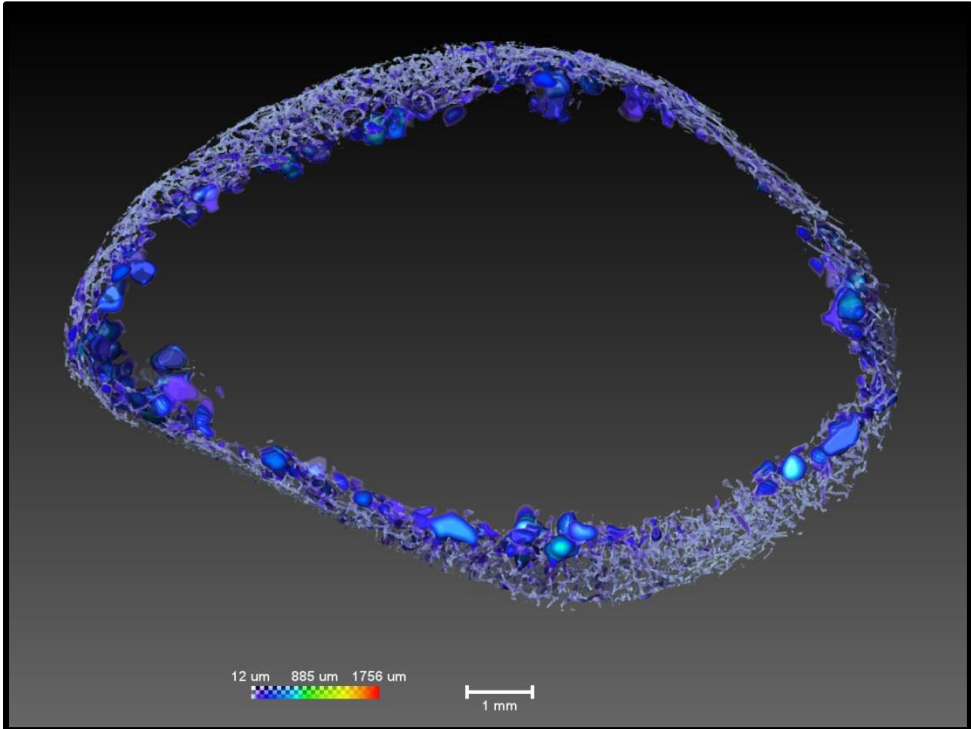
70F Vertebral Tilt View
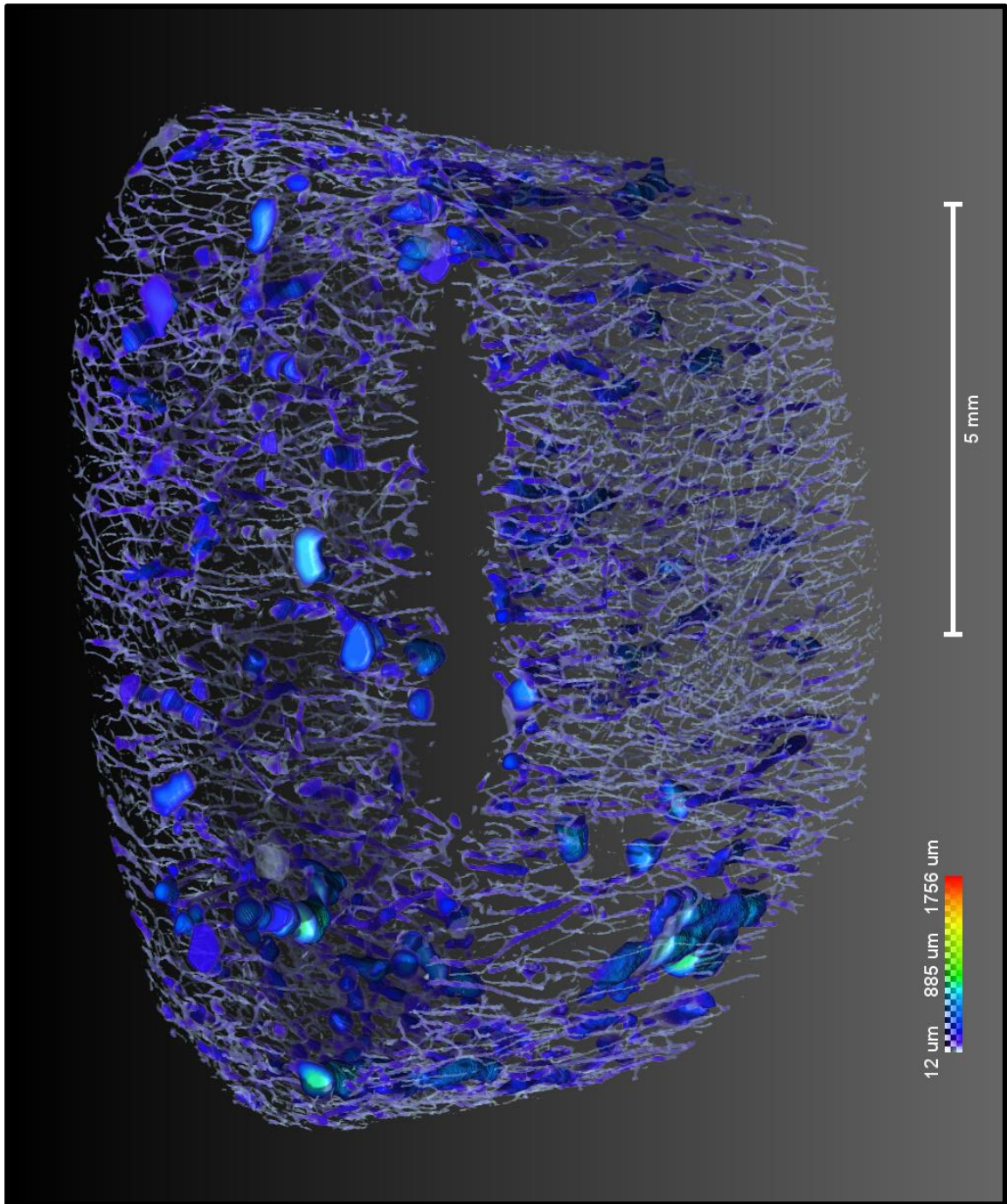
70F Vertebral Top and Side View

579

580
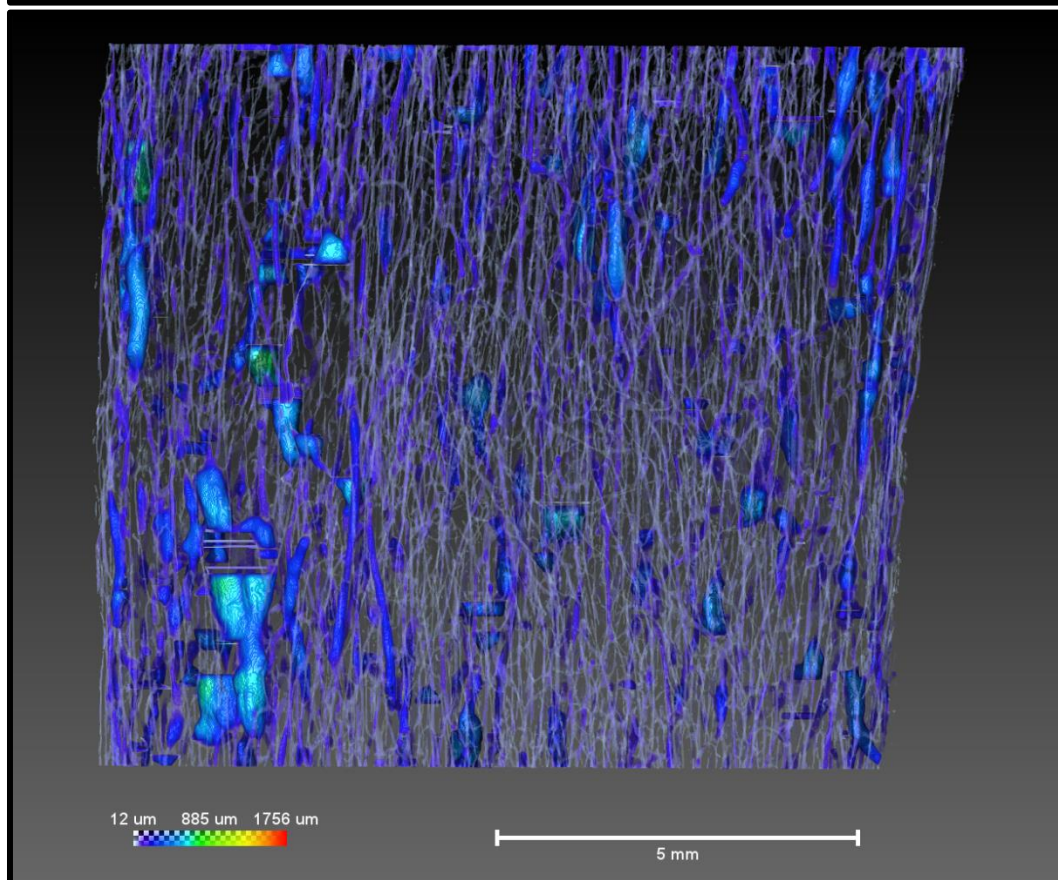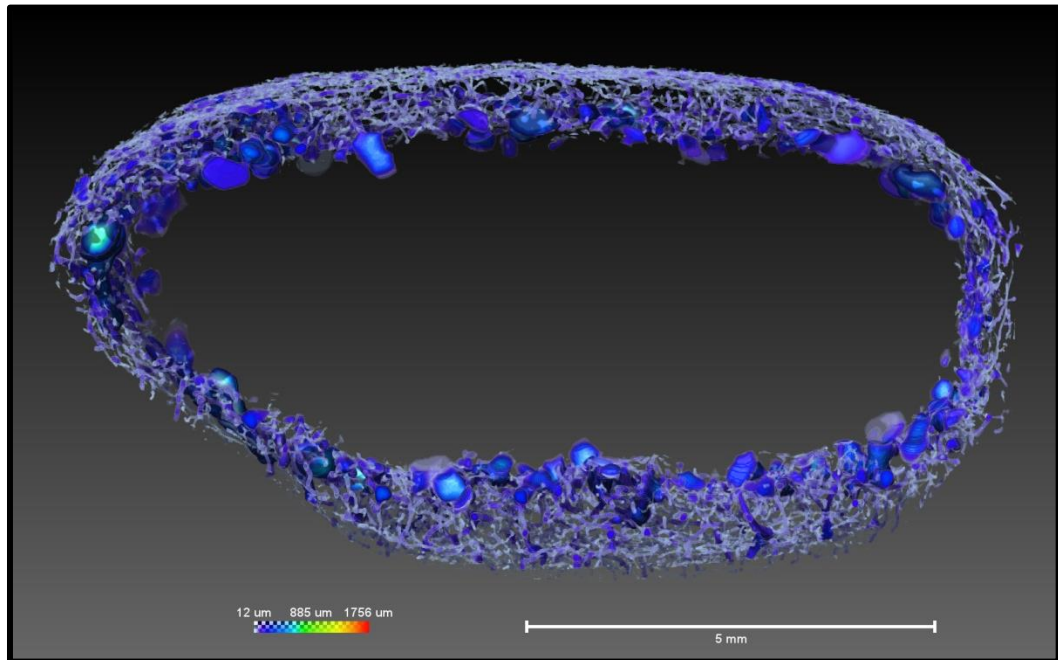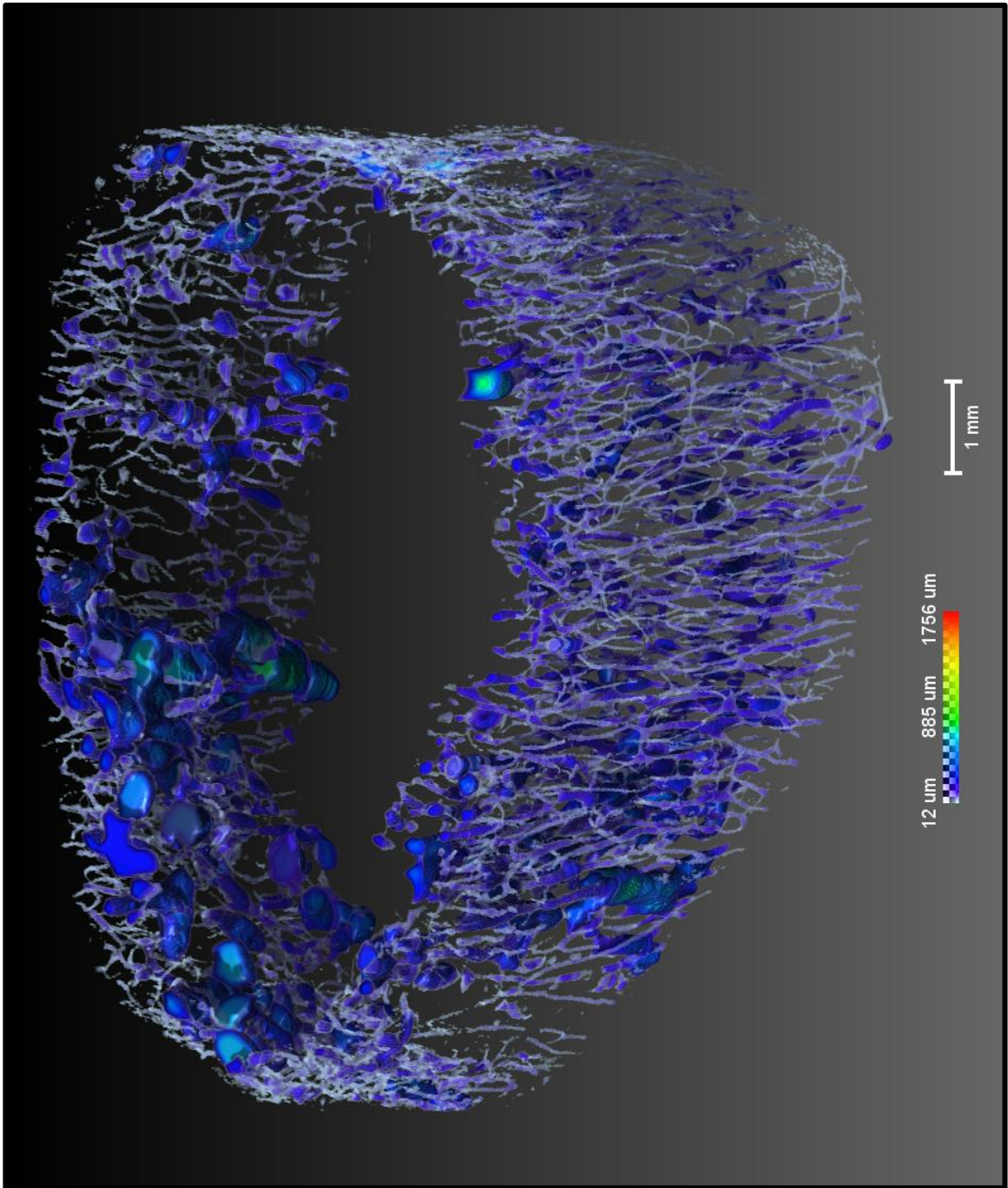
77M Vertebral Top and Side View

581
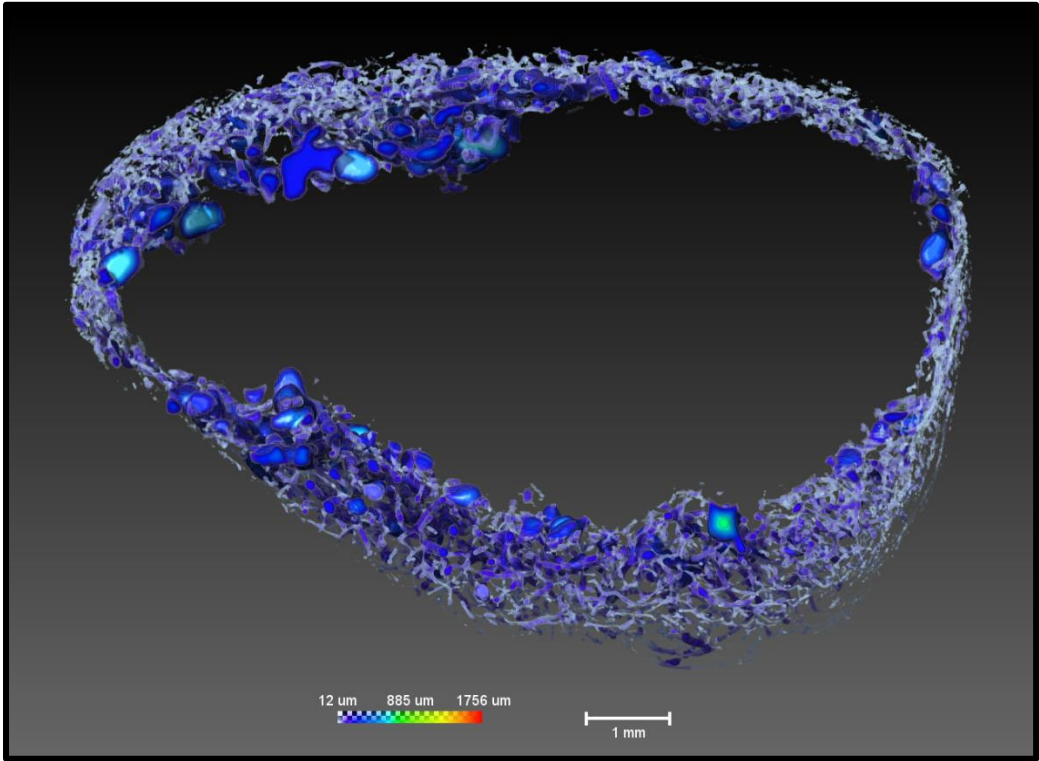
82F Vertebral Tilt View

582
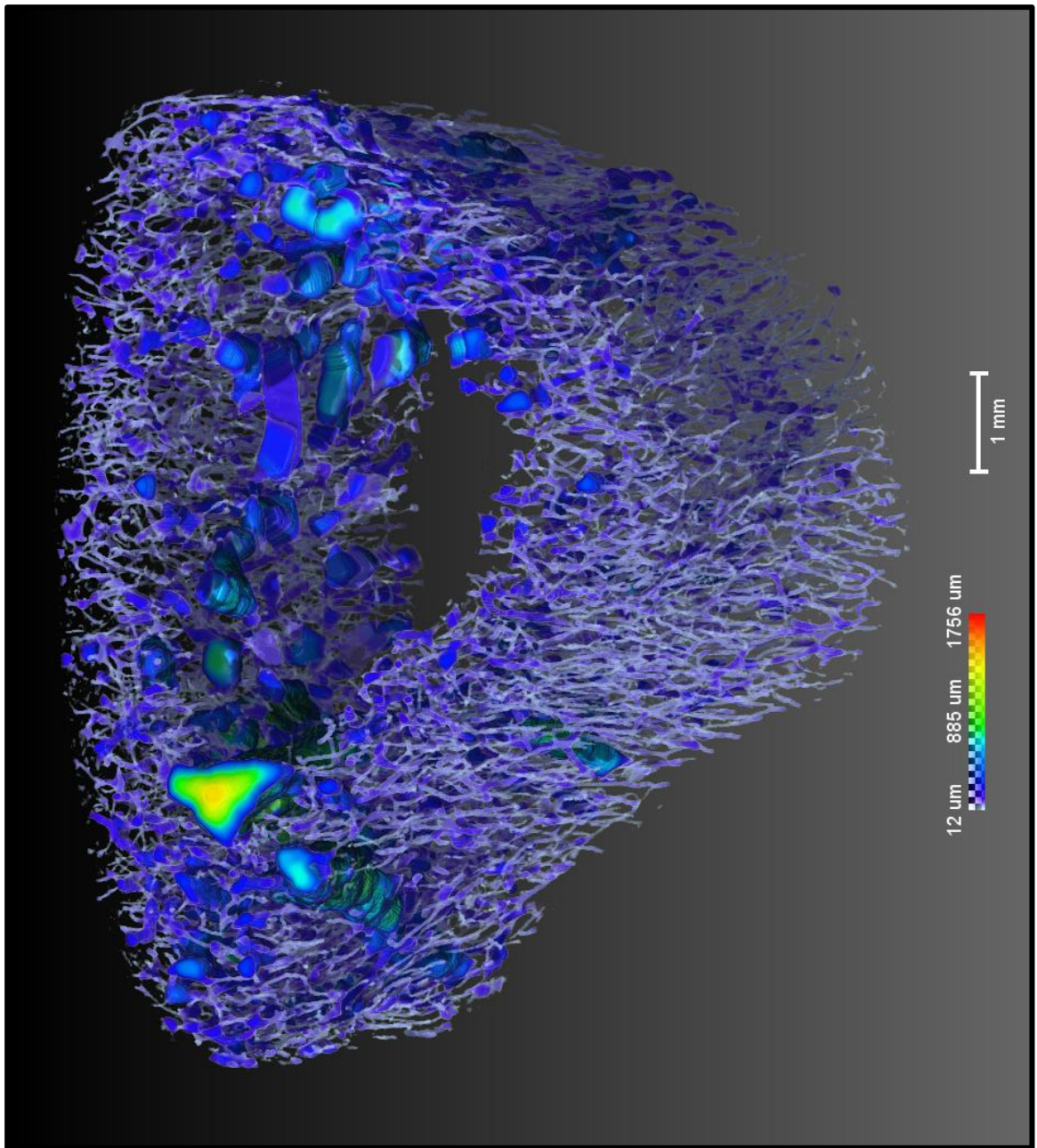
82F Vertebral Top and Side View

583

88M Vertebral Top and Side View

585